Leveraging Molecular Nanoclusters for Atomistic Insights into Reactive Interfaces

Benjamin S. Mitchell

A dissertation

submitted in partial fulfillment of the

requirements for the degree of

Doctor of Philosophy

University of Washington

2023

Reading Committee:

Alexandra Velian, Chair

Brandi Cossairt

Dianne Xiao

Program Authorized to Offer Degree:

Chemistry

University of Washington

Abstract

Leveraging Molecular Nanoclusters for Atomistic Insights into Reactive Interfaces

Benjamin S. Mitchell

Chair of the Supervisory Committee:
Alexandra Velian
Chemistry

Tuning metal/support interactions represents a powerful strategy to modulate catalytic activity, making supported single-site catalysts that harness these effects an active frontier of research. However, probing the complex interactions that occur at a heterogenous interface is a challenge and generally relies on surface imaging techniques which provide limited insight into the dynamic physiochemical processes that govern catalysis. To this end, we developed two classes of atomically precise nanoclusters which feature either three active sites, or one active site, in direct contact with a metal chalcogenide cluster support. In addition to facile synthetic tunability, these clusters are amenable to molecular characterization techniques which facilitate the systematic study of the electronic and structural changes that occur as the number and identity of the edge metal changes.

In the first part of this dissertation, the tri-edge cluster construct is probed, ultimately illustrating how judicial choice of edge identity can be used to tune the electronic structure of the nanocluster construct. Subsequent studies with this system elucidate multi-site communication of the edge sites, manifesting as allosteric ligand binding on the cluster surface. Harnessing this allostericity affords the tri-M cluster as a stimuli responsive nanoblock, which enabled the dimensional control of nanomaterial assembly.

In the second part of this dissertation, a single-edge cluster is presented, which circumvents the complexity of the multi-active site dynamics and allows for systematic study of the electronic and structural changes that occur as the identity of the edge metal changes and how that affects catalytic nitrene transfer reactivity. This study finds, that as the degree of electronic interaction between the edge and the support increases a cooperative regime is reached wherein the support can deliver electrons to the catalytic site, increasing the reactivity of key metal-nitrenoid intermediates. Subsequently, in depth interrogation of the Fe single-edge cluster illustrates the edge-support cooperativity upon inner- and outer-sphere oxidation reactions showcasing the redox flexibility of system. Ultimately, the catalytic properties of the tri-M and mono-M clusters are compared illustrating how the metal-support interactions in the two platforms regulate substrate binding and catalytic activity. The last chapter of this dissertation steps away from cluster chemistry and explores a simple organometallic construct and the effects of ligand binding and its reactivity with oxygen and oxo-atom donors. In total, this work presents a thorough analysis of how cluster supported active sites can be manipulated to enable atomistic insights into electronic and structural metal-support interactions.

TABLE OF CONTENTS

LIST OF FIGURES

LIST OF TABLES

LIST OF SCHEMES

ACKNOWLEDGEMENTS

This journey would not have been possible without the village that has supported me throughout these past five years. Firstly, I would like to thank Alexandra. From the very first day of graduate school to the very last, her excitement and passion about chemistry has propelled me to keep exploring. She has pushed me to be the best chemist I can be, and certainly I would not be where I am today without her guidance and mentorship. Her attention to detail and commitment to accurate and thorough scientific communication is woven throughout our work together and it is something that I cherish and will take with me to all my next adventures.

I would also like to thank my committee members, Prof. Cossairt, Prof. Xiao, and Prof. Kovacs. I am so honored to be a member of this department and it is because of you that we have such an open and collaborative environment here at UW. Your insights throughout the years on my exam committees have been incredibly helpful and your support gave me confidence during challenging times during my PhD.

I would like to thank Prof. Adam Johnson and Prof. Nancy Williams, who showed me the power of d-orbitals. Your commitment to education and mentorship made Claremont the perfect place to take my first steps as an inorganic chemist. I always look forward to seeing you at conferences and I can't wait to cross paths again and reiterate how influential you both have been in my professional and personal development.

To The Villains. Thank you for all the amazing memories and for all your insightful and inspiring conversations about chemistry. Andrei Chirila started the mono-metallated project, and his determination and ingenuity set the foundation for very fruitful research direction which I have been proud to carry on. Sebastian Krajewski is a chemistry encyclopedia and I loved chatting about baseball and science with him. Rob Love might be the greatest human I have ever met and is a ray of positivity in our lab. Daniel Zhou is an amazing office mate, and I am looking forward to beating him next year in fantasy football. Although I am better at basketball than him, Andrei Draguicevic is a great friend and I have loved our conversations about sports, life, and sometimes even chemistry. It has been one of the greatest honors of my PhD to mentor Kelsey Zimmerman, a

stellar undergraduate student who reignited my love for chemistry. She is going to do amazing things and I can't wait to see how her last year of undergraduate research goes, and what graduate program is lucky enough to recruit her. Andrew Boggiano, Mike Riehs, Ella Spurlock, Christine Chang, Yuka Sakazaki, Dan Tofan, Jiaying Yang, Camille Johnson, Steven Yu, David Hales, Catherine Romero, Isabel Friedrichs, and Edwin Lee have been amazing lab mates and I am thankful to all of them for making my time at UW filled with learning and laughter.

Since day one, Jon Kephart and Kendahl Walz Mitra have been by my side for every step of this journey. They have both been incredible lab mates and friends. I am eager to see all the amazing things they accomplish, and I can't wait for a Velian Group reunion in a couple years for us to sit down and reminisce about the highs and lows of grad school, coffee breaks at the Life Sciences Building, and of course Big Time.

I want to thank my amazing friends who have made my time in Seattle so special. I have had so many great meals and conversations with Milo Suvira and Noah Porter and every time we get together, I learn something new. I will cherish my conversations with Leo Porter-Zasada which have ranged from existential analyses of life, deep dish pizza, and the magical dark art of single crystal growth. Tavish Towner is a close friend from college and was a great roommate during my time in Seattle. He kept me sane during the COVID lockdowns and showed me how great life outside of the lab can be. Louise Guard is the Velian Group guardian angel, and she has been an amazing friend and mentor during graduate school. Ryan Allsop is an incredible friend and the best disc golf partner in the world.

There was a clear inflection point during my time in Seattle, and it all stems from meeting Natalie. I am eternally grateful for UW because it brought me to her. Your love and support have been integral during this journey, and I do not take it for granted for even one second. I love the life we have built together, and I can't wait for our next adventures. Thank you for being the best partner I could ask for. One of the many benefits of meeting Natalie has been becoming a member of her incredible family who have provided me with so much love and support throughout the years.

Lastly, I would not be here today without my family. Sam, I am so proud of you. I admire your fun-loving spirit, passion for literally anything (usually the thing that is in front of you in that moment), and how you know a little bit about everything. You are my best friend, and I can't wait to keep eating food and exploring the world together. Ruby and Danny, my second set of parents,

thank you for your support and fostering all of my crazy hobbies and interests. I will always remember building rockets in your garage, staying up late watching movies, and early morning fishing expeditions. And finally, Mom and Dad. You have given me every opportunity to succeed in my life. The way you explained the world to me gave me a perspective only two chemists could give a child. You gifted me with an appreciation for the physical world and a passion for asking questions and learning. There have been so many challenging days these past 5 years and having you in my corner is why I am able to submit this dissertation. I love you so much and thank you for everything you have done for Sam and me.

“Taking on a challenge is a lot like riding a horse, isn’t it? If you are comfortable while doing it you are probably doing it wrong.”

-Ted Lasso

This work is dedicated to my parents.

Chapter 1. TUNING THE ELECTRONIC STRUCTURE OF ATOMICALLY PRECISE SN/CO/SE NANOCLUSTERS VIA REDOX-MATCHING OF TIN(IV) SURFACE SITES

1.1 ABSTRACT

A new strategy is reported to tailor the electronic properties of a superatomic metal chalcogenide cluster by redox-matching the cluster core with surface Sn(IV) sites. Two ternary clusters $(SnR_2)_3Co_6Se_8L_6$ (R = Me, ^{n}Bu) are synthesized by salt metathesis from the hexalithiated salt $[Li_2(py)_2]_3Co_6Se_8L_6$ and R_2SnCl_2. Cyclic and differential pulse voltammetry studies reveal that the tristannylated clusters feature two new, near-degenerate, electronic states within the HOMO–LUMO gap of Co_6Se_8 core, that are attributed to the reduction of a surface tin site. Single crystal X-ray diffraction analysis reveals no Sn...Se coordination is present in the solid-state. The single crystal X-ray structure of the hexalithiated salt starting material is reported for the THF adduct variant $[Li_2(THF)_2]_6Co_6Se_8L_6$.

1.2 INTRODUCTION

Chevrel-type molecular clusters $M_6Ch_8L_6$ (M = Cr, Co, Re, Mo; Ch = S, Se, Te; L = organic ligand) have resurfaced in recent years as potent building blocks for hierarchical nanomaterials.[1–4] Highly symmetrical and chemically robust with rich electronic and magnetic properties, these clusters have attractive "superatomic" qualities, promising access to atomically precise materials with programmable functions. While their chemical stability enables these superatomic clusters to retain structural identity with minimal entropic changes upon assembly or redox manipulations, their large HOMO–LUMO gaps limit pathways to couple them and form electronic bands.

Reproduced in part with permission from:
Mitchell, B. S.; Kaminsky, W.; Velian, A. *Inorg. Chem.* **2021**, *60* (9), 6135–6139.

Strategies to tune their electronic properties have primarily focused on the nature of the capping ligands, but these have had limited impact.[5–7] Surface functionalization with energy-matched metals has been a successful strategy to tune the electronic structure of wide-band semiconductors.[8] Inspired by this approach, our group previously demonstrated that coordination of metals (M = Fe, Co, Zn) to the exposed chalcogens of Co_6Se_8 clusters is an effective strategy to narrow their HOMO–LUMO gaps (Figure 2b), while engendering catalytic activity[9,10] or directing their assembly into van der Waals 2D superatomic crystals.[4] Although the M–Se interaction is effective at stabilizing the LUMO level, the surface metals explored thus far did not introduce any new electronic states near the Co_6Se_8-localized frontier orbitals. Upon evaluating the reduction potentials of possible surface site metal candidates, tin stands out with a +4/+2 redox couple that is energetically matched with the band gap of the Co_6Se_8 cluster, and the attractive possibility of introducing two closely spaced low-lying electronic states near the frontier orbitals.

The relative instability of the +3 valence state, or "valence skipping", is a defining feature of tin chemistry that could also serve the goal of introducing multi-electron states near the frontier orbitals of the Co_6Se_8 cluster. In inorganic materials (e.g. InTe, SnAs, $Ag_{1-x}Sn_{1+x}Se_2$), this advantageous local electron pairing has attracted a lot of attention as it might be responsible for superconductivity, charge density waves, and other interesting solid-state physical phenomena.[11–14] While the redox properties, or valence skipping, in atomically precise tin chalcogenide clusters has been largely unexplored,[15] examples of mixed-valent, and Sn^{3+}–containing clusters have been reported.[16–18] Monometallic organotin complexes ($Sn^{IV}R_yX_{y-4}$; R = alkyl or aryl, X = halide) are known to undergo direduction to Sn^{2+} species via two closely spaced single electron transfer events, generally observed between *ca.* –1.1 to –1.6 V versus $Fc^{0/+}$ (Fc = ferrocene),[19–22] which lies within the HOMO–LUMO gap of the Co_6Se_8 cluster. Interestingly, bisalkyl tin fragments have been used extensively in cluster chemistry as cationic linkers to polyoxometallate anions, however their Sn^{4+}/Sn^{2+} reduction could not be observed in these otherwise redox-active systems.[23–26] Here we report that surface functionalization with dialkyl tin units introduces two energy accessible and closely spaced states within the band gap of the Co_6Se_8 cluster, demonstrating a new strategy to tune the electronic properties of this superatomic metal chalcogenide cluster.

1.3 SYNTHESIS AND STRUCTURAL CHARACTERIZATION

Our group has introduced the $Co_6Se_8L^H_6$ (**1**-H_6; L^H = $Ph_2PN(H)Tol$; Tol = 4-tolyl) cluster as an unusual metalloligand with three coordination sites on its surface. The synthetic protocol to access trimetallated $M_3Co_6Se_8L_6$ (**1**-M_3) clusters relies on $[Li_2(py)_2]_3Co_6Se_8L_6$ (**1**-$[Li_2(py)_2]_3$; py = pyridine) as a starting material.[9] Surprisingly stable to isolation, and with seemingly indefinite shelf-life, this formally hexa-anionic salt garnered special interest as its structure would shine light on how a single Co_6Se_8 cluster might accommodate six metals on its surface. In here, we found that simply exchanging the pyridine for tetrahydrofuran (THF) enabled the isolation of **1**-$[Li_2(THF)_2]_3$, which could be characterized by single crystal X-ray diffraction (Scheme 1.1, Figure 1.1a). Each pair of lithium ions, locked in a Li_2N_2 diamond core and anchored to the cluster via the two amides, is positioned directly above the two exposed selenium atoms, delineating a total of three $[LiNPSeCo]_2$ cages that extend the inorganic Co_6Se_8 core (Figure 1.1a). The multi-cage structure of this salt demonstrates the remarkable versatility of the $Co_6Se_8L_6$ metalloligand and raises interesting possibilities for how it might accommodate in this fashion other, more chemically versatile, metals.

To synthesize the tri-Sn derivatives, $(SnR_2)_3Co_6Se_8L_6$ (**1**-$(SnR_2)_3$; R = Me or ^{n}Bu), **1**-$[Li_2(py)_2]_3$ was treated with the respective R_2SnCl_2 (Scheme 1.1). Following a solvent workup to remove LiCl, **1**-$(SnR_2)_3$ was isolated pure as a dark-red solid (Me: 33%; ^{n}Bu: 56%). Multinuclear NMR analysis indicates that in solution **1**-$(SnR_2)_3$ are highly symmetrical, displaying single environments for the amidophosphines and SnR_2. Single broad peaks are observed by ^{31}P NMR

Scheme 1.1. Synthesis of **1**-$(SnR_2)_3$ clusters.

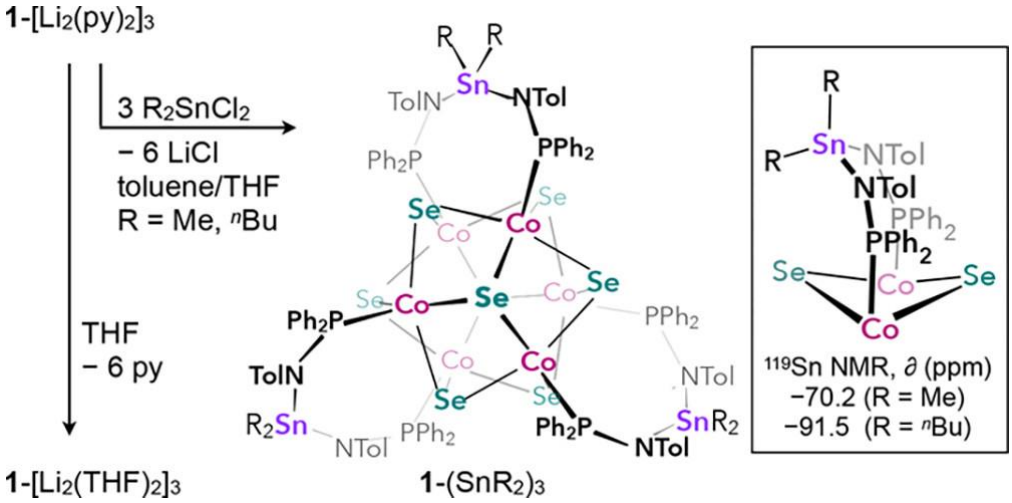

spectroscopy at +114.0 ($\nu_{1/2}$ = 303 Hz) and +115.3 ($\nu_{1/2}$ = 281 Hz) ppm for **1**-$(SnMe_2)_3$ and **1**-$(Sn^nBu_2)_3$, respectively, shifted downfield from +80.7 ppm for **1**-$[Li_2(py)_2]_3$. While not discernible in **1**-$(Sn^nBu_2)_3$, $^{117/119}$Sn satellites flank the ^{1}H NMR methyl resonance of **1**-$(Sn\mathit{Me}_2)_3$, with a coupling constant of 55 Hz.

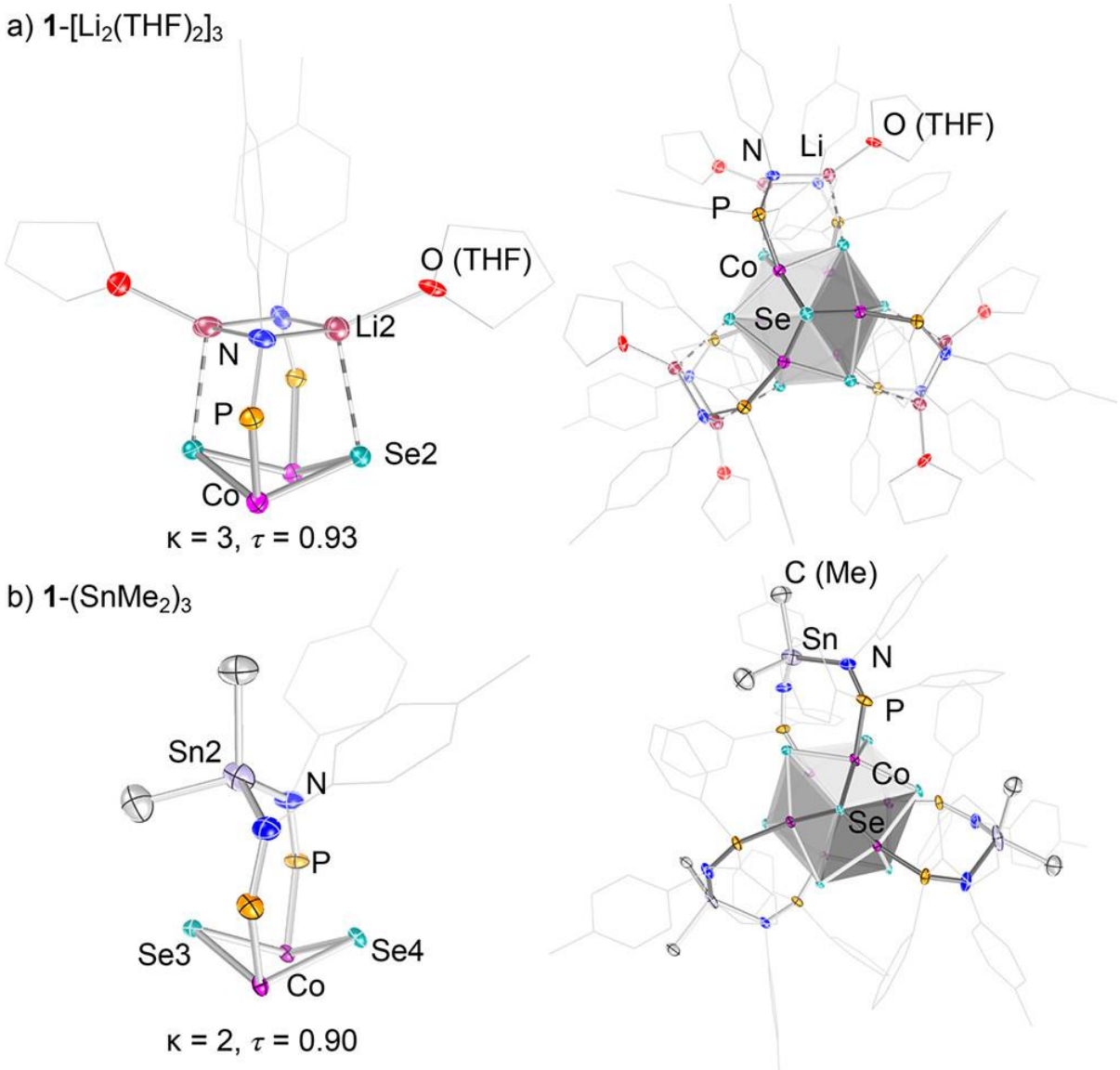

Figure 1.1. Solid-state structure of a) **1**-$[Li_2(THF)_2]_3$ and b) **1**-$(SnMe_2)_3$. Hydrogen atoms, co-crystallized solvent molecules, and disorder are omitted for clarity. Thermal ellipsoids are plotted at 50%.

With a wide NMR spectral window spanning from ca. +4000 to −2500 ppm, the chemical shift of the ^{119}Sn nucleus is a potent reporter on the chemical environment of the tin center.[27] For example, tetracoordinate Sn(IV) bisamide bisalkyl complexes display ^{119}Sn chemical shifts between −10 and +60 ppm,[28–30] while pentacoordinate Sn(IV) complexes feature signals at increasingly upfield values that empirically correlate with the strength of the interaction between the tin and the fifth ligand.[31–35] In solution, the three equivalent tin centers of **1**-$(SnR_2)_3$ each display a single resonance, at −70.2 ($\nu_{1/2}$ = 191 Hz) ppm for the methyl derivative, and at −91.5 ($\nu_{1/2}$ = 210 Hz) ppm for the *n*-butyl. While these upfield ^{119}Sn NMR chemical shifts suggests that a weak Se...Sn donor–acceptor interaction might occur in solution transiently, the solid-state structural data shows no formal coordination of a fifth Se ligand, as discussed below. Of all the surface functionalized Co_6Se_8 clusters reported thus far, including with Fe,[9,10] Co,[4] Zn[10] or Li, **1**-$(SnMe_2)_3$ is the only one in which the surface metal does not coordinate to the exposed Se, even as five and six-coordinate organometallic tin(IV) is ubiquitous.[36]

In contrast to the rigid and highly chelated structure of **1**-$[Li_2(THF)_2]_3$, metallation with Sn forms three flexible Sn/N/P/Co/Se macrocycles with the cluster surface (Figure 1.1b). In the solid-state, the Me_2Sn units of **1**-$(SnMe_2)_3$ are no longer equivalent as they appear in solution by NMR, but instead are locked in asymmetric orientations. Each Sn site leans toward one of the exposed Se, giving rise to one short and one long Sn…Se interatomic distance. The shortest Sn…Se contact (avg. 3.20 Å), however, remains significantly longer than 2.62 Å, the average value for a Sn–Se bond in five-coordinate Sn(IV) complexes.[36,37]

Compared to Fe, Co or Zn, the $SnMe_2$ unit is bulkier, causing a notable opening of the Co–P–N angles from 110.6±0.8° in the tri-iron derivative to 119±2°. This distortion is accompanied by a contraction in the average P–N bond distances from 1.69 Å, to 1.55 Å. While the $SnMe_2$ units put strain on the organic ligands (i.e. Ph_2P–N(Tol)), the inorganic Co_6Se_8 core remains virtually unchanged compared to **1**-H_6, forgoing the distortions previously observed upon surface metal (*i.e.* Fe, Co, Zn) coordination.[4,9,10] Indeed, the extent of the distortions in the Co_6Se_8 cluster core are proportional to the strength of the interaction between the surface metal M and the exposed Se. For example, zinc forms weaker bonds with selenium compared to iron, causing less distortion in the cobalt core.[4]

1.4 EFFECTS ON THE ELECTRONIC STRUCTURE

The stannylation is associated with a redshift in the electronic absorption spectrum of **1**-$(SnR_2)_3$ compared to **1**-H_6, and a new shoulder feature at ~680 nm (ε = 6,415 – 6,645 $M^{-1}cm^{-1}$), possibly related to the 503 nm absorption feature in **1**-H_6 (ε = 29,883 $M^{-1}cm^{-1}$;Figure 1.6 and Figure 1.6). This data provides a first indication that tin impacts the frontier orbital transitions, narrowing the HOMO-LUMO gap.

To further investigate how the three redox active Sn^{4+} sites affect the electronic structure of the ternary **1**-$(SnMe_2)_3$ cluster, cyclic and differential pulse voltammetry experiments were performed. Like all Co_6Se_8-based clusters, the tri-tin clusters **1**-$(SnR_2)_3$ reveal rich redox profiles, with six single-electron redox events (Figure 1.2a and Figure 1.8). The more electron rich dialkyl tin units shift the three cluster core-based oxidation events to more cathodic potentials by ca. 200-300 mV compared to the parent ligand (Table 1.1), however, they still closely resemble the electrochemical behavior of **1**-H_6 at anodic potentials.

More interestingly, the electrochemical reduction of **1**-$(SnR_2)_3$ proceeds markedly differently from that of the parent metalloligand **1**-H_6. The HOMO–LUMO gap, approximated electrochemically as the energy difference between the first oxidation and first reduction, contracts significantly from 1.44 eV in **1**-H_6 to 0.77 eV in **1**-$(SnMe_2)_3$ and 0.83 eV in **1**-$(Sn^nBu_2)_3$. Compared to the other one-electron redox events, the first reduction of **1**-$(SnR_2)_3$ features a notably larger area size suggestive of a multi-electron event. Differential pulse voltammetry was employed to better resolve this feature and revealed two closely spaced single-electron reductions (Figure 2a and S12). Considering the data and the literature on Sn^{4+} reduction,[19–22] we attribute the first two reductions of the **1**-$(SnR_2)_3$ clusters to the $Sn^{+4/+3}$ and $Sn^{+3/+2}$ couple, respectively, and only the third reduction (–3/–2) to $[Co_6Se_8]^{-1/0}$.

While tin introduces two new states to the ternary cluster, the lack of significant Sn...Se interactions are expected to result in no stabilization of the LUMO level of the Co_6Se_8 core. Indeed, although all redox events are shifted cathodically compared to **1**-H_6, the HOMO-LUMO gap of the Co/Se core (approximated by the energy difference between $[Co_6Se_8]^{-1/0}$ and $[Co_6Se_8]^{0/+1}$) remains almost constant upon stannylation, with values of 1.44, 1.47, and 1.51 eV for **1**-H_6, **1**-$(SnMe_2)_3$ and **1**-$(Sn^nBu_2)_3$, respectively (Figure 1.2b). In contrast, the HOMO–LUMO gap in **1**-M_3 derivatives becomes more narrow as the strength of the M...Se interaction increases. Notably,

switching the methyl groups in **1**-$(SnMe_2)_3$ with the more electron rich *n*-butyls has the most pronounced effect on the first two reduction events, which shift to more reducing potentials by 60 and 110 mV, respectively, whereas the third reduction attributed to the cobalt core shifts by only 30 mV.

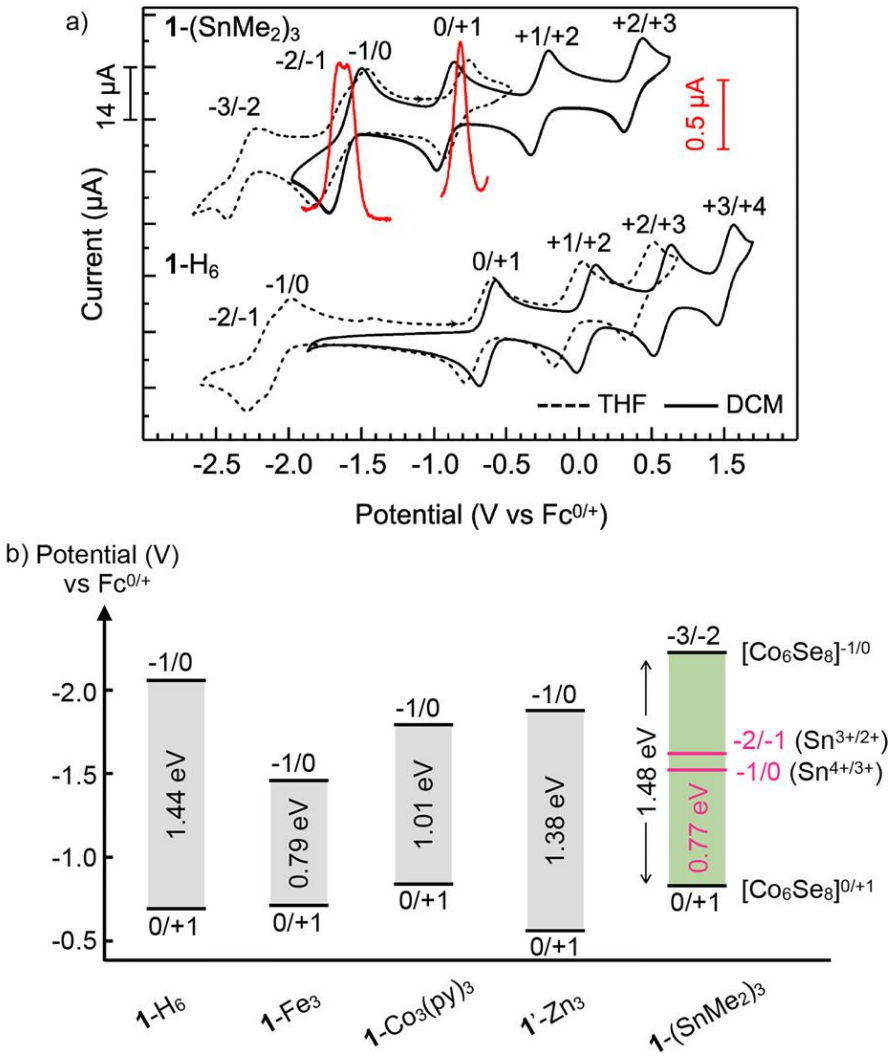

Figure 1.2. a) Cyclic voltammograms of **1**-$(SnMe_2)_3$ and **1**-H_6 recorded in DCM or THF (black), with overlaid differential pulse voltammograms (red, in THF). b) Relative energies of the HOMO (0/+1) and LUMO (–1/0) levels in Co_6Se_8-based clusters: **1**-H_6; **1**-Fe_3; **1**-Co_3; **1**'-Zn_3 ($Zn_3Co_6Se_8(Ph_2PN^iPr)_6$; ^{i}Pr = isopropyl) and **1**-$(SnMe_2)_3$, approximated from electrochemical data. For **1**-$(SnMe_2)_3$, the LUMO, LUMO+1, and LUMO+2 levels are plotted.

The metalloligand **1**-H_6 enforces a cis-orientation of the alkyl groups in the R_2Sn unit, while also providing sufficient flexibility to accommodate the seesaw geometry of a putative Sn(II) center formed upon reduction.[38,39] In contrast to the ubiquitous instances where the alkyl groups are positioned trans to each other, these features of the metalloligand minimize the entropic changes that occur upon reduction of Sn(IV) to Sn(II), positively impacting the reversibility of the process in **1**-$(SnMe_2)_3$.[21,22] However, although the electrochemical direduction attributed to one of the $SnMe_2$ sites is surprisingly well-behaved and quasireversible (Section 0),[40] the chemical reduction of **1**-$(SnMe_2)_3$ using decamethyl cobaltocene or sodium naphthalenide have thus far been unproductive towards conclusively observing or isolating the reduced cluster.

1.5 Conclusions

In conclusion, we introduced a new strategy to tune the electronic properties of a synthetically addressable cobalt chalcogenide cluster by matching the energies of surface-tethered redox-active sites. By judiciously choosing tin, a metal with an intrinsic preference for valence skipping that is redox-matched to the HOMO–LUMO gap of the cobalt cluster core, we deterministically introduce two new energetically accessible electronic states in the ternary cluster **1**-$(SnMe_2)_3$. The sequential direduction of **1**-$(SnMe_2)_3$ poses intriguing questions about the formation and electronic structure of the proposed mixed-valent $Sn^{II}Sn^{IV}Sn^{IV}$ site-differentiated cluster, the further investigation of which could shine light on complex physical phenomena such as valence skipping and two-electron defects in metal chalcogenide materials.

1.6 Synthetic Details and Characterization of Products

1.6.1 *General Experimental Considerations*

All syntheses were conducted under a dinitrogen atmosphere using standard Schlenk or glovebox techniques (LC Technology Solutions glovebox equipped with a freezer set to −35 °C). All glassware was dried at 160 °C for a minimum of 12 h and cooled in an evacuated antechamber prior to use in the glovebox. Solvents were purchased from Fischer Scientific and degassed, dried and purified using solvent purification columns housed in a stainless-steel cabinet and dispensed by a stainless-steel Schlenk line manufactured by JC Meyer Solvent Systems. Tetrahydrofuran (THF), diethyl ether, acetonitrile, and methylene chloride (DCM) are passed through two packed

columns of neutral alumina. In the cases of *n*-pentane and toluene, one of the columns is alumina and the other is Q5 reactant, a copper(II) oxide oxygen scavenger. All solvents were passed through an in-line, 2 μm filter, then stored over activated 3Å molecular sieves in the glovebox for a minimum of 72 h. 3Å molecular sieves were purchased from Sigma Aldrich and activated under vacuum at 300 °C for 48 h. Deuterated solvents (C_6D_6, CD_2Cl_2, CD_3CN) were purchased from Sigma Aldrich and stored over activated 3Å molecular sieves in the glovebox for a minimum of 72 h. Dimethyltin dichloride (98 %) was purchased from Alfa Aesar and used without further purification. Dibutyltin dichloride (96 %) and Naphthalene (99%) were purchased from Sigma Aldrich and used without further purification. Sodium metal (99.9%, cubes in mineral oil) was purchased from Sigma Aldrich and washed thoroughly with *n*-pentane under a nitrogen atmosphere. The aminophosphine $Ph_2PNHTol$ (Ph = phenyl, Tol = 4-tolyl),[41] $Co_6Se_8L^H{}_6$ (**1**-H_6), and $Li_6(py)_6Co_6Se_8L_6$ (**1**-$[Li_2(py)_2]_3$) were prepared according to literature.[9] UV-vis-*n*IR absorption spectra were acquired using a Varian Cary 5000 UV-Vis-*n*IR spectrometer, in *n*IR quartz cuvettes (Spectrocell Inc., 10 mm path length, 220–3500 nm spectral window). NMR spectra were acquired at 25 °C on Bruker 300 MHz or 500 MHz spectrometers. ^{1}H and ^{13}C NMR spectra were referenced to residual deuterated solvent peaks. ^{31}P and ^{119}Sn spectra were externally referenced to phosphoric acid and tetramethyltin, respectively. Electrochemical studies were conducted using a Gamry Interface 1010B potentiostat. Cyclic voltammetry and differential pulse voltammetry were conducted using a three-electrode cell setup with a glassy carbon disk working electrode, a platinum wire counter electrode, and a silver-wire pseudo-reference electrode. All potentials were referenced to the Fc/Fc^+ redox couple by adding a small amount of ferrocene after each measurement. All electrochemical measurements were conducted under a dinitrogen atmosphere, at 25 °C. Samples were prepared for elemental analysis by crushing single crystalline material into a powder and then placed under reduced pressure for 12 h. Co, Se, P elemental analysis was conducted using a PerkinElmer Nexion 2000B inductively-coupled plasma mass spectrometer (ICP-MS). Prior to ICP-MS analysis, samples were digested in neat nitric acid (Fisher Scientific, ICP-MS grade) at 50 °C.

1.7 Synthetic Details and Characterization of Products

1.7.1 *Synthesis of **1**-[Li$_2$(THF)$_2$]$_3$*

Exchange of pyridine with THF. A 100 mL Schlenk flask equipped with a Teflon valve was charged with **1**-[Li$_2$(py)$_2$]$_3$ (2.109 g, 0.650 mmol, 1 equiv) and a Teflon-coated stir bar. THF (70 mL) was added the flask and stirred at 55 °C in an oil bath for 2 h. The volatiles were removed under reduced pressure. This procedure was repeated once. The solids were triturated with diethyl ether (2 x 15 mL) and extracted with toluene (100 mL) through a plug of Celite over a medium-porosity fritted-glass filter. The volatiles were removed under reduced pressure to yield a spectroscopically pure, very dark red powder (1.785 g, 0.557 mmol, 86% yield).

^{1}H NMR (C_6D_6, 700 MHz) δ: 7.93 (t, 12H, *J* = 7.9 Hz, PPh_2 Ar***H***), 7.69 (t, 12H, *J* = 7.9 Hz, PPh_2 Ar***H***), 7.26 (s, 18H, PPh_2 Ar***H***), 7.12 (m, 12H, PPh_2 Ar***H***), 6.95 (m, 6H, PPh_2 Ar***H***), 6.58 (d, 12H, J = 6.8 Hz, tolyl *o*-Ar***H***), 6.34 (d, 12H, *J* = 6.5 Hz, tolyl *m*-Ar***H***), 3.38 (s, 24 H, LiO(C***H$_2$***)$_2$(CH_2)$_2$), 1.98 (s, 18 H, 4-tolyl-C***H$_3$***), 1.38 (s, 24 H, LiO(CH_2)$_2$(C***H$_2$***)$_2$) ppm. **^{31}P NMR** (C_6D_6, 283 MHz) δ: +80.65 ($\nu_{1/2}$ = 478 Hz) ppm. **^{7}Li NMR** (C_6D_6, 272 MHz) δ: +1.12 ($\nu_{1/2}$ = 20.7 Hz) ppm.

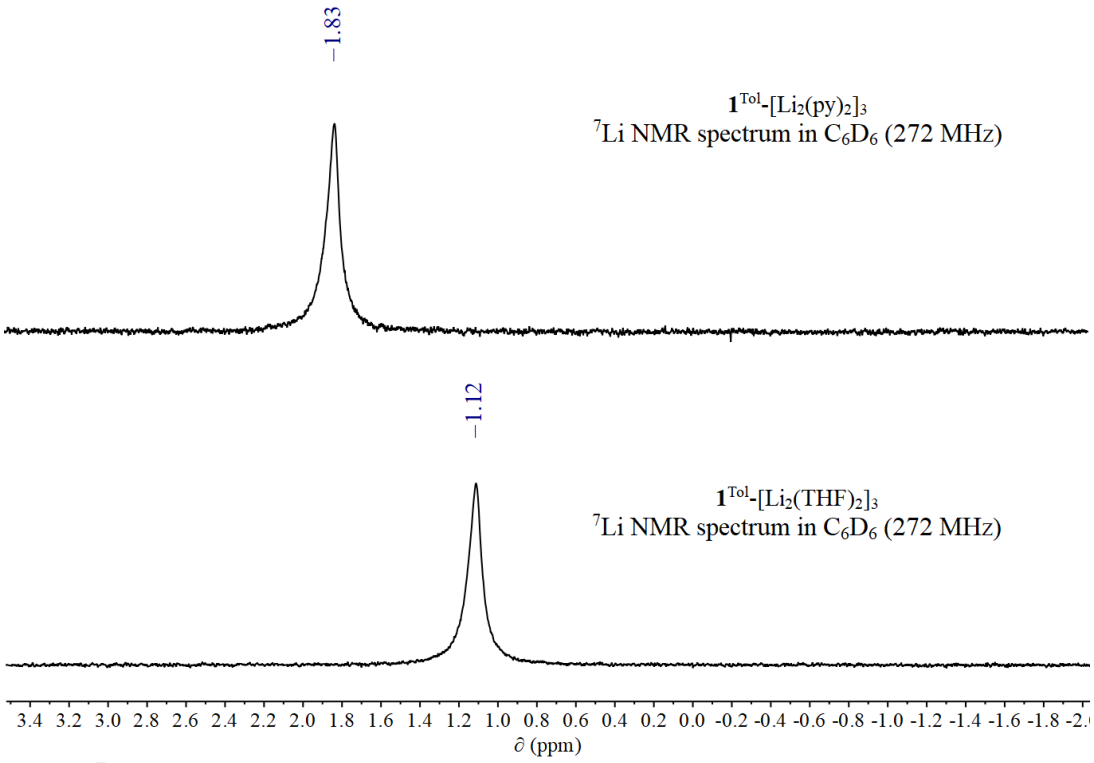

Figure 1.3. ^{7}Li NMR (C_6D_6, 25 °C, 272 MHz) spectra of **1**-[Li$_2$(py)$_2$]$_3$ and **1**-[Li$_2$(THF)$_2$]$_3$.

1.7.2 *Synthesis and Isolation of **1**-$(SnMe_2)_3$*

A 100 mL Teflon valved reaction vessel was charged with **1**-$[Li_2(py)_2]_3$ (1.998 g, 0.616 mmol, 1.0 equiv) and suspended in toluene (50 mL). Solid Me_2SnCl_2 (416.4 mg, 1.909 mmol, 3.1 equiv) was dissolved in THF (5 mL). The suspension of **1**-$[Li_2(py)_2]_3$ was placed in the glovebox coldwell for 20 minutes until the solvent was partially frozen. The reaction vessel was removed from the coldwell and allowed to thaw. Once stirring resumed, the Me_2SnCl_2 solution was added dropwise over the course of 2 minutes. The reaction flask was then degassed, sealed, and removed from the glovebox. The reaction mixture was stirred in a 60 °C oil bath for 20 hours. The volatiles were removed under reduced pressure. The crude solids were triturated with *n*-pentane (3 x 5 mL) and then extracted with toluene (~60 mL) through a plug of Celite over a medium porosity glass fritted filter. The volatiles were removed *in vacuo* to yield a very dark red solid. The solids were dissolved in minimal warm THF, filtered through a plug of Celite, layered with diethyl ether, and stored in the glovebox freezer (–35 °C). After 18 hours, a black (very dark red) precipitate formed and the solids were collected on a fine porosity glass fritted funnel (639 mg, 0.201 mmol, 33% yield). Crystals suitable for single crystal X-ray diffraction were grown via vapor diffusion of *n*-pentane into a saturated solution of THF at room temperature over the course of 7 days.

^{1}H NMR (C_6D_6, 500 MHz) δ: 7.84 - 7.76 (m, 24 H, PPh_2 *o*-Ar***H***), 7.25 (t, 12 H, *J* = 7.0 Hz, PPh_2 *p*-Ar***H***), 7.10 - 7.01 (m, 24 H, PPh_2 *m*-Ar***H***), 6.87 (d, 12 H, *J* = 8.4 Hz, 4-Tolyl *o*-Ar***H***), 6.57 (d, 12 H, *J* = 8.5 Hz, 4-Tolyl *m*-Ar***H***), 1.87 (s, 18 H, 4-Tolyl C***H₃***), 0.10 (s, 18 H, $J_{H\text{-}117/119Sn}$ = 57 Hz, Sn(C***H₃***)$_2$) ppm. **^{1}H NMR** (CD_2Cl_2, 500 MHz) δ: 7.38 (q, 24 H, J = 7.3 Hz, PPh_2 *o*-Ar***H***), 7.23 - 7.15 (m, 24 H, PPh_2 *p*-Ar***H***), 7.03 (t, 12 H, *J* = 7.6 Hz, PPh_2 *p*-Ar***H***), 6.51 (d, 12 H, J = 8.5 Hz, 4-Tolyl *o*-Ar***H***), 6.46 (d, 12 H, J = 8.4 Hz, 4-Tolyl *m*-Ar***H***), 2.06 (s, 18 H, 4-Tolyl C***H₃***), -0.35 (s, 18 H, $J_{H\text{-}117/119Sn}$ = 57 Hz Sn(C***H₃***)$_2$) ppm. **^{13}C NMR** (CD_2Cl_2, 125 MHz) δ: 146.84 (d, *J* = 10.1 Hz, C), 134.11 (d, *J* = 9.2 Hz, CH), 133.15 (s, C), 133.03 (s, CH), 132.95 (s, CH), 131.68 (s, CH), 128.60 (s, CH), 128.44 (s, C), S128.21 (s, CH), 126.97 (d, *J* = 9.2 Hz, CH), 126.63 (d, *J* = 9.2 Hz, CH), 20.8 (s, C-**C**H_3), 8.97 (s, Sn-**C**H_3) ppm. **^{31}P NMR** (C_6D_6, 283 MHz): δ +114.0 ($\nu_{1/2}$ = 303 Hz, $^{117/119}$Sn-P coupling was not resolved) ppm. **^{119}Sn NMR** (C_6D_6, 187 MHz): δ –70.2 ($\nu_{1/2}$ = 191 Hz, $^{117/119}$Sn-P coupling was not resolved) ppm. **Elemental analysis** found (calc.) for **1**-$(SnMe_2)_3$ (Formula: $C_{120}H_{120}Co_6N_6P_6Se_8Sn_3$): Co 11.45 (11.91), Se 19.95 (20.75), P 5.89 (6.13).

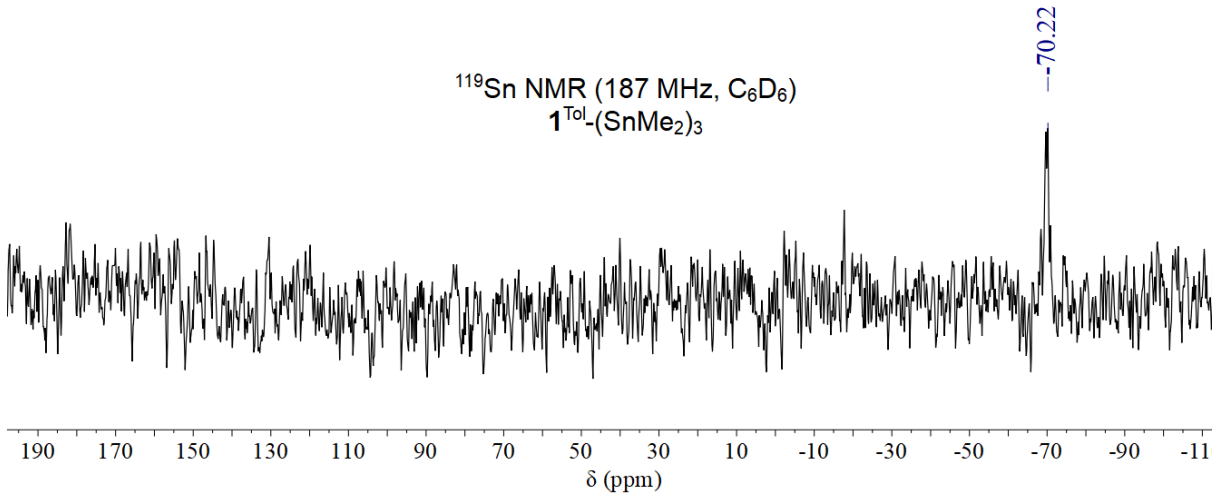

Figure 1.4. ^{119}Sn NMR (C_6D_6, 25 °C, 187 MHz) spectrum of **1**-$(SnMe_2)_3$.

1.7.3 Synthesis and Isolation of $(Sn^nBu_2)_3Co_6Se_8L_6$ - **1**-$(Sn^nBu_2)_3$

A 20 mL scintillation vial was charged with **1**-$[Li_2(py)_2]_3$ (200.0 mg, 0.062 mmol, 1.0 equiv) and suspended in toluene (10 mL). Solid $^nBu_2SnCl_2$ (56 mg, 0.186 mmol, 3.01 equiv) was dissolved in THF (1 mL). The suspension of **1**-$[Li_2(py)_2]_3$ was placed in the glovebox coldwell for 10 minutes until the solvent was partially frozen. The reaction vessel was removed from the coldwell and allowed to thaw. Once stirring resumed, the $^nBu_2SnCl_2$ solution was added dropwise to the vial. The reaction was stirred at 60 °C for 18 hours. The volatiles were removed under reduced pressure. The crude solids were triturated with *n*-pentane (3 x 5 mL) and then extracted with toluene (~10 mL) through a plug of Celite. The volatiles were removed *in vacuo* to yield a very dark red colored solid (119 mg, 0.035 mmol, 56% yield).

^{1}H NMR (C_6D_6, 500 MHz) δ: 7.82 (t, 24 H, *J* = 8.9 Hz, PPh_2 *o*-Ar***H***), 7.26 (m, 12 H, PPh_2 *p*-Ar***H***), 7.10 - 7.01 (m, 24 H, PPh_2 *m*-Ar***H***), 6.96 (d, 12 H, *J* = 7.9 Hz, 4-Tolyl *o*-Ar***H***), 6.62 (d, 12 H, *J* = 8.0 Hz, 4-Tolyl *m*-Ar***H***), 1.95 (s, 18 H, 4-Tolyl C***H₃***), 1.44 – 1.21 (m, 12 H, $Sn(C\boldsymbol{H_2}CH_2CH_2CH_3)_2$), 1.10 – 0.83 (m, 24 H, $Sn(CH_2C\boldsymbol{H_2}C\boldsymbol{H_2}CH_3)_2$), 0.72 (t, 18 H, *J* = 7.3 Hz, $Sn(CH_2CH_2CH_2C\boldsymbol{H_3})_2$) ppm. **^{13}C NMR** ($CD_2Cl_2$, 125 MHz) δ: 146.50 (d, *J* = 9.2 Hz, C), 133.00 (d, *J* = 10.0 Hz, CH), 132.81 (s, C), 131.83 (s, CH), 129.03 (s, CH), 128.59 (s, CH), (s, CH), 128.06 (s, C), 127.97 (s, CH), 127.65 (d, *J* = 10.0 Hz), 126.91 (d, *J* = 8.9 Hz), 126.66 (d, *J* = 9.5 Hz), 28.96 (s), 26.83 (s), 20.80 (s), 13.54 (s) ppm. **^{31}P NMR** (C_6D_6, 202 MHz): δ +115.3 ($\nu_{1/2}$

= 281 Hz, $^{117/119}$Sn-P coupling could not be resolved) ppm. **^{119}Sn NMR** (C_6D_6, 186 MHz): δ –91.5 ($\nu_{1/2}$ = 210 Hz, $^{117/119}$Sn-P coupling could not be resolved) ppm.

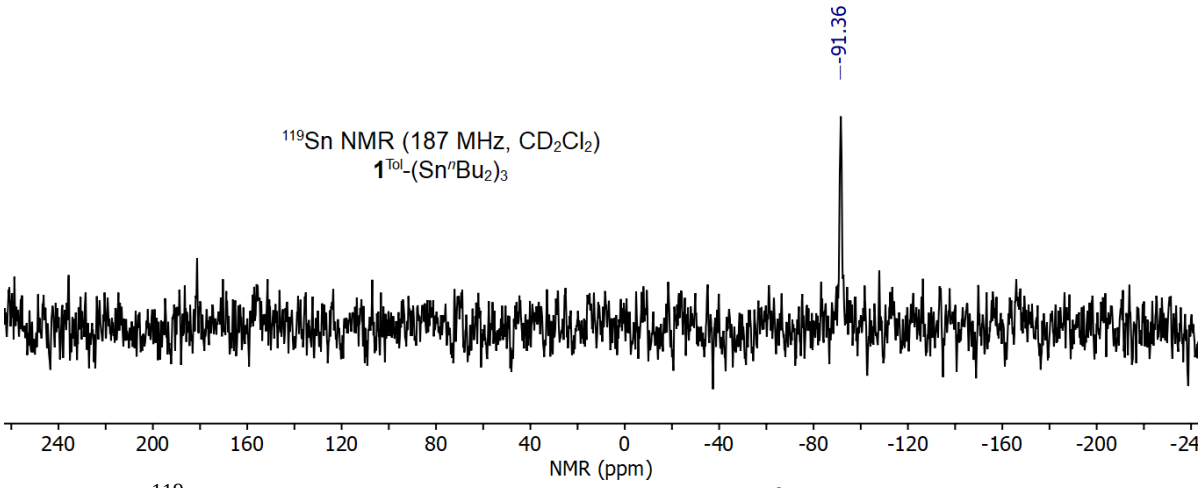

Figure 1.5. ^{119}Sn NMR (C_6D_6, 25 °C, 187 MHz) spectrum of **1**-(Sn^nBu_2)$_3$.

1.7.4 *UV-Vis-nIR Spectroscopy*

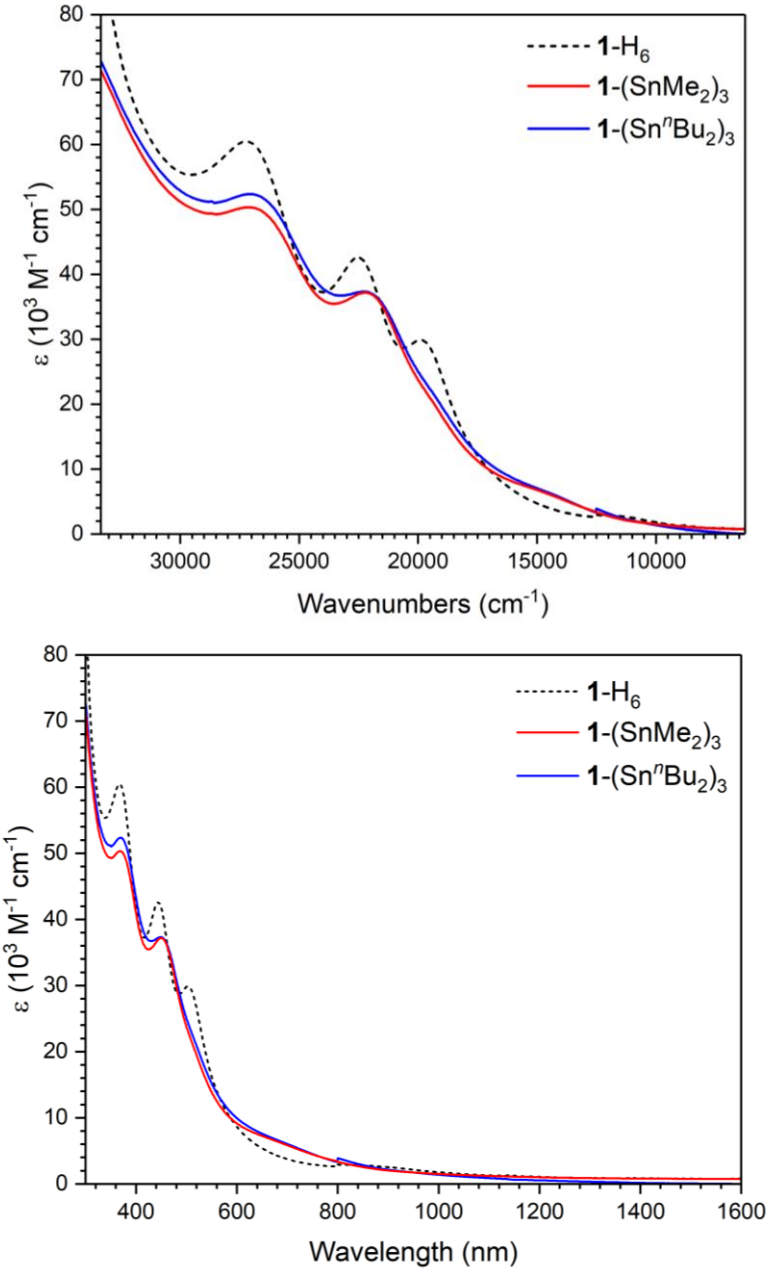

Figure 1.6. UV-Vis-*n*IR absorption spectrum of **1**-H_6, **1**-$(SnMe_2)_3$, and **1**-$(Sn^nBu_2)_3$ in toluene plotted in wavenumbers (top) and wavelength (bottom). The three bands observed in **1**-$(SnMe_2)_3$ are at 368 nm (ε = 50327 $M^{-1}\,cm^{-1}$), 450 nm (ε = 37180 $M^{-1}\,cm^{-1}$), and ~680 nm (ε = 6415 $M^{-1}\,cm^{-1}$). The three bands observed in **1**-$(Sn^nBu_2)_3$ are at 369 nm (ε = 52350 $M^{-1}\,cm^{-1}$), 449 nm (ε = 37325 $M^{-1}\,cm^{-1}$), and ~680 nm (ε = 6645 $M^{-1}\,cm^{-1}$).

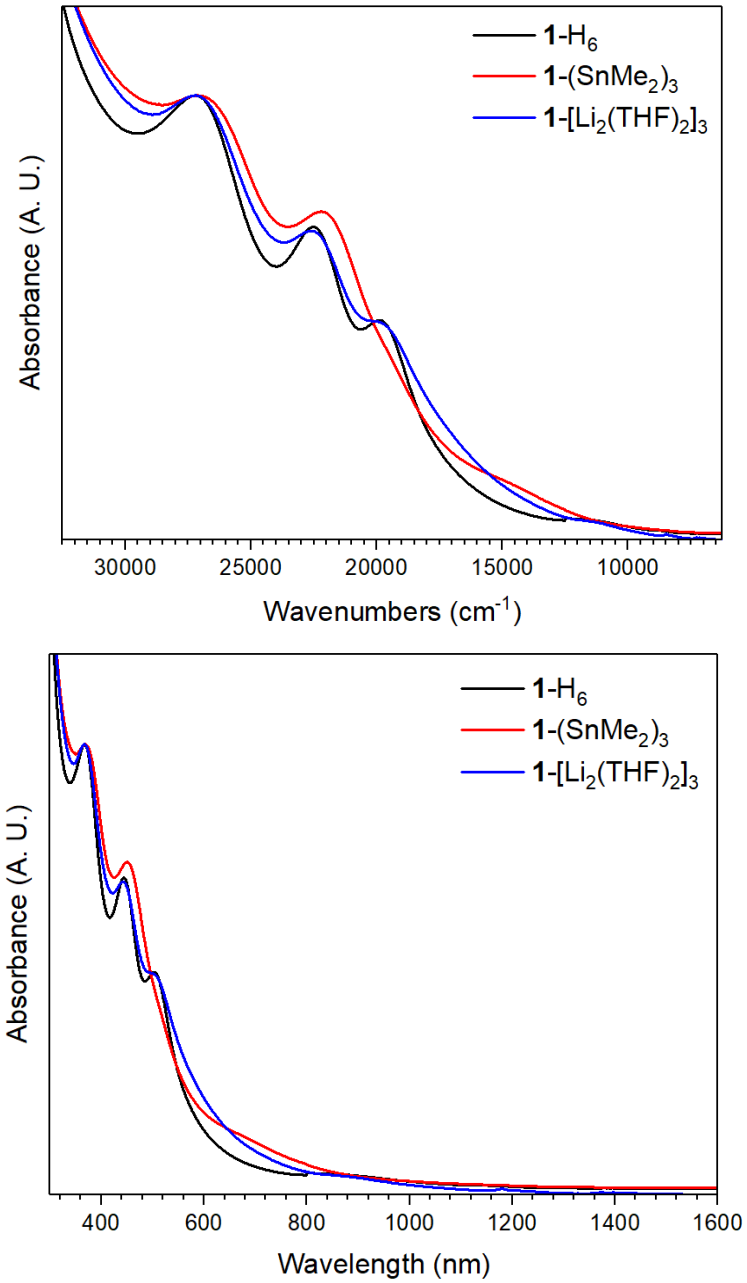

Figure 1.7. Normalized UV-Vis-*n*IR absorption spectrum of **1**-H_6 and **1**-$(SnMe_2)_3$ recorded in toluene and **1**-$[Li_2(THF)_2]_3$ recorded in THF, plotted in wavenumbers (top) and wavelength (bottom). Spectra were normalized to the highest energy peak (368 nm). The absorptivity values (Ɛ) for **1**-H_6, **1**-$(SnMe_2)_3$, and **1**-$[Li_2(THF)_2]_3$ at 368 nm are 60471 $M^{-1}\,cm^{-1}$, 50327 $M^{-1}\,cm^{-1}$, and 40885 $M^{-1}\,cm^{-1}$, respectively.

1.8 ELECTROCHEMISTRY

1.8.1 *Cyclic Voltammetry*

Table 1.1. Redox potentials ($E_{1/2}$) and peak-to-peak separation (ΔE_p) of **1**-H_6, **1**-$(SnMe_2)_3$ and **1**-$(Sn^nBu_2)_3$ at 200 mV/s in 0.1 M solutions of $TBAPF_6$ in DCM (or THF). *Potentials determined by peaks in DPV spectrum.

	$E_{1/2}$ (V vs $Fc^{0/+}$); ΔE_p(mV)		
	1-H_6	**1**-$(SnMe_2)_3$	**1**-$(Sn^nBu_2)_3$
+3/+4	1.01; 110	+2/+3	0.39; 146	0/+1	(–0.85, –0.76*); (205)
+2/+3	0.57 (0.41); 110 (201)	+1/+2	–0.27; 142		
+1/+2	0.05 (–0.08); 131 (201)		–0.92 (–0.84, –0.76*); 107 (155)		
0/+1	–0.63 (–0.69); 110 (191)	0/+1		–1/0	(–1.59*); N/A
		–1/0	(–1.53*); N/A	–2/–1	(–1.70*); N/A
–1/0	(–2.05); (N/A)	–2/–1	(–1.59*); N/A	–3/–2	(–2.36); (234)
–2/–1	(–2.21); (N/A)	–3/–2	(–2.33); (197)		

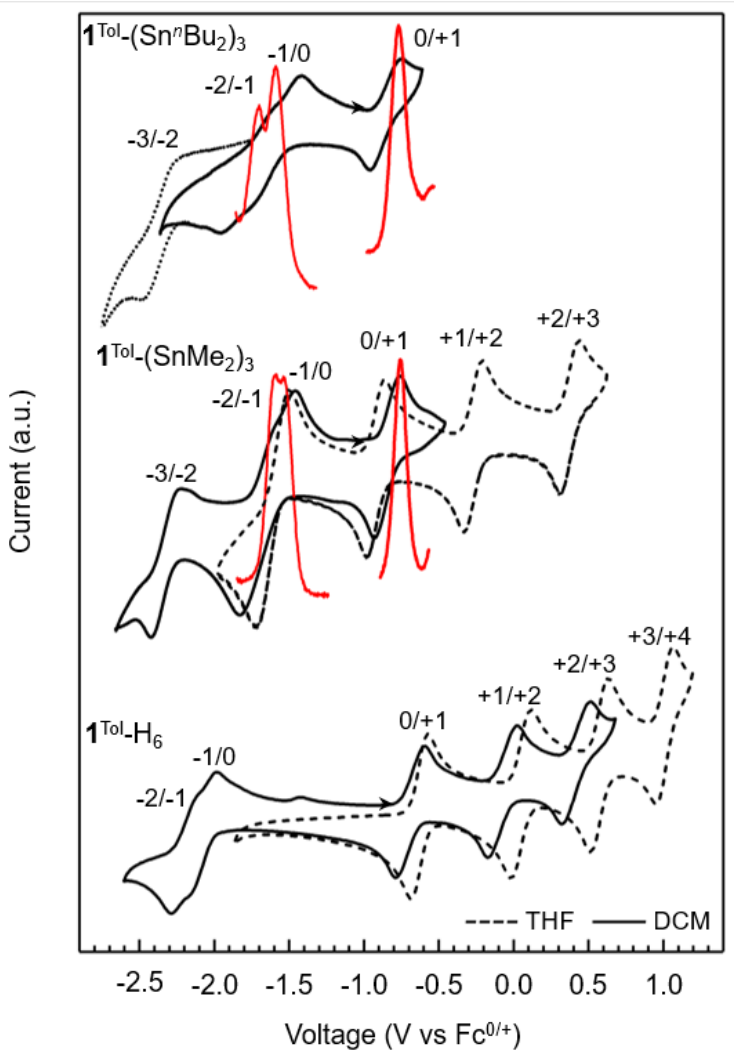

Figure 1.8. Cyclic voltammograms of $\mathbf{1}^{Tol}$-$(SnR_2)_3$ and $\mathbf{1}^{Tol}$-H_6 recorded in DCM (solid) and THF (dashed) solutions with $TBAPF_6$ (0.1 M) at 200 mV/s. Differential pulse voltammogram of $\mathbf{1}^{Tol}$-$(SnR_2)_3$ recorded in THF with $TBAPF_6$ (0.1 M) shown in red. The –3/–2 reduction for $\mathbf{1}^{Tol}$-$(Sn^nBu_2)_3$ is depicted with a dotted line due to the irreversibility of the event.

1.8.2 *Randles-Sevcik Analysis*

Large peak-to-peak separation potentials (ΔE_p) indicate quasi-reversible redox processes. To gauge the chemical reversibility of these electrochemical transformations, cyclic voltammograms were recorded at several scan rates between 50 and 500 mV s^{-1}. For a chemically reversible process, peak anodic and cathodic currents should exhibit a linear dependence on the square root of the scan rate.[42] This is demonstrated by fitting the electrochemical data to the Randles–Sevcik equation:

$$j_p = 269000 n_e^{3/2} D_0^{1/2} C_0 v^{1/2}$$

where j_p is the current density in A/cm^2, n_e is the number of electron equivalents transferred in the redox process, D_0 is the diffusion coefficient in cm^2/s, C_0 is the bulk concentration in mol/cm^3, and v is the potential scan rate in V/s. We found that the peak current densities exhibit a linear dependence on the square root of scan rate for the –3/–2, 0/+1, +1/+2, and +2/+3 events in **1**-$(SnMe_2)_3$.

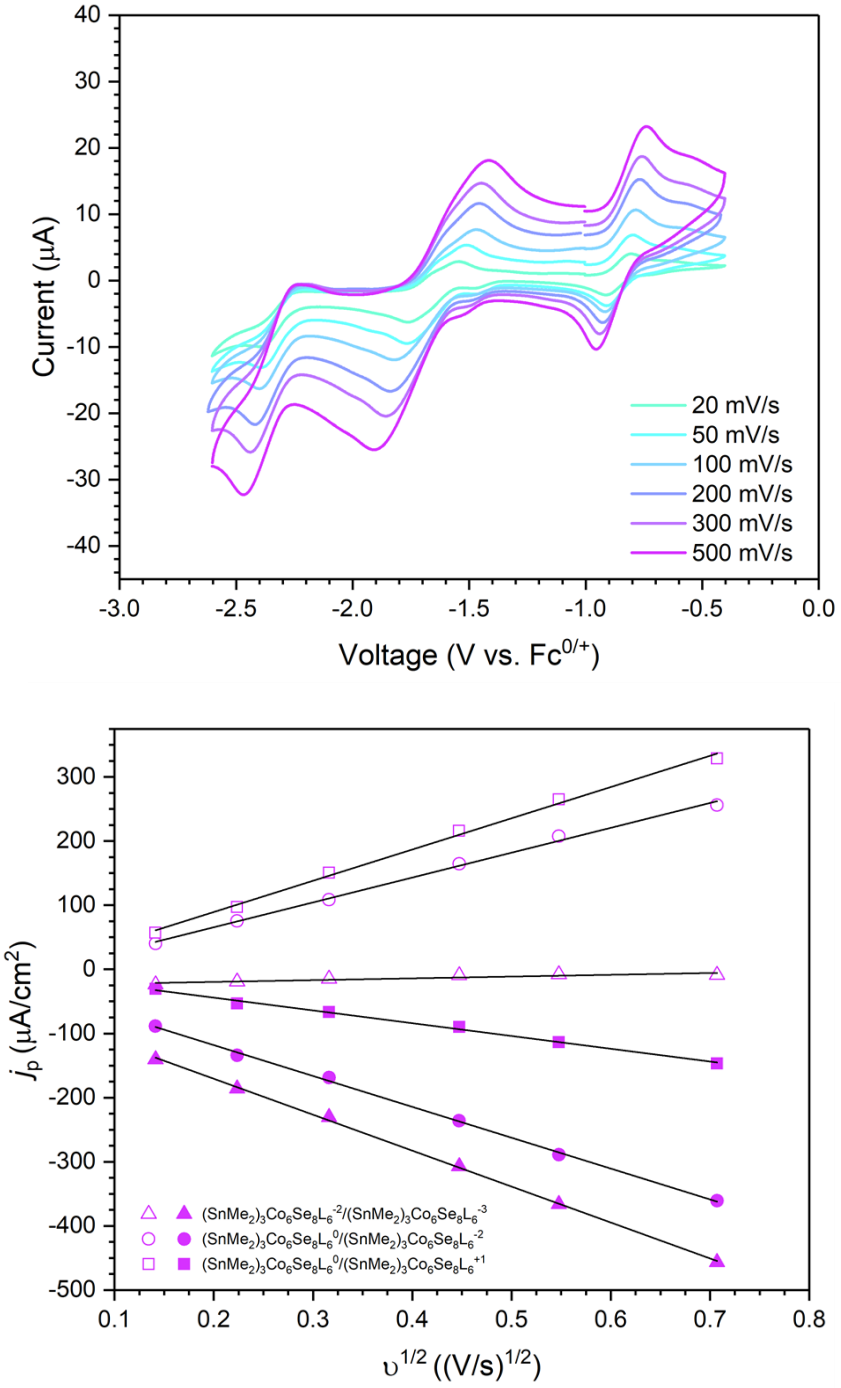

Figure 1.9. Cyclic voltammograms of **1**-$(SnMe_2)_3$ recorded between 20 and 500 mV/s in solutions of 0.1 M $TBAPF_6$ in THF referenced to ferrocene (top) and a plot of current density (j_p) versus the square root of scan rate ($\nu^{1/2}$) with linear fits used to model the data with the Randles-Sevcik equation (bottom).

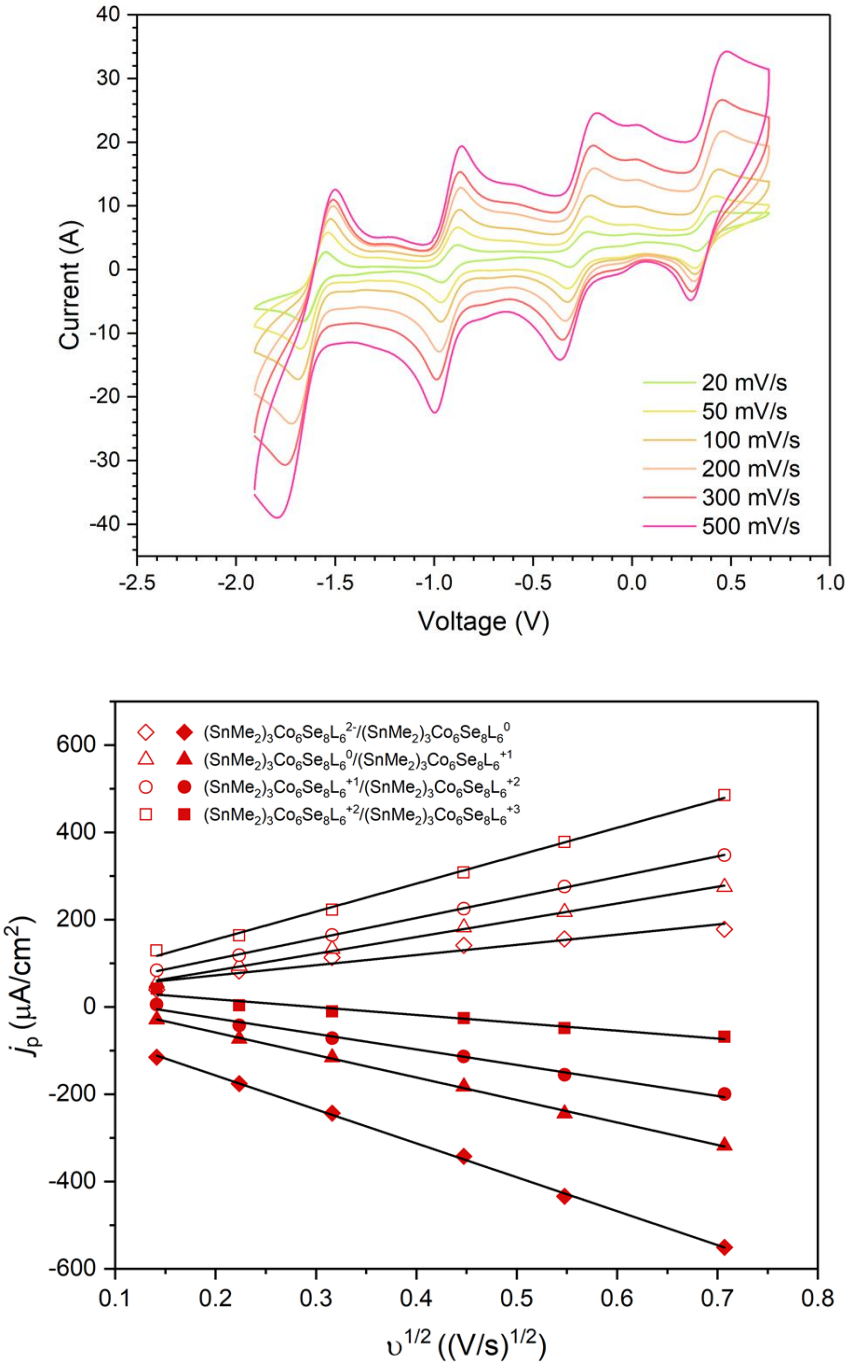

Figure 1.10. Cyclic voltammograms of **1**-$(SnMe_2)_3$ recorded between 20 and 500 mV/s in solutions of 0.1 M $TBAPF_6$ in DCM referenced to ferrocene (top) and a plot of current density (j_p) versus the square root of scan rate ($v^{1/2}$) with linear fits used to model the data with the Randles-Sevcik equation (bottom).

1.8.3 *Differential Pulse Voltammetry*

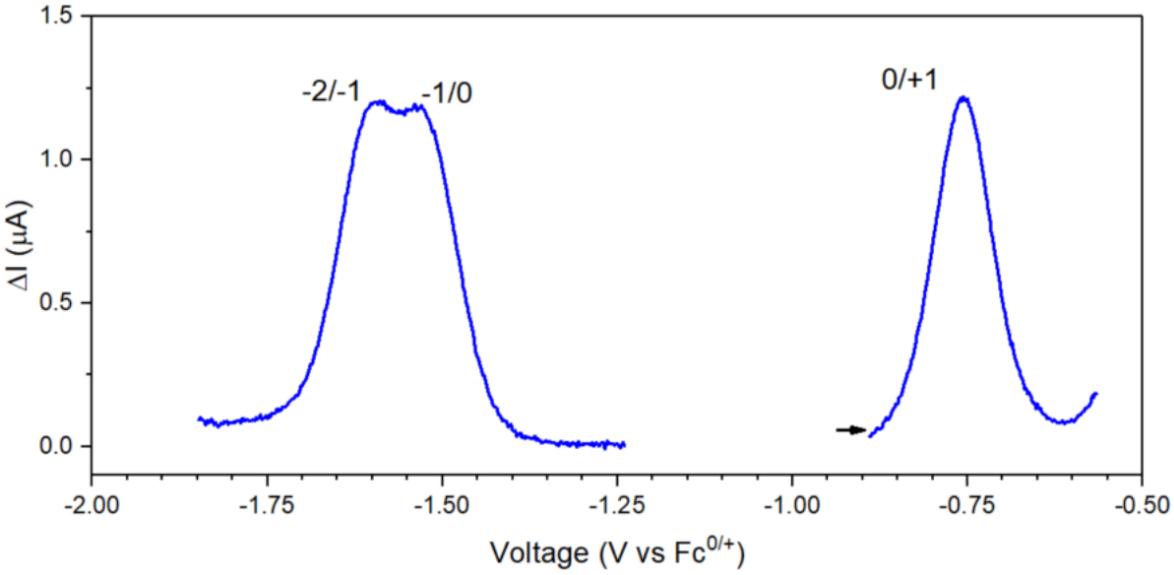

Figure 1.11. Differential pulse voltammogram of **1**-$(SnMe_2)_3$ in 0.1 M $TBAPF_6$ in THF solution. Step size = 2 mV, Pulse amplitude = 25 mV, Sample period = 2 s, Pulse time = 0.5 s.

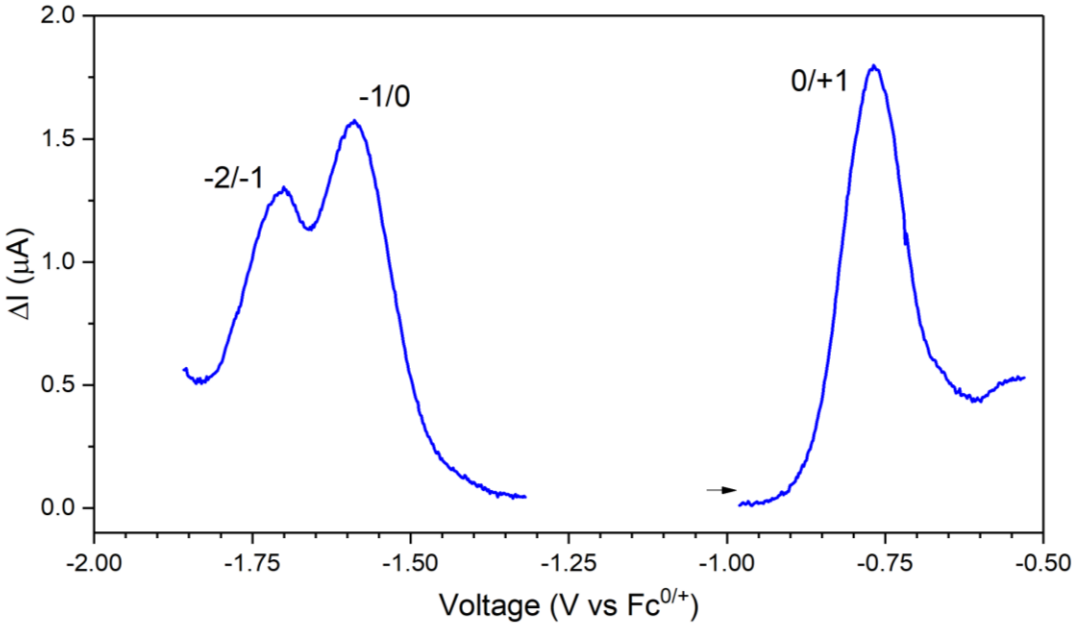

Figure 1.12. Differential pulse voltammogram of **1**-$(Sn^nBu_2)_3$ in 0.1 M $TBAPF_6$ in THF solution. Step size = 2 mV, Pulse amplitude = 25 mV, Sample period = 2 s, Pulse time = 0.5 s.

1.9 X-RAY DIFFRACTION STUDIES

Single crystals suitable for X-ray analysis were coated in deoxygenated paratone oil and mounted on a 20 µm CryoLoop™ (Hampton Research, 18 mm mount, 0.2 to 0.3 mm loop diameter). Data was collected at –173 °C on a Bruker APEX II single crystal X-ray diffractometer, with a Mo source. Data was integrated and scaled using SAINT, SADABS within the APEX2 software package by Bruker.[43] Solution by direct methods (SHELXT[44] or SIR97[45,46]) produced a complete heavy atom phasing model consistent with the proposed structure. Structures were completed by difference Fourier synthesis with SHELXL.[47–49] Scattering factors are from Waasmair and Kirfel.[50] Hydrogen atoms were placed in geometrically idealized positions and constrained to ride on their parent atoms with C–H distances in the range 0.95–1.00 Å. Isotropic thermal parameters U_{eq} were fixed such that they were $1.2U_{eq}$ of their parent atom Ueq for CHs and $1.5U_{eq}$ of their parent atom U_{eq} in case of methyl groups. All non-hydrogen atoms were refined anisotropically by full-matrix least-squares.

1.9.1 ***1***-*[Li$_2$(THF)$_2$]$_3$*

Dark red multi-faceted crystals suitable for X-ray diffraction analysis were grown via vapor diffusion of diethyl ether into a saturated THF filtrate over the course of 20 h at room temperature. The compound crystallized in trigonal $R\bar{3}$ and featuring a three-fold rotational axis through the axial Se atoms. The asymmetric unit contains a third of the molecule, and a diethyl ether and a THF molecule, some of which appeared disordered and necessitated removal through SQUEEZE.[51–53]

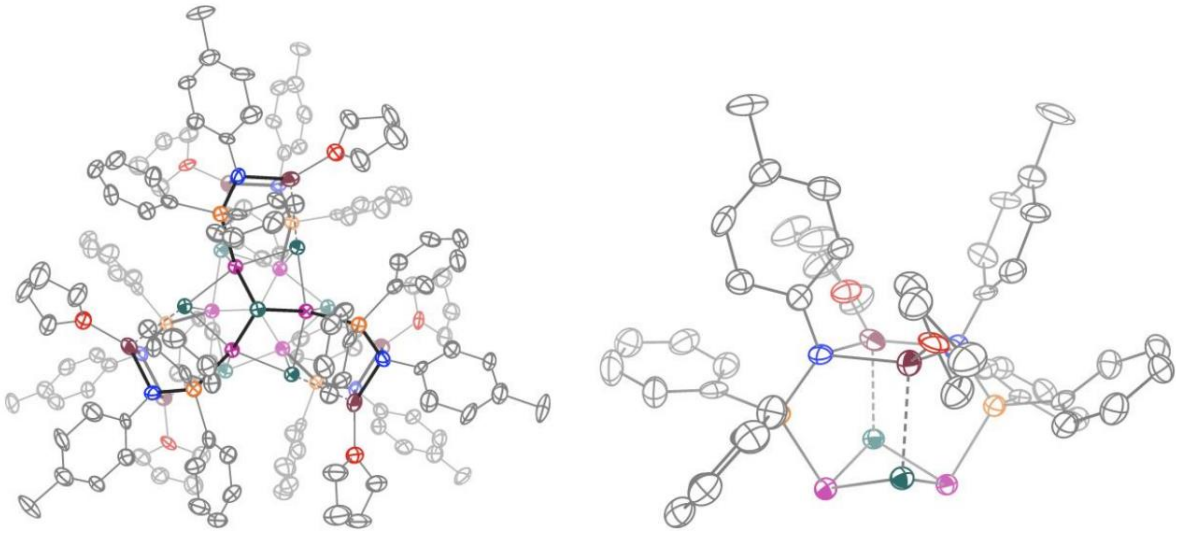

Figure 1.13. Molecular structure of **1**-[Li$_2$(THF)$_2$]$_3$ with thermal ellipsoids shown at a 50% probability level.

1.9.2 ***1***-*(SnMe$_2$)$_3$*

Dark red prisms suitable for X-ray diffraction analysis were grown via vapor diffusion of diethyl ether into a saturated THF filtrate over the course of 7 days at room temperature. The asymmetric unit of this structure contains two clusters, one of which is shown in Figure S16, the other which was disordered 1:1 and appeared partially folded on top of each other. A complete solution (with solvent SQUEEZEd) revealed that all clusters were identical, as the graphic below from the CheckCif report of the complete solution demonstrates. The R1 of this refinement, however, and the huge amount of restraints necessary to stabilize the refinement was unsatisfactory. Thus, the contribution of all disordered atoms and solvent to the diffraction pattern was removed with SQUEEZE.Crystallographic data reported in Table 1.2 corresponds to SQUEEZEd structure.

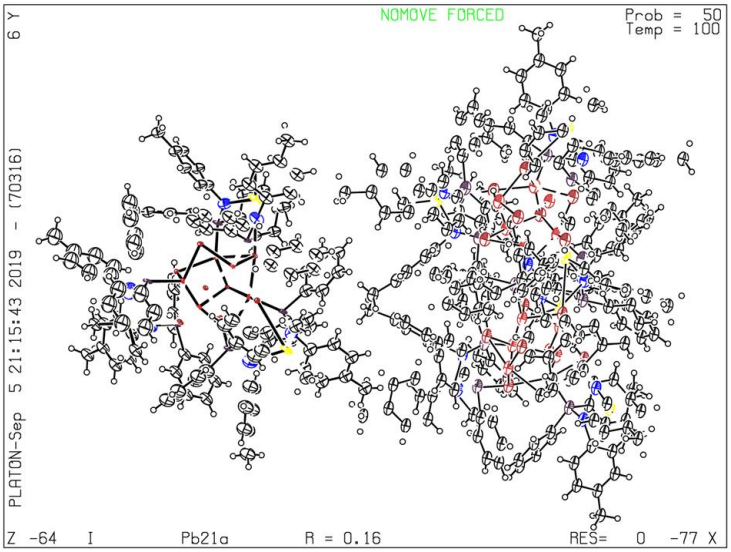

Figure 1.14. CheckCif ORTEP of the complete structure solution.

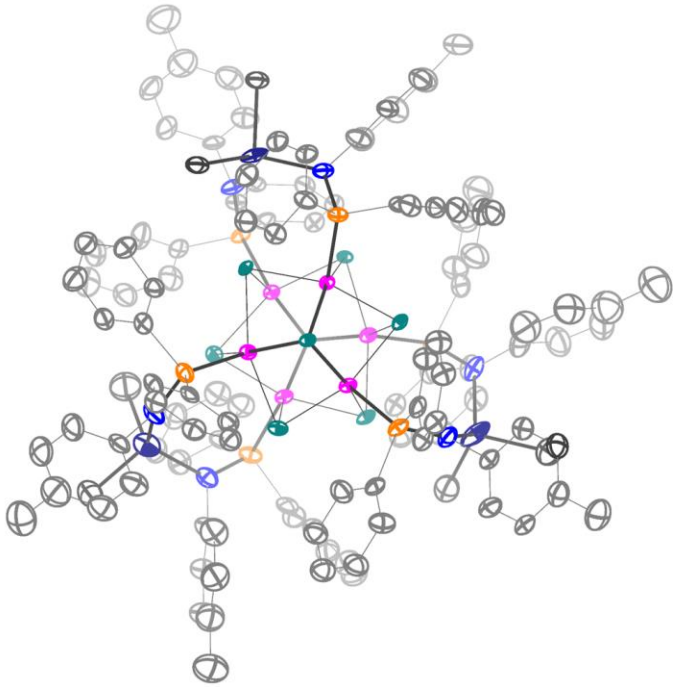

Figure 1.15. Molecular structure of **1**-$(SnMe_2)_3$ with thermal ellipsoids shown at a 50% probability level.

1.9.3 *X-ray Structure Tables*

Table 1.2. Crystallographic data for **1**-$[Li_2(THF)_2]_3$ and **1**-$(SnMe_2)_3$

Compound	**$Li_6(THF)_6Co_6Se_8L_6 \cdot 3$ THF**	**$(SnMe_2)_3Co_6Se_8L_6$**
Empirical formula	$C_{150}H_{174}Co_6Li_6N_6O_9P_6Se_8$	$C_{120}H_{120}Co_6N_6P_6Se_8Sn_3$
CCDC number	2052049	2052050
Formula weight	3417.66	3173.36
Temperature	100(2)	100(2)
Wavelength	0.71073	0.71073
Crystal system	Trigonal	Orthorhombic
Space group	$R\bar{3}$	$Pb2_1a$
a (Å)	21.6282(12)	31.6636(18)
b (Å)	21.6282(12)	25.169(3)
c (Å)	61.505(4)	33.635(3)
α (°)	90	90
β (°)	90	90
γ (°)	120	90
Volume ($Å^3$)	24916(3)	26805(4)
Z	6	4
ρ^{calc} (g cm^{-3})	1.367	0.786
Absorption coefficient (mm^{-1})	2.448	1.780
F(000)	10380	6224
Crystal size (mm^3)	0.210 x 0.190 x 0.180	0.380 x 0.080 x 0.030
Theta range for data collection (°)	1.713 to 25.179	1.371 to 25.091
Index ranges	$-25 \le h \le 25$, $-25 \le k \le 25$, $-73 \le l \le 73$	$-37 \le h \le 37$, $-29 \le k \le 30$, $-40 \le l \le 40$
Reflections collected	19442	92871
Independent reflections	9721 [R(int) = 0.0764]	47439 [R(int) = 0.2280]
Completeness to theta = 25.000°	97.4%	99.7%
Data / restraints / parameters	9721 / 102 / 592	47439 / 2149 / 1120
Goodness-of-fit on F^2	1.016	0.973
Final R indices [I>2sigma(I)]	R1 = 0.0701, wR2 = 0.1581	R1 = 0.1003, wR2 = 0.2176
R indices (all data)	R1 = 0.1274, wR2 = 0.1938	R1 = 0.1858, wR2 = 0.2620
Largest diff. peak and hole ($e^-Å^{-3}$)	3.022 and -1.017	2.097 and –2081

Table 1.3. Minimum and maximum values for selected interatomic distances as determined by single-crystal X-ray diffractometry

Compound	Interatomic Distance Range (Å)						
	Co-Se	Co…Co	M…Co	M…Se	Co-P	M-N	P-N
$Co_6Se_8L_6^H$	2.324(6) - 2.360(9)	2.917(7) - 2.974(4)	--	--	2.127(3) - 2.131(6)	--	1.676(6) - 1.716(7)
$Li_6(THF)_6Co_6Se_8L_6$	2.327(2) – 2.356(1)	2.851(2) – 3.045(1)	3.61(2) – 3.80(1)	2.536(18) – 2.537(12)	2.145(3) – 2.163(2)	2.06(2) – 2.11(1)	1.658(8) – 1.682(5)
$(SnMe_2)_3Co_6Se_8L_6$	2.303(4) – 2.391(4)	2.869(4) – 3.046(4)	4.161(3) – 4.211(3)	3.143(3) – 4.029(3)	2.094(5) – 2.123(5)	2.172(8) – 2.193(7)	1.542(8) – 1.549(8)

Table 1.4. Average values for selected interatomic distances as determined by single-crystal X-ray diffractometry.

Compound	Average Interatomic Distance ± Standard Deviation (Å)						
	Co-Se	Co…Co	M…Co	M…Se	Co-P	M-N	P-N
$Co_6Se_8L_6^H$	2.35 ± 0.02	2.94 ± 0.02	--	--	2.129 ± 0.002	--	1.69 ± 0.02
$Li_6(THF)_6Co_6Se_8L_6$	2.34 ± 0.01	2.97 ± 0.07			2.153 ± 0.009		1.67 ± 0.01
$(SnMe_2)_3Co_6Se_8L_6$	2.34 ± 0.02	2.95 ± 0.06			2.11 ± 0.01		1.546 ± 0.003

1.10 REFERENCES

(1) Roy, X.; Lee, C.-H.; Crowther, A. C.; Schenck, C. L.; Besara, T.; Lalancette, R. a; Siegrist, T.; Stephens, P. W.; Brus, L. E.; Kim, P.; Steigerwald, M. L.; Nuckolls, C. Nanoscale Atoms in Solid-State Chemistry. *Science* **2013**, *341* (6142), 157–160. https://doi.org/10.1126/science.1236259.

(2) Pinkard, A.; Champsaur, A. M.; Roy, X. Molecular Clusters: Nanoscale Building Blocks for Solid-State Materials. *Acc. Chem. Res.* **2018**, *51* (4), 919–929. https://doi.org/10.1021/acs.accounts.8b00016.

(3) Xie, J.; Wang, L.; S. Anderson, J. Heavy Chalcogenide-Transition Metal Clusters as Coordination Polymer Nodes. *Chemical Science* **2020**, *11* (32), 8350–8372. https://doi.org/10.1039/D0SC03429K.

(4) Kephart, J. A.; Romero, C. G.; Tseng, C.-C.; Anderton, K. J.; Yankowitz, M.; Kaminsky, W.; Velian, A. Hierarchical Nanosheets Built from Superatomic Clusters: Properties, Exfoliation and Single-Crystal-to-Single-Crystal Intercalation. *Chem. Sci.* **2020**, *11* (39), 10744–10751. https://doi.org/10.1039/D0SC03506H.

(5) Turkiewicz, A.; Paley, D. W.; Besara, T.; Elbaz, G.; Pinkard, A.; Siegrist, T.; Roy, X. Assembling Hierarchical Cluster Solids with Atomic Precision. *Journal of the American Chemical Society* **2014**, *136* (45), 15873–15876. https://doi.org/10.1021/ja508698w.

(6) Chauhan, V.; C. Reber, A.; N. Khanna, S. CO Ligands Stabilize Metal Chalcogenide Co 6 Se 8 (CO) n Clusters via Demagnetization. *Physical Chemistry Chemical Physics* **2017**, *19* (47), 31940–31948. https://doi.org/10.1039/C7CP07606A.

(7) Champsaur, A. M.; Hochuli, T. J.; Paley, D. W.; Nuckolls, C.; Steigerwald, M. L. Superatom Fusion and the Nature of Quantum Confinement. *Nano Lett.* **2018**, *18* (7), 4564–4569. https://doi.org/10.1021/acs.nanolett.8b01824.

(8) Liu, M.; Qiu, X.; Miyauchi, M.; Hashimoto, K. Energy-Level Matching of Fe(III) Ions Grafted at Surface and Doped in Bulk for Efficient Visible-Light Photocatalysts. *J. Am. Chem. Soc.* **2013**, *135* (27), 10064–10072. https://doi.org/10.1021/ja401541k.

(9) Kephart, J. A.; Mitchell, B. S.; Chirila, A.; Anderton, K. J.; Rogers, D.; Kaminsky, W.; Velian, A. Atomically Defined Nanopropeller Fe3Co6Se8(Ph2PNTol)6: Functional Model for the Electronic Metal–Support Interaction Effect and High Catalytic Activity for Carbodiimide

Formation. *J. Am. Chem. Soc.* **2019**, *141* (50), 19605–19610. https://doi.org/10.1021/jacs.9b12473.

(10) Kephart, J. A.; Boggiano, A. C.; Kaminsky, W.; Velian, A. Inorganic Clusters as Metalloligands: Ligand Effects on the Synthesis and Properties of Ternary Nanopropeller Clusters. *Dalton Trans.* **2020**, *49* (45), 16464–16473. https://doi.org/10.1039/D0DT02416C.

(11) Micnas, R.; Ranninger, J.; Robaszkiewicz, S. Superconductivity in Narrow-Band Systems with Local Nonretarded Attractive Interactions. *Rev. Mod. Phys.* **1990**, *62* (1), 113–171. https://doi.org/10.1103/RevModPhys.62.113.

(12) Wakita, T.; Paris, E.; Kobayashi, K.; Terashima, K.; Hacisalihoğlu, M. Y.; Ueno, T.; Bondino, F.; Magnano, E.; Píš, I.; Olivi, L.; Akimitsu, J.; Muraoka, Y.; Yokoya, T.; Saini, N. L. The Electronic Structure of Ag1−xSn1+xSe2 (x = 0.0, 0.1, 0.2, 0.25 and 1.0). *Phys. Chem. Chem. Phys.* **2017**, *19* (39), 26672–26678. https://doi.org/10.1039/C7CP05369J.

(13) Naijo, Y.; Hada, K.; Furukawa, T.; Itou, T.; Ueno, T.; Kobayashi, K.; Mazin, I. I.; Jeschke, H. O.; Akimitsu, J. Unusual Electronic State of Sn in AgSnSe 2. *Phys. Rev. B* **2020**, *101* (7), 075134. https://doi.org/10.1103/PhysRevB.101.075134.

(14) Hase, I.; Yasutomi, K.; Yanagisawa, T.; Odagiri, K.; Nishio, T. Electronic Structure of InTe, SnAs and PbSb: Valence-Skip Compound or Not? *Physica C: Superconductivity and its Applications* **2016**, *527*, 85–90. https://doi.org/10.1016/j.physc.2016.06.007.

(15) Peters, B.; Lichtenberger, N.; Dornsiepen, E.; Dehnen, S. Current Advances in Tin Cluster Chemistry. *Chem. Sci.* **2019**, *11* (1), 16–26. https://doi.org/10.1039/C9SC04363B.

(16) Suzuki, K.; Hanaya, T.; Sato, R.; Minato, T.; Yamaguchi, K.; Mizuno, N. Hexanuclear Tin(II) and Mixed Valence Tin(II,IV) Oxide Clusters within Polyoxometalates. *Chem. Commun.* **2016**, *52* (70), 10688–10691. https://doi.org/10.1039/C6CC05284C.

(17) Hassanzadeh Fard, Z.; Müller, C.; Harmening, T.; Pöttgen, R.; Dehnen, S. Thiostannate Tin–Tin Bond Formation in Solution: In Situ Generation of the Mixed-Valent, Functionalized Complex [(RSnIV)2(μ-S)23SnIII2S6]. *Angewandte Chemie International Edition* **2009**, *48* (24), 4441–4444. https://doi.org/10.1002/anie.200805719.

(18) Zheng, G.-L.; Ma, J.-F.; Su, Z.-M.; Yan, L.-K.; Yang, J.; Li, Y.-Y.; Liu, J.-F. A Mixed-Valence Tin–Oxygen Cluster Containing Six Peripheral Ferrocene Units. *Angewandte Chemie International Edition* **2004**, *43* (18), 2409–2411. https://doi.org/10.1002/anie.200353359.

(19) Sulaiman, S. T.; Al-Allaf, T. A. K.; Abeed, F. A. Differential Pulse Polarographic Determination of Some Organotin(IV) Compounds in Dimethyl Sulfoxide. *Microchemical Journal* **1987**, *35* (3), 257–262. https://doi.org/10.1016/0026-265X(87)90108-1.

(20) Abeed, F. A.; Al-Allaf, T. A. K.; Ahmed, K. S. Electrochemical Behaviour of Some Organotin(IV) Compounds by Rotating Disc Voltammetry in Non-Aqueous Solvents. *Applied Organometallic Chemistry* **1990**, *4* (2), 133–140. https://doi.org/10.1002/aoc.590040208.

(21) Shang, X.; Meng, X.; Alegria, E. C. B. A.; Li, Q.; Guedes da Silva, M. F. C.; Kuznetsov, M. L.; Pombeiro, A. J. L. Syntheses, Molecular Structures, Electrochemical Behavior, Theoretical Study, and Antitumor Activities of Organotin(IV) Complexes Containing 1-(4-Chlorophenyl)-1-Cyclopentanecarboxylato Ligands. *Inorg. Chem.* **2011**, *50* (17), 8158–8167. https://doi.org/10.1021/ic200635g.

(22) Shang, X.; Alegria, E. C. B. A.; Guedes da Silva, M. F. C.; Kuznetsov, M. L.; Li, Q.; Pombeiro, A. J. L. Redox-Active Cytotoxic Diorganotin(IV) Cycloalkylhydroxamate Complexes with Different Ring Sizes: Reduction Behaviour and Theoretical Interpretation. *Journal of Inorganic Biochemistry* **2012**, *117*, 147–156. https://doi.org/10.1016/j.jinorgbio.2012.08.019.

(23) Hussain, F.; Kortz, U. Polyoxoanions Functionalized by Diorganotin Groups: The Tetrameric, Chiral Tungstoarsenate(Iii), [{Sn(CH 3) 2 (H 2 O)} 2 {Sn(CH 3) 2 }As 3 (α-AsW 9 O 33) 4] 21−. *Chemical Communications* **2005**, No. 9, 1191–1193. https://doi.org/10.1039/B415901B.

(24) Hussain, F.; Kortz, U.; Keita, B.; Nadjo, L.; Pope, M. T. Tetrakis(Dimethyltin)-Containing Tungstophosphate [{Sn(CH3)2}4(H2P4W24O92)2]28-: First Evidence for a Lacunary Preyssler Ion. *Inorg. Chem.* **2006**, *45* (2), 761–766. https://doi.org/10.1021/ic051990y.

(25) Chen, W.-C.; Qin, C.; Li, Y.-G.; Zang, H.-Y.; Shao, K.-Z.; Su, Z.-M.; Wang, E.-B.; Liu, H.-S. Assembly of Tetrameric Dimethyltin-Functionalized Selenotungstates: From Nanoclusters to One-Dimensional Chains. *Chem. Commun.* **2015**, *51* (12), 2433–2436. https://doi.org/10.1039/C4CC08575B.

(26) Chen, W.-C.; Qin, C.; Wang, X.-L.; Wu, C.-X.; Li, Y.-G.; Zang, H.-Y.; Shao, K.-Z.; Su, Z.-M.; Wang, E.-B. Trimeric Hexa-Dimethyltin-Functionalized Selenotungstate [{Sn(CH3)2(CH3COO)}3{Sn(CH3)2}3{Se2W18O62(OH)(H2O)}3]18−. *CrystEngComm* **2016**, *18* (16), 2820–2824. https://doi.org/10.1039/C6CE00377J.

(27) Davies, A. G.; Gielen, M.; Pannell, K.; Tiekink, E. *Tin Chemistry: Fundamentals, Frontiers, and Applications*; John Wiley & Sons, Ltd, 2008. https://doi.org/10.1002/9780470758090.ch1.

(28) Davies, A. G.; Smith, P. J. 11 - Tin. In *Comprehensive Organometallic Chemistry*; Wilkinson, G., Stone, F. G. A., Abel, E. W., Eds.; Pergamon: Oxford, 1982; pp 519–627. https://doi.org/10.1016/B978-008046518-0.00019-2.

(29) van den Berghe, E. V.; van der Kelen, G. P. A Study of the 1H and 119Sn NMR Spectra of (CH3)4−nSn(NR2)n Compounds (R□CH3, C2H5). *Journal of Organometallic Chemistry* **1973**, *61*, 197–205. https://doi.org/10.1016/S0022-328X(00)86547-X.

(30) Kennedy, J. D.; McFarlane, W.; Pyne, G. S.; Wrackmeyer, B. Indirect Nuclear Spin Spin Coupling Constants of Tin-119 and Lead-207 to Nitrogen and Phosphorus in Organometallic Compounds. *Journal of Organometallic Chemistry* **1980**, *195* (3), 285–290. https://doi.org/10.1016/S0022-328X(00)93311-4.

(31) Hanau, K.; Rinn, N.; Argentari, M.; Dehnen, S. Organotin Selenide Clusters and Hybrid Capsules. *Chemistry – A European Journal* **2018**, *24* (45), 11711–11716. https://doi.org/10.1002/chem.201801652.

(32) Holeček, J.; Nádvorník, M.; Handlíř, K.; Lyčka, A. 13C and 119Sn NMR Study of Some Four- and Five-Coordinate Triphenyltin(IV) Compounds. *Journal of Organometallic Chemistry* **1983**, *241* (2), 177–184. https://doi.org/10.1016/S0022-328X(00)98505-X.

(33) Jia, W.-L.; Liu, Q.-D.; Wang, R.; Wang, S. Novel Phosphorescent Cyclometalated Organotin(IV) and Organolead(IV) Complexes of 2,6-Bis(2‘-Indolyl)Pyridine and 2,6-Bis[2‘-(7-Azaindolyl)]Pyridine. *Organometallics* **2003**, *22* (20), 4070–4078. https://doi.org/10.1021/om030404a.

(34) Kuchta, M. C.; Parkin, G. Terminal Sulfido and Selenido Complexes of Tin: Syntheses and Structures of [.Eta.4-Me8taa]SnE (E = S, Se). *J. Am. Chem. Soc.* **1994**, *116* (18), 8372–8373. https://doi.org/10.1021/ja00097a057.

(35) Athukorala Arachchige, K. S.; Diamond, L. M.; Knight, F. R.; Lechner, M.-L.; Slawin, A. M. Z.; Woollins, J. D. Synthetic, Structural, and Spectroscopic Studies of Sterically Crowded Tin–Chalcogen Acenaphthenes. *Organometallics* **2014**, *33* (21), 6089–6102. https://doi.org/10.1021/om500755w.

(36) Groom, C. R.; Bruno, I. J.; Lightfoot, M. P.; Ward, S. C. The Cambridge Structural Database. *Acta Cryst B* **2016**, *72* (2), 171–179. https://doi.org/10.1107/S2052520616003954.

(37) Yang, L.; R. Powell, D.; P. Houser, R. Structural Variation in Copper(i) Complexes with Pyridylmethylamide Ligands : Structural Analysis with a New Four-Coordinate Geometry Index, τ 4. *Dalton Transactions* **2007**, *0* (9), 955–964. https://doi.org/10.1039/B617136B.

(38) G. Harrison, P.; W. Thornton, E. Derivatives of Bivalent Germanium, Tin, and Lead. Part 21. Tin(II) Formate: A Reinvestigation. *Journal of the Chemical Society, Dalton Transactions* **1978**, *0* (10), 1274–1278. https://doi.org/10.1039/DT9780001274.

(39) R. Ewings, P. F.; G. Harrison, P.; J. King, T. Derivatives of Divalent Germanium, Tin, and Lead. Part VI. Crystal and Molecular Structure of Bis(1-Phenylbutane-1,3-Dionato)Tin(II). *Journal of the Chemical Society, Dalton Transactions* **1975**, *0* (14), 1455–1458. https://doi.org/10.1039/DT9750001455.

(40) Bard, A.; Faulkner, L. *Electrochemical Methods: Fundamentals and Applications*, 2nd ed.; Wiley: New York.

(41) Passarelli, V.; Benetollo, F. Reactivity of Novel N,N′-Diphosphino-Silanediamine-Based Rhodium(I) Derivatives. *Inorg. Chem.* **2011**, *50* (20), 9958–9967. https://doi.org/10.1021/ic2004408.

(42) Bard, A. J.; Faulkner, L. R. *Electrochemical Methods: Fundamentals and Applications*, 2nd ed.; Wiley: New York, 2001.

(43) *Bruker APEX2 (Version 2.1-4), SAINT (Version 7.34A), SADABS (Version 2007/4), 2007 BrukerAXS Inc, Madison, Wisconsin, USA.*

(44) *Sheldrick, G.M. Acta Cryst. 2015 A71, 3-8.*

(45) *Altomare, A.; Burla, C.; Camalli, M.; Cascarano, G. L.; Giacovazzo, C.; Guagliardi, A.; Moliterni, A.G.G.; Polidori, G.; Spagna, R. J. Appl. Crystallogr., 1999, 32, 115-119.*

(46) *Altomare, A.; Cascarano, G. L.; Giacovazzo, C.; Guagliardi, A. J. Appl. Crystallogr., 1993, 26, 343-350.*

(47) *Sheldrick, G. M. SHELXL-97, Program for the Refinement of Crystal Structures, 1997, University of Göttingen, Germany.*

(48) *Sheldrick, G. M. Acta Cryst. 2015, C71, 3–8.*

(49) *Mackay, S.; Edwards, C.; Henderson, A.; Gilmore, C.; Stewart, N.; Shankland, K.; Donald, A. MaXus: A Computer Program for the Solution and Refinement of Crystal Structures from Diffraction Data, 1997, University of Glasgow, Scotland.*

(50) *Waasmaier, D.; Kirfel, A. Acta Cryst., 1995, 51, 416-430.*

(51) Spek, A. L. Single-Crystal Structure Validation with the Program PLATON. *J Appl Cryst* **2003**, *36* (1), 7–13. https://doi.org/10.1107/S0021889802022112.

(52) van der Sluis, P.; Spek, A. L. BYPASS: An Effective Method for the Refinement of Crystal Structures Containing Disordered Solvent Regions. *Acta Cryst A* **1990**, *46* (3), 194–201. https://doi.org/10.1107/S0108767389011189.

(53) Spek, A. L. Structure Validation in Chemical Crystallography. *Acta Cryst D* **2009**, *65* (2), 148–155. https://doi.org/10.1107/S090744490804362X.

Chapter 2. REDOX-SWITCHABLE ALLOSTERIC EFFECTS IN MOLECULAR CLUSTERS

2.1 ABSTRACT

We demonstrate that allosteric effects and redox state changes can be harnessed to create a switch that selectively and reversibly regulates the coordination chemistry of a single site on the surface of a molecular cluster. This redox-switchable allostery is employed as a guiding force to assemble molecular clusters $Zn_3Co_6Se_8L'_6$ (L' =$Ph_2PN(H)Tol$, Ph = phenyl, Tol = 4-tolyl) into materials of pre-determined dimensionality (1 or 2-D), and to encode them with emissive properties. This work paves the path to program the assembly and function of inorganic clusters into stimuli-responsive, atomically precise materials.

2.2 INTRODUCTION

Reversibly activating a single coordination site on the surface of an inorganic cluster could enable unprecedented control over reactivity, opening uncharted paths for catalyst development and functional materials synthesis.[1,2] While redox cooperativity and charge redistribution among neighboring metals has been shown to lead to site-selective reactivity in some molecular clusters,[3–5] reversibly regulating the coordination chemistry of a single site on the surface of a molecular cluster remains elusive. More often, chemical differentiation, achieved either using the supporting ligand or by changing the identity of the metal itself, is required to direct the chemistry to a single site.[6–15] On an extended surface, the reactivity of chemically degenerate surface sites can become differentiated as a result of ligand binding via "inter-adsorbate interactions", giving rise to important phenomena like altered Sabatier volcano curves[16,17] or nanopatterning.[18] When a substrate binds at one site on a surface, it induces subtle structural and electronic changes at neighboring sites that alter their reactivity primarily by modifying adsorption energies. For

Reproduced in part with permission from:
Mitchell, B. S.; Krajewski, S. M.; Kephart, J. A.; Rogers, D.; Kaminsky, W.; Velian, A. *JACS Au* **2022**, *2* (1), 92–96.

Scheme 2.1. Redox-switchable allosteric effects: a powerful strategy to reversibly site-differentiate degenerate surface sites in inorganic clusters.

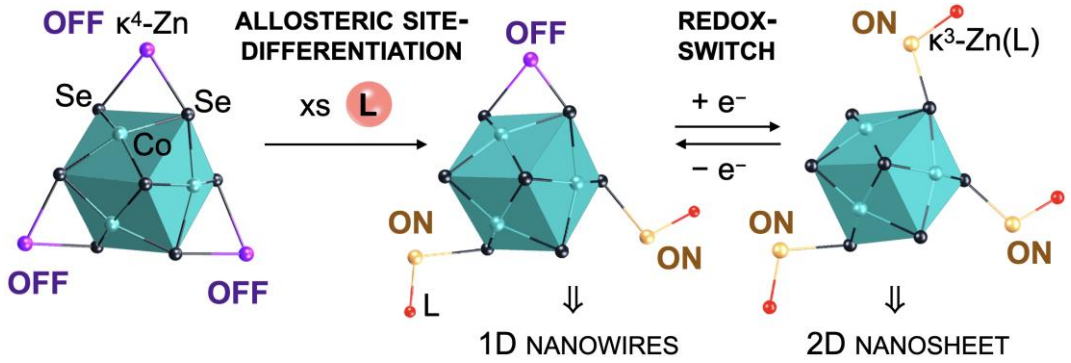

example, inter-adsorbate interactions inhibit CO adsorption at nearest-neighbor sites on Cu(100) due to decreased electron density around the initial CO adsorption site.[19] Similar effects are invoked as the major contributors for the coverage-dependent adsorption energy of H_2S on FeS_2.[20] Inspired by inter-adsorbate effects in extended materials, we set out to probe if site-differentiation of a molecular cluster could also be achieved based solely on ligand binding, and to investigate if redox state changes can be used as a switch for this differentiation.

Our group previously introduced a family of molecular clusters $M_3Co_6Se_8L'_6$ (**M3**, L' =$Ph_2PN(H)R$, Ph = phenyl, R = 4-tolyl; **M3***, R = isopropyl; M = Fe, Co, Zn, Sn) with three degenerate surface sites (M) that can engage with substrates and linkers,[21–24] enabling them to function as catalysts[21] and building blocks alike.[23] In this study, a redox innocent metal, Zn, was selected to decorate the cluster; therefore, a redox change in the Co_6Se_8 support would be unambiguously responsible for modifying the affinity of the cluster for linkers. Two main discoveries were made. First, the equivalent edge sites of **Zn3** become site-differentiated when exposed to ligands (Scheme 2.1). This is an illustration of inter-adsorbate effects wherein through-cluster electronic and structural rearrangements are propagated between the edge Zn sites upon ligand binding. Due to its similarity to allosteric effects in biological systems,[25,26] we refer to it as allosteric site-differentiation. Second, the site-differentiation can be reversibly switched "on" or "off" by simply changing the oxidation state of the cobalt selenide support. The utility of this redox-switchable allosteric effect is illustrated in the assembly of the atomically precise materials of pre-determined dimensionality, namely one-dimensional nanowires and two-dimensional nanosheets. While electrons are a convenient way to operate a molecular switch, we also demonstrate an inner-sphere electron transfer pathway relying on quinone reduction can be

employed to tag the **Zn$_3$** nanocluster. We use this strategy to equip the ditopic nanocluster building block **Zn$_3$**L$_2$ with a fluorophore, opening a new path to access stimuli-responsive, atomically precise nanomaterials.[27–29]

2.3 Results and Discussion

Zn$_3$ is prepared by salt metathesis from Li$_6$(py)$_6$Co$_6$Se$_8$L'$_6$ (1.0 equiv) and ZnCl$_2$ (3.3 equiv).[21,22] In the presence of coordinating ligands (L), the cluster is isolated exclusively as the site-differentiated bis-adduct **Zn$_3$**L$_2$ (L = py; 4.5 g, 80% yield, Figure 1a,b). Single crystal X-ray diffraction shines light on the site-differentiation, revealing an allosteric effect in which THF binding at two of the Zn edge sites effectively strengthens the Zn–Co$_6$Se$_8$ interactions at the third. Two Zn(THF) sites are chelated κ^3 by the cluster via two amides and one Se, while the third is bound κ^4, featuring a second Zn–Se bond (Figure 2.1c). The site-differentiation is retained in the

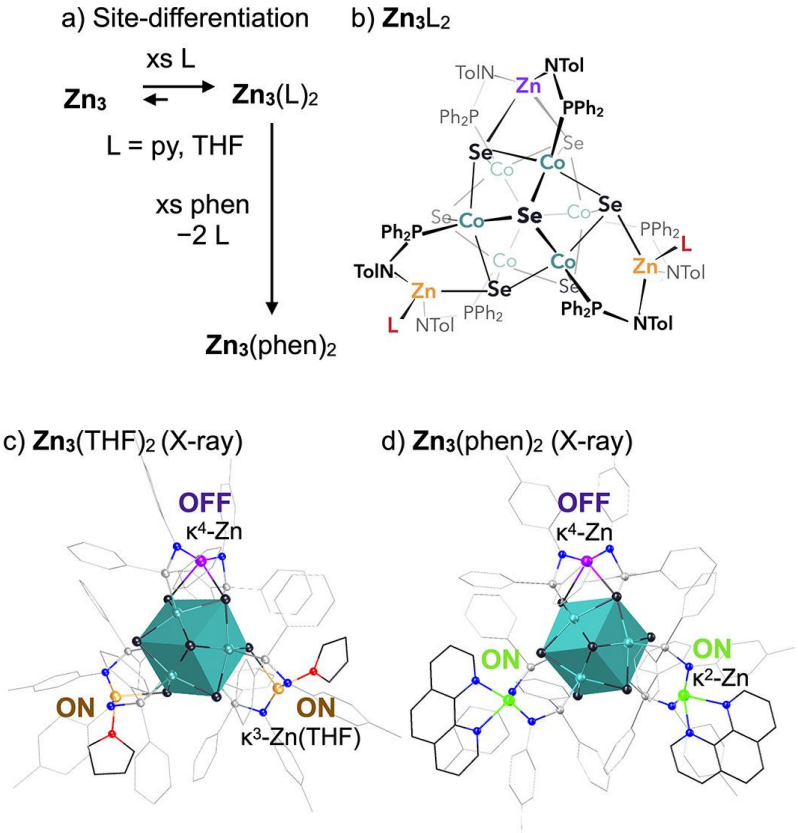

Figure 2.1. a) Synthesis of a ditopic nanoblock, and b) structure of **Zn$_3$**L$_2$ (L = THF or py). c) Single crystal X-ray diffraction structure of **Zn$_3$**(THF)$_2$, b) **Zn$_3$**(phen)$_2$. Hydrogen atoms, co-crystallized solvent and any disorder are omitted for clarity.

presence of excess 1,10-phenanthroline (phen), a chelating ligand with strong σ–donating properties. In the solid state, the bis-adduct **Zn3**(phen)2 (78% yield; Figure 2.1a) features one naked κ^4–Zn edge, and two κ^2–Zn sites in which both Zn—Se interactions have been replaced by coordination to phenanthroline (Figure 2.1d).[30–32] The allosteric effect set off by ligand binding in **Zn3** is enabled by the hemilability of the metal-support interactions.[21,22] We propose that breaking a Zn—Se bond upon ligand coordination begins a cascading effect through the Co_6Se_8 support which regains some electron density and presents at another Zn edge site by strengthening the Zn—Se interactions and diminishing its affinity for exogenous ligands.

Here the utility of the site-differentiation is harnessed to control the dimensionality of cluster assembled nanostructures. Typically, the chemically degenerate sites on the surface of inorganic clusters bind linkers indiscriminately, precluding dimensional control over the assembly. Synthetic pathways that enable deterministic assembly routes of low-dimensional structures is an active area of research.[33–37] With only two edge sites available to engage linkers, the **Zn3**(py)2 cluster is poised to encode the formation of a one-dimensional wire when mixed with a linear ditopic ligand. To mimic the coordination of pyridine and phenanthroline at the Zn edge sites, two types of nitrogen based linear linkers are employed: the monodentate 4,4'-bipyridine (bipy) and the chelating tetrapyrido[3,2-a:2′,3′-c:3″,2″-h:2‴,3‴-j] phenazine (tpphz), respectively. Black, prismatic crystals of the nanowires [**Zn3**(bipy)]n (**1**-bipy, 48% yield) and [**Zn3**(tpphz)]n (**1**-tpphz, 65% yield) grew over the course of 2–3 days of mixing **Zn3**(py)2 with excess bipy or tpphz (Figure 2.2a). Single crystal X-ray diffraction reveals the similarity of the cluster nodes with their molecular counterparts, which retain one edge site in the "off", κ^4–Zn state, and two linker-bound edge sites

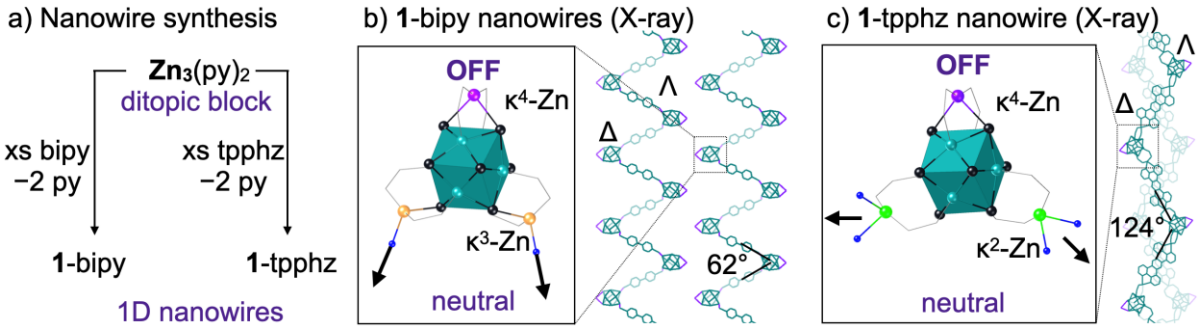

Figure 2.2. a) Synthesis of nanowires 1-bipy and 1-tpphz. Single crystal X-ray data of b) 1-bipy and c) 1-tpphz, with insets depicting a single cluster node of Δ-helicity. Organic ligands, H atoms and any co-crystallized solvent are not depicted for clarity.

that enable catenation of the wires (Figure 2.2b,c). While both nanowires exhibit a zig-zag motif, the κ^2–Zn versus κ^3–Zn linkages produce obvious structural differences. Most notably, the kinks of the wire measure 62° in **1**-bipy, and double, 124°, in **1**-tpphz where the chelating effect of tpphz disengages the Zn from the cluster enabling a more relaxed chain. Interestingly, in both wires, the racemic mixture of helical nanoclusters (Λ, Δ) of **Zn$_3$** assemble with alternating enantiomers, giving rise to the first examples of syndiotactic nanocluster wires. Typically, tacticity of hybrid inorganic/organic polymers is encoded based on the chirality of the organic linker rather than the intrinsic chirality of an inorganic node.[38–40] Tacticity in organic polymers is associated with drastic differences in physical properties; exploring the consequences of tacticity in inorganic hybrid materials could likewise be tied to interesting properties, but, in part due to lack of synthetic access, this remains a little explored frontier.

We previously observed that oxidation state changes affect the affinity for ligands of **Fe$_3$** clusters.[21] Here, we set out to explore if an increased affinity for ligands upon oxidation could turn the κ^4-Zn site into a redox switch. Electrochemically, **Zn$_3$** exhibits three single electron oxidation events (–0.37, 0.12, 0.49 V) and one reduction (–1.59 V) all of which are chemically reversible (Figure 2.11-Figure 2.13; referenced to Fc/Fc$^+$). The chemical oxidation of the neutral bis-adduct **Zn$_3$**(py)$_2$ in the presence of phenanthroline (3.3 equiv) is revealing. The tris-adduct [**Zn$_3$**(phen)$_3$][PF$_6$] (80%; Figure 2.3a) is formed as the sole product, and its solid state structure confirms the chemical equivalence of its three κ^2–Zn edge sites (Figure 2.3b). The formation of [**Zn$_3$**(phen)$_3$]$^+$ illustrates

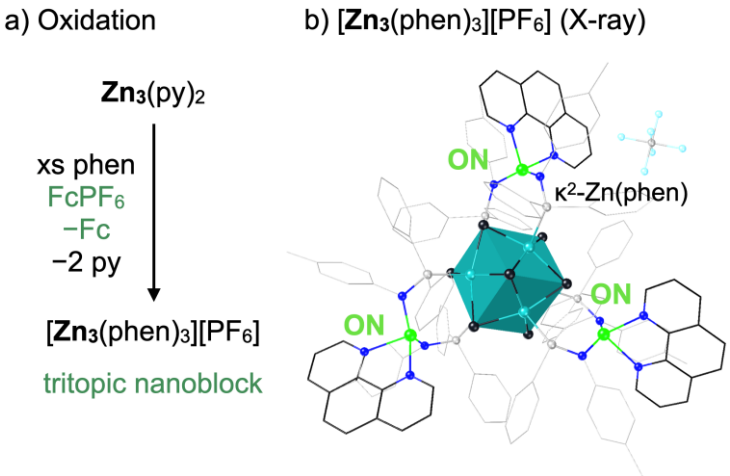

Figure 2.3. a) Synthesis of a tritopic nanoblock. b) Single crystal X-ray diffraction structure of [**Zn$_3$**(phen)$_3$][PF$_6$]. Hydrogen atoms, co-crystallized solvent and any disorder are omitted for clarity.

how removing a single electron from the cobalt core can be used to switch "on" the affinity for ligands at the κ^4–Zn site in the neutral cluster **Zn**$_3$(phen)$_2$. Due to the redox resilience of the Co_6Se_8 support, this process is electrochemically reversible (Figure 2.11). The ability to switch between the neutral and mono-oxidized nanoclusters using electrons in the transformation **Zn**$_3$(L)$_2$ + L ⇌ [**Zn**$_3$(L)$_3$]$^+$ + e$^-$, makes the zinc nanocluster an exceptional candidate for the assembly of stimuli-responsive materials.

Redox-switching "on" the affinity for ligands at the κ^4–Zn site turns the ditopic **Zn**$_3$(py)$_2$ cluster into a tritopic nanoblock, which in combination with linear linkers would give rise to two-dimensional nanosheets. Mixing the **Zn**$_3$(py)$_2$ nanocluster, the $FcPF_6$ oxidant and the bipy linker gives rise over the course of two days to black, prismatic crystals identified as [**Zn**$_3$(bipy)$_{1.5}$][PF_6] (**2**-bipy, 44% yield; Figure 2.4a). This material is identified as a layered two-dimensional van der Waals material, with each nanoblock in the +1 oxidation state using single crystal X-ray diffraction (Figure 2.4b). The structure of the individual nanosheets is remarkably similar to that of the previously reported $Co_3(bipy)_{1.5}Co_6Se_8L_6$ nanosheet,[34] with the only major differences being the presence of the PF_6^- anion and the orientation the sheets within the crystal lattice.

Beyond controlling dimensionality, electron transfer can be used to endow **Zn**$_3$(py)$_2$ with orthogonal emissive properties. The ruthenium complex [Ru(bipy)$_2$(phendione)][PF_6]$_2$ (bipy' = 2,2'-bipyridine, phendione = 1,1-phenanthroline-5,6-dione) is uniquely equipped to serve as both a fluorophore as well as an inner-sphere oxidant due to the dione moiety.[41–43] Upon treatment of **Zn**$_3$(py)$_2$ (1 equiv) with Ru(bipy')$_2$(phendione)][PF_6]$_2$ (1 equiv) produces a new species **3** (Figure

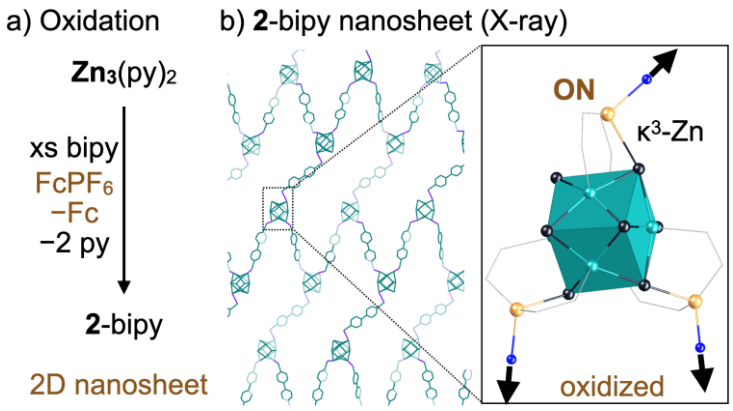

Figure 2.4. a) Synthesis of nanosheet **2**-bipy. b) Single crystal X-ray diffraction structure of **2**-bipy, with an inset depicting a tritopic node of Δ-helicity. Counterion PF_6^-, organic ligands, hydrogen atoms and any co-crystallized solvent are not depicted for clarity.

2.5), which is most consistent with the structure proposed in Figure 2.5b. Signaling the oxidation of the Co_6Se_8 core is the emergence of a single paramagnetic ^{31}P NMR resonance in **3** at −415 ppm (Figure 2.8). The monoreduction of the quinone to a semiquinone is reflected in the disappearance of the C=O stretch (1770 cm^{-1}) of starting material, and the appearance of a lower energy feature at 1464 cm^{-1}, attributed to the C–O stretch (Figure 2.9).[42,44] Upon excitation at λ_{max} (438 nm), **3** exhibits a broad emission band centered at 677 nm. Not only is this feature absent in $\mathbf{Zn_3}(py)_2$, but it is 50 nm redshifted from the parent Ru complex (Figure 2.5c). Preliminary studies reveal that **3** has potential as a nanoblock; treating it with bipy results in the formation of a material insoluble in common organic solvents –the hallmark of an extended framework.

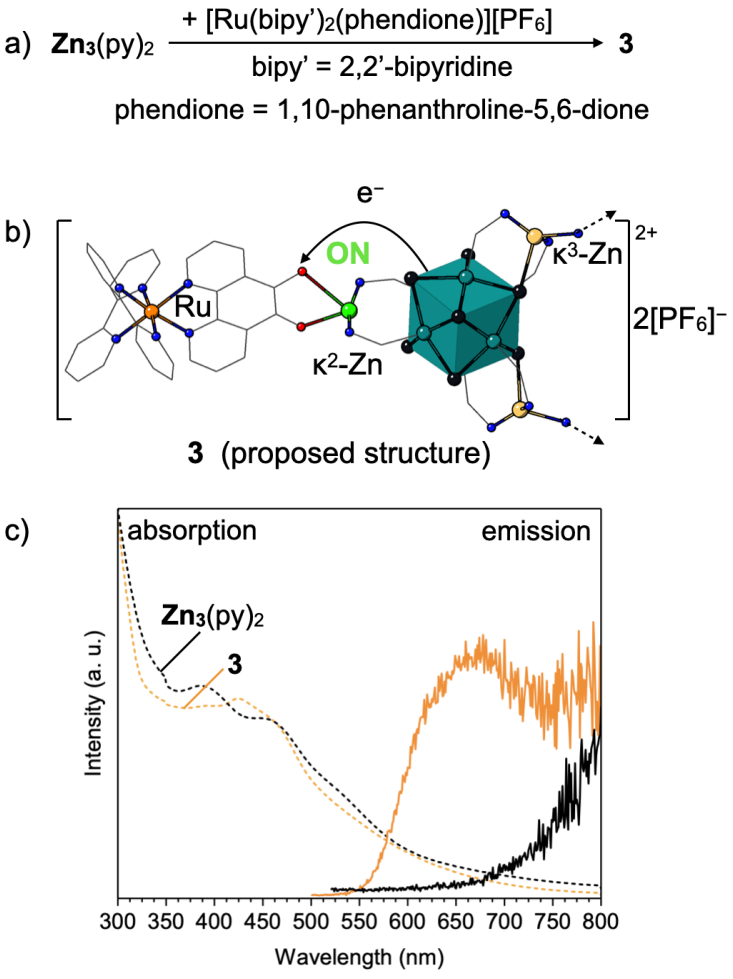

Figure 2.5. a) The synthesis of **3**, and b) structural model highlighting the inner sphere electron transfer from the cobalt core to the phendione unit. The dashed arrows indicate the possible linker-attachment points. c) Absorption and emission (438 nm excitation) profiles of $\mathbf{Zn_3}(py)_2$.

2.4 CONCLUSIONS

Traditionally, allosteric effects describe how the binding of a ligand at one site of a protein alters the properties of a distant site on the same protein.[25,26] In **Zn_3**, ligand binding at one edge site sets off a domino effect that changes the affinity for ligands at another Zn site. The hemilability of the interactions between the edge (Zn) and the redox-active support (Co_6Se_8) enables the creation of a switch, wherein electron transfer controls the affinity for ligands at a single Zn edge site. The redox-switchable allosteric site-differentiation of the **Zn_3** nanocluster turns it into a versatile building block which can be pre-encoded with desirable physicochemical information. This work illustrates a new approach to program dimensionality and function into stimuli-responsive atomically precise materials.

2.5 SYNTHETIC DETAILS AND CHARACTERIZATION OF PRODUCTS

2.5.1 *General Experimental Considerations*

No unexpected or unusually high safety hazards were encountered during the experimental work reported in here.

The syntheses were conducted under a dinitrogen atmosphere using standard Schlenk or glovebox techniques (LC Technology Solutions glovebox equipped with a freezer set to −35 °C). The glassware was dried at 160 °C for a minimum of 12 h and cooled in an evacuated antechamber prior to use in the glovebox.

Solvents were purchased from Fischer Scientific and degassed, dried and purified using solvent purification columns housed in a stainless-steel cabinet and dispensed by a stainless-steel Schlenk line manufactured by JC Meyer Solvent Systems. Tetrahydrofuran (THF), diethyl ether, acetonitrile, and methylene chloride (DCM) are passed through two packed columns of neutral alumina. In the cases of *n*-pentane and toluene, one of the columns is packed with alumina and the other with Q5 reactant, a copper(II) oxide oxygen scavenger. All solvents were passed through an in-line, 2 μm filter, then stored over activated 3Å molecular sieves in the glovebox for a minimum of 72 h before use. 3Å molecular sieves were purchased from Sigma Aldrich and activated under vacuum at 300 °C for 48 h.

Deuterated solvents ($CDCl_3$, C_6D_6, CD_2Cl_2, CD_3CN) were purchased from Sigma Aldrich and stored over activated 3Å molecular sieves in the glovebox for a minimum of 72 h prior to use. $Li_6(py)_6Co_6Se_8L_6$ was prepared via reported literature methods.[1] $ZnCl_2$ (99.99%-Zn, PURATREM) was purchased from Strem Chemicals, Inc. and used as received without further purification. 1,10-phenanthroline (99%, anhydrous) was purchased from Sigma Aldrich and used without further purification. Ferrocenium hexafluorophosphate was purchased from Sigma Aldrich and recrystallized from dry acetone and diethyl ether prior to use. Tetrapyrido[3,2-a:2′,3′-c:3″,2″-h:2‴,3‴-j]phenazine was prepared using reported literature methods.[2] Tetra(*n*-butyl)ammonium hexafluorophosphate (98%) was purchased from Sigma Aldrich; prior to use it was recrystallized from ethanol three times, and brought to constant mass under reduced pressure at 110 °C for 24 h. $[Ru(bpy)_2(phendione)][PF_6]_2$ was prepared using reported literature methods.[3] Samples were prepared for elemental analysis by first crushing crystalline material into a powder, bringing it to constant mass under reduced pressure (ca. 12 h). Co, Se, P elemental analysis was conducted using a Perkin-Elmer Nexion 200B inductively-coupled plasma mass spectrometer (ICP-MS). Prior to ICP-MS analysis, samples were digested in neat nitric acid (Fisher Scientific, ICP-MS grade) at 50 °C.

UV-vis-*n*IR absorption spectra were acquired using a Varian Cary 5000 UV-Vis-*n*IR spectrometer using *n*IR quartz cuvettes (Spectrocell Inc., 10 mm path length, 220–3500 nm spectral window). Emission spectra were acquired using a Horiba FluoroMax-4, using fluorometer optical borosilicate VIS cuvettes (Spectrocell Inc., 10 mm path length, 340-2000 nm spectral window).

NMR spectra were acquired at 25 °C on Bruker 300, 500, or 700 MHz spectrometers. ^{1}H and ^{13}C NMR spectra were referenced to residual deuterated solvent peaks. ^{31}P and ^{19}F NMR spectra were externally referenced to phosphoric acid and CCl_3F, respectively.

Cyclic voltammetry was conducted using a Gamry Interface 1010B potentiostat. A three-electrode cell setup was used with a glassy carbon disk working electrode, a platinum wire counter electrode, and a silver-wire pseudo-reference electrode. A three-electrode cell was also used for solid-state electrochemical measurements; in this instance, the analyte was dropcasted onto a carbon fiber paper electrode (1x1 cm, Spectracarb 2050A-1550) from a suspension of toluene. All potentials were referenced to the Fc/Fc^+ redox couple by adding a small amount of ferrocene (Fc) after each measurement. All electrochemical measurements were conducted under a dinitrogen atmosphere, at 25 °C.

2.5.2 *Synthesis and Isolation of $Zn_3(py)_2Co_6Se_8L_6$ (**$Zn_3(py)_2$**)*

A 100 mL Schlenk flask equipped with a 1-inch magnetic stir bar was loaded with $Li_6(py)_6Co_6Se_8$-L_6 (1.269 g, 0.391 mmol, 1.0 equiv) and toluene (60 mL), and the resulting mixture was partially frozen using the glovebox cold-well. Upon thawing, $ZnCl_2$ (0.176 g, 1.29 mmol, 3.3 equiv) dissolved in THF (6 mL) was added dropwise over the course of 2 minutes to the stirring mixture. The reaction flask was then degassed, sealed, and removed from the glovebox. The dark-red reaction mixture was then stirred at 60 °C for 20 h. Volatiles were removed under reduced pressure. The residue was first triturated with diethyl ether (3 x 5 mL), extracted in DCM (50 mL) and then passed through a plug of Celite on a fritted-glass funnel. The filtrate was placed under reduced pressure yielding a dark colored, black looking solid, which was slurried in acetonitrile (100 mL) for 1 h, and then recollected on a fine-porosity fritted-glass filter. The isolated solids were washed with a second portion of acetonitrile (30 mL) to yield **Zn$_3$**$(py)_2$ as an analytically pure, black, microcrystalline solid (0.811 g, 0.263 mmol, 67%).

^{1}H NMR (C_6D_6, 300 MHz) δ: 8.38 (br, 4 H, py-N(C*H*)$_2$(CH)$_2$CH), 7.71 (m, 24 H, PPh_2 Ar*H*), 7.08 (m, 18 H, PPh_2 Ar*H*), 6.98 (m, 6 H, PPh_2 Ar*H*), 6.76 (br, 4 H, py-N(CH)$_2$(C*H*)$_2$CH), 6.71 (d, 12 H, *J* = 8.0 Hz, tolyl *o*-Ar*H*), 6.51 (d, 12 H, *J* = 8.0 Hz, tolyl *m*-Ar*H*), 1.80 (s, 18 H, 4-tolyl-CH_3) ppm. ^{1}H NMR (CD_2Cl_2, 500 MHz) δ: 7.22−7.45 (m, 60 H, Ar*H*), 6.75 (d, 12 H, *J* = 8.2 Hz, tolyl *o*-Ar*H*), 6.25 (d, 12 H, *J* = 8.2 Hz, tolyl *m*-Ar*H*), 2.04 (s, 18 H, 4-tolyl-CH_3). ^{13}C NMR (CD_2Cl_2, 125 MHz) δ: 147.0 (d, 15.0 Hz, *i*-tolyl), 142.0 (d, *J* = 40 Hz, *i*-PPh_2), 139.6 (d, *J* = 40 Hz, *i*-PPh_2), 132.6 (d, *J* = 10.0 Hz, PPh *C*H), 132.1 (d, *J* = 10.0 Hz, PPh *C*H), 129.2 (s, PPh *p*-*C*H), 128.9 (s, tolyl *m*-(*C*H)$_2$, 128.7 (s, PPh *p*-*C*H), 128.5 (s, tolyl *C*CH_3), 127.6 (d, *J* =10.0 Hz, PPh *C*H), 127.3 (d, *J* =10.0 Hz, PPh *C*H), 122.9 (d, *J* = 10.0 Hz, tolyl *o*-(*C*H)$_2$), 20.4 (s, 4-tolyl-*C*H_3) ppm. ^{31}P NMR (C_6D_6, 283 MHz): δ +86.9 ($\nu_{1/2}$ = 333 Hz) ppm. UV-vis: Figure S10. Elemental analysis found (calc.) for **Zn$_3$**$(py)_2$ (Formula: $C_{124}H_{112}Co_6N_8P_6Se_8Zn_3$): Co 11.66 (11.47), Se 20.74 (20.50), P 5.86 (6.03).

2.5.3 *Isolation of **Zn_3** from **$Zn_3(py)_2$***

Removal of the coordinated pyridine ligands in **Zn$_3$**$(py)_2$ was accomplished by extensive trituration with diethyl ether. **Zn$_3$**$(py)_2$ was first slurried in diethyl ether under vigorous stirring for 3-8 hours, then placed under reduced pressure while being heated at 80 °C for 3-12 hours. This

process was repeated three times to ensure the coordinated pyridine was completely removed from the nanocluster.

^{1}H NMR (C_6D_6, 300 MHz) δ: 7.74 (m, 24 H, PPh_2 Ar*H*), 7.21 (s, 18 H, PPh_2 Ar*H*), 7.13 (m, 12 H, PPh_2 Ar*H*) , 7.05 (m, 6H, PPh_2 Ar*H*), 6.63 (d, 12 H, *J* = 8.1 Hz, tolyl *o*-Ar*H*), 6.51 (d, 12 H, *J* = 8.1 Hz, tolyl *m*-Ar*H*), 1.81 (s, 18 H, 4-tolyl-CH_3) ppm.

2.5.4 *Synthesis and isolation of $Zn_3(phen)_2Co_6Se_8L_6$ (**$Zn_3(phen)_2$**)*

Zn_3 $(py)_2$ (500 mg, 0.162 mmol, 1.0 equiv) was charged into a 20 mL scintillation vial and dissolved in DCM (10 mL). 1,10–Phenanthroline (93 mg, 0.513 mmol, 3.15 equiv) was dissolved separately in DCM (2 mL) and added to the **Zn_3**$(py)_2$ solution with stirring. The reaction was stirred at room temperature for 30 minutes. The reaction mixture was concentrated under reduced pressure to half of its original volume, layered with *n*-pentane (~15 mL), and placed in the glovebox freezer overnight. The dark, black looking precipitate was isolated *via* vacuum filtration through a fine porosity glass fritted funnel and identified as **Zn_3**$(phen)_2$ (437 mg, 0.133 mmol, 82% yield). The product showed very poor solubility in C_6D_6 and CD_3CN, however it was very soluble in CD_2Cl_2. Upon dissolution in pyridine-d_5 the phenanthroline ligands dissociate from the cluster. ^{1}H NMR spectrum reveals the formation of **Zn_3**$(py)_x$ cluster and uncoordinated 1,10-phenanthroline (Figure S5).

^{1}H NMR (CD_2Cl_2, 25 °C, 300 MHz) δ: 8.73 (s, br, 4 H, $\nu_{1/2}$ = 23.0 Hz, phen-NC*H*CH), 8.10 (s, br, 4 H, $\nu_{1/2}$ = 18.1 Hz, phen-NC*H*CH), 7.64 (s, 6 H,), 7.32 (s, br), 7.23 (s, br), 7.18 (s, br), 7.04 (s, br), 5.86 (s, br, 24 H, $\nu_{1/2}$ = 110.1 Hz, 4-tolyl-Ar*H*), 1.74 (s, br, 18 H, $\nu_{1/2}$ = 46.3 Hz, 4-tolyl-CH_3) ppm. ^{13}C NMR (CD_2Cl_2, 25 °C, 125 MHz) δ: 150.06, 136.90, 133.39, 132.87, 128.40, 128.01, 127.61, 126.93, 126.38, 123.92, 20.25 ppm. ^{31}P NMR (CD_2Cl_2, 25 °C, 283 MHz): δ +101.25 ($\nu_{1/2}$ = 710.3 Hz), +83.15 ($\nu_{1/2}$ = 1044.4 Hz) ppm. Elemental analysis found (calc.) for **Zn_3**$(phen)_2$ (Formula: $C_{138}H_{118}Co_6N_{10}P_6Se_8Zn_3$): Co 10.89 (10.77), Se 19.58 (19.24), P 5.50 (5.66).

2.5.5 *Synthesis and isolation of $[Zn_3(phen)_3Co_6Se_8L_6][PF_6]$ ($[$**$Zn_3(phen)_3$**$][PF_6]$)*

A 20 mL scintillation vial equipped with a magnetic stir bar was charged with **Zn_3**$(py)_2$ (217 mg, 0.071 mmol, 1.0 equiv) and DCM (8 mL) and cooled in the glovebox freezer (–35 °C) for 15 minutes. A solution of ferrocenium hexafluorophosphate (23 mg, 0.071 mmol, 1.0 equiv) in DCM (2 mL) was added dropwise to the cold stirring solution of **Zn_3**$(py)_2$. The reaction was allowed to

stir for 15 minutes at room temperature and a solution of 1,10-phenanthroline (40 mg, 0.223 mmol, 3.15 equiv) in DCM (1 mL) was added dropwise. After two hours the reaction mixture was concentrated to half of its volume *in vacuo*, layered with *n*-pentane, and placed in the glovebox freezer (–35 °C) for 1 hour. The precipitate was collected on a medium porosity glass fritted funnel to yield a dark, black looking solid, identified as $[Zn_3(phen)_3][PF_6]$ (202 mg, 0.057 mmol, 80% yield). Single crystals suitable for X-ray diffraction studies were grown *via* the vapor diffusion of diethyl ether into a saturated solution of the product in acetonitrile at room temperature over the course of 2 days.

^{1}H NMR (CD_2Cl_2, 300 MHz) δ: 8.76 (s, 6 H, phen-Ar*H*), 8.10 (d, 6 H, *J* = 8.1 Hz, phen-Ar*H*), 7.70 (t, 6 H, *J* = 7.1 Hz, PPh_2 p-Ar*H*), 7.67 (s, 6 H, phen-Ar*H*), 7.61 (t, 6 H, *J* = 7.1 Hz, PPh_2 p-Ar*H*), 7.39 (d, 12 H, PPh_2 o-Ar*H*), 7.30 (s, 12 H, PPh_2 o-Ar*H*), 7.02 (m, 6 H, phen-Ar*H*), 6.84 (t, 12 H, *J* = 6.2 Hz, PPh_2 m-Ar*H*), 6.46 (t, 12 H, *J* = 6.2 Hz, PPh_2 m-Ar*H*), 5.78 (d, 12 H, *J* = 5.6 Hz, tolyl Ar*H*), 5.57 (d, 12 H, *J* = 7.4 Hz, tolyl Ar*H*), 1.37 (s, 18 H, 4-tolyl-C*H*$_3$) ppm. ^{13}C NMR (CD_2Cl_2, 125 MHz) δ 145.48 (s, CH), 142.71 (s, C), 142.57 (s, C), 141.61 (s, C), 137.15 (s, CH), 134.36 (s, CH), 131.67 (s, CH), 128.72 (s, C), 128.32 (s, C), 128.22 (s, CH), 127.45 (s, CH), 127.27 (s, CH), 126.92 (s, CH), 126.52 (s, CH), 126.23 (s, CH), 125.42 (s, CH), 124.04 (s, CH), 20.63 (s, CH_3) ppm. ^{31}P NMR (CD_2Cl_2, 121 MHz): δ –143.92 (m, J_{FP} = 715 Hz), –521.23 ($\nu_{1/2}$ = 2283 Hz) ppm. ^{19}F NMR (CD_2Cl_2, 471 MHz) δ –73.85 (d, J_{PF} = 711 Hz) ppm. UV-vis: Figure S10. Elemental analysis found (calc.) for [**Zn$_3$**(phen)$_3$][PF_6] (Formula: $C_{150}H_{126}Co_6F_6N_{12}P_7Se_8Zn_3$): Co 9.82 (9.80), Se 17.79 (17.51), P 5.67 (6.01).

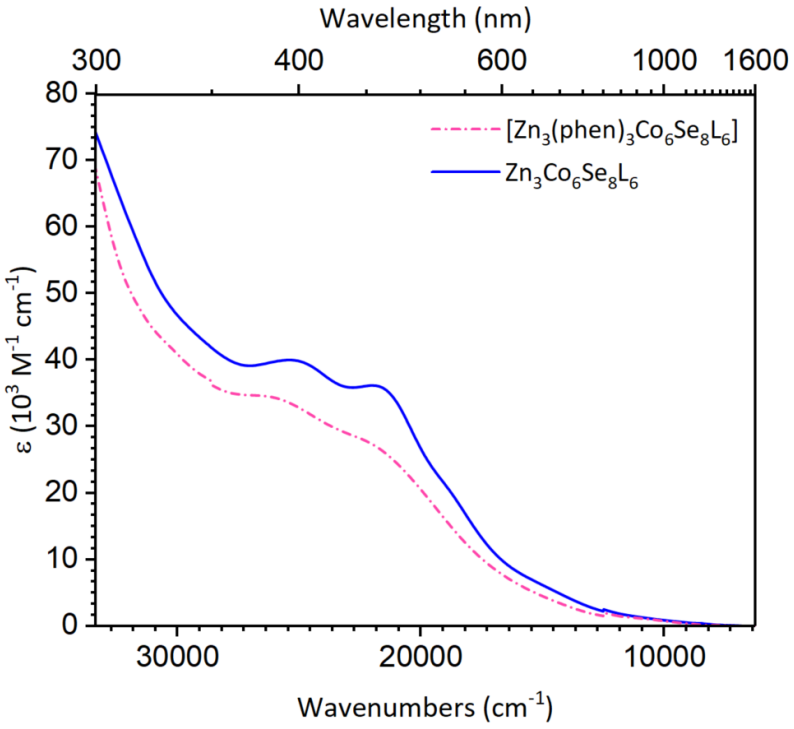

Figure 2.6. UV-Vis-*n*IR absorption spectrum of **Zn3** and [**Zn3**(phen)$_3$][PF$_6$] in THF.

2.5.6 *Synthesis and isolation of Zn$_3$(bipy)Co$_6$Se$_8$L$_6$ (**1**-bipy)*

Zn3(py)$_2$ (50 mg, 0.016 mmol, 1.0 equiv) was dissolved in toluene (5 mL) with gentle heating and stirring over the course of 30 minutes. The solution was filtered through a plug of Celite into a 20 mL scintillation vial charged with 4,4′-bipyridine (4 mg, 0.022 mmol, 1.8 equiv). The Celite plug was washed with additional toluene (2 mL). The reaction was allowed to sit undisturbed at 60 °C. Dark prismatic crystals suitable for single crystal X-ray diffraction formed on the sides of the vial. After 2 days, the mother liquor was decanted, and the crystals were soaked in toluene (3 x 5 mL; 15 minutes each cycle), decanting the supernatant after each treatment. The volatiles were removed *in vacuo* to yield **1**-bipy (25 mg, 0.0082 mmol, 51% yield). The material is insoluble in toluene and DCM but it dissolves in pyridine-d_5, reforming free monomer **Zn3**(py)$_2$ and 4,4′-bipyridine. Elemental analysis found (calc.) for **1**-bipy (Formula: $C_{124}H_{110}Co_6N_8P_6Se_8Zn_3$): Co 11.25 (11.47), Se 20.76 (20.50), P 6.32 (6.03).

2.5.7 *Formation and single crystal growth of $Zn_3(tpphz)Co_6Se_8L_6$ (**1**-tpphz)*

Tetrapyrido[3,2-a:2′,3′-c:3″,2″-h:2‴,3‴-j]phenazine (4 mg, 0.011 mmol, 1.0 equiv) was suspended in DCM (8 mL) and added to a solution of **Zn$_3$**(py)$_2$ (33 mg, 0.011 mmol, 1.0 equiv) in DCM (2 mL). The reaction was allowed to stand at room temperature in the glovebox without stirring. After one week, a crystalline solid was collected on a fine porosity sintered glass filter. The material was washed with toluene (~15 mL) and then DCM (~30 mL) until the filtrate ran clear. The solids were brought to constant mass *in vacuo* to yield **1**-tpphz as a dark crimson red solid (24 mg, 0.007 mmol, 65% yield). The material is insoluble in toluene and DCM but can be digested in pyridine-d_5 reforming free monomer **Zn$_3$**(py)$_2$. The insolubility of tpphz in pyridine-d_5 precludes its observation by NMR analysis after the digestion with pyridine.

^{1}H NMR (pyridine-d_5, 300 MHz) δ: 7.81 (m, 24 H), 7.40 (m, 6 H), 7.34 (m, 12 H), 7.28 (m, 12 H), 6.86 (d, 12 H, J = 7.9 Hz), 6.62 (d, 12 H, J = 8.0 Hz), 1.90 (s, 18 H) ppm. Elemental analysis found (calc.) for **1**-tpphz (Formula: $C_{138}H_{114}Co_6N_{12}P_6Se_8Zn_3$): Co 9.67 (10.69), Se 18.84 (19.10), P 6.01 (5.62). Incomplete digestion of **1**-tpphz in concentrated nitric acid at 80 °C for 18 hours precluded accurate ICP-MS analysis.

2.5.8 *Synthesis and Isolation of $[Zn_3(bpy)_{1.5}Co_6Se_8L_6][PF_6]$ (**2**-bipy)*

Zn$_3$(py)$_2$ (100 mg, 0.032 mmol, 1.0 equiv) and $FcPF_6$ (11 mg, 0.032 mmol, 1.0 equiv) were dissolved separately in DCM (7 mL and 3 mL, respectively). The $FcPF_6$ solution was added dropwise to the stirring solution of **Zn$_3$**(py)$_2$ and the reaction was allowed to stir at room temperature for 10 minutes. The reaction mixture was filtered through a plug of Celite into a 20 mL scintillation vial charged with 4,4′-bipyridine (11 mg, 0.068 mmol, 2.1 equiv). The Celite plug was washed with additional DCM (2 mL). The reaction was allowed to sit undisturbed at room temperature. Dark prismatic crystals suitable for single crystal X-ray diffraction formed on the sides of the vial. After 2 days, the mother liquor was decanted, and the crystals were soaked in DCM (3 x 5 mL; 15 minutes each cycle), decanting the supernatant after each treatment. The volatiles were removed *in vacuo* to yield **2**-bipy (45 mg, 0.014 mmol, 44% yield). The material is insoluble in toluene and DCM, however it dissolves in pyridine-d_5 forming free oxidized monomer, [**Zn$_3$**(py)$_3$][PF_6] and 4,4′-bipyridine.

Elemental analysis found (calc.) for **2**-bpy (Formula: $C_{129}H_{114}Co_6F_6N_9P_7Se_8Zn_3$): Co 10.50 (10.46), Se 18.89 (18.69), P 6.39 (6.42).

Characterization of [$\mathbf{Zn_3}(py)_3$][PF_6]:

^{1}H NMR (pyridine-d_5, 500 MHz) δ: 8.86 (m, 6 H), 8.22 (m, 12 H), 8.10 (m, 6 H), 7.91 (m, 6 H), 7.76 (s, 12 H), 7.61 (m, 6 H), 6.99 (s, 12 H), 6.85 (s, 12 H), 6.79 (d, 12 H, J = 8.0 Hz), 6.49 (d, 12 H, J = 7.0 Hz), 1.66 (s, 18 H) ppm. ^{13}C NMR (pyridine-d_5, 125 MHz) δ 151.64 (s), 145.76 (s), 134.12 (s), 131.25 (s), 130.20 (s), 128.93 (s), 128.73 (s), 127.72 (s), 126.05 (s), 124.77 (s), 122.15 (s), 21.32 (s) ppm. ^{31}P NMR (pyridine-d_5, 121 MHz): δ –142.30 (sept, J_{FP} = 712 Hz) ppm. The aminophosphine ^{31}P feature was not observed. ^{19}F NMR (pyridine-d_5, 470 MHz) δ –71.26 (d, J_{PF} = 710 Hz) ppm.

2.5.9 *Reaction of $\mathbf{Zn_3}(py)_2$ with $[Ru(bipy')_2(phendione)][PF_6]_2$: synthesis of **3***

A solution of $[Ru(bipy')_2(phendione)][PF_6]_2$ (11 mg, 0.012 mmol, 1.0 equiv) in acetonitrile (1 mL) was added dropwise to a stirring solution of $\mathbf{Zn_3}(py)_2$ (34 mg, 0.012, 1.0 equiv) in toluene (2 mL). The reaction was stirred at room temperature for 10 minutes and then concentrated under reduced pressure. The residue was triturated with diethyl ether (2 x 4 mL) and then washed with *n*-pentane (~10 mL) and diethyl ether (~10 mL). The product was completely solubilized in acetonitrile and passed through a plug Celite. Notably, the starting $\mathbf{Zn_3}(py)_2$ is completely insoluble in acetonitrile. The volatiles were removed *in vacuo* to yield a dark, black looking, solid (45 mg, 0.011 mmol, 92% yield)

^{1}H NMR (CD_3CN, 500 MHz) 8.47, 7.99, 7.83, 7.77, 7.66, 7.56, 7.52, 7.40, 7.33, 6.94, 6.88, 6.87, 6.81, 6.72, 6.59, 6.34, 6.27, 6.21, 1.74 (s, 12 H), 1.68 (s, 6 H) ppm. ^{31}P NMR (CD_3CN, 202 Hz) –144 (sept, J_{FP} = 707 Hz), –415 ($\nu_{1/2}$ = 1445 Hz) ppm. ATR-FTIR (film): ν_{SQ} = 1464 cm^{-1}. Elemental analysis found (calc.) for **3** (Formula: $C_{156}H_{134}Co_6F_{12}N_{14}O_2P_8RuSe_8Zn_3$): Co 8.56 (8.85), Se 16.16 (15.81), P 6.56 (6.20).

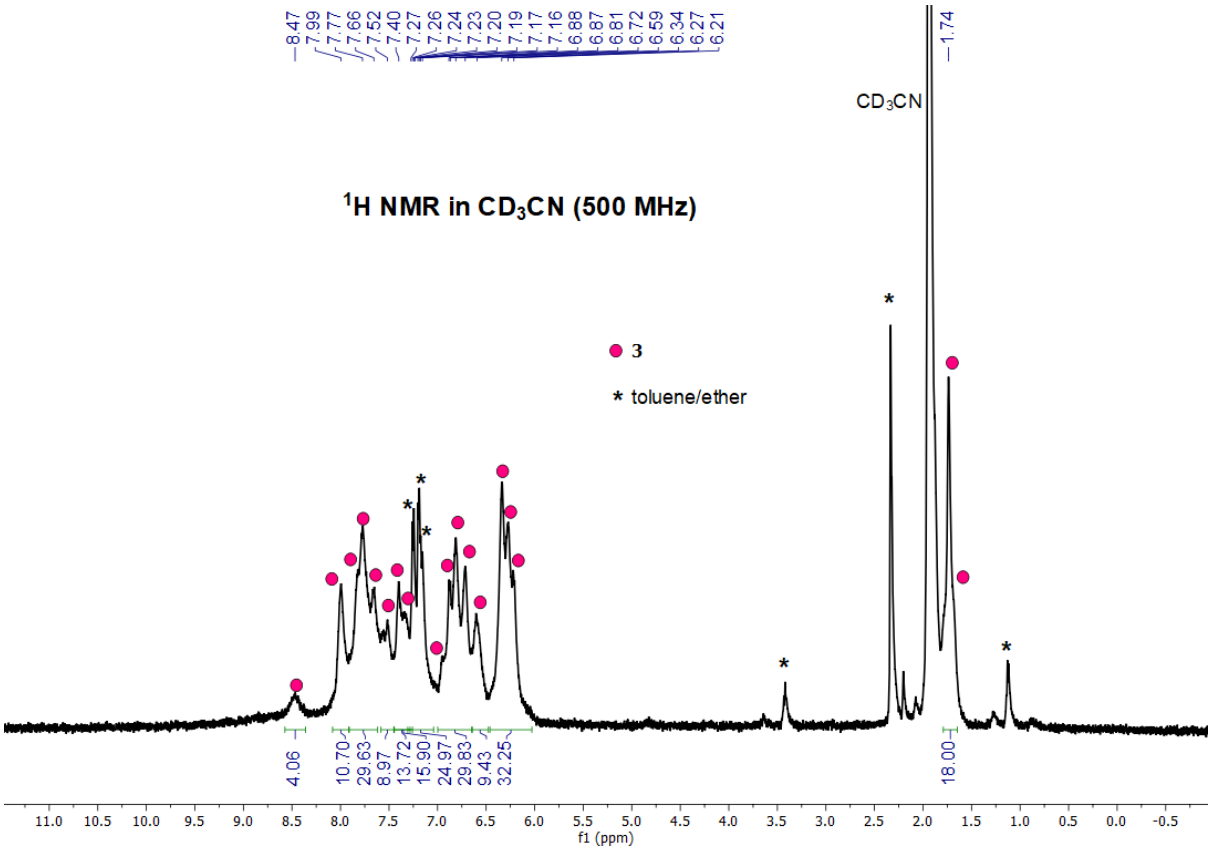

Figure 2.7. ^{1}H NMR (CD_3CN, 25 °C, 500 MHz) spectrum of **3**.

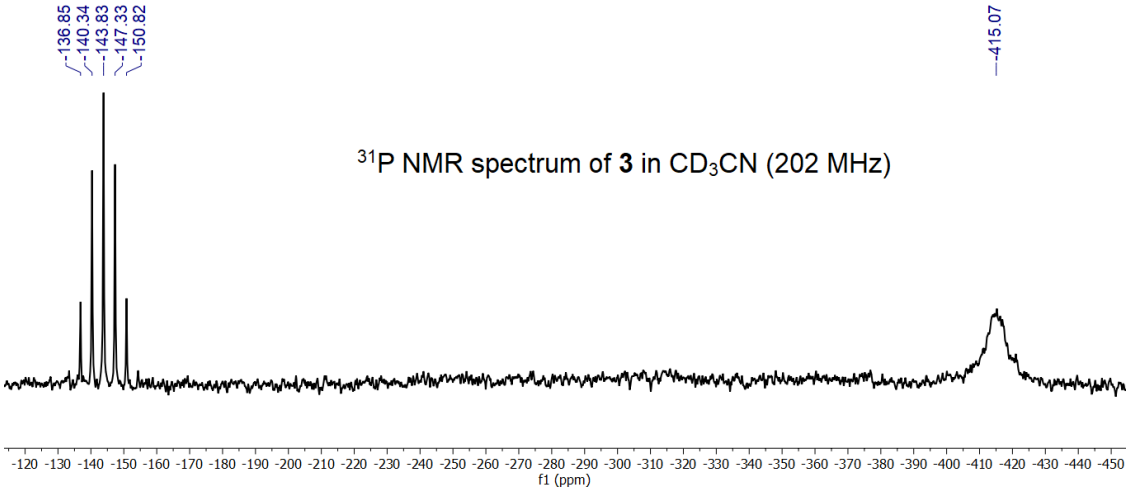

Figure 2.8. ^{31}P NMR (CD_3CN, 25 °C, 202 MHz) spectrum of **3**.

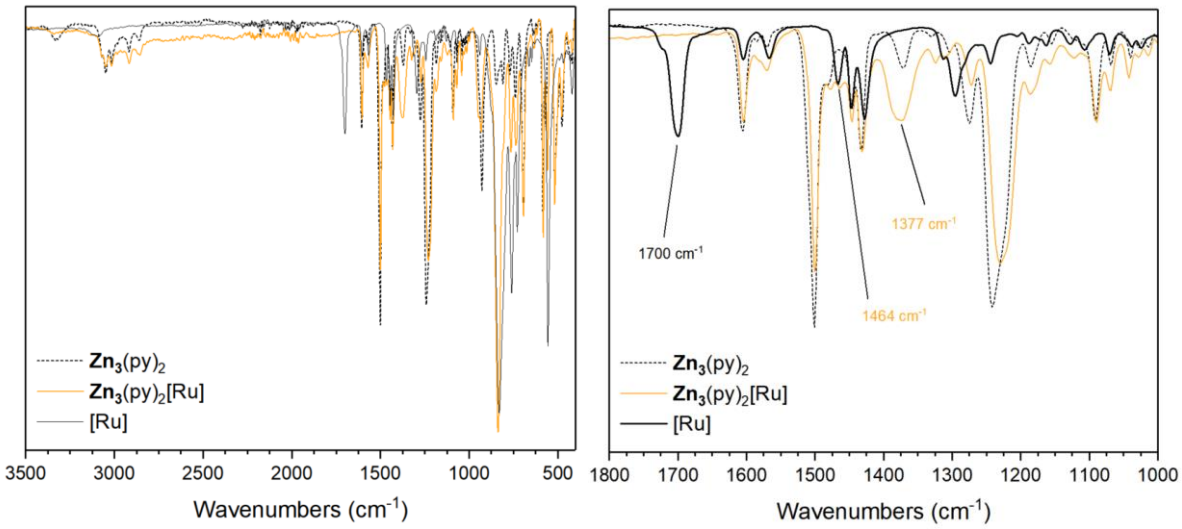

Figure 2.9. IR spectra of **Zn**$_3$(py)$_2$, [Ru(bipy')$_2$(phendione)][PF$_6$]$_2$, and **3**.

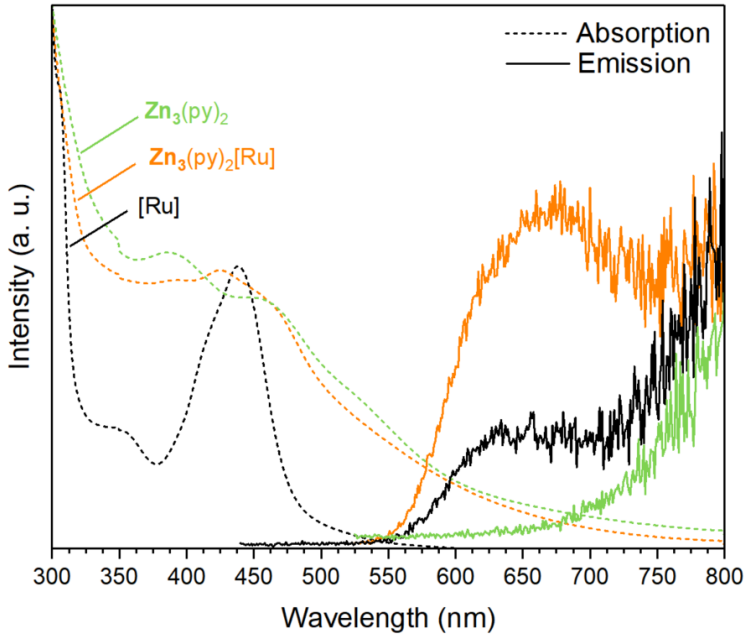

Figure 2.10. Absorption and emission spectra of **Zn**$_3$(py)$_2$, **3** and [Ru(bipy')$_2$(phendione)][PF$_6$]$_2$ in MeCN.

2.6 ELECTROCHEMISTRY

Table 2.1. Half-wave potentials ($E_{1/2}$) and peak-to-peak separation potentials (ΔE_p) of $Co_6Se_8L^H{}_6$ and **Zn3**$(py)_2$ recorded in 0.1 M $TBAPF_6$ DCM or THF solutions and **1**-tpphz drop casted onto a carbon paper electrode in a solution of 0.1 M $TBAPF_6$ in MeCN. All samples measured at a scan rate of 200 mV/s. Values recorded in DCM and THF solutions are reported with and without parenthesis, respectively.

redox couple (n_{red}/n_{ox})	$E_{1/2}$ (V vs $Fc^{0/+}$); ΔE_p (mV)		
	$Co_6Se_8{}^HL_6$	**Zn3**$(py)_2$	**1**-tpphz
+3/+4	1.01; 110	-	-
+2/+3	0.57 (0.41); 110 (201)	0.49; 131	-
+1/+2	0.05 (–0.08); 131 (201)	0.12 (–0.05); 181 (180)	–0.02 (irr)
0/+1	–0.63 (–0.69); 110 (191)	–0.37 (–0.67); 121 (190)	–0.65; 122
–1/0	–1.98 (–2.13); 151 (313)	–1.59 (–1.77); 111 (170)	–1.14 (irr)

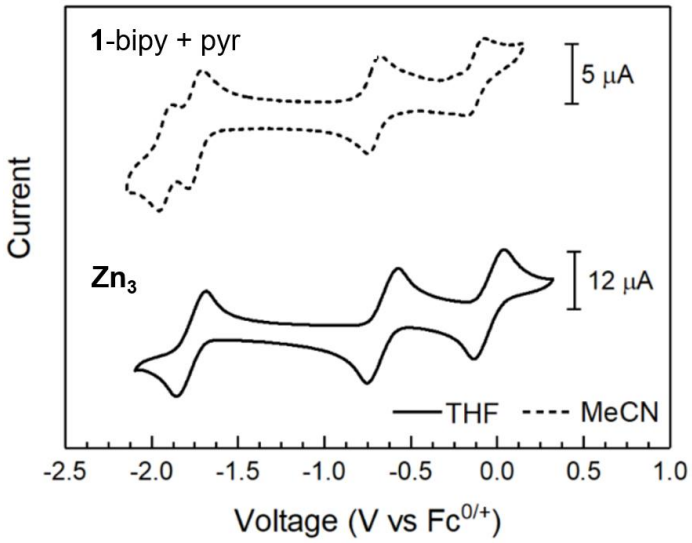

Figure 2.11. Cyclic voltammograms of **Zn**$_3$(py)$_2$ in THF (0.1 M TBAPF$_6$) and the **1**-bipy nanowire digested in pyridine and recorded in MeCN (0.1 M TBAPF$_6$).

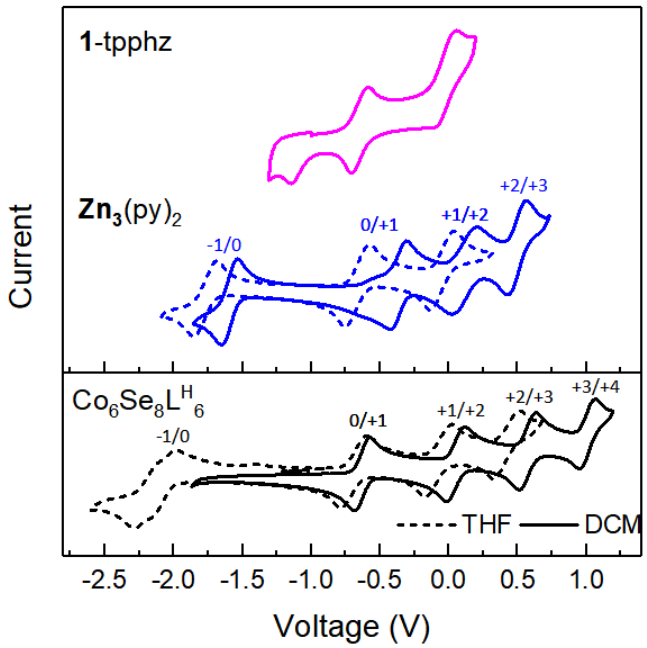

Figure 2.12. Cyclic voltammograms of $Co_6Se_8L^H{}_6$ and **Zn**$_3$(py)$_2$ recorded in DCM (solid) and THF (dashed) solutions with TBAPF$_6$ (0.1 M) at 200 mV/s. Due to the instability of the **1**-tpphz in THF and the limited electrochemical window of DCM, the solid state cyclic voltammogram of **1**-tpphz was recorded in a MeCN solution with TBAPF$_6$ (0.1 M) at 200 mV/s.

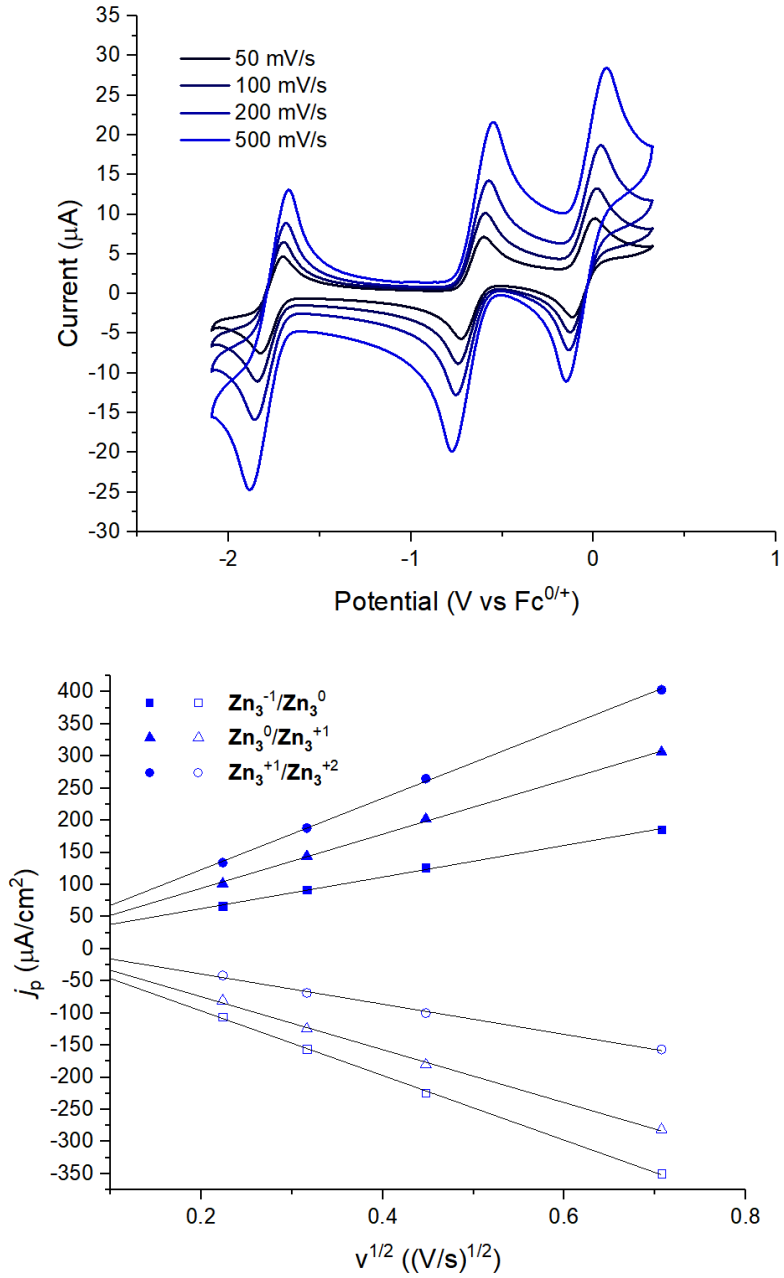

Figure 2.13. Cyclic voltammograms of **Zn$_3$**(py)$_2$ recorded between 50 and 500 mV s^{-1} in THF (0.1 M $TBAPF_6$) and referenced to ferrocene/ferrocenium (top) and plot of current density (j_p) versus the square root of scan rate ($v^{1/2}$) with linear fits used to model the data with the Randels-Sevcik equation (bottom).

2.7 X-RAY DIFFRACTION STUDIES

Single crystals suitable for X-ray analysis were coated in deoxygenated paratone oil and mounted on a 20 µm CryoLoop™ (Hampton Research, 18 mm mount, 0.2 to 0.3 mm loop diameter). Data was collected at –173 °C on a Bruker APEX II single crystal X-ray diffractometer, with a Mo source. Data was integrated and scaled using SAINT, SADABS within the APEX2 software package by Bruker.[4] Solution by direct methods (SHELXT[5] or SIR97[6,7]) produced a complete heavy atom phasing model consistent with the proposed structure. Structures were completed by difference Fourier synthesis with SHELXL.[8–10] Scattering factors are from Waasmair and Kirfel.[11] Hydrogen atoms were placed in geometrically idealized positions and constrained to ride on their parent atoms with C–H distances in the range 0.95–1.00 Å. Isotropic thermal parameters U_{eq} were fixed such that they were $1.2U_{eq}$ of their parent atom Ueq for CHs and $1.5U_{eq}$ of their parent atom U_{eq} in case of methyl groups. All non-hydrogen atoms were refined anisotropically by full-matrix least-squares.

2.7.1 ***Zn$_3$(THF)$_2$***

Thin, dark-red prismatic crystals suitable for X-ray analysis were grown via vapor diffusion of diethyl ether into a saturated solution of **Zn$_3$**(py)$_2$ in THF at room temperature over the course of 5 days. The asymmetric unit contains a full cluster with two of the three zinc atoms bound by THF, and an unbound, disordered THF molecule that was modeled over two positions.

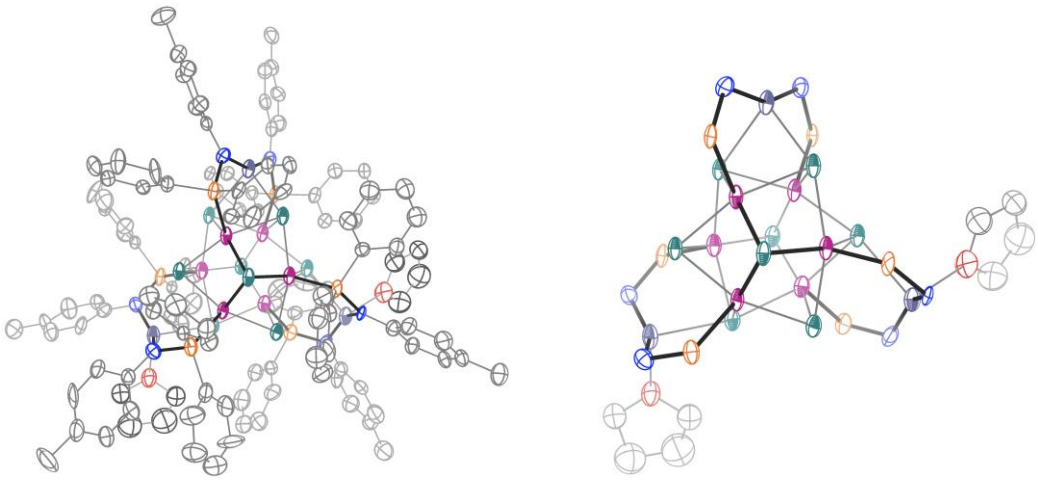

Figure 2.14. Molecular structure of **Zn$_3$**(THF)$_2$ with thermal ellipsoids shown at a 50%

2.7.2 ***Zn$_3$(phen)$_2$***

Dark-red prismatic crystals suitable for X-ray diffraction studies were grown over the course of two days *via* vapor diffusion of diethyl ether into a saturated solution of **Zn$_3$**(phen)$_2$ in THF at room temperature. The asymmetric unit contains two clusters of opposite helical chirality. The phenyl and tolyl groups of three aminophosphines are disordered over two positions.

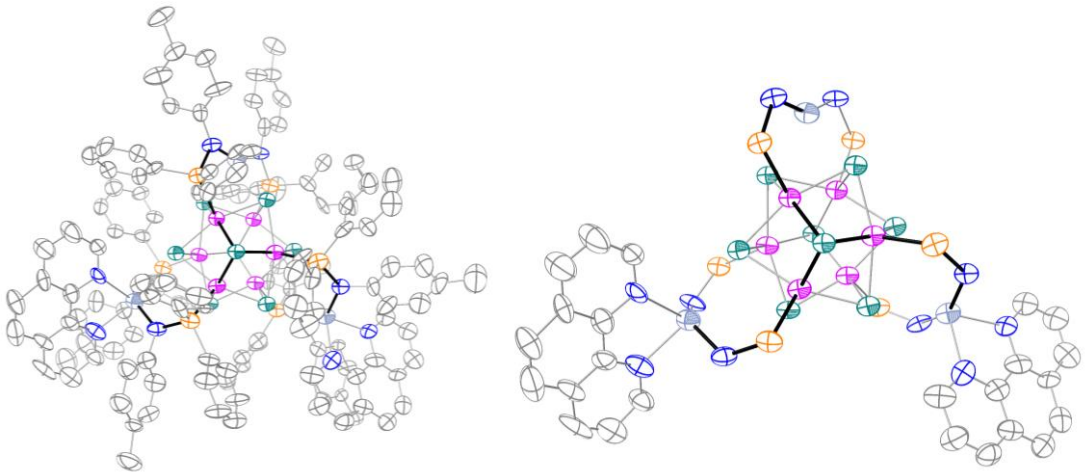

Figure 2.15. Molecular structure of **Zn$_3$**(phen)$_2$ with thermal ellipsoids shown at a 50%

2.7.3 *[**Zn**$_3$(phen)$_3$][PF$_6$]*

Dark-red prismatic crystals were grown *via* vapor diffusion of diethyl ether into a saturation solution [**Zn**$_3$(phen)$_3$][PF$_6$] in acetonitrile at room temperature over the course of two days. The asymmetric unit contains one cluster with a disordered PF_6^- anion, and two acetonitrile molecules and one diethyl ether molecule.

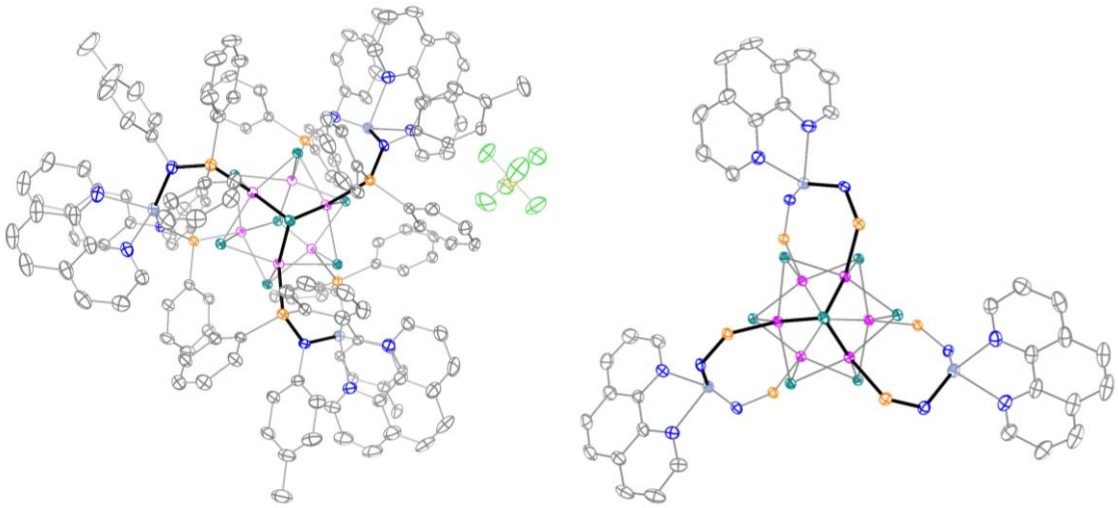

Figure 2.16. Molecular structure of [**Zn**$_3$(phen)$_3$][PF$_6$] with thermal ellipsoids shown at a 50% probability level.

2.7.4 ***1**-bipy*

Dark red prismatic crystals were grown from the reaction mixture at 60 °C over the course of two days. The data was of slightly reduced quality due to possible growth defects, and with some solvent toluene disorder present, a few restraints were required (ISOR on all carbon, nitrogen and DELU on carbon, nitrogen and connecting phosphorous, AFIX 66 on toluene rings, flat and EADP on disordered toluene) and 450 bad reflections were omitted (0.34%).

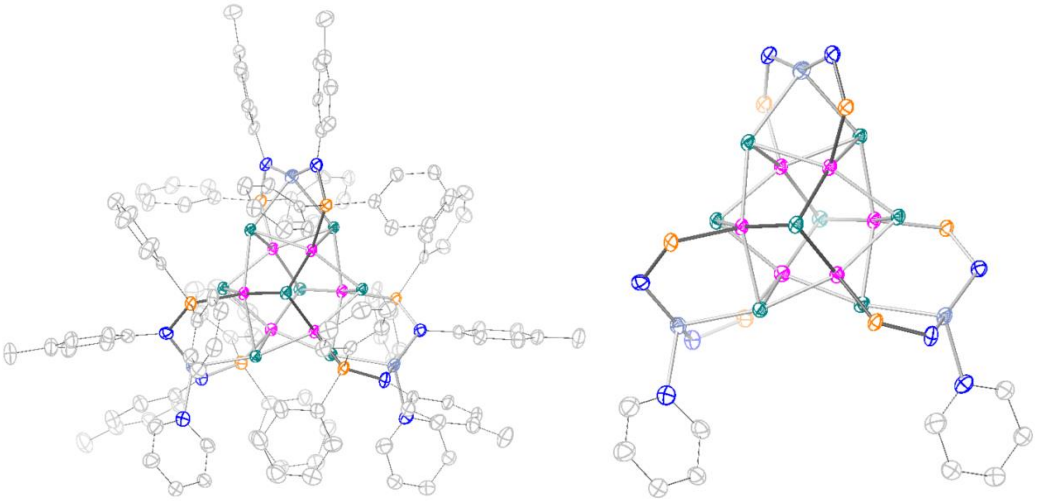

Figure 2.17. Molecular structure of **1**-bipy with thermal ellipsoids shown at a 50% probability level. Hydrogen atoms, disorder, and co-crystallized solvent molecules are omitted for clarity.

2.7.5 ***1*-*tpphz***

Dark red prismatic crystals were grown from the reaction mixture at room temperature over the course of one week. The unit cell contained disordered DCM solvent molecules which were removed with SQUEEZE.[12–14]

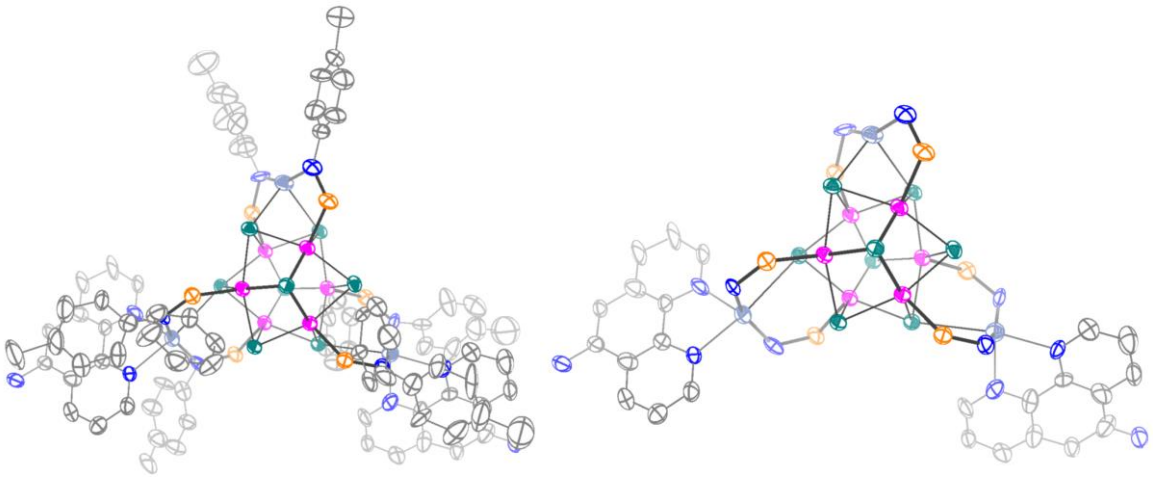

Figure 2.18. Structure of one **1**-tpphz unit with thermal ellipsoids shown at a 50% probability level.

2.7.6 ***2**-bipy*

Data was collected at -173° C on a Nonius Kappa CCD FR590 single crystal X-ray diffractometer, Mo-radiation. Small, dark red, prismatic crystals were grown from the reaction mixture at room temp over the course of 2 days. The contribution of about 18 disordered DCM solvent molecules per asymmetric unit to the diffraction pattern was removed with SQUEEZE (1563eV in voids).[12–14] Two PF_6^- anions were found, where one of which appeared disordered. The structure required several constraints and restraints. All phenyls were optimized with AFIX 66 … AFIX 0 loops. All complex motives aminophosphines were related with the SAME command. All pyridine halves of 4,4'-bipyridines were coupled with SAME. Pyridine moieties required FLAT restraints. Overall, an ISOR for carbons, nitrogen, and fluorine to prevent non-positive definite displacement matrices, and a DELU command including carbons, nitrogen and phosphorous were needed connecting the isotropic displacements along bonds. Some hydrogen atoms came slightly too close to each other which required their distances to be maintained with DFIX (since the data quality did not allow for a more detailed disorder model of phenyls and toluene) and 200 bad reflections were removed. While the small crystal size, the large unit cell (14771(12) $Å^3$), and solvent disorder resulted in weak higher angle scattering.

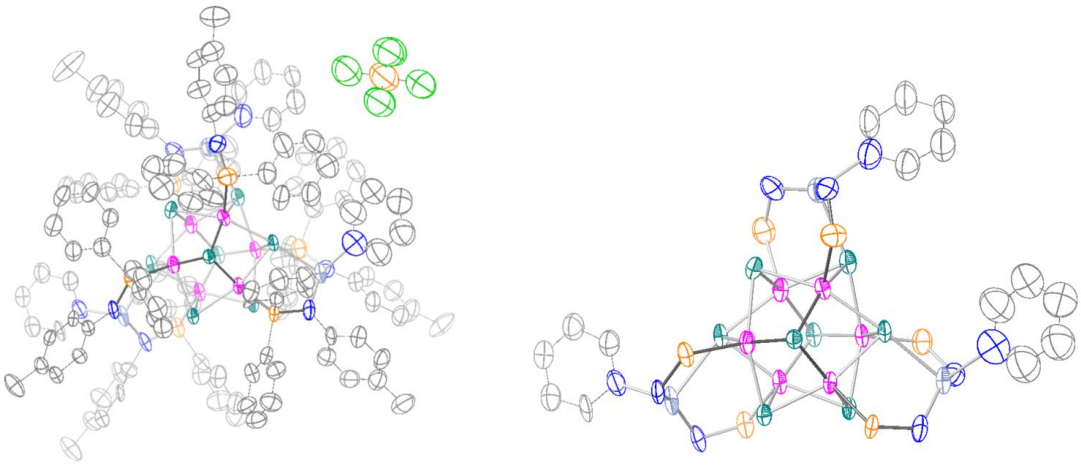

Figure 2.19. Structure of one $\mathbf{Zn_3}(bipy)_{1.5}$ unit with thermal ellipsoids shown at a 50% probability level.

2.7.7 *X-ray Structure Tables*

Table 2.2. Crystallographic data for **Zn$_3$**(THF)$_2$, **Zn$_3$**(phen)$_2$ and [**Zn$_3$**(phen)$_3$][PF$_6$]

Compound	**Zn$_3$**(THF)$_2$ · 2 THF	**Zn$_3$**(phen)$_2$	[**Zn$_3$**(phen)$_3$][PF$_6$]·Et$_2$O·2 MeCN
CCDC number	2102887	2102892	2102890
Empirical formula	$C_{256}H_{260}Co_{12}N_{12}O_7P_{12}Se_{16}Zn_6$	$C_{138}H_{118}Co_6N_{10}P_6Se_8Zn_3$	$C_{158}H_{142}Co_6F_6N_{14}OP_7Se_8Zn_3$
Formula weight	6351.12	3283.61	3765.01
Temperature (°K)	100(2)	100(2)	100(2)
Wavelength (Å)	0.71073	0.71073	0.71073
Crystal system	Monoclinic	Triclinic	Triclinic
Space group	P 2_1/c	P -1	P -1
a (Å)	23.165(4)	16.5919(16)	15.2771(8)
b (Å)	19.118(3)	18.8643(17)	25.6348(14)
c (Å)	28.120(4)	24.195(2)	26.4908(13)
α (°)	90	92.481(6)	117.056(3)
β (°)	92.232(9)	96.376(6)	102.934(3)
γ (°)	90	102.106(6)	95.533(3)
Volume (Å^3)	12444(3)	7560.0(12)	8766.7(8)
Z	2	2	2
ρ^{calc} (g cm^{-3})	1.695	1.442	1.426
Absorption coefficient (mm^{-1})	3.818	3.144	2.736
F(000)	6328	3260	3758
Crystal size (mm^3)	0.080 x 0.070 x 0.040	0.230 x 0.100 x 0.020	0.170 x 0.100 x 0.100
Theta range for data collection (°)	1.381 to 25.123	1.334 to 25.350	1.405 to 28.507
Index ranges	–27≤h ≤ 27, –22≤k≤22, –33≤l≤33	–19≤h≤19, –22≤k≤22, –30≤l≤30	–20≤h≤20, –34≤k≤34, –35≤l≤35
Reflections collected	43602	131590	87063
Independent reflections	22177 [R(int) = 0.1891]	27423 [R(int) = 0.2127]	43852 [R(int) = 0.0463]
Completeness to theta = 25.000°	99.8%	99.3%	99.8%
Data / restraints / parameters	22177 / 1255 / 1470	27473 / 544 / 1619	43852 / 159 / 1890
Goodness-of-fit on F^2	1.012	1.009	1.021
Final R indices [I>2sigma(I)]	R1 = 0.1138, wR2 = 0.2526	R1 = 0.0918, wR2 = 0.2106	R1 = 0.0380, wR2 = 0.0782
R indices (all data)	R1 = 0.2375, wR2 = 0.3103	R1 = 0.2344, wR2 = 02894	R1 = 0.0731, wR2 = 0.0881
Largest diff. peak and hole (e$^-$Å^{-3})	1.856 and –1.603	1.379 and -1.170	0.945 and -0.860

Table 2.3. Crystallographic data for **1**-bipy, **2**-bipy, and **1**-tpphz

Compound	**1**-bipy · 4 toluene	**2**-bipy	**1**-tpphz
CCDC number	2102891	2102888	2102889
Empirical formula	$C_{311}H_{292}Co_{12}N_{16}P_{12}Se_{16}Zn_6$	$C_{258}H_{228}Co_{12}F_{12}N_{18}P_{14}Se_{16}Zn_6$	$C_{138}H_{114}Co_6N_{12}OP_6Se_8Zn_3$
Formula weight	6987.97	6604.89	3307.60
Temperature (°K)	100(2)	100(2)	100(2)
Wavelength	0.71073	0.71073	0.71073
Crystal system	Monoclinic	Triclinic	Triclinic
Space group	P 2_1/n	P -1	P -1
a (Å)	26.093(3)	18.943(9)	19.1661(16)
b (Å)	18.874(3)	28.237(13)	20.5691(16)
c (Å)	30.338(4)	31.465(14)	21.9034(18)
α (°)	90	112.489(11)	69.547(4)
β (°)	106.615(4)	97.563(12)	65.685(4)
γ (°)	90	102.224(12)	86.539(4)
Volume (Å^3)	14317(3)	14771(12)	7337.6(11)
Z	2	2	2
ρ^{calc} (g cm^{-3})	1.621	1.485	1.497
Absorption coefficient (mm^{-1})	3.325	3.234	3.240
F(000)	6996	6536	3280
Crystal size (mm^3)	0.220 x 0.130 x 0.050	0.100 x 0.050 x 0.040	0.140 x 0.070 x 0.070
Theta range for data collection (°)	1.286 to 28.565	0.828 to 25.027	1.502 to 25.027
Index ranges	$-34\leq h\leq 34$, $-25\leq k\leq 25$, $-40\leq l\leq 40$	$-22\leq h\leq 22$, $-32\leq k\leq 32$, $-35\leq l\leq 35$	$-22\leq h\leq 22$, $-24\leq k\leq 24$, $-26\leq l\leq 26$
Reflections collected	133057	51575	50410
Independent reflections	35562 [R(int) = 0.1236]	51575 [R(int) = 0.2341]	25882 [R(int) = 0.1757]
Completeness to theta = 25.000°	98.2%	99.8%	99.8%
Data / restraints / parameters	35562 / 1576 / 1686	51575 / 6364 / 2614	25882 / 97 / 1575
Goodness-of-fit on F^2	1.144	1.012	0.929
Final R indices [I>2sigma(I)]	R1 = 0.1082, wR2 = 0.2726	R1 = 0.1495, wR2 = 0.2958	R1 = 0.0781, wR2 = 0.1631
R indices (all data)	R1 = 0.1508, wR2 = 0.2939	R1 = 0.3551, wR2 = 0.4257	R1 = 0.2194, wR2 = 0.2219
Largest diff. peak and hole (e$^-$Å^{-3})	2.533 and -1.776	2.131 and -1.378	1.258 and -1.033

2.8 REFERENCES

(1) Muetterties, E. L.; Rhodin, T. N.; Band, Elliot.; Brucker, C. F.; Pretzer, W. R. Clusters and Surfaces. *Chem. Rev.* **1979**, *79* (2), 91–137. https://doi.org/10.1021/cr60318a001.

(2) Somorjai, G. A.; Contreras, A. M.; Montano, M.; Rioux, R. M. Clusters, Surfaces, and Catalysis. *PNAS* **2006**, *103* (28), 10577–10583. https://doi.org/10.1073/pnas.0507691103.

(3) Eames, E. V.; Betley, T. A. Site-Isolated Redox Reactivity in a Trinuclear Iron Complex. *Inorg. Chem.* **2012**, *51* (19), 10274–10278. https://doi.org/10.1021/ic301241s.

(4) Petel, B. E.; Brennessel, W. W.; Matson, E. M. Oxygen-Atom Vacancy Formation at Polyoxovanadate Clusters: Homogeneous Models for Reducible Metal Oxides. *J. Am. Chem. Soc.* **2018**, *140* (27), 8424–8428. https://doi.org/10.1021/jacs.8b05298.

(5) Petel, B. E.; Meyer, R. L.; Maiola, M. L.; Brennessel, W. W.; Müller, A. M.; Matson, E. M. Site-Selective Halogenation of Polyoxovanadate Clusters: Atomically Precise Models for Electronic Effects of Anion Doping in VO2. *J. Am. Chem. Soc.* **2020**, *142* (2), 1049–1056. https://doi.org/10.1021/jacs.9b11874.

(6) Coucouvanis, D. Use of Preassembled Iron/Sulfur and Iron/Molybdenum/Sulfur Clusters in the Stepwise Synthesis of Potential Analogs for the Fe/Mo/S Site in Nitrogenase. *Acc. Chem. Res.* **1991**, *24* (1), 1–8. https://doi.org/10.1021/ar00001a001.

(7) Venkateswara Rao, P.; Holm, R. H. Synthetic Analogues of the Active Sites of Iron−Sulfur Proteins. *Chem. Rev.* **2004**, *104* (2), 527–560. https://doi.org/10.1021/cr020615+.

(8) de Ruiter, G.; Thompson, N. B.; Lionetti, D.; Agapie, T. Nitric Oxide Activation by Distal Redox Modulation in Tetranuclear Iron Nitrosyl Complexes. *J. Am. Chem. Soc.* **2015**, *137* (44), 14094–14106. https://doi.org/10.1021/jacs.5b07397.

(9) Champsaur, A. M.; Velian, A.; Paley, D. W.; Choi, B.; Roy, X.; Steigerwald, M. L.; Nuckolls, C. Building Diatomic and Triatomic Superatom Molecules. *Nano Lett.* **2016**, *16* (8), 5273–5277. https://doi.org/10.1021/acs.nanolett.6b02471.

(10) Hernández Sánchez, R.; Champsaur, A. M.; Choi, B.; Wang, S. G.; Bu, W.; Roy, X.; Chen, Y.-S.; Steigerwald, M. L.; Nuckolls, C.; Paley, D. W. Electron Cartography in Clusters. *Angewandte Chemie International Edition* **2018**, *57* (42), 13815–13820. https://doi.org/10.1002/anie.201806426.

(11) Nguyen, A. I.; Darago, L. E.; Balcells, D.; Tilley, T. D. Influence of a “Dangling” Co(II) Ion Bound to a [MnCo $_3$ O $_4$] Oxo Cubane. *J. Am. Chem. Soc.* **2018**, *140* (29), 9030–9033. https://doi.org/10.1021/jacs.8b04065.

(12) McSkimming, A.; Suess, D. L. M. Selective Synthesis of Site-Differentiated Fe4S4 and Fe6S6 Clusters. *Inorg. Chem.* **2018**, *57* (23), 14904–14912. https://doi.org/10.1021/acs.inorgchem.8b02684.

(13) Reed, C. J.; Agapie, T. A Terminal FeIII–Oxo in a Tetranuclear Cluster: Effects of Distal Metal Centers on Structure and Reactivity. *J. Am. Chem. Soc.* **2019**, *141* (24), 9479–9484. https://doi.org/10.1021/jacs.9b03157.

(14) Ye, M.; Thompson, N. B.; Brown, A. C.; Suess, D. L. M. A Synthetic Model of Enzymatic [Fe4S4]–Alkyl Intermediates. *J. Am. Chem. Soc.* **2019**, *141* (34), 13330–13335. https://doi.org/10.1021/jacs.9b06975.

(15) Sridharan, A.; Brown, A. C.; Suess, D. L. M. A Terminal Imido Complex of an Iron–Sulfur Cluster. *Angewandte Chemie International Edition* **2021**, *60* (23), 12802–12806. https://doi.org/10.1002/anie.202102603.

(16) Grabow, L. C.; Hvolbæk, B.; Nørskov, J. K. Understanding Trends in Catalytic Activity: The Effect of Adsorbate–Adsorbate Interactions for CO Oxidation Over Transition Metals. *Top Catal* **2010**, *53* (5), 298–310. https://doi.org/10.1007/s11244-010-9455-2.

(17) Qi, L.; Li, J. Adsorbate Interactions on Surface Lead to a Flattened Sabatier Volcano Plot in Reduction of Oxygen. *Journal of Catalysis* **2012**, *295*, 59–69. https://doi.org/10.1016/j.jcat.2012.07.019.

(18) Shong, B.; Bent, S. F. One-Dimensional Pattern Formation of Adsorbed Molecules on the Ge(100)-2 × 1 Surface Driven by Nearest-Neighbor Effects. *J. Phys. Chem. C* **2013**, *117* (2), 949–955. https://doi.org/10.1021/jp3078503.

(19) Borguet, E.; Dai, H.-L. Probing Surface Short Range Order and Inter-Adsorbate Interactions through IR Vibrational Spectroscopy: CO on Cu(100). *J. Phys. Chem. B* **2005**, *109* (17), 8509–8512. https://doi.org/10.1021/jp040527o.

(20) Krishnamoorthy, A.; Yildiz, B. Quantifying the Origin of Inter-Adsorbate Interactions on Reactive Surfaces for Catalyst Screening and Design. *Physical Chemistry Chemical Physics* **2015**, *17* (34), 22227–22234. https://doi.org/10.1039/C5CP03143E.

(21) Kephart, J. A.; Mitchell, B. S.; Chirila, A.; Anderton, K. J.; Rogers, D.; Kaminsky, W.; Velian, A. Atomically Defined Nanopropeller Fe3Co6Se8(Ph2PNTol)6: Functional Model for the Electronic Metal–Support Interaction Effect and High Catalytic Activity for Carbodiimide Formation. *J. Am. Chem. Soc.* **2019**, *141* (50), 19605–19610. https://doi.org/10.1021/jacs.9b12473.

(22) Kephart, J. A.; Boggiano, A. C.; Kaminsky, W.; Velian, A. Inorganic Clusters as Metalloligands: Ligand Effects on the Synthesis and Properties of Ternary Nanopropeller Clusters. *Dalton Trans.* **2020**, *49* (45), 16464–16473. https://doi.org/10.1039/D0DT02416C.

(23) Kephart, J. A.; Romero, C. G.; Tseng, C.-C.; Anderton, K. J.; Yankowitz, M.; Kaminsky, W.; Velian, A. Hierarchical Nanosheets Built from Superatomic Clusters: Properties, Exfoliation and Single-Crystal-to-Single-Crystal Intercalation. *Chem. Sci.* **2020**, *11* (39), 10744–10751. https://doi.org/10.1039/D0SC03506H.

(24) Mitchell, B. S.; Kaminsky, W.; Velian, A. Tuning the Electronic Structure of Atomically Precise Sn/Co/Se Nanoclusters via Redox Matching of Tin(IV) Surface Sites. *Inorg. Chem.* **2021**, *60* (9), 6135–6139. https://doi.org/10.1021/acs.inorgchem.1c00313.

(25) Monod, J.; Wyman, J.; Changeux, J.-P. On the Nature of Allosteric Transitions: A Plausible Model. *Journal of Molecular Biology* **1965**, *12* (1), 88–118. https://doi.org/10.1016/S0022-2836(65)80285-6.

(26) Changeux, J.-P. 50th Anniversary of the Word "Allosteric." *Protein Science* **2011**, *20* (7), 1119–1124. https://doi.org/10.1002/pro.658.

(27) Cheng, H. F.; d'Aquino, A. I.; Barroso-Flores, J.; Mirkin, C. A. A Redox-Switchable, Allosteric Coordination Complex. *J. Am. Chem. Soc.* **2018**, *140* (44), 14590–14594. https://doi.org/10.1021/jacs.8b09321.

(28) Lifschitz, A. M.; Rosen, M. S.; McGuirk, C. M.; Mirkin, C. A. Allosteric Supramolecular Coordination Constructs. *J. Am. Chem. Soc.* **2015**, *137* (23), 7252–7261. https://doi.org/10.1021/jacs.5b01054.

(29) Lorkovic, I. M.; Wrighton, M. S.; Davis, W. M. Use of a Redox-Active Ligand to Reversibly Alter Metal Carbonyl Electrophilicity. *Journal of the American Chemical Society* **1994**, *116* (14), 6220–6228. https://doi.org/10.1021/ja00093a023.

(30) Cambridge Structural Database. Zn-Se distances. Accessed: 5/27/20. 140 hits. Mean: 2.469 Å, Std Dev: 0.074 Å. Cambridge Structural Database. Zn-Se Distances. Accessed: 5/27/20. 140 Hits. Mean: 2.469 Å, Std Dev: 0.074 Å.

(31) Bruno, I. J.; Cole, J. C.; Edgington, P. R.; Kessler, M.; Macrae, C. F.; McCabe, P.; Pearson, J.; Taylor, R. New Software for Searching the Cambridge Structural Database and Visualizing Crystal Structures. *Acta Cryst B* **2002**, *58* (3), 389–397. https://doi.org/10.1107/S0108768102003324.

(32) Groom, C. R.; Bruno, I. J.; Lightfoot, M. P.; Ward, S. C. The Cambridge Structural Database. *Acta Cryst B* **2016**, *72* (2), 171–179. https://doi.org/10.1107/S2052520616003954.

(33) Champsaur, A. M.; Mézière, C.; Allain, M.; Paley, D. W.; Steigerwald, M. L.; Nuckolls, C.; Batail, P. Weaving Nanoscale Cloth through Electrostatic Templating. *J. Am. Chem. Soc.* **2017**, *139* (34), 11718–11721. https://doi.org/10.1021/jacs.7b07279.

(34) Kephart, J. A.; Romero, C. G.; Tseng, C.-C.; Anderton, K. J.; Yankowitz, M.; Kaminsky, W.; Velian, A. Hierarchical Nanosheets Built from Superatomic Clusters: Properties, Exfoliation and Single-Crystal-to-Single-Crystal Intercalation. *Chem. Sci.* **2020**. https://doi.org/10.1039/D0SC03506H.

(35) Xie, J.; Bu, X.; Zheng, N.; Feng, P. One-Dimensional Coordination Polymers Containing Penta-Supertetrahedral Sulfide Clusters Linked by Dipyridyl Ligands. *Chem. Commun.* **2005**, No. 39, 4916–4918. https://doi.org/10.1039/B508470A.

(36) Vaqueiro, P.; Romero, M. L.; Rowan, B. C.; Richards, B. S. Arrays of Chiral Nanotubes and a Layered Coordination Polymer Containing Gallium–Sulfide Supertetrahedral Clusters. *Chemistry – A European Journal* **2010**, *16* (15), 4462–4465. https://doi.org/10.1002/chem.200903425.

(37) Horwitz, N. E.; Xie, J.; Filatov, A. S.; Papoular, R. J.; Shepard, W. E.; Zee, D. Z.; Grahn, M. P.; Gilder, C.; Anderson, J. S. Redox-Active 1D Coordination Polymers of Iron–Sulfur Clusters. *J. Am. Chem. Soc.* **2019**, *141* (9), 3940–3951. https://doi.org/10.1021/jacs.8b12339.

(38) Wheaton, C. A.; Puddephatt, R. J. A Coordination Polymer of Gold(I) with Heterotactic Architecture and a Comparison of the Structures of Isotactic, Syndiotactic, and Heterotactic Isomers. *Angewandte Chemie International Edition* **2007**, *46* (24), 4461–4463. https://doi.org/10.1002/anie.200701325.

(39) Rasburn, J.; Foucher, D. A.; Reynolds, W. F.; Vancso, G. J. Solid State Polymerization of the Unsymmetrical [1]Ferrocenophane Fe(η-C5H4)2SiMePh; Synthesis of the First Stereoregular Organometallic Polymer. *Chem. Commun.* **1998**, No. 7, 843–844. https://doi.org/10.1039/A801042K.

(40) Ellis, W. W.; Schmitz, M.; Arif, A. A.; Stang, P. J. Preparation, Characterization, and X-Ray Crystal Structures of Helical and Syndiotactic Zinc-Based Coordination Polymers. *Inorg. Chem.* **2000**, *39* (12), 2547–2557. https://doi.org/10.1021/ic991315m.

(41) Bodini, M. E.; Copia, G.; Robinson, R.; Sawyer, D. T. Redox Chemistry of Metal-Catechol Complexes in Aprotic Media. 5. 3,5-Di-Tert-Butylcatecholato and 3,5-Di-Tert-Butyl-o-Benzosemiquinonato Complexes of Zinc(II). *Inorg. Chem.* **1983**, *22* (1), 126–129. https://doi.org/10.1021/ic00143a027.

(42) Shukla, A. D.; Das, A. Redox Responsive Binuclear Complexes Using 5,6-Dihydroxy-1,10-Phenanthroline as a Bridging Ligand: Synthesis, Characterization and Physicochemical Studies. *Polyhedron* **2000**, *19* (26), 2605–2611. https://doi.org/10.1016/S0277-5387(00)00563-5.

(43) Keyes, T. E.; Forster, R. J.; Jayaweera, P. M.; Coates, C. G.; McGarvey, J. J.; Vos, J. G. Modulation of Electronic Coupling across Dioxolene-Bridged Osmium and Ruthenium Dinuclear Complexes. *Inorg. Chem.* **1998**, *37* (22), 5925–5932. https://doi.org/10.1021/ic980293l.

(44) Schmidt, R. D.; Kent, C. A.; Concepcion, J. J.; Lin, W.; Meyer, T. J.; Forbes, M. D. E. A Little Spin on the Side: Solvent and Temperature Dependent Paramagnetism in [RuII(Bpy)2(Phendione)]2+. *Dalton Trans.* **2014**, *43* (47), 17729–17739. https://doi.org/10.1039/C4DT01868K.

(45) Chavan, H. V.; Adsul, L. K.; Bandgar, B. P. Polyethylene Glycol in Water: A Simple, Efficient and Green Protocol for the Synthesis of Quinoxalines. *J. Chem. Sci.* **2011**, *123* (4), 477–483. https://doi.org/10.1007/s12039-011-0081-8.

(46) Wachter, E.; Moyá, D.; Parkin, S.; Glazer, E. C. Ruthenium Complex "Light Switches" That Are Selective for Different G-Quadruplex Structures. *Chemistry – A European Journal* **2016**, *22* (2), 550–559. https://doi.org/10.1002/chem.201503203.

(47) *Bruker APEX2 (Version 2.1-4), SAINT (Version 7.34A), SADABS (Version 2007/4), 2007 BrukerAXS Inc, Madison, Wisconsin, USA.*

(48) *Sheldrick, G.M. Acta Cryst. 2015 A71, 3-8.*

(49) *Altomare, A.; Burla, C.; Camalli, M.; Cascarano, G. L.; Giacovazzo, C.; Guagliardi, A.; Moliterni, A.G.G.; Polidori, G.; Spagna, R. J. Appl. Crystallogr., 1999, 32, 115-119.*

(50) *Altomare, A.; Cascarano, G. L.; Giacovazzo, C.; Guagliardi, A. J. Appl. Crystallogr., 1993, 26, 343-350.*

(51) *Sheldrick, G. M. SHELXL-97, Program for the Refinement of Crystal Structures, 1997, University of Göttingen, Germany.*

(52) *Sheldrick, G. M. Acta Cryst. 2015, C71, 3–8.*

(53) *Mackay, S.; Edwards, C.; Henderson, A.; Gilmore, C.; Stewart, N.; Shankland, K.; Donald, A. MaXus: A Computer Program for the Solution and Refinement of Crystal Structures from Diffraction Data, 1997, University of Glasgow, Scotland.*

(54) *Waasmaier, D.; Kirfel, A. Acta Cryst., 1995, 51, 416-430.*

(55) Spek, A. L. Single-Crystal Structure Validation with the Program PLATON. *J Appl Cryst* **2003**, *36* (1), 7–13. https://doi.org/10.1107/S0021889802022112.

(56) Spek, A. L. Structure Validation in Chemical Crystallography. *Acta Cryst D* **2009**, *65* (2), 148–155. https://doi.org/10.1107/S090744490804362X.

(57) van der Sluis, P.; Spek, A. L. BYPASS: An Effective Method for the Refinement of Crystal Structures Containing Disordered Solvent Regions. *Acta Cryst A* **1990**, *46* (3), 194–201. https://doi.org/10.1107/S0108767389011189.

Chapter 3. METAL-SUPPORT INTERACTIONS IN MOLECULAR SINGLE-SITE CLUSTER CATALYSTS

3.1 ABSTRACT

This study provides atomistic insights into the interface between a single-site catalyst and a transition metal chalcogenide support and reveals that peak catalytic activity occurs when edge/support redox cooperativity is maximized. A molecular platform $MCo_6Se_8(PEt_3)_4(L)_2$ (**1**-M, M = Cr, Mn, Fe, Co, Cu, Zn) was designed in which the active site (M)/support (Co_6Se_8) interactions are interrogated by systematically probing the electronic and structural changes that occur as the identity of the metal varies. All 3d transition metal **1**-M clusters display remarkable catalytic activity for coupling tosyl azide and *tert*-butyl isocyanide, with Mn and Co derivatives showing the fastest turnover in the series. Structural, electronic, and magnetic characterization of the clusters was performed using single crystal X-ray diffraction, ^{1}H and ^{31}P nuclear magnetic resonance spectroscopy, electronic absorption spectroscopy, cyclic voltammetry, and computational methods. Distinct metal/support redox regimes can be accessed in **1**-M based on the energy of the edge metal's frontier orbitals with respect to those of the cluster support. As the degree of electronic interaction between the edge and the support increases, a cooperative regime is reached wherein the support can deliver electrons to the catalytic site, increasing the reactivity of key metal-nitrenoid intermediates.

3.2 INTRODUCTION

Tuning metal/support interactions represents a powerful strategy to modulate catalytic activity, making supported single-site catalysts that harness these effects an active frontier of research.[1–7] The electronic and geometric interactions with the atoms of the support can critically impact the performance of the active site, particularly when the support is chemically non-innocent as is the

Reproduced in part with permission from:
Mitchell, B. S.; Chirila, A.; Kephart, J. A.; Boggiano, A. C.; Krajewski, S. M.; Rogers, D.; Kaminsky, W.; Velian, A. *J. Am. Chem. Soc.* **2022**, *144* (40), 18459–18469.

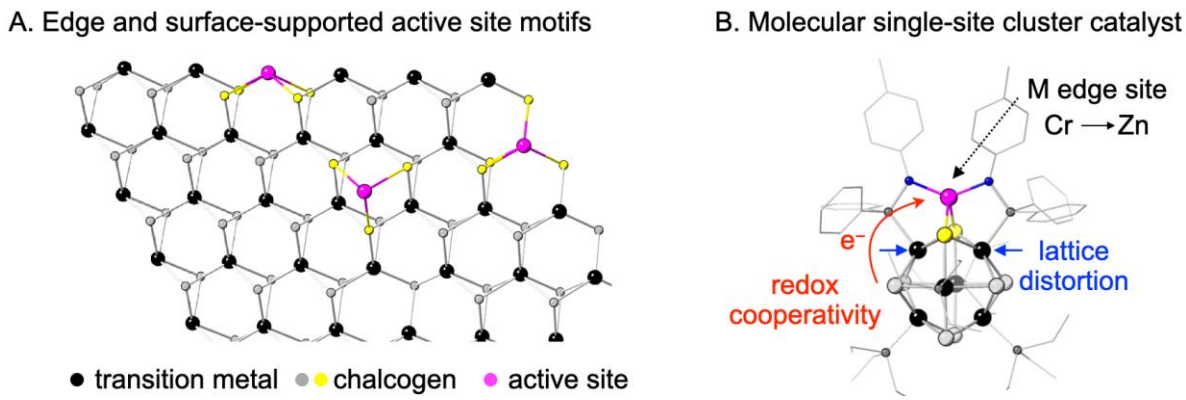

Figure 3.1. A) Types of edge and surface-supported active sites on a layered transition metal chalcogenide support. B) Single-site, atomically precise platform designed to study the electronic and structural changes at the metal/support interface, and their effects on catalytic activity.

case for transition metal chalcogenides.[8] For instance, the coordination environment of single Rh atoms installed at edge vacancies of MoS_2 nanosheets, as well as charge transfer between the active sites and the support impart optimal stability and high selectivity for aldehyde hydrogenation.[9] In a more molecularly-inspired approach, tuning the number of bonds between surface-anchored Co active sites and the WS_2 nanosheet support facilitates increased activity for electrochemical oxygen reduction.[10] More broadly, the interaction between surface or edge metal dopants and layered transition metal dichalcogenide supports has been extensively investigated in the context of identifying catalysts for industrially relevant processes, such as hydrotreatment and hydrogen evolution (Figure 3.1A).[11] In these materials metal dopants can serve as new catalytic centers,[9,10] or alter the activity of native sites indirectly, for example by engaging in charge transfer[12–14] or by inducing structural changes within the support.[15] However, the role of the metal dopant is complex and varies with the chemical transformation,[16,17] substrate identity,[18] and material morphology,[19–22] among other factors[23,24] precluding the determination of clear-cut structure-function relationships.

In contrast, coordinative non-innocence and electronic cooperativity between the ligand sphere and an active site have been extensively utilized and studied in molecular platforms.[25,26] For example, systematically tuning the identity of the metals in a simplified, bimetallic platform enabled exquisite insights into the role of the supporting metal center in modulating substrate binding, activation, and catalytic performance at the active site.[27–29] Extending this molecular

approach to investigate constructs that embody the complexities of a heterogenous active site could offer new perspectives for controlling catalytic activity or selectivity using metal/support interactions.

Due to their synthetic tunability and homogeneous nature, atomically precise nanoclusters are advantageous for this purpose and can serve as both functional models and as platforms for new catalyst development.[30,31] Examples of molecular clusters that feature metal/support architectures exist,[32–36] such as the catalytically competent $Au_n(SR)_m$ clusters in which the reactive surface gold atoms are chemically distinguished from those of the cluster core.[37] While tuning cluster size[38–40] and the coordination environment[41] of the active sites has been shown to modulate their catalytic activity, studies that identify the active site and systematically correlate how its identity impacts the metal/support interaction and the emerging catalytic activity have yet to materialize. To this end, our group has developed a class of nanoclusters (**M**$_3$; $M_3Co_6Se_8L_6$, M = Cr, Fe, Co, Zn, $SnMe_2$, L = $PPh_2N^{(-)}Tol$, Ph = phenyl, Tol = 4-tolyl) which feature three edge metals, M, anchored on the atomically precise Co_6Se_8 cluster.[42–46] This construct resembles edge- and surface-metals supported on transition metal chalcogenides, but their homogeneity enables the use of molecular characterization techniques. In **M**$_3$, the substrate-accessible edges facilitate not only catalytic activity[42,45] and dimensional control over nanomaterial growth,[43,44] but also provide atomic level insights into the evolution of the active sites under catalytic conditions, and their interconnected reactivity.[45]

Herein, the metal (M)/support (Co_6Se_8) interactions are interrogated by systematically probing the electronic and structural changes that occur at this interface as the identity of the metal varies in the 3d period. The role of the metal/support cooperativity in modulating reactivity is explored in the context of catalytic nitrene transfer. To this end, a single-site cluster platform $MCo_6Se_8(PEt_3)_4(L)_2$ (**1**-M, M = Cr, Mn, Fe, Co, Cu, Zn) was designed to i) circumvent the complexities of multi-site dynamics present in **M**$_3$, and ii) enable systematic modification of the edge metal identity (Figure 3.1B). This study reveals that distinct metal/support redox regimes can be accessed in **1**-M based on the energy of the edge metal's frontier orbitals with respect to those of the cluster support. As the degree of electronic interaction between the edge and the support increases, a cooperative regime is reached wherein the support can deliver electrons to the catalytic site, increasing the reactivity of key metal-nitrenoid intermediates. By using a cluster as a support,

this work provides an atomic level picture into how these effects manifest in a heterogenous single-site catalyst, and illustrates how metal/support interactions can be used to facilitate catalysis.

3.3 Synthesis of single-site clusters **1**-M (M = Cr, Mn, Fe, Co, Cu, Zn)

Site-differentiation of a cluster with chemically degenerate surface sites is a challenging synthetic pursuit. Successful strategies to accomplish this include stoichiometric control of reagents,[47–50] engineering sophisticated or very bulky ligand frameworks,[32,51,52] or by relying on allosteric effects between multiple edge sites.[44] Here, the synthesis of clusters with a single active site relies on access to isomerically pure samples of the site-differentiated cluster *cis*-$Co_6Se_8(PEt_3)_4(CO)_2$, in which two carbonyl groups localized on *cis*-cobalt sites can be precisely displaced by nucleophiles without scrambling on the cluster surface.[49] Photolysis of the *cis*-carbonyl cluster in the presence of excess aminophosphine $Ph_2PN(H)Tol$ (L^H) results in the formation of *cis*-$Co_6Se_8(PEt_3)_4(L^H)_2$ (**1**-H_2; 84% isolated yield; Scheme 3.1). The metalloligand **1**-H_2 features one well-defined binding site poised to anchor a single metal to the surface of the Co_6Se_8 support via amide chelation and up to two hemilabile M–Se interactions. Deprotonation of the aminophosphines of **1**-H_2 with *n*-butyllithium and subsequent treatment with the salt of a divalent metal (M^{2+} = Cr^{2+}, Mn^{2+}, Fe^{2+}, Co^{2+}, Cu^{2+} or Zn^{2+}) leads to the formation of a single new species identified as the monometallated cluster $MCo_6Se_8(PEt_3)_4(L)_2$ (**1**-M; 71-96% yield). With the exception of **1**-Cr(Sol) (Sol = THF, py) the monometallated clusters are isolated without bound exogenous ligands, which is in contrast to their trimetallated counterparts, typically isolated as solvent adducts $\mathbf{M_3}(Sol)_x$ (M = Cr, Fe, Co, Zn) despite their identical coordination environment at M.[42–45] This apparent lower affinity for

Scheme 3.1. Synthesis of single-site clusters.

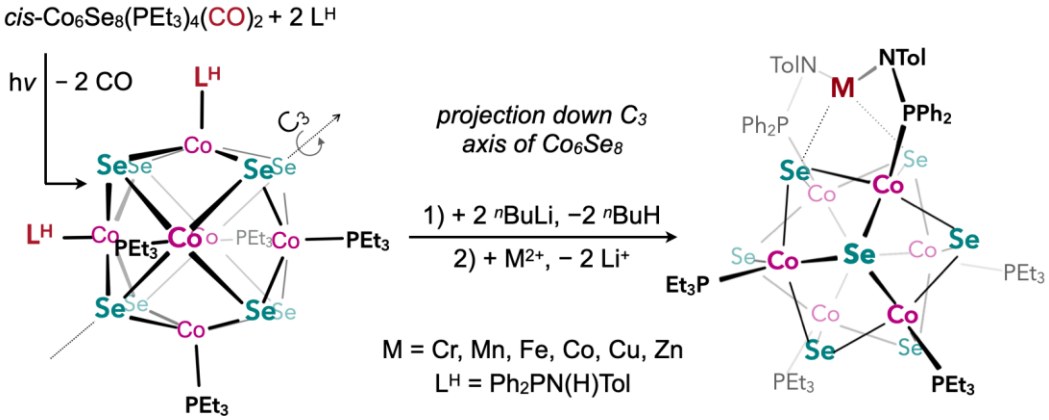

ligands is likely a consequence of the more electron rich Co_6Se_8 core in the **1**-M series,[53] which features just one Lewis acidic metal on its surface, and four electron donating triethylphosphine groups.

3.4 Trends in Catalytic Activity

Transition metal catalyzed N-group transfer is an attractive method to selectively and efficiently form carbon-nitrogen bonds.[54,55] We previously discovered that **Fe$_3$** and **Cr$_3$**(py)$_3$ are excellent catalysts for the coupling of tosyl azide (TsN_3) and *tert*-butyl isocyanide (^{t}BuNC) to form the asymmetric carbodiimide TsNCN^{t}Bu, therefore this transformation was used to benchmark the relative reactivity of the **1**-M series. Here, we discovered that all the monometallated clusters catalyze this transformation at room temperature with 1 mol% catalyst loading, whereas **1**-H_2 shows negligible activity (Figure 3.2; Figure 3.16). Inspecting the kinetic profiles of the homologues, **1**-Mn stands out as the most efficient catalyst with 50% conversion ($t_{1/2}$) achieved in just 5 min, followed by **1**-Co (10 min), **1**-Fe (22 min), **1**-Cr(py) (53 min) and **1**-Cu (66 min), respectively. In contrast to the other clusters, the conversion profile of **1**-Zn features a slow

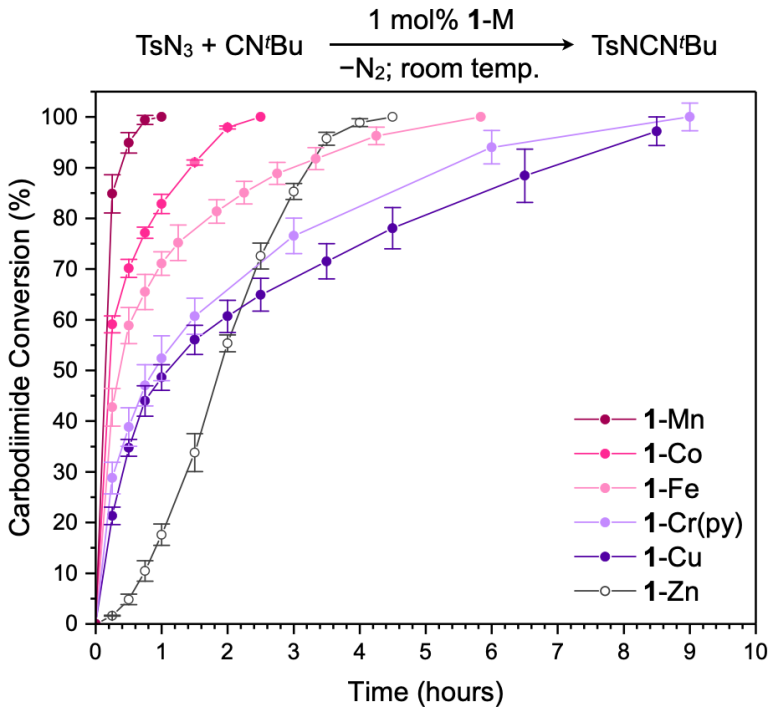

Figure 3.2. Catalytic conversion of carbodiimide (TsNCN^{t}Bu) with 1 mol% loading of **1**-M cluster. Conversion determined by ^{1}H NMR integrations of the product and reactants.

induction period followed by a very active catalytic regime, suggesting a different catalytic pathway is at play than in the other clusters, likely associated with a loss of structural integrity of the Zn/Co_6Se_8 construct. To assess the stability of the **1**-M clusters during this transformation, we analyzed the post-catalytic reaction mixtures using ^{1}H NMR spectroscopy at 10% **1**-M loading (Figure 3.18). Under these conditions, **1**-Co is completely regenerated. Although only ca. 60% of **1**-Fe is recovered upon substrate depletion, the remaining 40% is accounted for by the formation of a single new species, ostensibly the iron amido complex **1**-Fe(NHTs) (Figure 3.17). Some cluster fragmentation likely occurs for **1**-Zn and **1**-Cu where NMR analysis indicates that the resulting reaction mixture contains multiple unidentified species in addition to some recovered **1**-M cluster (17 and 23%, respectively). The spectroscopic analysis of the **1**-Cr and **1**-Mn samples does not suggest cluster degradation, but the broad, paramagnetic features of these clusters make a quantitative NMR analysis unreliable. While an extensive investigation into the speciation of the clusters under catalytic conditions is beyond the scope of this study, we point out that the trimetallated derivatives **Fe$_3$** and **Cr$_3$**$(py)_3$ catalyze this transformation without any observable cluster decomposition.[42,45] Carbodiimide formation typically occurs via the formation of metal-nitrenoid intermediates.[54,56–58] The recent isolation of catalytically competent metal-imido nanocluster intermediates (e.g. **Cr$_3$**$(NTs)_3$) demonstrated this is the case for the chromium derivative, confirming that the three edge sites are indeed catalytically active and that the edge/support construct is viable under catalytic conditions.[45]

3.5 Structural Analysis via Single Crystal X-ray Diffraction

Single crystal X-ray diffraction analysis of the **1**-M cluster series reveals that three different coordination geometries can be distinguished at the edge sites depending on the chemical identity of M (Figure 3.3A, B). The Mn, Fe, Co, and Zn edges feature distorted tetrahedral geometries, and are chelated κ^4 by the cluster via two amides and two Se atoms. Although the Ni congener has proven challenging to isolate experimentally, its geometry and electronic structure were modeled in silico and found to adopt a similar pseudo-tetrahedral edge coordination (Section S.8). In the Cr variant, characterized in the solid state as a THF adduct, the edge site features a pseudo-square pyramidal geometry similar to that observed for the trimetallated analogue **Cr$_3$**$(py)_3$, with one short and one long Cr–Se bond (2.581(6) and 2.772(7) Å).[45] In contrast, the edge site does not engage in bonding with Se in **1**-Cu (Cu….Se > 2.792(5) Å). The nearly linear N–Cu–N bond angle (ca.

173°) is a mark of Cu^{1+} and suggests that upon metallation with the Cu^{2+} salt an intramolecular electron transfer occurs between the edge and the support that gives rise to a $Cu^{1+}/Co_6Se_8^{1+}$ complex. A contraction in the Co…Co distances within the Co_6Se_8 core, typically associated with mono-oxidation,[59] is indeed observed in **1**-Cu (Figure 3.3C). Electrochemical, magnetic and nuclear magnetic resonance (NMR) data, as well as density functional theory (DFT) analysis also support this interpretation, as discussed in later sections. Monometallation gives rise to systematic distortions within the Co_6Se_8 core (Figure 3.3C, Table 3.5). These are primarily localized at the MCo_2Se_2 edge where the most striking change brought upon installing the edge site is an increased interatomic separation of the two Se atoms. The MCo_2Se_2 edge features elongated Co—Se bonds and contracted Co...Co distances compared to the rest of the Co_6Se_8 core, where the distortion trends are reversed such that overall the average metrics of the nonmetallated clusters (i.e. $Co_6Se_8L^H{}_6$ and $Co_6Se_8(PEt_3)_4(CO)_2$) are preserved. Comparison of the M…Se interatomic distances in the **1**-M series to the average distance for M–Se single bond in the Cambridge Structural Database suggests that the edge metal is bound strongest to the Se in the Mn and Co derivatives, followed by the Cr, Fe and Zn complexes, whereas no Cu…Se bonding interactions are present in **1**-Cu.[60–62]

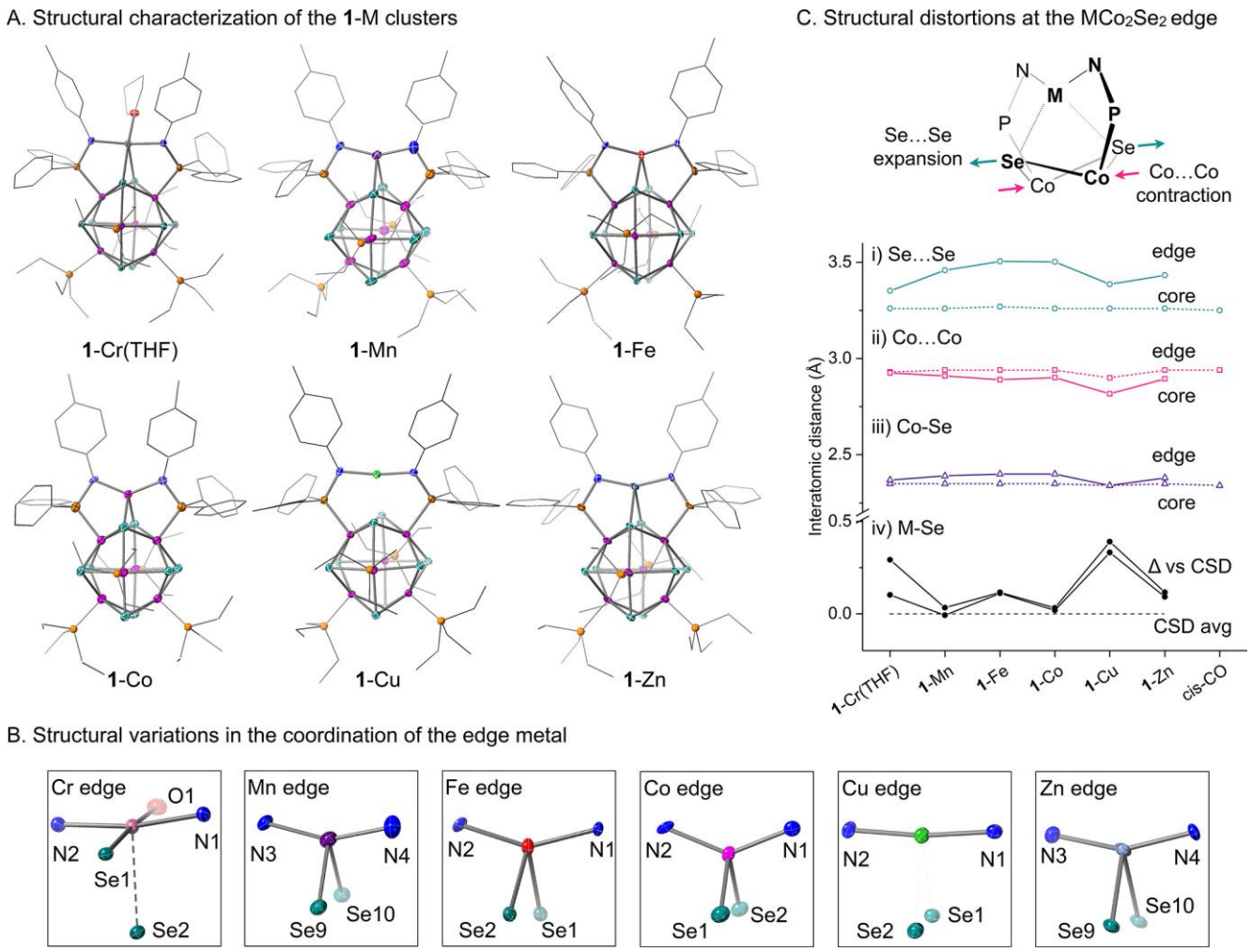

Figure 3.3. A) Single crystal X-ray structure of **1**-Cr(THF), **1**-Mn, **1**-Fe, **1**-Co, **1**-Cu, and **1**-Zn. Ellipsoids are plotted at 50% probability, and carbon backbones are depicted as wireframes. Disorder, hydrogen atoms and co-crystallized solvent molecules are omitted for clarity. B) Zoom ins on the edge site first coordination sphere. C) (i-iii) Edge (MCo_2Se_2) and core (Co_6Se_8) structural distortions upon monometallation. (iv) The deviation of the two M-Se interatomic distances from the average M-Se value reported in the Cambridge Structural Database.

3.6 Electronic Structure Investigations: magnetic moments, electronic absorption, and cyclic voltammetry

The magnetic response of the **1**-M nanoclusters was probed by solution phase magnetic susceptibility measurements using the Evans method.[63] The parent **1**-H_2 cluster is diamagnetic,[64] and remains closed-shell upon monometallation with zinc. **1**-Cr(py), **1**-Mn, **1**-Fe and **1**-Co are paramagnetic with effective magnetic moments of 4.6(3), 5.4(3), 4.9(3), and 3.8(3) μ_B, respectively, close to those expected for high-spin M^{2+} edge sites with S = 2, 5/2, 2 and 3/2. The high-spin state of the edge metals in **1**-Mn, **1**-Fe and **1**-Co is consistent with the pseudo-tetrahedral coordination environment enforced by the cluster support, and is in agreement with earlier investigations into the electronic structure of **Fe3** and **Co3**$(py)_3$ reported by our group.[42,43,53] DFT calculations predict that while most of the spin (64-90%) is localized on the edge metal's 3*d* orbitals in **1**-Cr(py), **1**-Mn, **1**-Fe, **1**-Co, and **1**-Ni, there is a contribution from the cobalt core (5-19%) which indicates some spin mixing between the paramagnetic edge metals and the Co_6Se_8 support (Figure 3.4, Table 3.6).[65] In contrast, the entirety of the spin density calculated for **1**-Cu is

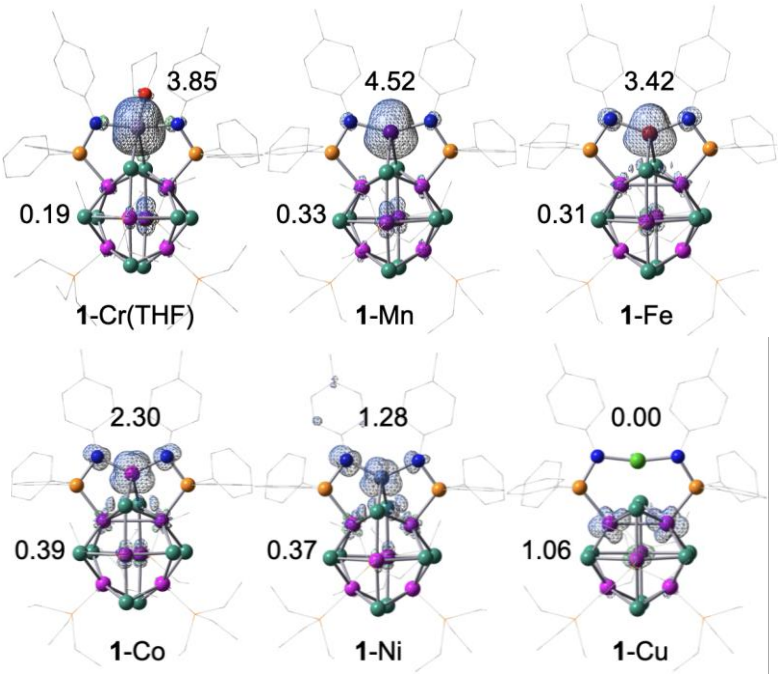

Figure 3.4. Mulliken spin density (α-β) plots of **1**-M series calculated at uB3LYP+/cc-pVTZ level of theory. Spin density values for the edge "M" and Co_6Se_8 core are included. Surfaces plotted at an isovalue of 0.004.

localized on the Co_6Se_8 support, which is in line with the proposed redistribution of charge between the edge and support that results in a diamagnetic Cu^{1+} site and a mono-oxidized S = 1/2 $[Co_6Se_8]^{1+}$ cluster core. Experimentally, **1**-Cu has an effective magnetic moment of 1.8(3) μ_B, which cannot be used to distinguish between $Cu^{1+}/[Co_6Se_8]^{1+}$ and $Cu^{2+}/[Co_6Se_8]^{0}$. It is interesting to note that the predicted distribution of the unpaired electrons in **1**-Cu is not uniform in the cluster core but is concentrated on the cobalt centers closest to the copper edge site. The localization of lattice distortion and spin closest to the edge site mirrors experimental observations and theoretical models for the interfacial perimeter in heterogeneous metal/support constructs.[4]

Electronic absorption spectroscopy and electrochemical measurements reveal that the electronic interaction between the edge and core is greatest in **1**-Fe, **1**-Co, and **1**-Cu, whereas metallation with Cr, Mn and Zn does not perturb the electronic structure of the metalloligand **1**-H_2 significantly (Figure 5). In **1**-Fe, **1**-Co, and **1**-Cu, the three characteristic UV absorption bands of the Co_6Se_8 core broaden, and the absorption in the visible and near IR spectral range intensifies significantly. For example, at 650 nm, the **1**-Cu derivative has an absorption coefficient of 6400 cm^{-1} M^{-1}, more than double that of **1**-H_2 (Figure 3.5C). Similar, but more pronounced electronic changes associated with edge/core interactions have been observed in the trimetallated analogues.[42] The increased absorption in the visible and IR range indicates decreased HOMO/LUMO gaps, which is corroborated by electrochemical analysis (Figure 3.5A). In contrast, the electronic absorption spectra of **1**-Cr(py), **1**-Mn, and **1**-Zn trace closely with that of **1**-H_2, with only a very small redshift in the absorption (< 5 nm) suggesting these metals have minimal influence on the electronic structure of the cobalt core.

Electrochemical analysis reinforces the trends observed in the optical spectra (Figure 3.5A, B). Cyclic voltammetry reveals that monometallation induces a narrowing of the HOMO/LUMO gap in **1**-Fe, **1**-Co and especially in **1**-Cu, whereas in **1**-Zn, **1**-Cr(py) and **1**-Mn it remains nearly identical to that of **1**-H_2. Here, the HOMO/LUMO gaps are estimated from the energetic difference between the first oxidation and first reduction events in tetrahydrofuran (THF). Overall, the **1**-M clusters retain rich redox profiles that are reminiscent of the metalloligand **1**-H_2, itself featuring four chemically reversible one-electron oxidations and one irreversible reduction. Notably, upon metallation the first reduction becomes chemically reversible for all derivatives except **1**-Mn and is stabilized in the series Mn < Fe < Co << Cu.

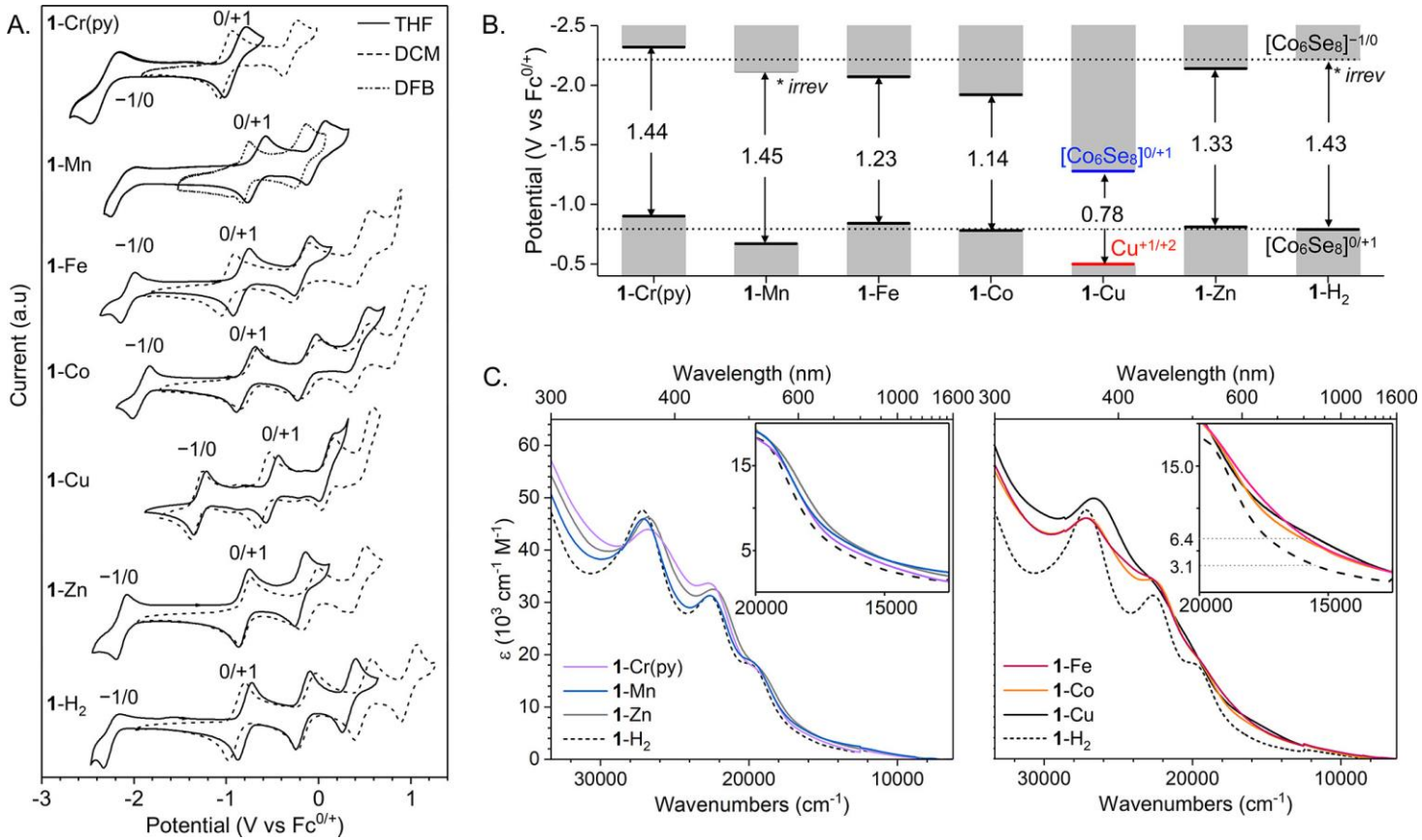

Figure 3.5. A) Cyclic voltammograms of **1**-M series recorded in 0.1 M solutions of $[(^{n}Bu)_4N]PF_6$ in tetrahydrofuran (THF), dichloromethane (DCM), or 1,2-difluorobenzene (DFB) at a scan rate of 200 mV/s and referenced to ferrocene/ferrocenium redox couple. B) Relative potentials of the HOMO/LUMO levels for each of the homologues in the **1**-M series, estimated from the 0/+1 and 0/−1 events in THF. C) Electronic absorption spectra collected in THF for the **1**-M series (left, M = Cr(py), Mn, Zn; right, M = Fe, Co, Cu) plotted vs the spectrum of **1**-H_2. Insets feature zoom-ins of the absorption in the visible and near-IR range. The extinction coefficient of **1**-Co was not measured.

Overall, the effect of monometallation on the electronic structure is proportional to the extent of structural distortion the edge site inflicts on the Co/Se cluster (Figure 3.3C). Thus, little electronic and structural distortions are observed for **1**-Cr, whereas in **1**-Fe and **1**-Co the decreased HOMO/LUMO gaps and redshift in the electronic absorption compared to **1**-H_2 are accompanied by pronounced structural distortions and increased M–Se interaction strength. Exceptions to this trend are the d^5 and d^{10} derivatives **1**-Mn and **1**-Zn, which feature structural distortions and relatively short M—Se bonding interactions but have HOMO/LUMO gaps and electronic absorption spectra resembling those of the parent ligand.

3.7 Paramagnetic ^{31}P NMR Spectroscopy Reports on the Electronic Structure of **1**-M

The chemically differentiated phosphines in **1**-M make them excellent reporters on the local electronic microenvironments. The ^{31}P NMR chemical shifts of the triethylphosphine ligands capping four of the six cobalt sites in Co_6Se_8 report directly on the support. The amidophosphines

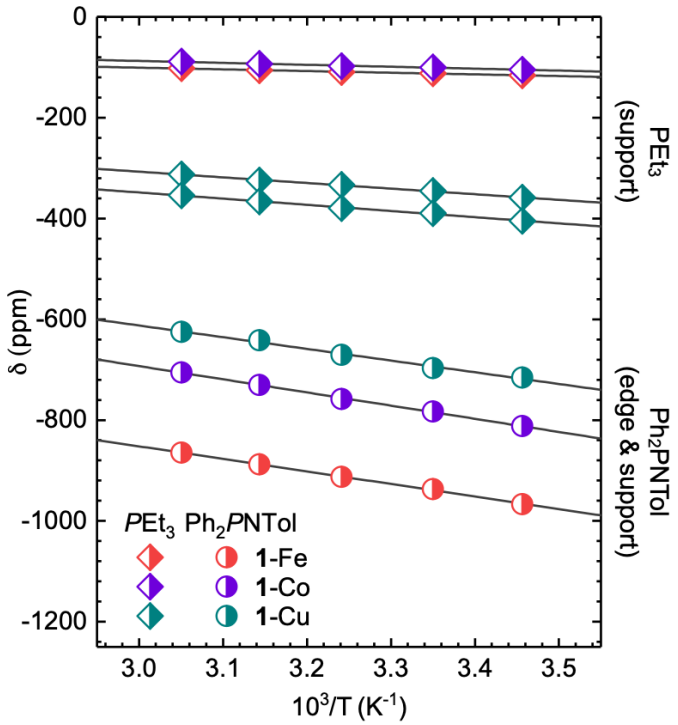

Figure 3.6. Curie behavior of **1**-Fe, **1**-Co and **1**-Cu reflected in the linear dependence of the ^{31}P NMR chemical shifts with inverse temperature in the 290 to 330 K range.

cap the remaining two cobalt centers in the cluster, but also directly anchor the surface metal, therefore informing on both the edge and the support.

While no ^{31}P NMR signals were detected for the Cr and Mn derivatives, **1**-Fe, **1**-Co, **1**-Cu, and **1**-Zn display diagnostic chemical shifts. The observed experimental chemical shift of a paramagnetic compound (δ_T^{obs}) is the sum contribution of the diamagnetic (δ^{dia}) and paramagnetic (δ_T^{para}) components, of which only the latter is temperature (1/T) and spin dependent (Equation 3.1).[66–68] The diamagnetic **1**-Zn cluster has chemical shifts similar to those of the free ligand. Meanwhile, the paramagnetic variants reveal a linear dependence of the ^{31}P NMR chemical shifts with the inverse of temperature (Figure 3.6). As the spin state of the clusters increases in the **1**-Cu (S = ½), **1**-Co (S = 3/2), **1**-Fe (S = 2) series, the ^{31}P chemical shifts associated with the amidophosphine become more negative (−663, −796, and –956 ppm, respectively). Spatially removed from high spin metal edge sites, the chemical shifts of the PEt_3 capping ligands are very similar for **1**-Fe and **1**-Co (−113, −98 ppm, respectively) where the Co_6Se_8 core is expected to stay diamagnetic. In contrast, they shift dramatically in **1**-Cu (−354, −400 ppm), corroborating our hypothesis that the cluster core is mono-oxidized (S = ½). While the C_{2v} cluster symmetry gives rise to two distinct PEt_3 environments in **1**-M, these are only resolved by ^{31}P NMR spectroscopy for the **1**-Cu derivative. We attribute this to the localization of the charge on the cobalt atoms proximal to the edge site, as predicted by DFT (Figure 3.4).

3.8 Calculated Electronic Structures

DFT calculations carried out at the uB3LYP+/cc-pVTZ level of theory closely reproduce structural and electrochemical experimental data of **1**-M (Figure 3.33).[69–72] Considering the large number of electronic states, the energetic overlap and relative contributions of the edge and core atoms to the valence orbitals and lowest energy unoccupied levels in the **1**-M clusters are more clearly visualized using density of states plots.[73] Inspecting Figure 3.7, we note that the energy of the d orbitals decreases in the atomic series Cr, Mn, Fe, Co and Ni.[12,74,75] This manifests at the LUMO levels where the edge metal contribution increases across the series, eventually peaking at Ni, where the first reduction is predicted to be primarily nickel, not Co_6Se_8-centered. The predicted increase in the edge metal contribution at the LUMO level correlates directly with the lowering in energy observed experimentally for the 0/−1 electrochemical reduction (Figure 3.5A). As expected, calculations reveal that there is no contribution to the LUMO levels from the d^{10} Zn^{2+}

and Cu^{1+} edges. **1**-Cu is electronically different from the rest of the series. Corroborating the structural, magnetic, NMR, and electrochemical data, DFT calculations predict that the HOMO level is localized on the Cu^{1+} edge site. Additionally, they reveal that the low-lying LUMO level is associated with the mono-oxidized core $[Co_6Se_8]^{1+}$, explaining the markedly lower 0/−1 reduction potential measured for **1**-Cu.

3.9 Deconstructing Edge/Core Cooperativity in **1**-M

The Co_6Se_8 cluster core ostensibly modulates the reactivity of the edge site by engaging in hemilabile edge–Se interactions on demand, or by providing electrons (or holes) to the reaction site. Empirically, the strength of the edge/core interaction in the **1**-M pre-catalysts is found to track linearly with the catalytic activity, such that the species with the shortest M–Se bonds in the solid state are also the most active catalysts (**1**-Mn > **1**-Co > **1**-Fe > **1**-Cr > **1**-Cu). This apparent trend in reactivity is illustrated in Figure 3.32 where the deviation of the edge M–Se bond lengths from the corresponding average values extracted from the Cambridge Structural Database,[60–62] is plotted against the observed catalytic activity for carbodiimide formation. We hypothesize that as the edge/support (M–Se) interaction becomes stronger, the edge/nitrenoid (M–NTs) interaction

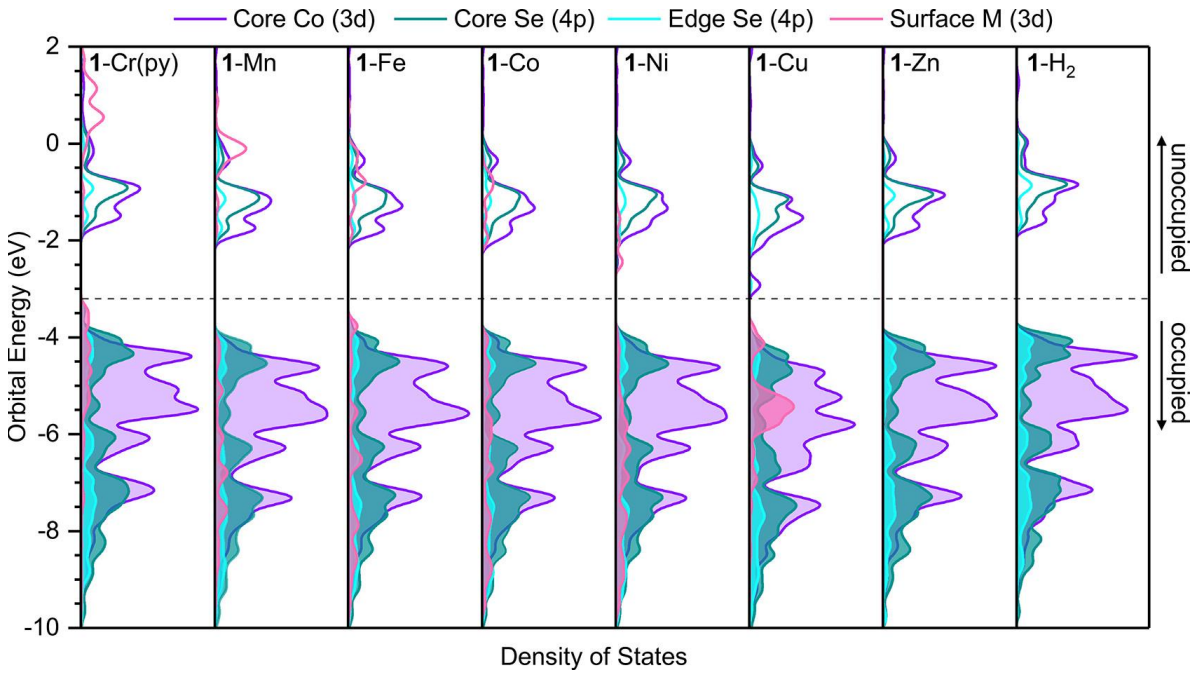

Figure 3.7. Partial density of states plots of **1**-M series calculated at uB3LYP+/cc-pVTZ level of theory.

weakens thereby becoming more reactive. Earlier studies into the trimetallated $\mathbf{M_3}$ nanoclusters corroborate this claim by revealing a strong interdependence in the substrate/edge site/support interaction dynamics.[42,44] For example, in the trichromium nanocluster $\mathbf{Cr_3}$, a catalyst for carbodiimide formation, edge sites that engage in stronger Cr–Se bonding interactions with the support form weaker edge/substrate (Cr–NTs) interactions,[45] although for this system the kinetic implications of this coordinative interplay could not be separated from isocyanide binding equilibria at the Cr(NTs) edge. In the **1**-M series, isocyanide binding is low for Zn, Cu, and Fe, intermediate for Mn and Co, and high for Cr, however, since the mechanism and rate determining step for each of these species is expected to vary, extracting direct correlations to catalytic activity is tenuous (Section 3.16). Ultimately, it is important to note that this trend in reactivity (Mn > Co > Fe > Cr > Cu) could also reflect the intrinsic periodic differences in reactivity of the 3d edge metal. For example, experimentally determined bond dissociation energies for metal-oxo fragments, isoelectronic with the putative metal-nitrenoid intermediates in azide activation, also increase in the series Mn < Co < Fe < Cr.[76]

The redox activity of the cobalt selenide support positions it to become electronically involved during a multielectron transformation such as azide activation and nitrene transfer, modulating the reactivity of the edge site. To identify the distinct regimes of edge/support redox cooperativity as a function of edge site identity, the calculated electronic structures of **1**-M were used to assess which derivatives energetically favor redox cooperativity. When M = Cr or Fe, the HOMO level is predicted to be primarily localized on the edge site, suggesting the cluster core is minimally involved with oxidation. When M = Cu, the edge metal has low-lying empty orbitals to which the core spontaneously transfers an electron, reducing the edge site. As in the case of Cr and Fe, here, the first oxidation is expected to be localized strictly on the edge metal (Cu^{1+}), with no cluster core participation. Finally, when M = Co, Mn, Ni, the similar energy of the edge atom and Co/Se core orbitals at the HOMO level positions the core to become electronically involved and, together with the strong M–Se interactions, facilitate edge/core charge redistribution during a redox reaction. This redox cooperative regime is empirically associated with the most active catalysts, **1**-Co and **1**-Mn. Its implications for the electronic structure of the metal-nitrenoid intermediate are explored below, and contrasted with the scenario in which the edge site is redox independent from the cluster core.

3.10 Role of Edge/Core Electronic Interactions in Modulating the M–NTs Multiple Bonds

To evaluate the role of the edge/support cooperativity in modulating the reactivity of **1**-M, the electronic structure of two metal-nitrenoid intermediates, ostensibly the key intermediates in azide activation and nitrene transfer, were investigated in silico. Two clusters were selected to illustrate the distinct regimes of electronic edge/support interactions, **1**-Cr(NTs), in which the Cr edge site is expected to be redox independent of the cluster core, and **1**-Co(NTs), in which the cobalt core is poised to become electronically involved. Electronic structure calculations of **1**-Cr(NTs) (S = 1) reproduce the experimental metrics for Cr(NTs) edge sites in the previously isolated **Cr$_3$** nanocluster system (Table 3.7),[45] and indicate that upon azide activation the oxidation is indeed localized on the chromium edge. This is reflected in the density of states plot of **1**-Cr(NTs) by the large Cr contribution at the LUMO levels, and the exclusive Co_6Se_8 contribution at the HOMO frontier levels (Figure 3.8C). Spin density plots reveal that the resulting Cr^{IV}-imido confines the unpaired spin on the Cr edge, while cobalt selenide core remains largely unaffected (Figure 3.8A and B).

In contrast to the edge/support redox independence in **1**-Cr, calculations suggest that the Co_6Se_8 support contributes an electron to activating tosyl azide in **1**-Co. The resulting **1**-Co(NTs) (S = 5/2) cluster features a Co^{2+}-iminyl edge on a mono-oxidized $[Co_6Se_8]^+$, whereas a Co^{3+}-iminyl might be expected in the absence of the cluster core participation. The density of states plot of **1**-Co(NTs) reveals the LUMO level is completely localized on the Co_6Se_8 core, while the Co edge metal contributes to the HOMO levels (Figure 3.8C). Metal-nitrenoid Cr,[58,77,78] Mn,[79,80] Fe,[81–84] Co,[85–88] Ni,[89–91] and Cu[92,93] species exist in a variety of electronic configurations,[56,94] and while no Co^{2+}-iminyl has yet been isolated, one has recently been implicated.[95] In general, metal centers with high oxidation states and low spin configurations impart stability to a metal-nitrenoid fragment. In contrast, lower oxidation states and high spin intermediates as those likely at play in **1**-Co are more reactive due to the population of antibonding orbitals and the increased electron-electron repulsion, both of which destabilize and weaken the M…N bond.[96,97] We therefore hypothesize that when M = Co, the cluster core localizes some of the charge created upon N_2 extrusion (+1), enabling the edge metal to retain a relatively lower oxidation state. In turn, this Co^{2+}-iminyl electronic structure is expected to feature a decreased bond order, and hence display

higher reactivity.[94] Therefore, in the case of **1**-Co, the edge/support cooperativity is poised to increase the reactivity of the M–NTs multiple bond fragment.

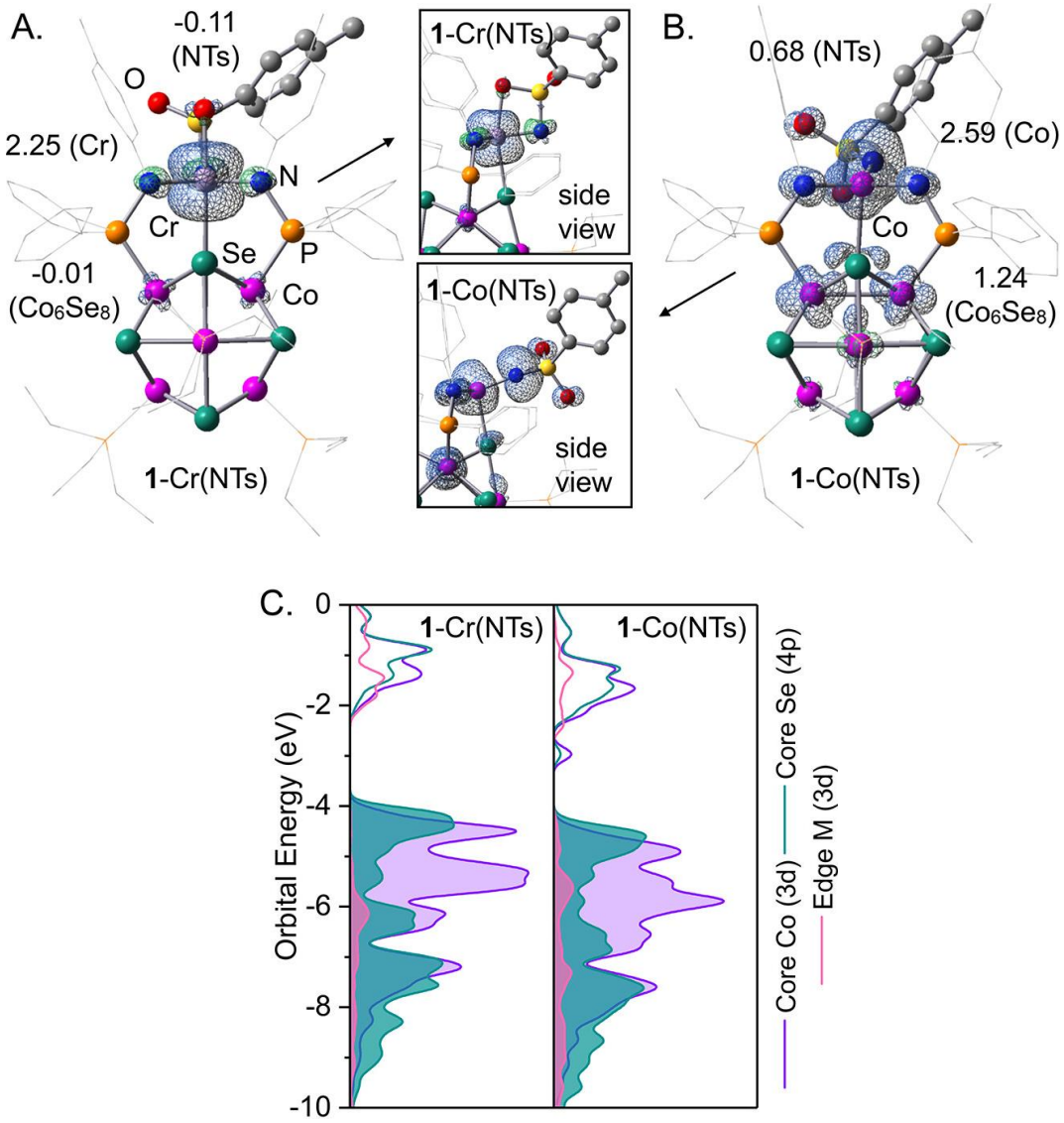

Figure 3.8. Mulliken spin density (α-β) plots of A) **1**-Cr(NTs), and B) **1**-Co(NTs) calculated at uB3LYP+/cc-pVTZ level of theory. Spin density values for the edge, NTs fragment, and Co_6Se_8 core are included. Surfaces plotted at an isovalue of 0.004. C) Corresponding partial density of states plots of **1**-Cr(NTs) and **1**-Co(NTs).

3.11 CONCLUSIONS

1-M is a molecular cluster that incorporates the complexities of a heterogeneous single-site catalyst in a tunable and monodisperse platform. Leveraging a molecular approach, this study provides atomistic insights into the metal/support interface, and how the ensuing cooperativity can be harnessed to dramatically alter catalytic activity in a redox transformation.

As a ligand, the Co_6Se_8 cluster is structurally and electronically responsive to the chemical identity of the edge site. The structural versatility is captured by the variety of coordination environments adopted by the edge metals in the solid-state: two coordinate linear (Cu), four-coordinate pseudo-tetrahedral (Mn, Fe, Co, Zn), or five-coordinate square pyramidal (Cr). The electronic effects of the metal/support interactions are probed by cyclic voltammetry, magnetic measurements, electronic absorption spectroscopy, paramagnetic ^{31}P NMR, and DFT calculations. The most obvious change observed is the narrowing of the HOMO/LUMO gaps, which is proportional to the degree of structural distortion inflicted by the edge site on the Co_6Se_8 cluster. Periodic trends in the valence orbital energies across the 3d series manifest in a stabilization of the LUMO levels across the **1**-M series up to copper, where edge/support charge redistribution occurs spontaneously to form a reduced Cu^{1+} edge and a mono-oxidized to $[Co_6Se_8]^+$ core. Ultimately, the use of molecular characterization techniques provides an atomic-level picture of the edge/cluster interface.

Metal/support interactions have been shown to enhance the catalytic activity of single-site heterogeneous catalysts. In **1**-M, the edge/support construct imparts remarkable activity for nitrene transfer across the 3d transition metal series, chemical versatility that is reserved to few molecular ligands.[98,99] The identity of the edge metal effectively tunes the observed catalytic rates, which peak for the Mn and Co derivatives. Empirically, the strength of edge/core (M–Se) bonding interaction correlates linearly with the catalytic activity of the 3d series. We hypothesize that due to dynamic push-pull substrate/active site/support interactions, the strength of the M–Se bonds and M–NTs multiple bonds are inversely related. Hence, the stronger the edge/core interaction, the weaker and more reactive the M(NTs) fragment in key metal nitrenoid catalytic intermediates. Identifying redox regimes wherein electronic cooperativity can occur between the active site and the cluster support provides a method to tune the reactivity of metal-ligand multiple bonds. The electronic interaction between the edge metal and the cluster support ranges from fully independent

(Cr) to cooperative (Co, Mn). In the latter, electron transfer from the cluster core to the edge site is predicted to increase the reactivity of the metal nitrenoid intermediate by ensuring a relatively lower oxidation state of the active site and weakening the M(NTs) bond.

In aggregate, this study provides an atomic level picture into the key structural and electronic factors underpinning metal/support interactions and their role in facilitating reactivity in a molecular single-site cluster, ultimately illustrating how their cooperativity can be leveraged to modulate catalytic performance.

3.12 Synthetic Details and Characterization of Products

3.12.1 *General Experimental Considerations*

All manipulations were performed under a nitrogen atmosphere using standard Schlenk or glovebox techniques (LC Technology Solutions glovebox equipped with a freezer set to −35 °C). All glassware was dried in an oven set to 160 °C for a minimum of 12 h and cooled in an evacuated antechamber prior to use in the glovebox.

Solvents were purchased from Fischer Scientific and degassed, dried and purified using solvent purification columns housed in a stainless-steel cabinet, and dispensed by a stainless steel Schlenk-line manufactured by JC Meyer Solvent Systems. Tetrahydrofuran (THF), diethyl ether (Et_2O), acetonitrile (MeCN), and methylene chloride (DCM) are passed through two packed columns of neutral alumina. *n*-Pentane and toluene are passed through one column of neutral alumina and one column of Q5 reactant, a copper (II) oxide oxygen scavenger. All solvents are passed through an in-line, 2 μm filter immediately before being dispensed which ensures that no packing material residue is dispensed with the solvent. Hexamethyldisiloxane (HMDSO) was purchased from Sigma Aldrich and degassed. Prior to use the solvents were stored over activated 3Å molecular sieves (purchased from Sigma Aldrich) in the glovebox for a minimum of 72 hours.

Deuterated solvents ($CDCl_3$, C_6D_6, CD_2Cl_2, CD_3CN) were purchased from Sigma Aldrich, degassed and dried over activated 3Å molecular sieves (purchased from Sigma Aldrich) in the glovebox for a minimum of 72 hours. $CrCl_2$ (99.99% purity), $MnCl_2$ (99.995% purity), $FeCl_2$ (98+% purity), $CoCl_2$ (98+% purity), $Cu(OTf)_2$ (98+% purity) and $ZnCl_2$ (99.99% purity) were purchased from Strem Chemicals, Inc. and dried under vacuum at 120 °C for 24 h prior to use. $Co_2(CO)_8$ (stabilized with 2-5% hexanes, Strem Chemicals, Inc.) was stored in the freezer and used

as received. Ethylmagnesium bromide (3.0 M in Et_2O), chlorodiphenylphosphine (97% purity), p-toluidine (99+% purity) were purchased from Alfa Aesar and used without further purification. Phosphorus trichloride (99% purity), selenium (99.5% purity, powder, 200 mesh), *n*-butyl lithium (2.5 M in hexanes) were purchased from Sigma Aldrich and used as received. Single element TraceCERT® standards for ICP were purchased from Sigma Aldrich. *N*-(p-tolyl)diphenyl-phosphinamine[1] and *cis*-$Co_6Se_8(PEt_3)_4(CO)_2$[2] were prepared according to the literature. Tosyl azide was synthesized according to a literature procedure,[3] and dried over activated 3Å molecular sieves in diethyl ether prior to use. *Tert*-butyl isocyanide (CN^tBu, 98%) was purchased from Sigma Aldrich, degassed, and stored over activated 3 Å molecular sieves in the glovebox for a minimum of 72 h prior to use.

Photolytic treatments were performed with a 450 W medium-pressure mercury vapor lamp (Hanovia Specialty Lighting, PC 451.050) emitting 200–400 nm broadband radiation. The lamp is hosted inside a quartz jacket continuously cooled using an automated water circulator.

NMR spectra were obtained on a Bruker 300, 500, or 700 MHz spectrometer. Chemical shifts are listed in parts per million and are referenced to the residual deuterated solvent peak for ^1H and ^{13}C-NMR. ^{31}P spectra are referenced to phosphoric acid.[4–6] All heteronuclear NMR measurements are proton decoupled ($X\{^1H\}$, X = ^{13}C, ^{31}P, ^{77}Se), unless specified otherwise.

The magnetic moments were determined using Evans method.[7] Each compound of interest was dissolved in a known in a mesitylene (1% v/v) solution in CD_2Cl_2. The solution, of known concentration, was transferred to an NMR tube together with a sealed capillary containing mesitylene (1% v/v) solution in CD_2Cl_2. Analysis of the mesitylene signals separation between the sample and capillary allowed the determination of the magnetic moment. Variable temperature measurements were recorded over a temperature range between 180 to 298K, calibrated using a CD_3OD standard.

UV/Visible spectra were recorded on a Varian Cary 5000 UV-Vis-NIR Spectrophotometer using Near-IR quartz cells (Spectrocell Inc., 10 mm path length, 220-3500 nanometers spectral window).

Automated Column Chromatography has been performed using a Teledyne ISCO CombiFlash Rf+ System using 300g Sillica columns packed in-house.

Cyclic voltammetry was conducted using a μAutolabbIII/FRA2 potentiostat by Metrohm and a Gamry Interface 1010B potentiostat. A three-electrode cell setup was used with a glassy carbon disk working electrode, a platinum wire counter electrode, and a silver wire pseudo-reference

electrode. All potentials were referenced Fc/Fc^+ redox couple by adding a small amount of ferrocene after each measurement. All electrochemical measurements were conducted under a dinitrogen atmosphere at room temperature.

EPR spectra were recorded on a Bruker EMX Nano spectrometer at 9.64 GHz as a frozen toluene solution.

Elemental Analysis measurements have been performed using the Inductively-Coupled Plasma Mass Spectrometer (ICP-MS) Perkin Elmer Nexion 2000B under operating conditions suitable for routine multi-element analysis. A known quantity of sample was added to 2 mL of a 60% HNO_3 solution in water and stirred overnight. The digestion was considered complete when solids are no longer observed. The instrument was calibrated using 0, 2, 5, 10, 20, 40, 60 parts per billion of certified multi-element ICP-MS standard calibration solutions for a range of elements prepared in 2% (v/v) nitric acid. The analyzed elements were Fe, Co, Zn, Cu, Se and P.

3.12.2 *Synthesis and Isolation of Triethylphosphine Selenide - ($SePEt_3$)*

Modified from a literature procedure.[8] A 2 L three-neck flask is first equipped with a mechanical stirrer and a pressure-equilibrated addition funnel capped with a rubber septum, and then connected to a nitrogen-flushed Schlenk manifold using an Airfree Schlenk adapter (see Figure 3.9a). A solution of ethylmagnesium bromide (1.00 mol, 333.0 mL of 3.0 M in diethylether, 3.0 equiv) is diluted with THF (350 mL) and cannula-transferred to a 2 L three-neck flask. The flask is then cooled to 0 °C using an ice bath. Inside the glovebox, phosphorus trichloride (45.78 g, 0.33 mol, 1.0 equiv) was diluted with THF (100 mL) inside a Schlenk flask. The sealed flask was connected to a Schlenk manifold and its contents were transferred using a cannula to the pressure-equalized addition funnel (see Figure 3.9b). The solution of phosphorus trichloride is added dropwise into the three-neck flask over the course of 2 hours, during which time a thick white precipitate is formed. The resulting white slurry is then allowed to stir for an additional hour, while warming the flask up to room temperature (see Figure 3.9c).

The volatile materials are then transferred using bulb-to-bulb vacuum distillation into a 1.0 L Schlenk flask containing selenium powder (26.30 g, 0.33 mol, 1.0 equiv; see Figure 3.9d). The resulting heterogeneous mixture is allowed to stir for 12 hours at room temperature. The unreacted selenium powder is removed by filtration over a Celite pad, which is then washed with additional EtOAc (100 mL). The filtrate is collected, and the volatile materials are removed *in vacuo*. The

resulting white solids are suspended in 100 mL of *n*-pentane. Filtration, and further washing with pentane (100 mL) affords the desired product ($SePEt_3$) as a spectroscopically pure white powder (39.05 g, 0.20 mol, 60.0%).

^1H NMR (700 MHz, C_6D_6) δ 1.40 (dq, $J_{H\text{-}H}$ = 7.5 Hz, $J_{H\text{-}P}$ = 11 Hz, 6H), 0.88 (dt, $J_{H\text{-}H}$ = 7.5 Hz, $J_{H\text{-}P}$ = 14 Hz, 9H) ppm. ^{31}P NMR (283.4 MHz, C_6D_6) δ 43.6 (s) ppm. ^{77}Se NMR (133.5 MHz, C_6D_6) δ −425.8 (d, $J_{P\text{-}Se}$=710 Hz) ppm. GC analysis: (Temp program: initial temp = 40° C, 15.00° C/min, final temp = 300° C, final time = 3.50 min) Retention time = 9.7 min. EI-MS m/z (intensity) = 198 (100), 170 (51), 142 (88), 111 (27), 57 (32).

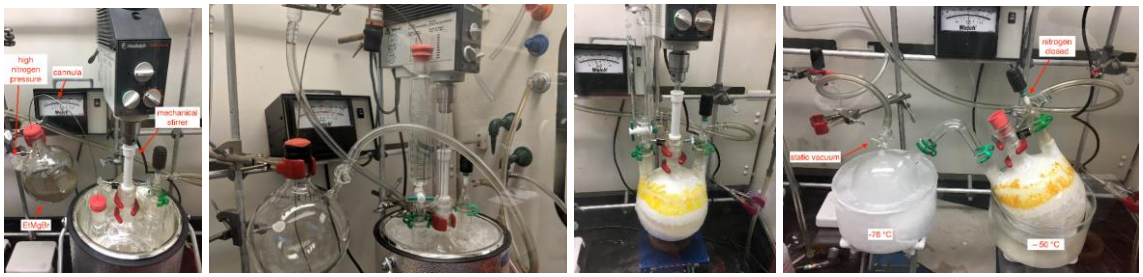

(a) (b) (c) (d)

Figure 3.9. Synthesis of $SePEt_3$; (a) initial set-up, followed by addition of EtMgBr, (b) Addition of PCl_3 to the dropping funnel, (c) Reaction mixture at the end of the reaction, (d) bulb-to-bulb distillation of the formed PEt_3

3.12.3 *Synthesis and Isolation of cis-$Co_6Se_8(PEt_3)_4(PPh2NHTol)_2$ (**1**-H_2)*

Inside the glovebox, *cis*-$Co_6Se_8(PEt_3)_4(CO)_2$ (0.83 g, 0.55 mmol, 1.0 equiv) and the *N*-(p-tolyl)diphenyl-phosphinamine (0.46 g, 1.64 mmol, 3.00 equiv) and toluene (25 mL) are added to a 100 mL Schlenk flask equipped with a magnetic stir bar. The reaction mixture is irradiated using a 450W Hg-lamp for 14 hours, while stirring. The reaction progress is monitored by IR spectroscopy *via* the disappearance of the CO stretch at 1972 cm^{-1}. Volatiles are evaporated *in vacuo*, the oily residue suspended and stirred in *n*-pentane (50 mL) for 12 hours and then triturated using *n*-pentane (2 × 15 mL) to yield a powder. The solids were washed with MeCN (30 mL) via vacuum filtration through a fine porosity glass fritted funnel. Removal of trace volatiles yields a spectroscopically pure red/brown powder (0.92 g, 0.55 mmol, 84% yield).

UV-vis-*n*IR (THF, 25 °C) λ: 368 (ε = 47,590 cm^{-1} M^{-1}), 441 (ε = 31,269 cm^{-1} M^{-1}), 505 (ε = 18,101 cm^{-1} M^{-1}) nm. ^1H NMR (500 MHz, C_6D_6) δ: 8.21 (m, 8H, -Ph), 7.16 (m, 8H, -Ph), 7.04 (m, 4H, -

Ph), 6.68 (d, J = 8.0 Hz, 4H, -C_6H_4-p-Me), 6.61 (d, J = 8.0 Hz, 4H, -C_6H_4-p-Me), 6.36 (d, J_{H-P} = 14.0 Hz, 4H, -NH), 1.94 (s, 6H, -Me), 1.87 (m, 12H, -CH_2), 1.72(m, 12H, -CH_2), 1.04 (m, 18H, -CH_3), 0.93 (m, 18H, -CH_3) ppm. ^{31}P NMR (283 MHz, C_6D_6) δ: 88.9 ($\nu_{1/2}$ = 643 Hz), 63.5 ($\nu_{1/2}$ = 668 Hz), 60.9 ($\nu_{1/2}$ = 636 Hz) ppm. ^{13}C NMR (176 MHz, C_6D_6) δ: 132.41, 132.35, 129.50, 128.51, 128.35, 127.60, 127.54, 118.49, 27.23, 22.72, 20.49, 14.27, 8.55, 8.41 ppm. Elemental Analysis (ICP-MS): Experimental (Calculated for $Co_6Se_8P_6C_{62}H_{96}N_2$) Co 17.39 (17.33), Se 31.22 (30.96), P 9.36 (9.11).

3.12.4 *Synthesis and Isolation of $FeCo_6Se_8(PEt_3)_4(PPh_2NTol)_2$ (**1**-Fe)*

Inside the glovebox, **1**-H_2 (0.204 g, 0.100 mmol, 1.0 equiv) is dissolved in an 8:2 THF/Toluene mixture (10 mL). The solution is then frozen in the glovebox coldwell. Upon thawing, *n*-BuLi (0.112 mmol, 90 μL of a 2.5 M solution in hexanes, 2.3 equiv) is added dropwise. The reaction mixture is then stirred at room temperature for 12 hours. Anhydrous $FeCl_2$ (0.014 g, 0.110 mmol, 1.1 equiv) is added as a solid and the reaction mixture is stirred for an additional 12 hours. The volatiles are removed in vacuo, and the resultant solids are triturated with *n*-pentane (15 mL). After trituration and removal of volatiles, the product is extracted in DCM (15 mL) and filtered through a plug of Celite. The filtrate is then evaporated, and solids triturated using n-pentane (2 × 10 mL). Recrystallization from toluene:*n*-pentane (1:5) followed by removal of the trace volatiles under reduced pressure yields a spectroscopically pure crystalline black solid (0.197 g, 0.094 mmol, 94% yield).

UV-vis-*n*IR (THF, 25 °C) λ: 367 (ε = 46,031 cm^{-1} M^{-1}), 443 (ε = 34,105 cm^{-1} M^{-1}) nm. ^{1}H NMR (500 MHz, C_6D_6) δ: 43.18 (s, 6H, -$C_6H_4CH_3$), 31.63 (s, 4H, -$C_6H_4CH_3$), 18.43 (s, 8H, -C_6H_5), 13.07 (s, 8H, -C_6H_5), 8.21 (s, 4H, -C_6H_5), 1.51 (s, 18H, -CH_2CH_3), 0.47 (s, 12H, -CH_2CH_3), -2.86 (s, 12H, -CH_2CH_3), -3.34 (s, 18H, -CH_2CH_3), -33.11 (s, 4H, -$C_6H_4CH_3$) ppm. ^{31}P NMR (283 MHz, C_6D_6) δ: -113.4, -955.6; (283 MHz, THF) δ: -111.2 ($\nu_{1/2}$ = 899 Hz), -915.0 ($\nu_{1/2}$ = 1819 Hz); (283 MHz, Tol/Py) δ: -80.8, -714.7 ppm. ^{13}C NMR (126 MHz, C_6D_6) δ: 222.1, 159.9, 144.4, 124.8, 110.4, 27.6, 12.3, 12.1, 6.8 ppm. μ_{eff} (Evans method, CD_2Cl_2, 298K) 4.9(3) μ_B. Elemental Analysis (ICP-MS): Experimental (Calculated for $Co_6Se_8P_6FeC_{62}H_{94}N_2$) Co 16.53 (16.88), Se 30.40 (30.16), P 8.72 (8.87), Fe 3.12 (2.67).

3.12.5 *Synthesis and Isolation of $CoCo_6Se_8(PEt_3)_4(PPh_2NTol)_2$ (**1**-Co)*

Inside the glovebox, **1**-H_2 (0.306 g, 0.150 mmol, 1.0 equiv) is dissolved in an 8:2 THF/Toluene mixture (16 mL). The solution is then frozen in the glovebox coldwell. Upon thawing, *n*-BuLi (0.315 mmol, 126 μL of a 2.5 M solution in hexanes, 2.1 equiv) is added dropwise. The reaction mixture is then stirred at room temperature for 12 hours. Next, anhydrous $CoCl_2$ (0.021 g, 0.165 mmol, 1.1 equiv) is added as a solid and the reaction mixture is stirred for an additional 12 hours. The volatiles are removed in vacuo, and the resultant solids are triturated using *n*-pentane (2 × 15 mL). After trituration and removal of volatiles, the product is dissolved in DCM (15 mL) and filtered through a plug of Celite. The filtrate is then evaporated and the solids triturated using n-pentane (2 × 10 mL). Further washing with MeCN (20 mL) and recrystallization from toluene:*n*-pentane (1:5) followed by removal of trace volatiles under reduced pressure yields a spectroscopically pure crystalline black solid (0.290 g, 0.138 mmol, 92% yield).

UV-vis-*n*IR (THF, 25 °C) λ: 369, 441 nm. ^{1}H NMR (500 MHz, C_6D_6) δ: 31.56 (s, 6H, -$C_6H_4CH_3$), 26.46 (s, 4H, -$C_6H_4CH_3$), 15.31 (s, 8H, -C_6H_5), 10.97 (s, 8H, -C_6H_5), 7.04 (s, 4H, -C_6H_5), 2.29 (s, 18H, -CH_2CH_3), 1.91 (s, 12H, -CH_2CH_3), -4.59 (s, 12H, -CH_2CH_3), -5.08 (s, 18H, -CH_2CH_3), -11.22 (s, 4H, -$C_6H_4CH_3$) ppm. ^{31}P NMR (121 MHz, C_6D_6) δ: -98.0 ($\nu_{1/2}$ = 588 Hz), -796.3 ($\nu_{1/2}$ = 1156 Hz) ppm. ^{13}C NMR (75 MHz, C_6D_6) δ: 197.37 (s, -Ar), 150.41 (d, -Ar), 140.43 (s, -Ar), 99.43 (s, broad,), 59.96 (s, -$C_6H_4CH_3$), 24.74 (d, -CH_2CH_3), 17.11 (s, -CH_2CH_3), 11.78 (d, -CH_2CH_3), 0.51 (s, -CH_2CH_3) ppm. μ_{eff} (Evans method, CD_2Cl_2, 298K) 3.7(3) μ_B. Elemental Analysis (ICP-MS): Experimental (Calculated for $Co_6Se_8P_6C_{62}H_{94}N_2Co$) Co 19.32 (19.67), Se 30.42 (30.12), P 8.78 (8.86).

3.12.6 *Synthesis and Isolation of $CuCo_6Se_8(PEt_3)_4(PPh_2NTol)_2$ (**1**-Cu)*

Inside the glovebox, 1-**H_2** (0.310 g, 0.150 mmol, 1.0 equiv) is dissolved in an 8:2 THF/Toluene mixture (18 mL). The solution is then frozen in the glovebox coldwell. Upon thawing, *n*-BuLi (0.340 mmol, 134 μL of a 2.5 M solution in hexanes, 2.3 equiv) is added dropwise. The reaction mixture is then stirred at room temperature for 12 hours. Next, anhydrous $Cu(OTf)_2$ (0.061 g, 0.17 mmol, 1.1 equiv) is added as a solid and the reaction mixture is stirred for an additional 12 hours. The volatiles are removed in vacuo, and the resultant solids triturated using *n*-pentane (2 × 15 mL). The solids are then extracted in DCM (15 mL) and filtered through a plug of Celite. The filtrate is then evaporated and the solids triturated with n-pentane (2 × 10 mL) again. Removal of the trace volatiles yields a spectroscopically pure crystalline brown solid (0.306 g, 0.144 mmol, 96% yield).
UV-vis-*n*IR (THF, 25 °C) λ: 375 (ε = 49,817 cm^{-1} M^{-1}), 443 (ε = 33,533 cm^{-1} M^{-1}) nm. ^{1}H NMR (500 MHz, C_6D_6) δ: 8.42 (d, J = 8.0 Hz, 8H, -C_6H_5), 7.55 (t, J = 8.0 Hz, 4H, -C_6H_5), 7.12 (d, J =

8.3 Hz, 4H, -$C_6H_4CH_3$), 6.75 (t, J = 8.0 Hz, 8H, -C_6H_5), 6.66 (d, J = 8.3 Hz, 4H, -$C_6H_4CH_3$), 1.84 (s, 6H, -$C_6H_4CH_3$), 0.36 (s, 18H, -CH_2CH_3), 0.13 (s, 18H, -CH_2CH_3), -0.18 (d, J = 7.5 Hz, 12H, -CH_2CH_3), -0.66 (d, J = 7.4 Hz, 12H, -CH_2CH_3) ppm. ^{31}P NMR (202 MHz, $CDCl_3$) δ: -354.1 ($\nu_{1/2}$ = 1751 Hz), -399.9 ($\nu_{1/2}$ = 2093 Hz), -663.4 ($\nu_{1/2}$ = 3494 Hz) ppm. ^{13}C NMR (126 MHz, $CDCl_3$) δ: 132.17, 128.20, 127.65, 124.89, 123.88, 20.69, 10.95 (d), -5.56, -10.95 ppm. μ_{eff} (Evans method, CD_2Cl_2, 298K) 1.8(3) μ_B. Elemental Analysis (ICP-MS): Experimental (Calculated for $C_{62}H_{94}Co_6N_2P_6Se_8Cu$) Co 16.80 (16.82), Se 29.78 (30.05), P 9.45 (8.84), Cu 3.15 (3.02).

3.12.7 *Synthesis and Isolation of $ZnCo_6Se_8(PEt_3)_4(PPh_2NTol)_2$ (**1**-Zn)*

Inside the glovebox, 1-**H_2** (0.300 g, 0.147 mmol, 1.0 equiv) is dissolved in a 8:2 THF/Toluene mixture (10 mL). The solution is then frozen in the glovebox coldwell. Upon thawing, *n*-BuLi (0.191 mmol, 130 μL of a 2.5 M solution in hexanes, 2.2 equiv) is added dropwise. The reaction mixture is then stirred at room temperature for 12 hours. Next, anhydrous $ZnCl_2$ (0.034 g, 0.191 mmol, 1.1 equiv) is added as a solid and the reaction mixture is stirred for an additional 12 hours. The volatiles are removed in vacuo, and the resultant solids triturated with *n*-pentane (15 mL). After trituration and removal of volatiles, the product is extracted in DCM (15 mL) and filtered through a plug of Celite. The filtrate is then evaporated and the solids triturated using n-pentane (2 × 10 mL). Further washing with MeCN (20 mL) followed by removal of the trace volatiles yields a spectroscopically pure crystalline black solid (0.220 g, 0.105 mmol, 71% yield).
UV-vis-*n*IR (THF, 25 °C) λ: 373 (ε = 46,254 cm^{-1} M^{-1}), 446 (ε = 32,507 cm^{-1} M^{-1}), 511 (ε = 18,203 cm^{-1} M^{-1}) nm. ^{1}H NMR (300 MHz, C_6D_6) δ: 8.34 (t, *J* = 7.8 Hz, 8H, -Ph), 7.23 (t, *J* = 7.8 Hz, 8H, -Ph), 7.07 (t, *J* = 7.8 Hz, 4H, -Ph), 6.91 (d, *J* = 7.5 Hz, 4H, -C_6H_4-CH_3), 6.63 (d, *J* = 7.5 Hz, 4H, -C_6H_4-CH_3), 1.86 (s, 6H, -C_6H_4-CH_3), 1.79-1.58 (m, 24H, -CH_2CH_3), 1.00-0.86 (m, 18H, -CH_2CH_3), 0.86-0.72 (m, 18H, -CH_2CH_3) ppm; (500 MHz, CD_2Cl_2) δ: 7.86 (t, *J* = 8.0cz Hz, 8H, -C_6H_5), 7.30-7.22 (m, 12H, -C_6H_5), 6.55 (d, *J* = 8.2 Hz, 4H, -C_6H_4-CH_3), 6.32 (d, *J* = 7.5 Hz, 4H, -C_6H_4-CH_3), 2.05 (s, 6H, -C_6H_4-CH_3), 1.73 (m, 12H, -CH_2CH_3), 1.58 (m, 12H, -CH_2CH_3), 0.99-0.91 (m, 36H, -CH_2CH_3) ppm. ^{31}P NMR (121 MHz, C_6D_6) δ: 83.08 ($\nu_{1/2}$ = 480 Hz), 61.88 ($\nu_{1/2}$ = 445 Hz), 56.71 ($\nu_{1/2}$ = 635 Hz) ppm; (202 MHz, CD_2Cl_2) δ 82.92, 61.38, 55.56 ppm. ^{13}C NMR (126 MHz, CD_2Cl_2) δ: 142.31, 142.00, 133.20, 133.12, 128.87, 128.48, 127.40, 127.32, 122.76, 122.68, 54.00, 27.40, 26.77, 20.61, 8.57, 8.28 ppm. Elemental Analysis (ICP-MS):

Experimental (Calculated for $C_{62}H_{94}Co_6N_2P_6Se_8Zn$) Co 17.05 (16.81), Se 29.89 (30.02), P 8.79 (8.83).

3.12.8 *Synthesis and Isolation of Cr(py)$Co_6Se_8(PEt_3)_4(PPh_2NTol)_2$ (**1**-Cr(py))*

Inside the glovebox, **1**-H_2 (0.200 g, 0.098 mmol, 1.0 equiv) is dissolved in toluene (9 mL) and a small amount of pyridine (9 drops). The solution is then frozen in the glovebox coldwell. Upon thawing, *n*-BuLi (0.245 mmol, 98 μL of a 2.5 M solution in hexanes, 2.5 equiv) is added dropwise. The reaction mixture is then stirred at room temperature for 12 hours. Next, anhydrous $CrCl_2$ (0.018 g, 0.147 mmol, 1.5 equiv) is added as a solid and the reaction mixture is stirred for an additional 22 hours. The volatiles are removed in vacuo, and the resultant solids were triturated using *n*-pentane (3 × 10 mL). Next, the product is extracted in toluene (15 mL) and the solution filtered through a plug of Celite. The filtrate is then evaporated, and the solids triturated with *n*-pentane (2 × 10 mL) again to yield a spectroscopically pure crystalline black solid (0.160 g, 0.073 mmol, 75% yield).

UV-vis-*n*IR (THF, 25 °C) λ: 373 (ε = 43,918 cm^{-1} M^{-1}), 440 (ε = 33,656 cm^{-1} M^{-1}), 512 (ε = 17,356 cm^{-1} M^{-1}) nm. ^{1}H NMR (300 MHz, C_6D_6) δ: 22.60 (s), 20.08 (s), 12.52 (s), 9.15 (s), 8.21 (s), 6.65 (s), 6.63 (s), 1.85 (s), 1.71 (s), 1.30 (s), 0.94 (s) ppm. ^{31}P NMR (202 MHz, C_6D_6) no signals observed between +2400 and -2400 ppm. μ_{eff} (Evans method, CD_2Cl_2, 298K) 4.6(3) μ_B.

3.12.9 *Synthesis and Isolation of $MnCo_6Se_8(PEt_3)_4(PPh_2NTol)_2$ (**1**-Mn)*

Inside the glovebox, **1**-H_2 (0.314 g, 0.154 mmol, 1.0 equiv) is dissolved in a 12:1 toluene/THF mixture (13 mL). The solution is then frozen in the glovebox cold trap. Upon thawing, *n*-BuLi (0.385 mmol, 154 μL of a 2.5 M solution in hexanes, 2.5 equiv) is added dropwise. The reaction mixture is then stirred at room temperature for 12 hours and then the volatiles are removed in vacuo. The solids are then redissolved in toluene (15 mL) and anhydrous $MnCl_2$ (0.048 g, 0.385 mmol, 2.5 equiv) is added as a solid and the reaction mixture is stirred at 110 °C for 48 hours. The volatiles are removed in vacuo, and the residue triturated extensively with *n*-pentane (5 × 10 mL). The solids were washed with HMDSO (~40 mL) and then subsequently *n*-pentane (~40 mL). The residual volatiles were thoroughly removed under reduced pressure and then the product was extracted in toluene (20 mL) through a plug of Celite. The filtrate is then evaporated, and the solids

triturated using *n*-pentane (2 × 10 mL) to yield a spectroscopically pure black powder (0.234 g, 0.112 mmol, 72% yield). This compound was found to decompose in DCM.

UV-vis-*n*IR (THF, 25 °C) λ: 369 (ε = 45,958 cm^{-1} M^{-1}), 442 (ε = 31,271 cm^{-1} M^{-1}), 510 (ε = 18,358 cm^{-1} M^{-1}) nm. ^{1}H NMR (300 MHz, C_6D_6) δ: 30.01 (s), 27.69 (s), 19.74 (s), 10.74 (s), 1.96 (s), 1.09 (s) ppm. ^{31}P NMR (202 MHz, C_6D_6) no signals observed between +2400 and -2400 ppm. μ_{eff} (Evans method, CD_2Cl_2, 298K) 5.4(3) μ_B. Elemental Analysis (ICP-MS): Experimental (Calculated for $C_{62}H_{94}Co_6N_2P_6Se_8Mn$) Co 17.11 (16.89), Se 29.83 (30.18), P 8.23 (8.88).

3.13 Cyclic Voltammetry

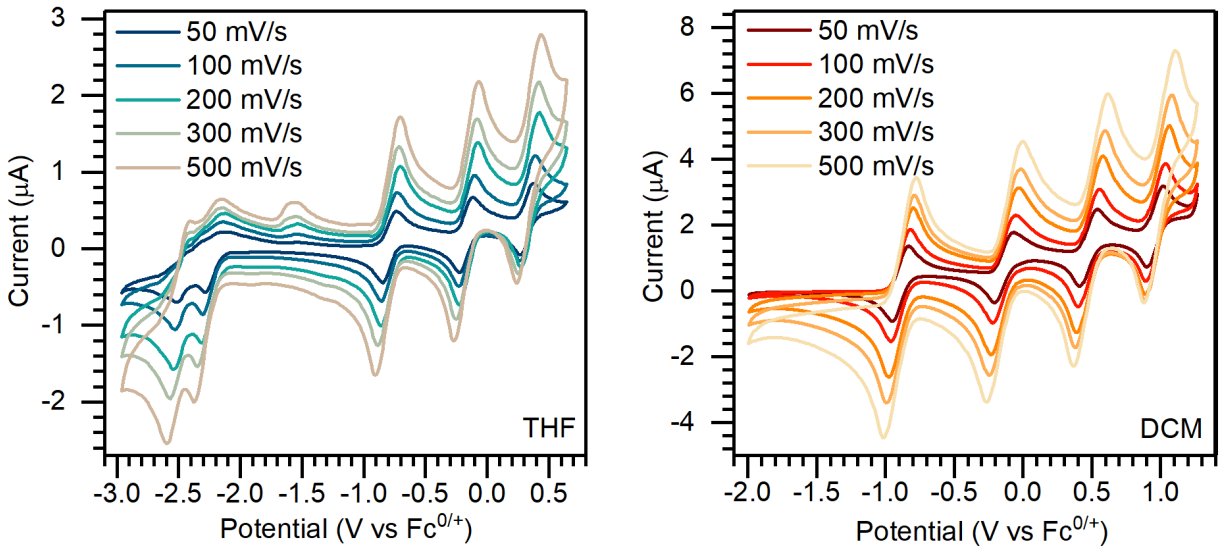

Figure 3.10. Cyclic Voltammogram at different scan rates of **1**-H_2 in (left) THF, and (right) DCM. Temperature: 298K; Electrolyte: 0.1M $TBAPF_6$; Potential vs Fc^+/Fc.

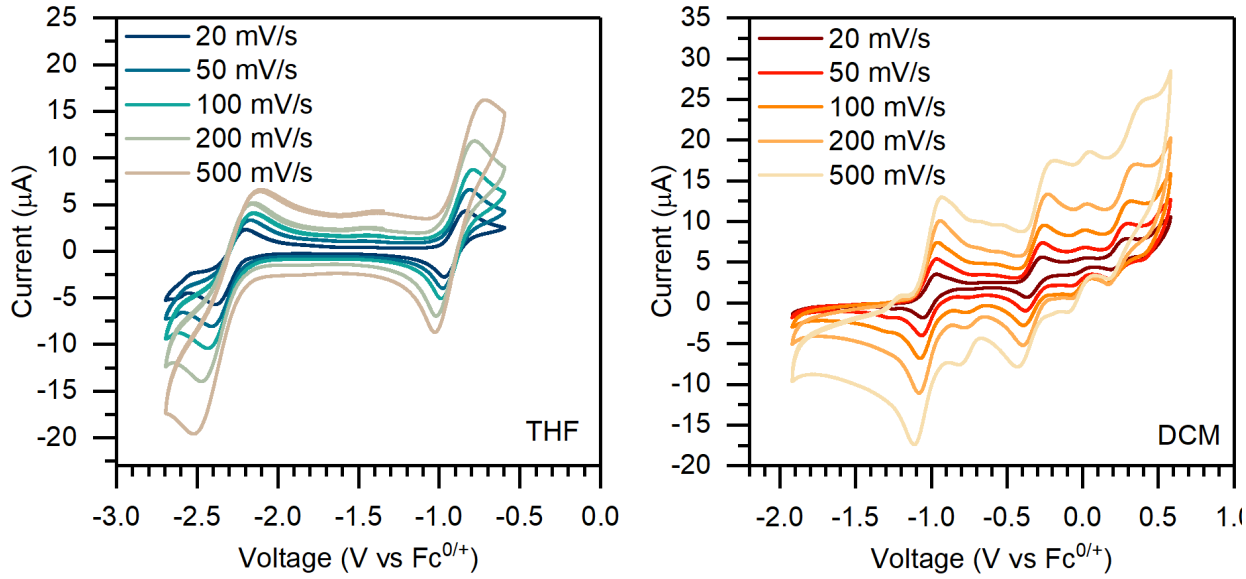

Figure 3.11. Cyclic Voltammogram at different scan rates of **1**-Cr(py) in (left) THF, and (right) DCM. Temperature: 298K; Electrolyte: 0.1M $TBAPF_6$; Potential vs Fc^+/Fc.

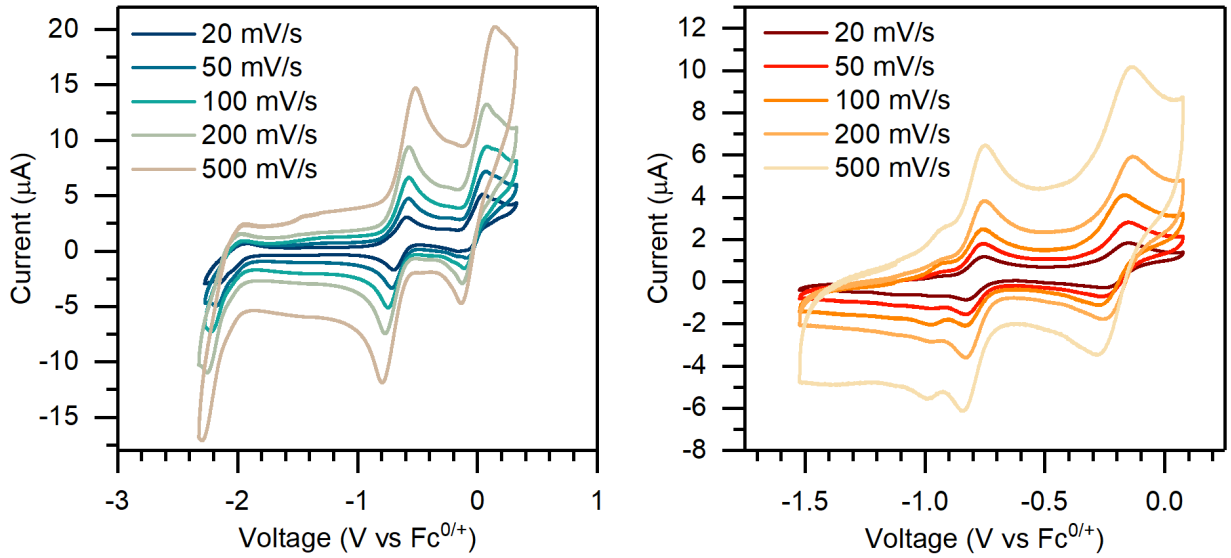

Figure 3.12. Cyclic Voltammogram at different scan rates of **1**-Mn in (left) THF and (right) DCM. Temperature: 298K; Electrolyte: 0.1M $TBAPF_6$ in THF; Potential vs Fc^+/Fc.

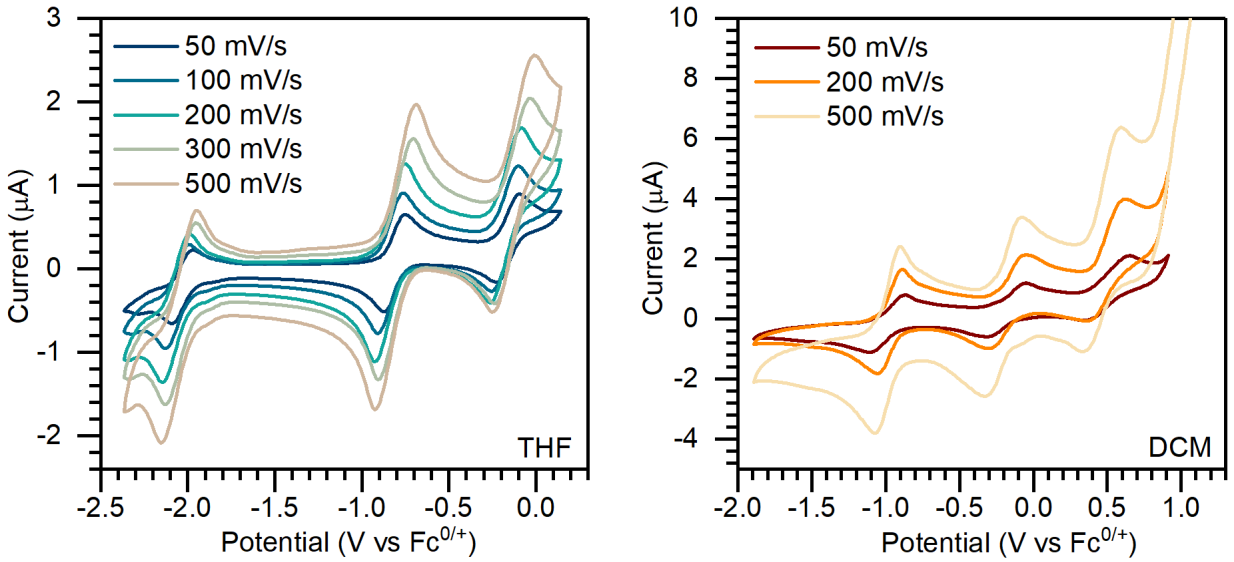

Figure 3.13. Cyclic Voltammogram at different scan rates of **1**-Fe in (left) THF and (right) DCM. Temperature: 298K; Electrolyte: 0.1M $TBAPF_6$; Potential vs Fc^+/Fc.

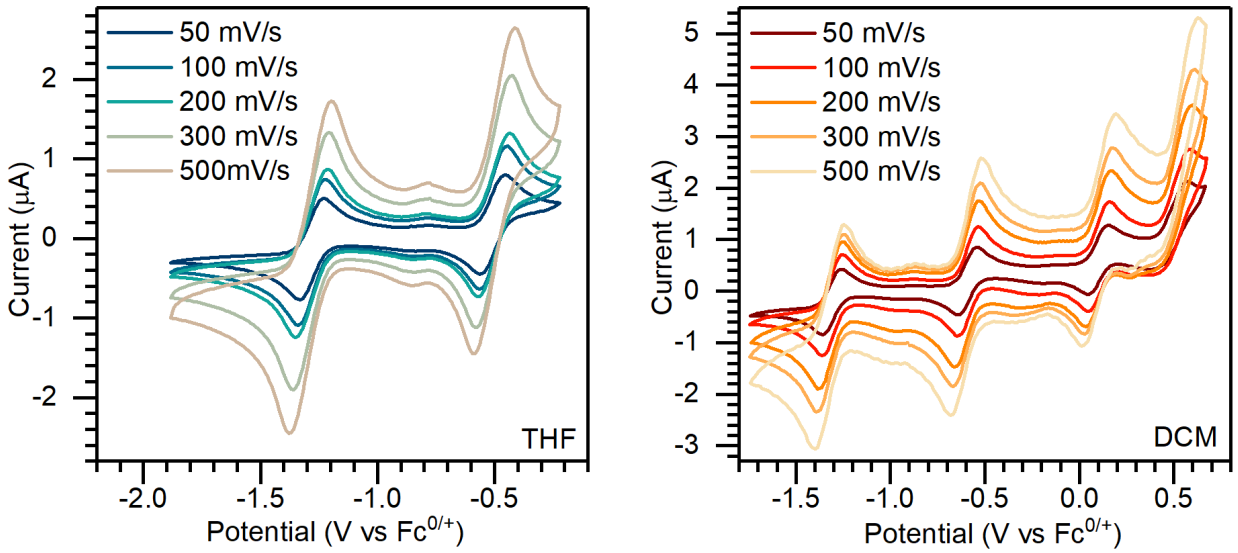

Figure 3.14. Cyclic Voltammogram at different scan rates of **1**-Cu in (left) THF and (right) DCM**.** Temperature: 298K; Electrolyte: 0.1M $TBAPF_6$ in THF; Potential vs Fc^+/Fc.

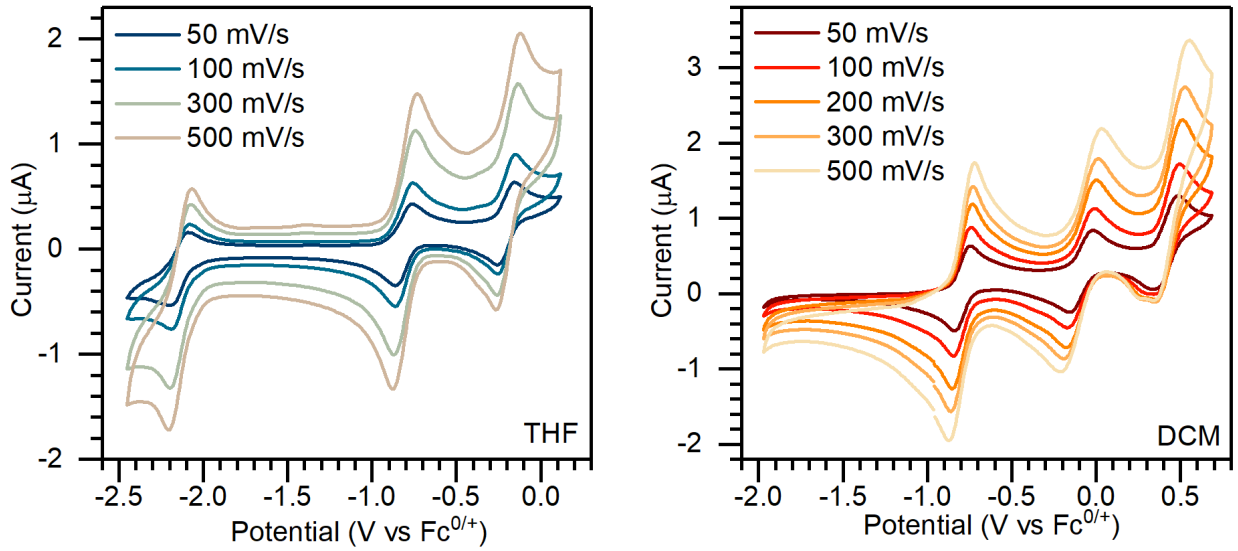

Figure 3.15. Cyclic Voltammogram at different scan rates of **1**-Zn in (left) THF and (right) DCM. Temperature: 298K; Electrolyte: 0.1M $TBAPF_6$ in THF; Potential vs Fc^+/Fc.

Table 3.1. Half-wave potentials ($E_{1/2}$) and peak-to-peak separation potentials (ΔE_p) of **1**-Cr(py), **1**-Mn, **1**-Fe, **1**-Co, **1**-Cu, **1**-Zn, and **1**-H_2 recorded in 0.1 M $TBAPF_6$ DCM or THF solutions at a scan rate of 200 mV/s. Values recorded in DCM and (THF) solutions. **1**-Mn was not stable in DCM under electrochemical conditions, so it was measured in 1,2-difluorobenzene.

redox couple (n_{red}/n_{ox})	$E_{1/2}$ (V vs $Fc^{0/+}$); ΔE_p (mV)		
	1-Cr(py)	**1**-Mn	**1**-Fe
+3/+4	-		-
+2/+3	-		0.46; 210
+1/+2	–0.31; 148	–0.20 (–0.02); 119 (200)	–0.19 (–0.17); 181 (176)
0/+1	–1.00 (–0.90); 138 (236)	–0.79 (–0.67); 76 (138)	–0.98 (–0.84); 141 (172)
–1/0	(–2.32); (319)	(–2.12); (274)	(–2.07); (151)
–2/–1	-	-	-

redox couple (n_{red}/n_{ox})	$E_{1/2}$ (V vs $Fc^{0/+}$); ΔE_p (mV)			
	1-Co	**1**-Cu	**1**-Zn	**1**-H_2
+3/+4	0.88; 274	-	-	0.98; 176
+2/+3	0.45 (0.42); 200 (263)	0.52; 171	0.43; 156	0.49 (0.35); 195 (151)
+1/+2	–0.08 (–0.13); 156 (205)	0.10; 131	–0.09 (–0.20); 171 (121)	–0.13 (–0.15); 200 (180)
0/+1	–0.74 (–0.78); 190 (205)	–0.59 (–0.50); 131 (131)	–0.80 (–0.81); 118 (110)	–0.89 (–0.79); 176 (162)
–1/0	(–1.92); (181)	–1.31 (–1.28); 141 (131)	(–2.14); (111)	(–2.22); (192)
–2/–1	-	-	-	(–2.48); (121)

3.14 Catalytic Synthesis of Carbodiimide with **1**-M Clusters

In a nitrogen atmosphere glovebox, a stock solution **1**-M in C_6D_6 (0.674 μmol, 0.01 equiv) was combined with a stock solution of ^{t}BuNC in C_6D_6 (111 μmol, 1.65 equiv) in an NMR tube. Neat C_6D_6 is added to the NMR tube to reach final volume is 0.6 mL (after TsN_3 is added). A stock solution of TsN_3 in C_6D_6 (67.4 μmol, 1.00 equiv) is added, and the reaction is removed from the glovebox and monitored by ^{1}H NMR spectroscopy. Conversion of TsN_3 and ^{t}BuNC to TsNCN^{t}Bu at 25 °C was monitored by ^{1}H NMR integrations of the reagents and products versus one another. Catalytic runs were carried out in triplicate and the average value is reported with error bars representing the standard deviation. Control experiments with **1**-H_2 and *cis*-$Co_6Se_8(PEt_3)_4(CO)_2$ was carried out under the same conditions however 2.5 mol% of the cluster was used.

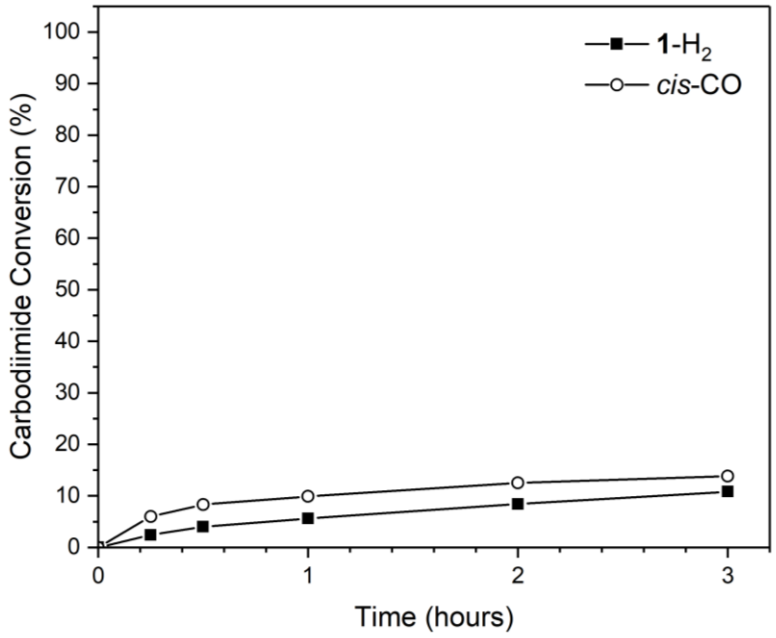

Figure 3.16. Catalytic conversion of carbodiimide (TsNCN^{t}Bu) with 2.5 mol% loading of **1**-H_2 and *cis*-$Co_6Se_8(PEt_3)_4(CO)_2$ clusters.

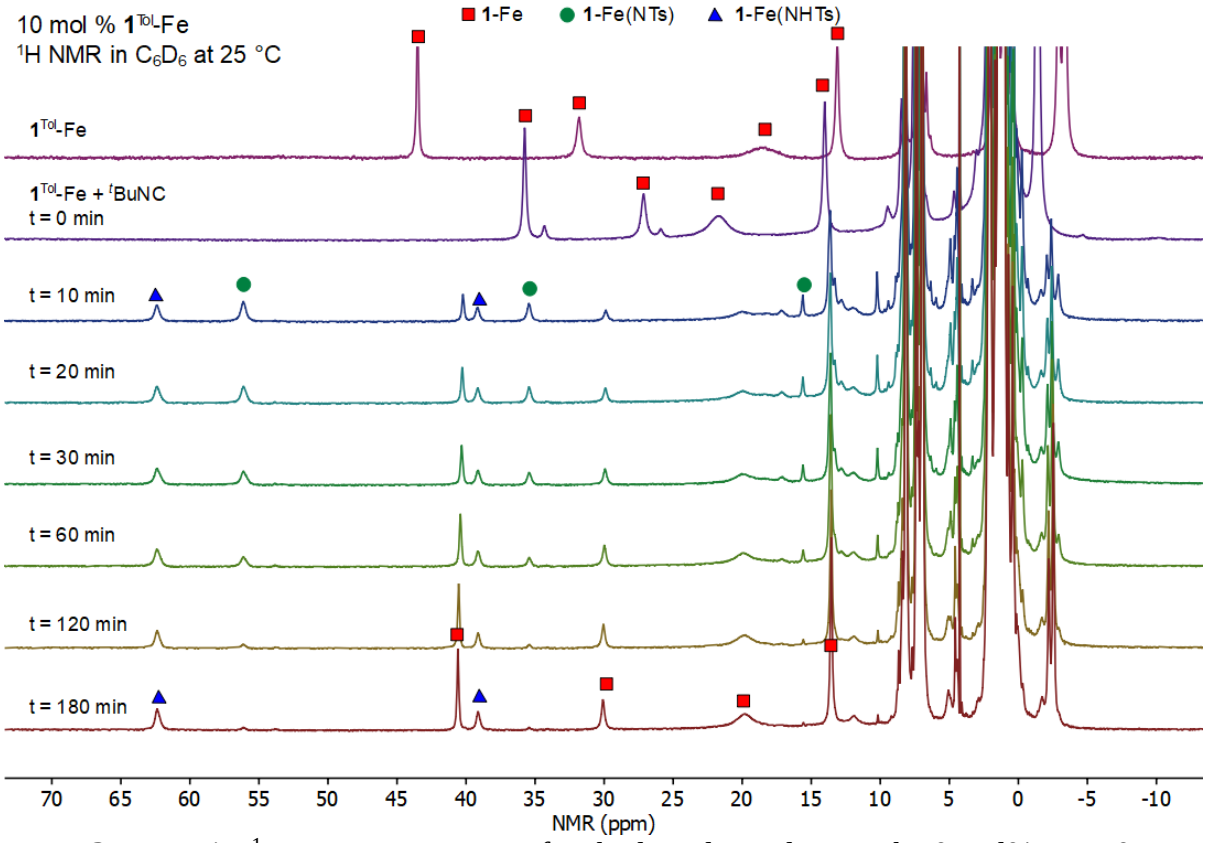

Figure 3.17. *In situ* ^{1}H NMR monitoring of carbodiimide catalysis with 10 mol% **1**-Fe, 0.11 M TsN_3, and 0.19 M ^{t}BuNC in C_6D_6.

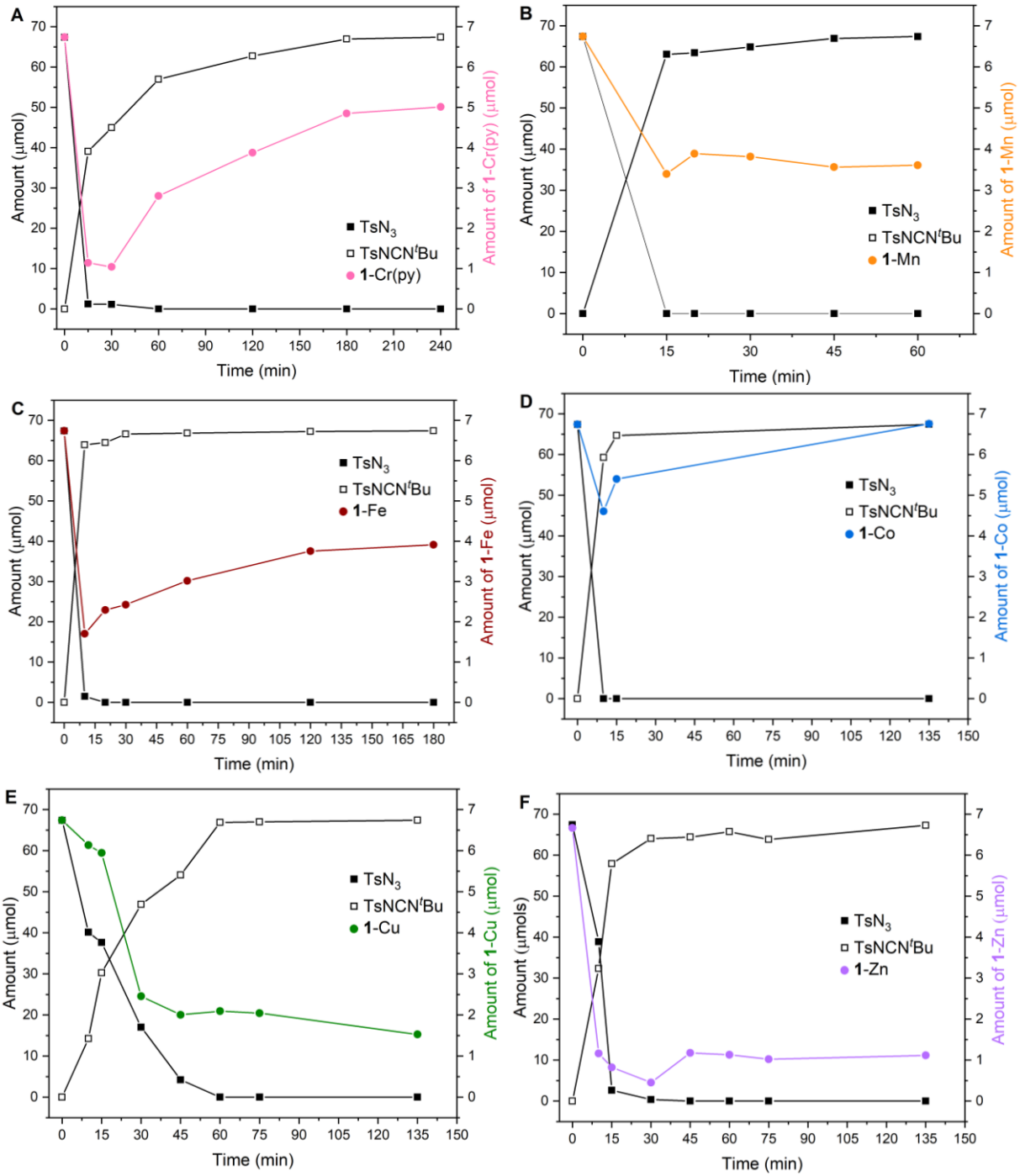

Figure 3.18. Evolution of **1**-M, tosyl azide, and carbodiimide product (TsNCNtBu) during catalysis. NMR scale reactions in C_6D_6 with 10 mol% **1**-M, 0.11 M TsN_3, and 0.19 M ^{t}BuNC were carried out with an external capillary standard (5 % DCM in C_6D_6 by volume). Amounts were determined via single scan NMR integrations versus the external standard. All prepared **1**-M complexes were analyzed a) **1**-Cr(py), b) **1**-Mn, c) **1**-Fe, d) **1**-Co, e) **1**-Cu, and f) **1**-Zn.

3.14.1 *In situ Catalyst Recycling Studies (1-Mn and 1-Cr)*

In a nitrogen atmosphere glovebox, **1**-M (0.00674 mmol, 0.01 equiv) was dissolved in C_6D_6 (0.5 mL) with a mesitylene internal standard and transferred to a J-young NMR tube. Neat ^{t}BuNC (12.5 µL, 0.111 mmol, 1.65 equiv) and TsN_3 (10.3 µL, 0.0674 mmol, 1.00 equiv) were added at room temperature and the reaction was monitored by ^{1}H NMR spectroscopy. After complete consumption of TsN_3 (~1 hr for **1**-Mn and ~6 hrs for **1**-Cr), the reaction mixture was filtered through Celite plug and more TsN_3 (10.3 µL, 0.0674 mmol, 1.00 equiv) and ^{t}BuNC (7.6 µL, 0.0674 mmol, 1.00 equiv) was added for an additional round of catalysis. Both **1**-Mn and **1**-Cr show good activity for the subsequent catalytic cycle with complete conversion of the substrates on a similar time scale to the initial round of catalysis.

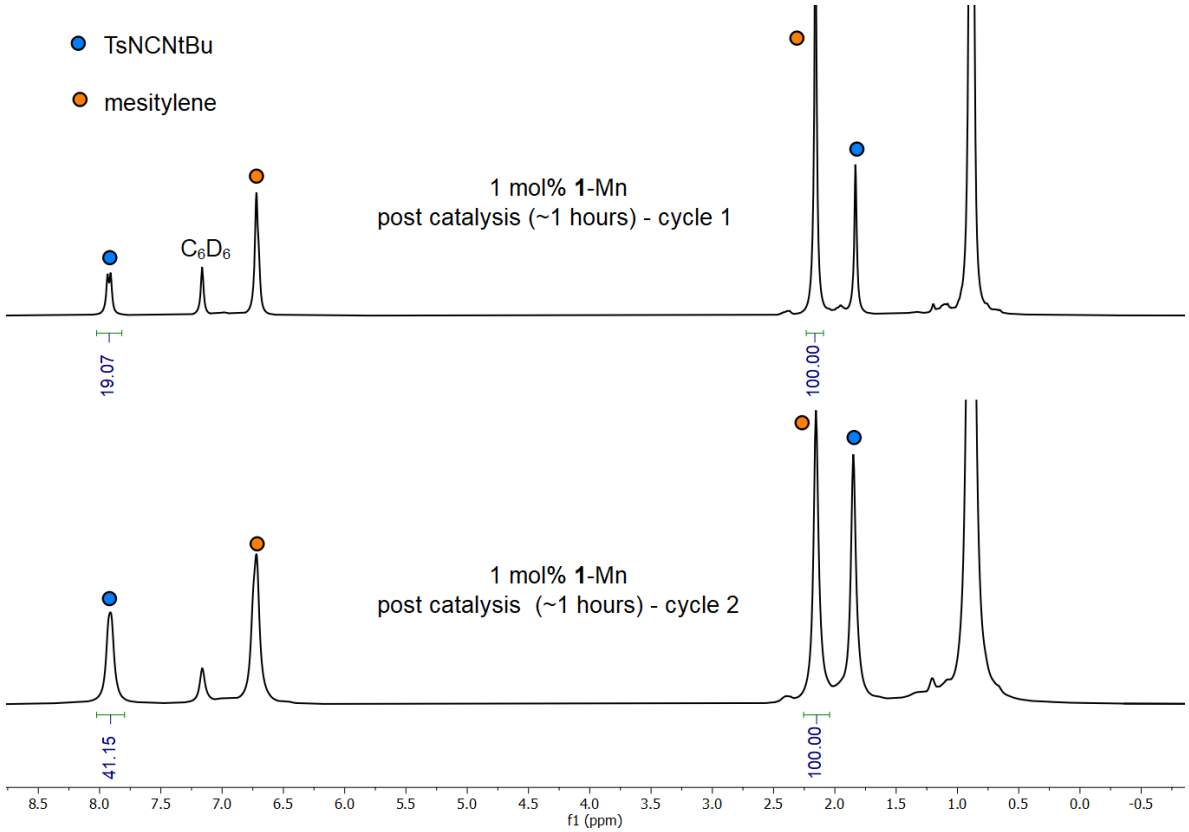

Figure 3.19. ^{1}H NMR (300 MHz, C_6D_6, 25 °C) spectra demonstrating that **1**-Mn (1 mol %) can be recycled for the catalytic synthesis of TsNCN^{t}Bu.

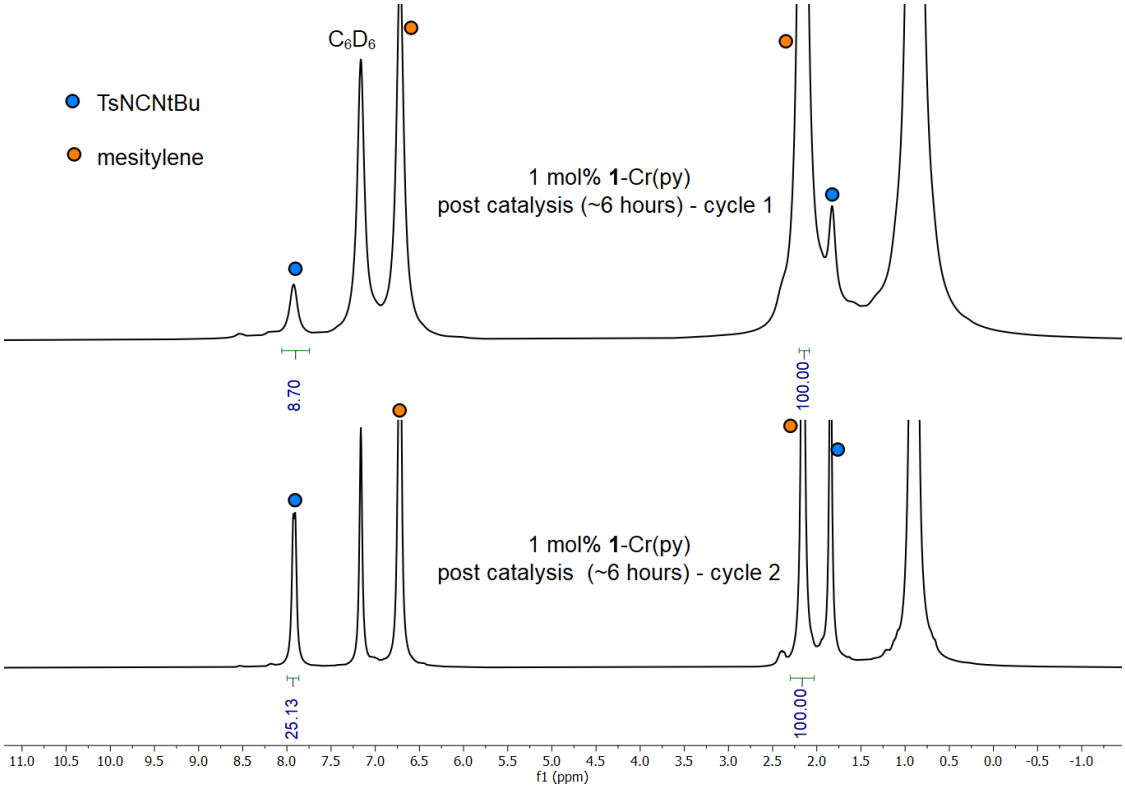

Figure 3.20. ^{1}H NMR (300 MHz, C_6D_6, 25 °C) spectra demonstrating that **1**-Cr(py) (1 mol %) can be recycled for the catalytic synthesis of TsNCN^{t}Bu.

3.15 Paramagnetic ^{31}P NMR Studies

The observed experimental chemical shift of a paramagnetic compound is given by equation (S1),[1,2,3]

$$\delta_T^{obs} = \delta^{dia} + \delta_T^{para} = \delta^{dia} + \frac{S(S+1)\beta_e}{3k_bT\gamma_N} gA \qquad (3.1)$$

in which δ^{dia} and δ^{para} are the diamagnetic and respectively the paramagnetic contributions to the chemical shift, S is total spin of the system, β_e is the Bohr magneton, k_b the Boltzmann constant, T the absolute temperature, γ_N the nuclear gyromagnetic ratio, g the g-tensor, and A the hyperfine tensor. Paramagnetic ^{31}P NMR spectra for **1**-Fe, **1**-Co, and **1**-Cu were collected at 290, 300, 310, 320, and 330 K on a 300 MHz NMR instrument. The temperature was calibrated using an 80% ethylene glycol/DMSO-d_6 external standard.

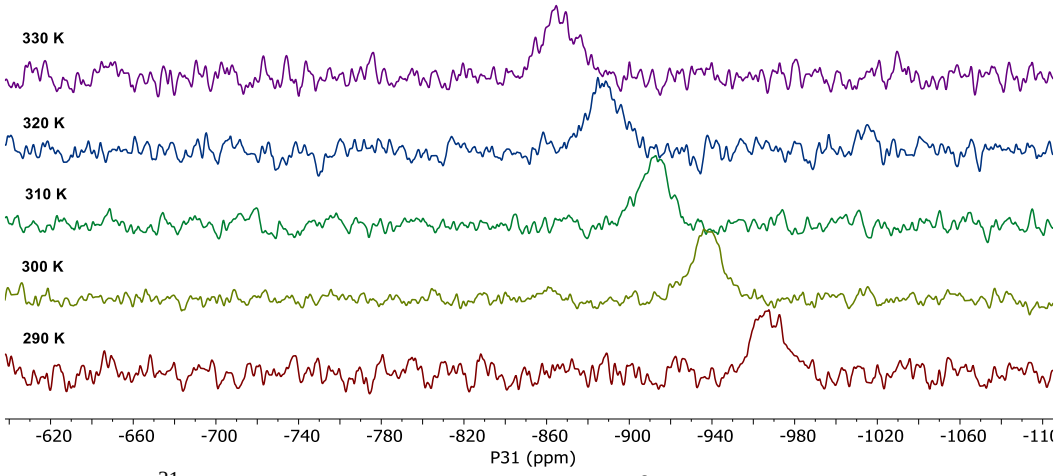

Figure 3.21. VT-^{31}P-NMR (C_6D_6, 121 MHz) spectra of **1**-Fe (-630 to -1100 ppm range)

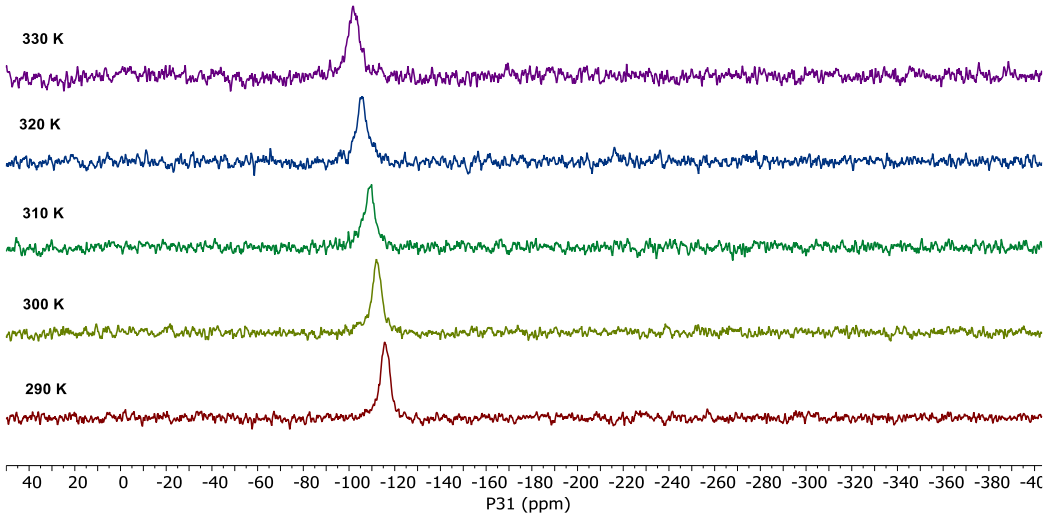

Figure 3.22. VT-^{31}P-NMR (C_6D_6, 121 MHz) spectra of **1**-Fe (50 to -400 ppm range)

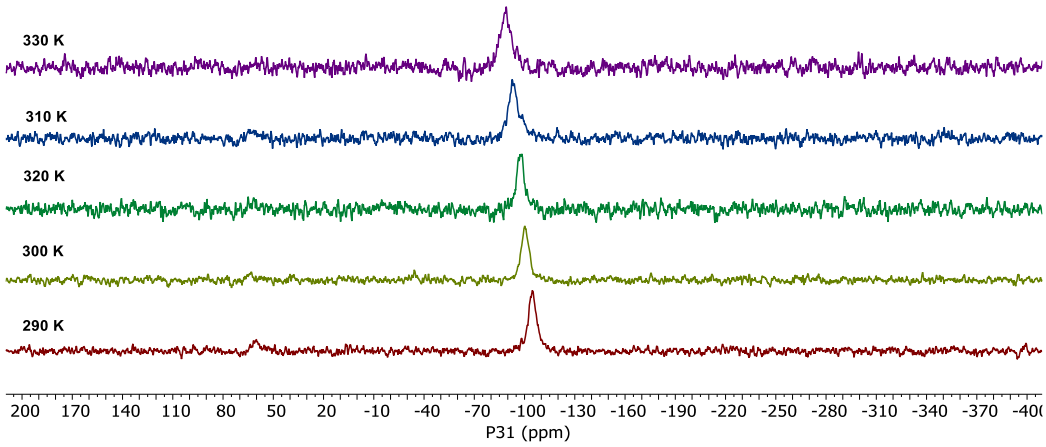

Figure 3.23. VT-^{31}P-NMR (C_6D_6, 121 MHz) spectra of **1**-Co (200 to -400 ppm range).

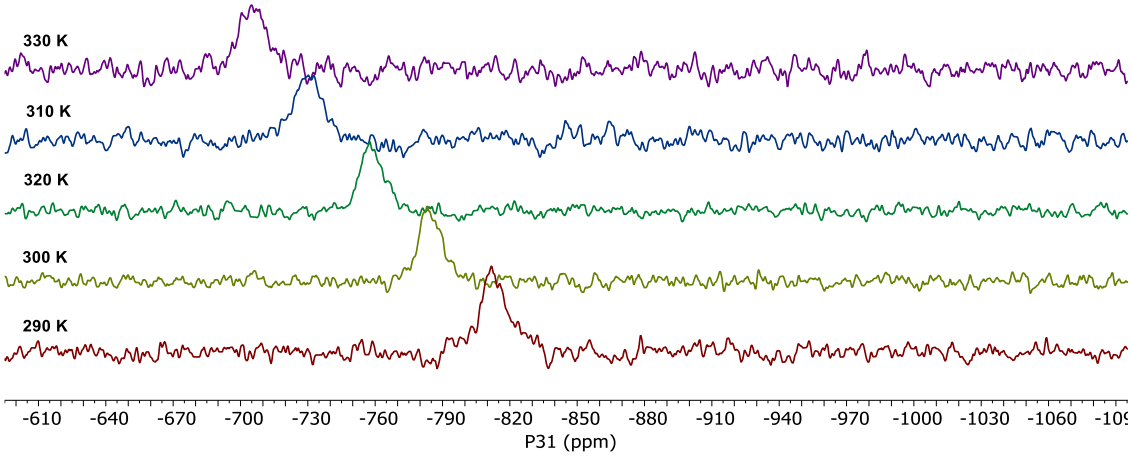

Figure 3.24. VT-^{31}P-NMR (C_6D_6, 121 MHz) spectra of **1**-Co (-620 to -1050 ppm range)

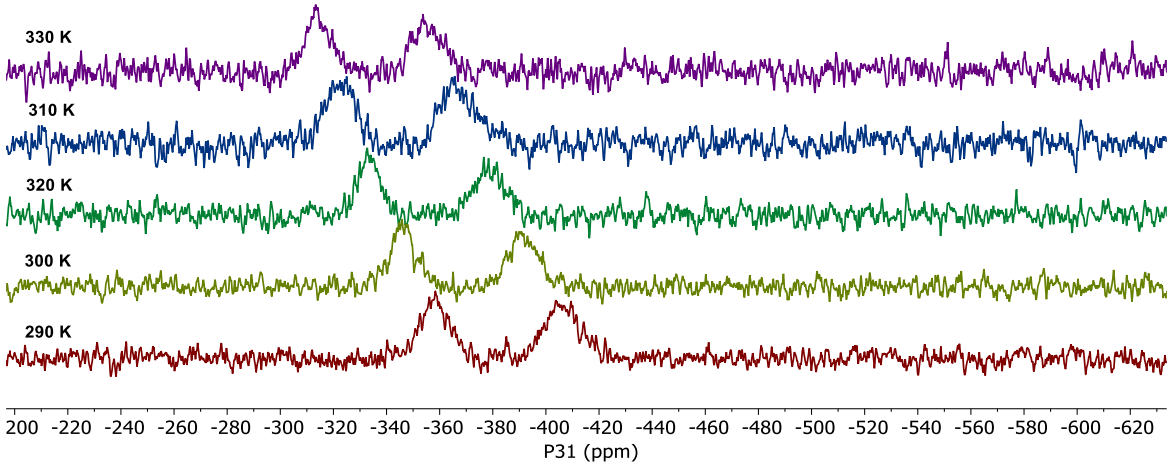

Figure 3.25. VT-^{31}P-NMR (C_6D_6, 121 MHz) spectra of **1**-Cu (-200 to -630 ppm range)

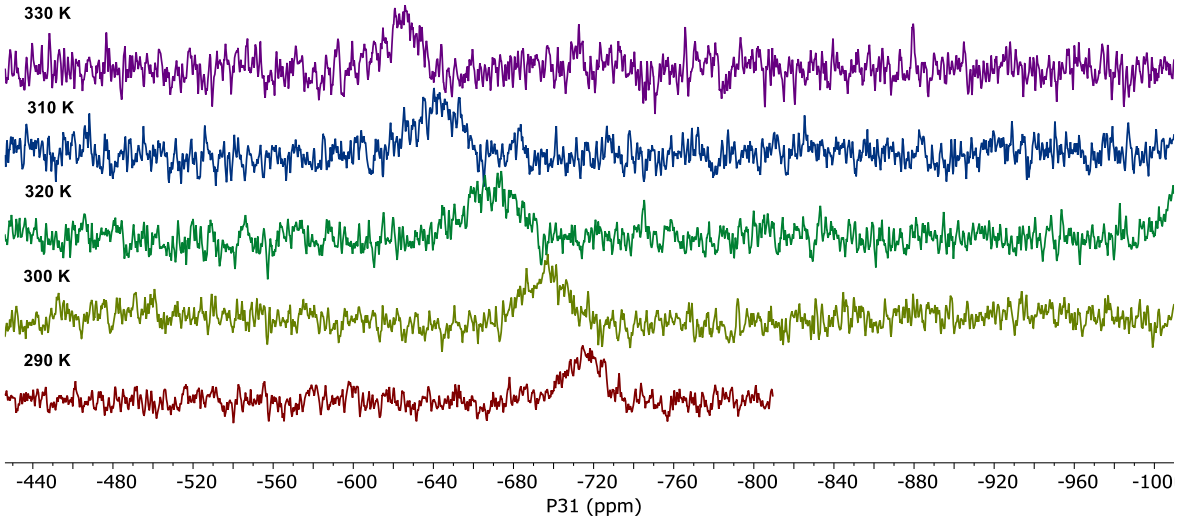

Figure 3.26. VT-^{31}P-NMR (C_6D_6, 121 MHz) spectra of **1**-Cu (-430 to -1000 ppm range)

3.16 *Isocyanide* Coordination Experiments and Determination of the Binding Constant

For the equilibrium,

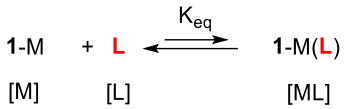

the equilibrium constant can be written as

$$K_{eq} = \frac{[ML]}{[M][L]}$$

and, for a known total concentration of **1**-M containing species, $[M^{tot}] = [M] + [ML]$ and L, $[L^{tot}] = [L] + [ML]$, the equilibrium constant can be defined as

$$K_{eq} = \frac{[ML]}{([M^{tot}] - [ML])([L^{tot}] - [L])}$$

It is then possible to fit the equilibrium constant to the ^{1}H NMR data obtained by treating **1**-M with increasing amounts of L. This utilizes the ability to treat the chemical shift, δ, of a peak from these spectra as a weighted average of the chemical shift of that peak in the absence of L, δ_0, and in the presence of an infinite excess of L, δ_{max} such that

$$\delta = \frac{[M]\delta_0 + [ML]\delta_{max}}{[M^{tot}]}$$

After substituting the known concentrations we obtain the [ML] as a function of **1**-M initial concentration and chemical shift.

$$[ML] = [M^{tot}]\frac{\delta - \delta_0}{\delta_{max} - \delta_0}$$

In practice, it is also necessary to fit δ_{max}, as it is not possible to achieve an infinite excess of L.

3.16.1 *Experimental Details of Coordination Studies*

A *J*-young NMR tube was charged with a solution of **1**-M (1.0 equiv) in C_6D_6 (0.5 mL). A stock solution of ^{t}BuNC in C_6D_6 (0.5 M) was then added as aliquots and the reaction was monitored using ^{1}H NMR spectroscopy. The binding constant was determined using the equations presented above

Table 3.2. Approximate ^{t}BuNC binding constant of **1**-M clusters determined by ^{1}H NMR spectroscopy.

	^{t}BuNC binding constant (M^{-1})
1-Cr(py)	1413 (1^{st}), 5 (2^{nd})
1-Mn	ca. 268
1-Fe	26
1-Co	362
1-Cu	23
1-Zn	6

3.17 X-Ray Diffraction Studies

Data was collected at 100K on a Bruker APEX II single crystal X-ray diffractometer using Mo-radiation. The data was integrated and scaled using SAINT, SADABS within the APEX2 software package by Bruker.[9] Solution by direct methods (SHELXT[10] or SIR97[11,12]) produced a complete heavy atom phasing model consistent with the proposed structure. The structure was completed by difference Fourier synthesis with SHELXL.[10,13,14] Scattering factors are from Waasmair and Kirfel.[15] Hydrogen atoms were placed in geometrically idealized positions and constrained to ride on their parent atoms with C-H distances in the range 0.95-1.00 Angstrom. Isotropic thermal parameters U_{eq} were fixed such that they were $1.2U_{eq}$ of their parent atom U_{eq} for CH's and $1.5U_{eq}$ of their parent atom U_{eq} in case of methyl groups. All non-hydrogen atoms were refined anisotropically by full-matrix least-squares.

3.17.1 ***1*-*Cr(THF)***

Diffraction quality, dark red crystals of **1**-Cr(THF) were grown via vapor diffusion of *n*-pentane into a saturated solution of toluene at 25 °C over the course of 3 days. The asymmetric unit contains one **1**-Cr cluster bound by a THF ligand, and three toluene molecules. The refinement was routine.

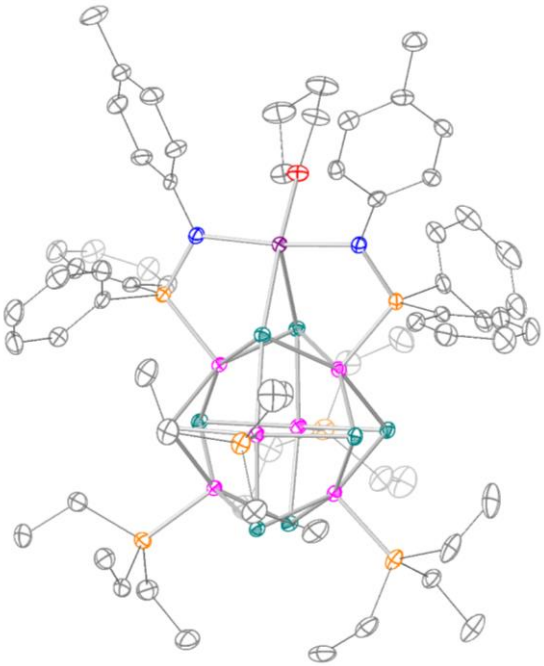

Figure 3.27. ORTEP of **1**-Cr(THF) with thermal ellipsoids at the 50% probability level. Hydrogen atoms and co-crystallized toluene molecules are omitted for clarity.

3.17.2 ***1*-*Mn***

Diffraction quality crystals of **1**-Mn was grown via vapor diffusion of pentane into a saturated solution of toluene at room temperature over the course of 3 days. Crystals were dissected from a larger conglomerate which resulted in either some damage or a remaining small piece of another grain. A twin law was found, and two domain integration was tried however the data statistics became worse with less reflections integrated and still some larger residual density peaks remaining. The displacement parameters of carbon atoms were stabilized with an ISOR card and 250 bad reflections were removed from the refinement as a result of the possible twinning. The asymmetric unit contains two clusters with no solvent molecules or disordered moieties.

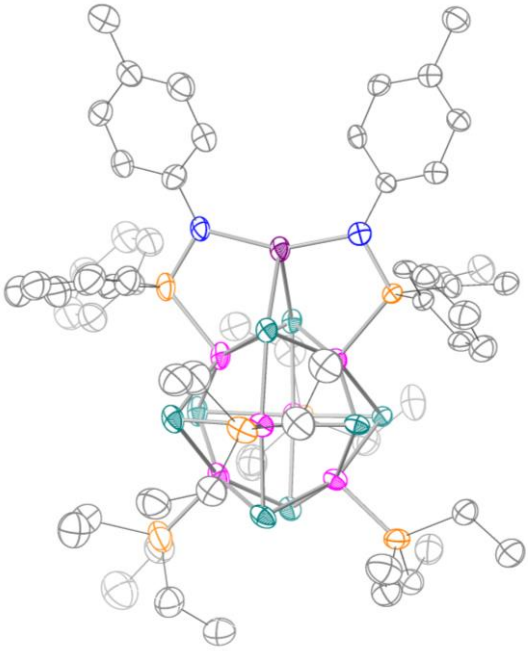

Figure 3.28. ORTEP of **1**-Mn with thermal ellipsoids at the 50% probability level. Hydrogen atoms are omitted for clarity.

3.17.3 ***1-Fe***

Diffraction-quality, dark red crystals of **1**-Fe were grown at −35 °C from a saturated Et_2O solution. The asymmetric unit contains a disordered Et_2O solvent and a half of a chemically disordered **1**-Fe cluster complex, with one component at 88.3(4)% containing Fe, the other at 11.7% lacking the Fe, but showing the nitrogen protonated. Additional structural disorder includes split nitrogen positions resulting from the presence versus absence of the Fe.

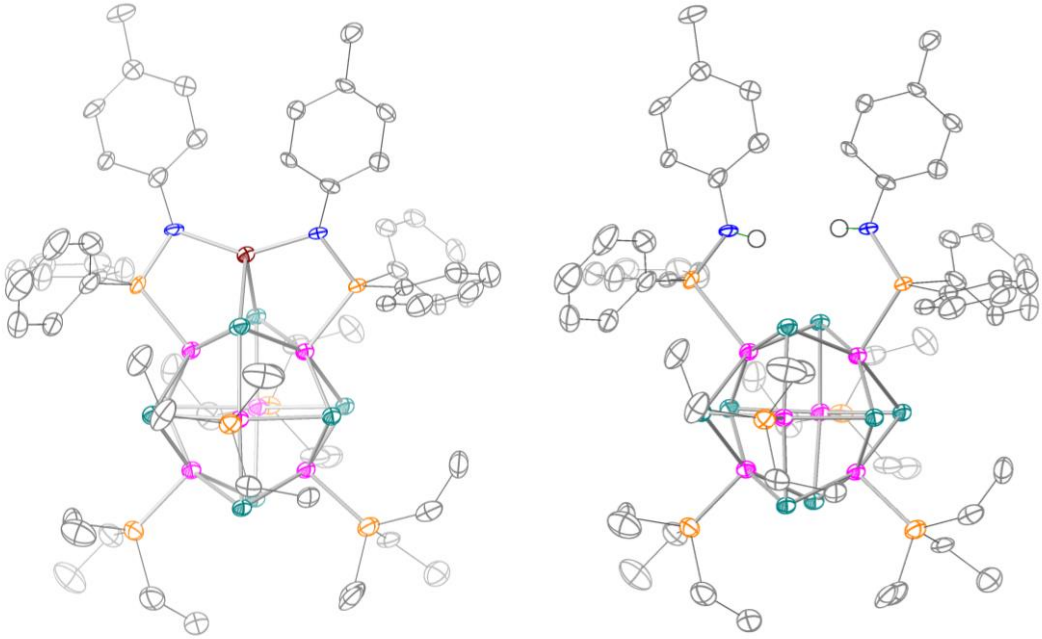

Figure 3.29. ORTEP of **1**-Fe (left) and **1**-H_2 (right) with, with thermal ellipsoids at the 50% probability level. Hydrogen atoms, PEt_3 disorder, and Et_2O molecule are omitted for clarity.

3.17.4 ***1*-*Co***

Diffraction-quality, dark red crystals of **1**-Co were grown at −35 °C from a saturated Et_2O solution. The asymmetric unit contains a disordered Et_2O solvent which was removed with SQUEEZE, and a chemically disordered **1**-Co cluster complex, with one component at 75% containing Co, the other at 25% being the protonated **1**-H_2 ligand. Some thermal restraints were required on disordered triethyl moieties and a few other atoms. 77 bad diffraction peaks were omitted.

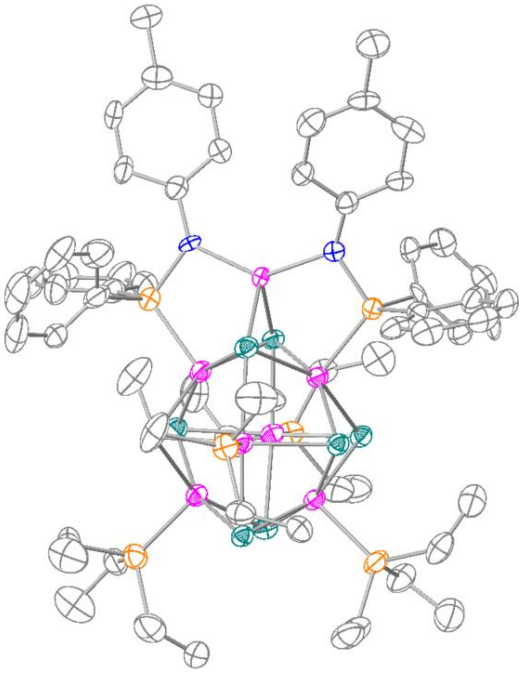

Figure 3.30. ORTEP of **1**-Co with thermal ellipsoids at the 50% probability level. Hydrogen atoms and **1**-H_2 disordered component are omitted for clarity.

3.17.5 ***1*-*Zn***

Diffraction-quality, dark colored prismatic crystals of **1**-Zn were grown via vapor diffusion of *n*-pentane into a saturated solution of **1**-Zn in toluene at room temperature over the course of 4 days. The structure is pseudo-merohedrally twinned and the asymmetric unit contains two clusters.

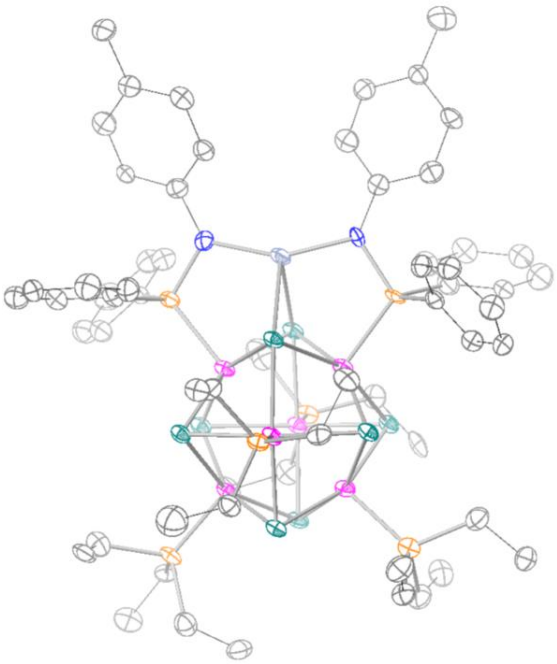

Figure 3.31. ORTEP of **1**-Zn with thermal ellipsoids at the 50% probability level. Hydrogen atoms omitted for clarity.

Table 3.3. Crystallographic data for **1**-Fe, **1**-Co, and **1**-Cr(THF)

Compound	**88.3%** 1-**Fe • 11.7%** 1-H_2 • Et_2O	**75%** 1-**Co • 25%** 1-H_2	**2** 1-**Cr(THF) • 3 toluene**
CCDC Number	2113026	2113027	2113030
Empirical formula	$C_{66}H_{104.23}Co_6Fe_{0.88}N_2OP_6Se_8$	$C_{62}H_{94.5}Co_{6.75}N_2P_6Se_8$	$C_{167}H_{244}Co_{12}Cr_2N_4O_2P_{12}Se_{16}$
Formula weight	2162.11	2083.17	4785.81
Temperature (K)	100(2)	100(2)	100(2)
Wavelength (Å)	0.71073	0.71073	0.71073
Crystal system	Monoclinic	Monoclinic	Monoclinic
Space group	P 2_1/n	P $2_{1/n}$	C 2/c
a (Å)	17.3857(10)	17.3986(10)	23.673(3)
b (Å)	26.0557(17)	25.9589(16)	15.506(3)
c (Å)	17.8253(10)	17.8366(11)	50.796(9)
α (°)	90	90	90
β (°)	93.551(4)	93.233(3)	96.503(7)
γ (°)	90	90	90
Volume (Å^3)	8059.3(8)	8043.1(8)	18526(6)
Z	4	4	4
Calculated Density (g cm^{-3})	1.782	1.720	1.716
Absorption coefficient (mm^{-1})	5.131	5.133	4.452
F(000)	4277	4099	9544
Crystal size (mm^3)	0.150 x 0.070 x 0.040	0.170 x 0.090 x 0.060	0.160 x 0.100 x 0.080
Theta range for data collection (°)	1.386 to 28.398	1.387 to 25.350	1.573 to 28.706
Index ranges	$-23 \le h \le 23$, $-34 \le k \le 34$, $0 \le l \le 23$	$-20 \le h \le 20$, $-31 \le k \le 31$, $0 \le l \le 21$	$-31 \le h \le 31$, $-20 \le k \le 20$, $-68 \le l \le 67$
Reflections collected	39471	28941	86106
Independent reflections	20042 [R(int) = 0.1524]	14650 [R(int) = 0.0493]	23249 [R(int) = 0.0549]
Completeness to theta = 25.000°	99.9 %	99.5 %	100.0 %
Data / restraints / parameters	20042 / 116 / 883	14650 / 178 / 729	23249 / 15 / 1005
Goodness-of-fit on F^2	0.906	1.072	1.060
Final R indices [I>2sigma(I)]	R_1 = 0.0595, wR_2 = 0.1064	R_1 = 0.0811, wR_2 = 0.2053	R_1 = 0.0363, wR_2 = 0.0617
R indices (all data)	R_1 = 0.1950, wR_2 = 0.1440	R_1 = 0.1202, wR_2 = 0.2294	R_1 = 0.0562, wR_2 = 0.0662
Largest diff. peak and hole (e$^-$Å^{-3})	1.294 and -0.924	2.672 and -1.227	1.512 and -0.855

Table 3.4. Crystallographic data for **1**-Mn, **1**-Cu, and **1**-Zn.

Compound	1-**Mn**	1-**Cu • 2 pentane**	1-**Zn**
CCDC Number	2113029	2113031	2113028
Empirical formula	$C_{62}H_{94}Co_6MnN_2P_6Se_8$	$C_{72}H_{118}Co_6CuN_2P_6Se_8$	$C_{62}H_{94}Co_6N_2P_6Se_8Zn$
Formula weight	2093.41	2246.30	2103.84
Temperature (K)	100(2)	100(2)	100(2)
Wavelength (Å)	0.71073	0.71073	0.71073
Crystal system	Triclinic	Triclinic	Triclinic
Space group	P -1	P -1	P -1
a (Å)	17.6675(12)	14.3457(7)	17.804(2)
b (Å)	17.9931(13)	18.2058(10)	17.951(2)
c (Å)	24.7981(17)	19.0993(10)	24.568(3)
α (°)	91.591(4)	111.022(2)	90.220(5)
β (°)	109.615(4)	90.795(2)	109.065(4)
γ (°)	93.499(4)	112.790(2)	91.102(5)
Volume (Å^3)	7402.1(9)	4224.5(4)	7419.6(14)
Z	4	2	4
Calculated Density (g cm^{-3})	1.878	1.766	1.883
Absorption coefficient (mm^{-1})	5.578	4.996	5.718
F(000)	4116	2234	4136
Crystal size (mm^3)	0.170 x 0.150 x 0.130	0.230 x 0.120 x 0.110	0.170 x 0.120 x 0.120
Theta range for data collection (°)	1.135 to 25.027	1.321 to 28.358	1.135 to 26.610
Index ranges	$-21 \le h \le 21$, $-21 \le k \le 21$, $-29 \le l \le 29$	$-19 \le h \le 19$, $-24 \le k \le 24$, $-25 \le l \le 25$	$-22 \le h \le 22$, $-22 \le k \le 22$, $-30 \le l \le 30$
Reflections collected	51698	237092	59806
Independent reflections	25864 [R(int) = 0.0621]	21056 [R(int) = 0.0723]	30289 [R(int) = 0.1043]
Completeness to theta = 25.000°	99.0 %	100.0 %	100.0 %
Data / restraints / parameters	25864 / 744 / 1535	21056 / 149 / 920	30289 / 768 / 1536
Goodness-of-fit on F^2	1.084	1.013	1.037
Final R indices [I>2sigma(I)]	R_1 = 0.1103, wR_2 = 0.2803	R_1 = 0.0371, wR_2 = 0.0796	R_1 = 0.1103, wR_2 = 0.2884
R indices (all data)	R_1 = 0.1550, wR_2 = 0.3217	R_1 = 0.0691, wR_2 = 0.0927	R_1 = 0.1774, wR_2 = 0.3495
Largest diff. peak and hole (e$^-$Å^{-3})	5.484 and -2.499	1.190 and -0.917	3.300 and -2.247

Table 3.5. Select interatomic distances (Å).

Compound	intra-Co_6Se_8 (avg, Å)			MCo_2Se_2 edge unit (Å)							Geometry Index
	Co–Se	Co...Co	Se...Se	Co–Se	Co...Co	Se...Se	M...Se		M...Co		
1-Cr(THF)	2.35	2.93	3.26	2.37	2.925(1)	3.351(6)	2.581(6)	2.772(7)	3.263(3)	3.284(5)	$\tau_5 = 0.12$
1-Mn	2.35	2.94	3.26	2.39	2.909(6)	3.458(5)	2.572(7)	2.532(6)	2.974(6)	3.059(6)	$\tau_4 = 0.73$
1-Fe	2.35	2.94	3.27	2.40	2.890(8)	3.504(8)	2.501(7)	2.506(6)	2.94(1)	2.937(5)	$\tau_4 = 0.77$
1-Co	2.35	2.94	3.26	2.40	2.901(2)	3.502(3)	2.379(4)	2.391(4)	2.758(3)	2.806(3)	$\tau_4 = 0.81$
1-Cu	2.34	2.90	3.26	2.34	2.816(3)	3.386(2)	2.792(5)	2.850(3)	3.344(4)	3.345(7)	-
1-Zn	2.35	2.94	3.26	2.38	2.895(8)	3.432(5)	2.562(7)	2.586(7)	3.069(8)	3.087(9)	$\tau_4 = 0.75$
$Co_6Se_8(PEt_3)_4(CO)_2$ [i]	2.34	2.94	3.25	-	-	-	-	-	-	-	-
$Co_6Se_8L^H_6$ [i]	2.34	2.95	3.25	-	-	-	-	-	-	-	-

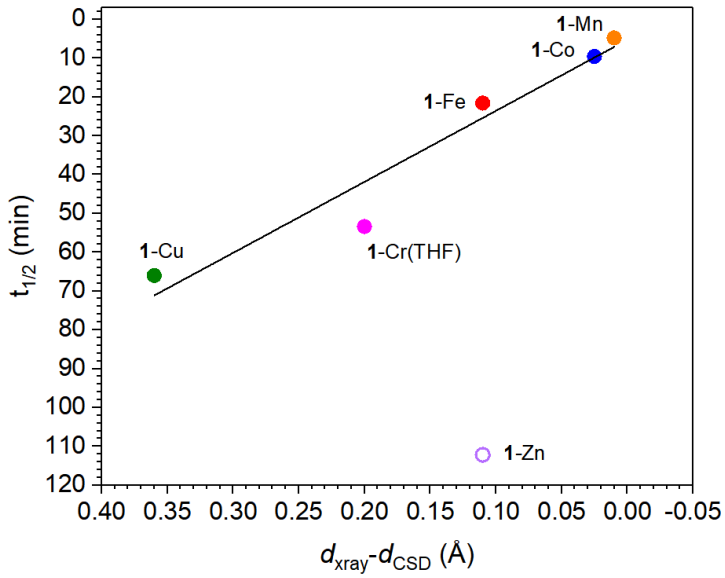

Figure 3.32. Linear correlation between spatial overlap (d_{xray}-d_{CSD}) and $t_{1/2}$ of carbodiimide catalysis by **1**-M series. **1**-Zn is represented as hollow circle to differentiate it from the series due to the ostensibly different reaction mechanism compared to the other **1**-M clusters.

3.18 DFT Calculations

All calculations were performed using Gaussian 16, Revision A.03 quantum chemistry program package for the Linux operating system.[17] The initial starting point geometries were obtained from the corresponding crystallographically obtained structures and optimized to a minimum, followed by analytical frequency calculations (Hessian) to confirm that no imaginary frequencies were present. The geometry optimizations were performed using unrestricted DFT calculations at a pure GGA functional level using Becke's 1988 gradient-corrected exchange functional and Perdew's 1986 electron correlation functional (uBPV86) and def2SVP basis set. Using the optimized geometries, single point calculations were performed at the uB3LYP+/cc-pVTZ that were used for orbital energy diagrams and spin density calculations. Multiwfn was used to generate partial density of states plots.[18]

Example of geometry optimizations:

%nprocshared=28

%mem=64GB

%chk=FeCo6Se8Tol_0_5_u_bvp86_def2SVP_OPT_FREQ.chk

#p opt freq ubvp86/def2SVP scf=maxcycle=3072 gfinput pop=(full,nbo)

FeCo6Se8Tol_0_5_u_bvp86_def2SVP_OPT_FREQ

0 5

coordinates from X-ray structure

Example of single point calculations:

%nprocshared=28

%mem=80GB

%oldchk= FeCo6Se8Tol_0_5_u_bvp86_def2SVP_OPT_FREQ.chk

%chk=Fe6Se8Tol_0_5_u_b3lyp_plus_ccpVTZ_NMR.chk

#p ub3lyp IOp(3/76=1000001500) IOp(3/77=0720008000) IOp(3/78=0810010000) cc-pVTZ guess=read geom=check scf=maxcycle=3072 gfinput pop=full IOp(6/82=1)

FeCo6Se8Tol_0_5_u_b3lyp_plus_ccpVTZ_NMR

0 5

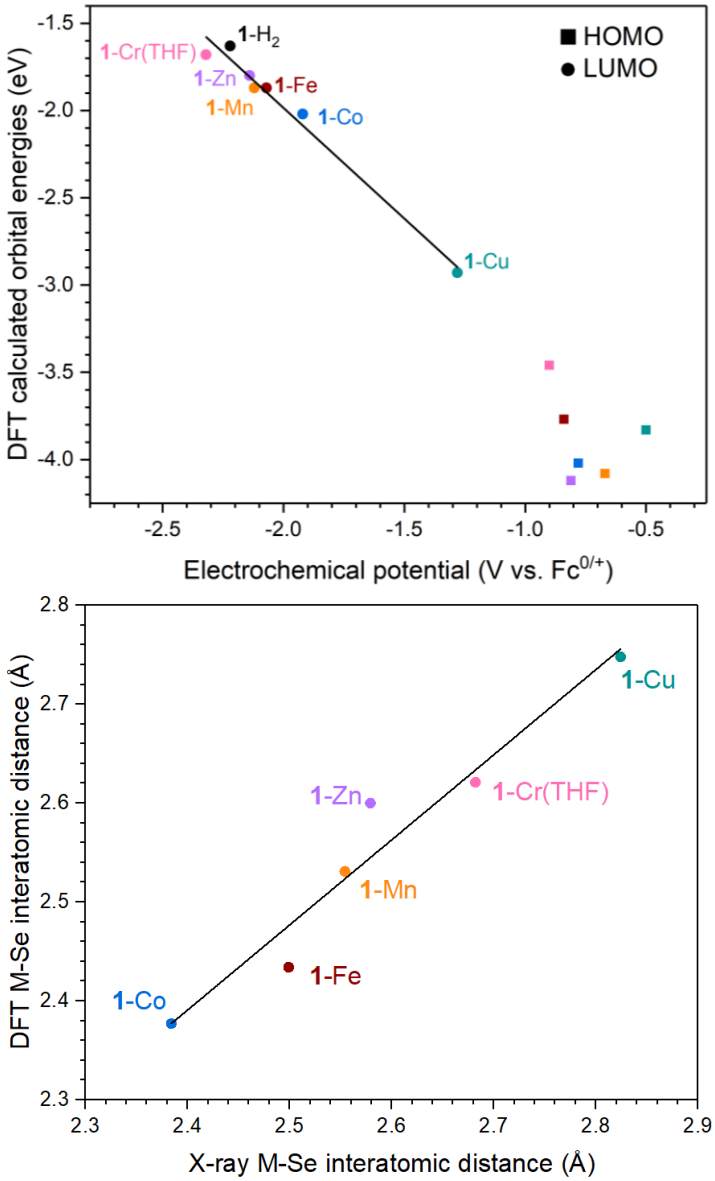

Figure 3.33. DFT calculated HOMO and LUMO energies plotted versus electrochemical oxidation and reduction potentials obtained from cyclic voltammetry (200 mV/s, 0.1 M $TBAPF_6$ in THF) (top). DFT optimized M-Se interatomic distances plotted versus interatomic distances obtained from single crystal X-ray structures. (bottom)

3.18.1 *Spin Density Calculations*

Table 3.6. Mulliken spin density (α-β) values for **1**-M series. Calculations performed using B3LYP+ functional at the cc-pVTZ level for all atoms.

	Mulliken Spin Densities (α-β)				
	Edge "M"	Co_6Se_8 core	Total Spin	% spin on edge	% spin on core
1-Cr(THF)	3.85	0.19	4	96.3	4.8
1-Mn	4.52	0.33	5	90.3	6.6
1-Fe	3.42	0.31	4	85.4	7.7
1-Co	2.30	0.39	3	76.7	12.9
1-Ni	1.28	0.37	2	64.0	18.6
1-Cu	0.00	1.06	1	0	105.6

3.18.2 *DFT Calculations of Putative **1**-M(NTs) Intermediates*

The initial starting point geometries for **1**-Cr(NTs) and **1**-Co(NTs) were obtained by replicating the edge site geometry in the previously reported **Cr**$_3$(NTs)$_3$ cluster.[19] The optimization and single-point calculations were done with the same functionals and basis sets as the **1**-M cluster calculations (see above). **1**-Cr(NTs) optimized with sulfonyl chelation, similar to what is observed with the **Cr**$_3$ variants, however **1**-Co(NTs) exhibits end on nitrene coordination with no sulfonyl chelation. The interatomic distances in **1**-Cr(NTs) replicate well the experimental distances obtained from single crystal X-ray diffraction of the similar Cr(NTs) edges reported for the **Cr**$_3$ clusters (Table S5).

Table 3.7. Comparison of Cr(NTs) edge site bond metrics between DFT optimized structure of **1**-Cr(NTs), and the single crystal X-ray structures of the **Cr**$_3$ variants.

Cr(NTs) edge site bond metrics (Å)		
Compound	**DFT optimized geometry (uBPV86/def2SVP)**	
	Cr–Se	**Cr-N**
1-Cr(NTs)	2.49	1.84
	X-ray crystallography (avg. interatomic distance)	
Cr$_3$(NTs)$_3$	2.48	1.82
Cr$_3$(NTs)(CNtBu)$_2$	2.44	1.86
***Cr**$_3$(NTs)$_3$(CNtBu)$_3$	2.61	1.75

*Sulfonyl chelation is broken resulting in a different edge site geometry

3.19 REFERENCES

(1) Tauster, S. J. Strong Metal-Support Interactions. *Acc. Chem. Res.* **1987**, *20* (11), 389–394. https://doi.org/10.1021/ar00143a001.

(2) Campbell, C. T. Catalyst–Support Interactions: Electronic Perturbations. *Nature Chemistry* **2012**, *4* (8), 597–598. https://doi.org/10.1038/nchem.1412.

(3) Bruix, A.; Rodriguez, J. A.; Ramírez, P. J.; Senanayake, S. D.; Evans, J.; Park, J. B.; Stacchiola, D.; Liu, P.; Hrbek, J.; Illas, F. A New Type of Strong Metal–Support Interaction and the Production of H2 through the Transformation of Water on Pt/CeO2(111) and Pt/CeOx/TiO2(110) Catalysts. *J. Am. Chem. Soc.* **2012**, *134* (21), 8968–8974. https://doi.org/10.1021/ja302070k.

(4) Deelen, T. W. van; Mejía, C. H.; Jong, K. P. de. Control of Metal-Support Interactions in Heterogeneous Catalysts to Enhance Activity and Selectivity. *Nat Catal* **2019**, *2* (11), 955–970. https://doi.org/10.1038/s41929-019-0364-x.

(5) Liu, L.; Corma, A. Metal Catalysts for Heterogeneous Catalysis: From Single Atoms to Nanoclusters and Nanoparticles. *Chem. Rev.* **2018**, *118* (10), 4981–5079. https://doi.org/10.1021/acs.chemrev.7b00776.

(6) Qi, K.; Chhowalla, M.; Voiry, D. Single Atom Is Not Alone: Metal–Support Interactions in Single-Atom Catalysis. *Materials Today* **2020**, *40*, 173–192. https://doi.org/10.1016/j.mattod.2020.07.002.

(7) Wang, A.; Li, J.; Zhang, T. Heterogeneous Single-Atom Catalysis. *Nature Reviews Chemistry* **2018**, *2* (6), 65–81. https://doi.org/10.1038/s41570-018-0010-1.

(8) Wang, X.; Zhang, Y.; Wu, J.; Zhang, Z.; Liao, Q.; Kang, Z.; Zhang, Y. Single-Atom Engineering to Ignite 2D Transition Metal Dichalcogenide Based Catalysis: Fundamentals, Progress, and Beyond. *Chem. Rev.* **2022**, *122* (1), 1273–1348. https://doi.org/10.1021/acs.chemrev.1c00505.

(9) Lou, Y.; Zheng, Y.; Li, X.; Ta, N.; Xu, J.; Nie, Y.; Cho, K.; Liu, J. Pocketlike Active Site of Rh1/MoS2 Single-Atom Catalyst for Selective Crotonaldehyde Hydrogenation. *J. Am. Chem. Soc.* **2019**, *141* (49), 19289–19295. https://doi.org/10.1021/jacs.9b06628.

(10) Hong, W.; Meza, E.; Li, C. W. Controlling the Co–S Coordination Environment in Co-Doped WS2 Nanosheets for Electrochemical Oxygen Reduction. *J. Mater. Chem. A* **2021**, *9* (35), 19865–19873. https://doi.org/10.1039/D1TA02468J.

(11) Chhowalla, M.; Shin, H. S.; Eda, G.; Li, L.-J.; Loh, K. P.; Zhang, H. The Chemistry of Two-Dimensional Layered Transition Metal Dichalcogenide Nanosheets. *Nature Chem* **2013**, *5* (4), 263–275. https://doi.org/10.1038/nchem.1589.

(12) Harris, S.; Chianelli, R. R. Catalysis by Transition Metal Sulfides: A Theoretical and Experimental Study of the Relation between the Synergic Systems and the Binary Transition Metal Sulfides. *Journal of Catalysis* **1986**, *98* (1), 17–31. https://doi.org/10.1016/0021-9517(86)90292-7.

(13) Raybaud, P.; Hafner, J.; Kresse, G.; Kasztelan, S.; Toulhoat, H. Structure, Energetics, and Electronic Properties of the Surface of a Promoted MoS2 Catalyst: An Ab Initio Local Density Functional Study. *Journal of Catalysis* **2000**, *190* (1), 128–143. https://doi.org/10.1006/jcat.1999.2743.

(14) Berhault, G.; Lacroix, M.; Breysse, M.; Maugé, F.; Lavalley, J.-C.; Nie, H.; Qu, L. Characterization of Acidic Sites of Silica-Supported Transition Metal Sulfides by Pyridine and 2,6 Dimethylpyridine Adsorption: Relation to Activity in CH3SH Condensation. *Journal of Catalysis* **1998**, *178* (2), 555–565. https://doi.org/10.1006/jcat.1998.2196.

(15) Bolar, S.; Shit, S.; Murmu, N. C.; Samanta, P.; Kuila, T. Activation Strategy of MoS2 as HER Electrocatalyst through Doping-Induced Lattice Strain, Band Gap Engineering, and Active Crystal Plane Design. *ACS Appl. Mater. Interfaces* **2021**, *13* (1), 765–780. https://doi.org/10.1021/acsami.0c20500.

(16) Jaramillo, T. F.; Jørgensen, K. P.; Bonde, J.; Nielsen, J. H.; Horch, S.; Chorkendorff, I. Identification of Active Edge Sites for Electrochemical H2 Evolution from MoS2 Nanocatalysts. *Science* **2007**. https://doi.org/10.1126/science.1141483.

(17) Bonde, J.; Moses, P. G.; Jaramillo, T. F.; Nørskov, J. K.; Chorkendorff, I. Hydrogen Evolution on Nano-Particulate Transition Metal Sulfides. *Faraday Discuss.* **2008**, *140* (0), 219–231. https://doi.org/10.1039/B803857K.

(18) Tuxen, A. K.; Füchtbauer, H. G.; Temel, B.; Hinnemann, B.; Topsøe, H.; Knudsen, K. G.; Besenbacher, F.; Lauritsen, J. V. Atomic-Scale Insight into Adsorption of Sterically Hindered

Dibenzothiophenes on MoS2 and Co–Mo–S Hydrotreating Catalysts. *Journal of Catalysis* **2012**, *295*, 146–154. https://doi.org/10.1016/j.jcat.2012.08.004.

(19) Lauritsen, J. V.; Nyberg, M.; Nørskov, J. K.; Clausen, B. S.; Topsøe, H.; Lægsgaard, E.; Besenbacher, F. Hydrodesulfurization Reaction Pathways on MoS2 Nanoclusters Revealed by Scanning Tunneling Microscopy. *Journal of Catalysis* **2004**, *224* (1), 94–106. https://doi.org/10.1016/j.jcat.2004.02.009.

(20) Lauritsen, J. V.; Kibsgaard, J.; Olesen, G. H.; Moses, P. G.; Hinnemann, B.; Helveg, S.; Nørskov, J. K.; Clausen, B. S.; Topsøe, H.; Lægsgaard, E.; Besenbacher, F. Location and Coordination of Promoter Atoms in Co- and Ni-Promoted MoS2-Based Hydrotreating Catalysts. *Journal of Catalysis* **2007**, *249* (2), 220–233. https://doi.org/10.1016/j.jcat.2007.04.013.

(21) Kibsgaard, J.; Tuxen, A.; Knudsen, K. G.; Brorson, M.; Topsøe, H.; Lægsgaard, E.; Lauritsen, J. V.; Besenbacher, F. Comparative Atomic-Scale Analysis of Promotional Effects by Late 3d-Transition Metals in MoS2 Hydrotreating Catalysts. *Journal of Catalysis* **2010**, *272* (2), 195–203. https://doi.org/10.1016/j.jcat.2010.03.018.

(22) Tuxen, A.; Kibsgaard, J.; Gøbel, H.; Lægsgaard, E.; Topsøe, H.; Lauritsen, J. V.; Besenbacher, F. Size Threshold in the Dibenzothiophene Adsorption on MoS2 Nanoclusters. *ACS Nano* **2010**, *4* (8), 4677–4682. https://doi.org/10.1021/nn1011013.

(23) Rangarajan, S.; Mavrikakis, M. On the Preferred Active Sites of Promoted MoS2 for Hydrodesulfurization with Minimal Organonitrogen Inhibition. *ACS Catal.* **2017**, *7* (1), 501–509. https://doi.org/10.1021/acscatal.6b02735.

(24) Mom, R. V.; Louwen, J. N.; Frenken, J. W. M.; Groot, I. M. N. In Situ Observations of an Active MoS2 Model Hydrodesulfurization Catalyst. *Nat Commun* **2019**, *10* (1), 2546. https://doi.org/10.1038/s41467-019-10526-0.

(25) Chirik, P. J.; Wieghardt, K. Radical Ligands Confer Nobility on Base-Metal Catalysts. *Science* **2010**, *327* (5967), 794–795. https://doi.org/10.1126/science.1183281.

(26) Praneeth, V. K. K.; Ringenberg, M. R.; Ward, T. R. Redox-Active Ligands in Catalysis. *Angewandte Chemie International Edition* **2012**, *51* (41), 10228–10234. https://doi.org/10.1002/anie.201204100.

(27) Eisenhart, R. J.; Clouston, L. J.; Lu, C. C. Configuring Bonds between First-Row Transition Metals. *Acc. Chem. Res.* **2015**, *48* (11), 2885–2894. https://doi.org/10.1021/acs.accounts.5b00336.

(28) Cammarota, R. C.; Clouston, L. J.; Lu, C. C. Leveraging Molecular Metal–Support Interactions for H2 and N2 Activation. *Coordination Chemistry Reviews* **2017**, *334*, 100–111. https://doi.org/10.1016/j.ccr.2016.06.014.

(29) Bosnich, B. Cooperative Bimetallic Redox Reactivity. *Inorg. Chem.* **1999**, *38* (11), 2554–2562. https://doi.org/10.1021/ic990164k.

(30) Tyo, E. C.; Vajda, S. Catalysis by Clusters with Precise Numbers of Atoms. *Nature Nanotech* **2015**, *10* (7), 577–588. https://doi.org/10.1038/nnano.2015.140.

(31) Du, X.; Jin, R. Atomically Precise Metal Nanoclusters for Catalysis. *ACS Nano* **2019**, *13* (7), 7383–7387. https://doi.org/10.1021/acsnano.9b04533.

(32) Reed, C. J.; Agapie, T. A Terminal FeIII–Oxo in a Tetranuclear Cluster: Effects of Distal Metal Centers on Structure and Reactivity. *J. Am. Chem. Soc.* **2019**, *141* (24), 9479–9484. https://doi.org/10.1021/jacs.9b03157.

(33) Carr, C. R.; Taheri, A.; Berben, L. A. Fast Proton Transfer and Hydrogen Evolution Reactivity Mediated by [Co13C2(CO)24]4–. *J. Am. Chem. Soc.* **2020**, *142* (28), 12299–12305. https://doi.org/10.1021/jacs.0c04034.

(34) McSkimming, A.; Suess, D. L. M. Dinitrogen Binding and Activation at a Molybdenum–Iron–Sulfur Cluster. *Nat. Chem.* **2021**, *13* (7), 666–670. https://doi.org/10.1038/s41557-021-00701-6.

(35) Amtawong, J.; Balcells, D.; Wilcoxen, J.; Handford, R. C.; Biggins, N.; Nguyen, A. I.; Britt, R. D.; Tilley, T. D. Isolation and Study of Ruthenium–Cobalt Oxo Cubanes Bearing a High-Valent, Terminal RuV–Oxo with Significant Oxyl Radical Character. *J. Am. Chem. Soc.* **2019**, *141* (50), 19859–19869. https://doi.org/10.1021/jacs.9b10320.

(36) Schreiber, E.; Fertig, A. A.; Brennessel, W. W.; Matson, E. M. Oxygen-Atom Defect Formation in Polyoxovanadate Clusters via Proton-Coupled Electron Transfer. *J. Am. Chem. Soc.* **2022**, *144* (11), 5029–5041. https://doi.org/10.1021/jacs.1c13432.

(37) Li, G.; Jin, R. Atomically Precise Gold Nanoclusters as New Model Catalysts. *Acc. Chem. Res.* **2013**, *46* (8), 1749–1758. https://doi.org/10.1021/ar300213z.

(38) Zhu, Y.; Qian, H.; Jin, R. An Atomic-Level Strategy for Unraveling Gold Nanocatalysis from the Perspective of Aun(SR)m Nanoclusters. *Chemistry – A European Journal* **2010**, *16* (37), 11455–11462. https://doi.org/10.1002/chem.201001086.

(39) Liu, Y.; Tsunoyama, H.; Akita, T.; Xie, S.; Tsukuda, T. Aerobic Oxidation of Cyclohexane Catalyzed by Size-Controlled Au Clusters on Hydroxyapatite: Size Effect in the Sub-2 Nm Regime. *ACS Catal.* **2011**, *1* (1), 2–6. https://doi.org/10.1021/cs100043j.

(40) Chen, W.; Chen, S. Oxygen Electroreduction Catalyzed by Gold Nanoclusters: Strong Core Size Effects. *Angewandte Chemie* **2009**, *121* (24), 4450–4453. https://doi.org/10.1002/ange.200901185.

(41) Jin, R.; Li, G.; Sharma, S.; Li, Y.; Du, X. Toward Active-Site Tailoring in Heterogeneous Catalysis by Atomically Precise Metal Nanoclusters with Crystallographic Structures. *Chem. Rev.* **2021**, *121* (2), 567–648. https://doi.org/10.1021/acs.chemrev.0c00495.

(42) Kephart, J. A.; Mitchell, B. S.; Chirila, A.; Anderton, K. J.; Rogers, D.; Kaminsky, W.; Velian, A. Atomically Defined Nanopropeller Fe3Co6Se8(Ph2PNTol)6: Functional Model for the Electronic Metal–Support Interaction Effect and High Catalytic Activity for Carbodiimide Formation. *J. Am. Chem. Soc.* **2019**, *141* (50), 19605–19610. https://doi.org/10.1021/jacs.9b12473.

(43) Kephart, J. A.; Romero, C. G.; Tseng, C.-C.; Anderton, K. J.; Yankowitz, M.; Kaminsky, W.; Velian, A. Hierarchical Nanosheets Built from Superatomic Clusters: Properties, Exfoliation and Single-Crystal-to-Single-Crystal Intercalation. *Chem. Sci.* **2020**, *11* (39), 10744–10751. https://doi.org/10.1039/D0SC03506H.

(44) Mitchell, B. S.; Krajewski, S. M.; Kephart, J. A.; Rogers, D.; Kaminsky, W.; Velian, A. Redox-Switchable Allosteric Effects in Molecular Clusters. *JACS Au* **2022**, *2* (1), 92–96. https://doi.org/10.1021/jacsau.1c00491.

(45) Kephart, J. A.; Mitchell, B. S.; Kaminsky, W.; Velian, A. Multi-Active Site Dynamics on a Molecular Cr/Co/Se Cluster Catalyst. *J. Am. Chem. Soc.* **2022**, *144* (21), 9206–9211. https://doi.org/10.1021/jacs.2c00234.

(46) Mitchell, B. S.; Kaminsky, W.; Velian, A. Tuning the Electronic Structure of Atomically Precise Sn/Co/Se Nanoclusters via Redox Matching of Tin(IV) Surface Sites. *Inorg. Chem.* **2021**, *60* (9), 6135–6139. https://doi.org/10.1021/acs.inorgchem.1c00313.

(47) Jin, S.; Venkataraman, D.; DiSalvo, F. J. Ligand Substitution Reactions of W6S8L6 with Tricyclohexylphosphine (L = 4-Tert-Butylpyridine or n-Butylamine): 31P NMR and Structural Studies of W6S8(PCy3)n(4-Tert-Butylpyridine)6-n ($0 < n \leq 6$) Complexes. *Inorg. Chem.* **2000**, *39* (13), 2747–2757. https://doi.org/10.1021/ic991426l.

(48) Eames, E. V.; Betley, T. A. Site-Isolated Redox Reactivity in a Trinuclear Iron Complex. *Inorg. Chem.* **2012**, *51* (19), 10274–10278. https://doi.org/10.1021/ic301241s.

(49) Champsaur, A. M.; Velian, A.; Paley, D. W.; Choi, B.; Roy, X.; Steigerwald, M. L.; Nuckolls, C. Building Diatomic and Triatomic Superatom Molecules. *Nano Lett.* **2016**, *16* (8), 5273–5277. https://doi.org/10.1021/acs.nanolett.6b02471.

(50) Petel, B. E.; Brennessel, W. W.; Matson, E. M. Oxygen-Atom Vacancy Formation at Polyoxovanadate Clusters: Homogeneous Models for Reducible Metal Oxides. *J. Am. Chem. Soc.* **2018**, *140* (27), 8424–8428. https://doi.org/10.1021/jacs.8b05298.

(51) Venkateswara Rao, P.; Holm, R. H. Synthetic Analogues of the Active Sites of Iron−Sulfur Proteins. *Chem. Rev.* **2004**, *104* (2), 527–560. https://doi.org/10.1021/cr020615+.

(52) McSkimming, A.; Suess, D. L. M. Selective Synthesis of Site-Differentiated Fe4S4 and Fe6S6 Clusters. *Inorg. Chem.* **2018**, *57* (23), 14904–14912. https://doi.org/10.1021/acs.inorgchem.8b02684.

(53) Kephart, J. A.; Boggiano, A. C.; Kaminsky, W.; Velian, A. Inorganic Clusters as Metalloligands: Ligand Effects on the Synthesis and Properties of Ternary Nanopropeller Clusters. *Dalton Trans.* **2020**, *49* (45), 16464–16473. https://doi.org/10.1039/D0DT02416C.

(54) Driver, T. G. Recent Advances in Transition Metal-Catalyzed N-Atom Transfer Reactions of Azides. *Org. Biomol. Chem.* **2010**, *8* (17), 3831–3846. https://doi.org/10.1039/C005219C.

(55) Roizen, J. L.; Harvey, M. E.; Du Bois, J. Metal-Catalyzed Nitrogen-Atom Transfer Methods for the Oxidation of Aliphatic C–H Bonds. *Acc. Chem. Res.* **2012**, *45* (6), 911–922. https://doi.org/10.1021/ar200318q.

(56) Wigley, D. E. Organoimido Complexes of the Transition Metals. In *Progress in Inorganic Chemistry*; John Wiley & Sons, Ltd, 1994; pp 239–482. https://doi.org/10.1002/9780470166437.ch4.

(57) Cowley, R. E.; Golder, M. R.; Eckert, N. A.; Al-Afyouni, M. H.; Holland, P. L. Mechanism of Catalytic Nitrene Transfer Using Iron(I)–Isocyanide Complexes. *Organometallics* **2013**, *32* (19), 5289–5298. https://doi.org/10.1021/om400379p.

(58) Yousif, M.; Tjapkes, D. J.; Lord, R. L.; Groysman, S. Catalytic Formation of Asymmetric Carbodiimides at Mononuclear Chromium(II/IV) Bis(Alkoxide) Complexes. *Organometallics* **2015**, *34* (20), 5119–5128. https://doi.org/10.1021/acs.organomet.5b00703.

(59) Choi, B.; Yu, J.; Paley, D. W.; Trinh, M. T.; Paley, M. V.; Karch, J. M.; Crowther, A. C.; Lee, C.-H.; Lalancette, R. A.; Zhu, X.; Kim, P.; Steigerwald, M. L.; Nuckolls, C.; Roy, X. Van Der Waals Solids from Self-Assembled Nanoscale Building Blocks. *Nano Lett.* **2016**, *16* (2), 1445–1449. https://doi.org/10.1021/acs.nanolett.5b05049.

(60) Bruno, I. J.; Cole, J. C.; Edgington, P. R.; Kessler, M.; Macrae, C. F.; McCabe, P.; Pearson, J.; Taylor, R. New Software for Searching the Cambridge Structural Database and Visualizing Crystal Structures. *Acta Cryst B* **2002**, *58* (3), 389–397. https://doi.org/10.1107/S0108768102003324.

(61) Groom, C. R.; Bruno, I. J.; Lightfoot, M. P.; Ward, S. C. The Cambridge Structural Database. *Acta Cryst B* **2016**, *72* (2), 171–179. https://doi.org/10.1107/S2052520616003954.

(62) A Search for All M…Se Single Bond Lengths in the Cambridge Structural Database (Accessed 2/11/22) Yielded 82 Hits for Cr…Se with a Mean of 2.482 Å and a Standard Deviation of 0.072 Å, 173 Hits for Mn…Se with a Mean of 2.544 Å and a Standard Deviation of 0.104 Å, 591 Hits for Fe…Se with a Mean of 2.389 Å and a Standard Deviation of 0.057 Å, 182 Hits for Co…Se with a Mean of 2.359 Å and a Standard Deviation of 0.062 Å, 237 Hits for Ni…Se with a Mean of 2.350 Å and a Standard Deviation of 0.080 Å, 467 Hits for Cu…Se with a Mean of 2.464 Å with a Standard Deviation of 0.120 Å, and 140 Hits for Zn…Se with a Mean of 2.469 Å with a Standard Deviation of 0.074 Å.

(63) Evans, D. F. The Determination of the Paramagnetic Susceptibility of Substances in Solution by Nuclear Magnetic Resonance. *Journal of the Chemical Society* **1959**, 2003–2005. https://doi.org/10.1039/JR9590002003.

(64) Pinkard, A.; Champsaur, A. M.; Roy, X. Molecular Clusters: Nanoscale Building Blocks for Solid-State Materials. *Acc. Chem. Res.* **2018**, *51* (4), 919–929. https://doi.org/10.1021/acs.accounts.8b00016.

(65) Ganguly, S.; Ghosh, A. Seven Clues to Ligand Noninnocence: The Metallocorrole Paradigm. *Acc. Chem. Res.* **2019**, *52* (7), 2003–2014. https://doi.org/10.1021/acs.accounts.9b00115.

(66) Köhler, F. H. Paramagnetic Complexes in Solution: The NMR Approach. In *Encyclopedia of Magnetic Resonance*; John Wiley & Sons, Ltd: Chichester, UK, 2011. https://doi.org/10.1002/9780470034590.emrstm1229.

(67) Luca, O. R.; Konezny, S. J.; Paulson, E. K.; Habib, F.; Luthy, K. M.; Murugesu, M.; Crabtree, R. H.; Batista, V. S. Study of an S = 1 NiII Pincer Electrocatalyst Precursor for Aqueous Hydrogen Production Based on Paramagnetic 1H NMR. *Dalton Transactions* **2013**, *42* (24), 8802. https://doi.org/10.1039/c3dt50528f.

(68) Roquette, P.; Maronna, A.; Reinmuth, M.; Kaifer, E.; Enders, M.; Himmel, H.-J. Combining NMR of Dynamic and Paramagnetic Molecules: Fluxional High-Spin Nickel(II) Complexes Bearing Bisguanidine Ligands. *Inorg. Chem.* **2011**, *50* (5), 1942–1955. https://doi.org/10.1021/ic102420x.

(69) Frisch, M. J.; Trucks, G. W.; Schlegel, H. B.; Scuseria, G. E.; Robb, M. A.; Cheeseman, J. R.; Scalmani, G.; Barone, V.; Petersson, G. A.; Nakatsuji, H.; Li, X.; Caricato, M.; Marenich, A. V.; Bloino, J.; Janesko, B. G.; Gomperts, R.; Mennucci, B.; Hratchian, H. P.; Ortiz, J. V.; Izmaylov, A. F.; Sonnenberg, J. L.; Williams; Ding, F.; Lipparini, F.; Egidi, F.; Goings, J.; Peng, B.; Petrone, A.; Henderson, T.; Ranasinghe, D.; Zakrzewski, V. G.; Gao, J.; Rega, N.; Zheng, G.; Liang, W.; Hada, M.; Ehara, M.; Toyota, K.; Fukuda, R.; Hasegawa, J.; Ishida, M.; Nakajima, T.; Honda, Y.; Kitao, O.; Nakai, H.; Vreven, T.; Throssell, K.; Montgomery Jr., J. A.; Peralta, J. E.; Ogliaro, F.; Bearpark, M. J.; Heyd, J. J.; Brothers, E. N.; Kudin, K. N.; Staroverov, V. N.; Keith, T. A.; Kobayashi, R.; Normand, J.; Raghavachari, K.; Rendell, A. P.; Burant, J. C.; Iyengar, S. S.; Tomasi, J.; Cossi, M.; Millam, J. M.; Klene, M.; Adamo, C.; Cammi, R.; Ochterski, J. W.; Martin, R. L.; Morokuma, K.; Farkas, O.; Foresman, J. B.; Fox, D. J. Gaussian 16 Rev. A.03; Wallingford, CT, 2016.

(70) Becke, A. D. Density-functional Thermochemistry. III. The Role of Exact Exchange. *J. Chem. Phys.* **1993**, *98* (7), 5648–5652. https://doi.org/10.1063/1.464913.

(71) Stephens, P. J.; Devlin, F. J.; Chabalowski, C. F.; Frisch, M. J. Ab Initio Calculation of Vibrational Absorption and Circular Dichroism Spectra Using Density Functional Force Fields. *J. Phys. Chem.* **1994**, *98* (45), 11623–11627. https://doi.org/10.1021/j100096a001.

(72) Kendall, R. A.; Dunning, T. H.; Harrison, R. J. Electron Affinities of the First-row Atoms Revisited. Systematic Basis Sets and Wave Functions. *J. Chem. Phys.* **1992**, *96* (9), 6796–6806. https://doi.org/10.1063/1.462569.

(73) Lu, T.; Chen, F. Multiwfn: A Multifunctional Wavefunction Analyzer. *Journal of Computational Chemistry* **2012**, *33* (5), 580–592. https://doi.org/10.1002/jcc.22885.

(74) Wu, M.; Yao, X.; Hao, Y.; Dong, H.; Cheng, Y.; Liu, H.; Lu, F.; Wang, W.; Cho, K.; Wang, W.-H. Electronic Structures, Magnetic Properties and Band Alignments of 3d Transition Metal Atoms Doped Monolayer MoS2. *Physics Letters A* **2018**, *382* (2), 111–115. https://doi.org/10.1016/j.physleta.2017.10.024.

(75) Gangwar, R.; Pandey, D.; Kancharlapalli, S.; Raychaudhuri, D.; Chakrabarti, A.; Banerjee, A.; Ghanty, T. K. Ab Initio Study of Adsorption of Fission Gas Atoms Xe and Kr on MoS2 Monolayer Functionalized with 3d Transition Metals. *J. Phys. Chem. C* **2021**, *125* (2), 1493–1508. https://doi.org/10.1021/acs.jpcc.0c08888.

(76) Armentrout, P. B.; Halle, L. F.; Beauchamp, J. L. Periodic Trends in Transition Metal-Hydrogen, Metal-Carbon, and Metal-Oxygen Bond Dissociation Energies. Correlation with Reactivity and Electronic Structure. *J. Am. Chem. Soc.* **1981**, *103* (21), 6501–6502. https://doi.org/10.1021/ja00411a043.

(77) Edwards, N. Y.; Eikey, R. A.; Loring, M. I.; Abu-Omar, M. M. High-Valent Imido Complexes of Manganese and Chromium Corroles. *Inorg. Chem.* **2005**, *44* (10), 3700–3708. https://doi.org/10.1021/ic0484506.

(78) Dong, Y.; M. Clarke, R.; Zheng, S.-L.; A. Betley, T. Synthesis and Electronic Structure Studies of a Cr-Imido Redox Series. *Chemical Communications* **2020**, *56* (21), 3163–3166. https://doi.org/10.1039/D0CC00108B.

(79) Shi, H.; Xie, J.; Lam, W. W. Y.; Man, W.-L.; Mak, C.-K.; Yiu, S.-M.; Lee, H. K.; Lau, T.-C. Generation and Reactivity of a One-Electron-Oxidized Manganese(V) Imido Complex with a Tetraamido Macrocyclic Ligand. *Chemistry – A European Journal* **2019**, *25* (56), 12895–12899. https://doi.org/10.1002/chem.201902405.

(80) Zdilla, M. J.; Abu-Omar, M. M. Mechanism of Catalytic Aziridination with Manganese Corrole: The Often Postulated High-Valent Mn(V) Imido Is Not the Group Transfer Reagent. *J. Am. Chem. Soc.* **2006**, *128* (51), 16971–16979. https://doi.org/10.1021/ja0665489.

(81) King, E. R.; Hennessy, E. T.; Betley, T. A. Catalytic C−H Bond Amination from High-Spin Iron Imido Complexes. *J. Am. Chem. Soc.* **2011**, *133* (13), 4917–4923. https://doi.org/10.1021/ja110066j.

(82) Iovan, D. A.; Betley, T. A. Characterization of Iron-Imido Species Relevant for N-Group Transfer Chemistry. *J. Am. Chem. Soc.* **2016**, *138* (6), 1983–1993. https://doi.org/10.1021/jacs.5b12582.

(83) Cowley, R. E.; Eckert, N. A.; Vaddadi, S.; Figg, T. M.; Cundari, T. R.; Holland, P. L. Selectivity and Mechanism of Hydrogen Atom Transfer by an Isolable Imidoiron(III) Complex. *J. Am. Chem. Soc.* **2011**, *133* (25), 9796–9811. https://doi.org/10.1021/ja2005303.

(84) Cowley, R. E.; Holland, P. L. Ligand Effects on Hydrogen Atom Transfer from Hydrocarbons to Three-Coordinate Iron Imides. *Inorg. Chem.* **2012**, *51* (15), 8352–8361. https://doi.org/10.1021/ic300870y.

(85) Goswami, M.; Lyaskovskyy, V.; Domingos, S. R.; Buma, W. J.; Woutersen, S.; Troeppner, O.; Ivanović-Burmazović, I.; Lu, H.; Cui, X.; Zhang, X. P.; Reijerse, E. J.; DeBeer, S.; van Schooneveld, M. M.; Pfaff, F. F.; Ray, K.; de Bruin, B. Characterization of Porphyrin-Co(III)-'Nitrene Radical' Species Relevant in Catalytic Nitrene Transfer Reactions. *J. Am. Chem. Soc.* **2015**, *137* (16), 5468–5479. https://doi.org/10.1021/jacs.5b01197.

(86) Gu, Z.-Y.; Liu, Y.; Wang, F.; Bao, X.; Wang, S.-Y.; Ji, S.-J. Cobalt(II)-Catalyzed Synthesis of Sulfonyl Guanidines via Nitrene Radical Coupling with Isonitriles: A Combined Experimental and Computational Study. *ACS Catal.* **2017**, *7* (6), 3893–3899. https://doi.org/10.1021/acscatal.7b00798.

(87) Baek, Y.; Betley, T. A. Catalytic C–H Amination Mediated by Dipyrrin Cobalt Imidos. *J. Am. Chem. Soc.* **2019**, *141* (19), 7797–7806. https://doi.org/10.1021/jacs.9b01262.

(88) Baek, Y.; Das, A.; Zheng, S.-L.; Reibenspies, J. H.; Powers, D. C.; Betley, T. A. C–H Amination Mediated by Cobalt Organoazide Adducts and the Corresponding Cobalt Nitrenoid Intermediates. *J. Am. Chem. Soc.* **2020**, *142* (25), 11232–11243. https://doi.org/10.1021/jacs.0c04252.

(89) Dong, Y.; Lukens, J. T.; Clarke, R. M.; Zheng, S.-L.; Lancaster, K. M.; Betley, T. A. Synthesis, Characterization and C–H Amination Reactivity of Nickel Iminyl Complexes. *Chem. Sci.* **2020**, *11* (5), 1260–1268. https://doi.org/10.1039/C9SC04879K.

(90) Dong, Y.; Lund, C. J.; Porter, G. J.; Clarke, R. M.; Zheng, S.-L.; Cundari, T. R.; Betley, T. A. Enantioselective C–H Amination Catalyzed by Nickel Iminyl Complexes Supported by Anionic Bisoxazoline (BOX) Ligands. *J. Am. Chem. Soc.* **2021**, *143* (2), 817–829. https://doi.org/10.1021/jacs.0c09839.

(91) Dong, Y.; Clarke, R. M.; Porter, G. J.; Betley, T. A. Efficient C–H Amination Catalysis Using Nickel-Dipyrrin Complexes. *J. Am. Chem. Soc.* **2020**, *142* (25), 10996–11005. https://doi.org/10.1021/jacs.0c02126.

(92) Bagchi, V.; Paraskevopoulou, P.; Das, P.; Chi, L.; Wang, Q.; Choudhury, A.; Mathieson, J. S.; Cronin, L.; Pardue, D. B.; Cundari, T. R.; Mitrikas, G.; Sanakis, Y.; Stavropoulos, P. A Versatile Tripodal Cu(I) Reagent for C–N Bond Construction via Nitrene-Transfer Chemistry: Catalytic Perspectives and Mechanistic Insights on C–H Aminations/Amidinations and Olefin Aziridinations. *J. Am. Chem. Soc.* **2014**, *136* (32), 11362–11381. https://doi.org/10.1021/ja503869j.

(93) Carsch, K. M.; DiMucci, I. M.; Iovan, D. A.; Li, A.; Zheng, S.-L.; Titus, C. J.; Lee, S. J.; Irwin, K. D.; Nordlund, D.; Lancaster, K. M.; Betley, T. A. Synthesis of a Copper-Supported Triplet Nitrene Complex Pertinent to Copper-Catalyzed Amination. *Science* **2019**, *365* (6458), 1138–1143. https://doi.org/10.1126/science.aax4423.

(94) Kuijpers, P. F.; van der Vlugt, J. I.; Schneider, S.; de Bruin, B. Nitrene Radical Intermediates in Catalytic Synthesis. *Chemistry – A European Journal* **2017**, *23* (56), 13819–13829. https://doi.org/10.1002/chem.201702537.

(95) Baek, Y.; Betley, T. A. Reversible C−C Bond Cleavage of a Cobalt Diketimide into an Elusive Cobalt Aryl Nitrenoid Complex. *Angewandte Chemie International Edition* **2022**, *61* (17), e202115437. https://doi.org/10.1002/anie.202115437.

(96) Wilding, M. J. T.; Iovan, D. A.; Wrobel, A. T.; Lukens, J. T.; MacMillan, S. N.; Lancaster, K. M.; Betley, T. A. Direct Comparison of C–H Bond Amination Efficacy through Manipulation of Nitrogen-Valence Centered Redox: Imido versus Iminyl. *J. Am. Chem. Soc.* **2017**, *139* (41), 14757–14766. https://doi.org/10.1021/jacs.7b08714.

(97) Crabtree, R. H. *The Organometallic Chemistry of the Transition Metals*, 4th ed.; Jon Wiley & Sons, Inc, 2005.

(98) Haber, J.; Mlodnicka, T.; Poltowicz, J. Metal-Dependent Reactivity of Some Metalloporphyrins in Oxidation with Dioxygen. *Journal of Molecular Catalysis* **1989**, *54* (3), 451–461. https://doi.org/10.1016/0304-5102(89)80160-9.

(99) Feng, X.-T.; Yu, J.-G.; Lei, M.; Fang, W.-H.; Liu, S. Toward Understanding Metal-Binding Specificity of Porphyrin: A Conceptual Density Functional Theory Study. *J. Phys. Chem. B* **2009**, *113* (40), 13381–13389. https://doi.org/10.1021/jp905885y.

(100) Greenwood, B. P.; Forman, S. I.; Rowe, G. T.; Chen, C.-H.; Foxman, B. M.; Thomas, C. M. Multielectron Redox Activity Facilitated by Metal−Metal Interactions in Early/Late

Heterobimetallics: Co/Zr Complexes Supported by Phosphinoamide Ligands. *Inorganic Chemistry* **2009**, *48* (13), 6251–6260. https://doi.org/10.1021/ic900552b.

(101) Kim, J. Y.; Park, S. H.; Ryu, J.; Cho, S. H.; Kim, S. H.; Chang, S. Rhodium-Catalyzed Intermolecular Amidation of Arenes with Sulfonyl Azides via Chelation-Assisted C–H Bond Activation. *J. Am. Chem. Soc.* **2012**, *134* (22), 9110–9113. https://doi.org/10.1021/ja303527m.

(102) Fulmer, G. R.; Miller, A. J. M.; Sherden, N. H.; Gottlieb, H. E.; Nudelman, A.; Stoltz, B. M.; Bercaw, J. E.; Goldberg, K. I. NMR Chemical Shifts of Trace Impurities: Common Laboratory Solvents, Organics, and Gases in Deuterated Solvents Relevant to the Organometallic Chemist. *Organometallics* **2010**, *29* (9), 2176–2179. https://doi.org/10.1021/om100106e.

(103) Gottlieb, H. E.; Kotlyar, V.; Nudelman, A. NMR Chemical Shifts of Common Laboratory Solvents as Trace Impurities. *The Journal of Organic Chemistry* **1997**, *62* (21), 7512–7515. https://doi.org/10.1021/jo971176v.

(104) Babij, N. R.; McCusker, E. O.; Whiteker, G. T.; Canturk, B.; Choy, N.; Creemer, L. C.; Amicis, C. V. D.; Hewlett, N. M.; Johnson, P. L.; Knobelsdorf, J. A.; Li, F.; Lorsbach, B. A.; Nugent, B. M.; Ryan, S. J.; Smith, M. R.; Yang, Q. NMR Chemical Shifts of Trace Impurities: Industrially Preferred Solvents Used in Process and Green Chemistry. *Organic Process Research & Development* **2016**, *20* (3), 661–667. https://doi.org/10.1021/acs.oprd.5b00417.

(105) Evans, D. F. 400. The Determination of the Paramagnetic Susceptibility of Substances in Solution by Nuclear Magnetic Resonance. *Journal of the Chemical Society (Resumed)* **1959**, *81* (1), 2003. https://doi.org/10.1039/jr9590002003.

(106) Evans, C. M.; Evans, M. E.; Krauss, T. D. Mysteries of TOPSe Revealed: Insights into Quantum Dot Nucleation. *Journal of the American Chemical Society* **2010**, *132* (32), 10973–10975. https://doi.org/10.1021/ja103805s.

(107) Kaupp, M.; Köhler, F. H. Combining NMR Spectroscopy and Quantum Chemistry as Tools to Quantify Spin Density Distributions in Molecular Magnetic Compounds. *Coordination Chemistry Reviews* **2009**, *253* (19–20), 2376–2386. https://doi.org/10.1016/j.ccr.2008.12.020.

(108) *Solution NMR of Paramagnetic Molecules: Applications to Metallobiomolecules and Models*; Bertini, I., Luchinat, C., Parigi, G., Eds.; Current methods in inorganic chemistry; Elsevier Science Ltd: Amsterdam ; New York, 2001.

(109) Bruker APEX2 (Version 2.1-4), SAINT (Version 7.34A), SADABS (Version 2007/4), 2007 BrukerAXS Inc, Madison, Wisconsin, USA.

(110) Sheldrick, G. M. *SHELXT* – Integrated Space-Group and Crystal-Structure Determination. *Acta Crystallogr A Found Adv* **2015**, *71* (1), 3–8. https://doi.org/10.1107/S2053273314026370.
(111) Altomare, A.; Burla, M. C.; Camalli, M.; Cascarano, G. L.; Giacovazzo, C.; Guagliardi, A.; Moliterni, A. G. G.; Polidori, G.; Spagna, R. SIR97: A New Tool for Crystal Structure Determination and Refinement. *J Appl Cryst* **1999**, *32* (1), 115–119. https://doi.org/10.1107/S0021889898007717.
(112) Altomare, A.; Cascarano, G.; Giacovazzo, C.; Guagliardi, A. Completion and Refinement of Crystal Structures with SIR92. *J Appl Cryst* **1993**, *26* (3), 343–350. https://doi.org/10.1107/S0021889892010331.
(113) Sheldrick, G.M., SHELXL-97, Program for the Refinement of Crystal Structures, 1997, University of Göttingen, Germany.
(114) Mackay, S.; Edwards, C.; Henderson, A.; Gilmore, C.; Stewart, N.; Shankland, K.; Donald, A., MaXus: A Computer Program for the Solution and Refinement of Crystal Structures from Diffraction Data, 1997, University of Glasgow, Scotland.
(115) Waasmaier, D.; Kirfel, A. New Analytical Scattering-Factor Functions for Free Atoms and Ions. *Acta Cryst A* **1995**, *51* (3), 416–431. https://doi.org/10.1107/S0108767394013292.
(116) Frisch, M. J.; Trucks, G. W.; Schlegel, H. B.; Scuseria, G. E.; Robb, M. A.; Cheeseman, J. R.; Scalmani, G.; Barone, V.; Petersson, G. A.; Nakatsuji, H.; Li, X.; Caricato, M.; Marenich, A. V.; Bloino, J.; Janesko, B. G.; Gomperts, R.; Mennucci, B.; Hratchian, H. P.; Ortiz, J. V.; Izmaylov, A. F.; Sonnenberg, J. L.; Williams; Ding, F.; Lipparini, F.; Egidi, F.; Goings, J.; Peng, B.; Petrone, A.; Henderson, T.; Ranasinghe, D.; Zakrzewski, V. G.; Gao, J.; Rega, N.; Zheng, G.; Liang, W.; Hada, M.; Ehara, M.; Toyota, K.; Fukuda, R.; Hasegawa, J.; Ishida, M.; Nakajima, T.; Honda, Y.; Kitao, O.; Nakai, H.; Vreven, T.; Throssell, K.; Montgomery Jr., J. A.; Peralta, J. E.; Ogliaro, F.; Bearpark, M. J.; Heyd, J. J.; Brothers, E. N.; Kudin, K. N.; Staroverov, V. N.; Keith, T. A.; Kobayashi, R.; Normand, J.; Raghavachari, K.; Rendell, A. P.; Burant, J. C.; Iyengar, S. S.; Tomasi, J.; Cossi, M.; Millam, J. M.; Klene, M.; Adamo, C.; Cammi, R.; Ochterski, J. W.; Martin, R. L.; Morokuma, K.; Farkas, O.; Foresman, J. B.; Fox, D. J. *Gaussian 16 Rev. A.03*; Wallingford, CT, 2016.
(117) Lu, T.; Chen, F. Multiwfn: A Multifunctional Wavefunction Analyzer. *Journal of Computational Chemistry* **2012**, *33* (5), 580–592. https://doi.org/10.1002/jcc.22885.

Chapter 4. PROBING EDGE/SUPPORT ELECTRONIC COOPERATIVITY IN SINGLE EDGE Fe/Co_6Se_8 CLUSTERS

4.1 Abstract

This study provides insights into the electronic structure of an atomically precise Fe/Co_6Se_8 cluster and the extent of redox cooperativity between the Fe active site and the non-innocent Co_6Se_8 support. Chemical oxidation studies enable the isolation of two types of oxidized Fe/Co_6Se_8 clusters, in which the nature of the counterion (I^- or OTf^-) significantly impacts the structural interactions between Fe and the Co_6Se_8 unit. Experimental characterization by single crystal X-ray diffraction, ^{57}Fe Mössbauer spectroscopy, and $^{31}P\{^1H\}$ NMR spectroscopy is complemented by computational analysis. In aggregate, the study reveals that upon oxidation, the charge is shared between the Fe edge site and the Co_6Se_8 core.

4.2 Introduction

Multimetallic cooperativity holds the promise of imbuing base metals with the ability to achieve desirable multielectron transformations that are uncharacteristic of a single metal.[1] The power of multi-site cooperativity is illustrated by nature's reliance on base metal clusters to carry out some of the most complex and energetically difficult processes, such as cleaving dinitrogen during ammonia biosynthesis.[2,3] Although the mode of operation and electronic structure of the FeMo cofactor are still topics of debate,[4–6] this polymetallic cluster provides the active site for substrate binding and reduction, and mediates the transfer of the electrons required for nitrogen fixation.[3,7–9]

Molecular clusters have the synthetic tunability to systematically probe and ultimately control how multiple metals interact to achieve complex redox transformations.[10–16] Towards this goal, chemical oxidation studies provide valuable insights and can reveal how the metal identity,[11]

Reproduced in part with permission from:
Mitchell, B. S.; Chirila, A.; Anderton, K. J.; Kaminsky, W.; Velian, A. *Inorg. Chem.* **2023**, *Accepted*.

ligand binding[17,18] or the ligand framework impact charge distribution within a multimetallic platform.[19–22] For example, inner-sphere oxidation of an all-ferrous Fe_3 cluster was shown to result in anion coordination at one Fe center, and localization of the generated charge on the two distal sites.[17] On the contrary, outer-sphere oxidation of a Cu_4S cluster results in complete charge delocalization between the four Cu centers.[18] The Fe_3 and Cu_4S clusters illustrate instances of distinct regimes for multi-site electronic interactions in structurally unrelated platforms. By anchoring base metals on the surface of a redox-noninnocent cluster (Co_6Se_8), our group introduced a modular platform that enables access to a range of redox regimes within the same framework that is also catalytically competent.[23–25] Recently, we have shown that the identity of the edge metal M in the single edge clusters $MCo_6Se_8(PEt_3)_4L'_2$ (**1**-M, M = Cr, Mn, Fe, Co, Cu, Zn; L' = $PPh_2N^{(-)}Tol$; Tol = 4-Tolyl, Ph = phenyl, Et = ethyl) determines the extent to which the active site and the support interact electronically (Figure 4.1), and have begun elucidating the consequences of the ensuing cooperativity in catalysis.[25,26]

In this study, we investigate the chemical oxidation of the single-edge cluster **1**-Fe to explicate the extent of edge/support electronic interactions in localizing the resulting charge.[27] Whereas ^{57}Fe Mössbauer spectroscopy reveals the Fe site undergoes oxidation, single crystal X-ray diffraction studies, $^{31}P\{^1H\}$ NMR spectroscopic analyses, and DFT calculations suggest that the Co_6Se_8 core shares the burden of the charge.

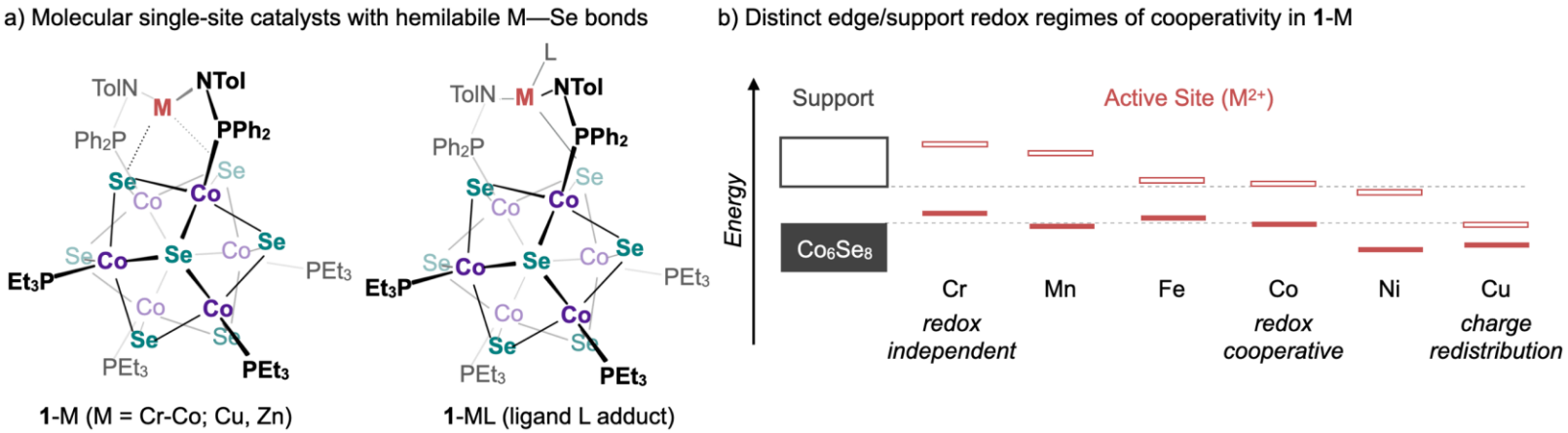

Figure 4.1. a) Single edge clusters $MCo_6Se_8(PEt_3)_4L'_2$ (**1**-M; κ^4-M), and monoadduct **1**-ML (κ^3-M). b) Distinct redox regimes of electronic cooperativity as a result of the energetic and spatial overlap between the edge/support frontier orbitals. Energies approximated from DFT calculations.

4.3 CHEMICAL OXIDATION

Scheme 4.1. Chemical oxidation of **1**-Fe, **1**-H_2, and **1**-Zn.

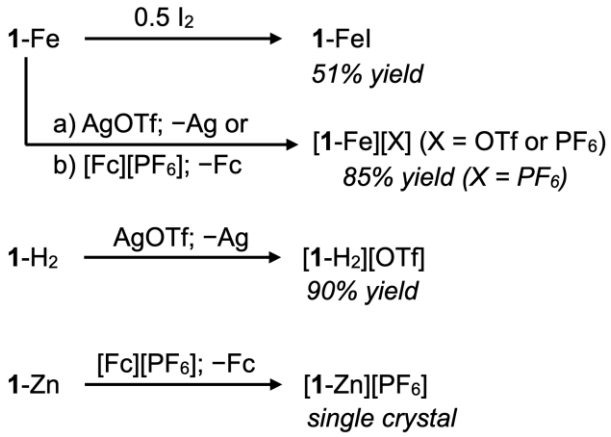

Electrochemical measurements have previously revealed that the single edge cluster **1**-Fe, formally $Fe^{2+}/[Co_6Se_8]^0$, can be oxidized reversibly multiple times.[25] Here, the chemical mono-oxidation of **1**-Fe is accomplished using a series of inner and outer sphere oxidants of appropriate oxidative strength,[28] such as iodine, silver triflate (AgOTf), and ferrocenium hexafluorophosphate ([Fc][PF_6]; Scheme 4.1). The resulting mono-oxidized clusters are therefore obtained either as salts [**1**-Fe][X] (X = OTf, PF_6), with the counterion dissociated from Fe as in [**1**-Fe][OTf] or [**1**-Fe][PF_6], or as neutral species with the anion directly bound to the edge site, as in **1**-FeI. From a synthetic standpoint, [Fc][PF_6] is a more convenient reagent, as it enables the isolation of [**1**-Fe][PF_6] as an analytically pure compound (85% yield). While [**1**-Fe][OTf] is not isolated pure, it is characterized in the solid state (Figure 4.2). The similar spectroscopic signatures of the [**1**-Fe][PF_6] and [**1**-Fe][OTf] salts suggests that in the solid state the latter is also representative of the former, and the two compounds are considered interchangeable in this text.

The solubility properties of the oxidized clusters align with the extent of anion association at Fe. In contrast to **1**-FeI, the hexafluorophosphate salt [**1**-Fe][PF_6] is insoluble in non-polar solvents (i.e. toluene, benzene). Interestingly, [**1**-Fe][OTf] readily dissolves in benzene, suggesting a closer association of the ions occurs in this solvent. ^{19}F NMR spectroscopy indicates that while the triflate ion remains completely dissociated from the Fe edge in polar solvents ($\delta = -78$ ppm in acetonitrile-d_3), it is weakly associated in non-polar ones ($\delta = -60$ ppm in benzene-d_6).[29]

To compare the structural and electronic changes incurred in the Fe/Co_6Se_8 cluster upon oxidation, **1**-Zn and **1**-H_2 which feature either a redox inactive edge metal (Zn) or no edge metal at all are also oxidized and analysed. The cluster ligand salt [**1**-H_2][OTf] is produced in good yield (90%) upon treatment with AgOTf. X-ray quality crystals of [**1**-Zn][PF_6] are grown from a crude reaction mixture between **1**-Zn and [Fc][PF_6] (Section 4.8.6).

4.4 Structural Analysis

Diffraction quality crystals of [**1**-Fe][OTf] and **1**-FeI are obtained from layered solutions of toluene, or benzene-d_6, and *n*-pentane stored at −35 °C (Figure 4.2). Their analysis illustrates the flexible ligand/active site/support interactions, and shines light on the structural changes incurred at the Fe edge upon oxidation of **1**-Fe.[25] Table 4.1 summarizes key interatomic distances of the clusters discussed in this section.

Binding an exogenous ligand at Fe can occur when the incoming ligand has sufficient coordinative strength to outcompete Se. In turn, the nucleophilicity of the Se sites and the Fe—Se bond strength are responsive to redox changes of the Co_6Se_8 core, the ligand framework, or binding activity at neighboring edge sites when they are present.[26,30] The structures of [**1**-Fe][OTf] and **1**-FeI capture a switching point: iodide is sufficiently nucleophilic to break an Fe—Se bond and give rise to a κ^3-Fe edge in **1**-FeI. In contrast, triflate remains an outer sphere counterion as it cannot outcompete Se coordination. In [**1**-Fe][OTf], the κ^4-Fe edge site retains the two Fe—Se bonds of the parent complex **1**-Fe, previously characterized in the solid state and depicted in Figure 4.2a for comparison.[25]

Inspecting the $FeCo_2Se_2$ edge units indicates that anion coordination, as well as oxidation leads to significant restructuring that propagates through the entire cluster. For example, to accommodate a κ^4-bound Fe edge on the Co_6Se_8 surface, the Co—Se bonds elongate from 2.35 Å in **1**-FeI, to 2.42 Å in [**1**-Fe]$^+$, and the vicinal selenium atoms are pushed apart increasing the Se…Se interatomic distance from 3.42 Å to 3.58 Å. Since the average interatomic Co…Se and Se…Se distances of the Co/Se cores remain virtually unchanged, these local distortions are compensated by deformations in the rest of the Co/Se core. Inspecting the edge metrics of [**1**-Fe]$^+$ also reveals that the "appended" Fe center becomes truly incorporated by the Co_6Se_8 cluster. This is reflected in Fe…Co distances of 2.754(6) and 2.805(6) Å that are notably shorter than the average Co…Co distances of the Co_6Se_8 core (2.92 Å).

The edge/support interaction strength (Fe—Se bonds), and the Co…Co distances within the Co_6Se_8 cluster inform on the localization of the charge within the Fe/Co_6Se_8 construct. We hypothesize that if oxidation is localized on the Co_6Se_8 core, the Fe—Se bonds will elongate due to the decreased electron richness of the Se sites. This scenario is illustrated in the mono-oxidized zinc cluster [**1**-Zn][PF_6], where the charge is unambiguously confined on Co_6Se_8, and the two Zn—Se contacts elongate from an average of 2.55 in **1**-Zn to 2.64 Å (Figure 4.14). Instead, the opposite is observed when oxidizing **1**-Fe in the presence of a weakly coordinating anion: the two Fe—Se bonds contract from an average of 2.50 to 2.40 Å in [**1**-Fe][OTf], suggesting that unlike in the zinc congener, the edge site participates in localizing the charge. As discussed in the next section, Mössbauer spectroscopy corroborates this proposal.

Another empirical structural reporter that adds nuance to this claim is the average interatomic distance between neighboring Co atoms within the Co_6Se_8 core. When oxidation is strictly confined to the Co_6Se_8 core, as is the case in [**1**-Zn][PF_6], **1**-Cu,[25] or [$Co_6Se_8L^H_6$][OTf],[23] the Co…Co average distance consistently contracts from 2.94 to 2.90 avg. Å.[23,31] The Co…Co distance is therefore a reporter on the extent of Co_6Se_8 oxidation between 0/+1 charge. If the charge was completely localized on the Fe center upon monooxidation of **1**-Fe, we would expect an average Co…Co distance of 2.94 Å. Instead, this distance contracts to 2.92 Å in **1**-FeI and [**1**-Fe][OTf], suggesting partial oxidation of the Co_6Se_8 core.

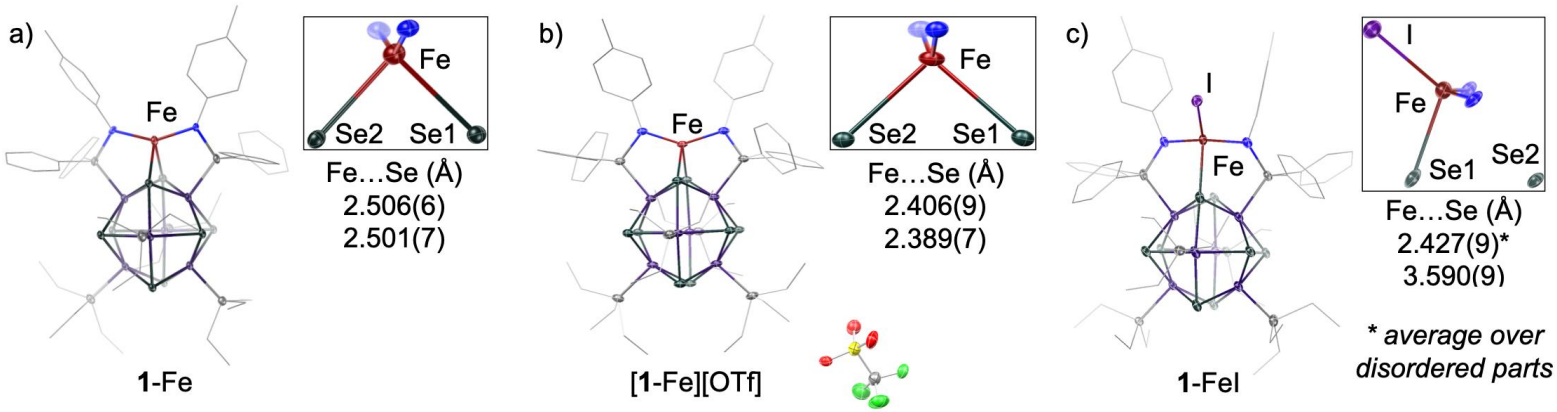

Figure 4.2. Comparison of bonding metrics at the Fe edge upon mono-oxidation. Single crystal X-ray diffraction of a) **1**-Fe, b) [**1**-Fe][OTf], and c) **1**-FeI. Hydrogen atoms, co-crystallized solvent molecules, and disorder in **1**-FeI are omitted for clarity. Carbon atoms are depicted as wireframe.

Table 4.1. Select interatomic distances (Å) for single edge clusters **1**-M, and unmetallated clusters $Co_6Se_8L'_6{}^H$ (**2**-H_6), and [**2**-H_6][OTf]. Standard error propagation was used to estimate the error for average distances.

Compound	intra-Co_6Se_8 (avg, Å)			MCo_2Se_2 edge unit (Å)						
	Co–Se	Co...Co	Se...Se	Co–Se	Co...Co	Se...Se	M...Se		M...Co	
1-Fe [i]	2.353(1)	2.940(2)	3.266(2)	2.397(3)	2.890(8)	3.504(8)	2.501(7)	2.506(6)	2.94(1)	2.937(5)
1-FeI	2.345(1)	2.921(1)	3.257(1)	2.354(2)	2.805(3)	3.423(2)	2.61(1) 2.248(8)	3.59(1) 3.46(1)	3.698(6) 3.407(7)	3.65(1) 3.42(1)
[**1**-Fe][OTf]	2.352(2)	2.916(3)	3.243(3)	2.420(8)	2.85(1)	3.58(1)	2.389(7)	2.406(9)	2.754(6)	2.805(6)
1-Zn [i]	2.350(1)	2.938(1)	3.262(1)	2.382(3)	2.895(6)	3.432(5)	2.537(7)	2.562(7)	3.069(8)	3.087(9)
[**1**-Zn][PF_6]	2.342(2)	2.895(2)	3.257(2)	2.380(3)	2.88(1)	3.44(1)	2.615(8)	2.66(1)	3.104(9)	3.123(9)
2-H_6[i]	2.35(2)	2.944(2)	3.254(2)	-	-	-	-	-	-	-
[**2**-H_6][OTf] [i]	2.34(1)	2.903(1)	3.260(1)	-	-	-	-	-	-	-

4.5 Electronic Investigations Using Mössbauer Spectroscopy

Two limiting scenarios would localize the charge in [**1**-Fe][X] and **1**-FeI either on the Co_6Se_8 core ($Fe^{2+}/[Co_6Se_8]^{1+}$), or on the iron edge site ($Fe^{3+}/[Co_6Se_8]^{0}$). Structural analysis, discussed in the previous section, suggests the charge is distributed between Fe and Co_6Se_8. Solution phase magnetic measurements using Evans method[32] confirm, as expected, that [**1**-Fe][OTf] and **1**-FeI have five unpaired electrons each, but do not report on the location of the unpaired electron gained upon oxidation of **1**-Fe. To experimentally probe these possibilities, **1**-Fe, [**1**-Fe][PF_6], and **1**-FeI are analysed using zero-field ^{57}Fe Mössbauer spectroscopy (Figure 4.3a). While the neutral **1**-Fe

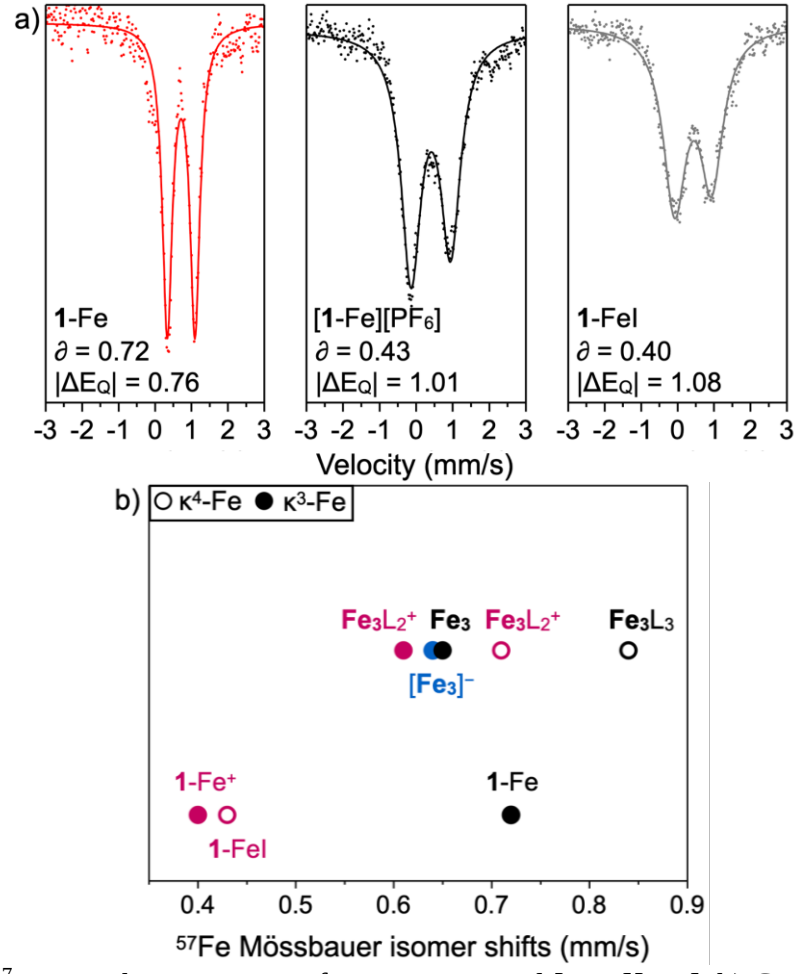

Figure 4.3. a) ^{57}Fe Mössbauer spectra of **1**-Fe, **1**-FeI, and [**1**-Fe][PF_6]. b) Comparison of ^{57}Fe Mössbauer isomer shifts between monoiron (**1**-Fe, **1**-FeI, [**1**-Fe][PF_6]), and triiron (**Fe$_3$**, **Fe$_3$**L_3, [**Fe$_3$**L_2][PF_6], [TBA][**Fe$_3$**]; L = CN^tBu) clusters redox series. Mono-oxidized clusters are depicted pink, neutral in black, and monoreduced in blue.

cluster has an isomer shift most consistent with a high spin Fe(II) edge (δ = 0.72 mm/s), the oxidized clusters [**1**-Fe][PF_6] and **1**-FeI have isomer shifts (δ = 0.43, 0.40 mm/s, respectively) typically associated with high spin $Fe^{2.5+}$ or Fe^{3+} centers.[17,33–35] Although the coordination environments of the two κ^4-Fe edges in **1**-Fe and **1**-Fe^+ are nearly identical (τ_4 = 0.78 and 0.77, respectively[36]), the shortened Fe—Se bonds, decreased ∠N-Fe-N angle, and electronic changes at Fe give rise to significantly different quadrupole splitting ($|\Delta E_Q|$ = 0.76, 1.01 mm/s, respectively). The quadrupole splitting of **1**-Fe^+ is nearly identical to that of **1**-FeI ($|\Delta E_Q|$ = 1.08 mm/s; τ_4 = 0.82), perhaps a reflection of their similar oxidation states and comparable polarizability of Se and I.[37]

In contrast to the tri-Fe clusters $Fe_3Co_6Se_8L_6$' (**Fe_3**) characterized previously by our group,[38] the mono-Fe clusters discussed here incur a significantly stronger response in the ^{57}Fe Mössbauer isomer shifts upon oxidation (Figure 4.3b). Mössbauer and electrochemical measurements have previously led us to propose that the frontier orbitals of tri-Fe clusters are primarily localized on the Co_6Se_8 core, giving rise to a redox regime wherein the edge sites remain isovalent (Fe^{2+}) upon chemical mono-oxidation or monoreduction.[23] Here, the Mössbauer data indicates that the iron edge undergoes significant oxidation, implying a comparatively lower contribution from the Co_6Se_8 core than in the trimetallated analogues. While limiting scenarios of localizing the charge on the iron or core are attractive in their simplicity, it is also possible, and likely, that *"the distribution of electron density does not occur in 1e$^-$* jumps*"*.[39] Therefore, we propose that the charge is distributed between the Fe edge(s) and the cobalt core, to different extents depending on the number of edge sites and bound exogenous ligands, placing **1**-Fe and **Fe_3** in an intermediate, and dynamic edge/support redox regime.[25]

4.6 $^{31}P\{^1H\}$ NMR Spectroscopy and DFT Calculations Inform on Edge/Core Charge Distribution

NMR spectroscopy furnishes detailed insights into the electronic and structural characteristics of the single edge clusters **1**-M.[25] In particular, the $^{31}P\{^1H\}$ NMR chemical shifts of the phosphines are sensitive reporters for electronic and chemical changes occurring at the edge site (*P*Ph_2NTol) or the Co_6Se_8 core (*P*Et_3).

Here, we set out to investigate if the $^{31}P\{^1H\}$ NMR chemical shifts of **1**-Fe, **1**-FeI and [**1**-Fe][PF_6] shine light on the relative distribution of charge between the edge and the Co_6Se_8 core, and corroborate the findings with electronic structure calculations. Additionally, variable temperature

NMR spectroscopy measurements, previously reported[25] for $^{31}P\{^{1}H\}$ and appended here for ^{1}H signals, reveal a Curie behaviour for **1**-Fe, whereas inversion recovery experiments enable the complete assignment of the ^{1}H and $^{31}P\{^{1}H\}$ NMR signals in **1**-Fe (Figure 4.8-Figure 4.10).[40,41] Figure 4.4 compares the $^{31}P\{^{1}H\}$ NMR of three pairs of compounds: the κ^4-complexes **1**-Fe/[**1**-Fe][X], the κ^3-complexes **1**-Fe(py)/**1**-FeX, and the parent cluster ligands **1**-H_2/[**1**-H_2][OTf]. The $^{31}P\{^{1}H\}$ NMR chemical shifts are also summarized in

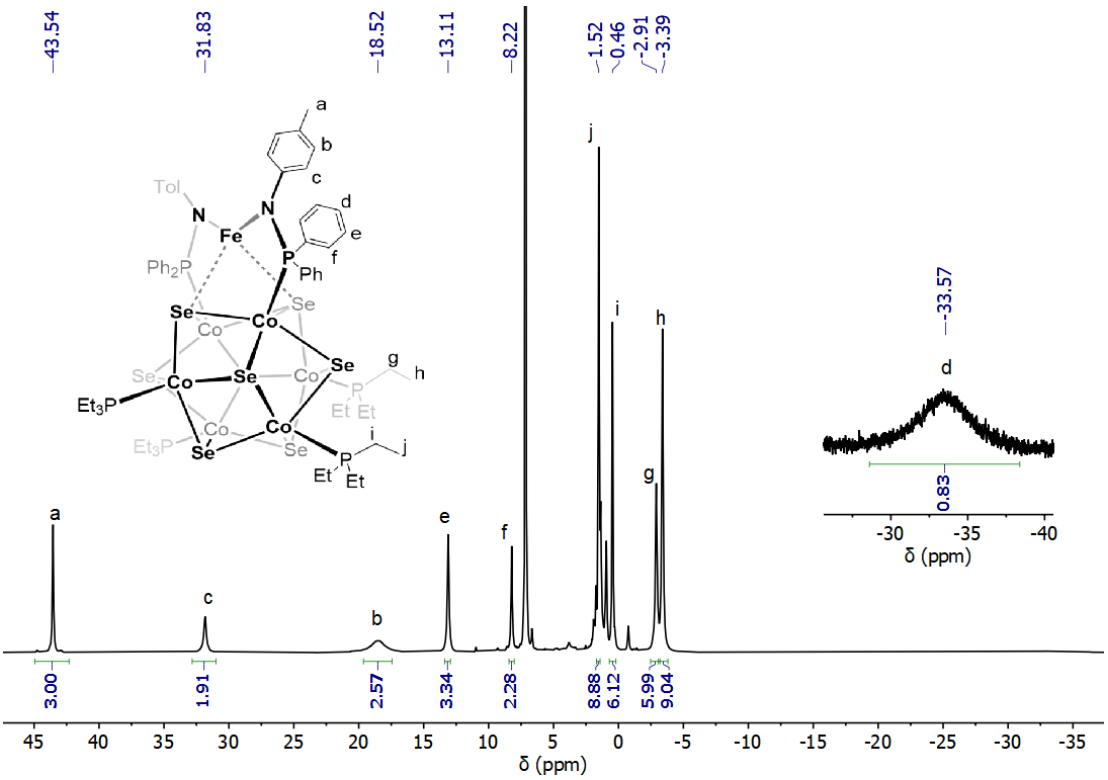

Figure 4.10. Assignment of ^{1H} NMR features in **1-Fe** determined by relaxation time studies.

Table 4.2.

Oxidation has a large impact on the chemical shift of the PEt_3 groups in the κ^4-Fe complexes **1**-Fe/[**1**-Fe][X], indicating that Co_6Se_8 gains unpaired electron density (Figure 4.4). Indeed, the PEt_3 groups shift from −113 ppm in **1**-Fe to −632 ppm in the [**1**-Fe]$^+$ cation, whereas the PPh_2NTol groups, already proximal to a paramagnetic center, are minimally affected. The oxidized metalloligand, [**1**-H_2][OTf], which confines the charge exclusively to the Co_6Se_8 core, exhibits a ca. 400 ppm negative shift for both the PEt_3 and the PPh_2NTol groups compared to the neutral cluster **1**-H_2.

The transition from κ^4 to κ^3 coordination at Fe is also associated with diagnostic changes in the $^{31}P\{^1H\}$ NMR chemical shifts, as seen comparing the [**1**-Fe]$^+$/**1**-FeI and **1**-Fe/**1**-Fe(py) pairs (Figure 4.4). For example, ligand coordination leads to shifts of ca. 200 ppm to higher frequencies for the PPh_2NTol groups in both the neutral and the oxidized clusters. Although distal to the Fe site, the PEt_3 are especially sensitive to anion coordination. Two distinct PEt_3 signals are resolved for **1**-FeI clusters, marking their permanent desymmetrization. Their chemical shifts undergo dramatic changes upon anion coordination, from −633 ppm in [1-Fe]$^+$ to −355 and −183 ppm in **1**-FeI, the latter ostensibly associated with the distal PEt_3.

To probe how the electronic structure of **1**-Fe is impacted by oxidation and anion coordination, we turned to DFT calculations (uB3LYP+/ccpVTZ).[42–45] Figure 5b depicts the Mulliken spin density

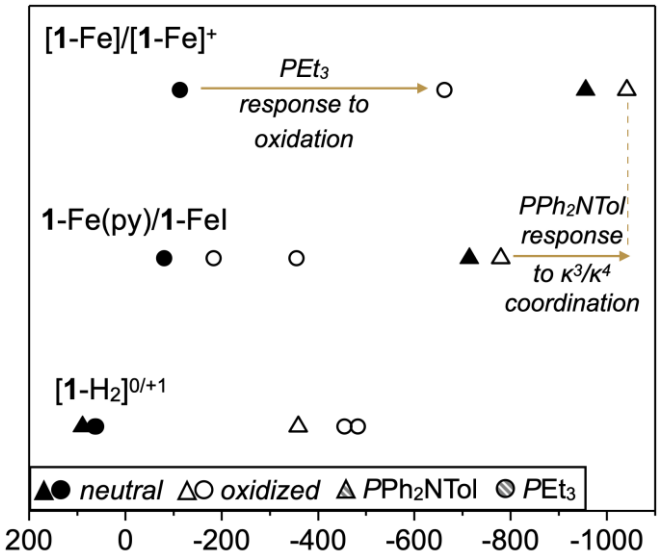

Figure 4.4. $^{31}P\{^1H\}$ NMR chemical shifts of amidophosphine PPh_2NTol (triangles) and triethylphosphine PEt_3 (circles) groups in the neutral clusters **1**-H_2, **1**-Fe, and **1**-Fe(py) (filled), and mono-oxidized clusters [**1**-H_2]$^+$, [**1**-Fe]$^+$, and **1**-FeI (hollow).

(α-β) plots for **1**-Fe,[25] **1**-FeI, [**1**-Fe]$^+$, indicating that the spin density on the Co_6Se_8 core more than doubles upon oxidizing the neutral **1**-Fe (0.31) to [**1**-Fe]$^+$ (0.77). These calculations corroborate therefore the proposal that the charge is shared between the edge and the Co_6Se_8 support in [**1**-Fe]$^+$.

Since the phosphines report on the electronic structure of Fe/Co_6Se_8 construct, their $^{31}P\{^1H\}$ NMR chemical shifts were plotted against the spin densities calculated for edge and support (Figure 4.5a,b). The $^{31}P\{^1H\}$ NMR chemical shifts of the PEt_3 groups on the neutral **1**-H_2 were used as a reference point for a completely diamagnetic cluster. The calculated spin density on the Co_6Se_8 support and experimental $^{31}P\{^1H\}$ NMR data for the PEt_3 groups roughly correlate, reaffirming the proposal that upon oxidation of **1**-Fe the charge is partly localized on the Co_6Se_8 support. At the same time, the relatively small change in the spin density at the edge sites is consistent with minor differences in the chemical shifts of the *P*Ph_2NTol groups in **1**-Fe, **1**-FeI, and [**1**-Fe]$^+$ where the most significant variation occurs as a result of the κ^4 to κ^3 transition at Fe upon anion binding.

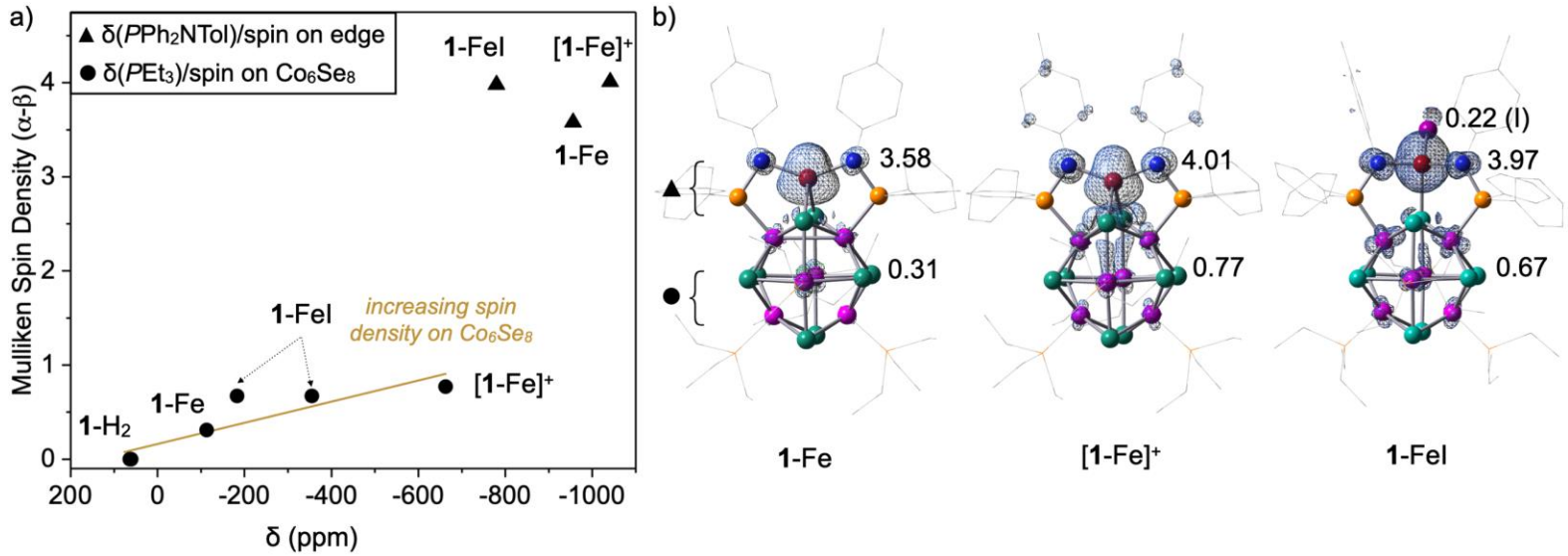

Figure 4.5. a) Relationship between the calculated Mulliken spin density calculated for the core or edge, and $^{31}P\{^{1}H\}$ NMR chemical shift of PEt_3 and PPh_2NTol. b) Mulliken spin density (α-β) plots of **1**-Fe, [**1**-Fe]$^+$, and **1**-FeBr calculated at the DFT uB3LYP+/cc-pVTZ level of theory.

4.7 Conclusions

In conclusion, this study reveals atom level insights into the structural and electronic effects of chemical oxidation of **1**-Fe. Outer- and inner-sphere oxidation illustrates the versatility of the cluster construct to accommodate charge and ancillary ligands. The combination of experimental and computational methods highlights an interesting regime of redox delocalization where the charge is shared between the Fe edge and the Co_6Se_8 core.

4.8 Synthetic Details and Characterization of Products

4.8.1 *General Experimental Considerations*

All manipulations were performed under a dry and oxygen free nitrogen atmosphere using standard Schlenk or glovebox techniques (LC Technology Solutions glovebox equipped with a freezer set to −35 °C). All glassware was dried in an oven set to 160 °C for a minimum of 12 h and cooled in an evacuated antechamber prior to use in the glovebox.

Solvents were purchased from Fischer Scientific and degassed, dried and purified using solvent purification columns housed in a stainless steel cabinet, and dispensed by a stainless steel Schlenk-line manufactured by JC Meyer Solvent Systems. Tetrahydrofuran (THF), diethyl ether (Et_2O), acetonitrile (MeCN), and methylene chloride (DCM) are passed through two packed columns of neutral alumina. In the cases of n-pentane, benzene, and toluene one of the columns is alumina and the other is Q5 reactant, a copper(II) oxide oxygen scavenger. Dimethylformamide (DMF) is dried by passage over two columns of activated molecular sieves. All solvents are passed through an in-line, 2 micron filter immediately before being dispensed which ensures that no packing material residue is dispensed with the solvent. Prior to use the solvents were stored over activated 3Å molecular sieves (purchased from Sigma Aldrich) in the glovebox for a minimum of 72 hours.

Deuterated solvents (C_6D_6 and CD_2Cl_2) were purchased from Cambridge Isotope Laboratories, Inc. or Sigma Aldrich, degassed and dried over activated 3Å molecular sieves (purchased from Sigma Aldrich) in the glovebox for a minimum of 72 hours.

1-H_2, **1**-Fe, and **1**-Zn were prepared using known literature procedures.[25] Ferrocenium hexafluorophosphate was purchased from Sigma Aldrich and recrystallized from dry acetone and

diethyl ether prior to its use. Silver trifluoromethanesulfonate (99%) was purchased from Strem Chemicals and used without further purification.

NMR spectra were obtained on a Bruker 300 or 500 MHz spectrometer. Chemical shifts are listed in parts per million and are referenced to the residual deuterated solvent peak for ^{1}H. ^{31}P and 19F spectra are referenced to phosphoric acid (0 ppm) and $CFCl_3$ (0 ppm), respectively.[46–48] All heteronuclear NMR measurements are proton decoupled ($X\{^{1}H\}$, X = ^{19}F, ^{31}P).

The magnetic moments were determined using Evans method using an NMR instrument.[49] A precisely measured quantity of each compound was dissolved in a known amount of a mesitylene (1% v/v) solution in CD_2Cl_2. The solution was transferred to an NMR tube together with a capillary containing mesitylene (1% v/v) solution in CD_2Cl_2. Analysis of the mesitylene signals separation between the sample and capillary allows for determination of the magnetic moment for the compound.

GC-MS measurements were performed using an Agilent Technologies instrument - MS: Model 5973; GC: Model 6890 equipped with Model 7683 autosampler. The GC Column used is a 30 meters Agilent Technologies J&W HP-5ms (part no.19091S-433).

Zero-field ^{57}Fe Mössbauer spectra were measured with a constant acceleration spectrometer (SEE Co., Minneapolis, MN) at 90 K. Solid samples (ca. 40 mg) were restrained with Parabar 10312 (Hampton Research Co., Aliso Viejo, CA). Isomer shifts are given relative to α-Fe metal at 298 K. The data were analyzed and simulated with Igor Pro 7 software (WaveMetrics, Inc., Portland, OR) using Lorentzian fitting functions.

EPR spectra were recorded on a Bruker EMX Nano spectrometer at 9.64 GHz as a frozen toluene solution.

X-ray crystallographic data was recorded on a Bruker APEX II single crystal X-ray diffractometer using Mo radiation.

Samples were prepared for elemental analysis by crushing crystalline material into a powder and then placed under reduced pressure for 12 h. Co, Se, P elemental analysis was conducted using a PerkinElmer Nexion 2000B inductively-coupled plasma mass spectrometer (ICP-MS). Prior to ICP-MS analysis, samples were digested in neat nitric acid (Fisher Scientific, ICP-MS grade) at 50 °C.

4.8.2 *Synthesis and isolation of [**1**-H_2][OTf]*

Inside the glovebox, **1**-H_2 (0.100 g, 0.049 mmol, 1.0 equiv) is dissolved in DCM (4 mL). The solution is then frozen in the glovebox coldwell. Upon thawing, a silver triflate (0.0126 g, 0.049 mmol, 1.0 equiv) solution in acetonitrile (2 mL) is added dropwise and the resulting reaction mixture is stirred at room temperature for 3 hours. The volatiles are then removed *in vacuo* and the residue triturated with *n*-pentane (5 mL), dissolved in DCM (10 mL) and filtered through Celite to remove the silver black. Evaporation of the volatiles under vacuum followed by trituration with *n*-pentane (2 × 10 mL) lead to a dark red crystalline solid (0.096 g, 90% yield).

^{1}H NMR (300 MHz, C_6D_6) δ 7.92 (d, J_{H-H} = 7.5 Hz, 8H, -C_6H_5), 7.31 (t, J_{H-H} = 7.5 Hz, 4H, -C_6H_5), 6.88 (m, 12H, -C_6H_5 and -$C_6H_4CH_3$), 6.61 (d, J_{H-H} = 8.0 Hz, 4H, -$C_6H_4CH_3$), 5.63 (s, 2H, -N*H*Tol), 1.79 (s, 6H, -$C_6H_4CH_3$), 0.26 (s, 18H, -CH_2CH_3), 0.01 (s, 18H, -CH_2CH_3), -0.86 (d, J_{H-P} = 6.2 Hz, 12H, -CH_2CH_3), -1.17 (d, J_{H-P} = 6.2 Hz, 12H, -CH_2CH_3); ^{31}P NMR (121 MHz, C_6D_6) δ -348.8 ($\nu_{1/2}$ = 832 Hz), -455.1 ($\nu_{1/2}$ = 746 Hz), -483.5 ($\nu_{1/2}$ = 825 Hz). Elemental Analysis (ICP-MS): Experimental (Calculated for $C_{63}H_{96}Co_6F_3N_2O_3P_6SSe_8$) Co 16.54 (16.15), Se 28.52 (28.85), P 8.50 (8.49).

4.8.3 *Synthesis and isolation of [**1**-Fe][OTf]*

Inside the glovebox, 1-**Fe** (0.105 g, 0.050 mmol, 1.0 equiv) is dissolved in DCM (7 mL). The solution is then frozen in the glovebox coldwell. Upon thawing, a solution of silver triflate (0.050 mmol, 0.5 mL of a 0.1 M acetonitrile solution, 1.0 equiv) is added dropwise and the resulting reaction mixture stirred at room temperature for 3 hours. The volatiles are then removed *in vacuo* and the residue triturated with *n*-pentane (2 × 10 mL), dissolved in DCM (20 mL) and filtered through Celite to remove the silver black. Evaporation of the volatiles under vacuum followed by trituration with *n*-pentane (2 × 10 mL) lead to a black crystalline solid (0.095 g, 0.042 mmol, 85% yield).

^{1}H NMR (500 MHz, C_6D_6) δ 85.73, 53.99, 14.65, 12.71, 6.49, 1.89, 0.45, 0.26, -0.14, -1.59; ^{31}P NMR (283 MHz, C_6D_6) δ -632.5 ($\nu_{1/2}$ = 3274 Hz), -936.1 ($\nu_{1/2}$ = 1332 Hz); ^{19}F NMR (470 MHz, C_6D_6) δ -60.17; μ_{eff} (Evans method, CD_2Cl_2, 298K) 5.8(3) μ_B.

4.8.4 *Synthesis and isolation of [**1**-Fe][PF_6]*

Inside the glovebox, **1**-Fe (0.096 g, 0.046 mmol, 1.0 equiv) is dissolved in DCM (5 mL). The solution is then frozen in the glovebox coldwell. Upon thawing, a solution of ferrocenium hexafluorophosphate (15 mg, 0.046 mmol, 1.0 equiv) in DCM (2 mL) is added dropwise and the resulting reaction mixture stirred at room temperature for 3 hours. The reaction mixture was concentrated to half of its original volume under reduce pressure, filtered through Celite, layered with *n*-pentane (10 mL), and left undisturbed in the glovebox freezer overnight. Evaporation of the volatiles under vacuum followed by trituration with *n*-pentane (2 × 10 mL) lead to a black crystalline solid (0.095 g, 0.042 mmol, 85% yield).

^{1}H NMR (300 MHz, CD_2Cl_2) δ 91.63, 57.06, 15.04, 7.70, 7.60, 6.99, 2.06, 0.26, -1.62 ppm. ^{31}P NMR (283 MHz, CD_2Cl_2) δ -639.8, -941.3; μ_{eff} (Evans method, CD_2Cl_2, 298K) 5.8(3) μ_B. Elemental Analysis (ICP-MS): Experimental (Calculated for $C_{62}H_{94}Co_6F_6FeN_2P_7Se_8$) Co 16.12 (15.79), Se 28.48 (28.21), P 9.86 (9.68).

4.8.5 *Oxidation of 1-Fe with 0.5 equiv of I_2: synthesis of **1**-Fe(I)*

Inside the glovebox, **1**-Fe (60.0 mg, 0.029 mmol, 1.0 equiv) was dissolved in DCM (3 mL). The solution was frozen in the glovebox coldwell, and upon thawing I_2 (3.6 mg, 0.014 mmol, 0.5 equiv) was added as a solution in DCM (2 mL) and the resultant reaction mixture was stirred at room temperature for 45 minutes. The volatiles were removed *in vacuo* and the solids were dissolved in a minimal amount of toluene (~1.5 mL), filtered through a plug of Celite, and layered with *n*-pentane (~7 mL). After 48 hours at –35 °C, a black precipitate was isolated *via* vacuum filtration with a fine porosity glass fritted funnel (32.4 mg, 0.015 mmol, 51% yield).

^{1}H NMR (300 MHz, C_6D_6) δ 62.12, 43.98, 31.28, 26.45, 14.91, 12.41, 10.52, 1.88, 0.68, 0.28, –39.77; ^{31}P NMR (283 MHz, C_6D_6) δ –180.36, –350.48, –774.30; μ_{eff} (Evans method, CD_2Cl_2, 298K) 5.7(3) μ_B. Elemental Analysis (ICP-MS): Experimental (Calculated for $C_{62}H_{94}Co_6FeIN_2P_6Se_8$) Co 15.83 (15.92), Se 28.63 (28.44), P 8.39 (8.37).

4.8.6 *In situ oxidation of **1**-Zn with $FcPF_6$*

Inside the glovebox, **1**-Zn (12 mg, 0.0055 mmol, 1.0 equiv) is dissolved in DCM (3 mL). The solution is then frozen in the glovebox coldwell. Upon thawing, a solution of ferrocenium hexafluorophosphate (111 μL, 0.05 M in MeCN, 1.0 equiv) is added dropwise and the resulting reaction mixture stirred at room temperature for 3 hours. The reaction mixture was concentrated under reduce pressure, dissolved in benzene-d_6, filtered through Celite, and analyzed by NMR spectroscopy. The NMR sample was then brought back into the glovebox and layered with *n*-pentane, and left undisturbed at room temperature for 1 week to yield high quality single crystals suitable for X-ray diffraction analysis. The crystal analyzed by X-ray diffraction is described in Section 4.11.3, and represented in Figure 4.13, as well as in Figure 4.14 as a comparison with the parent cluster **1**-Zn.

4.9 EPR SPECTROSCOPY

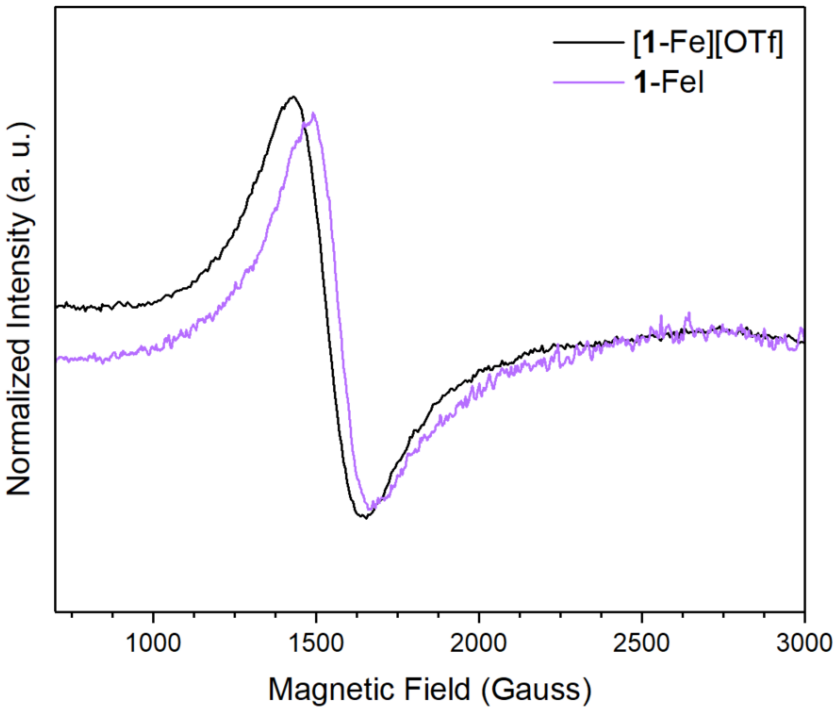

Figure 4.6. X-Band EPR spectra of [**1**-Fe][OTf] and **1**-FeI at 9.64 GHz in frozen toluene at 100 K. **[1**-Fe][OTf] g = 4.35 and **1**-FeI g = 4.46.

4.10 PARAMAGNETIC NMR STUDIES

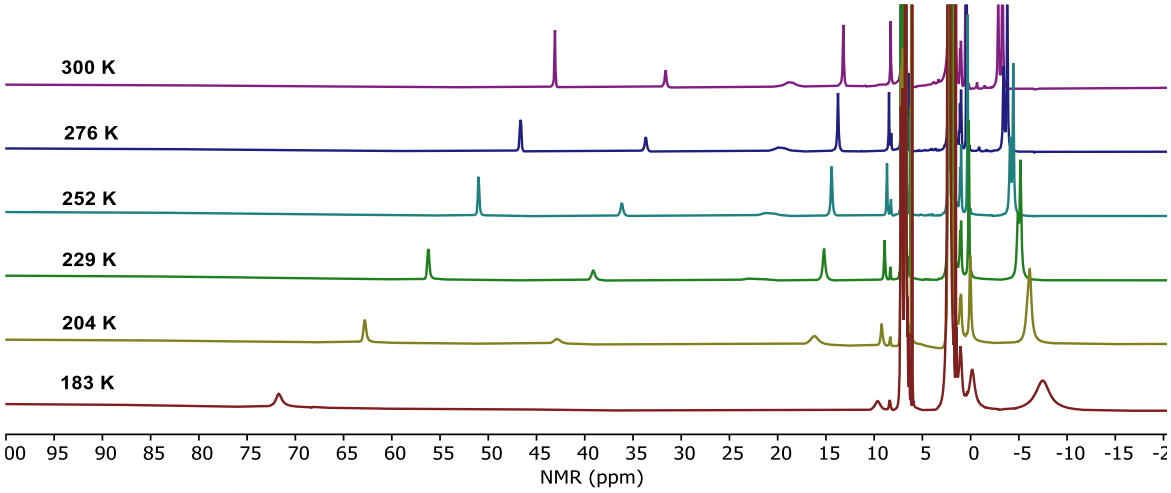

Figure 4.7. VT-^{1}H-NMR (C_6D_6, 500 MHz) spectra of **1**-Fe from 183K to 300K.

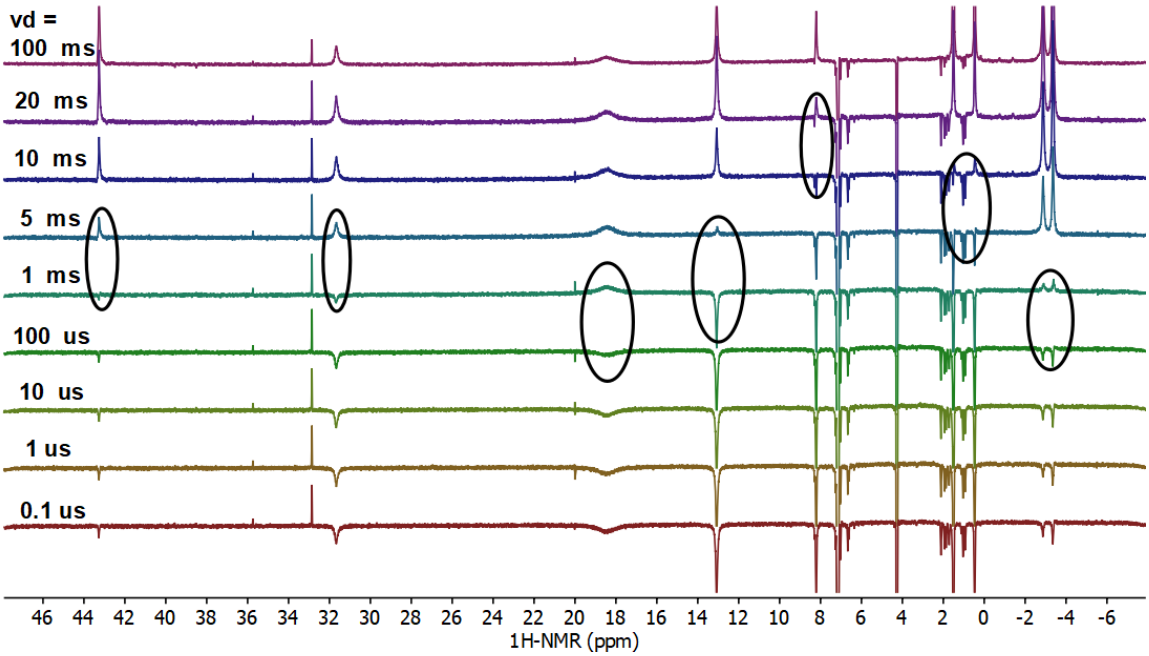

Figure 4.8. ^{1}H NMR T_1 relaxation determination of **1**-Fe by monitoring the phase inversion for each peak. The lowest determined T1 is 0.7 ms while the highest is 22 ms.

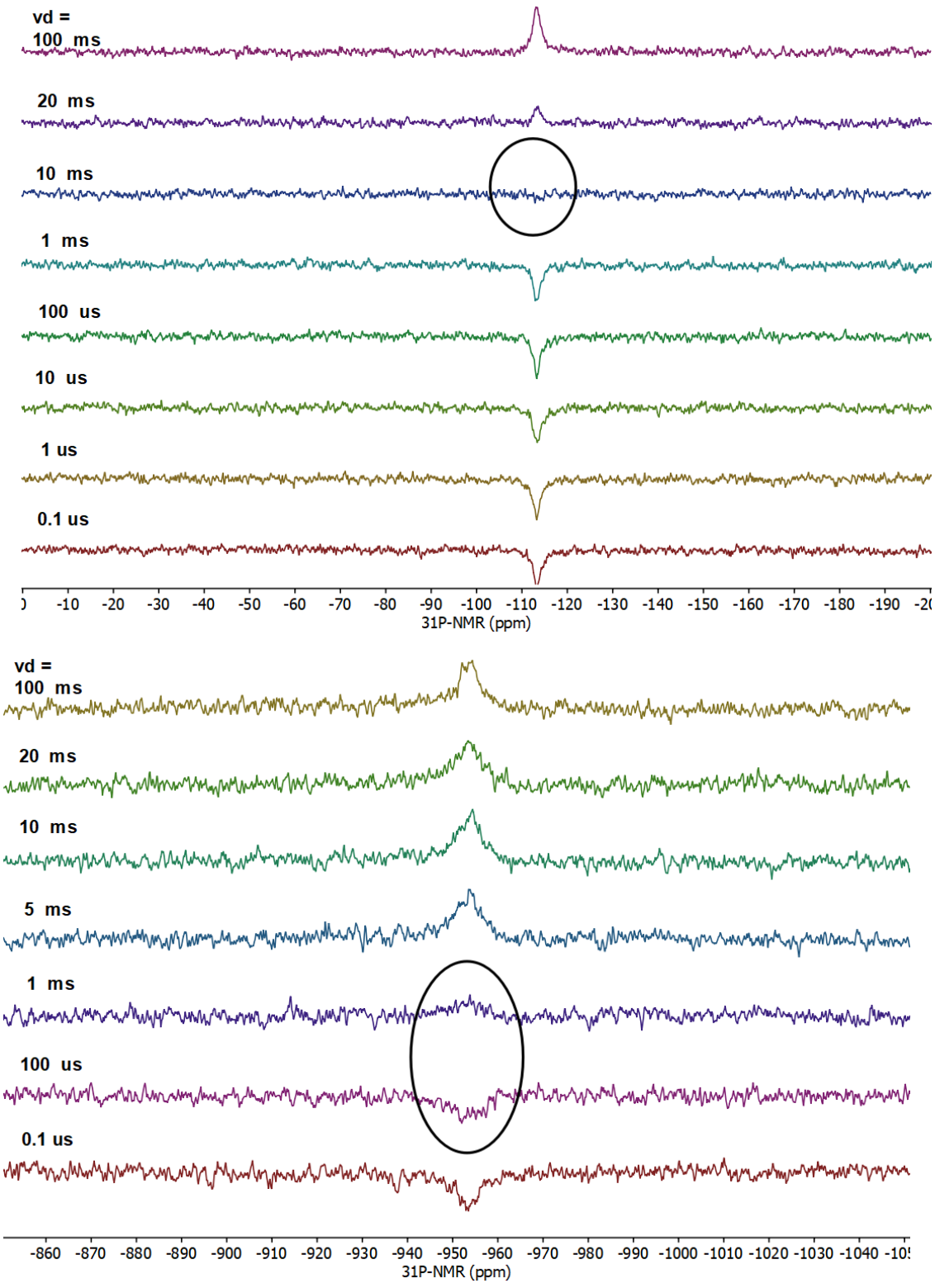

Figure 4.9. ^{31}P NMR T1 relaxation determination of **1**-Fe. T1=14 ms for the signal at −113ppm (top) and T1=0.7ms for the signal at −955ppm (bottom).

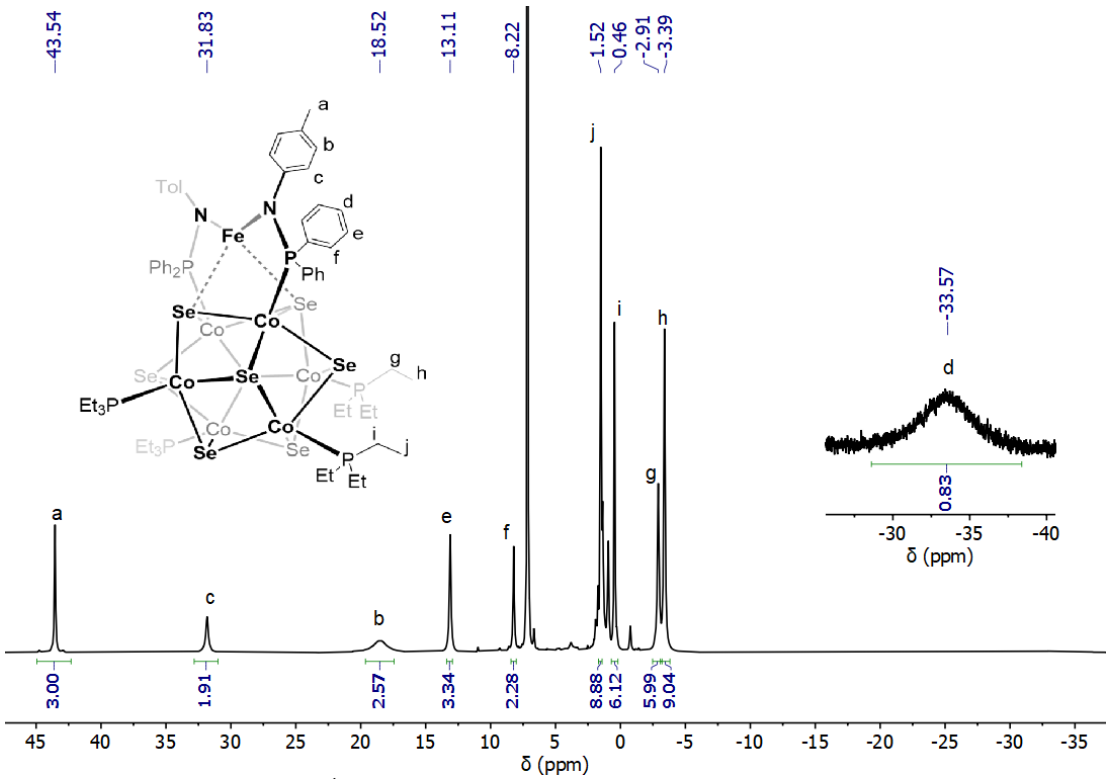

Figure 4.10. Assignment of ^{1}H NMR features in **1**-Fe determined by relaxation time studies.

Table 4.2. $^{31}P\{^{1}H\}$ NMR chemical shifts.

Compound	δ(*P*Et$_3$) (ppm)	δ(*P*N$^{(-)}$Tol) (ppm)
1-H$_2$*	64; 61	89
[**1**-H$_2$][OTf]	–455; –484	–359
1-Fe*	–113	–956
[**1**-Fe][OTf]	–633	–936
[**1**-Fe][PF$_6$]	–663	–999
1-Fe(py)	–81	–715
1-Fe(THF)	–111	–915
1-FeI	–183, –355	–780

4.11 X-RAY DIFFRACTION STUDIES

Data was collected at 100K on a Bruker APEX II single crystal X-ray diffractometer using Mo-radiation. The data was integrated and scaled using SAINT, SADABS within the APEX2 software package by Bruker.[50] Solution by direct methods (SHELXT[51] or SIR97[52,53]) produced complete heavy atom phasing models consistent with the proposed structures. Structure were completed by difference Fourier synthesis with SHELXL.[51,54,55] Scattering factors are from Waasmair and Kirfel.[56] Hydrogen atoms were placed in geometrically idealized positions and constrained to ride on their parent atoms with C-H distances in the range 0.95-1.00 Angstrom. Isotropic thermal parameters U_{eq} were fixed such that they were $1.2U_{eq}$ of their parent atom U_{eq} for CH's and $1.5U_{eq}$ of their parent atom U_{eq} in case of methyl groups. All non-hydrogen atoms were refined anisotropically by full-matrix least-squares.

4.11.1 *[**1**-Fe][OTf]*

Diffraction-quality, dark colored crystals of [**1**-Fe][OTf] were grown at −35 °C from a layered solution of toluene/*n*-pentane. A shard of a crystal, measuring 0.09 × 0.07 × 0.07 mm^3 was mounted on a loop with Paratone® oil. The data appeared twinned via 4 degrees about (0 -0.377 1) (CELL_NOW[57]) and after multi-domain integration (SAINT, SADABS within the APEX2 software package by Bruker[50]) the data was merged utilizing TWINABS[58]. The asymmetric unit includes two toluene solvent molecules. The space group is chiral and twin analysis on chirality revealed the compound to be practically enantiopure (Flack parameter = 0.02(3)).

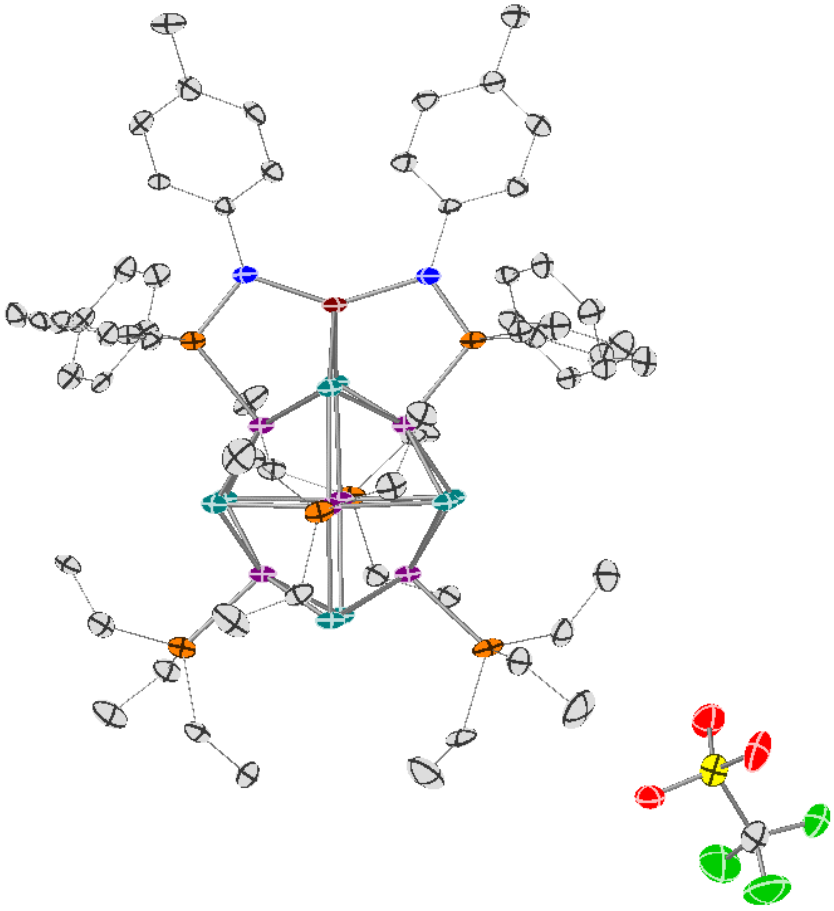

Figure 4.11. ORTEP of [**1**-Fe][OTf] with thermal ellipsoids at the 50% probability level.

4.11.2 ***1*-*Fe(Br)***

Diffraction-quality, dark colored crystals of **1**-Fe(I) were grown at room temperature from a layered solution of benzene-d_6/*n*-pentane. A black prism, measuring 0.09 x 0.08 x 0.06 mm^3 was mounted on a loop with Paratone® oil. The Fe-I and all PEt_3 units were disordered requiring DELU/ISOR and some EADP restraints for those moieties as well as linking the related geometries via SAME.

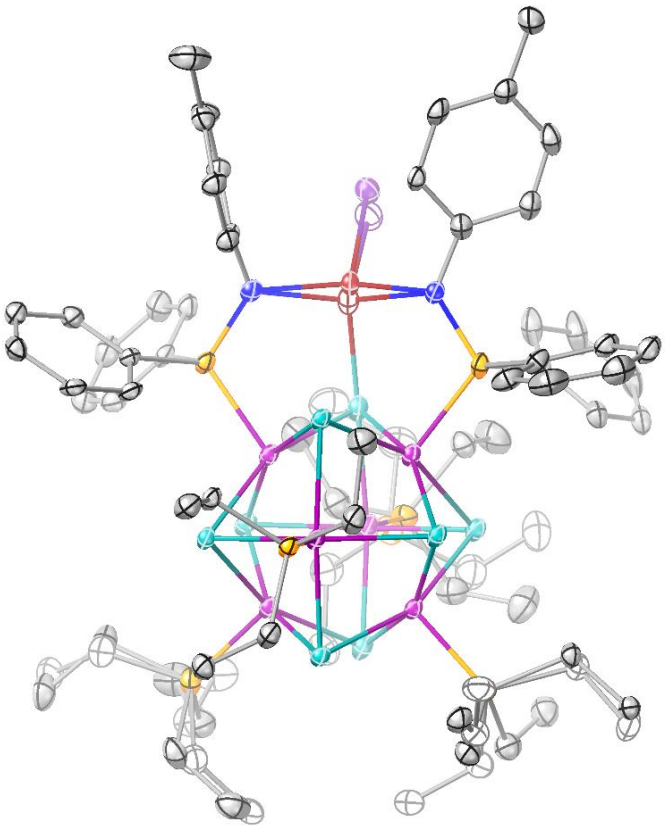

Figure 4.12. ORTEP of **1**-FeI with thermal ellipsoids shown at 50% probability level. Disordered Fe-I and PEt_3 moieties are represented as hollow atoms. Hydrogen atoms are omitted for clarity

4.11.3 *[**1**-Zn][PF$_6$]*

Diffraction quality crystals of [**1**-Zn][PF$_6$] were grown at room temperature from a layered solution of benzene-d_6/pentane. The data appears to be pseudo-merohedrally twinned via a 180 degrees rotation about [-1 0 2] and a twin-matrix was added that considerably improved the R1: (-1 0 0, 0 -1 0, -1 0 1). The structure contains some partially disordered C_6D_6.

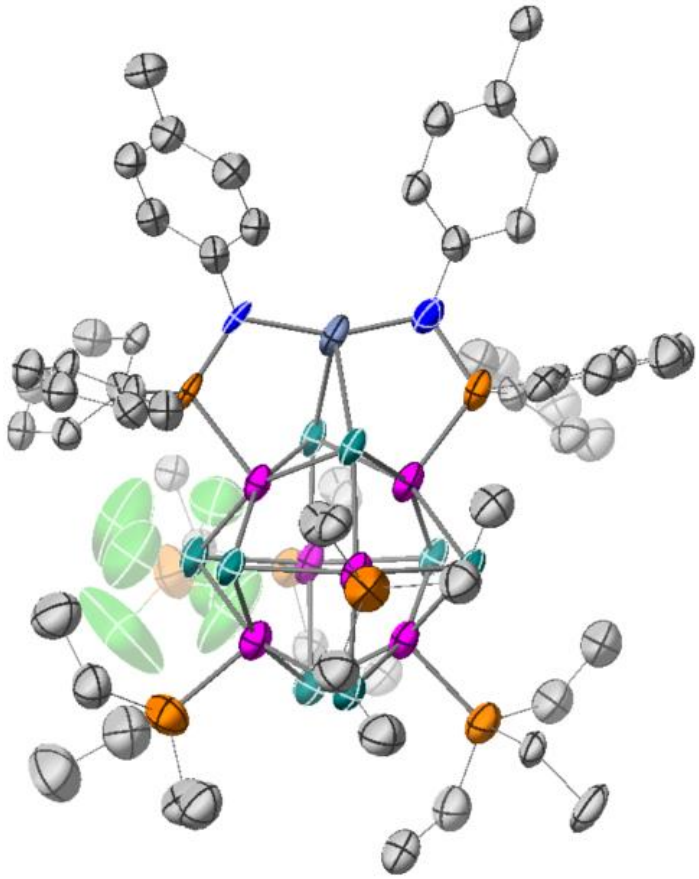

Figure 4.13. ORTEP of [**1**-Zn][PF$_6$] with thermal ellipsoids at the 50% probability level. Disordered benzene-d_6 molecules are omitted for clarity.

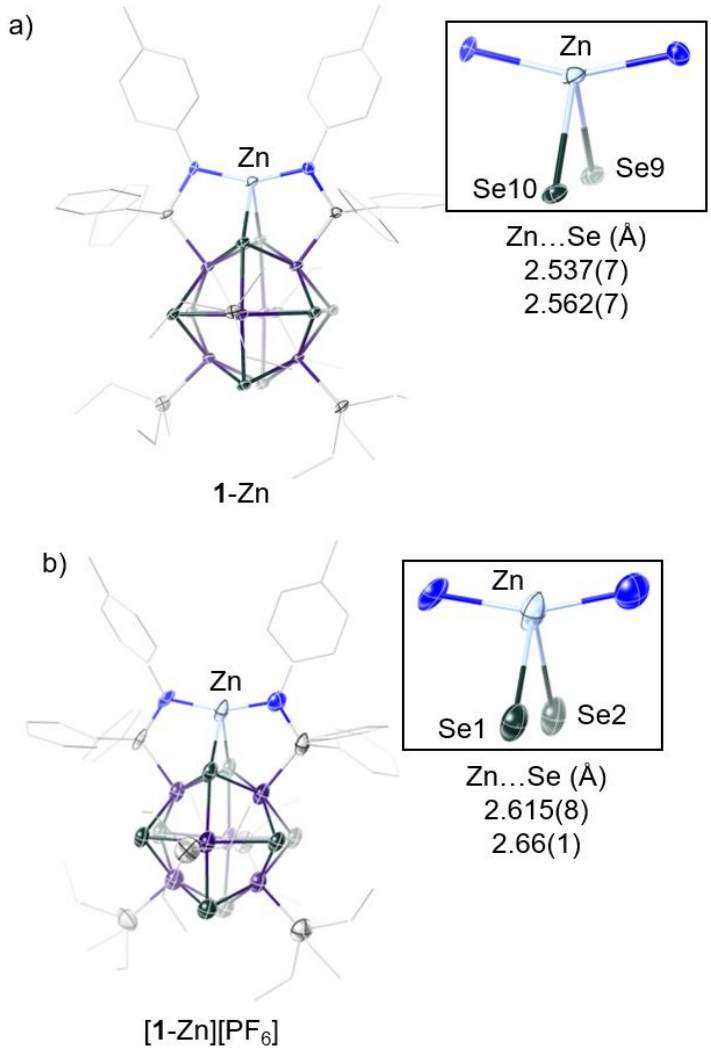

Figure 4.14. Single crystal X-ray diffraction of a) **1**-Zn and b) [**1**-Zn][PF_6]. Hydrogen atoms, co-crystallized solvent molecules, disorder, and PF_6 anion are omitted for clarity.

4.11.4 *X-ray Structure Tables*

Table 4.3. Crystallographic data for [**1**-Fe][OTf], **1**-FeI, and [**1**-Zn][PF_6]

Compound	**[1-Fe][**OTf] • toluene	**1**-FeI	**[1-Zn][**OTf] • 3 C_6D_6
CCDC deposition number	2225100	2260994	2225102
Empirical formula	$C_{77}H_{110}Co_6FeN_2O_3F_3P_6SSe_8$	$C_{62}H_{94}Co_6FeIN_2P_6Se_8$	$C_{80}H_{94}Co_6D_{18}F_6N_2P_7Se_8Zn$
Formula weight	2427.65	2221.22	2501.24
Temperature (K)	100(2)	100(2)	100(2)
Wavelength (Å)	0.71073	0.71073	0.71073
Crystal system	Monoclinic	Triclinic	Triclinic
Space group	P 2_1	P -1	P -1
a (Å)	14.384(3)	12.9948(10)	14.3074(13)
b (Å)	21.020(4)	14.6453(10)	15.1878(11)
c (Å)	14.851(3)	21.9847(16)	22.741(2)
α (°)	90	99.096(4)	86.131(5)
β (°)	95.859(14)	92.427(4)	72.325(5)
γ (°)	90	114.259(3)	78.487(5)
Volume (Å^3)	4466.5(16)	3739.7(5)	4613.5(7)
Z	2	2	2
Calculated Density (g cm^{-3})	1.805	1.973	1.801
Absorption coefficient (mm^{-1})	4.687	5.959	4.639
F(000)	2406	2166	2458
Crystal size (mm^3)	0.090 x 0.070 x 0.070	0.090 x 0.080 x 0.060	0.160 x 0.110 x 0.100
Theta range for data collection (°)	1.423 to 25.186	1.554 to 28.443	1.521 to 25.028
Index ranges	-14 ≤ h≤14, -20 ≤ k ≤ 20, -16 ≤ l ≤ 16	-17 ≤ h ≤ 17, -19 ≤ k ≤ 19, -29 ≤ l ≤ 29	-16 ≤ h ≤ 16, -18 ≤ k ≤ 18, -27 ≤ l ≤ 27
Reflections collected	15528	36970	
Independent reflections	15528 [R(int) = 0.117]	18711 [R(int) = 0.0667]	16226 [R(int) = 0.1441]
Completeness to theta = 25.000°	99.0 %	100.0 %	99.8 %
Data / restraints / parameters	15528 / 970 / 879	18711 / 577 / 952	16226 / 1045 / 1014
Goodness-of-fit on F^2	0.960	1.006	1.029
Final R indices [I>2sigma(I)]	R_1 = 0.1113, wR_2 = 0.1850	R_1 = 0.0445, wR_2 = 0.0973	R_1 = 0.1210, wR_2 = 0.2595
R indices (all data)	R_1 = 0.2593, wR_2 = 0.2214	R_1 = 0.0890, wR_2 = 0.1168	R_1 = 0.2366, wR_2 = 0.3324
Largest diff. peak and hole (e$^-$Å^{-3})	2.342 and -1.287	0.905 and -1.798	2.301 and -1.880

4.12 DFT CALCULATIONS

All calculations were performed using Gaussian 16, Revision A.03 quantum chemistry program package for the Linux operating system.[59] The initial starting point geometries were obtained from the corresponding crystallographically obtained structures and optimized to a minimum, followed by analytical frequency calculations (Hessian) to confirm that no imaginary frequencies were present. The geometry optimizations were performed using unrestricted DFT calculations at a pure GGA functional level using Becke's 1988 gradient-corrected exchange functional and Perdew's 1986 electron correlation functional (uBPV86) and def2SVP basis set. Using the optimized geometries, single point calculations were performed at the uB3LYP+/cc-pVTZ that were used for orbital energy diagrams and spin density calculations. [43–45,59] For **1**-FeI, an alternate basis set was employed, cc-pVTZ-PP.[60–62]

Example of geometry optimizations:

%nprocshared=28
%mem=64GB
%chk=FeCo6Se8Tol_1_6_u_bvp86_def2SVP_OPT_FREQ.chk
#p opt freq ubvp86/def2SVP scf=maxcycle=3072 gfinput pop=(full,nbo)

FeCo6Se8Tol_1_6_u_bvp86_def2SVP_OPT_FREQ

1 6
coordinates from X-ray structure

Example of single point calculations:

%nprocshared=28
%mem=80GB
%oldchk= FeCo6Se8Tol_1_6_u_bvp86_def2SVP_OPT_FREQ.chk
%chk=Fe6Se8Tol_1_6_u_b3lyp_plus_ccpVTZ.chk
#p ub3lyp IOp(3/76=1000001500) IOp(3/77=0720008000) IOp(3/78=0810010000) cc-pVTZ guess=read geom=check scf=maxcycle=3072 gfinput pop=full IOp(6/82=1)

FeCo6Se8Tol_1_6_u_b3lyp_plus_ccpVTZ

1 6

Input file for single point calculation of **1**-FeI

%mem=107GB
%LindaWorker=n2128,n2129,n2130,n2131
%usessh
%nprocshared=28
%RWF=FeICo6Se8Tol_0_6_u_b3lyp_plus_ccpVTZ.rwf
%NoSave
%oldchk=FeICo6Se8Tol_0_6_u_bvp86_def2SVP_OPT_FREQ.chk
%chk=FeICo6Se8Tol_0_6_u_b3lyp_plus_ccpVTZ.chk
#p ub3lyp/GEN IOp(3/76=1000001500) IOp(3/77=0720008000) IOp(3/78=0810010000) geom=check scf=(restart,maxcycle=3072) gfinput pop=full IOp(6/82=1)

FeICo6Se8Tol_0_6_u_b3lyp_plus_ccpVTZ

0 6

Co Se P N Fe C 0
cc-pVTZ
****
I 0
S 11 1.00
5.546500D+03 1.560000D-04
8.382140D+02 9.860000D-04
1.821870D+02 2.792000D-03
3.121230D+01 -4.325100D-02
1.953140D+01 2.341340D-01

8.240990D+00 -7.509430D-01
2.194550D+00 8.829680D-01
1.109110D+00 4.620610D-01
3.746410D-01 2.228600D-02
1.770800D-01 -4.353000D-03
8.106100D-02 1.102000D-03
S 1 1.00
3.746410D-01 1.000000D+00
S 1 1.00
1.770800D-01 1.000000D+00
S 11 1.00
5.546500D+03 -7.300000D-05
8.382140D+02 -5.080000D-04
1.821870D+02 -1.158000D-03
3.121230D+01 1.219300D-02
1.953140D+01 -8.785400D-02
8.240990D+00 3.382000D-01
2.194550D+00 -5.765500D-01
1.109110D+00 -4.092980D-01
3.746410D-01 5.674590D-01
1.770800D-01 6.124890D-01
8.106100D-02 1.432310D-01
S 1 1.00
1.001000D-01 1.000000D+00
P 9 1.00
1.889880D+02 5.850000D-04
2.128680D+01 3.692300D-02
1.003960D+01 -2.353240D-01
3.451800D+00 3.414830D-01
1.974560D+00 5.347880D-01
1.024200D+00 2.651410D-01

```
     4.494370D-01         2.578700D-02
     1.866480D-01         5.220000D-04
     7.348100D-02         6.060000D-04
P    1   1.00
     5.981000D-01         1.000000D+00
P    9   1.00
     1.889880D+02        -2.560000D-04
     2.128680D+01        -1.168200D-02
     1.003960D+01         8.319200D-02
     3.451800D+00        -1.569700D-01
     1.974560D+00        -2.245180D-01
     1.024200D+00        -1.144510D-01
     4.494370D-01         3.753560D-01
     1.866480D-01         5.751360D-01
     7.348100D-02         2.459170D-01
P    1   1.00
     9.618000D-02         1.000000D+00
D    9   1.00
     1.326620D+02         5.720000D-04
     3.760540D+01         4.402000D-03
     1.038910D+01        -4.092200D-02
     6.490170D+00         9.966100D-02
     3.454510D+00         3.226630D-01
     1.844130D+00         4.003430D-01
     9.624780D-01         2.683060D-01
     4.728530D-01         8.484700D-02
     1.932000D-01         7.632000D-03
D    1   1.00
     4.728530D-01         1.000000D+00
D    1   1.00
     1.932000D-01         1.000000D+00
```

```
F    1   1.00
     4.064000D-01          1.000000D+00
****

I    0
I-ECP    4    28
g potential
 1
2      1.00000000           0.00000000
s-g potential
 3
2     40.03337600          49.98964900
2     17.30057600         281.00655600
2      8.85172000          61.41673900
p-g potential
 4
2     15.72014100          67.41623900
2     15.20822200         134.80769600
2      8.29418600          14.56654800
2      7.75394900          28.96842200
d-g potential
 4
2     13.81775100          35.53875600
2     13.58780500          53.33975900
2      6.94763000           9.71646600
2      6.96009900          14.97750000
f-g potential
 4
2     18.52295000         -20.17661800
2     18.25103500         -26.08807700
2      7.55790100          -0.22043400
```

2 7.59740400 -0.22164600

****

$NBO PLOT FILE=FeICo6Se8Tol_0_6_u_b3lyp_plus_ccpVTZ $END

4.13 REFERENCES

(1) Cammarota, R. C.; Clouston, L. J.; Lu, C. C. Leveraging Molecular Metal–Support Interactions for H2 and N2 Activation. *Coordination Chemistry Reviews* **2017**, *334*, 100–111. https://doi.org/10.1016/j.ccr.2016.06.014.

(2) Ross, M. O.; Rosenzweig, A. C. A Tale of Two Methane Monooxygenases. *J Biol Inorg Chem* **2017**, *22* (2), 307–319. https://doi.org/10.1007/s00775-016-1419-y.

(3) Hoffman, B. M.; Lukoyanov, D.; Yang, Z.-Y.; Dean, D. R.; Seefeldt, L. C. Mechanism of Nitrogen Fixation by Nitrogenase: The Next Stage. *Chem. Rev.* **2014**, *114* (8), 4041–4062. https://doi.org/10.1021/cr400641x.

(4) Benediktsson, B.; Bjornsson, R. QM/MM Study of the Nitrogenase MoFe Protein Resting State: Broken-Symmetry States, Protonation States, and QM Region Convergence in the FeMoco Active Site. *Inorg. Chem.* **2017**, *56* (21), 13417–13429. https://doi.org/10.1021/acs.inorgchem.7b02158.

(5) Henthorn, J. T.; Arias, R. J.; Koroidov, S.; Kroll, T.; Sokaras, D.; Bergmann, U.; Rees, D. C.; DeBeer, S. Localized Electronic Structure of Nitrogenase FeMoco Revealed by Selenium K-Edge High Resolution X-Ray Absorption Spectroscopy. *J. Am. Chem. Soc.* **2019**, *141* (34), 13676–13688. https://doi.org/10.1021/jacs.9b06988.

(6) Bjornsson, R.; Neese, F.; DeBeer, S. Revisiting the Mössbauer Isomer Shifts of the FeMoco Cluster of Nitrogenase and the Cofactor Charge. *Inorg. Chem.* **2017**, *56* (3), 1470–1477. https://doi.org/10.1021/acs.inorgchem.6b02540.

(7) Arnett, C. H.; Bogacz, I.; Chatterjee, R.; Yano, J.; Oyala, P. H.; Agapie, T. Mixed-Valent Diiron μ-Carbyne, μ-Hydride Complexes: Implications for Nitrogenase. *J. Am. Chem. Soc.* **2020**, *142* (44), 18795–18813. https://doi.org/10.1021/jacs.0c05920.

(8) Doan, P. E.; Telser, J.; Barney, B. M.; Igarashi, R. Y.; Dean, D. R.; Seefeldt, L. C.; Hoffman, B. M. 57Fe ENDOR Spectroscopy and 'Electron Inventory' Analysis of the Nitrogenase E4 Intermediate Suggest the Metal-Ion Core of FeMo-Cofactor Cycles Through Only One Redox Couple. *J. Am. Chem. Soc.* **2011**, *133* (43), 17329–17340. https://doi.org/10.1021/ja205304t.

(9) Pickett, C. J.; Vincent, K. A.; Ibrahim, S. K.; Gormal, C. A.; Smith, B. E.; Best, S. P. Electron-Transfer Chemistry of the Iron–Molybdenum Cofactor of Nitrogenase: Delocalized and Localized Reduced States of FeMoco which Allow Binding of Carbon Monoxide to Iron and

Molybdenum. *Chemistry – A European Journal* **2003**, *9* (1), 76–87. https://doi.org/10.1002/chem.200390033.

(10) Thomas, C. M. Metal-Metal Multiple Bonds in Early/Late Heterobimetallic Complexes: Applications Toward Small Molecule Activation and Catalysis. *Comments on Inorganic Chemistry* **2011**, *32* (1), 14–38. https://doi.org/10.1080/02603594.2011.593213.

(11) Eisenhart, R. J.; Clouston, L. J.; Lu, C. C. Configuring Bonds between First-Row Transition Metals. *Acc. Chem. Res.* **2015**, *48* (11), 2885–2894. https://doi.org/10.1021/acs.accounts.5b00336.

(12) de Ruiter, G.; Carsch, K. M.; Gul, S.; Chatterjee, R.; Thompson, N. B.; Takase, M. K.; Yano, J.; Agapie, T. Accelerated Oxygen Atom Transfer and C−H Bond Oxygenation by Remote Redox Changes in Fe3Mn-Iodosobenzene Adducts. *Angewandte Chemie* **2017**, *129* (17), 4850–4854. https://doi.org/10.1002/ange.201701319.

(13) Arnett, C. H.; Chalkley, M. J.; Agapie, T. A Thermodynamic Model for Redox-Dependent Binding of Carbon Monoxide at Site-Differentiated, High Spin Iron Clusters. *J. Am. Chem. Soc.* **2018**, *140* (16), 5569–5578. https://doi.org/10.1021/jacs.8b01825.

(14) Amtawong, J.; Nguyen, A. I.; Tilley, T. D. Mechanistic Aspects of Cobalt–Oxo Cubane Clusters in Oxidation Chemistry. *J. Am. Chem. Soc.* **2022**, *144* (4), 1475–1492. https://doi.org/10.1021/jacs.1c11445.

(15) Kim, Y.; Sridharan, A.; Suess, D. L. M. The Elusive Mononitrosylated [Fe4S4] Cluster in Three Redox States. *Angewandte Chemie International Edition* **2022**, *61* (47), e202213032. https://doi.org/10.1002/anie.202213032.

(16) Brown, A. C.; Thompson, N. B.; Suess, D. L. M. Evidence for Low-Valent Electronic Configurations in Iron–Sulfur Clusters. *J. Am. Chem. Soc.* **2022**, *144* (20), 9066–9073. https://doi.org/10.1021/jacs.2c01872.

(17) Eames, E. V.; Betley, T. A. Site-Isolated Redox Reactivity in a Trinuclear Iron Complex. *Inorg. Chem.* **2012**, *51* (19), 10274–10278. https://doi.org/10.1021/ic301241s.

(18) Johnson, B. J.; Antholine, W. E.; Lindeman, S. V.; Graham, M. J.; Mankad, N. P. A One-Hole Cu4S Cluster with N2O Reductase Activity: A Structural and Functional Model for CuZ*. *J. Am. Chem. Soc.* **2016**, *138* (40), 13107–13110. https://doi.org/10.1021/jacs.6b05480.

(19) Hernández Sánchez, R.; Zheng, S.-L.; Betley, T. A. Ligand Field Strength Mediates Electron Delocalization in Octahedral [(HL)2Fe6(L′)m]N+ Clusters. *J. Am. Chem. Soc.* **2015**, *137* (34), 11126–11143. https://doi.org/10.1021/jacs.5b06453.

(20) Arnett, C. H.; Kaiser, J. T.; Agapie, T. Remote Ligand Modifications Tune Electronic Distribution and Reactivity in Site-Differentiated, High-Spin Iron Clusters: Flipping Scaling Relationships. *Inorg. Chem.* **2019**, *58* (23), 15971–15982. https://doi.org/10.1021/acs.inorgchem.9b02470.

(21) Hernández Sánchez, R.; Champsaur, A. M.; Choi, B.; Wang, S. G.; Bu, W.; Roy, X.; Chen, Y.-S.; Steigerwald, M. L.; Nuckolls, C.; Paley, D. W. Electron Cartography in Clusters. *Angewandte Chemie International Edition* **2018**, *57* (42), 13815–13820. https://doi.org/10.1002/anie.201806426.

(22) Brown, A. C.; Suess, D. L. M. Valence Localization in Alkyne and Alkene Adducts of Synthetic [Fe4S4]+ Clusters. *Inorg. Chem.* **2022**. https://doi.org/10.1021/acs.inorgchem.2c01353.

(23) Kephart, J. A.; Mitchell, B. S.; Chirila, A.; Anderton, K. J.; Rogers, D.; Kaminsky, W.; Velian, A. Atomically Defined Nanopropeller Fe3Co6Se8(Ph2PNTol)6: Functional Model for the Electronic Metal–Support Interaction Effect and High Catalytic Activity for Carbodiimide Formation. *J. Am. Chem. Soc.* **2019**, *141* (50), 19605–19610. https://doi.org/10.1021/jacs.9b12473.

(24) Kephart, J.; Mitchell, B.; Kaminsky, W.; Velian, A. *Multi-Active Site Dynamics on a Molecular Cr/Co/Se Cluster Catalyst*; preprint; Chemistry, 2022. https://doi.org/10.26434/chemrxiv-2022-zkfsp.

(25) Mitchell, B. S.; Chirila, A.; Kephart, J. A.; Boggiano, A. C.; Krajewski, S. M.; Rogers, D.; Kaminsky, W.; Velian, A. Metal–Support Interactions in Molecular Single-Site Cluster Catalysts. *J. Am. Chem. Soc.* **2022**, *144* (40), 18459–18469. https://doi.org/10.1021/jacs.2c07033.

(26) Mitchell, B.; Chirila, A.; Zhou, D.; Kephart, J.; Velian, A. *Metal-Support Interactions Regulate Substrate Binding in Fe/Co/Se Cluster Catalysts*; preprint; Chemistry, 2022. https://doi.org/10.26434/chemrxiv-2022-f19xz.

(27) Mitchell, B. S.; Chirila, A.; Anderton, K.; Kaminsky, W.; Velian, A. Probing Edge/Support Electronic Cooperativity in Single Edge Fe/Co6Se8 Clusters. ChemRxiv December 30, 2022. https://doi.org/10.26434/chemrxiv-2022-4mtw9.

(28) Connelly, N. G.; Geiger, W. E. Chemical Redox Agents for Organometallic Chemistry. *Chem. Rev.* **1996**, *96* (2), 877–910. https://doi.org/10.1021/cr940053x.

(29) England, J.; Britovsek, G. J. P.; Rabadia, N.; White, A. J. P. Ligand Topology Variations and the Importance of Ligand Field Strength in Non-Heme Iron Catalyzed Oxidations of Alkanes. *Inorg. Chem.* **2007**, *46* (9), 3752–3767. https://doi.org/10.1021/ic070062r.

(30) Mitchell, B. S.; Krajewski, S. M.; Kephart, J. A.; Rogers, D.; Kaminsky, W.; Velian, A. Redox-Switchable Allosteric Effects in Molecular Clusters. *JACS Au* **2021**. https://doi.org/10.1021/jacsau.1c00491.

(31) Choi, B.; Yu, J.; Paley, D. W.; Trinh, M. T.; Paley, M. V.; Karch, J. M.; Crowther, A. C.; Lee, C.-H.; Lalancette, R. A.; Zhu, X.; Kim, P.; Steigerwald, M. L.; Nuckolls, C.; Roy, X. Van Der Waals Solids from Self-Assembled Nanoscale Building Blocks. *Nano Lett.* **2016**, *16* (2), 1445–1449. https://doi.org/10.1021/acs.nanolett.5b05049.

(32) Evans, D. F. The Determination of the Paramagnetic Susceptibility of Substances in Solution by Nuclear Magnetic Resonance. *J. Chem. Soc.* **1959**, No. 0, 2003–2005. https://doi.org/10.1039/JR9590002003.

(33) Fultz, B. Mössbauer Spectrometry. In *Characterization of Materials*; John Wiley & Sons, Ltd, 2012; pp 1–21. https://doi.org/10.1002/0471266965.com069.pub2.

(34) Pandelia, M.-E.; Lanz, N. D.; Booker, S. J.; Krebs, C. Mössbauer Spectroscopy of Fe/S Proteins. *Biochimica et Biophysica Acta (BBA) - Molecular Cell Research* **2015**, *1853* (6), 1395–1405. https://doi.org/10.1016/j.bbamcr.2014.12.005.

(35) Spreer, L. O.; Li, A.; MacQueen, D. B.; Allan, C. B.; Otvos, J. W.; Calvin, M.; Frankel, R. B.; Papaefthymiou, G. C. Characterization of a Delocalized Mixed-Valence Bis-Macrocyclic Diiron Compound. *Inorg. Chem.* **1994**, *33* (9), 1753–1755. https://doi.org/10.1021/ic00087a006.

(36) Yang, L.; Powell, D. R.; Houser, R. P. Structural Variation in Copper(I) Complexes with Pyridylmethylamide Ligands: Structural Analysis with a New Four-Coordinate Geometry Index, T4. *Dalton Trans.* **2007**, No. 9, 955–964. https://doi.org/10.1039/B617136B.

(37) Rumble, J. *CRC Handbook of Chemistry and Physics*, 103rd ed.; CRC Press/Taylor and Francis: Boca Raton, FL, 2022.

(38) Kephart, J. A.; Mitchell, B. S.; Chirila, A.; Anderton, K. J.; Rogers, D.; Kaminsky, W.; Velian, A. Atomically Defined Nanopropeller $Fe_3Co_6Se_8(Ph_2PNTol)_6$: Functional Model for the Electronic Metal–Support Interaction Effect and High Catalytic Activity for Carbodiimide Formation. *J. Am. Chem. Soc.* **2019**, *141* (50), 19605–19610. https://doi.org/10.1021/jacs.9b12473.

(39) Wolczanski, P. T. Flipping the Oxidation State Formalism: Charge Distribution in Organometallic Complexes As Reported by Carbon Monoxide. *Organometallics* **2017**, *36* (3), 622–631. https://doi.org/10.1021/acs.organomet.6b00820.

(40) Williams, T. J.; Kershaw, A. D.; Li, V.; Wu, X. An Inversion Recovery NMR Kinetics Experiment. *J. Chem. Educ.* **2011**, *88* (5), 665–669. https://doi.org/10.1021/ed1006822.

(41) Bernassau, J.-M.; Hyafil, F. Choice of Delay Time Sequence in Spin-Lattice Relaxation Time Measurements by Inversion-Recovery. *Journal of Magnetic Resonance (1969)* **1980**, *40* (2), 245–258. https://doi.org/10.1016/0022-2364(80)90248-6.

(42) Frisch, M. J.; Trucks, G. W.; Schlegel, H. B.; Scuseria, G. E.; Robb, M. A.; Cheeseman, J. R.; Scalmani, G.; Barone, V.; Petersson, G. A.; Nakatsuji, H.; Li, X.; Caricato, M.; Marenich, A. V.; Bloino, J.; Janesko, B. G.; Gomperts, R.; Mennucci, B.; Hratchian, H. P.; Ortiz, J. V.; Izmaylov, A. F.; Sonnenberg, J. L.; Williams; Ding, F.; Lipparini, F.; Egidi, F.; Goings, J.; Peng, B.; Petrone, A.; Henderson, T.; Ranasinghe, D.; Zakrzewski, V. G.; Gao, J.; Rega, N.; Zheng, G.; Liang, W.; Hada, M.; Ehara, M.; Toyota, K.; Fukuda, R.; Hasegawa, J.; Ishida, M.; Nakajima, T.; Honda, Y.; Kitao, O.; Nakai, H.; Vreven, T.; Throssell, K.; Montgomery Jr., J. A.; Peralta, J. E.; Ogliaro, F.; Bearpark, M. J.; Heyd, J. J.; Brothers, E. N.; Kudin, K. N.; Staroverov, V. N.; Keith, T. A.; Kobayashi, R.; Normand, J.; Raghavachari, K.; Rendell, A. P.; Burant, J. C.; Iyengar, S. S.; Tomasi, J.; Cossi, M.; Millam, J. M.; Klene, M.; Adamo, C.; Cammi, R.; Ochterski, J. W.; Martin, R. L.; Morokuma, K.; Farkas, O.; Foresman, J. B.; Fox, D. J. Gaussian 16 Rev. A.03; Wallingford, CT, 2016.

(43) Becke, A. D. Density-functional Thermochemistry. III. The Role of Exact Exchange. *J. Chem. Phys.* **1993**, *98* (7), 5648–5652. https://doi.org/10.1063/1.464913.

(44) Kendall, R. A.; Dunning, T. H.; Harrison, R. J. Electron Affinities of the First-row Atoms Revisited. Systematic Basis Sets and Wave Functions. *J. Chem. Phys.* **1992**, *96* (9), 6796–6806. https://doi.org/10.1063/1.462569.

(45) Stephens, P. J.; Devlin, F. J.; Chabalowski, C. F.; Frisch, M. J. Ab Initio Calculation of Vibrational Absorption and Circular Dichroism Spectra Using Density Functional Force Fields. *J. Phys. Chem.* **1994**, *98* (45), 11623–11627. https://doi.org/10.1021/j100096a001.

(46) Fulmer, G. R.; Miller, A. J. M.; Sherden, N. H.; Gottlieb, H. E.; Nudelman, A.; Stoltz, B. M.; Bercaw, J. E.; Goldberg, K. I. NMR Chemical Shifts of Trace Impurities: Common Laboratory

Solvents, Organics, and Gases in Deuterated Solvents Relevant to the Organometallic Chemist. *Organometallics* **2010**, *29* (9), 2176–2179. https://doi.org/10.1021/om100106e.

(47) Gottlieb, H. E.; Kotlyar, V.; Nudelman, A. NMR Chemical Shifts of Common Laboratory Solvents as Trace Impurities. *The Journal of Organic Chemistry* **1997**, *62* (21), 7512–7515. https://doi.org/10.1021/jo971176v.

(48) Babij, N. R.; McCusker, E. O.; Whiteker, G. T.; Canturk, B.; Choy, N.; Creemer, L. C.; Amicis, C. V. D.; Hewlett, N. M.; Johnson, P. L.; Knobelsdorf, J. A.; Li, F.; Lorsbach, B. A.; Nugent, B. M.; Ryan, S. J.; Smith, M. R.; Yang, Q. NMR Chemical Shifts of Trace Impurities: Industrially Preferred Solvents Used in Process and Green Chemistry. *Organic Process Research & Development* **2016**, *20* (3), 661–667. https://doi.org/10.1021/acs.oprd.5b00417.

(49) Evans, D. F. 400. The Determination of the Paramagnetic Susceptibility of Substances in Solution by Nuclear Magnetic Resonance. *Journal of the Chemical Society (Resumed)* **1959**, *81* (1), 2003. https://doi.org/10.1039/jr9590002003.

(50) Bruker APEX2 (Version 2.1-4), SAINT (Version 7.34A), SADABS (Version 2007/4), 2007 BrukerAXS Inc, Madison, Wisconsin, USA.

(51) Sheldrick, G. M. *SHELXT* – Integrated Space-Group and Crystal-Structure Determination. *Acta Crystallogr A Found Adv* **2015**, *71* (1), 3–8. https://doi.org/10.1107/S2053273314026370.

(52) Altomare, A.; Burla, M. C.; Camalli, M.; Cascarano, G. L.; Giacovazzo, C.; Guagliardi, A.; Moliterni, A. G. G.; Polidori, G.; Spagna, R. SIR97: A New Tool for Crystal Structure Determination and Refinement. *J Appl Cryst* **1999**, *32* (1), 115–119. https://doi.org/10.1107/S0021889898007717.

(53) Altomare, A.; Cascarano, G.; Giacovazzo, C.; Guagliardi, A. Completion and Refinement of Crystal Structures with SIR92. *J Appl Cryst* **1993**, *26* (3), 343–350. https://doi.org/10.1107/S0021889892010331.

(54) Sheldrick, G.M., SHELXL-97, Program for the Refinement of Crystal Structures, 1997, University of Göttingen, Germany.

(55) Mackay, S.; Edwards, C.; Henderson, A.; Gilmore, C.; Stewart, N.; Shankland, K.; Donald, A., MaXus: A Computer Program for the Solution and Refinement of Crystal Structures from Diffraction Data, 1997, University of Glasgow, Scotland.

(56) Waasmaier, D.; Kirfel, A. New Analytical Scattering-Factor Functions for Free Atoms and Ions. *Acta Cryst A* **1995**, *51* (3), 416–431. https://doi.org/10.1107/S0108767394013292.

(57) Sheldrick, G. M., CELL_NOW, 2005, University of Göttingen, Germany.

(58) Sheldrick, G. M., TWINABS, 2007, University of Göttingen, Germany.

(59) Frisch, M. J.; Trucks, G. W.; Schlegel, H. B.; Scuseria, G. E.; Robb, M. A.; Cheeseman, J. R.; Scalmani, G.; Barone, V.; Petersson, G. A.; Nakatsuji, H.; Li, X.; Caricato, M.; Marenich, A. V.; Bloino, J.; Janesko, B. G.; Gomperts, R.; Mennucci, B.; Hratchian, H. P.; Ortiz, J. V.; Izmaylov, A. F.; Sonnenberg, J. L.; Williams; Ding, F.; Lipparini, F.; Egidi, F.; Goings, J.; Peng, B.; Petrone, A.; Henderson, T.; Ranasinghe, D.; Zakrzewski, V. G.; Gao, J.; Rega, N.; Zheng, G.; Liang, W.; Hada, M.; Ehara, M.; Toyota, K.; Fukuda, R.; Hasegawa, J.; Ishida, M.; Nakajima, T.; Honda, Y.; Kitao, O.; Nakai, H.; Vreven, T.; Throssell, K.; Montgomery Jr., J. A.; Peralta, J. E.; Ogliaro, F.; Bearpark, M. J.; Heyd, J. J.; Brothers, E. N.; Kudin, K. N.; Staroverov, V. N.; Keith, T. A.; Kobayashi, R.; Normand, J.; Raghavachari, K.; Rendell, A. P.; Burant, J. C.; Iyengar, S. S.; Tomasi, J.; Cossi, M.; Millam, J. M.; Klene, M.; Adamo, C.; Cammi, R.; Ochterski, J. W.; Martin, R. L.; Morokuma, K.; Farkas, O.; Foresman, J. B.; Fox, D. J. *Gaussian 16 Rev. A.03*; Wallingford, CT, 2016.

(60) Peterson, K. A.; Figgen, D.; Goll, E.; Stoll, H.; Dolg, M. Systematically Convergent Basis Sets with Relativistic Pseudopotentials. II. Small-Core Pseudopotentials and Correlation Consistent Basis Sets for the Post-d Group 16–18 Elements. *The Journal of Chemical Physics* **2003**, *119* (21), 11113–11123. https://doi.org/10.1063/1.1622924.

(61) Peterson, K. A.; Shepler, B. C.; Figgen, D.; Stoll, H. On the Spectroscopic and Thermochemical Properties of ClO, BrO, IO, and Their Anions. *J. Phys. Chem. A* **2006**, *110* (51), 13877–13883. https://doi.org/10.1021/jp065887l.

(62) Pritchard, B. P.; Altarawy, D.; Didier, B.; Gibson, T. D.; Windus, T. L. New Basis Set Exchange: An Open, Up-to-Date Resource for the Molecular Sciences Community. *J. Chem. Inf. Model.* **2019**, *59* (11), 4814–4820. https://doi.org/10.1021/acs.jcim.9b00725.

Chapter 5. METAL-SUPPORT INTERACTIONS REGULATE SUBSTRATE BINDING AFFINITY IN FE/CO/SE CLUSTER CATALYSTS

5.1 ABSTRACT

Here, we investigate the stereo-electronic requirements of a family of Fe/Co_6Se_8 molecular clusters to achieve a Goldilocks regime of substrate affinity for the catalytic coupling of tosyl azide and *tert*-butyl isocyanide. The reactivity of a catalytically competent iron-nitrenoid intermediate, observed *in situ*, is explored towards nitrene transfer and hydrogen atom abstraction. The dual role of isocyanide, which on one hand prevents catalyst degradation, but, in large amounts, slows down reactivity is exposed. The impact of distal changes (number of neighboring active sites and identity of supporting ligands) on substrate affinity, electronic properties, and catalytic activity is investigated. Overall, the study reveals that the dynamic, push-pull interactions between the substrate (^{t}BuNC), active site (Fe), and support (Co_6Se_8) create a regime where increased substrate activation occurs with facile dissociation.

5.2 INTRODUCTION

The Sabatier principle intuitively states that optimal catalytic activity is reached when the active site has a moderate affinity for substrates or the resulting products, underscoring the tension between engaging and releasing key adsorbates that ensures continuous reactivity at the active sites.[1–3] While weak adsorption may limit reactions from occurring, strong substrate/active site interactions can inhibit catalytic turnovers by blocking the active site, or by electronically deactivating neighboring ones.[4] Structurally uniform platforms enable systematic studies that uncover the requirements for optimal conditions of adsorbate/active site interactions for a given transformation, and elucidate the nature of the cooperativity between the active site and the support. For example, numerous *in silico* and experimental studies have shown how size,

Reproduced in part with permission from:
Mitchell, B. S.; Chirila, A.; Zhou, D. Y.; Kephart, J. A.; Velian, A. *Inorg. Chem.* **2023**, *Accepted*.

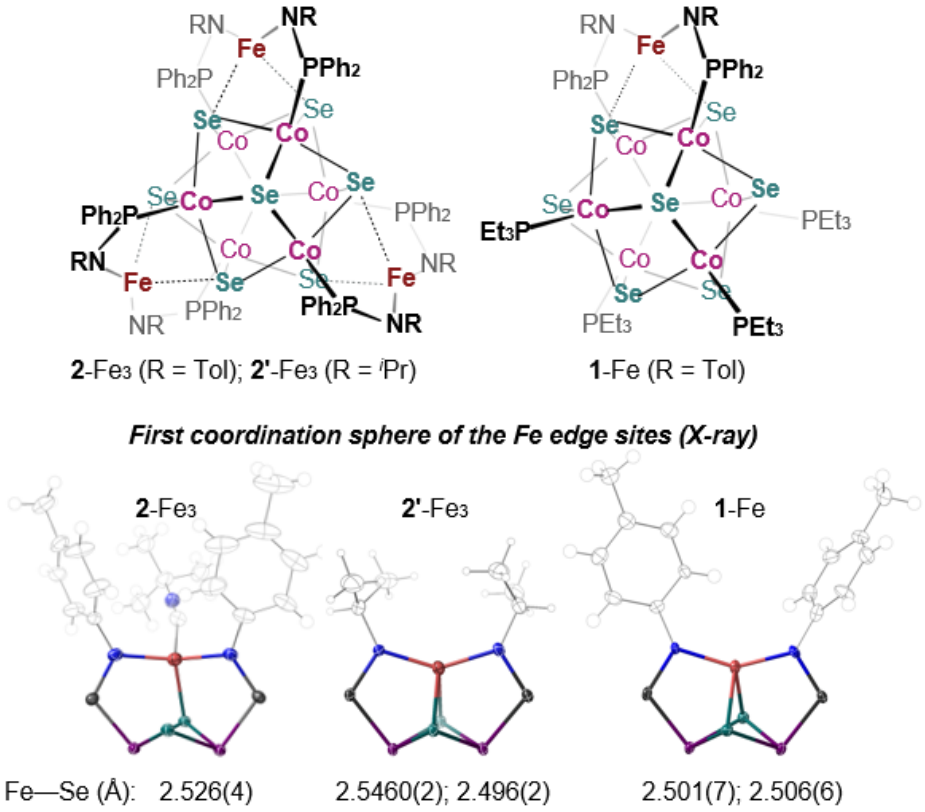

Figure 5.1. Connectivity and first coordination sphere of the Fe edge sites in **2**-Fe_3, **2′**-Fe_3, and **1**-Fe from previously reported single crystal X-ray structures.

morphology, dopants or active site identity in the single layer limit of MoS_2 clusters impact the strength of adsorbate/catalyst interactions[5–9] and break linear scaling relationships.[10]

Elucidating how multiple metals cooperate to bind and activate substrates to unearth catalyst design principles for complex multi-electron transformations is the focus of numerous molecular efforts.[11–14] To this end, our group introduced a molecular construct in which the identity and number of active sites installed on an atomically precise inorganic cluster support can be systematically tuned.[15–19] This synthetic innovation has enabled systematic investigations into the nature of the active site/support cooperativity[15,16] and the role of multi-active site dynamics in modulating catalytic activity for azide activation and asymmetric carbodiimide synthesis.[18]

In this study, we investigate the stereo-electronic requirements of the active site to access a Goldilocks regime of substrate affinity at a family of Fe/Co_6Se_8 molecular cluster catalysts (Figure 5.1). Distal changes, such as the number of neighboring active sites and identity of supporting ligands, impact substrate affinity and modulate the ensuing catalytic activity towards coupling

tosyl azide and *tert*-butyl isocyanide. The study uncovers how the dynamic substrate/active site/support interactions coalesce to maximize catalytic activity. Strong metal/support interactions promote substrate (isocyanide) dissociation, while simultaneously enabling π-backbonding and increased substrate activation. Additionally, this study illustrates the duality of isocyanide as a substrate: on one hand, the isocyanide prevents catalyst degradation, but, in large amounts, it slows down reactivity ostensibly by blocking the active site. The complex kinetic dependence of isocyanide in carbodiimide formation has been previously observed, and mechanistic pathways for its involvement proposed.[20–25] Here, the nature of the metal-support interactions, the presence of multiple substrate binding sites, and the steric profile at the active site dramatically alter the observed catalytic activity towards nitrene transfer.[17]

5.3 Results and Discussion

We have previously isolated catalytically competent metal-imido intermediates formed by the trichromium cluster $Cr_3(py)_3Co_6Se_8L_6$ (L = $PPh_2N^{(-)}Tol$, Ph = phenyl, Tol = 4-tolyl) demonstrating that the edges are the locus of reactivity.[18] In contrast, identification of iron nitrenoid intermediates for the triiron $Fe_3Co_6Se_8L_6$ (**2**-Fe_3) or monoiron derivative $FeCo_6Se_8(PEt_3)_4(L)_2$ (**1**-Fe; Et = ethyl) has been elusive.[15,16] We hypothesized that the presence of a single active site could make observing intermediates and interpreting the reactivity of **1**-Fe more accessible than for the triiron congener **2**-Fe_3. Indeed, at 10% **1**-Fe loading, we have previously observed the formation of two paramagnetic species by ^{1}H NMR spectroscopy during the course of the carbodiimide formation.[15] To probe the identity of these species, here, the reaction between **1**-Fe and TsN_3 was evaluated first under stoichiometric conditions (Scheme 5.1). Slow addition of the azide to a thawing solution

Scheme 5.1. Stoichiometric azide activation and nitrene transfer to (a) an isocyanide, or (b) a phosphine.

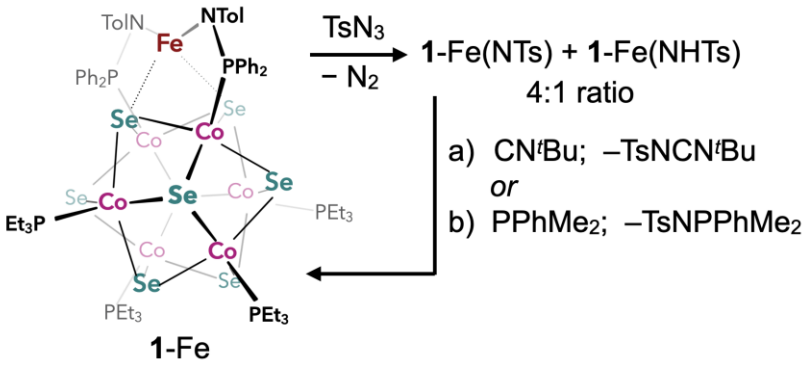

of the iron complex leads to rapid effervescence and the consumption of the azide, as evinced by the disappearance of the diagnostic tosyl azide stretch (2123 cm^{-1}; Figure 5.5) in the associated infrared spectrum. Analysis of the crude reaction mixture by ^{1}H and ^{31}P NMR spectroscopy indicates complete conversion of **1**-Fe to two new species assigned as **1**-Fe(NTs) and **1**-Fe(NHTs), and formed in a 4:1 molar ratio (Scheme 5.1; Figure 5.4 and Figure 5.6). The ability of only one of the species to transfer the nitrene group and regenerate **1**-Fe led to its identification as **1**-Fe(NTs). Indeed, treating a freshly prepared mixture of these two species with stoichiometric isocyanide[26] (^{t}BuNC) incurs the complete consumption of **1**-Fe(NTs), while **1**-Fe(NHTs) remains unreacted (Figure 5.10). The starting material **1**-Fe is regenerated quantitatively, along with the corresponding nitrene transfer product. Similar results are obtained if a phosphine[27] ($PPhMe_2$) is used instead to trap the nitrene group, giving rise to the iminophosphorane coproduct $TsNPPhMe_2$ (Figure 5.7 and Figure 5.8).

Iron-nitrenoid complexes are often difficult to isolate, due to reactive iminyl character favoring hydrogen abstraction chemistry to form iron-amido products.[23,28] To probe the identity of the azide activation co-product, ostensibly **1**-Fe(NHTs), a well-known hydrogen atom source, 9,10-dihydroanthracene (DHA; 15 or 30 equiv),[29] was added in excess to the reaction between **1**-Fe and TsN_3 and the resulting mixture monitored by NMR (Scheme 5.2a; Figure 5.11). After 4 h at 60 °C, ^{1}H NMR spectroscopy indicates that no **1**-Fe(NTs) persists in the reaction mixture. Instead, the dominant species is the amido complex **1**-Fe(NHTs), generated alongside intractable paramagnetic byproducts. The relatively slow reaction between **1**-Fe(NTs) and DHA, perhaps due to the steric bulk at Fe, fosters decomposition, but increasing the DHA amount from 15 to 30 equivalents

Scheme 5.2. Probing the formation of **1**-Fe(NHTs).

a) Favoring H atom abstraction with dihydroanthracene (DHA)

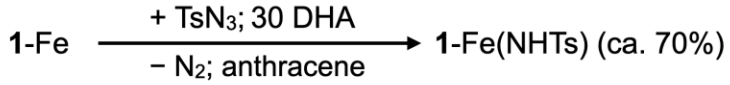

b) Suppressing H atom abstraction with excess CN^{t}Bu

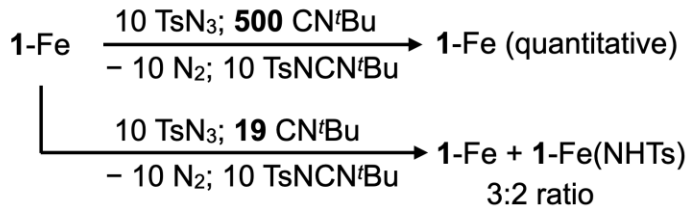

enhances the conversion to **1**-Fe(NHTs) from ca. 54 to 70% spectroscopic yield. Similar results are obtained using other hydrogen atom donors (Section 5.5.6).[29–31]Over time, or upon purification attempts, both **1**-Fe(NTs) and **1**-Fe(NHTs) were found to degrade, precluding their separation or further characterization as pure species.

We hypothesized that increasing the isocyanide concentration would accelerate nitrene transfer and prevent hydrogen abstraction from occurring. Indeed, monitoring the catalytic reaction by NMR spectroscopy at 10% **1**-Fe loading revealed that a large excess of isocyanide (500 equiv; 5.6 M) completely halts the formation of **1**-Fe(NHTs) (Scheme 5.2b; Figure 5.19). In contrast, at low isocyanide concentration (19 equiv, 0.2 M) ca. 40% of the catalyst is consumed in the off-cycle formation of the amido complex **1**-Fe(NHTs).[15] It is noteworthy that under similar conditions the triiron cluster **2**-Fe_3 also degrades, possibly undergoing fragmentation,[16] whereas decomposition is shut off when a large excess of a coordinating ligand (*tert*-butyl isocyanide or pyridine) is present (Figure 5.18 and Figure 5.20).[16]

To uncover how the number of edge sites and the isocyanide concentration modulate the catalytic activity, the **1**-Fe and **2**-Fe_3 clusters are compared under high isocyanide concentration, when both clusters are recovered quantitatively. **2**-Fe_3 features three times more Fe edge sites than **1**-Fe, yet under the same conditions (2.5% cluster loading, 5.6 M ^{t}BuNC) **1**-Fe reaches 50% conversion ($t_{1/2}$)

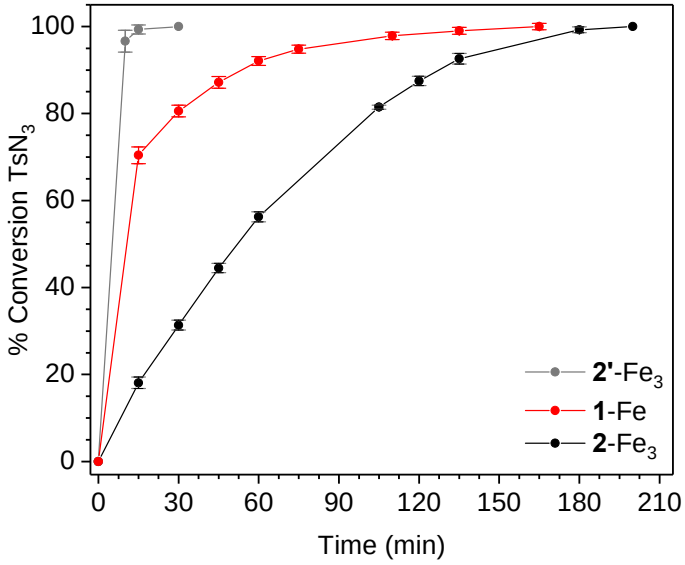

Figure 5.2. Comparing the catalytic activity of **1**-Fe, **2**-Fe_3, and **2′**-Fe_3 towards carbodiimide formation from TsN_3 and ^{t}BuNC at 2.5% cluster loading, 5.6 M ^{t}BuNC, in benzene-d_6 at room temperature.

significantly faster than **2**-Fe_3 (ca. 10 vs 50 minutes; Figure 5.2). This indicates that although the

edge sites in **1**-Fe and **2**-Fe_3 have chemically identical first coordination environments (Figure 5.1), the former is significantly more reactive. We hypothesized that the difference in reactivity between **1**-Fe and **2**-Fe_3 is a result of modulating the electronic richness of the active site by distal changes in the cluster (i.e. number of active sites or ancillary ligands), which in turn regulates the affinity for substrates (^{t}BuNC). To probe this hypothesis, $Fe_3Co_6Se_8L'_6$ (**2′**-Fe_3 ; L′ = $PPh_2N^{(-)i}Pr$, ^{i}Pr = isopropyl), which like **2**-Fe_3 features three Fe edge sites but like **1**-Fe has minimal affinity for exogenous ligands,[32] was included in this comparison. Under the same conditions, **2′**-Fe_3 was found to be the fastest catalyst in the series, with a $t_{1/2}$ of ca. 5 min (Figure 5.2). At first sight the trend in catalytic activities **2′**-Fe_3 > **1**-Fe > **2**-Fe_3 is surprising. To investigate the origins of the differential reactivity in the series, electrochemical, structural, substrate affinity, and vibrational data are compared and discussed below, revealing that catalytic activity peaks when metal/support interactions are strongest, and the affinity for the isocyanide lowest.

We hypothesize that in part, this trend in reactivity stems from the dual role that isocyanide plays in this transformation. While increased amounts of ^{t}BuNC prevent cluster degradation, ostensibly by accelerating nitrene transfer, they also inhibit reactivity by blocking azide coordination at Fe. This concentration effect is qualitatively illustrated in the slower catalytic activity for **1**-Fe upon increasing the concentration of isocyanide from 0.2 vs 5.6 M (Figure 5.17). In **2**-Fe_3 and **2′**-Fe_3, this effect is compounded by inter-adsorbate effects stemming from the presence of multiple active sites.

Comparing the relative HOMO energies of the clusters – approximated from cyclic voltammetry measurements, indicates that the clusters are increasingly electron rich in the series **2**-Fe_3 < **2′**-Fe_3 < **1**-Fe with the 0/+1 oxidation event ranging from –0.6 to –1.0 V vs Fc/Fc^+ (Figure 5.3a).[15,16,32] This cathodic shift can be rationalized by the relative number of Lewis acidic edges (one in **1**-Fe vs three in **2**-Fe_3 and **2′**-Fe_3), and the donating properties of the ancillary ligands (PEt_3 in **1**-Fe vs $PPh_2N^{(-)}Tol$ in **2**-Fe_3; and $PPh_2N^{(-)}Tol$ in **2**-Fe_3 vs $PPh_2N^{(-)i}Pr$ in **2′**-Fe_3).

Structural information provided from previously reported single crystal X-ray measurements[15,16,32] reveals that Fe—Se bonds are strongest in **1**-Fe, where the Se sites are most electron rich, and weakest in **2**-Fe_3, where they are most electronically depleted. In **1**-Fe and **2′**-Fe_3 the edge sites are bound κ^4 to the Co/Se cluster support via two amide and two selenium atoms, whereas in **2**-$Fe_3(CN^tBu)_3$, crystallized as a trisadduct, the Fe sites are bound κ^3 to a single Se site and two amides (Figure 5.1).[15,16,32]

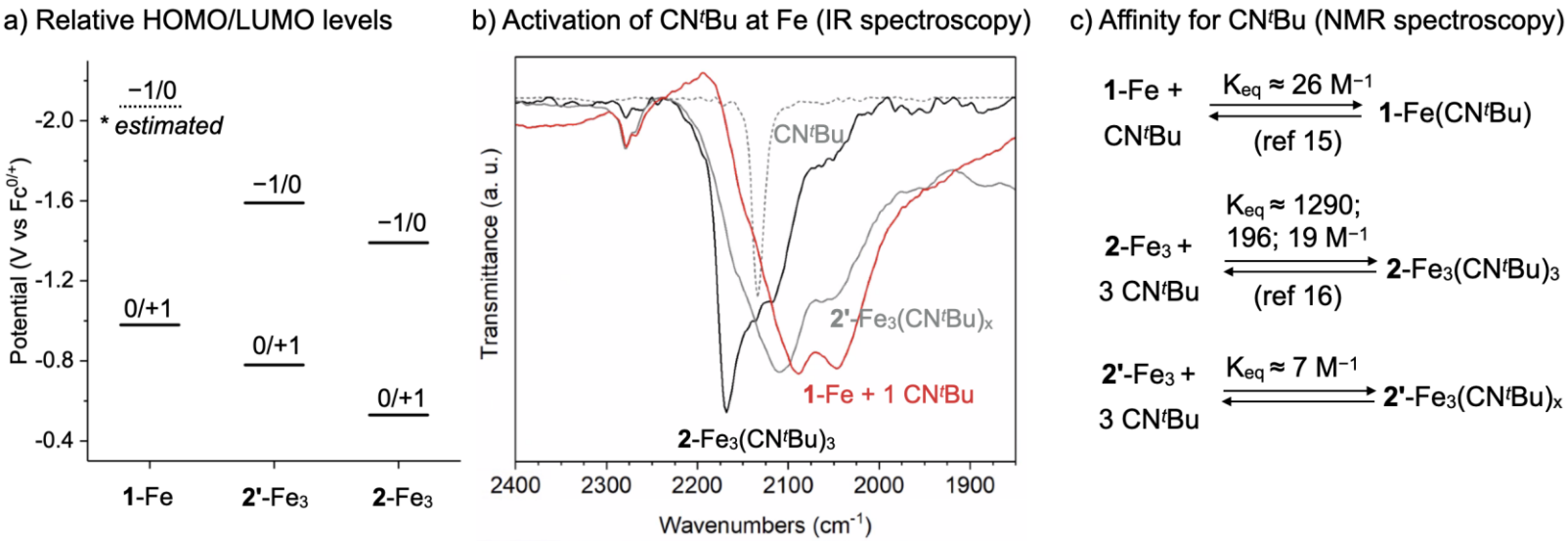

Figure 5.3. Comparing the electronic properties of the Fe edge sites in **1**-Fe, **2**-Fe$_3$, and **2′**-Fe$_3$. (a) HOMO/LUMO energies estimated electrochemically. (b) Electrophilicity of the Fe edge sites as proxied by the energy of bound isocyanide, measured via infrared spectroscopy. (c) Affinity for isocyanide, measured by NMR spectroscopy.

Finally, the strengths of the metal/substrate and metal/support interactions are inversely related, and the nature of the Fe—CN^{t}Bu interaction is highly sensitive to distal changes in the clusters. The affinity for isocyanide at Fe, estimated using ^{1}H NMR spectroscopy, is low for the electron-rich clusters **1**-Fe and **2′**-Fe$_3$ (ca. 26, and 7 M^{-1}, respectively; Figure 5.22), and significantly higher for the more electron deficient **2**-Fe$_3$, where three binding constants could be resolved (1290, 196, and 19 M^{-1}, respectively),[15,16] ostensibly for each Fe edge. In line with the estimated isocyanide affinities, **1**-Fe and **2′**-Fe$_3$ crystallize free of exogeneous ligands even in the presence of a large excess of ^{t}BuNC (100 equiv), whereas **2**-Fe$_3$ can be isolated as the tris-adduct **2**-Fe$_3$(CN^{t}Bu)$_3$. Noteworthy, the increased steric bulk at Fe imparted by the amido isopropyl substituents in **2′**-Fe$_3$[32] could also account for a lower affinity for isocyanide in this species compared to the more electron rich **1**-Fe (7 vs 26 M^{-1}). Beyond the affinity for ligands, infrared spectroscopy reveals that the edge sites in **1**-Fe and **2′**-Fe$_3$ are sufficiently electron rich to π-backbond and activate the isocyanide (ν_{CN} = 2088 and 2104 cm^{-1}, respectively), whereas the blue-shifted CN stretch in **2**-Fe$_3$(CN^{t}Bu)$_x$ (ν_{CN} = 2168 cm^{-1}) signals that only σ-bonding is present (Figure 5.3b). Therefore, the strongest isocyanide activation occurs at the Fe edge sites with the lowest affinity for this ligand, which are also the least Lewis acidic.

It is attractive to propose that the increased catalytic activity of **2′**-Fe$_3$ vs **1**-Fe stems from a higher number of active sites (three vs one). Both clusters are more active catalysts than **2**-Fe$_3$, in line with their decreased affinity for isocyanide, and increased electronic richness. However, it is important to point out that in spite of the electronic and structural similarities, replacing the tolyl substituents with bulkier isopropyl groups might completely alter the mechanism of azide activation and carbodiimide formation at Fe.[20,33–35] Furthermore, the extent Co$_6$Se$_8$ electronic participation in the **1**-Fe, **2′**-Fe$_3$, and **2**-Fe$_3$ series could vary, giving rise to different edge/core redox regimes and distinguishing the reactivity of Fe-nitrenoid species formed along the way.[15]

5.4 Conclusions

In conclusion, adjusting the electronic profile of the Fe edge sites via distal changes in the cluster, such as number of neighboring active sites or nature of capping ligands, regulates the affinity for substrates at the Fe edge and tunes catalytic activity. As the support cluster becomes more electronically rich, the metal/support interactions (Fe—Se bonds) are strengthened, while the metal/substrate (Fe—CN^{t}Bu) interactions become more labile. The dynamic, push-pull

interactions between the substrate (^{t}BuNC), active site (Fe), and support (Co_6Se_8) foster a substrate binding behavior, wherein substrate activation occurs concomitantly with its expedited release enabling increased catalytic activity.

5.5 Experimental Details

5.5.1 *General Considerations*

All manipulations were performed under a dry and oxygen free nitrogen atmosphere using standard Schlenk or glovebox techniques (LC Technology Solutions glovebox equipped with a freezer set to −35 °C). All glassware was dried in an oven set to 160 °C for a minimum of 12 h and cooled in an evacuated antechamber prior to use in the glovebox. Solvents were purchased from Fischer Scientific and degassed, dried and purified using solvent purification columns housed in a stainless steel cabinet, and dispensed by a stainless steel Schlenk-line manufactured by JC Meyer Solvent Systems. Tetrahydrofuran (THF), diethyl ether (Et_2O), acetonitrile (MeCN), and methylene chloride (DCM) are passed through two packed columns of neutral alumina. In the cases of n-pentane, benzene, and toluene one of the columns is alumina and the other is Q5 reactant, a copper(II) oxide oxygen scavenger. All solvents are passed through an in-line, 2 micron filter immediately before being dispensed which ensures that no packing material residue is dispensed with the solvent. Prior to use the solvents were stored over activated 3Å molecular sieves (purchased from Sigma Aldrich) in the glovebox for a minimum of 72 hours. Deuterated solvents (C_6D_6 and CD_2Cl_2) were purchased from Cambridge Isotope Laboratories, Inc. or Sigma Aldrich, degassed and dried over activated 3Å molecular sieves (purchased from Sigma Aldrich) in the glovebox for a minimum of 72 hours. **1**-Fe,[15] **2**-Fe_3,[16] **2′**-Fe_3,[32] and tosyl azide[36] were prepared using known literature procedures. *tert*-Butyl isocyanide was purchased from Sigma Aldrich and degassed and dried over activated 3Å molecular sieves for a minimum of 72 hours. NMR spectra were obtained on a Bruker 300 or 500 MHz spectrometer. Chemical shifts are listed in parts per million and are referenced to the residual deuterated solvent peak for ^{1}H.[37–39] ^{31}P spectra are proton decoupled ($^{31}P\{^1H\}$) and referenced to phosphoric acid (0 ppm). Attenuated total reflectance infrared (ATR-IR) spectra were recorded on a Bruker Alpha IR instrument equipped with a Platinum ATR accessory.

5.5.2 *Stoichiometric reaction of **1**-Fe with TsN_3*

An NMR tube was charged with a solution of **1**-Fe (10.5 mg, 5.0 µmol, 1.0 equiv) in C_6D_6 (0.5 mL) and frozen in the glovebox freezer. Upon thawing, a solution of TsN_3 in C_6D_6 (0.5 M, 10.5 µL, 5.25 µmol, 1.05 equiv) was added dropwise resulting in immediate effervescence. Quantitative consumption of **1**-Fe and TsN_3 starting materials is confirmed by ^{1}H NMR and IR spectroscopy.

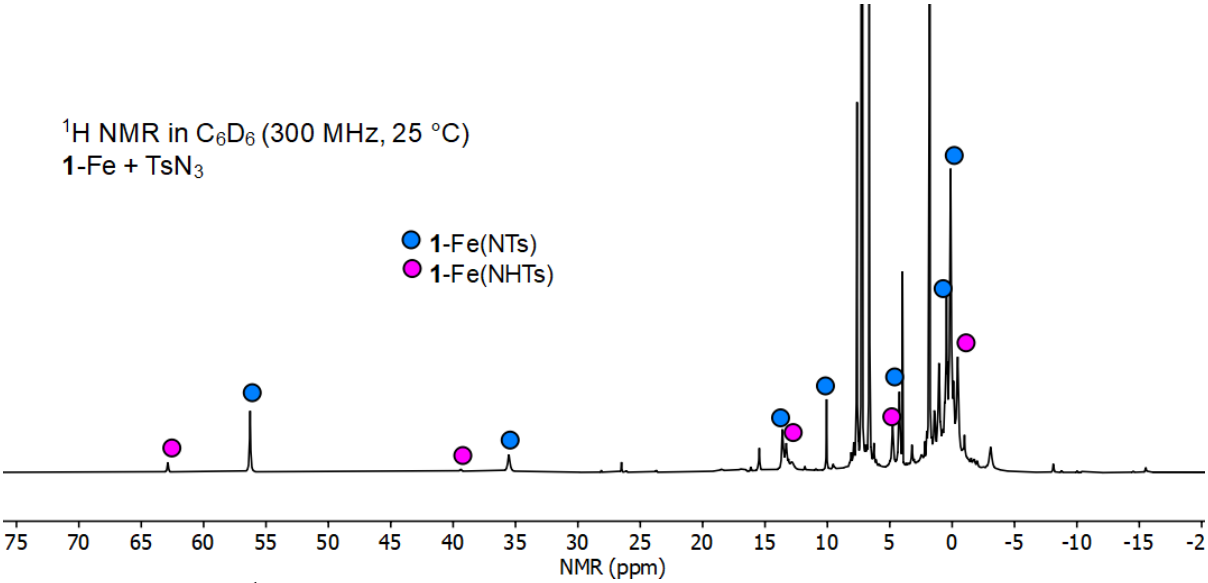

Figure 5.4. In situ ^{1}H NMR (C_6D_6, 300 MHz, 25 °C) spectrum of the reaction of **1**-Fe with TsN_3 after 15 minutes.

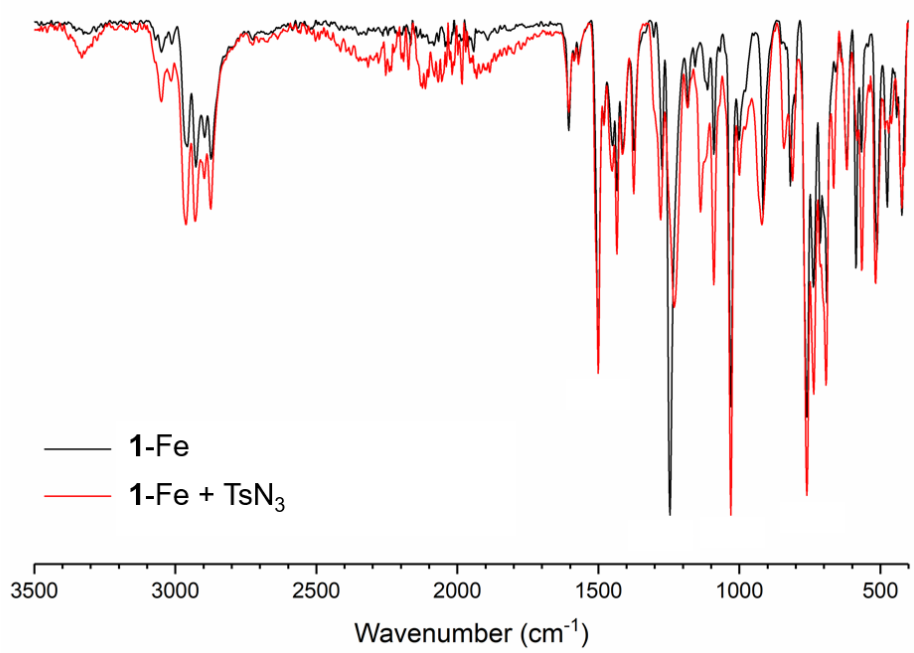

Figure 5.5. IR spectra in C_6D_6 of **1**-Fe and the crude reaction 15 minutes after the addition of TsN_3 to **1**-Fe. No unreacted TsN_3 is observed (2123 cm^{-1}).

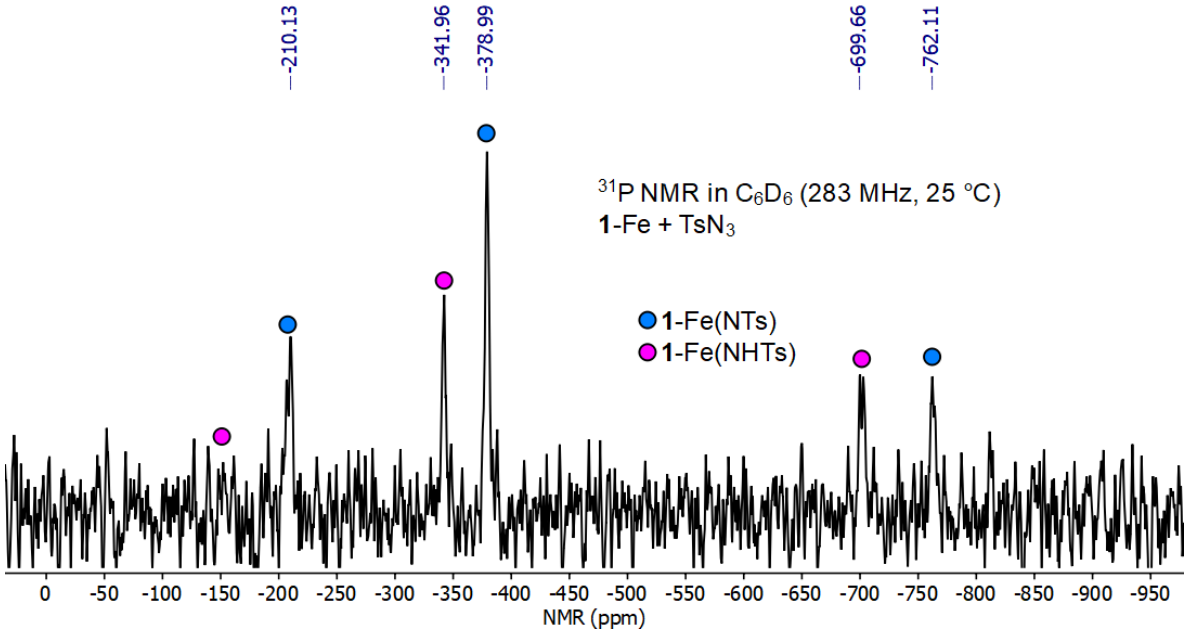

Figure 5.6. In situ ^{31}P NMR (C_6D_6, 283 MHz, 25 °C) spectrum of the reaction of **1**-Fe with TsN_3 after 30 minutes.

5.5.3 *Stoichiometric reaction of **1**-Fe with TsN_3 and subsequent transfer to Me_2PPh*

An NMR tube was charged with a solution of **1**-Fe (10.5 mg, 5.0 µmol, 1.0 equiv) in C_6D_6 (0.5 mL). A 0.5 M solution of TsN_3 in C_6D_6 was prepared and the appropriate aliquot was added to the reaction (10.0 µL, 5.0 µmol, 1.0 equiv). The solution immediately developed effervescence. After 30 minutes, A 0.5 M solution of Me_2PhP in C_6D_6 was added to the reaction (100.0 µL, 50.0 µmol, 10.0 equiv). After addition, the reaction is monitored using ^1H NMR. After 24 hours, a ^{31}P NMR spectra was recorded showing the presence of the iminophosphorane product and coordinated PMe_2Ph.

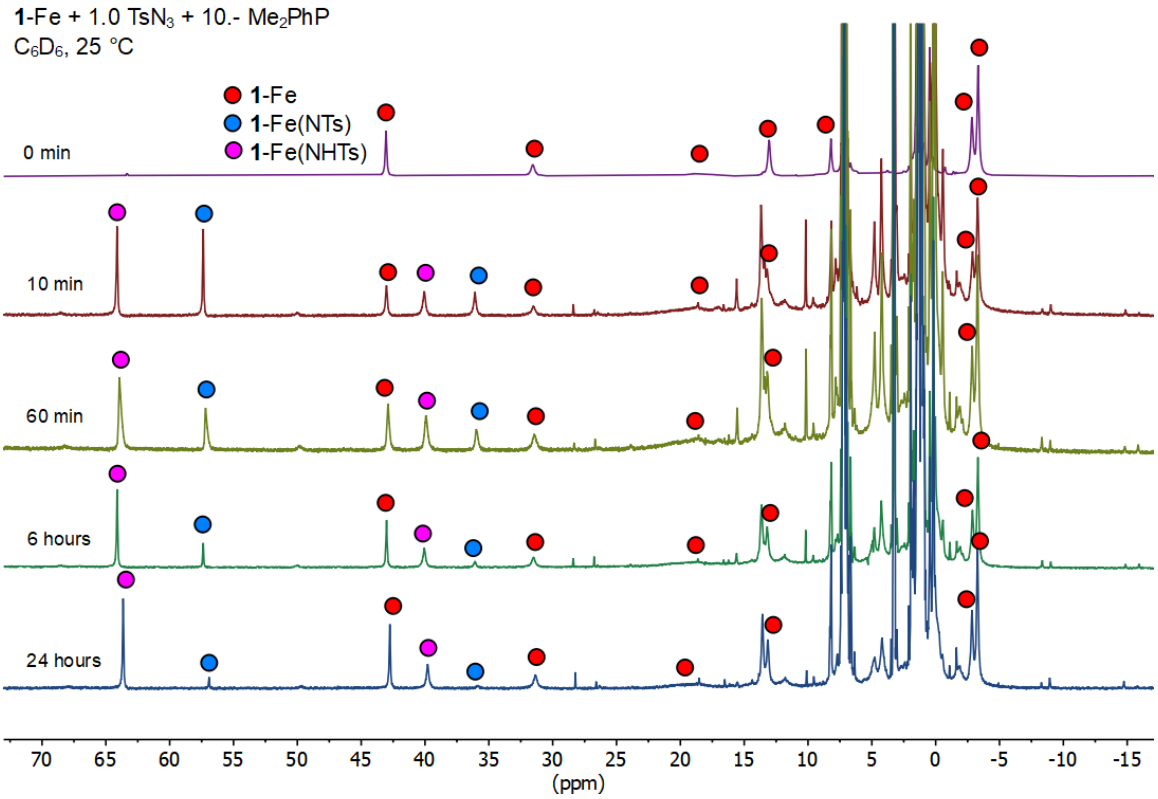

Figure 5.7. ^1H NMR (C_6D_6, 298K, 300 MHz) monitoring of the sub-stoichiometric reaction of **1**-Fe with TsN_3 followed by the addition of excess Me_2PhP.

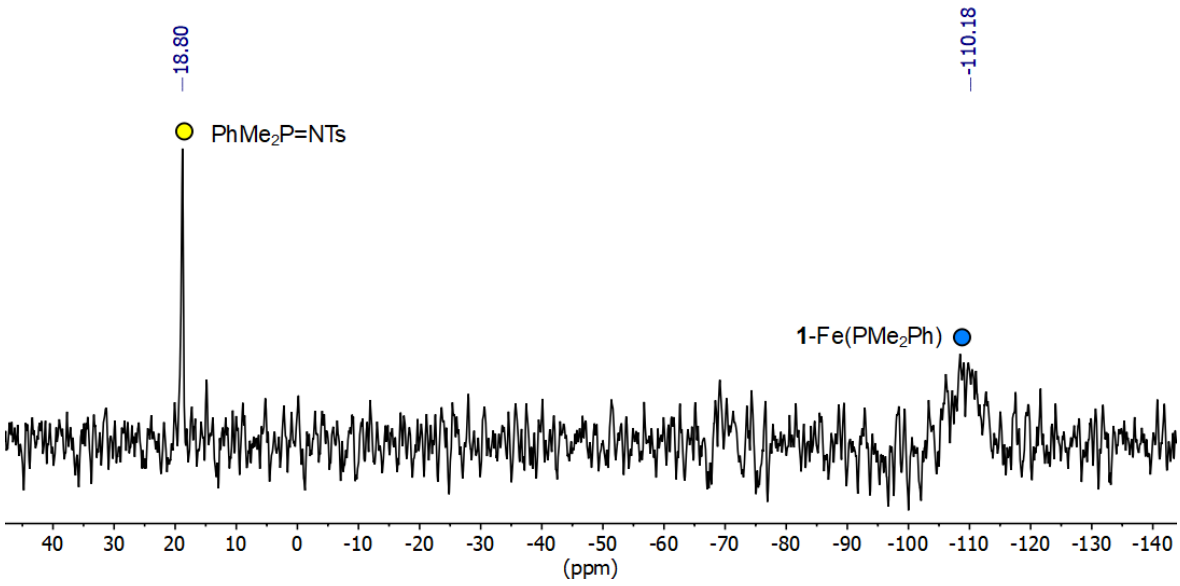

Figure 5.8. ^{31}P NMR (C_6D_6, 298K, 121 MHz) 24 hours after the addition of Me_2PhP.

Me_2PPh ligand binding studies

Since no free Me_2PPh is observed in the ^{31}P NMR spectrum in the nitrene transfer studies with excess phosphine, we explored ligand binding studies with Me_2PPh. An NMR sample in benzene-*d_6* of 1-Fe was treated with 1, 10, and 30 equiv of Me_2PPh and monitored by ^{31}P NMR spectroscopy. The ^{31}P NMR spectra of varying concentrations of Me_2PPh shows a single ^{31}P signal in the +150 and -350 ppm window, attributed to the PEt_3 resonance of 1-Fe, which shifts as a function of Me_2PPh concentration (-99 to -114 ppm). No free Me_2PPh is observed.

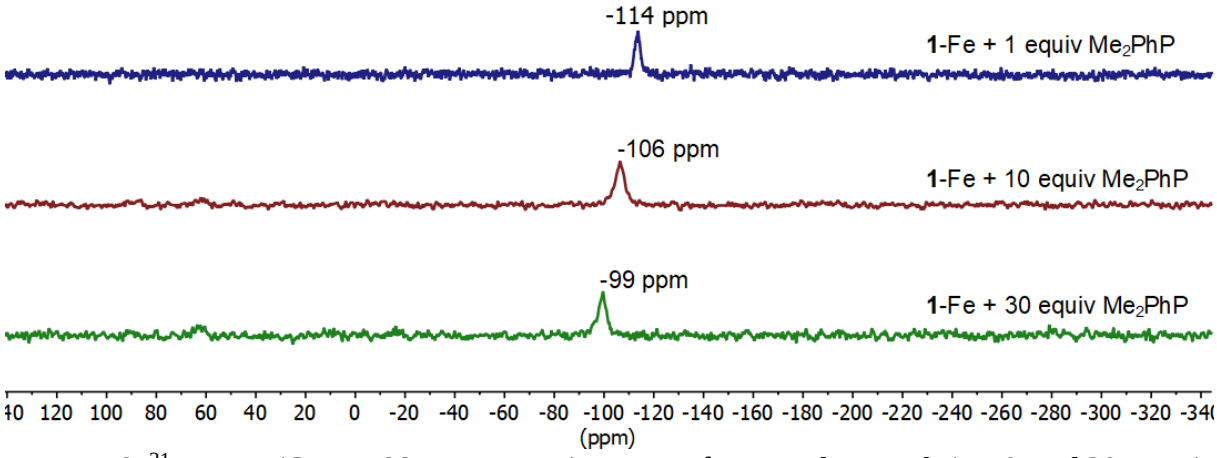

Figure 5.9. ^{31}P NMR (C_6D_6, 298K, 121 MHz) spectra of **1**-Fe and PMe_2Ph (1, 10, and 30 equiv).

5.5.4 *Stoichiometric reaction of 1-Fe with TsN_3 and transfer to ^tBuNC*

An NMR tube was charged with a solution of **1**-Fe (10 mg, 0.0048 mmol, 1.0 equiv) in C_6D_6 (0.5 mL) and an internal mesitylene standard (1% by volume). An initial ^1H NMR spectrum was recorded. The reaction was frozen in the glovebox freezer and upon thawing TsN_3 was added as a stock solution in C_6D_6 (0.1 M, 48 µL, 0.048 mmol, 1.0 equiv). After the effervescence subsided (~1 minute) the NMR sample was frozen in the glovebox freezer and ^{t}BuNC was added as a stock solution in C_6D_6 (0.93 M, 50 µL, 0.048 µmol, 10 equiv). The reaction was thawed and monitored using ^1H NMR spectroscopy until complete consumption of **1**-Fe(NTs) was observed.

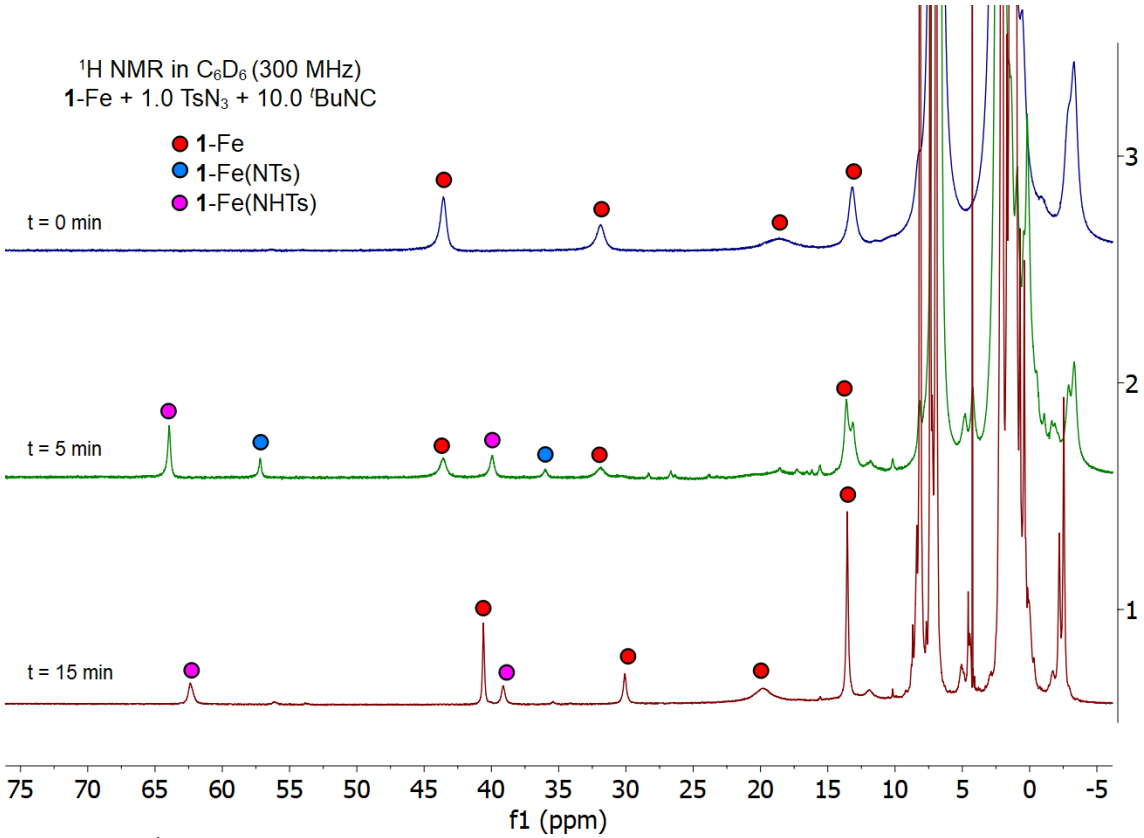

Figure 5.10. ^1H NMR (C_6D_6, 298K, 300 MHz) monitoring of the stoichiometric reaction of **1**-Fe with TsN_3 followed by the addition of excess ^{t}BuNC. **1**-Fe at 15 min is shifted from the t = 0 min timepoint due to coordination of the excess ^{t}BuNC to the Fe center.

5.5.5 *Hydrogen atom abstraction with 9,10-dihydroanthracene (DHA)*

1-Fe (15.0 mg, 0.0072 mmol, 1.0 equiv) and DHA (15 or 30 equiv) were dissolved in C_6D_6 (0.5 mL) and transferred to a J-young NMR tube with an internal mesitylene standard (1% by volume). A t=0 time point was recorded by ^{1}H NMR. The reaction mixture was frozen in the glovebox freezer and upon thawing, a solution of TsN_3 in C_6D_6 (0.025 mL, 55 mg/mL, 0.0072 mmol, 1.0 equiv) was added, and the reaction was heated at 60 °C and monitored by ^{1}H NMR spectroscopy. The control reaction without DHA was carried out with identical procedures however in the absence of 9,10-dihydroanthracene.

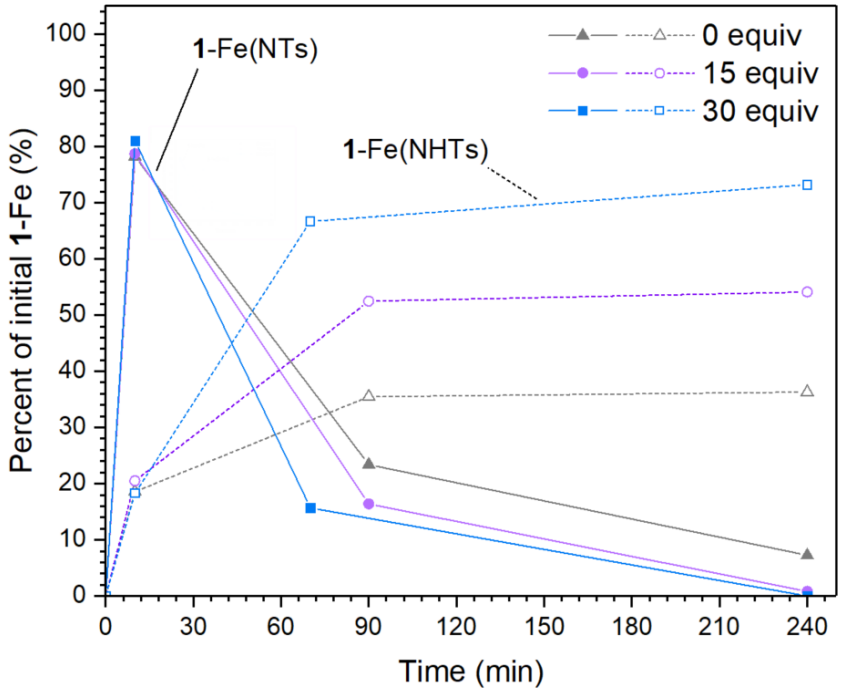

Figure 5.11. Evolution of **1**-Fe(NTs) and **1**-Fe(NHTs) species over time with 0, 15, and 30 equiv of 9,10-dihydroanthracene at 60 °C. Percent is determined by integration of tolyl-C*H*$_3$ feature (**1**-Fe = 43 ppm; **1**-Fe(NTs) = 57 ppm; 1-Fe(NHTs) = 64 ppm) versus the internal mesitylene standard (1% by volume).

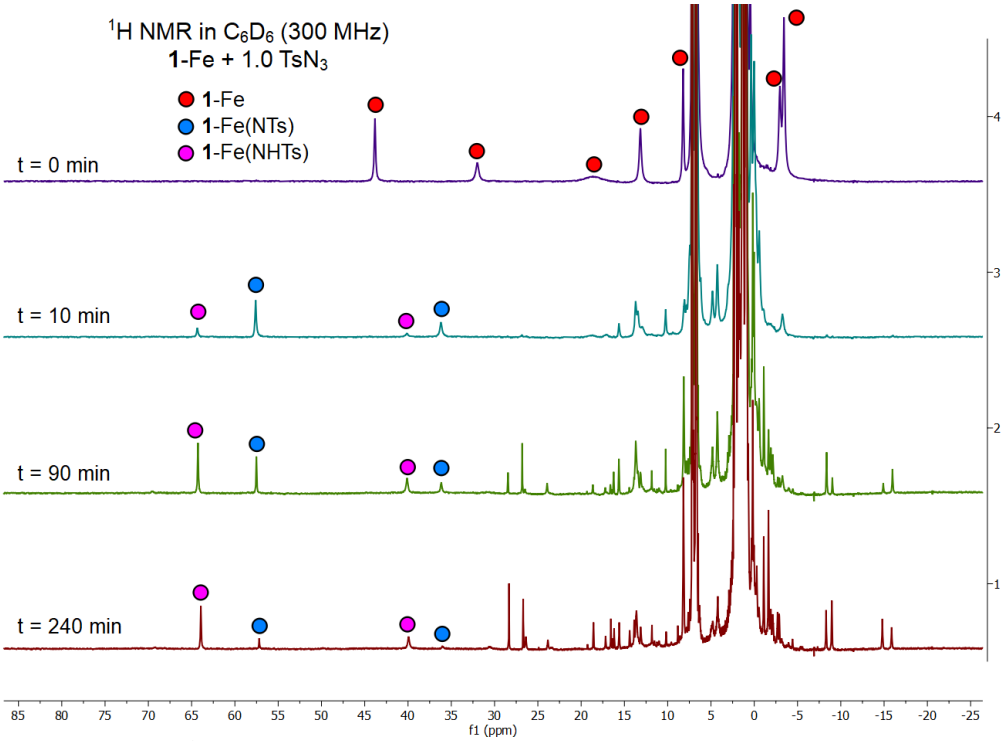

Figure 5.12. In situ ^{1}H NMR (C_6D_6, 300 MHz, 25 °C) monitoring of the **1**-Fe(NTs) and **1**-Fe(NHTs) at 60 °C. Spectra are referenced to the internal mesitylene standard (1% by volume).

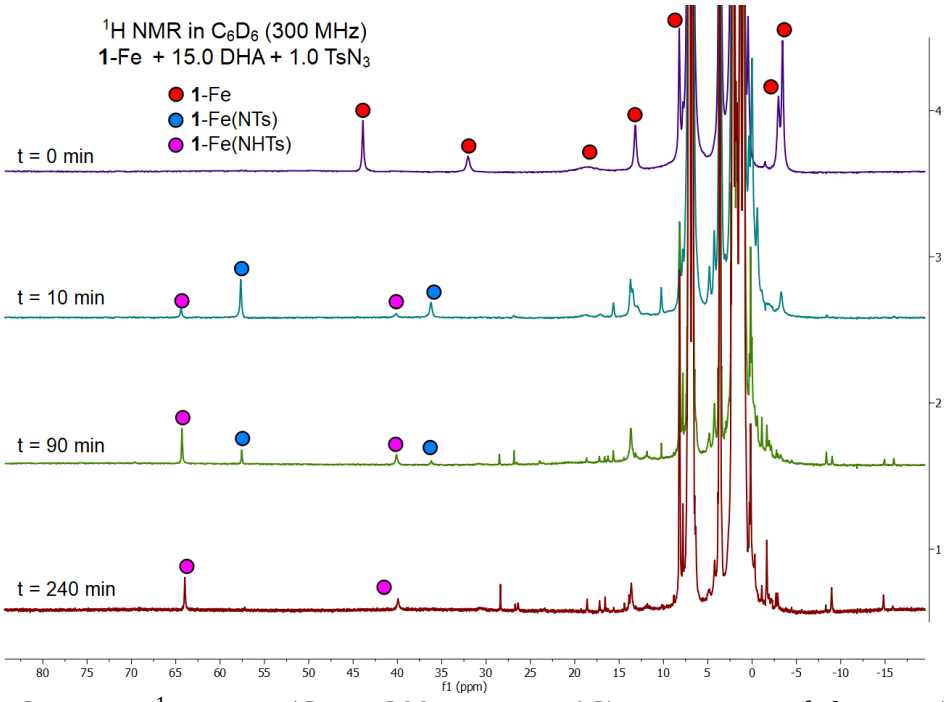

Figure 5.13. In situ ^{1}H NMR (C_6D_6, 300 MHz, 25 °C) monitoring of the **1**-Fe(NTs) and **1**-Fe(NHTs) in the presence of 15 equiv of 9,10-dihydroathracene at 60 °C. Spectra are referenced to the internal mesitylene standard (1% by volume).

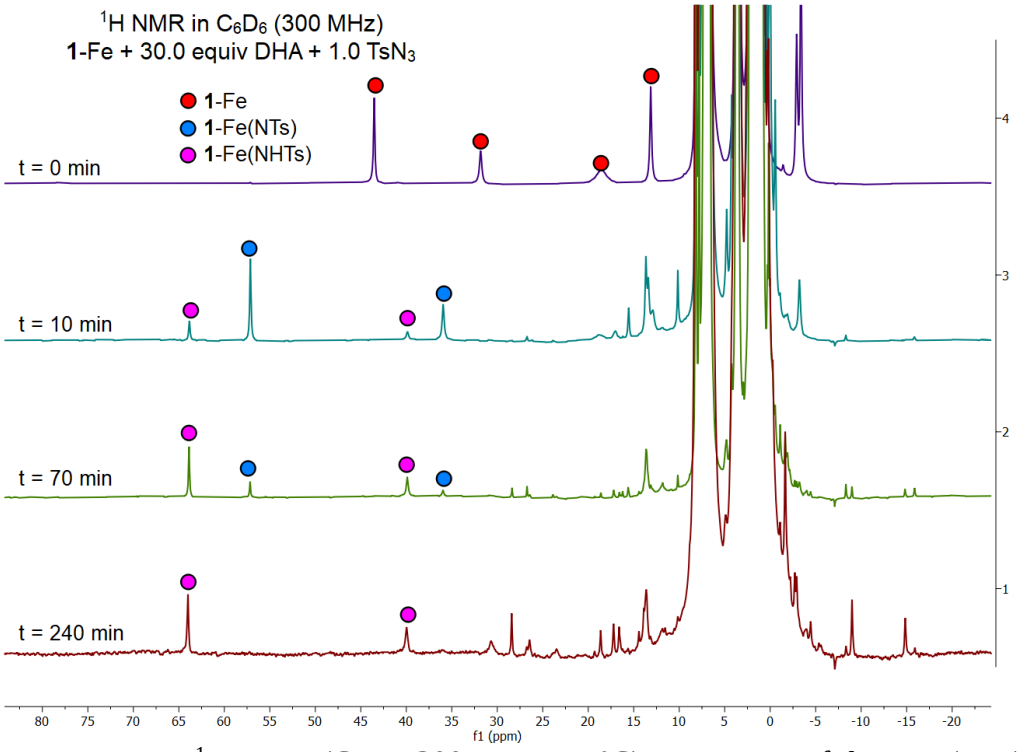

Figure 5.14. In situ ^{1}H NMR (C_6D_6, 300 MHz, 25 °C) monitoring of the **1**-Fe(NTs) and **1**-Fe(NHTs) in the presence of 30 equiv of 9,10-dihydroathracene at 60 °C. Spectra are referenced to the internal mesitylene standard (1% by volume).

5.5.6 *Hydrogen atom transfer with butylated hydroxytoluene (BHT)*

An NMR tube was charged with a solution of **1**-Fe (10 mg, 0.0048 mmol, 1.0 equiv) in C_6D_6 (0.5 mL) and an internal mesitylene standard (1% by volume). An initial ^{1}H NMR spectrum was recorded. The reaction was frozen in the glovebox freezer and upon thawing stock solutions of TsN_3 (0.1 M in C_6D_6, 48 µL, 0.048 mmol, 1.0 equiv) and BHT (0.1 M in C_6D_6, 48 µL, 0.048 mmol, 1.0 equiv) were added. The reaction was monitored using ^{1}H NMR spectroscopy until complete consumption of **1**-Fe(NTs) was observed.

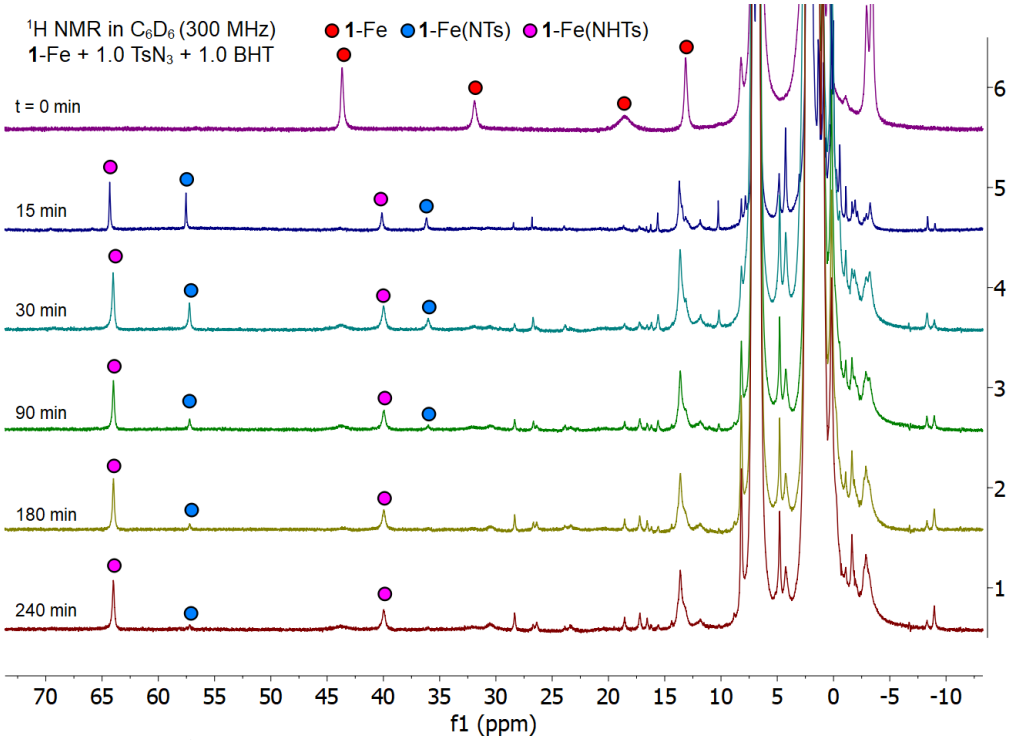

Figure 5.15. In situ ^{1}H NMR (C_6D_6, 300 MHz, 25 °C) monitoring of the **1**-Fe(NTs) and **1**-Fe(NHTs) in the presence of 1 equiv of butylated hydroxytoluene (BHT) at 25 °C. Spectra are referenced to the internal mesitylene standard (1% by volume).

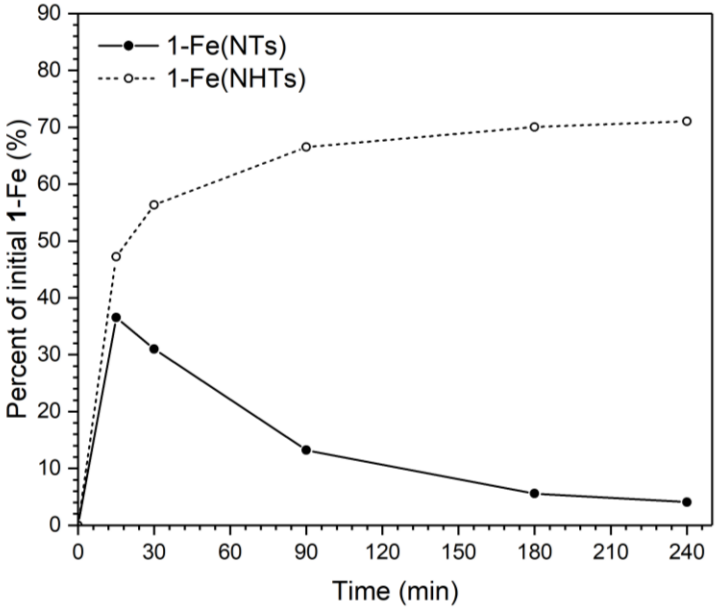

Figure 5.16. Evolution of **1**-Fe(NTs) and **1**-Fe(NHTs) species over time with 1 equiv of butylated hydroxytoluene (BHT) at 25 °C. Percent is determined by integration of tolyl-C*H*$_3$ feature (**1**-Fe = 43 ppm; **1**-Fe(NTs) = 57 ppm; **1**-Fe(NHTs) = 64 ppm) versus the internal mesitylene standard (1% by volume).

5.5.7 *Carbodiimide Catalysis*

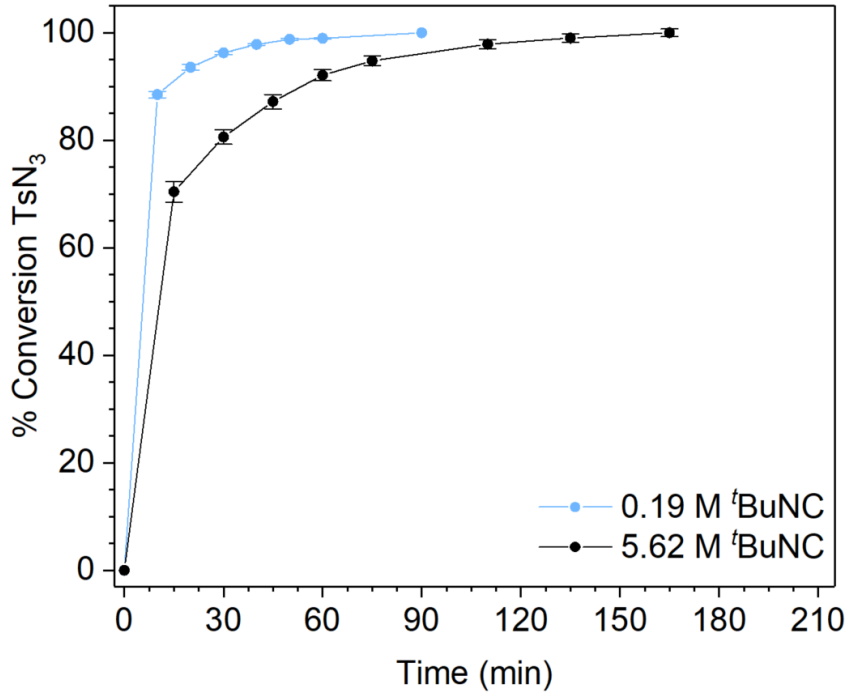

Figure 5.17. Catalytic synthesis of carbodiimide with 2.5 mol % **1**-Fe with varying amounts of ^{t}BuNC (0.19 or 5.62 M).

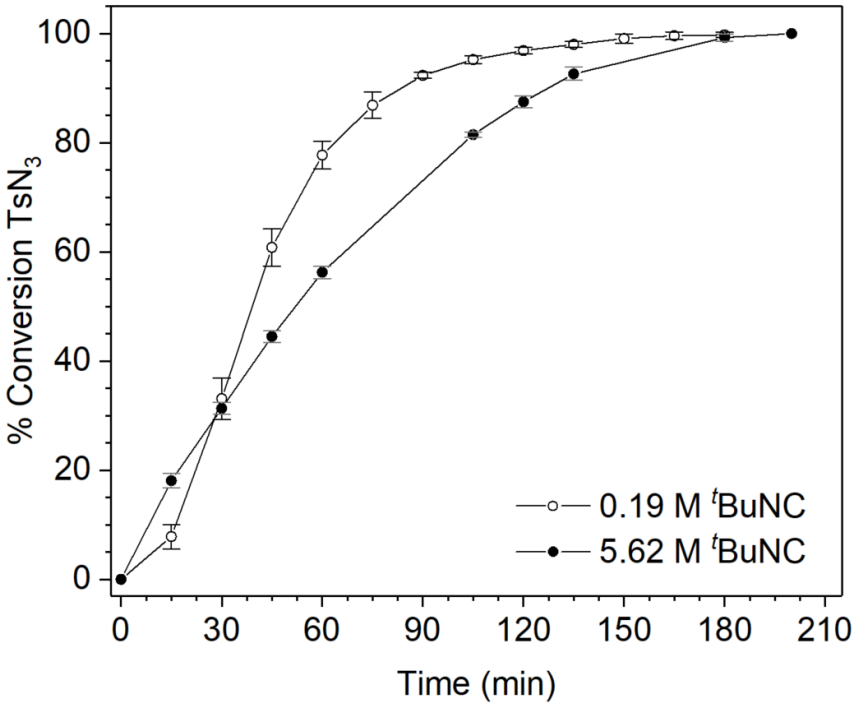

Figure 5.18. Catalytic synthesis of carbodiimide with 2.5 mol % **2**-Fe_3 with varying amounts

5.5.8 *Catalyst Recycling Studies*

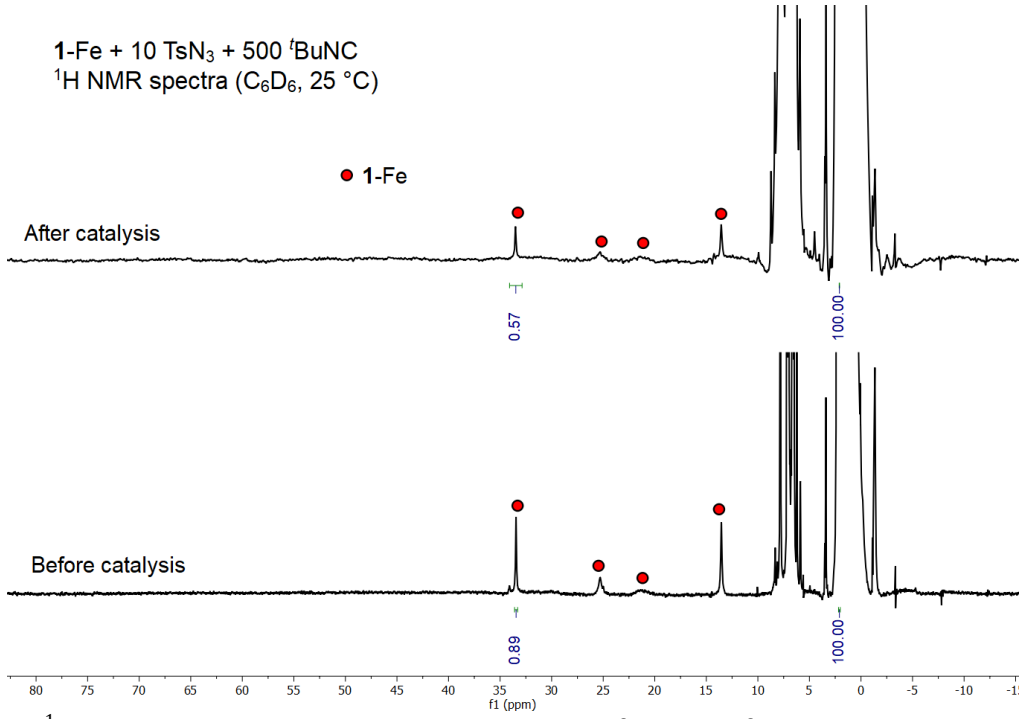

Figure 5.19. ^{1}H NMR spectra (500 MHz, C_6D_6, 25 °C) before and after carbodiimide catalysis with 10 mol % **1**-Fe with 500 equiv of ^{t}BuNC. Integrations are versus internal mesitylene standard.

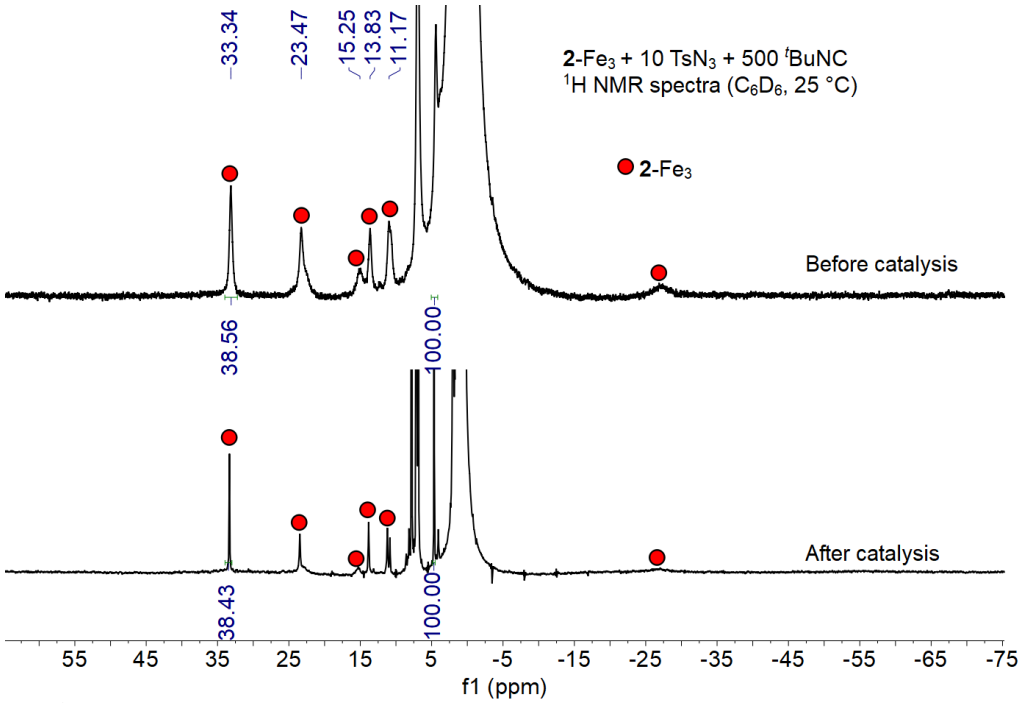

Figure 5.20. ^{1}H NMR spectra (300 MHz, C_6D_6, 25 °C) before and after carbodiimide catalysis with 10 mol % **2**-Fe_3 with 500 equiv of ^{t}BuNC. Integrations are versus internal mesitylene standard.

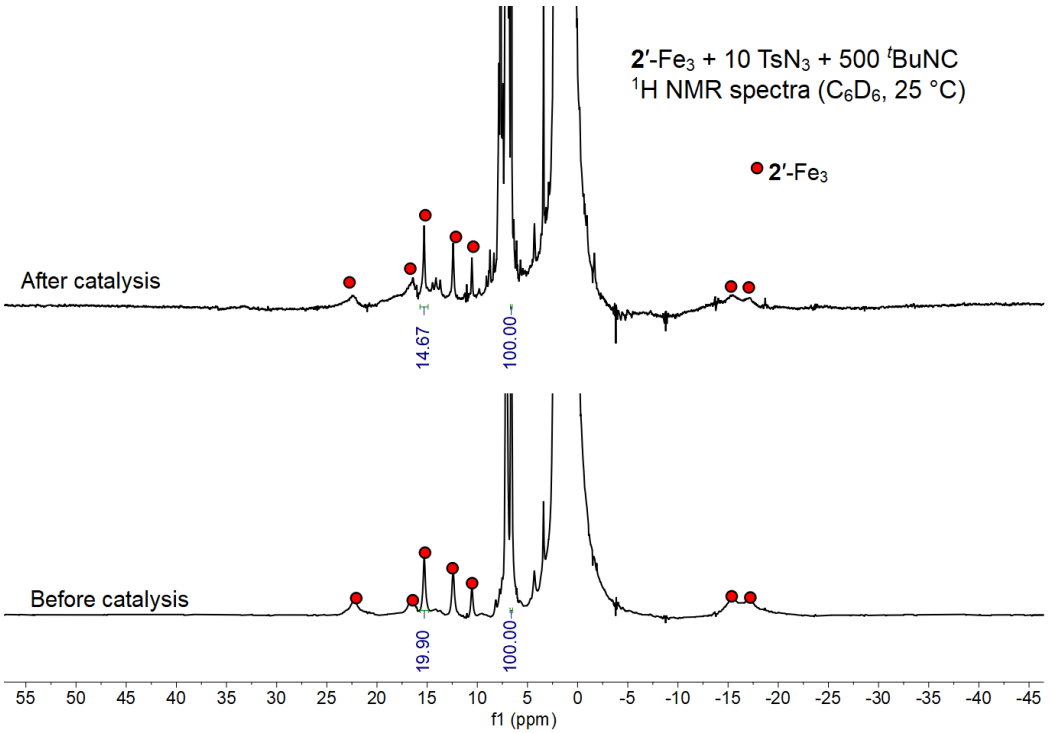

Figure 5.21. ^{1}H NMR spectra (300 MHz, C_6D_6, 25 °C) before and after carbodiimide catalysis with 10 mol % **2′**-Fe_3 with 500 equiv of ^{t}BuNC. Integrations are versus internal mesitylene standard.

5.5.9 *Approximation of tBuNC Binding Constant for **2′**-Fe$_3$*

^{1}H NMR binding constant was determined by previously reported methods.[16] An average K_{eq} was found from the analysis of the features at 19.95 and 8.88 ppm (in the initial spectrum).

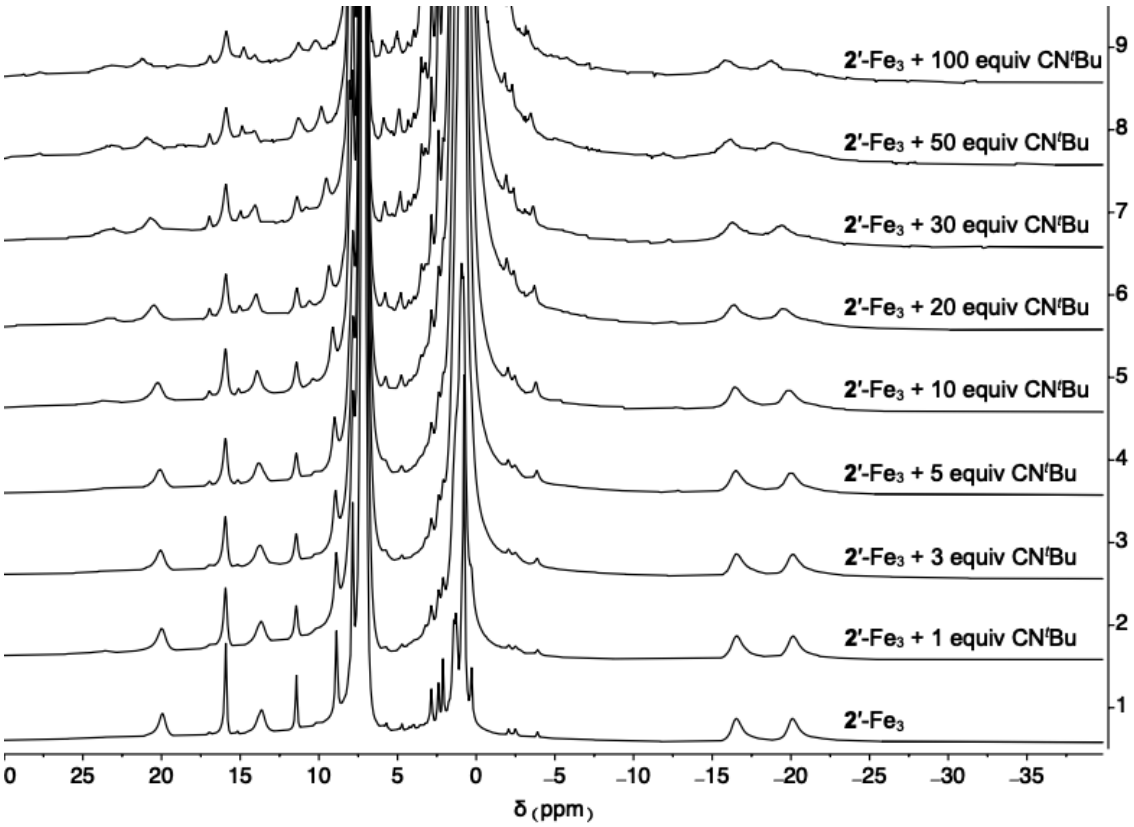

Figure 5.22. ^{1}H NMR spectra (300 MHz, C_6D_6, 25 °C) of **2′**-Fe$_3$ with varying equivalents of ^{t}BuNC. K_{eq} = 7 M^{-1}. From 20-100 equivalents of ^{t}BuNC, solids were observed on the walls of the NMR tube.

5.6 REFERENCES

(1) Sabatier, P. (1854-1941) A. du texte. *La Catalyse En Chimie Organique*; 1913.

(2) Trasatti, S. Work Function, Electronegativity, and Electrochemical Behaviour of Metals: III. Electrolytic Hydrogen Evolution in Acid Solutions. *Journal of Electroanalytical Chemistry and Interfacial Electrochemistry* **1972**, *39* (1), 163–184. https://doi.org/10.1016/S0022-0728(72)80485-6.

(3) Medford, A. J.; Vojvodic, A.; Hummelshøj, J. S.; Voss, J.; Abild-Pedersen, F.; Studt, F.; Bligaard, T.; Nilsson, A.; Nørskov, J. K. From the Sabatier Principle to a Predictive Theory of Transition-Metal Heterogeneous Catalysis. *Journal of Catalysis* **2015**, *328*, 36–42. https://doi.org/10.1016/j.jcat.2014.12.033.

(4) Oudar, J. *Deactivation and Poisoning of Catalysts*; CRC Press, 1985.

(5) Chikan, V.; Kelley, D. F. Size-Dependent Spectroscopy of MoS2 Nanoclusters. *J. Phys. Chem. B* **2002**, *106* (15), 3794–3804. https://doi.org/10.1021/jp011898x.

(6) Tuxen, A.; Kibsgaard, J.; Gøbel, H.; Lægsgaard, E.; Topsøe, H.; Lauritsen, J. V.; Besenbacher, F. Size Threshold in the Dibenzothiophene Adsorption on MoS2 Nanoclusters. *ACS Nano* **2010**, *4* (8), 4677–4682. https://doi.org/10.1021/nn1011013.

(7) Bruix, A.; V. Lauritsen, J.; Hammer, B. Effects of Particle Size and Edge Structure on the Electronic Structure, Spectroscopic Features, and Chemical Properties of Au(111)-Supported MoS 2 Nanoparticles. *Faraday Discussions* **2016**, *188* (0), 323–343. https://doi.org/10.1039/C5FD00203F.

(8) Wu, Z.; Fang, B.; Wang, Z.; Wang, C.; Liu, Z.; Liu, F.; Wang, W.; Alfantazi, A.; Wang, D.; Wilkinson, D. P. MoS2 Nanosheets: A Designed Structure with High Active Site Density for the Hydrogen Evolution Reaction. *ACS Catal.* **2013**, *3* (9), 2101–2107. https://doi.org/10.1021/cs400384h.

(9) Hakala, M.; Kronberg, R.; Laasonen, K. Hydrogen Adsorption on Doped MoS2 Nanostructures. *Sci Rep* **2017**, *7* (1), 15243. https://doi.org/10.1038/s41598-017-15622-z.

(10) Pérez-Ramírez, J.; López, N. Strategies to Break Linear Scaling Relationships. *Nat Catal* **2019**, *2* (11), 971–976. https://doi.org/10.1038/s41929-019-0376-6.

(11) Arnett, C. H.; Kaiser, J. T.; Agapie, T. Remote Ligand Modifications Tune Electronic Distribution and Reactivity in Site-Differentiated, High-Spin Iron Clusters: Flipping Scaling

Relationships. *Inorg. Chem.* **2019**, *58* (23), 15971–15982. https://doi.org/10.1021/acs.inorgchem.9b02470.

(12) Hernández Sánchez, R.; Champsaur, A. M.; Choi, B.; Wang, S. G.; Bu, W.; Roy, X.; Chen, Y.-S.; Steigerwald, M. L.; Nuckolls, C.; Paley, D. W. Electron Cartography in Clusters. *Angewandte Chemie International Edition* **2018**, *57* (42), 13815–13820. https://doi.org/10.1002/anie.201806426.

(13) Amtawong, J.; Nguyen, A. I.; Tilley, T. D. Mechanistic Aspects of Cobalt–Oxo Cubane Clusters in Oxidation Chemistry. *J. Am. Chem. Soc.* **2022**, *144* (4), 1475–1492. https://doi.org/10.1021/jacs.1c11445.

(14) Sridharan, A.; Brown, A. C.; Suess, D. L. M. A Terminal Imido Complex of an Iron–Sulfur Cluster. *Angewandte Chemie International Edition* **2021**, *60* (23), 12802–12806. https://doi.org/10.1002/anie.202102603.

(15) Mitchell, B. S.; Chirila, A.; Kephart, J. A.; Boggiano, A. C.; Krajewski, S. M.; Rogers, D.; Kaminsky, W.; Velian, A. Metal–Support Interactions in Molecular Single-Site Cluster Catalysts. *J. Am. Chem. Soc.* **2022**, *144* (40), 18459–18469. https://doi.org/10.1021/jacs.2c07033.

(16) Kephart, J. A.; Mitchell, B. S.; Chirila, A.; Anderton, K. J.; Rogers, D.; Kaminsky, W.; Velian, A. Atomically Defined Nanopropeller Fe3Co6Se8(Ph2PNTol)6: Functional Model for the Electronic Metal–Support Interaction Effect and High Catalytic Activity for Carbodiimide Formation. *J. Am. Chem. Soc.* **2019**, *141* (50), 19605–19610. https://doi.org/10.1021/jacs.9b12473.

(17) Mitchell, B. S.; Krajewski, S. M.; Kephart, J. A.; Rogers, D.; Kaminsky, W.; Velian, A. Redox-Switchable Allosteric Effects in Molecular Clusters. *JACS Au* **2022**, *2* (1), 92–96. https://doi.org/10.1021/jacsau.1c00491.

(18) Kephart, J. A.; Mitchell, B. S.; Kaminsky, W.; Velian, A. Multi-Active Site Dynamics on a Molecular Cr/Co/Se Cluster Catalyst. *J. Am. Chem. Soc.* **2022**, *144* (21), 9206–9211. https://doi.org/10.1021/jacs.2c00234.

(19) Mitchell, B. S.; Kaminsky, W.; Velian, A. Tuning the Electronic Structure of Atomically Precise Sn/Co/Se Nanoclusters via Redox Matching of Tin(IV) Surface Sites. *Inorg. Chem.* **2021**, *60* (9), 6135–6139. https://doi.org/10.1021/acs.inorgchem.1c00313.

(20) Cowley, R. E.; Golder, M. R.; Eckert, N. A.; Al-Afyouni, M. H.; Holland, P. L. Mechanism of Catalytic Nitrene Transfer Using Iron(I)–Isocyanide Complexes. *Organometallics* **2013**, *32* (19), 5289–5298. https://doi.org/10.1021/om400379p.

(21) Beaumier, E. P.; McGreal, M. E.; Pancoast, A. R.; Wilson, R. H.; Moore, J. T.; Graziano, B. J.; Goodpaster, J. D.; Tonks, I. A. Carbodiimide Synthesis via Ti-Catalyzed Nitrene Transfer from Diazenes to Isocyanides. *ACS Catal.* **2019**, *9* (12), 11753–11762. https://doi.org/10.1021/acscatal.9b04107.

(22) Laskowski, C. A.; Hillhouse, G. L. Group-Transfer Reactions of Ni(II)−Ni(II) Bridging Imido Complexes. Catalytic Formation of Carbodiimides and Isocyanates via Nitrene Transfer from Organoazides. *Organometallics* **2009**, *28* (20), 6114–6120. https://doi.org/10.1021/om900783u.

(23) Spasyuk, D. M.; Carpenter, S. H.; Kefalidis, C. E.; Piers, W. E.; Neidig, M. L.; Maron, L. Facile Hydrogen Atom Transfer to Iron(III) Imido Radical Complexes Supported by a Dianionic Pentadentate Ligand. *Chem. Sci.* **2016**, *7* (9), 5939–5944. https://doi.org/10.1039/C6SC01433J.

(24) Nguyen, A. I.; Zarkesh, R. A.; Lacy, D. C.; Thorson, M. K.; Heyduk, A. F. Catalytic Nitrene Transfer by a Zirconium(IV) Redox-Active Ligand Complex. *Chem. Sci.* **2010**, *2* (1), 166–169. https://doi.org/10.1039/C0SC00414F.

(25) Yousif, M.; Tjapkes, D. J.; Lord, R. L.; Groysman, S. Catalytic Formation of Asymmetric Carbodiimides at Mononuclear Chromium(II/IV) Bis(Alkoxide) Complexes. *Organometallics* **2015**, *34* (20), 5119–5128. https://doi.org/10.1021/acs.organomet.5b00703.

(26) Harlan, E. W.; Holm, R. H. Molybdenum-Mediated Imido Group Transfer: Stoichiometric and Catalytic Reactions and Structures. *J. Am. Chem. Soc.* **1990**, *112* (1), 186–193. https://doi.org/10.1021/ja00157a030.

(27) Wilding, M. J. T.; Iovan, D. A.; Betley, T. A. High-Spin Iron Imido Complexes Competent for C–H Bond Amination. *J. Am. Chem. Soc.* **2017**, *139* (34), 12043–12049. https://doi.org/10.1021/jacs.7b06682.

(28) King, E. R.; Hennessy, E. T.; Betley, T. A. Catalytic C−H Bond Amination from High-Spin Iron Imido Complexes. *J. Am. Chem. Soc.* **2011**, *133* (13), 4917–4923. https://doi.org/10.1021/ja110066j.

(29) Mayer, J. M. Understanding Hydrogen Atom Transfer: From Bond Strengths to Marcus Theory. *Acc. Chem. Res.* **2011**, *44* (1), 36–46. https://doi.org/10.1021/ar100093z.

(30) Roberts, B. P. Polarity-Reversal Catalysis of Hydrogen-Atom Abstraction Reactions: Concepts and Applications in Organic Chemistry. *Chemical Society Reviews* **1999**, *28* (1), 25–35. https://doi.org/10.1039/A804291H.

(31) Bietti, M.; Cucinotta, E.; DiLabio, G. A.; Lanzalunga, O.; Lapi, A.; Mazzonna, M.; Romero-Montalvo, E.; Salamone, M. Evaluation of Polar Effects in Hydrogen Atom Transfer Reactions from Activated Phenols. *J. Org. Chem.* **2019**, *84* (4), 1778–1786. https://doi.org/10.1021/acs.joc.8b02571.

(32) Kephart, J. A.; Boggiano, A. C.; Kaminsky, W.; Velian, A. Inorganic Clusters as Metalloligands: Ligand Effects on the Synthesis and Properties of Ternary Nanopropeller Clusters. *Dalton Trans.* **2020**, *49* (45), 16464–16473. https://doi.org/10.1039/D0DT02416C.

(33) Yang, Y.; Diederich, F.; Valentine, J. S. Lewis Acidic Catalysts for Olefin Epoxidation by Iodosylbenzene. *J. Am. Chem. Soc.* **1991**, *113* (19), 7195–7205. https://doi.org/10.1021/ja00019a016.

(34) Li, Z.; Quan, R. W.; Jacobsen, E. N. Mechanism of the (Diimine)Copper-Catalyzed Asymmetric Aziridination of Alkenes. Nitrene Transfer via Ligand-Accelerated Catalysis. *J. Am. Chem. Soc.* **1995**, *117* (21), 5889–5890. https://doi.org/10.1021/ja00126a044.

(35) R. Roose, T.; S. Verdoorn, D.; Mampuys, P.; Ruijter, E.; W. Maes, B. U.; A. Orru, R. V. Transition Metal-Catalysed Carbene- and Nitrene Transfer to Carbon Monoxide and Isocyanides. *Chemical Society Reviews* **2022**, *51* (14), 5842–5877. https://doi.org/10.1039/D1CS00305D.

(36) Kim, J. Y.; Park, S. H.; Ryu, J.; Cho, S. H.; Kim, S. H.; Chang, S. Rhodium-Catalyzed Intermolecular Amidation of Arenes with Sulfonyl Azides via Chelation-Assisted C–H Bond Activation. *J. Am. Chem. Soc.* **2012**, *134* (22), 9110–9113. https://doi.org/10.1021/ja303527m.

(37) Fulmer, G. R.; Miller, A. J. M.; Sherden, N. H.; Gottlieb, H. E.; Nudelman, A.; Stoltz, B. M.; Bercaw, J. E.; Goldberg, K. I. NMR Chemical Shifts of Trace Impurities: Common Laboratory Solvents, Organics, and Gases in Deuterated Solvents Relevant to the Organometallic Chemist. *Organometallics* **2010**, *29* (9), 2176–2179. https://doi.org/10.1021/om100106e.

(38) Gottlieb, H. E.; Kotlyar, V.; Nudelman, A. NMR Chemical Shifts of Common Laboratory Solvents as Trace Impurities. *The Journal of Organic Chemistry* **1997**, *62* (21), 7512–7515. https://doi.org/10.1021/jo971176v.

(39) Babij, N. R.; McCusker, E. O.; Whiteker, G. T.; Canturk, B.; Choy, N.; Creemer, L. C.; Amicis, C. V. D.; Hewlett, N. M.; Johnson, P. L.; Knobelsdorf, J. A.; Li, F.; Lorsbach, B. A.;

Nugent, B. M.; Ryan, S. J.; Smith, M. R.; Yang, Q. NMR Chemical Shifts of Trace Impurities: Industrially Preferred Solvents Used in Process and Green Chemistry. *Organic Process Research & Development* **2016**, *20* (3), 661–667. https://doi.org/10.1021/acs.oprd.5b00417.

Chapter 6. MIMICKING THE EDGE: IRON AND COBALT COMPLEXES WITH AMINOPHOSPHINE SELENIDE LIGANDS

6.1 INTRODUCTION

Nature commonly employs chalcogenide ligands, particularly sulfur, in the primary coordination sphere of metalloenzymes. Compared to oxygen, sulfur has better orbital overlap with 3d transition metals,[1] and the softer coordination enables flexibility of the enzymatic active sites, critical for efficient multi-step chemical transformations.[2–4] Moving down the group 14 elements, selenium has increased polarizability and nucleophilicity, and a lower oxidation potential.[5] Biologically, selenium-containing protein architectures are more rare, however they can serve many functions, most notably as enzymes for oxidoreductase processes.[6,7] Additionally, due to the spectroscopic and electronic differences, synthetically replacing sulfur with selenium presents many interesting opportunities to interrogate the electronic structure and catalytic mechanism of enzymatic processes.[8–11] For instance, replacing an active site cysteine residue with the more electron donating selenocysteine in cytochrome P450 resulted improved C-H bond cleavage reactivity which enabled insights into the key H-atom abstraction step.[9]

Particularly with respect to oxygen binding and activation, biomimetic models with sulfur have been extensively developed and investigated.[12–14] In contrast, molecular complexes probing the role of selenium in oxygen activation is much more rare. One example, is a ruthenium complex with a proximal arylselenium tether which was competent for O_2 activation and subsequent O-atom transfer.[15] While the Se is not in the primary coordination sphere, the pendant Se promotes O_2 cleavage and then subsequently stabilizes the cleaved product resulting in a Ru-O-Se motif.[15]

In this study, we explore a simple organometallic construct (ML_2; M = Co or Fe, L = $SePPh_2NTol$; Tol = 4-tolyl) with hemilabile Se contacts and gain insights into the structural and electronic effects of ligand coordination and its reactivity with oxygen and oxo atom donors. This $M(EPR_2NR')_2$ construct (M = Ti, V, Cr, Mn, Fe, Co, Ni, Zn, Cd; E = S, Se, Te; R = *tert*-butyl, ethyl ; R' = *iso*-propyl, cyclohexyl, methyl, ethyl, *tert*-butyl, cyclohexyl, phenyl) has been previously prepared in the late 1980's and early 1990's and studied for its ability as single source precursors for the

deposition of metal chalcogenide phases.[16–19] However, the reactivity of these complexes with 3d transition metals, has not been explored.

6.2 Synthesis of ML_2 (M = Fe or Co)

The aminophosphine selenide ligand, $SePPh_2NHTol$ (L^H; Tol = 4-tolyl, Ph = phenyl), was prepared by combing the aminophosphine (1.0 equiv) and excess selenium powder (1.3 equiv) in toluene. After two hours of stirring at room temperature the unreacted Se was removed via vacuum filtration and after removal of the volatiles, L^H was isolated as a pure off-white solid (99% yield). The ^{31}P NMR spectrum of L^H is shifted from the aminophosphine starting material and it features Se^{77} satellites (49 ppm, J_{SeP} = 357 Hz). While a plethora of aminophosphine selenides have been prepared through similar methods, this is the first report of this complex with the 4-tolyl substituent on the amino group.

While other reported preparations of related ML_2 complex use *n*-butyl lithium to deprotonate the aminophosphine chalcogenide, we found that this resulted in the formation of noxious fumes, presumably due to the decomposition of the ligand into volatile alkyl selenide species. We found that preparing the M(HMDS) precursor *in situ* alleviated this danger. The salt metathesis of the anhydrous metal dichloride (1 equiv) and lithium bis(trimethylsilyl)amide (2 equiv) followed by the addition of the aminophosphine selenide (2 equiv) resulted in the formation of ML_2 as the major product (Scheme 6.1). A brief solvent workup, targeted at removal of LiCl from the reaction mixture, followed by bulk crystallization from a layered solution of toluene and *n*-pentane yielded both CoL_2 and FeL_2 in good yield and purity (92% and 59% yield, respectively). Both CoL_2 and FeL_2 exhibit six paramagnetic ^1H NMR signals indicating a highly symmetric species with a single ligand environment (Figure 6.9Figure 6.10). No ^{31}P NMR feature was observed for either complex within a +2400 to –2400 ppm range. As determined by Evan's method, the ML_2 complexes have

Scheme 6.1. Synthesis of ML_2 complexes.

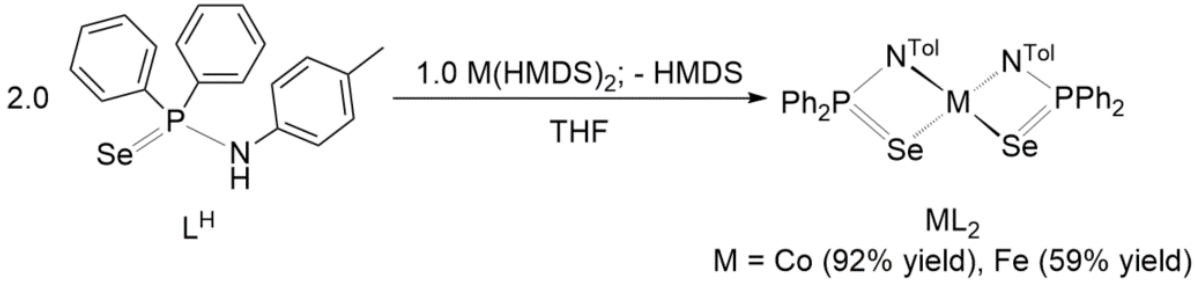

L^H ML_2

M = Co (92% yield), Fe (59% yield)

magnetic moments of 3.9(3) μ_B for Co and 4.9(3) μ_B for Fe, both characteristic of a high spin M^{2+} center.[20]

6.3 Solid State Structural Analysis of ML_2

High quality single crystals of CoL_2 and FeL_2 were grown via the vapor diffusion of pentane into a saturated solution of ML_2 in toluene. Both complexes feature a pseudo tetrahedral geometry (τ^4 = 0.85 and 0.72, for CoL_2 and FeL_2, respectively)[21] with κ^2 chelation from the amidophosphine selenide (Figure 6.1), as seen previously in the literature.[16–19] For both complexes, the P-N and P-Se interatomic distances are nearly identical, however the Fe-Se and Fe-N distances (2.50 and 2.02 avg. Å, respectively) are slightly elongated compared to the Co-Se and Co-N distances (2.49 and

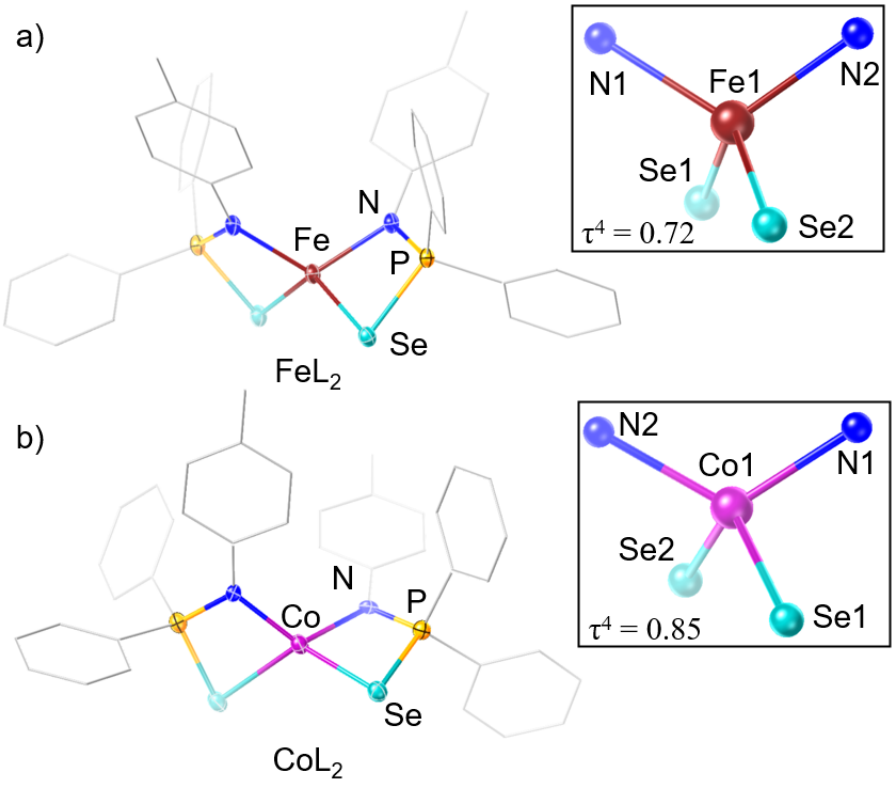

Figure 6.1. Solid state structures of FeL_2 (a) and CoL_2 (b). Hydrogen atoms, co-crystallized solvent molecules, and disorder are omitted for clarity. Carbons are depicted as wireframe. Thermal ellipsoids are plotted at 50% probability. Select interatomic distances (Å) in FeL_2: Fe1-N1 2.020(2), Fe1-N2 2.021(2), Fe1-Se1 2.507(3), Fe1-Se2 2.500(3). Select interatomic distances (Å) in CoL_2: Co1-N1 1.984(8), Co1-N2 1.985(8), Co1-Se1 2.486(6), Co1-Se2 2.493(8)

1.98 avg. Å, respectively). The N-P-Se and N-M-Se angles are also similar between the two complexes (Table 6.4).

6.4 Ancillary Ligand Coordination in CoL_2

The flexibility of this ligand framework is demonstrated by ancillary ligand coordination studies. Crystals of the pyridine adduct, CoL_2(py) were grown by adding excess pyridine to a crystallization of CoL_2 which resulted in the formation of red needle-like crystals (Figure 6.24). The presence of the fifth ligand results in a structural rearrangement in which the aminophosphine selenide ligands rearrange into the equatorial plane with the pyridine ligand in the apical position, resulting in distorted square pyramidal geometry ($\tau^5 = 0.04$; Figure 6.2). The τ^5 value close to zero suggests almost perfect square pyramidal geometry, however this metric does not capture the distortion stemming from the Co atom being pulled out of the XY plane.

While the amide contact is minimally affected upon ligand coordination, the dative Co…Se interactions are elongated from 2.49 avg. Å in CoL_2 to 2.66 avg. Å in CoL_2(py) presumably due to the increased electron-electron repulsion incurred by axial ligand coordination. Additionally, pyridine coordination results in minor structural perturbations of the ligand which manifest as a contraction in the P-Se interatomic distance (2.16 avg. Å versus 2.14 avg Å) and changes in the

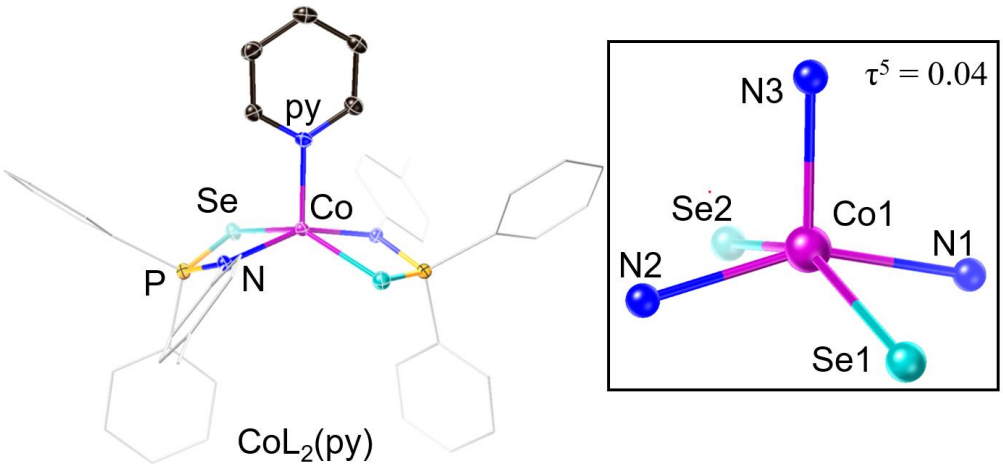

Figure 6.2. Solid state structure of CoL_2(py). Hydrogen atoms, co-crystallized solvent molecules, and disorder are omitted for clarity. Carbons are depicted as wireframe. Thermal ellipsoids are plotted at 50% probability. Select interatomic distances (Å): Co1-N1 2017(2), Co1-N2 2.018(2), Co1-Se1 2.675(2), Co1-Se2 2.6414(8), Co1-N3 2.074(2).

average N-Co-Se and N-P-Se angles (N-Co-Se: 82.0° to 77.5°, N-P-Se: 101.9° to 103.2°; Table 6.4).

The electronic absorption profile captures the dramatic color change upon ligand coordination. CoL_2 exhibits a λ_{max} at 596 nm with other smaller absorption features at 521 and 596 nm (Figure 6.3). Upon treatment excess pyridine, the λ_{max} shifts over 30 nm to higher energy (562 nm), indicative of the color change to red (Figure 6.3).

The solution magnetic susceptibility of $CoL_2(py)$ was measured to report on the magnetic impacts incurred by the shift in geometry, however Evan's method suggests a S = 3/2 spin state (4.1(3) μ_B), similar to CoL_2.[20]

Intrigued by ligand coordination in this simple molecular construct we investigated coordination of π-accepting ligands. Treatment with *tert*-butyl isocyanide (^{t}BuNC) results in color change from green to yellow which is represented by a large increase in absorption in the UV range (Figure 6.3). ^{1}H NMR analysis of the $CoL_2(CN^tBu)$ adduct reveals bound isocyanide and shifting of the amidophosphine resonances, indicative of ligand coordination (Figure 6.12). However, the Co-CN^tBu interaction is very weak, and the isocyanide ligand is lost under reduced pressure which precluded isolation of the $CoL_2(CN^tBu)$ product. In fact, crystallization in the presence of a large

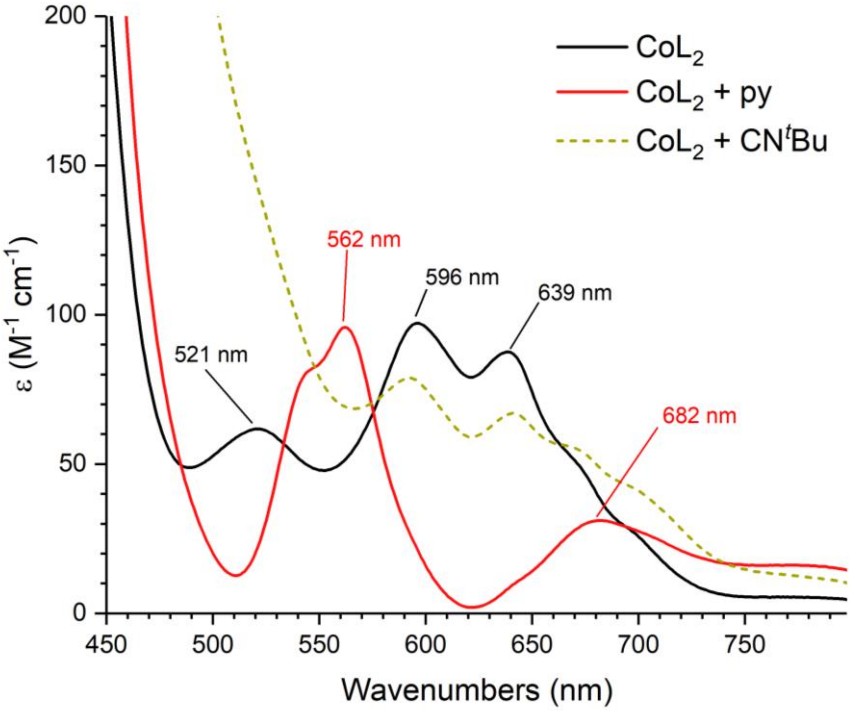

Figure 6.3. Absorption spectra of CoL_2, $CoL_2(py)$, and $CoL_2(CN^tBu)$ recorded in toluene at 25 °C.

excess of CNtBu (500+ equiv) results in only the CoL_2 complex. IR spectroscopy reveals a strictly sigma donating Co-CN^{t}Bu interaction (ν_{NC} = 2278 cm^{-1}) with no pi-backbonding to stabilize the adduct. In line with this, no coordination of carbon monoxide (CO) is observed by ^{1}H NMR or IR spectroscopy upon sparging CO into a solution of CoL_2 in toluene at room temperature for 15 minutes.

6.5 Chemical Oxidation of FeL_2 with Iodine

Scheme 6.2. Chemical oxidation of FeL_2 with iodine.

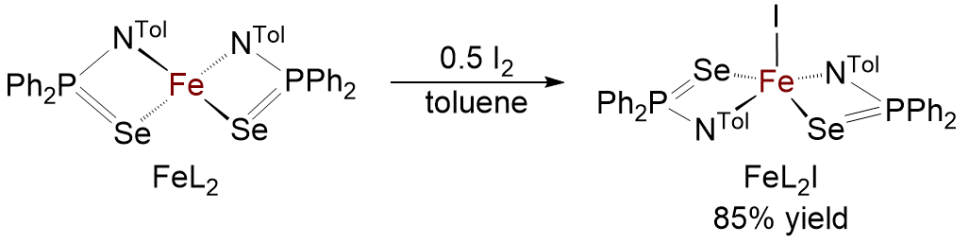

We set out to probe how this ligand construct might accommodate anionic ligands. Inner sphere chemical oxidation of the Fe derivative, FeL_2 (1 equiv), was accomplished with iodine (0.5 equiv) to yield the oxidized FeL_2I complex (Scheme 6.2, 85% yield). Oxidation results in a color change from yellow to dark red, and the resulting product is soluble in non-polar solvents (eg. toluene and benzene-d_6) suggesting close association of anion and the complex. The ^{1}H NMR spectrum exhibits one set of amidophosphine chalcogenide resonances indicating that upon anion coordination the product is still symmetric (Figure 6.11). FeL_2 is isolated as a brilliant yellow solid with an almost featureless absorption profile from 300-1200 nm (Figure 6.4). However, upon oxidation with iodine, FeL_2I exhibits absorption features at 419 nm (4017 M^{-1} cm^{-1}) and 564 nm (3145 M^{-1} cm^{-1}; Figure 6.4).

High quality single crystals of FeL_2I were grown via vapor diffusion of *n*-pentane into toluene at –35 °C. The solid state structure reveals that, similar to CoL_2(py), the solid state structure the amidophosphine ligands reorganize and the anionic I^- ligand coordinates in the apical position resulting in a distorted tetrahedral geometry (τ^5 = 0.29; Figure 6.5). Compared to CoL_2(py), the Fe center is pulled even farther out of the XY plane presumably due to the stronger Fe-I interaction compared to the dative Co-pyridine interaction. Upon oxidation and anion coordination, the Fe—Se contacts elongate from 2.50 avg Å to 2.58 avg Å coupled with a less dramatic increase in the Fe—N distances (2.02 to 2.03 avg. Å). Slight contractions in the P—Se (2.17 to 2.16 avg. Å) and

slight elongations in the P—N (1.63 to 1.64 avg. Å) bonds compared to FeL_2 are also observed (Table 6.4). Additionally, both the N-P-Se and N-Fe-Se angles contract by 2° and 3°, respectively, in FeL_2I compared to FeL_2.

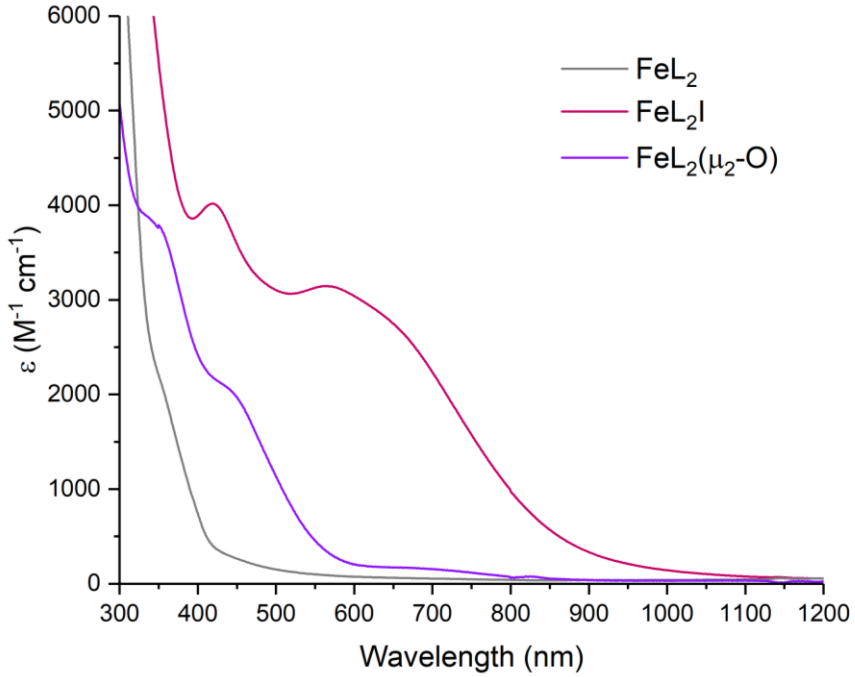

Figure 6.4. Absorption spectra of FeL_2, FeL_2I, and $FeL_2(\mu_2\text{-O})$ recorded in toluene at 25 °C.

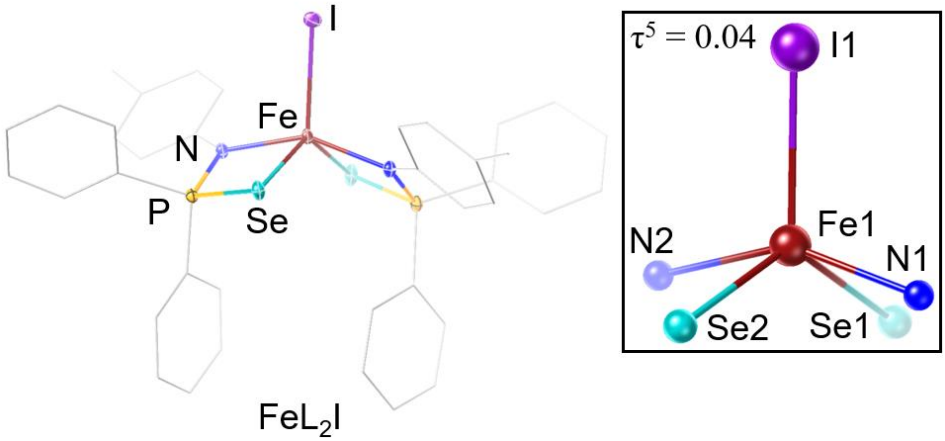

Figure 6.5. Solid state structure of FeL_2I. Hydrogen atoms, co-crystallized solvent molecules, and disorder are omitted for clarity. Carbons are depicted as wireframe. Thermal ellipsoids are plotted at 50% probability. Select interatomic distances (Å): Fe1-N1 2.034(2), Fe1-N2 2.028(2), Fe1-Se1 2.575(1), Fe1-Se2 2.566(1), Fe1-I1 2.5880(6).

6.6 Reactivity with O_2, Mesityl nitrile oxide, Iodosobenzene, and Pyridine-N-Oxide

Intrigued by the structural flexibility and the redox properties, we tested their reactivity with neat O_2. Degassed samples of ML_2 in toluene were sparged with O_2 for 1 minute. FeL_2 reacted quickly with O_2 which was observed by a rapid color change from yellow to red, while no color change was observed for CoL_2 even after 24 hours.

In situ ^{1}H NMR studies of FeL_2 exposed to air reveal that over the course of 1 hour, FeL_2 converts to a new species with ^{1}H NMR resonances shifted toward the diamagnetic region, a transient paramagnetic intermediate, and a red precipitate (Figure 6.15Figure 6.16). Intrigued by the evolution of species in this reaction, we set out to identify the products.

Using oxo atom donors can be an effective method for generating and studying metal oxo intermediates.[22,23] FeL_2 was treated with mesityl nitrile oxide (1 equiv; MesCNO) resulting a color change from yellow to dark red and the formation of a red precipitate. ^{1}H NMR of the soluble material in benzene-d_6 shows the same paramagnetic species observed in the *in situ* reaction with air. The paramagnetic product exhibits 10 ^{1}H NMR signals indicating a deviation from the symmetry observed in FeL_2 and FeL_2I (Figure 6.17).

The red precipitate, on the other hand, is completely insoluble in polar and non-polar organic solvents leading us to hypothesize its identity as red Se, an amorphous allotrope of Se. Conversion from red Se to the crystalline grey Se can be accomplished with moderate heating, and indeed upon heating the reaction mixture at 80 °C for 4 hours the red solids converted to grey solids.[24] In order to quantify the Se produced, the solids were isolated via vacuum filtration and then suspended in a solution of PPh_3 (3 equiv) in toluene. After stirring at room temperature for 2 hours, the reaction became homogenous indicating the formation of triphenyl phosphine selenide ($SePPh_3$). The solution was then analyzed by ^{31}P NMR spectroscopy and integrations of the PPh_3 versus $SePPh_3$ illustrated that upon stoichiometric treatment of FeL_2 with MesCNO, 1 equivalent of Se is produced (Figure 6.18). P-Se bond cleavage in the presence of oxo atom donors has be observed previously.[25] Since no other species are observed in the ^{1}H NMR or ^{31}P NMR spectra, we hypothesize that paramagnetic species observed in the reaction with O_2, and with MesCNO, is a mixed ligated complex where the Fe is chelated by one amidophosphine selenide and one amidophosphine oxide.

Scheme 6.3. Synthesis of $[CoLL']_2$.

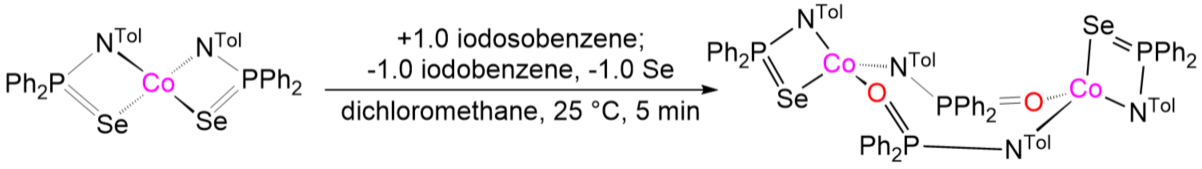

Experimental data to support this putative mixed ligated species was obtained from studying the reaction of CoL_2 with iodosobenzene (Scheme 6.3). Treating CoL_2 with stoichiometric iodosobenzene results in an immediate color change from green to blue with the concomitant precipitation of red Se. Upon removal of the solids, the filtrate was analyzed by ^{1}H NMR which reveals a single desymmetrized paramagnetic species (Figure 6.13). Crystals of this complex were grown from a layered solution of *n*-pentane and dichloromethane at –35 °C over the course of two days. This species is a mixed ligated complex with one amidophosphine selenide and one amidophosphine oxide (L' = $OPPh_2NTol$), wherein the oxide ligand is bridging between two Fe centers to form a bimetallic complex ($[CoLL']_2$; Figure 6.6). In the solid state, the eight-membered ring (Co-N-P-O-Co-N-P-O) is in a boat-chair confirmation, the most stable conformer of cyclooctane.[26,27]

We hypothesized that the use of a weaker oxo atom donor might prevent ligand oxidation and favor oxo atom transfer to the metal center. Treating CoL_2 with pyridine-*N*-oxide in benzene-d_6 results in clean formation of a new species which did not evolve under thermolysis or photolysis (Figure 6.14). High quality single crystals of this species were grown from a solution of *n*-pentane and C_6D_6 at room temperature to reveal CoL_2(Opy), where the pyridine-*N*-oxide ligand is coordinated in the apical position similar to the pyridine ligand in CoL_2(py) (Figure 6.7). Furthermore, the structural and bonding metrics are similar in CoL_2(Opy) and CoL_2(py) (Table 6.4).

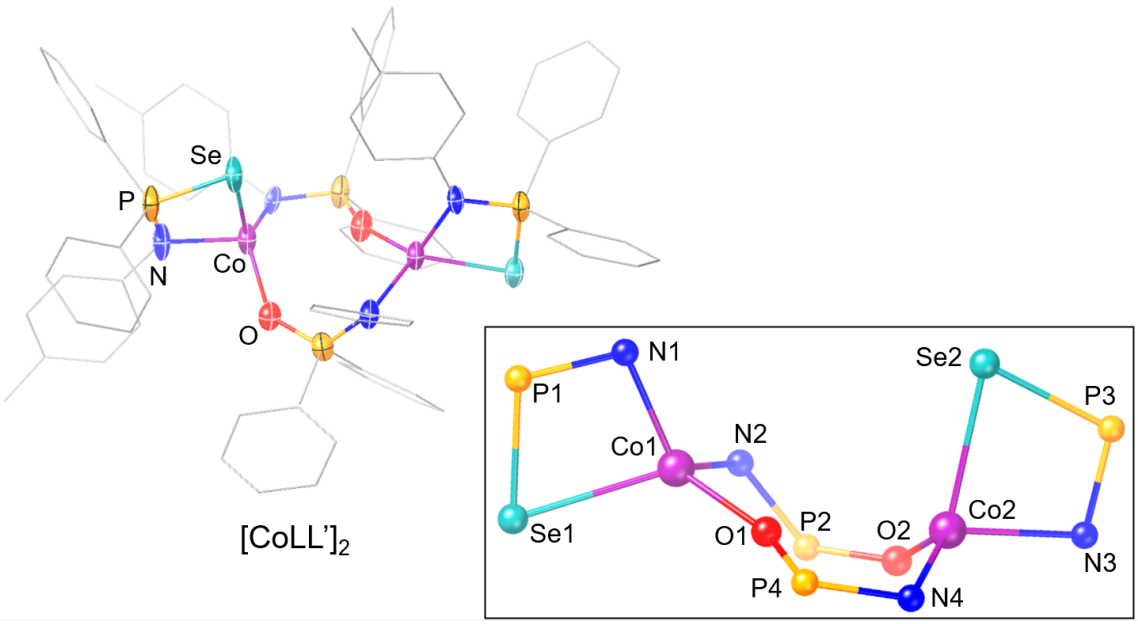

Figure 6.6. Solid state structure of $[CoLL']_2$. Hydrogen atoms, co-crystallized solvent molecules, and disorder are omitted for clarity. Carbons are depicted as wireframe. Thermal ellipsoids are plotted at 50% probability. Inset depicts a ball and stick model with carbons omitted. Select interatomic distances (Å): Co1-N1 1.991(7), Co1-N2 1.976(8), Co1-Se1 2.512(4), Co1-O1 1.946(7), Co2-N3 2.028(8), Co2-N4 1.979(7), Co2-Se2 2.522(7), Co2-O2 1.940(7), P2-O2 1.534(7), P4-O1 1.524(5), P1-Se1 2.165(4), P3-Se2 2.154(8).

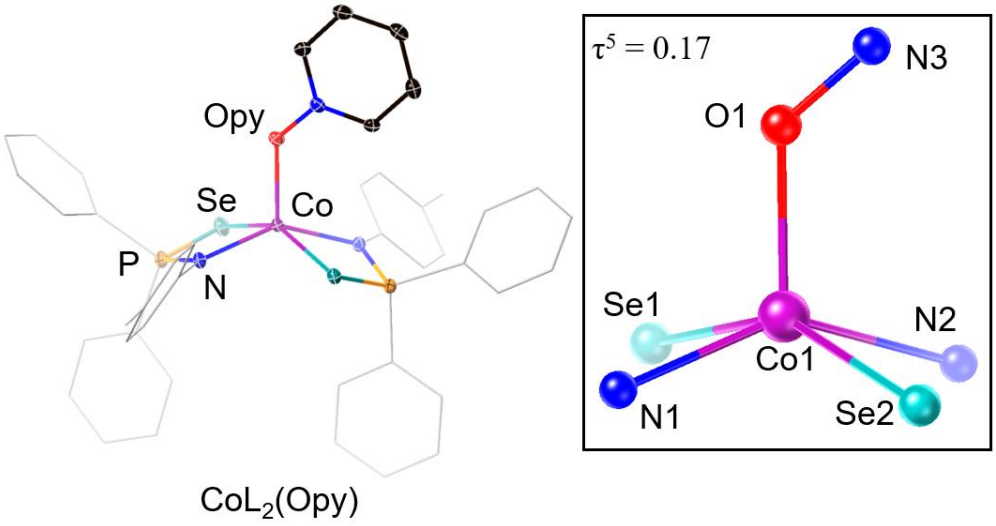

Figure 6.7. Solid state structure of $CoL_2(Opy)$. Hydrogen atoms, co-crystallized solvent molecules, and disorder are omitted for clarity. Carbons are depicted as wireframe. Thermal ellipsoids are plotted at 50% probability. Select interatomic distances (Å): Co1-N1 2.013(3), Co1-N2 2.049(2), Co1-Se1 2.6604(8), Co1-Se2 2.727(2), Co1-O1 2.011(2), O1-N3 1.336(3).

Similarly, monitoring the stoichiometric reaction between FeL_2 and pyridine-*N*-oxide by ^1H NMR in benzene-d_6, results in a shift in the proton resonances (Figure 6.19). However, contrary to CoL_2, upon heating at 60 °C the complex cleanly converts to a new species with ^1H NMR resonances shifted dramatically toward the diamagnetic region (previously observed in the reaction with O_2) accompanied by the release of pyridine (Figure 6.19).

Preparative scale synthesis of this complex enabled characterization and ultimately of identification of the product as a μ-oxo dimer, $FeL_2(\mu_2\text{-}O)$ (Scheme 6.4, Figure 6.20). Crystals suitable for X-ray diffraction studies were grown via vapor diffusion of *n*-pentane into toluene at room temperature. The solid state structure reveals two square pyramidal FeL_2 centers (τ^5 = 0.08 and 0.19) bridged by an oxo atom (Figure 6.8).

Scheme 6.4. Synthesis of $FeL_2(\mu_2\text{-}O)$.

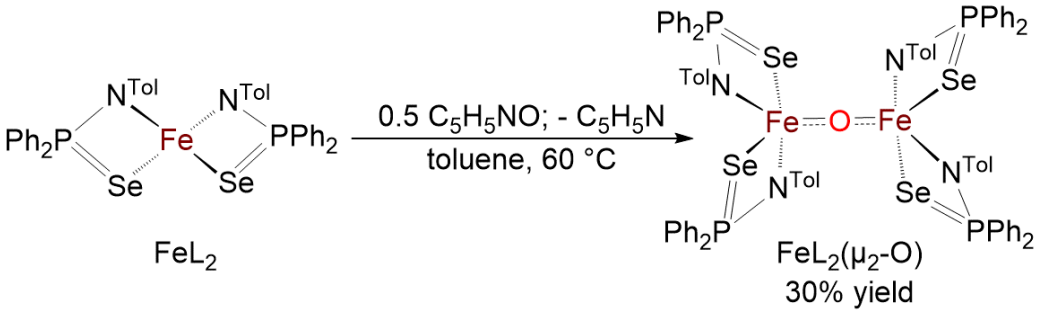

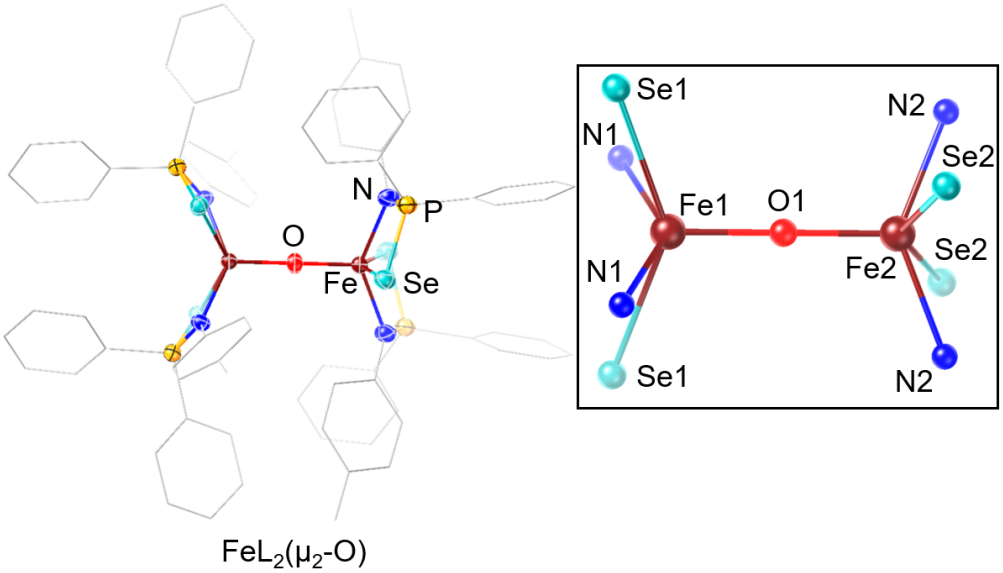

Figure 6.8. Solid state structure of $FeL_2(\mu_2\text{-}O)$. Hydrogen atoms, co-crystallized solvent molecules, and disorder are omitted for clarity. Carbons are depicted as wireframe. Thermal ellipsoids are plotted at 50% probability. Select interatomic distances (Å): Fe1-N1 1.772(5), Fe1-Se1 2.640(2), Fe2-N2 2.039(5), Fe2-Se2 2.653(3), Fe1-O1 1.771(5), Fe2-O1 1.755(5).

Binuclear iron oxo dimers have been extensively studied due to their relevance in biological systems.[28,29] Nature harnesses these dimer fragments as reversible oxygen carriers[30] and active sites for enzymatic catalysis (methane oxidation, ribonucleotide reduction).[31–33] Abiotically, these species have been investigated for their interesting magnetism and spectroscopy, as well as their ability activate O_2 and catalyze oxidation reactions.[29,34–36]

Since the first synthetic Fe-O-Fe dimer posited Pfeiffer et al in 1933,[37] many synthetic reports of this inorganic unit have emerged and been reviewed by multiple accounts.[38–41] Generally these complexes are stabilized by O, N, or S chelating ligands. To the best of our knowledge this is the first structural report of an iron μ_2-oxo dimer with Se in the primary coordination sphere.

The low magnetic moment of $FeL_2(\mu_2\text{-O})$ (1.0(3) μ_B)[20] is characteristic of these complexes and it is attributed to antiferromagnetic coupling of the two Fe(III) S = 5/2 centers. Extensive research into the magnetism of these dimers has found that the degree of magnetic coupling is dependent on the Fe-O-Fe angle and the Fe-Fe interatomic distance.[42,43] $FeL_2(\mu_2\text{-O})$ has a perfectly linear Fe-O-Fe angle (180.0°) which results in maximal magnetic coupling between the Fe centers. The Fe-O interatomic distances in $FeL_2(\mu_2\text{-O})$ are rather standard and asymmetric (1.771(5) and 1.755(5) Å) which is not unusual in this moiety.[39]

Features at 350 (ε = 3,794 M^{-1} cm^{-1}) and 441 (ε = 2,054 M^{-1} cm^{-1}) nm are observed in the electronic absorption spectrum (Figure 6.4). Previous studies have identified the former of these bands as oxo to Fe charge transfer transitions.[44] Comparison of the FT-IR spectra of FeL_2 and $FeL_2(\mu_2\text{-O})$ lead us to putatively identify the Fe-O-Fe asymmetric stretching frequency (852 cm^{-1}), which aligns closely with literature reports for μ-oxo dimers.[39]

The FeL_2 fragments in $FeL_2(\mu_2\text{-O})$ exhibit structural consequences similar to FeL_2I, albeit more dramatic. In the solid state the Fe—Se interatomic distances (2.50 to 2.64 avg Å) and the Fe—N distances (2.02 to 2.04 avg Å) are elongated compared to the parent complex, FeL_2 (Table 6.4). Furthermore, the P-N and P-Se contacts contract in $FeL_2(\mu_2\text{-O})$ (Table 6.4).

6.7 CONCLUSIONS

In conclusion, we synthesized and characterized a simple amidophosphine selenide complex, ML_2 (M = Fe or Co), in good yield and high purity. In the solid state, ML_2 exhibits tetrahedral geometry, however upon neutral or anionic ancillary ligand coordination the amidophosphine ligands reorganize resulting in square pyramidal geometry. Additionally, we explored their reactivity with

oxo atom donors. Interestingly, depending on the identity of the donor either the ligand or the metal center is oxidized. Mesityl nitrile oxide and iodosobenzene, cause direct oxidation of the amidophosphine selenide resulting in ligand fragmentation. However, we found that pyridine-*N*-oxide pre-coordinates to the metal center, and in the case of FeL_2, upon thermolysis pyridine is lost and a μ-oxo dimer is formed. Furthermore, $FeL_2(\mu_2\text{-}O)$ is formed in the reaction of FeL_2 with O_2, suggesting the FeL_2 construct is competent for O_2 activation. In aggregate, this study provides insight into a structurally dynamic organometallic complex and its ability to activate oxygen and form metal oxos. While Fe-oxo dimers are widely reported, this work provides an interesting example of a μ_2-oxo dimer with Se in the primary coordination sphere.

6.8 Synthetic Details and Characterization of Products

6.8.1 *General Experimental Considerations*

Safety Consideration: Deprotonation of aminophosphine selenide ligands with *n*-butyl lithium results in decomposition of the ligand and the formation of compounds with highly noxious vapors. The syntheses were conducted under a dinitrogen atmosphere using standard Schlenk or glovebox techniques (LC Technology Solutions glovebox equipped with a freezer set to −35 °C). The glassware was dried at 160 °C for a minimum of 12 h and cooled in an evacuated antechamber prior to use in the glovebox.

Solvents were purchased from Fischer Scientific and degassed, dried and purified using solvent purification columns housed in a stainless-steel cabinet and dispensed by a stainless-steel Schlenk line manufactured by JC Meyer Solvent Systems. Tetrahydrofuran (THF), diethyl ether, acetonitrile, and methylene chloride (DCM) are passed through two packed columns of neutral alumina. In the cases of *n*-pentane and toluene, one of the columns is packed with alumina and the other with Q5 reactant, a copper(II) oxide oxygen scavenger. All solvents were passed through an in-line, 2 μm filter, then stored over activated 3Å molecular sieves in the glovebox for a minimum of 72 h before use. 3Å molecular sieves were purchased from Sigma Aldrich and activated under vacuum at 300 °C for 48 h.

Deuterated solvents ($CDCl_3$, C_6D_6, CD_2Cl_2, CD_3CN) were purchased from Sigma Aldrich and stored over activated 3Å molecular sieves in the glovebox for a minimum of 72 h prior to use. The aminophosphine $Ph_2PNHTol$ (Ph = phenyl, Tol = 4-tolyl; L^H) was prepared according to the

literature.[45] Selenium (99.5%, powder, 200 mesh) was purchased from Sigma Aldrich and used without further purification. $CoCl_2$ (98+%) was purchased from Strem Chemicals, Inc. and dried under vacuum at 120 °C for 24 h prior to use. $FeCl_2$ (98+%) was purchased from Strem Chemicals, Inc. and dried under vacuum at 120 °C for 24 h prior to use. *Tert*-butyl isocyanide (^{t}BuNC, 98%) was purchased from Sigma Aldrich and stored over activated 3Å molecular sieves in the glovebox for 72 h prior to use. Lithium bis(trimethylsilyl)amide was purchased from Sigma Aldrich and used without further purification. Mesityl nitrile oxide was prepared by literature methods.[46]

Samples were prepared for elemental analysis by first crushing crystalline material into a powder, bringing it to constant mass under reduced pressure (ca. 12 h). Co, Se, P elemental analysis was conducted using a Perkin-Elmer Nexion 200B inductively-coupled plasma mass spectrometer (ICP-MS). Prior to ICP-MS analysis, samples were digested in neat nitric acid (Fisher Scientific, ICP-MS grade) at 50 °C.

UV-vis-*n*IR absorption spectra were acquired using a Varian Cary 5000 UV-Vis-*n*IR spectrometer using *n*IR quartz cuvettes (Spectrocell Inc., 10 mm path length, 220–3500 nm spectral window).

NMR spectra were acquired at 25 °C on Bruker 300 or 500 MHz spectrometers. ^{1}H and ^{13}C NMR spectra were referenced to residual deuterated solvent peaks. ^{31}P spectra were externally referenced to phosphoric acid.

6.8.2 *Synthesis and Isolation of $Fe(SePPh_2PNTol)_2$: FeL_2*

A 125 mL filter flask equipped with a 1-inch magnetic stir bar was loaded with anhydrous $FeCl_2$ (319 mg, 2.52 mmol, 1.0 equiv) and THF (5 mL). A solution of Li(HMDS) (842 mg, 5.04 mmol, 2.0 equiv) in THF (7 mL) was added dropwise to the stirring suspension of $FeCl_2$ and stirred at room temperature for 30 minutes. A solution of $SePPh_2NHTol$ (1.864 g, 5.04 mmol, 2.0 equiv) in THF (15 mL) added dropwise and the reaction was stirred for an additional 1 hour. The volatiles were removed under reduced pressure and the crude solids were triturated with *n*-pentane (3×5 mL) and extracted in warm toluene (~20 mL) through a medium porosity glass fritted funnel and plug of Celite. Once the filtrate had cooled to room temperature, the solution was layered with *n*-pentane and the mixture was left undisturbed for 18 hours to yield a crop of crystals which were collected via vacuum filtration through a fine porosity glass fritted funnel. The crystals were washed with *n*-pentane (20 mL) to yield FeL_2 as a yellow solid (1.18 g, 1.48 mmol, 59%). ^{1}H NMR (C_6D_6, 300 MHz) δ: 33.04 ($\nu_{1/2}$ = 129 Hz), 28.36 ($\nu_{1/2}$ = 34 Hz), 11.00 ($\nu_{1/2}$ = 158 Hz), 8.27 ($\nu_{1/2}$ =

26 Hz), 5.81 ($\nu_{1/2}$ = 21 Hz), –10.64 ($\nu_{1/2}$ = 536 Hz) ppm. μ_{eff} (Evans method, C_6D_6, 298K) 4.9(3) μ_B.

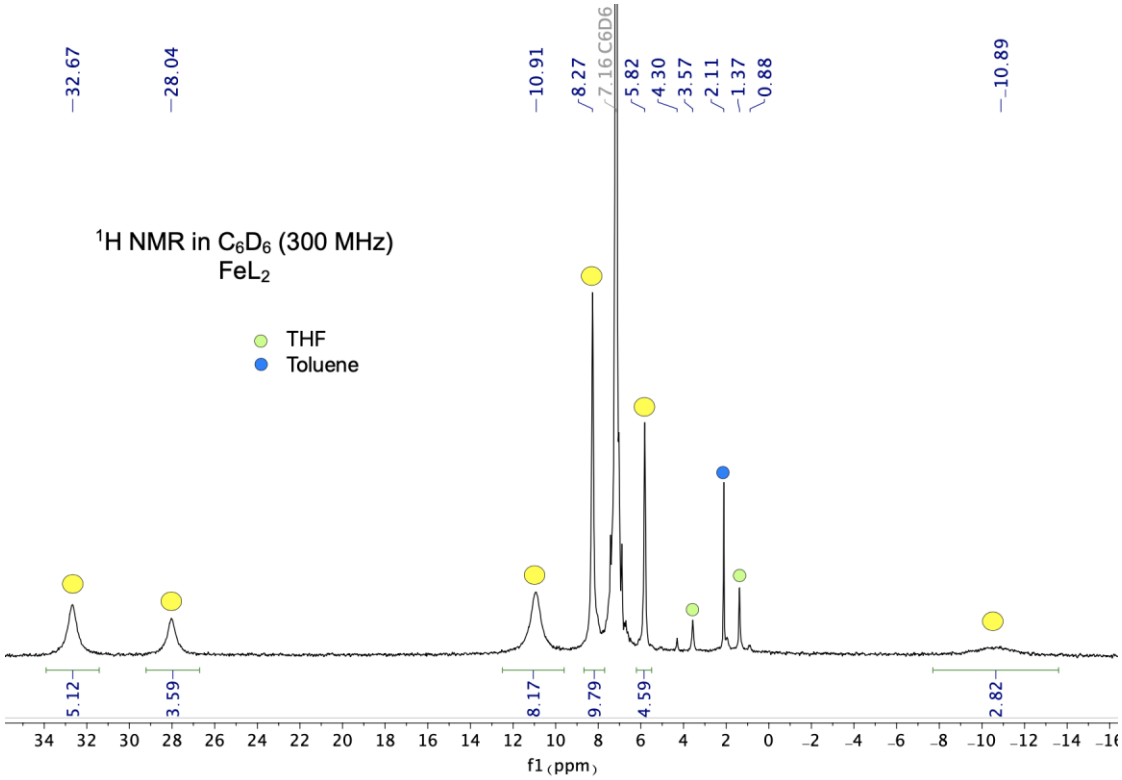

Figure 6.9. ^{1}H NMR (C_6D_6, 25 °C, 500 MHz) spectrum of FeL_2.

6.8.3 *Synthesis and Isolation of Co(SePPh$_2$PNTol)$_2$: CoL$_2$*

A 125 mL filter flask equipped with a 1-inch magnetic stir bar was loaded with anhydrous $CoCl_2$ (500 mg, 3.85 mmol, 1.0 equiv) and THF (10 mL). A solution of Li(HMDS) (1.289 g, 7.70 mmol, 2.0 equiv) in THF (10 mL) was added dropwise to the stirring suspension of MCl_2. In a separate 20 mL scintillation vial $Ph_2PNHTol$ (2.243 g, 7.70 mmol, 2.0 equiv), Se (700 mg, 8.87 mmol, 2.3 equiv), and THF (15 mL) were combined and stirred at room temperature. After both reaction mixtures were stirred for 30 minutes, the phosphine selenide solution was added to the $Co(HMDS)_2$ solution via vacuum filtration through a medium porosity fritted funnel and a plug of Celite. After an additional 1 hour, the volatiles were removed under reduced pressure. The crude solids were triturated with *n*-pentane (3×5 mL) and dissolved in warm toluene and filtered through a medium porosity glass fritted funnel and plug of Celite. Once the filtrate had cooled to room

temperature, the solution was layered with *n*-pentane and the mixture was left undisturbed for 18 hours to yield a crop of crystals which were collected via vacuum filtration through a fine porosity glass fritted funnel. The crystals were washed with *n*-pentane (20 mL) to yield CoL_2 as a green solid (2.92 g, 3.66 mmol, 95%). ^{1}H NMR (C_6D_6, 500 MHz) δ: 88.41 ($\nu_{1/2}$ = 2288 Hz), 30.83 ($\nu_{1/2}$ = 243 Hz), 23.59 ($\nu_{1/2}$ = 137 Hz), 17.27 ($\nu_{1/2}$ = 25 Hz), –4.02 ($\nu_{1/2}$ = 162 Hz) ppm. UV-vis-*n*IR (toluene, 25 °C) 521, 596, 639 nm. μ_{eff} (Evans method, C_6D_6, 298K) 3.9(3) μ_B.

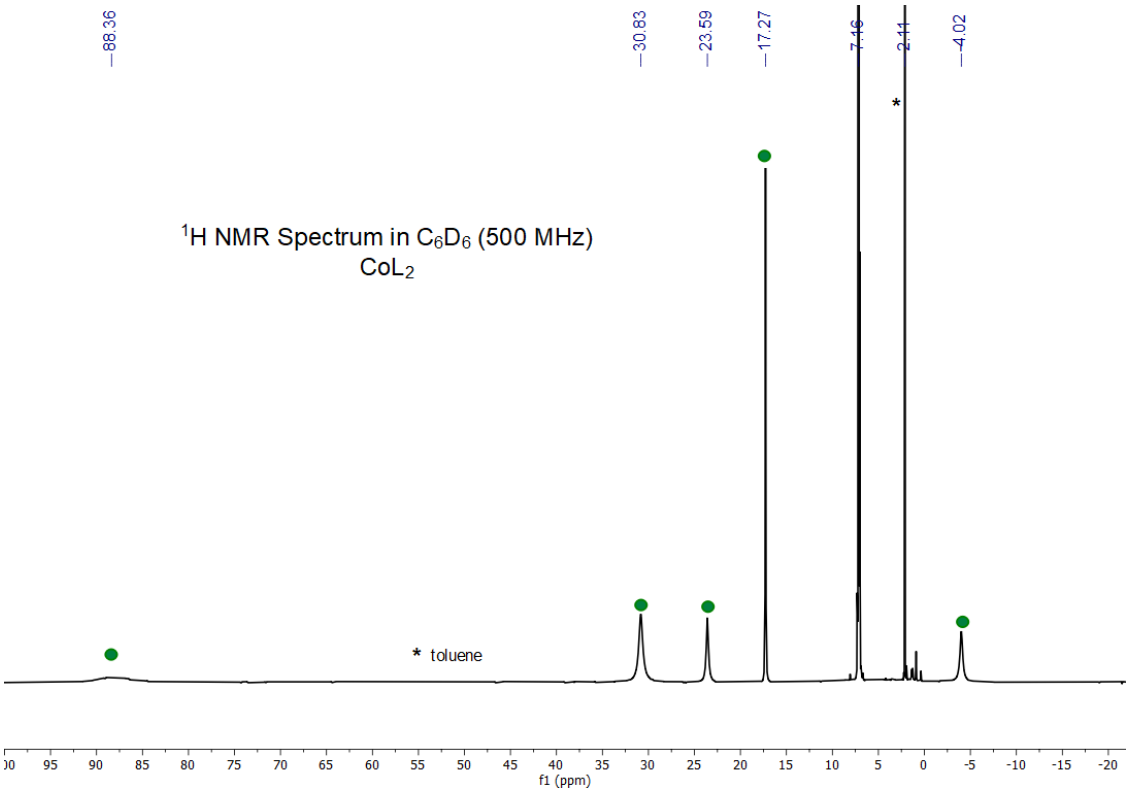

Figure 6.10. ^{1}H NMR (C_6D_6, 25 °C, 500 MHz) spectrum of CoL_2.

6.8.4 *Chemical Oxidation of FeL_2 with Iodine*

FeL_2 (500 mg, 0.629 mmol, 1 equiv) was dissolved in DCM (5 mL) and cooled to −35 °C. A solution of iodine (80 mg, 0.314 mmol, 0.5 equiv) in DCM (2 mL) was added dropwise to the stirring solution of FeL_2. The reaction was left to stir at room temperature for 1 hour at which point the volatiles were removed under reduced pressure. The solids were dissolved in minimal toluene (~3 mL), filtered through a plug of Celite, layered with *n*-pentane (~10 mL) and left undisturbed in the glovebox freezer. After 18 hours solids were collected via vacuum filtration through a fine porosity glass fritted funnel to yield FeL_2I as a black crystalline solid (495 mg, 0.537 mmol, 85%

yield). UV-vis-*n*IR (toluene, 25 °C) 419 (ε = 4,017 M^{-1} cm^{-1}) 564 (ε = 3,145 M^{-1} cm^{-1}) nm. ^{1}H NMR (C_6D_6, 300 MHz) δ: 76.22 ($\nu_{1/2}$ = 47 Hz), 59.77 ($\nu_{1/2}$ = 115 Hz), 14.44 ($\nu_{1/2}$ = 834 Hz), −0.08 ($\nu_{1/2}$ = 143 Hz), −25.16 ($\nu_{1/2}$ = 1703 Hz) ppm.

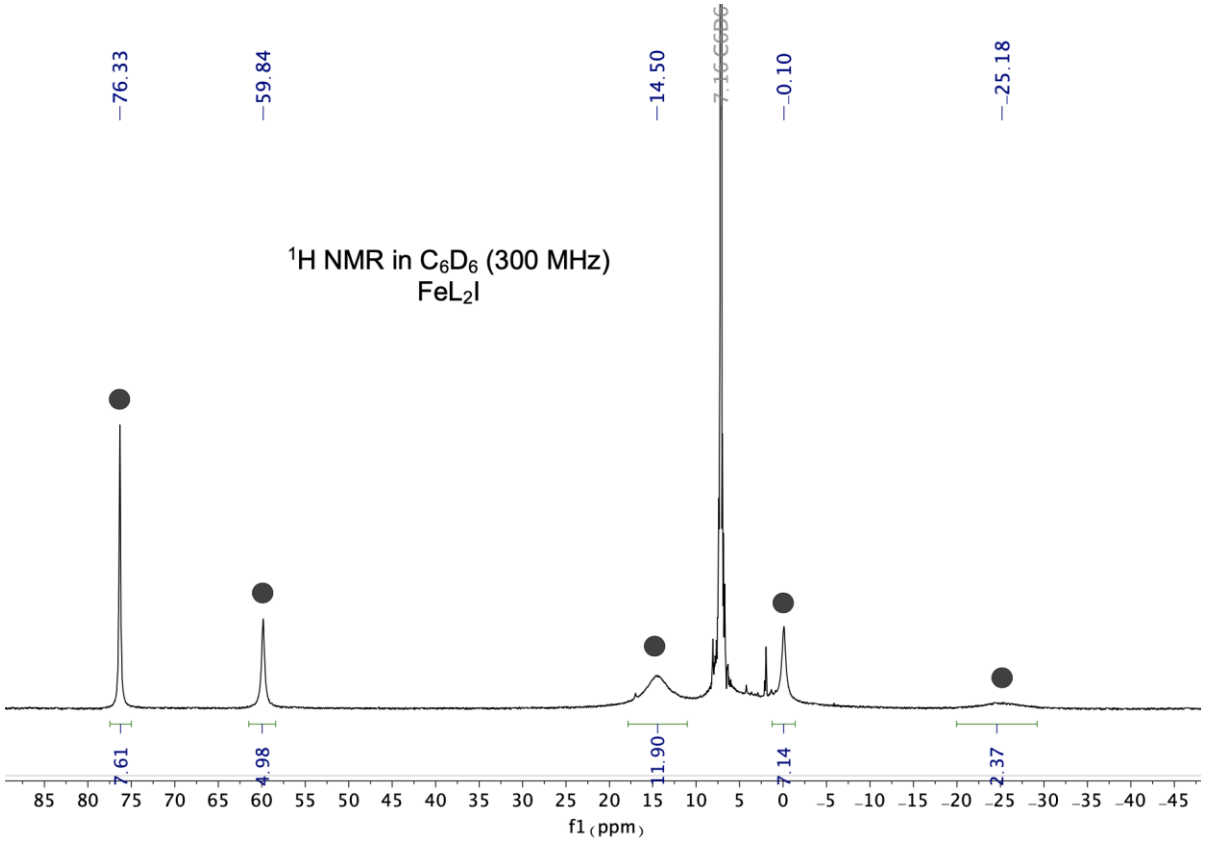

Figure 6.11. ^{1}H NMR (C_6D_6, 25 °C, 300 MHz) spectrum of FeL_2I.

6.8.5 *Synthesis of CoL_2(py)*

CoL_2 (90 mg, 0.113 mmol, 1 equiv) was massed into a 20 mL scintillation vial and dissolved in dichloromethane (5 mL). Pyridine (0.5 mL) was added and the reaction immediately changed from green to red. The solution was filtered through a Celite plug, layered with *n*-pentane (~10 mL), and left undisturbed in the glovebox freezer (−35 °C) overnight. The red crystals were collected via vacuum filtration through a fine porosity glass fritted funnel to yield CoL_2(py) (86 mg, 0.098 mmol, 87% yield). The material precipitates from benzene-d_6 and dichlormethane-d_2 so no NMR spectra was recorded.

6.8.6 *In Situ Formation of $CoL_2(CN^tBu)$*

A solution of ^{t}BuNC (92 mg/mL in C_6D_6, 11 μL, 0.0123 mmol, 1.0 equiv) was added to a solution of CoL_2 (7.5 mg, 0.0123 mmol, 1.0 equiv) in C_6D_6 (0.5 mL). ^{1}H NMR (C_6D_6, 300 MHz) δ: 59.55 ($\nu_{1/2}$ = 1809 Hz), 23.10 ($\nu_{1/2}$ = 80 Hz), 16.64 ($\nu_{1/2}$ = 103 Hz), 9.61 ($\nu_{1/2}$ = 166 Hz), 1.80 ($\nu_{1/2}$ = 16 Hz) ppm. UV-vis-*n*IR (toluene, 25 °C) 596, 639, 673, 702 nm. FT-IR ν_{CN} = 2278 cm^{-1}.

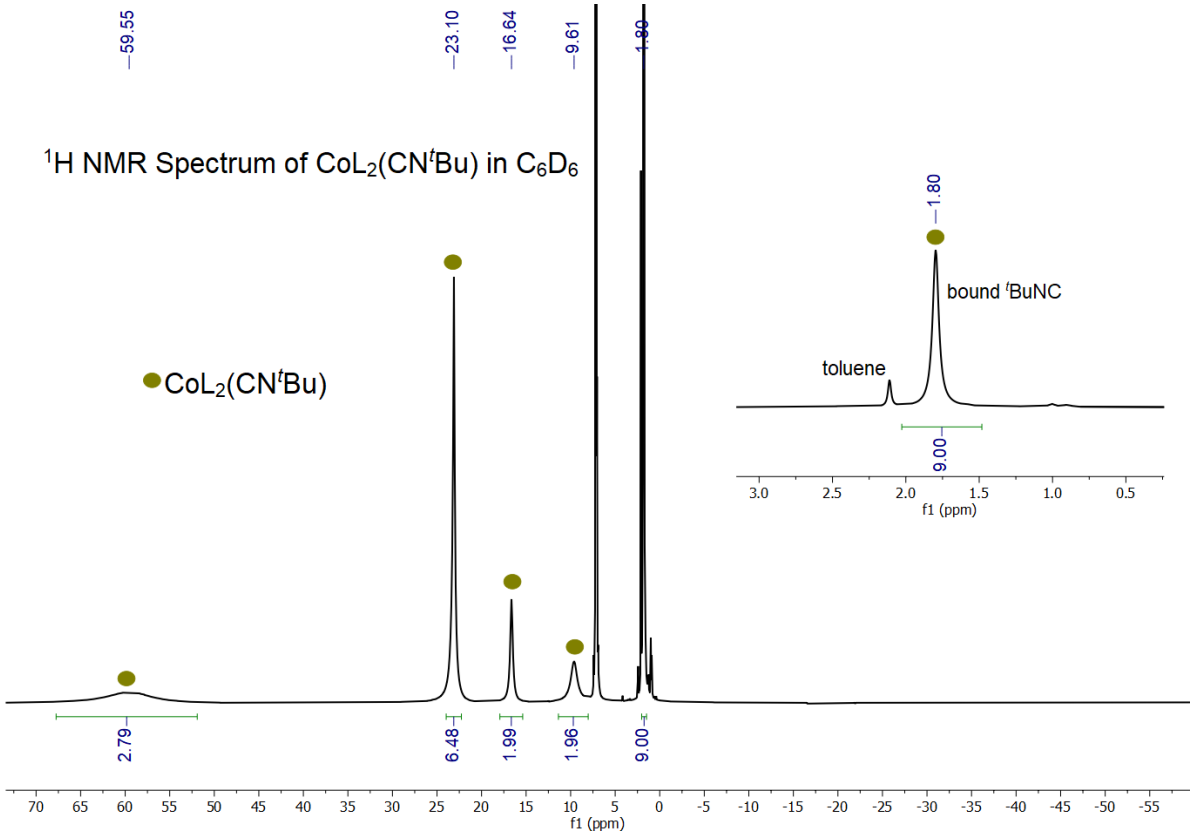

Figure 6.12. ^{1}H NMR (C_6D_6, 25 °C, 300 MHz) spectrum of $CoL_2(CN^tBu)$.

6.8.7 *Synthesis of $[CoLL']_2$*

CoL_2 (39 mg, 0.064 mmols, 1 equiv) was dissolved in dichloromethane (4 mL). A slurry of iodosobenzene (14 mg, 0.064 mmol, 1 equiv) in DCM was added. The reaction immediately changed color from green to midnight blue with the concomitant formation of a heterogenous red powder. After 5 minutes the red solids were removed via filtration through a Celite plug resulting. The filtrate was layered with *n*-pentane and stored in the glovebox freezer for two days. Crude ^{1}H

NMR of the filtrate (CD_3CN, 25 °C, 300 MHz) 70.77, 33.78, 26.66, 25.58, 23.25, 22.93, 20.87, 13.91, 12.20, −10.18, −40.68, −63.56 ppm.

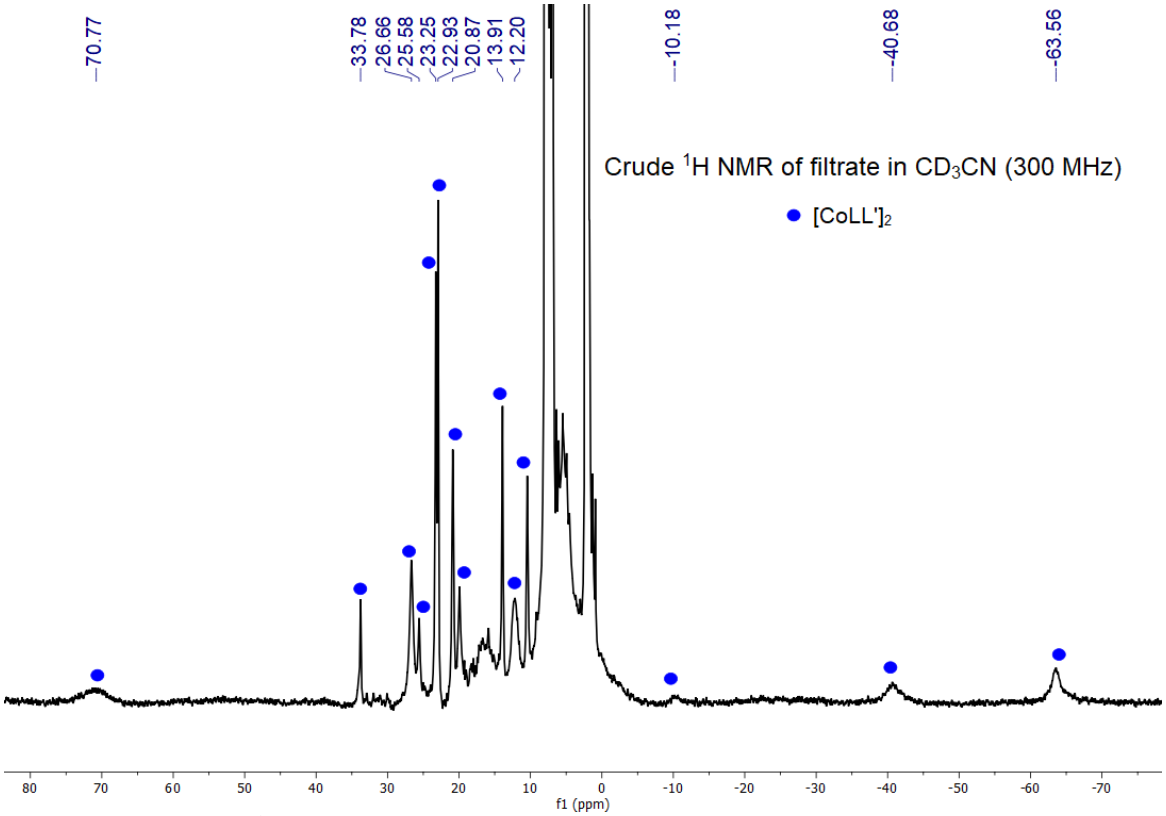

Figure 6.13. Crude ^{1}H NMR (CD_3CN, 25 °C, 300 MHz) of the filtrate from the reaction between CoL_2 and iodosobenzene.

6.8.8 *Synthesis of CoL_2(Opy)*

CoL_2 (15 mg, 0.025 mmol, 1 equiv) and pyridine-*N*-oxide (2 mg, 0.025 mmol, 1 equiv) were dissolved in benzene-d_6 (0.6 mL total) and combined in a J-young NMR tube. No color change occured however a new species by ^{1}H NMR spectroscopy was observed. No change in the ^{1}H NMR spectrum was observed after heating for 12 hours at 60 °C or after 3 hours under photolytic conditions (450 W Hg lamp). High quality single crystals were grown via vapor diffusion of *n*-pentane into the NMR sample yielding blue needle-like crystals. ^{1}H NMR (C_6D_6, 25 °C, 500 MHz)

46.19 ($\nu_{1/2}$ = 1160 Hz), 23.16 ($\nu_{1/2}$ = 29 Hz), 19.54 ($\nu_{1/2}$ = 118 Hz), 15.17 ($\nu_{1/2}$ = 161 Hz), 13.55 ($\nu_{1/2}$ = 71 Hz), 9.25 ($\nu_{1/2}$ = 37 Hz), 4.52 ($\nu_{1/2}$ = 121 Hz), −3.01 ($\nu_{1/2}$ = 127 Hz) ppm.

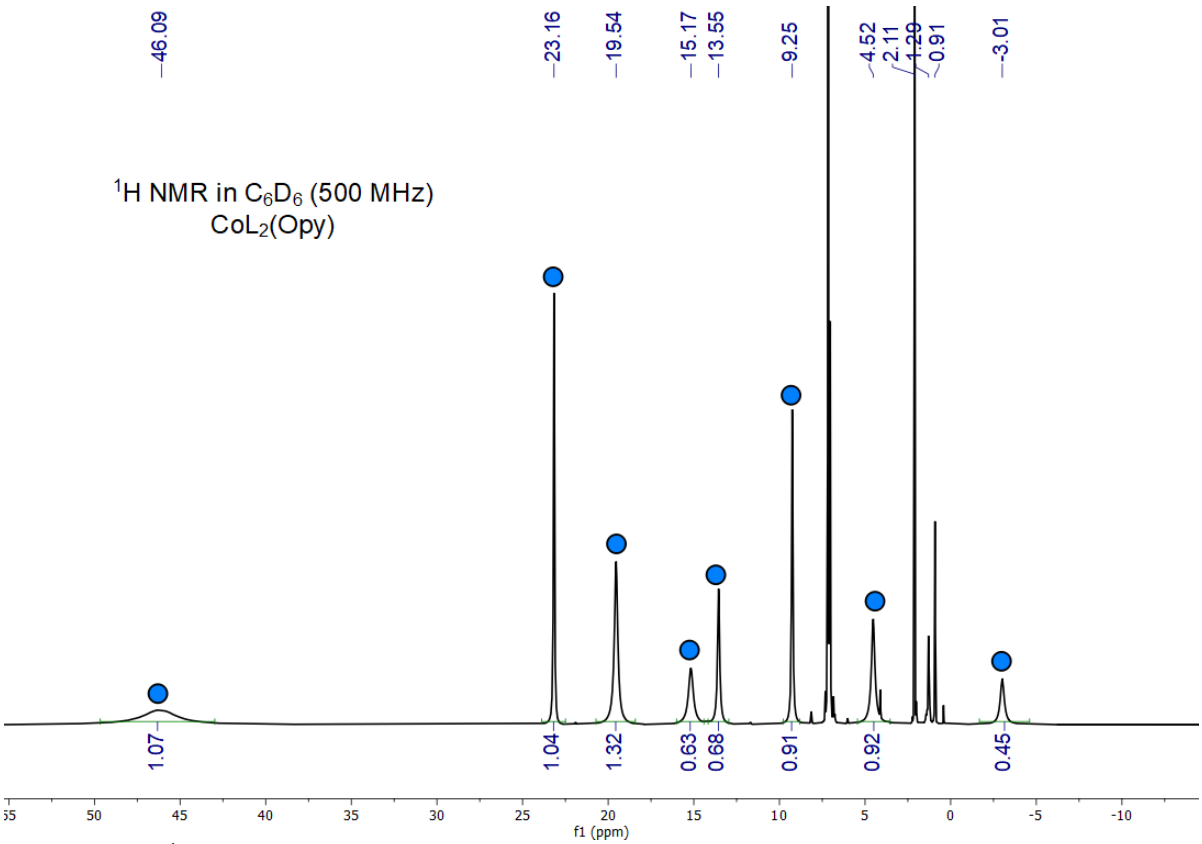

Figure 6.14. ^{1}H NMR (C_6D_6, 25 °C, 500 MHz) spectrum of CoL_2(Opy).

6.8.9 *In Situ Reaction Monitoring of FeL_2 Exposed to Air*

FeL_2 was dissolved in benzene-d_6 and a t = 0 ^{1}H NMR was acquired. The NMR sample was then exposed to air for ~1 min and then the NMR sample was shaken to ensure mixing. The reaction was monitored by ^{1}H NMR spectroscopy.

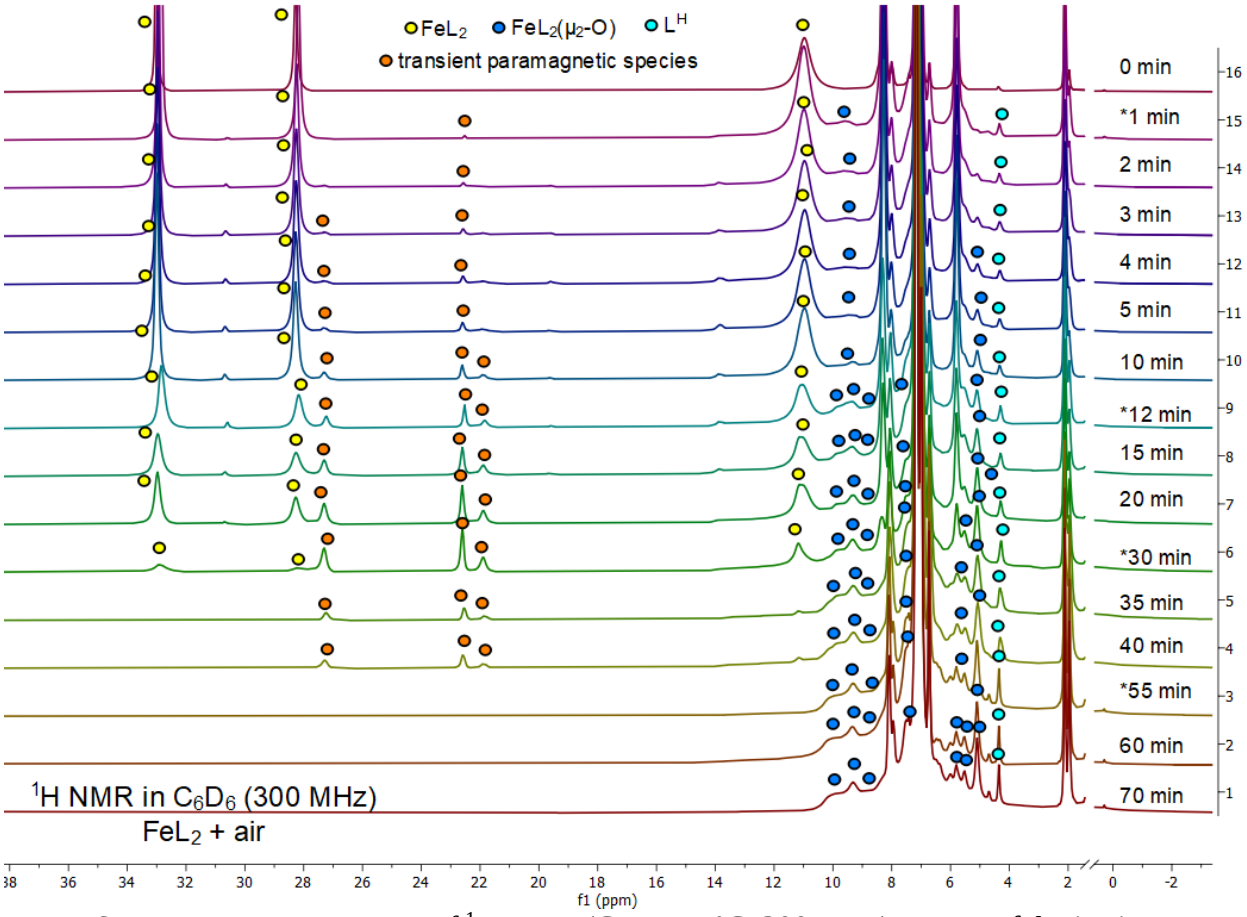

Figure 6.15. Paramagnetic region of ^{1}H NMR (C_6D_6, 25 °C, 300 MHz) spectra of the *in situ* reaction of FeL_2 exposed to air.

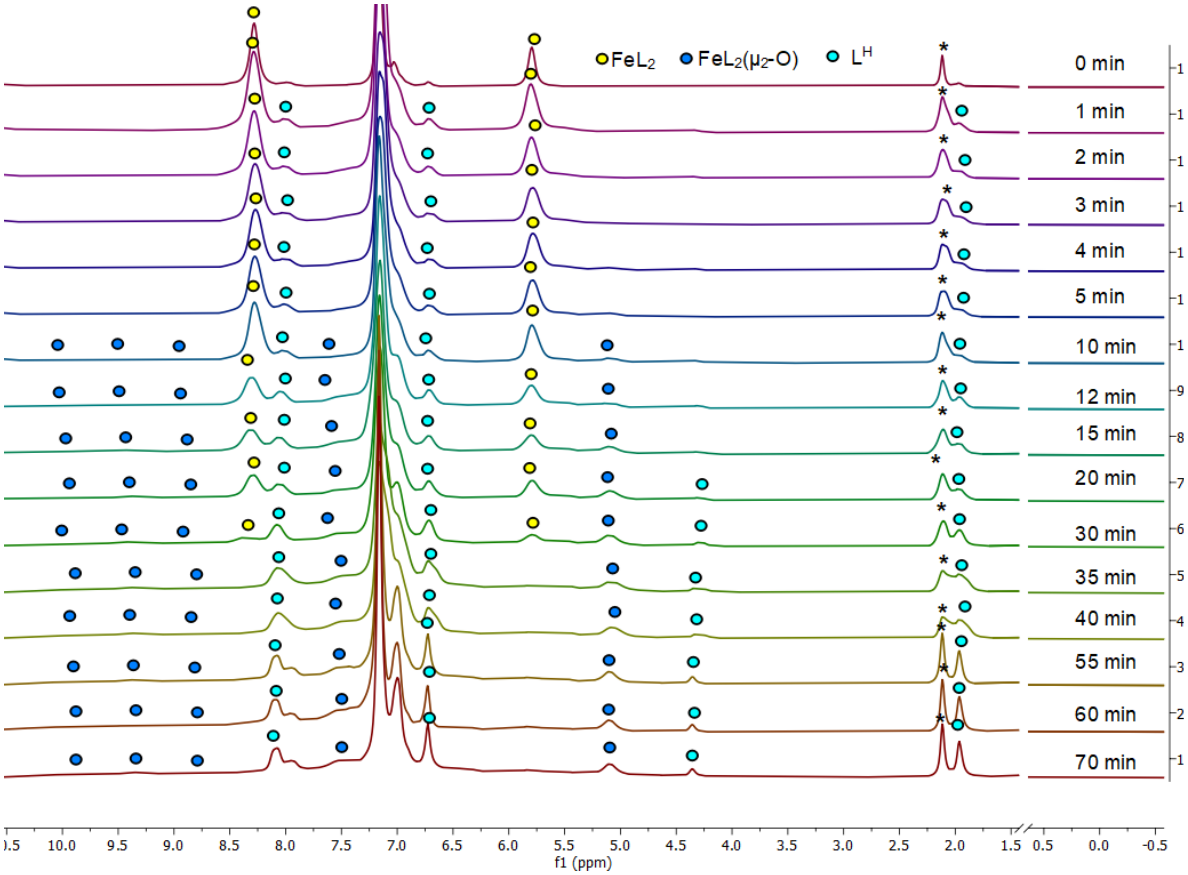

Figure 6.16. Diamagnetic region of ^{1}H NMR (C_6D_6, 25 °C, 300 MHz) spectra of the *in situ* reaction of FeL_2 exposed to air.

6.8.10 *Reaction of FeL_2 and Mesityl Nitrile Oxide*

FeL_2 (100 mg, 0.126 mmol, 1 equiv) was dissolved in toluene (8 mL) and cooled in the glovebox freezer. Mesityl nitrile oxide was added as a stock solution in toluene (0.5 M, 252 µL, 0.126 mmol, 1 equiv) dropwise. The reaction was stirred at room temperature for 30 minutes which resulted in the formation of a red precipitate. The reaction was then heated at 80 °C for 4 hours at which point the precipitate changed color from red to grey. The solids were removed via vacuum filtration through a plug of Celite.

Probing the soluble products

The filtrate was concentrated under reduced pressure to yield dark red solids which were analyzed by ^{1}H NMR spectroscopy in benzene-d_6. The resulting spectrum revealed the presence of a desymmetrized paramagnetic species, MesCN, and a small amount of L^H. ^{1}H NMR (C_6D_6, 25 °C, 300 MHz) 27.32 ($\nu_{1/2}$ = 52 Hz), 22.62 ($\nu_{1/2}$ = 24 Hz), 21.91 ($\nu_{1/2}$ = 58 Hz), 19.90 (vb), 11.19 ($\nu_{1/2}$

= 60 Hz), 9.38 (vb), 7.68 ($\nu_{1/2}$ = 42 Hz) 6.72 (MesCN Ar***H***, $\nu_{1/2}$ = 13 Hz), 6.37 ($\nu_{1/2}$ = 13 Hz), 2.19 (MesCN 2 C***H*****$_3$**, $\nu_{1/2}$ = 12 Hz), 1.85 (MesCN C***H*****$_3$**, $\nu_{1/2}$ = 12 Hz), −12.27 ($\nu_{1/2}$ = 612 Hz), −51.97 ($\nu_{1/2}$ = 1180 Hz) ppm.

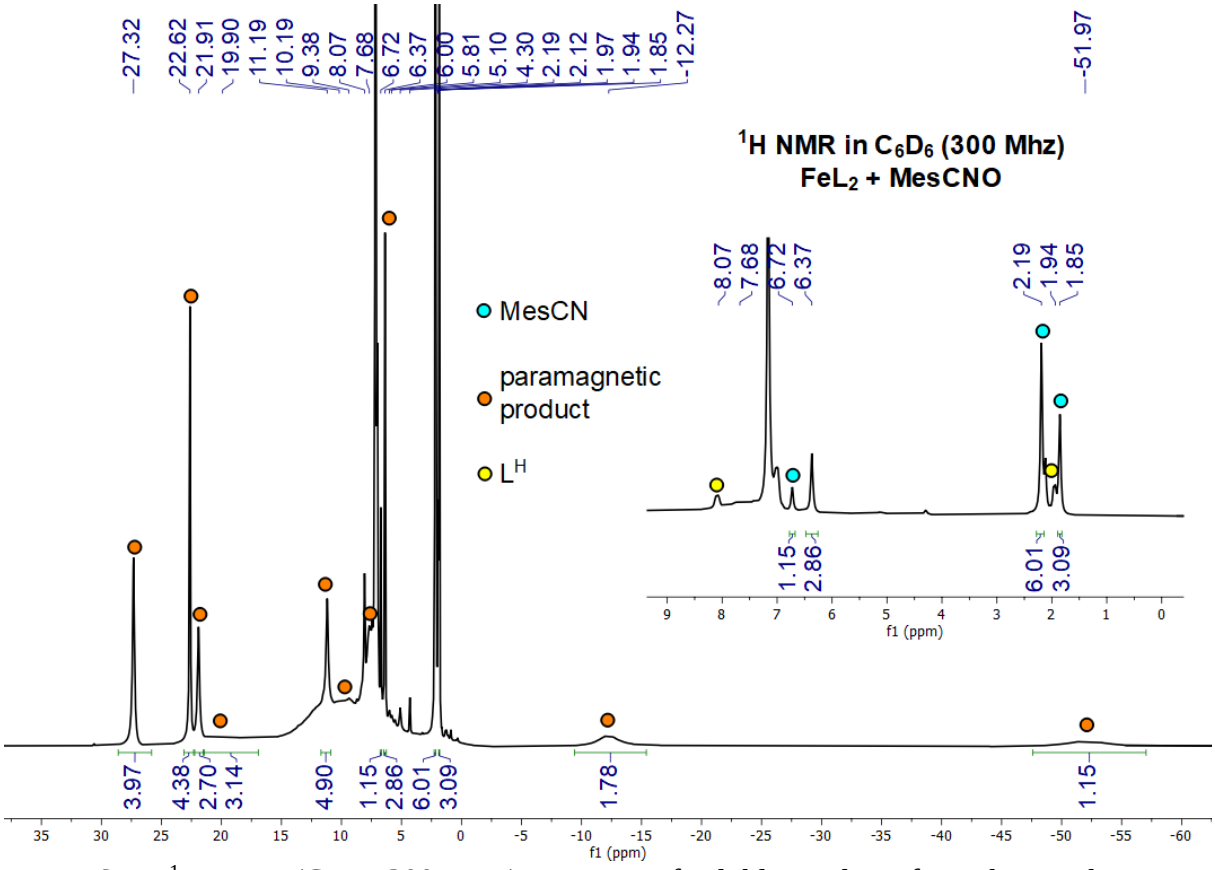

Figure 6.17. ^{1}H NMR (C_6D_6, 300 MHz) spectrum of soluble products from the stoichiometric reaction of FeL_2 and MesCNO.

Probing the identity of the precipitate

The grey solids collected on the Celite plug were stirred in a solution of excess triphenyl phosphine (99 mg, 0.378 mmol, 3 equiv) in toluene (5 mL) for 3 hours. Although beginning heterogenous over the course 3 hours the grey solids were solubilized and the reaction appeared homogenous. The solution was filtered through a pipette filter and analyzed by ^{31}P NMR spectroscopy in toluene. Two resonances are present in the ^{31}P spectrum which are attributed to PPh_3 and $SePPh_3$ integrating in a 2:1 ratio suggesting that upon treatment with 1 equivalent of MesCNO, 1 equivalent of Se is produced. ^{31}P NMR (toluene, 121 MHz, 25 °C) 35.84 (Se***P***Ph_3, 1 equiv, $J_{P\text{-}Se}$ = 379 Hz), −4.67 (***P***Ph_3, 2 equiv) ppm.

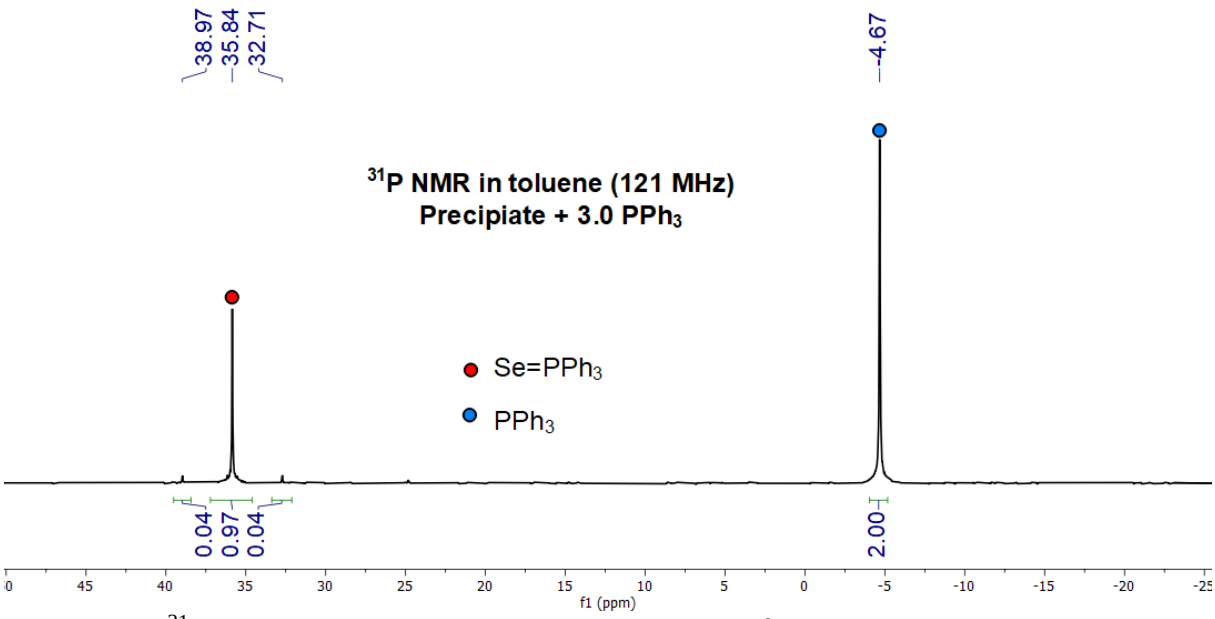

Figure 6.18. ^{31}P NMR (toluene, 121 Hz, 25 °C) spectrum of the precipitate treated with excess PPh_3 (3 equiv).

6.8.11 *In Situ Reaction of FeL_2 and Pyridine-N-Oxide*

FeL_2 (15 mg, 0.025 mmol, 1 equiv) and pyridine-*N*-oxide (2 mg, 0.025 mmol, 1 equiv) were dissolved in benzene-d6 (0.6 mL total) and combined in a J-young NMR tube. The reaction was monitored by ^{1}H NMR spectroscopy for 30 minutes at room temperature, at which point the reaction was heated to 60 °C and monitored for an addition 2 hours. Upon heating a color change for pale orange to dark red was observed.

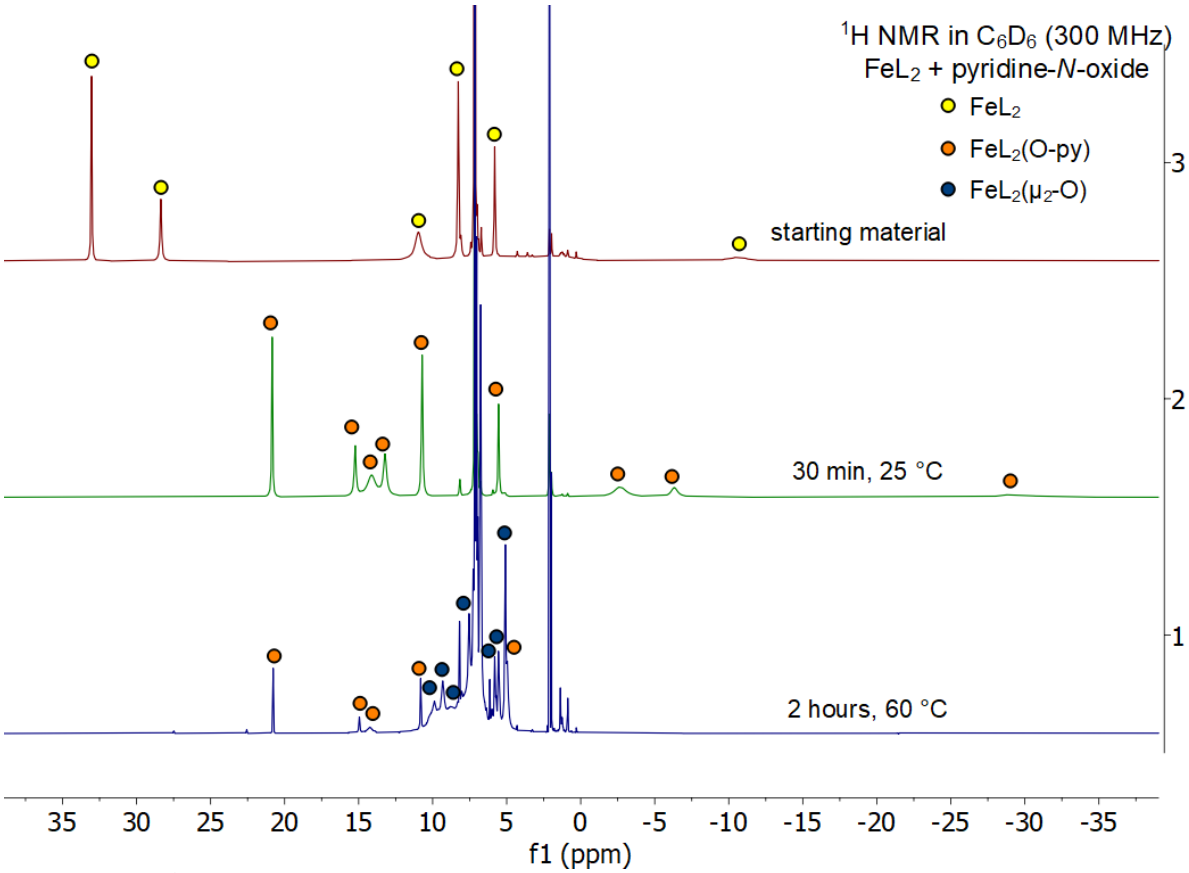

Figure 6.19. ^{1}H NMR (C_6D_6, 25 °C, 500 MHz) spectra of the *in situ* reaction of FeL_2 and pyridine-*N*-oxide.

6.8.12 *Synthesis and Isolation of $FeL_2(\mu_2\text{-}O)$*

FeL_2 (200 mg, 0.251 mmol, 1 equiv) was dissolved in toluene (5 mL) and pyridine-*N*-oxide (14 mg, 0.151 mmol, 0.6 equiv) was added as a solution in toluene (2 mL). The reaction was stirred at 60 °C for 24 hours upon which the solution turned from pale yellow to dark red. The solvent was removed under reduced pressure and the solids were triturated with *n*-pentane (3 x 3 mL). The solids were dissolved in minimal toluene (~3 mL), layered with *n*-pentane (~10 mL), and stored in the glovebox freezer overnight. The solids were then collected on a fine porosity fritted funnel via vacuum filtrate, and then washed with diethyl ether until the filtrate ran clear (~25 mL). The solids were then redissolved in minimal THF (~2 mL), layered with *n*-pentane, and left undisturbed for 18 hours in the glovebox freezer. The solids were isolated via vacuum filtration through a fine porosity fritted funnel to yield a dark red solid (62 mg, 0,039 mmol, 30% yield). UV-vis-*n*IR

(toluene, 25 °C) 350 (ε = 3,794 M^{-1} cm^{-1}) 441 (ε = 2,054 M^{-1} cm^{-1}) nm. ^1H NMR (C_6D_6, 300 MHz) 9.86, 9.33, 7.53, 6.89, 5.80, 5.53, 5.10 ppm. FT-IR ν_{FeOFe} = 852 cm^{-1}.

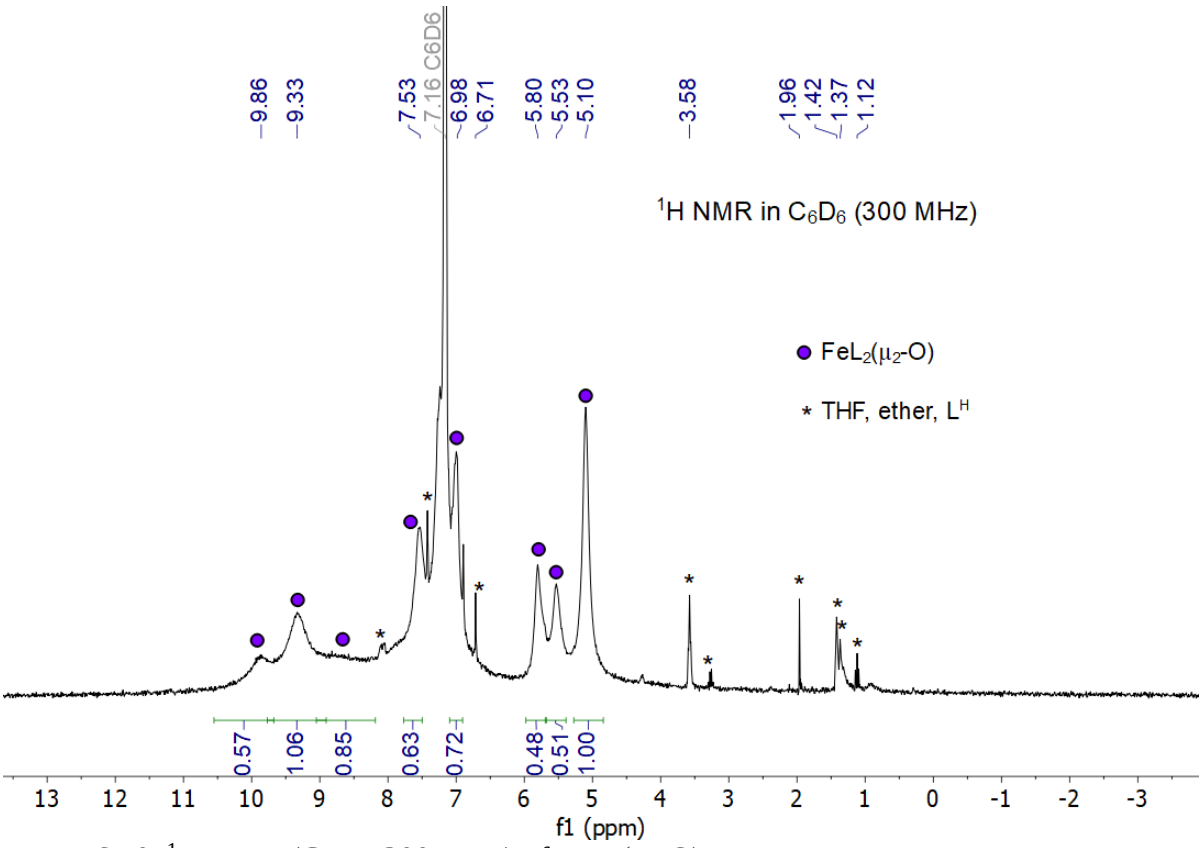

Figure 6.20. ^1H NMR (C_6D_6, 300 MHz) of $FeL_2(\mu_2\text{-}O)$.

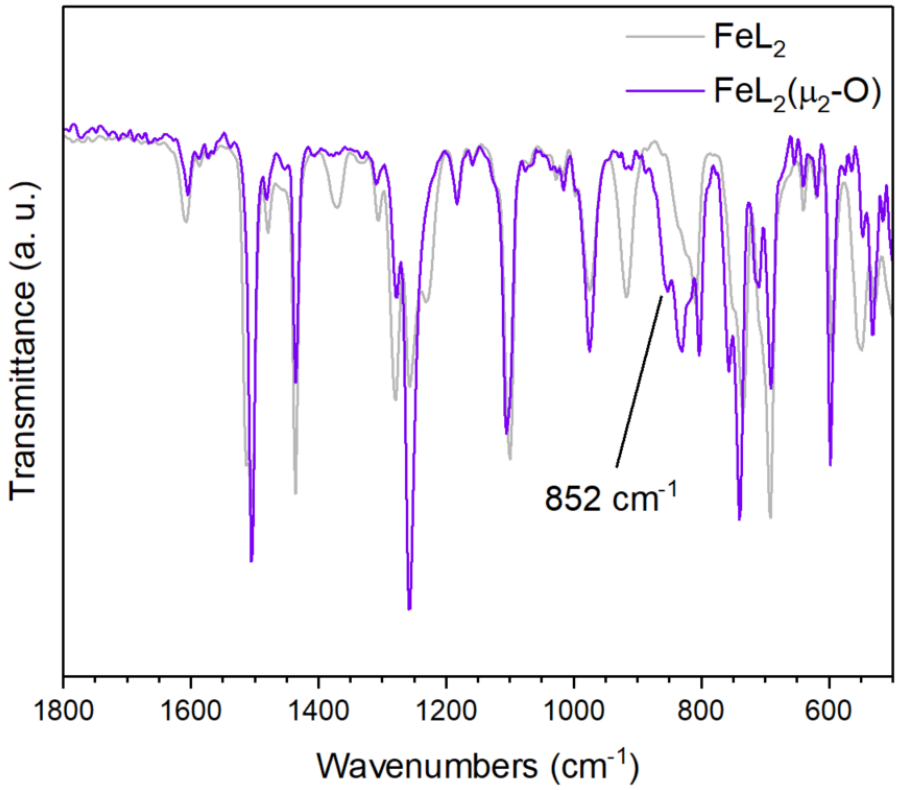

Figure 6.21. FT-IR spectrum of $FeL_2(\mu_2\text{-}O)$ and FeL_2 drop casted from benzene-d_6 between 1800 and 500 cm^{-1}. 852 cm^{-1} is the putative Fe-O-Fe asymmetric stretching frequency.

6.9 X-RAY DIFFRACTION STUDIES

Single crystals suitable for X-ray analysis were coated in deoxygenated paratone oil and mounted on a 20 µm CryoLoop™ (Hampton Research, 18 mm mount, 0.2 to 0.3 mm loop diameter). Data was collected at –173 °C on a Bruker APEX II single crystal X-ray diffractometer, with a Mo source. Data was integrated and scaled using SAINT, SADABS within the APEX2 software package by Bruker.[47] Solution by direct methods (SHELXT[48] or SIR97[49,50]) produced a complete heavy atom phasing model consistent with the proposed structure. Structures were completed by difference Fourier synthesis with SHELXL.[51–53] Scattering factors are from Waasmair and Kirfel.[54] Hydrogen atoms were placed in geometrically idealized positions and constrained to ride on their parent atoms with C–H distances in the range 0.95–1.00 Å. Isotropic thermal parameters U_{eq} were fixed such that they were $1.2U_{eq}$ of their parent atom Ueq for CHs and $1.5U_{eq}$ of their parent atom U_{eq} in case of methyl groups. All non-hydrogen atoms were refined anisotropically by full-matrix least-squares.

6.9.1 *FeL₂*

Yellow crystals were grown via vapor diffusion of *n*-pentane into a saturated solution of FeL_2 in toluene over the course of 2 days at room temperature. The asymmetric unit (shown below) contains one FeL_2 molecule and one toluene molecule distributed over two positions.

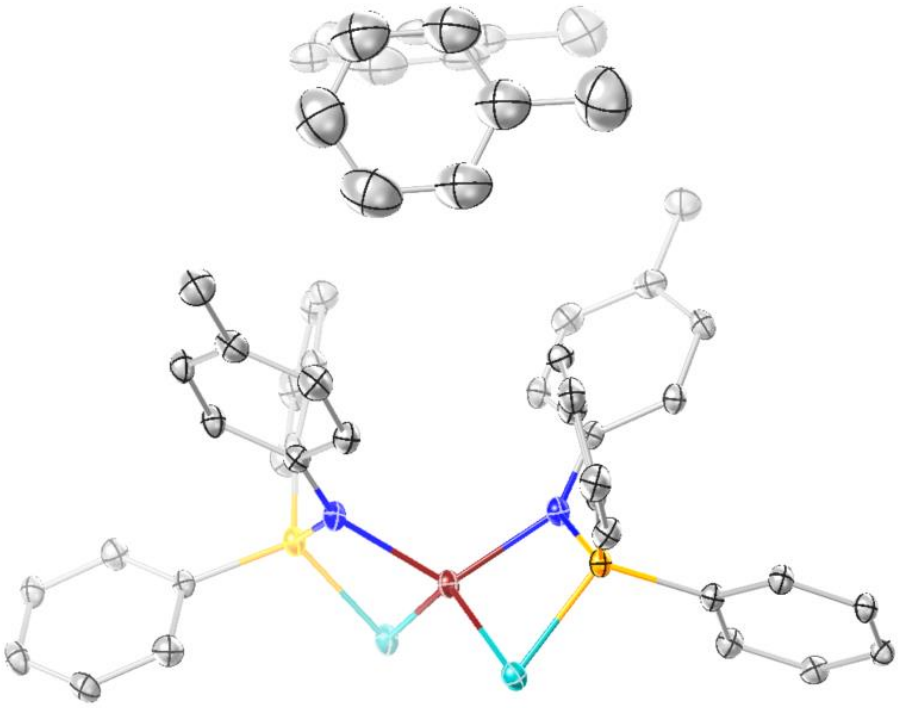

Figure 6.22. ORTEP of FeL_2 and one co-crystalized toluene molecule disordered over two positions with thermal ellipsoids shown at 50% probability level. Hydrogen atoms are omitted for clarity.

6.9.2 *CoL_2*

Green crystals were grown via vapor diffusion of n-pentane into a saturated solution of CoL_2 in toluene over the course of 2 days at room temperature. The unit cell contains four CoL_2 molecules and four toluene molecules each of which are disordered over two positions. The asymmetric unit (shown below) contains one CoL_2 molecule and two toluene molecules.

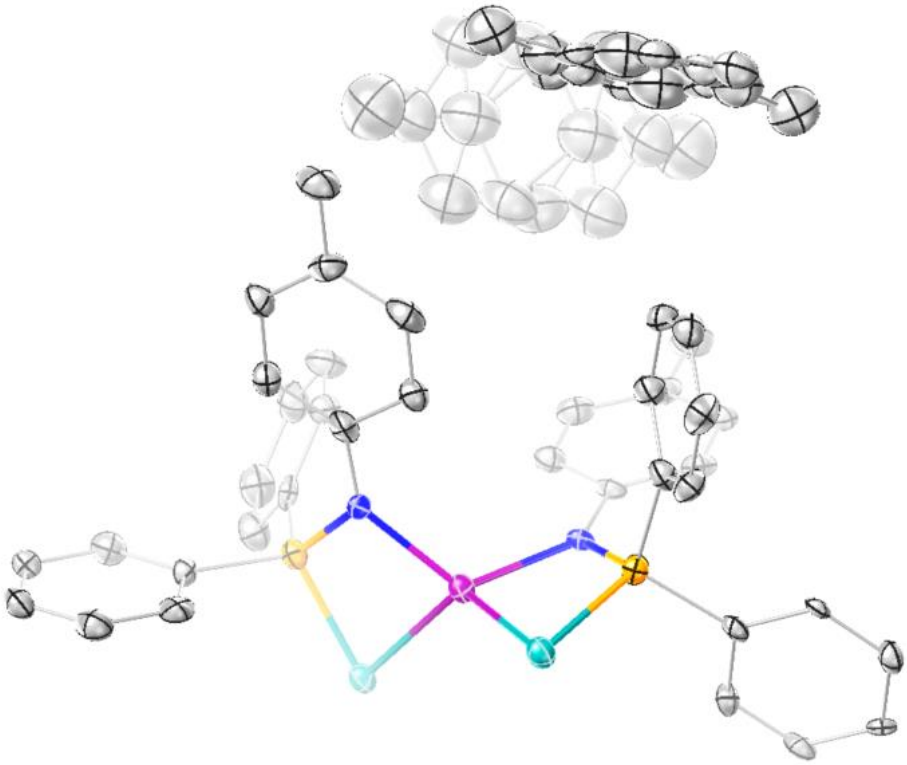

Figure 6.23. ORTEP of CoL_2 and co-crystalized toluene molecules disordered over two positions with thermal ellipsoids shown at 50% probability level. Hydrogen atoms are omitted for clarity.

6.9.3 *$CoL_2(py)$*

Red needles were grown over the course of 2 days via vapor diffusion of *n*-pentane into a saturated solution of CoL_2 in toluene with a few drops of pyridine added. The unit cell contains four $CoL_2(py)$ molecules with no disorder and no co-crystalized solvent molecules.

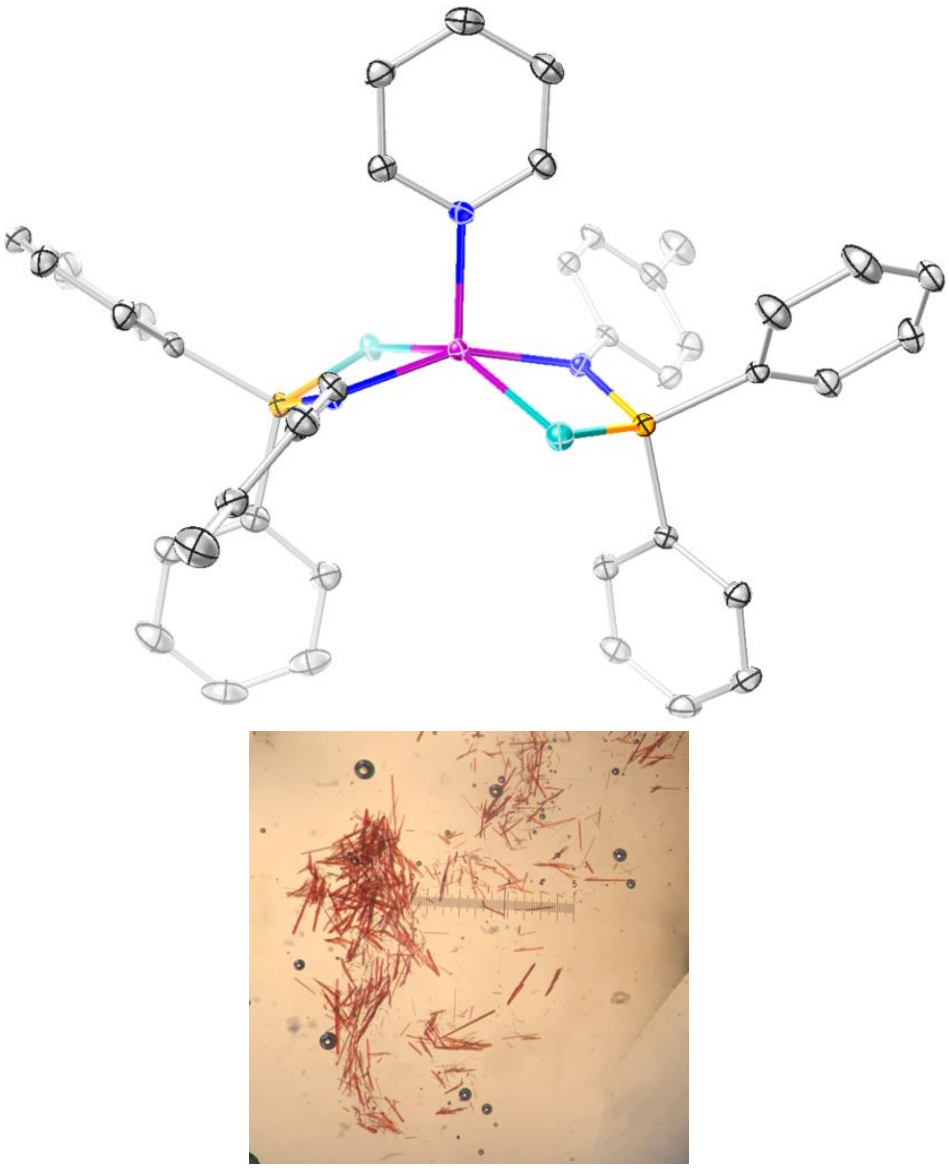

Figure 6.24. ORTEP of $CoL_2(py)$ plotted at 50% probability level with hydrogens omitted for clarity (top). Microscope image of $CoL_2(py)$ crystals (bottom).

6.9.4 *FeL_2I*

Dark red prismatic crystals were grown via vapor diffusion of *n*-pentane into a saturated solution of FeL_2I in toluene over the course of 2 days at room temperature. The asymmetric unit contains one FeL2I molecule and one disordered toluene molecule.

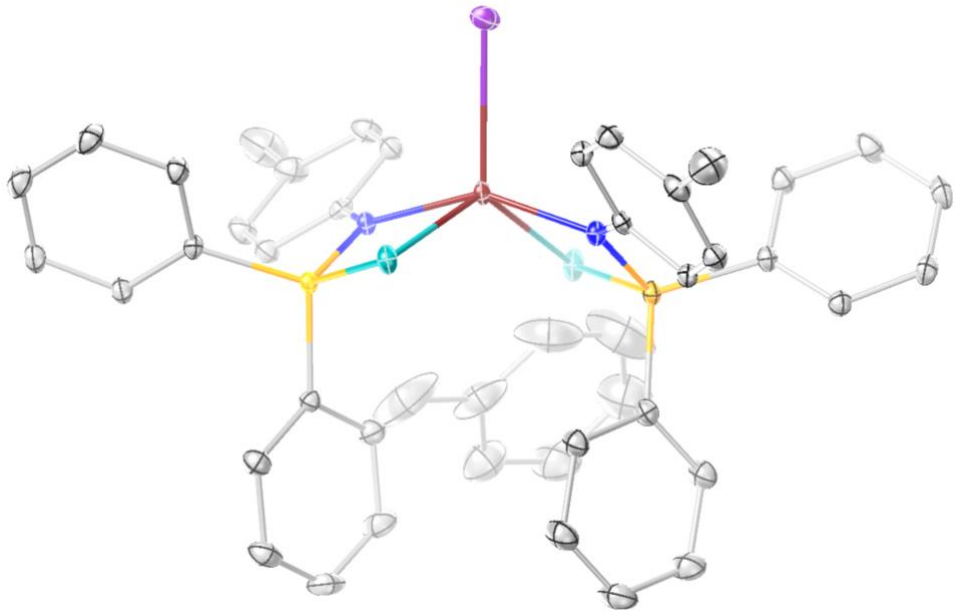

Figure 6.25. ORTEP of FeL_2I and one co-crystalized toluene molecule (disorder omitted) with thermal ellipsoids shown at 50% probability level. Hydrogen atoms are omitted for clarity.

6.9.5 *CoL_2(Opy)*

Blue needles were grown over the course of two days via the vapor diffusion of n-pentane into a saturation solution of CoL_2(Opy) in benzene-d_6 at room temperature. The asymmetric unit contains one CoL_2(Opy) unit and no disorder or co-crystallized solvent molecules. The refinement was routine.

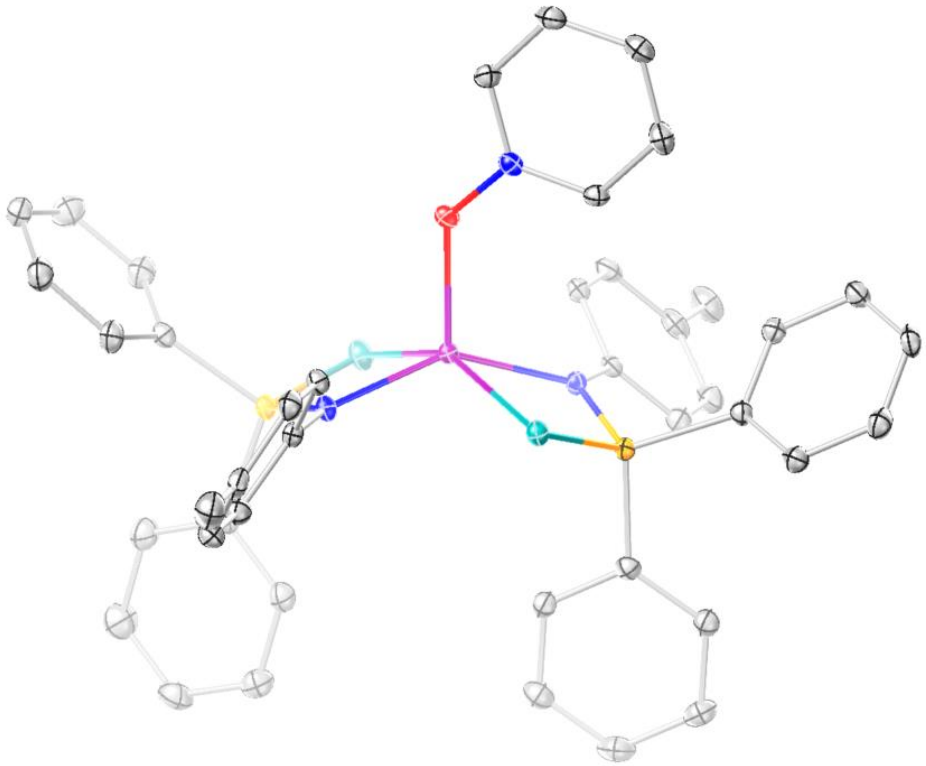

Figure 6.26. ORTEP of CoL_2(Opy) with thermal ellipsoids shown at 50% probability level. Hydrogen atoms are omitted for clarity.

6.9.6 *[CoLL']$_2$*

Blue crystals were grown over the course of 2 days from a layered solution of *n*-pentane and dichloromethane at -35 °C. With the exception of a few DELU – displacement parameter stabilizations of two tolyl moieties and ISOR for two other atoms, the structure was freely refined. One DCM was found and the contribution of heavily disordered additional pentane to the diffraction pattern was removed with SQUEEZE.[55–57]

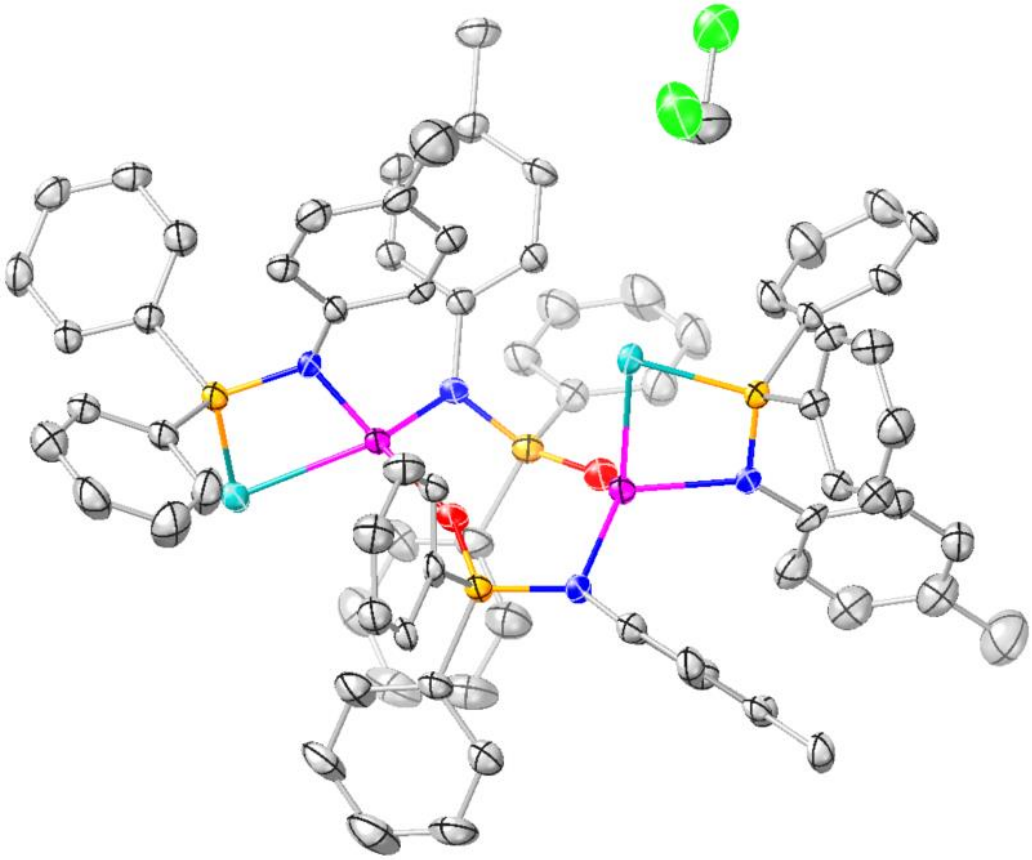

Figure 6.27. ORTEP of [CoLL']$_2$ and one co-crystalized dichloromethane molecule with thermal ellipsoids shown at 50% probability level. Hydrogen atoms are omitted for clarity.

6.9.7 *$FeL_2(\mu_2\text{-}O)$*

Dark red crystals were grown via vapor diffusion of *n*-pentane into a saturated solution of $FeL_2(\mu_2\text{-}O)$ in toluene over the course of one week at room temperature. The dimer crystallized with three toluene molecules which were mostly disordered and required some restraints to stabilize the displacement parameters. The toluene molecules were related with SAME commands and the four-fold disordered molecules required FLAT to planarize.

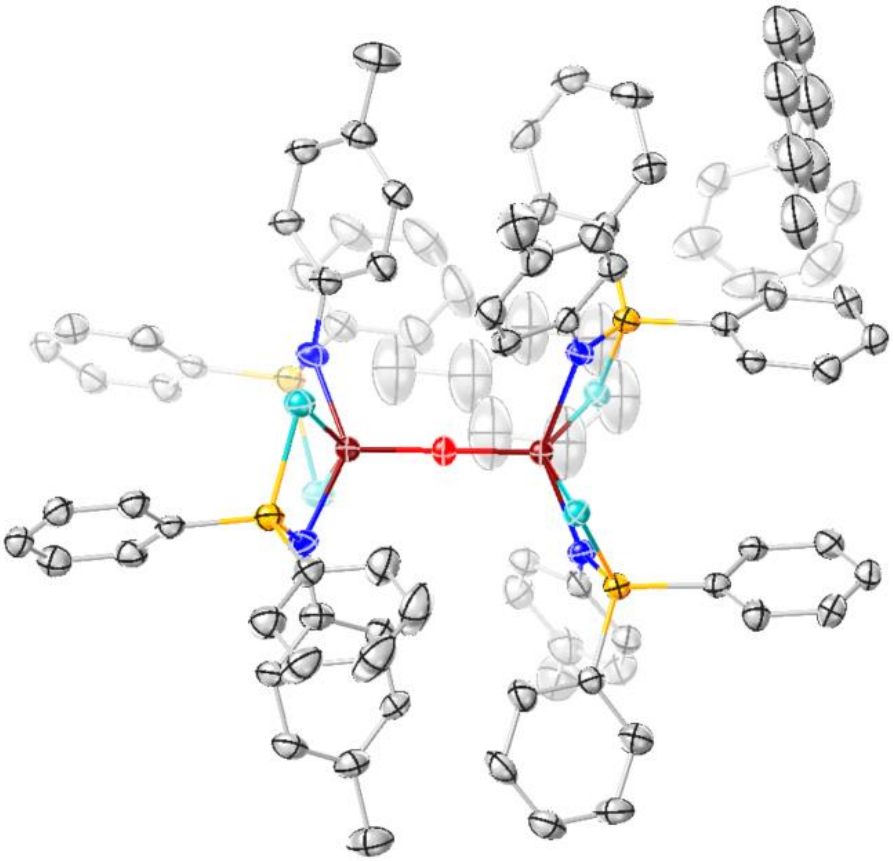

Figure 6.28. ORTEP of $FeL_2(\mu_2\text{-}O)$ and three co-crystalized toluene molecules (disorder omitted) with thermal ellipsoids shown at 50% probability level. Hydrogen atoms are omitted for clarity.

6.9.8 *X-ray Structure Tables*

Table 6.1. Crystallographic data for FeL_2, FeL_2I, and $FeL_2(\mu_2\text{-}O)$.

Compound	FeL_2 • toluene	2 FeL_2I • toluene	$FeL_2(\mu_2\text{-}O)$
CCDC number			
Empirical formula	$C_{45}H_{42}FeN_2P_2Se_2$	$C_{97}H_{92}Fe_2I_2N_4P_4Se_4$	$C_{111}H_{108}Fe_2N_4OP_4Se_4$
Formula weight	886.51	2118.96	2065.43
Temperature (°K)	100(2)	100(2)	100(2)
Wavelength (Å)	0.71073	0.71073	0.71073
Crystal system	Monoclinic	Monoclinic	Monoclinic
Space group	P $2_1/c$	P $2_1/c$	C 2/c
a (Å)	19.9536(12)	14.2731(6)	15.5700(9)
b (Å)	18.2820(10)	20.6687(8)	25.0763(13)
c (Å)	11.2339(7)	15.3137(6)	25.1124(18)
α (°)	90	90	90
β (°)	99.051(3)	92.457(2)	97.116(3)
γ (°)	90	90	90
Volume ($Å^3$)	4047.0(4)	4513.5(3)	9729.3(10)
Z	4	2	4
ρ^{calc} (g cm^{-3})	1.455	1.559	1.410
Absorption coefficient (mm^{-1})	2.284	2.737	1.912
F(000)	1800	2112	4232
Crystal size (mm^3)	0.170 x 0.150 x 0.040	0.240 x 0.180 x 0.180	0.090 x 0.080 x 0.080
Theta range for data collection (°)	1.519 to 28.600	1.656 to 28.490	1.548 to 25.464
Index ranges	$-26\le h \le 26$, $-24\le k\le 24$, $0\le l\le 15$	$-19\le h \le 19$, $-27\le k\le 27$, $-20\le l\le 20$	$-18\le h \le 18$, $-30\le k\le 30$, $0\le l\le 30$
Reflections collected	20092	4482	17728
Independent reflections	10242 [R(int) = 0.0469]	11352 [R(int) = 0.0274]	8982 [R(int) = 0.0712]
Completeness to theta = 25.000°	100.0%	99.9%	100.0%
Data / restraints / parameters	10242 / 204 / 504	11352 / 72 / 532	8982 / 158 / 557
Goodness-of-fit on F^2	0.928	1.029	0.926
Final R indices [I>2sigma(I)]	R1 = 0.0363, wR2 = 0.0735	R1 = 0.0217, wR2 = 0.0521	R1 = 0.0551, wR2 = 0.1253
R indices (all data)	R1 = 0.0718, wR2 = 0.0813	R1 = 0.0263, wR2 = 0.0540	R1 = 0.1215, wR2 = 0.1444
Largest diff. peak and hole ($e^-Å^{-3}$)	0.814 and –0.734	0.889 and –0.412	1.621 and –0.715

Table 6.2. Crystallographic data for CoL_2, $CoL_2(py)$, and $[CoLL']_2$

Compound	CoL_2 • toluene	$CoL_2(py)$	$[CoLL']_2$• DCM
CCDC number			
Empirical formula	$C_{45}H_{42}CoN_2P_2Se_2$	$C_{43}H_{39}CoN_3P_2Se_2$	$C_{77}H_{70}Cl_2Co_2N_4OP_4Se_2$
Formula weight	889.59	876.56	1553.93
Temperature (°K)	100(2)	100(2)	100(2)
Wavelength (Å)	0.71073	0.71073	0.71073
Crystal system	Monoclinic	Monoclinic	Triclinic
Space group	P $2_1/c$	P $2_1/c$	P 1
a (Å)	19.8631(14)	9.1037(6)	12.6942(12)
b (Å)	18.2281(12)	38.905(2)	15.1453(14)
c (Å)	11.2418(14)	10.8792(6)	22.622(2)
α (°)	90	90	83.006(6)
β (°)	99.061(7)	92.318(3)	78.299(5)
γ (°)	90	90	83.775(6)
Volume ($Å^3$)	4019.5(6)	3850.0(4)	4211.5(7)
Z	4	4	2
ρ^{calc} (g cm^{-3})	1.470	1.512	1.225
Absorption coefficient (mm^{-1})	2.352	2.455	1.439
F(000)	1804	1772	1584
Crystal size (mm^3)	0.170 x 0.100 x 0.030	0.250 x 0.130 x 0.110	0.580 x 0.050 x 0.030
Theta range for data collection (°)	1.525 to 25.027	1.945 to 28.345	1.360 to 25.155
Index ranges	$-23 \le h \le 23$, $-21 \le k \le 21$, $-13 \le l \le 13$	$-12 \le h \le 12$, $-51 \le k \le 51$, $-14 \le l \le 14$	$-15 \le h \le 15$, $-18 \le k \le 18$, $-27 \le l \le 27$
Reflections collected	13819	19078	30057
Independent reflections	13819 [R(int) = 0.1198]	9615 [R(int) = 0.0276]	15094 [R(int) = 0.1392]
Completeness to theta = 25.000°	99.8%	100.0%	99.9%
Data / restraints / parameters	13819 / 129 / 513	9615 / 0 / 462	15094 / 32 / 842
Goodness-of-fit on F^2	1.010	1.016	0.946
Final R indices [I>2sigma(I)]	R1 = 0.0704, wR2 = 0.1111	R1 = 0.0253, wR2 = 0.0522	R1 = 0.0699, wR2 = 0.1553
R indices (all data)	R1 = 0.1494, wR2 = 0.1351	R1 = 0.0387, wR2 = 0.0560	R1 = 0.1654, wR2 = 0.1947
Largest diff. peak and hole ($e^-Å^{-3}$)	0.813 and –0.637	0.428 and –0.362	1.222 and –0.860

Table 6.3. Crystallographic data for CoL_2(Opy).

Compound	CoL_2(Opy) • DCM
CCDC number	
Empirical formula	$C_{43}H_{39}CoN_3OP_2Se_2$
Formula weight	892.56
Temperature (°K)	100(2)
Wavelength (Å)	0.71073
Crystal system	Monoclinic
Space group	P 2_1/n
a (Å)	9.5190(4)
b (Å)	36.8473(15)
c (Å)	10.8054(5)
α (°)	90
β (°)	91.229(3)
γ (°)	90
Volume (Å^3)	3789(3)
Z	4
ρ^{calc} (g cm^{-3})	1.565
Absorption coefficient (mm^{-1})	2.498
F(000)	1804
Crystal size (mm^3)	0.100 x 0.070 x 0.060
Theta range for data collection (°)	1.105 to 28.352
Index ranges	$-12 \leq h \leq 12$, $-49 \leq k \leq 49$, $-14 \leq l \leq 14$
Reflections collected	18735
Independent reflections	9444 [R(int) = 0.0332]
Completeness to theta = 25.000°	100.0%
Data / restraints / parameters	9444 / 0 / 471
Goodness-of-fit on F^2	1.018
Final R indices [I>2sigma(I)]	R1 = 0.0325, wR2 = 0.0642
R indices (all data)	R1 = 0.0517, wR2 = 0.0703
Largest diff. peak and hole (e$^-$Å^{-3})	0.596 and –0.625

Table 6.4. Select structural parameters for CoL_2, CoL_2(py), CoL_2(Opy), FeL_2, FeL_2I, and $FeL_2(\mu_2\text{-}O)$.

Compound	Select interatomic distances (Å)									Geometry Index (τ^4 or τ^5)	Avg bond angles (°)	
	M-Se		M-N		M-X	P-Se		P-N			N-P-Se	N-M-Se
CoL_2	2.486(6)	2.493(8)	1.984(8)	1.985(8)	-	2.162(3)	2.163(4)	1.62(1)	1.63(1)	0.85	101.9	82.0
CoL_2(py)	2.678(2)	2.641(1)	2.017(2)	2.018(2)	2.074(2)	2.137(1)	2.139(3)	1.631(2)	1.628(2)	0.04	103.2	77.5
CoL_2(Opy)	2.6604(8)	2.727(2)	2.013(3)	2.049(2)	2.011(2)	2.144(3)	2.1434(8)	1.630(2)	1.626(2)	0.17	102.9	76.4
FeL_2	2.507(3)	2.500(3)	2.020(2)	2.021(2)	-	2.167(2)	2.1703(9)	1.624(3)	1.630(3)	0.72	102.6	81.7
FeL_2I	2.575(1)	2.566(1)	2.034(2)	2.028(2)	2.5880(6)	2.162(1)	2.160(1)	1.637(1)	1.638(1)	0.29	100.4	78.4
$FeL_2(\mu_2\text{-}O)$	2.640(2)	2.653(3)	2.035(4)	2.039(5)	1.755(5) 1.771(5)	2.147(3)	2.151(2)	1.613(5)	1.615(5)	0.08 0.19	102.8	77.2

6.10 REFERENCES

(1) Beinert, H. Iron-Sulfur Proteins: Ancient Structures, Still Full of Surprises. *JBIC* **2000**, *5* (1), 2–15. https://doi.org/10.1007/s007750050002.

(2) Gennari, M.; Pécaut, J.; DeBeer, S.; Neese, F.; Collomb, M.-N.; Duboc, C. A Fully Delocalized Mixed-Valence Bis-μ(Thiolato) Dicopper Complex: A Structural and Functional Model of the Biological CuA Center. *Angewandte Chemie International Edition* **2011**, *50* (25), 5662–5666. https://doi.org/10.1002/anie.201100605.

(3) Brazzolotto, D.; Wang, L.; Tang, H.; Gennari, M.; Queyriaux, N.; Philouze, C.; Demeshko, S.; Meyer, F.; Orio, M.; Artero, V.; Hall, M. B.; Duboc, C. Tuning Reactivity of Bioinspired [NiFe]-Hydrogenase Models by Ligand Design and Modeling the CO Inhibition Process. *ACS Catal.* **2018**, *8* (11), 10658–10667. https://doi.org/10.1021/acscatal.8b02830.

(4) Tang, H.; Hall, M. B. Biomimetics of [NiFe]-Hydrogenase: Nickel- or Iron-Centered Proton Reduction Catalysis? *J. Am. Chem. Soc.* **2017**, *139* (49), 18065–18070. https://doi.org/10.1021/jacs.7b10425.

(5) Huber, R. E.; Criddle, R. S. Comparison of the Chemical Properties of Selenocysteine and Selenocystine with Their Sulfur Analogs. *Archives of Biochemistry and Biophysics* **1967**, *122* (1), 164–173. https://doi.org/10.1016/0003-9861(67)90136-1.

(6) Labunskyy, V. M.; Hatfield, D. L.; Gladyshev, V. N. Selenoproteins: Molecular Pathways and Physiological Roles. *Physiol Rev* **2014**, *94* (3), 739–777. https://doi.org/10.1152/physrev.00039.2013.

(7) Lu, J.; Holmgren, A. Selenoproteins *. *Journal of Biological Chemistry* **2009**, *284* (2), 723–727. https://doi.org/10.1074/jbc.R800045200.

(8) Henthorn, J. T.; Arias, R. J.; Koroidov, S.; Kroll, T.; Sokaras, D.; Bergmann, U.; Rees, D. C.; DeBeer, S. Localized Electronic Structure of Nitrogenase FeMoco Revealed by Selenium K-Edge High Resolution X-Ray Absorption Spectroscopy. *J. Am. Chem. Soc.* **2019**, *141* (34), 13676–13688. https://doi.org/10.1021/jacs.9b06988.

(9) Onderko, E. L.; Silakov, A.; Yosca, T. H.; Green, M. T. Characterization of a Selenocysteine-Ligated P450 Compound I Reveals Direct Link between Electron Donation and Reactivity. *Nature Chem* **2017**, *9* (7), 623–628. https://doi.org/10.1038/nchem.2781.

(10) Solomon, J. B.; Tanifuji, K.; Lee, C. C.; Jasniewski, A. J.; Hedman, B.; Hodgson, K. O.; Hu, Y.; Ribbe, M. W. Characterization of a Nitrogenase Iron Protein Substituted with a Synthetic [Fe4Se4] Cluster. *Angewandte Chemie International Edition* **2022**, *61* (19), e202202271. https://doi.org/10.1002/anie.202202271.

(11) Yu, S. B.; Papaefthymiou, G. C.; Holm, R. H. Comprehensive Iron-Selenium-Thiolate Cluster Chemistry. *Inorg. Chem.* **1991**, *30* (18), 3476–3485. https://doi.org/10.1021/ic00018a018.

(12) Taut, J.; Chambron, J.-C.; Kersting, B. Fifty Years of Inorganic Biomimetic Chemistry: From the Complexation of Single Metal Cations to Polynuclear Metal Complexes by Multidentate Thiolate Ligands. *European Journal of Inorganic Chemistry* **2023**, *26* (10), e202200739. https://doi.org/10.1002/ejic.202200739.

(13) Wang, L.; Gennari, M.; Cantú Reinhard, F. G.; Padamati, S. K.; Philouze, C.; Flot, D.; Demeshko, S.; Browne, W. R.; Meyer, F.; de Visser, S. P.; Duboc, C. O2 Activation by Non-Heme Thiolate-Based Dinuclear Fe Complexes. *Inorg. Chem.* **2020**, *59* (5), 3249–3259. https://doi.org/10.1021/acs.inorgchem.9b03633.

(14) Dedushko, M. A.; Greiner, M. B.; Downing, A. N.; Coggins, M.; Kovacs, J. A. Electronic Structure and Reactivity of Dioxygen-Derived Aliphatic Thiolate-Ligated Fe-Peroxo and Fe(IV) Oxo Compounds. *J. Am. Chem. Soc.* **2022**, *144* (19), 8515–8528. https://doi.org/10.1021/jacs.1c07656.

(15) Laskavy, A.; Shimon, L. J. W.; Konstantinovski, L.; Iron, M. A.; Neumann, R. Activation of Molecular Oxygen by a Dioxygenase Pathway by a Ruthenium Bis-Bipyridine Compound with a Proximal Selenium Site. *J. Am. Chem. Soc.* **2010**, *132* (2), 517–523. https://doi.org/10.1021/ja9047027.

(16) Fuchs, M.; Kuchen, W.; Peters, W. Übergangsmetallkomplexe [Et2P(S)NR]M/n, Vierringchelate mit Thiophosphinsäure-Organylamidato-Liganden [1]. *Zeitschrift für anorganische und allgemeine Chemie* **1987**, *545* (2), 75–82. https://doi.org/10.1002/zaac.19875450209.

(17) Deeg, A.; Kuchen, W.; Langsch, D.; Mootz, D.; Peters, W.; Wunderlich, H. Nickel(II)- und Cobalt(II)-Thiophosphinsäure-N-Organylamidato-Chelate [R2P(S)NR′]2M: Magnetische Eigenschaften und Kristallstrukturen. *Zeitschrift für anorganische und allgemeine Chemie* **1991**, *606* (1), 119–132. https://doi.org/10.1002/zaac.19916060113.

(18) Song, X.; Bochmann, M. Synthesis of Phosphinochalcogenoic Amidato Complexes of Divalenttransition Metals and Their Thermolysis to Metal Selenide and Telluridephases. *J. Chem. Soc., Dalton Trans.* **1997**, No. 15, 2689–2692. https://doi.org/10.1039/A702460F.

(19) Bochmann, M.; Bwembya, G. C.; Hursthouse, M. B.; Coles, S. J. Synthesis of Phosphinochalcogenoic Amidato Complexes of Zinc and Cadmium. The Crystal and Molecular Structure of [Zn{But2P(Se)NPri}2]. *J. Chem. Soc., Dalton Trans.* **1995**, No. 17, 2813–2817. https://doi.org/10.1039/DT9950002813.

(20) Evans, D. F. The Determination of the Paramagnetic Susceptibility of Substances in Solution by Nuclear Magnetic Resonance. *J. Chem. Soc.* **1959**, No. 0, 2003–2005. https://doi.org/10.1039/JR9590002003.

(21) Yang, L.; R. Powell, D.; P. Houser, R. Structural Variation in Copper(i) Complexes with Pyridylmethylamide Ligands : Structural Analysis with a New Four-Coordinate Geometry Index, τ 4. *Dalton Transactions* **2007**, *0* (9), 955–964. https://doi.org/10.1039/B617136B.

(22) Palluccio, T. D.; Rybak-Akimova, E. V.; Majumdar, S.; Cai, X.; Chui, M.; Temprado, M.; Silvia, J. S.; Cozzolino, A. F.; Tofan, D.; Velian, A.; Cummins, C. C.; Captain, B.; Hoff, C. D. Thermodynamic and Kinetic Study of Cleavage of the N–O Bond of N-Oxides by a Vanadium(III) Complex: Enhanced Oxygen Atom Transfer Reaction Rates for Adducts of Nitrous Oxide and Mesityl Nitrile Oxide. *J. Am. Chem. Soc.* **2013**, *135* (30), 11357–11372. https://doi.org/10.1021/ja405395z.

(23) Stang, P. J.; Zhdankin, V. V. Organic Polyvalent Iodine Compounds. *Chem. Rev.* **1996**, *96* (3), 1123–1178. https://doi.org/10.1021/cr940424+.

(24) K.C. Mills. *Thermodynamic Data for Inorganic Sulphides, Selenides and Tellurides*; Butterworths: London, 1974.

(25) Mielniczak, G.; Opusiski, A. Iodosobenzene and Iodoxybenzene as Reagents for Oxygen Transfer in Organophosphorus Chemistry. *Synlett* **2001**, *2001* (04), 0505–0508. https://doi.org/10.1055/s-2001-12312.

(26) Hendrickson, J. B. Molecular Geometry. V. Evaluation of Functions and Conformations of Medium Rings. *J. Am. Chem. Soc.* **1967**, *89* (26), 7036–7043. https://doi.org/10.1021/ja01002a036.

(27) Dorofeeva, O. V.; Mastryukov, V. S.; Allinger, N. L.; Almenningen, A. The Molecular Structure and Conformation of Cyclooctane as Determined by Electron Diffraction and Molecular

Mechanics Calculations. *J. Phys. Chem.* **1985**, *89* (2), 252–257. https://doi.org/10.1021/j100248a015.

(28) Lippard, S. J. Oxo-Bridged Polyiron Centers in Biology and Chemistry. *Angewandte Chemie International Edition in English* **1988**, *27* (3), 344–361. https://doi.org/10.1002/anie.198803441.

(29) Jasniewski, A. J.; Que, L. Jr. Dioxygen Activation by Nonheme Diiron Enzymes: Diverse Dioxygen Adducts, High-Valent Intermediates, and Related Model Complexes. *Chem. Rev.* **2018**, *118* (5), 2554–2592. https://doi.org/10.1021/acs.chemrev.7b00457.

(30) Wilkins, P. C.; Wilkins, R. G. The Coordination Chemistry of the Binuclear Iron Site in Hemerythrin. *Coordination Chemistry Reviews* **1987**, *79* (3), 195–214. https://doi.org/10.1016/0010-8545(87)80003-6.

(31) Lammers, M.; Follmann, H. The Ribonucleotide Reductases — A Unique Group of Metalloenzymes Essential for Cell Proliferation. In *Inorganic Elements in Biochemistry*; Connett, P. H., Folłmann, H., Lammers, M., Mann, S., Odom, J. D., Wetterhahn, K. E., Eds.; Structure and Bonding; Springer: Berlin, Heidelberg, 1983; pp 27–91. https://doi.org/10.1007/BFb0111318.

(32) Lund, J.; Woodland, M. P.; Dalton, H. Electron Transfer Reactions in the Soluble Methane Monooxygenase of Methylococcus Capsulatus (Bath). *European Journal of Biochemistry* **1985**, *147* (2), 297–305. https://doi.org/10.1111/j.1432-1033.1985.tb08750.x.

(33) Woodland, M. P.; Dalton, H. Purification and Characterization of Component A of the Methane Monooxygenase from Methylococcus Capsulatus (Bath). *Journal of Biological Chemistry* **1984**, *259* (1), 53–59. https://doi.org/10.1016/S0021-9258(17)43620-9.

(34) Sorokin, A. B.; Tuel, A. Heterogeneous Oxidation of Aromatic Compounds Catalyzed by Metallophthalocyanine Functionalized Silicas. *New Journal of Chemistry* **1999**, *23* (5), 473–476. https://doi.org/10.1039/A901689I.

(35) Pergrale, C.; Sorokin, A. B. Designing a Dimeric Phthalocyanine-Supported Catalyst for the Selective Oxidation of Aromatic Compounds. *Comptes Rendus de l'Académie des Sciences - Series IIC - Chemistry* **2000**, *3* (10), 803–810. https://doi.org/10.1016/S1387-1609(00)01186-5.

(36) Gopakumar, G.; Belanzoni, P.; Baerends, E. J. Hydroxylation Catalysis by Mononuclear and Dinuclear Iron Oxo Catalysts: A Methane Monooxygenase Model System versus the Fenton Reagent FeIVO(H2O)52+. *Inorg. Chem.* **2012**, *51* (1), 63–75. https://doi.org/10.1021/ic200754w.

(37) Pfeiffer, P.; Breith, E.; Lübbe, E.; Tsumaki, T. Tricyclische Orthokondensierte Nebenvalenzringe. *Justus Liebigs Annalen der Chemie* **1933**, *503* (1), 84–130. https://doi.org/10.1002/jlac.19335030106.

(38) Murray, K. S. Binuclear Oxo-Bridged Iron(Iii) Complexes. *Coordination Chemistry Reviews* **1974**, *12* (1), 1–35. https://doi.org/10.1016/S0010-8545(00)80384-7.

(39) Kurtz, D. M. Jr. Oxo- and Hydroxo-Bridged Diiron Complexes: A Chemical Perspective on a Biological Unit. *Chem. Rev.* **1990**, *90* (4), 585–606. https://doi.org/10.1021/cr00102a002.

(40) Guchhait, T.; Sasmal, S.; Khan, F. S. T.; Rath, S. P. Oxo- and Hydroxo-Bridged Diiron(III) Porphyrin Dimers: Inorganic and Bio-Inorganic Perspectives and Effects of Intermacrocyclic Interactions. *Coordination Chemistry Reviews* **2017**, *337*, 112–144. https://doi.org/10.1016/j.ccr.2017.02.008.

(41) Sorokin, A. B. Recent Progress on Exploring M-Oxo Bridged Binuclear Porphyrinoid Complexes in Catalysis and Material Science. *Coordination Chemistry Reviews* **2019**, *389*, 141–160. https://doi.org/10.1016/j.ccr.2019.03.016.

(42) Weihe, H.; Güdel, H. U. Angular and Distance Dependence of the Magnetic Properties of Oxo-Bridged Iron(III) Dimers. *J. Am. Chem. Soc.* **1997**, *119* (28), 6539–6543. https://doi.org/10.1021/ja970320r.

(43) Mukherjee, R. N.; Stack, T. D. P.; Holm, R. H. Angle Dependence of the Properties of the [Fe2X]4+ Bridge Unit (X = O, S): Structures, Antiferromagnetic Coupling, and Properties in Solution. *J. Am. Chem. Soc.* **1988**, *110* (6), 1850–1861. https://doi.org/10.1021/ja00214a030.

(44) Reem, R. C.; McCormick, J. M.; Richardson, D. E.; Devlin, F. J.; Stephens, P. J.; Musselman, R. L.; Solomon, E. I. Spectroscopic Studies of the Coupled Binuclear Ferric Active Site in Methemerythrins and Oxyhemerythrin: The Electronic Structure of Each Iron Center and the Iron-Oxo and Iron-Peroxide Bonds. *J. Am. Chem. Soc.* **1989**, *111* (13), 4688–4704. https://doi.org/10.1021/ja00195a024.

(45) Passarelli, V.; Benetollo, F. Reactivity of Novel N,N'-Diphosphino-Silanediamine-Based Rhodium(I) Derivatives. *Inorg. Chem.* **2011**, *50*, 9958–9967. https://doi.org/10.1021/ic2004408.

(46) Barybin, M. V.; Diaconescu, P. L.; Cummins, C. C. Coordination Chemistry of a Chelating Amidoximato Ligand. *Inorg. Chem.* **2001**, *40* (12), 2892–2897. https://doi.org/10.1021/ic0100370.

(47) *Bruker APEX2 (Version 2.1-4), SAINT (Version 7.34A), SADABS (Version 2007/4), 2007 BrukerAXS Inc, Madison, Wisconsin, USA.*

(48) *Sheldrick, G.M. Acta Cryst. 2015 A71, 3-8.*

(49) *Altomare, A.; Burla, C.; Camalli, M.; Cascarano, G. L.; Giacovazzo, C.; Guagliardi, A.; Moliterni, A.G.G.; Polidori, G.; Spagna, R. J. Appl. Crystallogr., 1999, 32, 115-119.*

(50) *Altomare, A.; Cascarano, G. L.; Giacovazzo, C.; Guagliardi, A. J. Appl. Crystallogr., 1993, 26, 343-350.*

(51) *Sheldrick, G. M. SHELXL-97, Program for the Refinement of Crystal Structures, 1997, University of Göttingen, Germany.*

(52) *Sheldrick, G. M. Acta Cryst. 2015, C71, 3–8.*

(53) *Mackay, S.; Edwards, C.; Henderson, A.; Gilmore, C.; Stewart, N.; Shankland, K.; Donald, A. MaXus: A Computer Program for the Solution and Refinement of Crystal Structures from Diffraction Data, 1997, University of Glasgow, Scotland.*

(54) *Waasmaier, D.; Kirfel, A. Acta Cryst., 1995, 51, 416-430.*

(55) Spek, A. L. Single-Crystal Structure Validation with the Program PLATON. *J Appl Cryst* **2003**, *36* (1), 7–13. https://doi.org/10.1107/S0021889802022112.

(56) van der Sluis, P.; Spek, A. L. BYPASS: An Effective Method for the Refinement of Crystal Structures Containing Disordered Solvent Regions. *Acta Cryst A* **1990**, *46* (3), 194–201. https://doi.org/10.1107/S0108767389011189.

(57) Spek, A. L. Structure Validation in Chemical Crystallography. *Acta Cryst D* **2009**, *65* (2), 148–155. https://doi.org/10.1107/S090744490804362X.

APPENDIX A: DFT OPTIMIZED GEOMETRY COORDINATES

1-H_2				**1**-Fe			
0 1				0 5			
C	1.36329623	4.65873952	0.85798495	C	2.44766761	-3.61503408	-1.87451731
C	0.16862869	5.30575076	0.46674976	C	3.52988782	-3.23862379	-2.69685204
H	-0.45275559	4.86645113	-0.33085662	H	4.23002531	-2.46782601	-2.34222525
C	-0.24412870	6.48658598	1.10362000	C	3.71312612	-3.84297905	-3.95248529
H	-1.17170703	6.98474878	0.78081060	H	4.56645766	-3.54367680	-4.58071195
C	0.51246257	7.02210849	2.16107079	C	2.81740788	-4.82754963	-4.40134409
H	0.18404486	7.94406099	2.66549332	H	2.96658182	-5.30660602	-5.38150217
C	1.68065973	6.36549059	2.57868865	C	1.72292560	-5.19163591	-3.59706305
H	2.27232175	6.76783633	3.41569282	H	1.00789065	-5.95181019	-3.94844987
C	2.10517322	5.19089728	1.93238484	C	1.53081705	-4.58103453	-2.34727437
H	3.01722376	4.67944486	2.27149396	H	0.65699305	-4.85504726	-1.73685197
C	2.48109132	3.63405173	-1.64022359	C	2.28807713	-4.16160143	1.00464083
C	2.02654163	4.80748750	-2.27720737	C	2.41054928	-5.52735691	0.67493303
H	1.32110303	5.47736448	-1.76585664	H	2.45970055	-5.84107546	-0.37773281
C	2.48237726	5.14510176	-3.56341455	C	2.49142806	-6.50160996	1.68557392
H	2.11821785	6.06706854	-4.04291415	H	2.58654905	-7.56340157	1.40922714
C	3.40256638	4.31928523	-4.22914575	C	2.46574635	-6.12419259	3.03694131
H	3.76368736	4.58818641	-5.23393956	H	2.53620988	-6.88750897	3.82735049
C	3.86633248	3.15152860	-3.59899583	C	2.35722265	-4.76347715	3.37426154
H	4.59639748	2.50164816	-4.10584132	H	2.34671454	-4.45567592	4.43124885
C	3.40760967	2.81033734	-2.31760812	C	2.26098894	-3.79158401	2.36794364
H	3.77628264	1.89555134	-1.83182116	H	2.16976521	-2.72686964	2.63731904
C	4.65186968	3.11914466	0.79538013	C	-2.08347031	-2.07575916	4.75284257
C	4.99456150	4.39317923	0.28650462	H	-2.55375073	-1.88137363	5.74097783
H	4.21706499	5.05170553	-0.12269279	H	-2.89821717	-2.36873295	4.05839196
C	6.32941557	4.82822370	0.29973778	C	-1.04703953	-3.19667124	4.87455570
H	6.56143376	5.82617589	-0.10673318	H	-0.54076160	-3.39134672	3.90751703
C	7.37239371	4.03581381	0.81760557	H	-1.53657183	-4.14176493	5.18870613
C	7.01970369	2.76576487	1.32665381	H	-0.27061785	-2.96352976	5.63088927
H	7.80223699	2.10855626	1.74022174	C	-2.73321065	0.74966310	4.79746462
C	5.69696367	2.31141505	1.31381931	H	-2.46819151	1.74057415	4.37327261

H	5.45693199	1.31169028	1.71015198
C	8.80719385	4.51230915	0.83034577
H	8.89992438	5.53350865	0.41086836
H	9.46648901	3.84553529	0.23412139
H	9.22384833	4.53442372	1.86002927
C	2.44581737	-3.49268898	2.02909746
C	3.49637862	-3.00442173	2.83419529
H	4.18281252	-2.25110801	2.42132533
C	3.66615006	-3.47228956	4.14842560
H	4.49511369	-3.08399939	4.76040179
C	2.78869167	-4.43351917	4.67681454
H	2.92732658	-4.80632703	5.70358696
C	1.72894230	-4.91382838	3.88759645
H	1.02900745	-5.65938367	4.29594267
C	1.55138036	-4.44033717	2.57722816
H	0.69988755	-4.80300014	1.98297534
C	2.26460344	-4.29072539	-0.79318828
C	2.38952047	-5.62771956	-0.36366200
H	2.45323004	-5.86208650	0.70874514
C	2.45239141	-6.67514078	-1.30038910
H	2.54905904	-7.71376299	-0.94746652
C	2.40621795	-6.39899243	-2.67535858
H	2.46113904	-7.21950245	-3.40750368
C	2.29555118	-5.06683051	-3.11234772
H	2.26594717	-4.83946159	-4.18916874
C	2.21639283	-4.02323294	-2.17969491
H	2.11732660	-2.98220412	-2.52433840
C	4.95841192	-2.48524369	-0.32418190
C	5.42567084	-3.75686459	0.07990649
H	4.77528629	-4.42495806	0.65872268
C	6.72590528	-4.17371799	-0.24613031
H	7.05687998	-5.17234119	0.08290339
C	7.61649746	-3.35679009	-0.96967414
C	7.14385439	-2.08442833	-1.36211594
H	7.80632112	-1.40861014	-1.92764594
C	5.84782993	-1.65703514	-1.05590006
H	5.50809200	-0.66068723	-1.38128000
H	-3.68418696	0.45937700	4.30202567
C	-2.90048270	0.83029811	6.31801022
H	-3.17529915	-0.14485442	6.77006226
H	-3.71081343	1.54346830	6.57707497
H	-1.98087670	1.18638370	6.82458101
C	0.03475874	-0.13176037	5.17951885
H	-0.23988522	-0.43656651	6.21352734
H	0.80877757	-0.84578610	4.82903074
C	0.58483549	1.29612387	5.15351930
H	0.86953732	1.60335052	4.12744298
H	1.49195276	1.37378796	5.78676066
H	-0.14832544	2.03670570	5.53167664
C	-3.42099574	-4.70709749	-1.27338911
H	-2.38990388	-4.91538954	-0.91866494
H	-4.06254738	-5.54349147	-0.92097326
C	-3.46020974	-4.61977468	-2.80217091
H	-4.49144971	-4.48577453	-3.18656149
H	-3.06045476	-5.55193000	-3.25239028
H	-2.83929762	-3.77903976	-3.17266491
C	-5.62055280	-2.82846998	-1.10898873
H	-5.41023691	-2.47388106	-2.13929754
H	-6.14800065	-3.80352753	-1.20243875
C	-6.48521890	-1.80562098	-0.36983323
H	-6.74925972	-2.13905264	0.65432413
H	-7.43329815	-1.62587362	-0.91768388
H	-5.95387525	-0.83713767	-0.27780043
C	-4.37160081	-3.87102250	1.33728795
H	-3.40493106	-4.25287525	1.73007779
H	-4.61673372	-2.98664400	1.96264102
C	-5.46987958	-4.93470823	1.43297501
H	-6.45792733	-4.55159459	1.10623454
H	-5.58476968	-5.27398041	2.48364124
H	-5.24401846	-5.83678098	0.82815327
C	-5.83941464	2.49615545	-0.41475272
H	-6.07039310	1.46872561	-0.06360078
H	-6.54809807	3.18020694	0.09987389
C	-6.01737039	2.59943426	-1.93127663

C	9.01209874	-3.81686934	-1.32533196
H	9.26292844	-4.77539433	-0.82943460
H	9.77952370	-3.07214153	-1.02609499
H	9.12655248	-3.97089109	-2.42039512
P	-0.63048717	-0.01276497	-4.18151301
C	0.08175175	1.53998836	-4.95552068
H	0.88660671	1.86401119	-4.26324400
H	0.57414103	1.23553097	-5.90412233
C	-0.89436587	2.68949507	-5.22052137
H	-0.34658889	3.56934534	-5.61633907
H	-1.67023203	2.41972803	-5.96542296
H	-1.40171347	3.01002492	-4.28874537
C	0.58929265	-1.30442360	-4.78131915
H	1.55107548	-1.01341016	-4.30703461
H	0.28323257	-2.24670971	-4.28079205
C	0.75460866	-1.50915335	-6.29051782
H	1.53535993	-2.27238160	-6.49086840
H	-0.17841741	-1.86543983	-6.77239921
H	1.06956879	-0.58407943	-6.81566676
C	-2.13657671	-0.32614961	-5.24484402
H	-2.87251891	0.45200556	-4.95474113
H	-1.85382398	-0.12830176	-6.30231656
C	-2.75311370	-1.71761453	-5.08812202
H	-3.68581685	-1.80331623	-5.68317733
H	-2.06711359	-2.52087999	-5.42573191
H	-3.00556426	-1.91518558	-4.02758129
P	-3.79639670	-3.15172117	-0.16129727
C	-3.29028007	-4.78362808	0.60688440
H	-3.09584257	-4.55234265	1.67533789
H	-4.17920268	-5.45099658	0.57765865
C	-2.07556235	-5.46951699	-0.02100674
H	-1.81984073	-6.39485458	0.53574683
H	-2.25665311	-5.75828203	-1.07622673
H	-1.18728467	-4.80651215	-0.00926127
C	-4.28861632	-3.63676398	-1.89902393
H	-4.68436838	-2.70437469	-2.35362776
H	-3.33027199	-3.83505310	-2.42341631
H	-5.83787960	3.62821110	-2.30380522
H	-7.05352378	2.32294888	-2.21709992
H	-5.32865207	1.91276679	-2.46289306
C	-4.54056924	3.21531981	2.06047683
H	-4.90611997	2.24446676	2.45803922
H	-3.55861428	3.38430353	2.54965740
C	-5.51497030	4.35226410	2.38473027
H	-6.51893903	4.19638155	1.93965220
H	-5.66017580	4.43057943	3.48251606
H	-5.14419245	5.33758987	2.03616741
C	-3.79618244	4.56185925	-0.43822849
H	-3.59818591	4.40472129	-1.51880549
H	-4.74025527	5.14559455	-0.36358714
C	-2.62991397	5.31913117	0.20186631
H	-2.80533375	5.52810638	1.27680939
H	-2.47217178	6.29228077	-0.30676831
H	-1.68853660	4.73956004	0.11566151
C	-2.59977409	1.09157165	-5.03474140
H	-2.45159943	1.03544235	-6.13513550
H	-3.38700652	0.35280351	-4.77608570
C	-3.02672250	2.49921389	-4.61579981
H	-3.15070782	2.56567838	-3.51653044
H	-3.99464076	2.76992964	-5.08587379
H	-2.28470863	3.26703708	-4.91527044
C	0.26653970	1.64440987	-4.83977644
H	0.09953323	2.57711647	-4.26043473
H	1.23052461	1.23842890	-4.46687536
C	0.33119613	1.92382894	-6.34468477
H	0.52609898	1.00604839	-6.93600320
H	1.15446915	2.63372987	-6.56929591
H	-0.60309067	2.37989593	-6.73074593
C	-0.75338961	-1.06955333	-5.28908104
H	-1.53189966	-1.79400328	-4.96910919
H	-0.98574230	-0.79171811	-6.34057518
C	0.63875400	-1.69568971	-5.18635775
H	1.43148643	-1.01195126	-5.55182226
H	0.69467965	-2.62129561	-5.79437599

C	-5.26850498	-4.80160048	-2.07095814
H	-5.48207325	-4.97038289	-3.14717973
H	-4.86610842	-5.75329734	-1.66805804
H	-6.24170106	-4.61230982	-1.57348272
C	-5.44494750	-2.91862427	0.69725387
H	-5.95691670	-3.90520326	0.72681959
H	-5.19029083	-2.65383242	1.74486552
C	-6.34955405	-1.85024034	0.08188865
H	-7.25448577	-1.69445473	0.70488049
H	-5.81748066	-0.88187440	0.00470476
H	-6.69114664	-2.12937811	-0.93577894
P	-4.08709917	2.82549669	-0.05754999
C	-4.12835751	4.03650530	-1.48644787
H	-4.90606993	4.79848656	-1.26076034
H	-3.14794616	4.55642307	-1.45619405
C	-4.35890057	3.41355716	-2.86471988
H	-4.27689015	4.18200196	-3.66085187
H	-3.60986604	2.62323437	-3.07302665
H	-5.36374541	2.95195325	-2.95014539
C	-5.80285849	2.08300187	-0.09057219
H	-5.80427499	1.40447422	-0.96943831
H	-5.84095883	1.41533258	0.79555185
C	-7.00072972	3.03731025	-0.12041473
H	-7.95107571	2.46368057	-0.13219953
H	-7.03383304	3.70034815	0.76817787
H	-7.00243622	3.68455359	-1.02109985
C	-4.17696851	4.03422101	1.37085277
H	-3.19436199	4.55124140	1.37661433
H	-4.94535852	4.79740965	1.11845717
C	-4.45753828	3.41235522	2.74062021
H	-4.41293495	4.18474248	3.53605459
H	-5.46115842	2.94253788	2.78826057
H	-3.70865680	2.63084050	2.98122380
P	-1.03885606	-0.07517588	4.23302536
C	-2.65088245	-0.51679170	5.07724629
H	-2.51991663	-0.33803634	6.16686507
H	-3.38515792	0.23162203	4.71212065
H	0.88580765	-1.97187970	-4.14185996
C	2.13623918	4.21988245	-0.82278726
C	2.10970602	5.58215104	-0.45945635
H	2.04723747	5.87224495	0.59932575
C	2.18319124	6.58427908	-1.44323115
H	2.16143568	7.64327150	-1.14174665
C	2.29757803	6.23932129	-2.79876278
H	2.36180129	7.02517184	-3.56730943
C	2.33780532	4.88299057	-3.16773250
H	2.43984392	4.60196476	-4.22741356
C	2.25007664	3.88199584	-2.18979201
H	2.27652175	2.82045622	-2.48278913
C	2.16480798	3.60522375	2.04769803
C	1.16184630	4.48777891	2.50858397
H	0.29377813	4.71620323	1.87236692
C	1.25702747	5.07030840	3.78282852
H	0.47301783	5.76382135	4.12494535
C	2.34271026	4.76341484	4.62191642
H	2.41553990	5.22017237	5.62116749
C	3.32826296	3.86458330	4.18183379
H	4.17728409	3.61076747	4.83542808
C	3.23995555	3.28697459	2.90360724
H	4.00979027	2.58133328	2.55835778
P	-1.45906922	-0.43317979	4.09699710
P	-3.94515791	-3.16522135	-0.34561976
P	-1.03547794	0.44864892	-4.23097199
P	-4.13018389	2.86067710	0.26562478
Co	0.51879393	-1.42780760	-0.14685187
Co	-1.07394482	0.15674793	-2.09152558
Co	-2.53705113	-1.55028224	-0.25501365
Co	-2.61466155	1.35559789	0.02417997
Co	-1.23184705	-0.27455778	1.95848844
Co	0.45042406	1.37218354	0.13743121
Se	1.30724951	0.15506655	-1.78725137
Se	-0.94916494	-2.16046630	-1.86475767
Se	-3.38809127	0.03037887	-1.77221119
Se	-3.52328145	-0.28670792	1.45779087

C	-3.16070137	-1.93542493	4.81503872	Se	-1.16631178	2.04103364	1.73632272
H	-4.15162819	-2.08914305	5.29035292	Se	1.16768994	-0.20195585	1.83542195
H	-3.27049108	-2.12063413	3.72731060	Se	-1.05421121	2.38036790	-1.40929628
H	-2.47369915	-2.70635488	5.21953874	Se	-1.03565223	-2.50804271	1.27572113
C	-0.65764556	1.53207095	5.11448030	Fe	2.85116948	0.03768788	0.09038162
H	-1.43196297	2.24689489	4.76484768	P	2.05273455	2.80064112	0.37854436
H	-0.83666502	1.36551399	6.19936264	P	2.20169681	-2.77704728	-0.23803706
C	0.74109871	2.10479234	4.87576389	N	3.57292068	-1.79947744	0.04925794
H	0.85614314	3.07664657	5.39837027	N	3.48877046	1.90238892	0.15884426
H	1.53736409	1.42897384	5.24888952	C	4.84720784	-2.22529002	0.45993511
H	0.92530659	2.27999622	3.79679360	C	5.66458834	-1.31857748	1.18948831
C	0.18258755	-1.27759476	4.97623865	H	5.26089630	-0.32190479	1.43135179
H	-0.05895172	-2.26087098	4.52102948	C	6.95364517	-1.66640973	1.60274221
H	1.16565549	-0.99983744	4.54176370	H	7.55091849	-0.92668339	2.16097454
C	0.25503652	-1.37157165	6.50329359	C	7.49963608	-2.94147592	1.32944354
H	1.01626281	-2.12157676	6.80265175	C	6.68712421	-3.84483797	0.61646600
H	0.54481408	-0.40931657	6.97304370	H	7.07524481	-4.85026797	0.38334067
H	-0.70786924	-1.68786509	6.95458859	C	5.39564337	-3.50435128	0.18445976
N	3.33911058	2.62115903	0.82705463	H	4.80993990	-4.24238762	-0.37965785
N	3.68117673	-1.99322446	-0.00764689	C	8.89060478	-3.31147514	1.79166663
P	1.87008069	3.07541179	0.02816096	H	9.65632055	-2.61282981	1.39146374
P	2.17828866	-2.80588069	0.32718235	H	9.16863212	-4.33382714	1.46721424
Co	0.44252188	1.50390237	0.06424725	H	8.97793940	-3.27796564	2.89920771
Co	0.54820724	-1.45763262	0.10290055	C	4.75785211	2.39746725	-0.18381260
Co	-0.89026512	-0.00600520	-2.05043501	C	5.22064923	3.70322659	0.12217122
Co	-2.40094657	-1.53019164	-0.04940481	H	4.56630348	4.40627457	0.65484236
Co	-2.49360316	1.39648650	-0.03151446	C	6.51263298	4.11477201	-0.24080681
Co	-1.04397835	-0.03077888	2.09337693	H	6.83317564	5.13851595	0.01424244
Se	1.28049644	0.06240511	1.74840279	C	7.40876158	3.25979607	-0.91214545
Se	1.40403304	0.04881079	-1.51563065	C	6.94737823	1.95864987	-1.21680535
Se	-0.83281411	-2.32115061	-1.60647907	H	7.61199734	1.25516213	-1.74495806
Se	-3.23031542	-0.08352241	-1.71781291	C	5.65924487	1.53967466	-0.87224605
Se	-3.34436330	-0.09488292	1.57336424	H	5.32197618	0.52449888	-1.13719026
Se	-1.10983172	2.27597471	1.65238992	C	8.79959899	3.70678383	-1.30085766
Se	-0.99042400	-2.33161473	1.65327586	H	8.94204123	3.69424912	-2.40315725
Se	-1.00347801	2.30763436	-1.60206059	H	9.57989783	3.04203394	-0.87227100
H	3.48563700	-1.05296766	-0.37131473	H	9.00862189	4.73708091	-0.95073543

H	3.21974292	1.71702350	1.30111507				

1-Co				**1**-Cu			
0 4				0 2			
C	-2.59744042	3.37999735	-2.09536185	C	-2.40211500	3.51341124	-1.98905955
C	-3.77533635	3.00217172	-2.77293406	C	-3.55099260	3.18403556	-2.73953164
H	-4.47744038	2.31099118	-2.28388720	H	-4.27854735	2.47406112	-2.31960236
C	-4.04877826	3.50462536	-4.05677074	C	-3.76619692	3.75849802	-4.00405103
H	-4.97352735	3.20314076	-4.57287875	H	-4.67129217	3.49471088	-4.57294735
C	-3.15175282	4.39046195	-4.67613036	C	-2.83854167	4.66924979	-4.53566824
H	-3.37085528	4.78921363	-5.67886803	H	-3.01308245	5.12674497	-5.52197713
C	-1.96718436	4.75813767	-4.01361241	C	-1.67931926	4.98499745	-3.80579483
H	-1.25220445	5.44114811	-4.49834469	H	-0.93738102	5.68431485	-4.22207741
C	-1.68420332	4.24666998	-2.73685686	C	-1.45530708	4.40106125	-2.54809087
H	-0.73902441	4.51402087	-2.24043774	H	-0.52454736	4.62753482	-2.00736230
C	-2.28104880	4.18836556	0.70640816	C	-2.10735729	4.13683287	0.88078056
C	-2.30160457	5.52305793	0.25139471	C	-1.84285318	5.47971297	0.54377973
H	-2.31810128	5.74141408	-0.82605691	H	-1.68271414	5.76833359	-0.50425398
C	-2.32291406	6.58898686	1.16815459	C	-1.81086835	6.47374269	1.53778782
H	-2.33817514	7.62507215	0.79507987	H	-1.60639291	7.51808044	1.25396249
C	-2.33806574	6.33628694	2.54861184	C	-2.05273492	6.14273052	2.88000161
H	-2.36273851	7.17194227	3.26514450	H	-2.03589717	6.92364760	3.65603208
C	-2.32965403	5.00801242	3.00979846	C	-2.33020127	4.80778096	3.22331075
H	-2.35342170	4.79842766	4.09033911	H	-2.54035027	4.53884601	4.27013318
C	-2.29313605	3.94345868	2.09779764	C	-2.35302550	3.81376554	2.23432957
H	-2.28102921	2.90455439	2.46462780	H	-2.58061227	2.77125148	2.50664654
C	2.05428583	2.40845014	4.59487706	C	2.07306083	2.31763201	4.64103181
H	2.52733886	2.29015744	5.59367351	H	2.55493966	2.17131106	5.63181078
H	2.86445472	2.66557229	3.88104477	H	2.88105697	2.56780713	3.92243118
C	0.99996701	3.51822092	4.63940742	C	1.04413892	3.44941013	4.71793741
H	0.48919984	3.63624392	3.66248480	H	0.51432740	3.59223194	3.75466677
H	1.47470883	4.49085409	4.88451045	H	1.54534094	4.40801202	4.96531398
H	0.22849037	3.32681764	5.41228816	H	0.28395212	3.26605330	5.50355769
C	2.74435635	-0.39639848	4.84177686	C	2.68513303	-0.51165493	4.85665118
H	2.50030749	-1.41770931	4.48231765	H	2.40880015	-1.52157197	4.48856965
H	3.69541567	-0.12318794	4.33701907	H	3.64426279	-0.26374674	4.35419638
C	2.89673474	-0.37173273	6.36590107	C	2.83585298	-0.50507907	6.38116413

H	3.14825442	0.63675992	6.75383425	H	3.12110484	0.49078693	6.77810523
H	3.71753707	-1.04998104	6.67986897	H	3.63238784	-1.21375367	6.69014496
H	1.97859059	-0.71074333	6.88669753	H	1.90569638	-0.81708791	6.89750476
C	-0.03942372	0.46481887	5.14514048	C	-0.07836873	0.42200508	5.15415339
H	0.22535815	0.83705702	6.15937526	H	0.18643692	0.77355266	6.17585521
H	-0.81974799	1.14578628	4.74624839	H	-0.83478373	1.12991744	4.75644797
C	-0.57225927	-0.96862294	5.20487860	C	-0.64819429	-0.99772368	5.19107655
H	-0.83663931	-1.34536317	4.19662747	H	-0.91391950	-1.35724754	4.17692274
H	-1.48787627	-1.01699983	5.82857910	H	-1.57076962	-1.02930317	5.80526201
H	0.16469428	-1.67320009	5.64031583	H	0.06513097	-1.72640082	5.62592549
C	3.41868498	4.61429109	-1.58999068	C	3.43116285	4.63884118	-1.45780471
H	2.38472591	4.83701486	-1.25300560	H	2.39744286	4.85651233	-1.11694126
H	4.05290675	5.47539705	-1.28742245	H	4.06855577	5.48506665	-1.12194492
C	3.46632914	4.43389309	-3.11045377	C	3.48560091	4.51199243	-2.98339320
H	4.50079874	4.28749110	-3.48141787	H	4.52163703	4.37708664	-3.35407502
H	3.05969241	5.33295031	-3.61820868	H	3.08303716	5.42923882	-3.46069138
H	2.85585138	3.56586465	-3.43209724	H	2.87605337	3.65706642	-3.33996059
C	5.62232179	2.75329969	-1.31084832	C	5.61065613	2.73769794	-1.24933279
H	5.40914639	2.33380449	-2.31585648	H	5.38342858	2.35026782	-2.26403791
H	6.14791053	3.72111582	-1.46763041	H	6.14879394	3.70216777	-1.38227621
C	6.49042976	1.78056952	-0.51054508	C	6.46934189	1.72979336	-0.48338852
H	6.75415175	2.17744762	0.49080810	H	6.74823201	2.09464233	0.52590233
H	7.43856886	1.56984029	-1.04710867	H	7.40903416	1.51912267	-1.03452754
H	5.96198373	0.81809248	-0.35861863	H	5.92569450	0.77258332	-0.35353947
C	4.38142736	3.95467167	1.06523905	C	4.40197518	3.88796235	1.17020197
H	3.41684866	4.36668025	1.43189414	H	3.44692369	4.30844415	1.55179973
H	4.62455101	3.11509511	1.75015116	H	4.63194131	3.02538635	1.83060660
C	5.48370434	5.01841816	1.08521709	C	5.52442437	4.92974533	1.21315280
H	6.46958838	4.61015366	0.78332998	H	6.50183919	4.50984032	0.90021905
H	5.60218559	5.42864456	2.10983228	H	5.65162551	5.31291524	2.24705080
H	5.25954204	5.87765526	0.42030173	H	5.31603871	5.80874162	0.56926077
C	5.84961733	-2.51348704	-0.22599734	C	5.81669224	-2.51563784	-0.35160226
H	6.07312355	-1.45811809	0.03548846	H	6.04226595	-1.46321167	-0.08080370
H	6.56143519	-3.14564402	0.34732611	H	6.54131037	-3.15329835	0.19907972
C	6.03399571	-2.74655673	-1.72744455	C	5.96889579	-2.72850461	-1.85945524
H	5.85775211	-3.80388190	-2.01116241	H	5.79453856	-3.78339511	-2.15299289
H	7.07125995	-2.49408863	-2.03099067	H	6.99695457	-2.46358709	-2.18271209

H	5.34805266	-2.10952086	-2.32060601	H	5.26497754	-2.08856277	-2.42790471
C	4.55705315	-3.04287096	2.29736568	C	4.57472326	-3.08781986	2.19058190
H	4.93383080	-2.04643012	2.61272561	H	4.95879270	-2.09665920	2.51367652
H	3.57661908	-3.16195608	2.80383345	H	3.60470087	-3.21381105	2.71494037
C	5.52276323	-4.15896957	2.70802626	C	5.54720301	-4.21118193	2.56387063
H	6.52242324	-4.05607285	2.23838629	H	6.53718390	-4.10193410	2.07566085
H	5.68200907	-4.14202038	3.80651653	H	5.72863646	-4.21073182	3.65895384
H	5.13546534	-5.16614954	2.45273975	H	5.15348373	-5.21404031	2.30154771
C	3.81256004	-4.58090343	-0.08978275	C	3.78613716	-4.58816145	-0.20787610
H	3.61934197	-4.50888167	-1.18025532	H	3.58226104	-4.49957508	-1.29509216
H	4.75790300	-5.15422873	0.03372197	H	4.73172304	-5.16447706	-0.10218504
C	2.64571479	-5.29092785	0.60165409	C	2.62523156	-5.30581061	0.48512784
H	2.81357769	-5.40991380	1.69142924	H	2.80161253	-5.43715447	1.57212045
H	2.49919937	-6.30378366	0.17344015	H	2.47475210	-6.31329805	0.04620731
H	1.70040051	-4.72874039	0.46160457	H	1.67899145	-4.74209379	0.35792262
C	2.62683537	-1.41708987	-4.94671151	C	2.50979646	-1.26874254	-5.03828667
H	2.47826567	-1.43412748	-6.04829905	H	2.33671156	-1.25546568	-6.13638468
H	3.40418663	-0.65303052	-4.73630588	H	3.27684685	-0.49621206	-4.82117828
C	3.07073517	-2.78929996	-4.43734981	C	2.99031897	-2.64683535	-4.58096969
H	3.19237601	-2.78359656	-3.33583451	H	3.13681712	-2.67160000	-3.48268094
H	4.04342374	-3.07701967	-4.88696961	H	3.95791497	-2.90193562	-5.06016664
H	2.33950280	-3.58422326	-4.68866158	H	2.26858063	-3.44779915	-4.84038074
C	-0.22868262	-2.00346161	-4.70622426	C	-0.33109936	-1.91876025	-4.73441079
H	-0.04878222	-2.88971497	-4.06178935	H	-0.12132507	-2.81676051	-4.11602646
H	-1.19960465	-1.58727401	-4.36432499	H	-1.29783654	-1.52646414	-4.35499686
C	-0.28697080	-2.38907525	-6.18786420	C	-0.42438253	-2.27171178	-6.22238736
H	-0.49371848	-1.51795724	-6.84255526	H	-0.66976076	-1.39133025	-6.85079608
H	-1.10007786	-3.12432829	-6.36207909	H	-1.22576534	-3.02130632	-6.38862998
H	0.65408082	-2.85812730	-6.54044119	H	0.51580620	-2.71176149	-6.61265156
C	0.73834389	0.68857292	-5.34517425	C	0.56730980	0.80658133	-5.33347224
H	1.50562316	1.44751618	-5.08365248	H	1.33785735	1.56774160	-5.08869378
H	0.96809100	0.33977555	-6.37580923	H	0.75827737	0.48012046	-6.37919242
C	-0.66465573	1.29477291	-5.27543075	C	-0.83722345	1.39681636	-5.19555973
H	-1.44672263	0.57304096	-5.58672086	H	-1.62458483	0.66951294	-5.47925803
H	-0.74180174	2.17489108	-5.94558209	H	-0.95269189	2.28211573	-5.85280811
H	-0.90975192	1.63779403	-4.25040274	H	-1.04230485	1.72919851	-4.15839533
C	-2.13852700	-4.23194121	-0.53481954	C	-1.98712796	-4.20640814	-0.67248496

C	-2.05925503	-5.55336920	-0.04873649	C	-1.63889373	-5.51657471	-0.28633369
H	-1.99910796	-5.74361043	1.03253877	H	-1.40880397	-5.74381268	0.76386466
C	-2.07711944	-6.64234142	-0.93827789	C	-1.61163415	-6.55700957	-1.23210228
H	-2.01386660	-7.66783808	-0.54174540	H	-1.34153155	-7.57516475	-0.91061905
C	-2.18802276	-6.42649663	-2.32067311	C	-1.94098130	-6.30557185	-2.57295969
H	-2.20950869	-7.28055495	-3.01526426	H	-1.92683691	-7.12294866	-3.31055017
C	-2.27944449	-5.11193520	-2.81153219	C	-2.30321363	-5.00426768	-2.96346095
H	-2.37988403	-4.93233285	-3.89318207	H	-2.58434012	-4.79939162	-4.00820804
C	-2.24685630	-4.02381413	-1.92783747	C	-2.32183810	-3.96383556	-2.02351134
H	-2.31255890	-2.99537022	-2.31662913	H	-2.61576039	-2.94796626	-2.32999366
C	-2.32423211	-3.36815694	2.26114197	C	-2.15064138	-3.44400867	2.17586646
C	-1.32987758	-4.16097330	2.87681610	C	-1.14446479	-4.26426519	2.73421000
H	-0.39605545	-4.38705033	2.34056570	H	-0.23462060	-4.49311880	2.16063179
C	-1.51598886	-4.65002567	4.18003438	C	-1.28016340	-4.77713750	4.03492435
H	-0.73645130	-5.27388234	4.64459885	H	-0.49081183	-5.42288171	4.45065670
C	-2.68661076	-4.33630096	4.89293186	C	-2.41160129	-4.45996614	4.80635795
H	-2.82974496	-4.71743228	5.91603781	H	-2.51648429	-4.86179202	5.82619997
C	-3.66799863	-3.52787088	4.29613925	C	-3.40163981	-3.61996415	4.27106070
H	-4.58433460	-3.27027961	4.84968535	H	-4.28753899	-3.35673445	4.86967256
C	-3.48963490	-3.04625435	2.98784226	C	-3.27285468	-3.11453759	2.96607777
H	-4.25805287	-2.41503211	2.51809319	H	-4.04805581	-2.45753664	2.54547395
P	1.45733076	0.71498335	4.05382440	P	1.43363349	0.64681146	4.08092900
P	3.94978577	3.13723482	-0.56520413	P	3.95085351	3.12596524	-0.48110925
P	1.05353398	-0.74640224	-4.18528891	P	0.94245910	-0.65122491	-4.22351117
P	4.14133940	-2.82987908	0.48169358	P	4.12583246	-2.84800978	0.38634143
Co	-0.50271195	1.42425635	-0.26089939	Co	-0.43868582	1.34899396	-0.22973394
Co	1.09319713	-0.30356050	-2.06956570	Co	1.03235539	-0.26308087	-2.10413900
Co	2.54329419	1.52879641	-0.36068354	Co	2.51937643	1.53516726	-0.32432806
Co	2.62123198	-1.34996411	0.12564509	Co	2.59428084	-1.37146157	0.08005795
Co	1.24185045	0.40479240	1.92895704	Co	1.20893334	0.36993094	1.95760458
Co	-0.42932693	-1.37492460	0.23918349	Co	-0.37453952	-1.30396208	0.18503163
Se	-1.26698707	-0.30276838	-1.77496957	Se	-1.30579424	-0.24624902	-1.70615602
Se	0.96559902	2.02960988	-2.02474804	Se	0.98021017	2.06819367	-2.00183734
Se	3.40529254	-0.15636563	-1.75729899	Se	3.36648139	-0.12796459	-1.77981621
Se	3.53281592	0.39089856	1.43817008	Se	3.51455935	0.34271346	1.44365321
Se	1.17808391	-1.92785253	1.88778747	Se	1.18806989	-1.96683180	1.84923079
Se	-1.13349806	0.34311574	1.81028896	Se	-1.14894268	0.27274207	1.73736348

Se	1.07438331	-2.48271581	-1.23355014	Se	1.07095178	-2.46547735	-1.32301231
Se	1.04330323	2.59505149	1.09170305	Se	1.05035895	2.57563404	1.16197126
Co	-2.72606902	-0.02549073	0.08109538	Cu	-3.34580321	-0.03817981	0.07871159
P	-2.10669853	-2.71171620	0.53924667	P	-2.04205817	-2.72257909	0.45958877
P	-2.24786325	2.69622561	-0.40795676	P	-2.17103606	2.70979428	-0.32411744
N	-3.58775897	1.72305907	0.01814446	N	-3.59224391	1.87115248	0.03481522
N	-3.51279802	-1.80592708	0.18723233	N	-3.51348367	-1.95478411	0.15022434
C	-4.81189715	2.14566116	0.55426188	C	-4.82375664	2.45334213	0.37900532
C	-5.55749953	1.22789472	1.34439943	C	-5.79998506	1.63445645	1.01487202
H	-5.12825435	0.22934631	1.52033633	H	-5.53669218	0.58401811	1.22526786
C	-6.80045476	1.57293252	1.88071362	C	-7.05973341	2.12699243	1.36542845
H	-7.34475659	0.82871953	2.48551708	H	-7.77952290	1.44697247	1.85096940
C	-7.37342148	2.84796239	1.66508962	C	-7.42527503	3.47062016	1.11965750
C	-6.63664223	3.75652751	0.87955354	C	-6.46030513	4.28673831	0.49833723
H	-7.05125033	4.75930275	0.68345155	H	-6.70346589	5.34108392	0.28486323
C	-5.38810053	3.42371619	0.33184479	C	-5.19491240	3.80193519	0.13015259
H	-4.85863176	4.16441075	-0.28282588	H	-4.49221625	4.48525994	-0.36446720
C	-8.71595618	3.21109150	2.25727234	C	-8.78778246	3.99665835	1.51040848
H	-9.50899776	2.49769145	1.94640578	H	-9.60643215	3.42852356	1.01813337
H	-9.03729372	4.22505483	1.94667658	H	-8.90740092	5.06237555	1.23085719
H	-8.69254209	3.19506844	3.36858673	H	-8.96175959	3.91839763	2.60557256
C	-4.74672146	-2.28159308	-0.27577249	C	-4.73999936	-2.59245011	-0.09906843
C	-5.25241415	-3.58340676	-0.02130541	C	-5.04482900	-3.94311097	0.21885564
H	-4.65524170	-4.29976174	0.55920558	H	-4.28996086	-4.58088021	0.69734089
C	-6.51595902	-3.97076299	-0.49352274	C	-6.30947607	-4.48680389	-0.05853552
H	-6.87395298	-4.99048904	-0.27463099	H	-6.50004846	-5.54033482	0.20625096
C	-7.33773933	-3.09561741	-1.23120113	C	-7.33827570	-3.72985899	-0.65175804
C	-6.83468406	-1.79705359	-1.47877326	C	-7.03893616	-2.38387682	-0.96492733
H	-7.44639704	-1.07769090	-2.04818233	H	-7.81069012	-1.74895054	-1.43137156
C	-5.57778385	-1.39766175	-1.01800918	C	-5.78114783	-1.83315200	-0.70543993
H	-5.20424254	-0.38136350	-1.21762852	H	-5.57053433	-0.78242709	-0.96697694
C	-8.69816259	-3.51593466	-1.73866888	C	-8.69945489	-4.31911224	-0.94478459
H	-8.75535792	-3.46939003	-2.84774473	H	-8.93630616	-4.29088669	-2.03056483
H	-9.50340510	-2.85519204	-1.35158456	H	-9.51057900	-3.76124165	-0.42891790
H	-8.94294247	-4.55344490	-1.43621685	H	-8.76321684	-5.37642280	-0.61883083

1-Zn				**1**-Cr(THF)			
0 1				0 5			
C	-2.42747893	3.60820589	-1.89576706	C	-1.9103751	5.6897146	3.8322789
C	-3.51785988	3.25704585	-2.71855921	C	-2.0922025	6.2563213	2.5607122
H	-4.23063749	2.49689978	-2.36615598	C	-1.6931173	4.3053722	3.9434961
C	-3.69379270	3.87205961	-3.97013573	C	-2.0629318	5.4476291	1.4106695
H	-4.55364972	3.59111398	-4.59798550	C	3.4774479	2.3426410	4.4978907
C	-2.78276252	4.84409632	-4.41505761	C	-1.6484401	3.5010230	2.7937790
H	-2.92586144	5.33185608	-5.39184054	C	2.0968805	1.8093722	4.8819358
C	-1.68043205	5.18384894	-3.61088318	C	4.1014214	6.0397649	-0.7444724
H	-0.95258372	5.93317828	-3.95925089	C	-1.8398625	4.0557831	1.5083366
C	-1.49572693	4.56133876	-2.36586568	C	-6.3648567	4.2363883	0.4706420
H	-0.61306941	4.81249287	-1.75859729	C	-8.7566495	4.0638336	-0.4070153
C	-2.27506887	4.12279416	0.99312456	C	3.2492967	4.8001556	-0.4544640
C	-2.29252787	5.49843552	0.68490324	C	-5.0408369	3.7808238	0.5735251
H	-2.27719033	5.83205675	-0.36254371	C	5.3715328	3.3493164	0.8693361
C	-2.35355131	6.45964890	1.70940335	C	-7.3430247	3.5449522	-0.2735248
H	-2.36744672	7.52965551	1.44915373	C	3.1334965	-1.0341884	6.3040424
C	-2.41148284	6.06019199	3.05330248	C	0.1083435	-0.2078140	5.1549628
H	-2.46675764	6.81373685	3.85421183	C	-0.8598668	5.0502627	-1.5318695
C	-2.40779303	4.68985399	3.36888233	C	-0.8386112	5.9184394	-2.6338697
H	-2.46526234	4.36490654	4.41925740	C	-5.9459003	1.0514486	3.2940239
C	-2.33301614	3.73031715	2.34918803	C	6.5412142	2.3620637	0.8676079
H	-2.32623254	2.65785837	2.60181476	C	-4.5139926	0.8506546	2.8020584
C	2.08647532	2.13586244	4.75456574	C	-1.8796122	4.0799819	-1.3974305
H	2.56239675	1.95252332	5.74216361	C	-4.6140646	2.5941320	-0.0820713
H	2.89647142	2.42654768	4.05363665	C	-1.8262710	5.8192285	-3.6306027
C	1.04471794	3.25251206	4.87060099	C	2.9022346	-1.0126435	4.7900526
H	0.52935073	3.43308234	3.90568193	C	-0.4201914	-1.6389219	5.0571396
H	1.53176153	4.20377294	5.16955840	C	-6.9266098	2.3610000	-0.9220864
H	0.27564453	3.02446908	5.63587174	C	-6.6037365	-0.2894434	2.9275545
C	2.74183919	-0.68864014	4.83334775	C	5.1321584	3.1647453	-2.0083785
H	2.48397464	-1.68288732	4.41284610	C	-2.8518863	3.9728531	-2.4120570
H	3.69605137	-0.39766069	4.34451750	C	-2.8264735	4.8407524	-3.5188222
C	2.89477390	-0.75838240	6.35593328	C	-5.6055091	1.9046615	-0.8374987
H	3.15793652	0.22157766	6.80459632	C	4.3684137	3.3097138	-3.3264233
H	3.70726154	-1.46426602	6.62776703	C	-5.9702092	-0.6038676	1.5716515

H	1.97241755	-1.11786196	6.85510830	C	-3.2929579	-3.9187627	3.9952374
C	-0.03504920	0.19042458	5.18459785	C	-2.3507250	-4.8418761	4.4780115
H	0.23166745	0.49338083	6.22133414	C	-3.1258796	-3.3357463	2.7271482
H	-0.80005439	0.90966101	4.82554128	C	6.6325470	-1.5393123	-0.5866763
C	-0.59269707	-1.23421614	5.15215362	C	-1.2287016	-5.1623056	3.6935120
H	-0.86678850	-1.53849190	4.12234295	C	4.8479792	-3.3842450	1.6617158
H	-1.50713476	-1.30715963	5.77532598	C	-2.0158526	-3.6680799	1.9236788
H	0.13222790	-1.97901016	5.53788150	C	-0.7787244	1.8676955	-4.9847871
C	3.41007799	4.71690058	-1.28504523	C	-1.0554258	-4.5719987	2.4307273
H	2.37782225	4.92180130	-0.93196848	C	5.9152760	-4.4747043	1.7955843
H	4.04969790	5.55076411	-0.92326718	C	0.6209158	1.3009916	-5.2297201
C	3.45560919	4.64277709	-2.81424302	C	-5.1193047	-1.9401694	-1.6755907
H	4.48848626	4.51294497	-3.19565162	C	-4.4308128	-2.6299754	-0.6382873
H	3.05737133	5.57900175	-3.25734647	C	5.7598512	-2.7087292	-1.0448156
H	2.83599876	3.80524287	-3.19403240	C	-6.3020189	-2.4387669	-2.2347029
C	5.60000961	2.82284365	-1.14128614	C	-4.9811218	-3.8757491	-0.2316007
H	5.37920892	2.46650985	-2.16879089	C	-6.8557834	-3.6688544	-1.8142562
H	6.13243876	3.79443718	-1.24156366	C	-6.1578578	-4.3739803	-0.8118029
C	6.46366138	1.79677797	-0.40534795	C	2.5817711	-0.7791062	-5.1863010
H	6.74032589	2.13302487	0.61448870	C	-8.1376825	-4.1982542	-2.4163279
H	7.40480323	1.60618027	-0.96135918	C	-1.8403532	-4.3209183	-0.9222770
H	5.92541462	0.83313188	-0.30359382	C	3.7243126	-4.6725469	-0.7264295
C	4.38006211	3.87451413	1.31459557	C	-0.2493612	-1.4786283	-4.8919077
H	3.42072251	4.26897233	1.71262428	C	2.5796495	-5.3898757	-0.0087088
H	4.61909819	2.98946224	1.94123170	C	-1.8353846	-4.0089487	-2.3004359
C	5.49169322	4.92527432	1.39843654	C	-1.8847477	-5.6756885	-0.5360006
H	6.47319102	4.52905640	1.06765139	C	3.0945322	-2.1848523	-4.8668713
H	5.61672955	5.26788516	2.44684619	C	-0.4088190	-1.6486010	-6.4060223
H	5.27319266	5.82737564	0.79089104	C	-1.8722668	-5.0252416	-3.2653179
C	5.85037565	-2.45844638	-0.41565229	C	-1.9062696	-6.6954766	-1.5050070
H	6.07077247	-1.41814606	-0.09723145	C	-1.8999905	-6.3748870	-2.8709584
H	6.57659442	-3.11642483	0.10837512	H	-1.9366651	6.3231917	4.7325296
C	6.00885487	-2.60186627	-1.93097227	H	-2.2647197	7.3392450	2.4572544
H	5.84263960	-3.64372857	-2.27188456	H	-1.5471004	3.8474820	4.9346178
H	7.03569114	-2.31534324	-2.23958327	H	3.6437182	3.3498944	4.9327489
H	5.30081232	-1.94265885	-2.47160878	H	3.4781745	6.9560012	-0.6790674
C	4.60264015	-3.13671635	2.09518199	H	-6.6459088	5.1633877	0.9983626

H	4.97494201	-2.15564368	2.46006369	H	2.0078575	1.7023363	5.9851258
H	3.63123760	-3.29352203	2.60846298	H	-2.2319237	5.9109563	0.4280110
C	5.58519127	-4.26416840	2.42773934	H	1.3064624	2.5199132	4.5602015
H	6.57738793	-4.12343877	1.95207937	H	-9.0225062	4.7444536	0.4267324
H	5.75900002	-4.30920994	3.52322339	H	4.9330658	6.1669402	-0.0213456
H	5.20479057	-5.25915035	2.11933977	H	2.7644652	4.8661088	0.5430455
C	3.83513312	-4.54903055	-0.36143904	H	-4.3287566	4.3498202	1.1835687
H	3.63608199	-4.42010505	-1.44544804	H	4.2949341	1.6845241	4.8565362
H	4.78387749	-5.12285790	-0.27140597	H	5.7490834	4.3910431	0.7831739
C	2.67430413	-5.29898655	0.29642398	H	3.5733367	2.4252408	3.3967215
H	2.84593492	-5.47233576	1.37828967	H	3.4733860	-0.0525025	6.6928386
H	2.53005536	-6.28896294	-0.18294486	H	4.8114682	3.2870338	1.8253328
H	1.72749254	-4.73219902	0.18705115	H	0.3557802	0.0535264	6.2072240
C	2.62308594	-1.09904190	-5.05864056	H	-1.4575988	2.4197367	2.8889543
H	2.47408106	-1.04145997	-6.15886249	H	4.5428162	6.0200021	-1.7617300
H	3.40115602	-0.35132286	-4.79780032	H	-5.9899038	1.2832928	4.3765000
C	3.06605143	-2.50284608	-4.64292554	H	-9.4987465	3.2392483	-0.4221821
H	3.18191478	-2.57322722	-3.54308451	H	-0.0749006	5.1262585	-0.7633591
H	4.04073068	-2.75874240	-5.10720231	H	-0.0422384	6.6743856	-2.7185834
H	2.33618830	-3.27874503	-4.95120617	H	-0.6640894	0.5150492	4.8175208
C	-0.23605394	-1.70089138	-4.83495975	H	-6.4240519	1.8855325	2.7402374
H	-0.05214583	-2.62540059	-4.24798712	H	-8.8953752	4.6371057	-1.3504682
H	-1.20082547	-1.30357273	-4.45530542	H	2.2205350	-1.3188313	6.8657597
C	-0.30971656	-1.99420936	-6.33679437	H	2.4153586	4.7106938	-1.1816395
H	-0.52616572	-1.08520312	-6.93421341	H	7.2122426	2.5573250	1.7297587
H	-1.12206299	-2.72077325	-6.54717021	H	-4.0078650	1.7797261	2.4796772
H	0.62892489	-2.43720515	-6.72753334	H	3.9183114	-1.7748772	6.5650243
C	0.73090589	1.02741642	-5.31325857	H	-3.8752018	0.3315701	3.5500656
H	1.50105046	1.76709147	-5.00846889	H	-1.3434636	-1.7570634	5.6600992
H	0.95261736	0.74642890	-6.36622265	H	5.8709881	3.9867829	-1.8821397
C	-0.67048638	1.62948049	-5.19312356	H	7.1559920	2.4438037	-0.0514943
H	-1.45579158	0.93059908	-5.54578572	H	-1.8108176	6.5012987	-4.4949954
H	-0.75107254	2.55225240	-5.80253310	H	3.8356038	-0.7674963	4.2406344
H	-0.90727301	1.90408924	-4.14576451	H	-7.7084036	-0.2353652	2.8658743
C	-2.09509547	-4.19727198	-0.83265826	H	6.1827974	1.3167232	0.9546056
C	-1.93053788	-5.55877871	-0.50597154	H	0.3143247	-2.3807251	5.4308287
H	-1.78017226	-5.86397370	0.53939345	H	-6.3426787	-1.0698272	3.6732729

C	-1.98110480	-6.54434663	-1.50771758	H	3.8098099	4.2657550	-3.3862094
H	-1.85179309	-7.60319792	-1.23395216	H	2.5962053	-2.0113698	4.4130770
C	-2.20927480	-6.18486276	-2.84491199	H	-7.6512636	1.7869014	-1.5235537
H	-2.25606389	-6.95845481	-3.62702338	H	-0.6674542	-1.9106923	4.0118460
C	-2.38783167	-4.83005322	-3.17672568	H	5.7030673	2.2130355	-2.0046099
H	-2.58254721	-4.53820250	-4.22041846	H	-3.6374594	3.2090575	-2.3348851
C	-2.32443087	-3.84466337	-2.18135990	H	-3.6005097	4.7498186	-4.2967402
H	-2.46183445	-2.78424946	-2.44528737	H	-6.5192399	-0.1209293	0.7360577
C	-2.11818323	-3.61832419	2.05138619	H	-4.1684106	-3.6524831	4.6083217
C	-1.10158241	-4.48600395	2.51105251	H	5.0669192	3.2756403	-4.1881584
H	-0.22451919	-4.69103710	1.87967871	H	-5.3100795	0.9903515	-1.3765356
C	-1.18986877	-5.07842253	3.78126976	H	-2.4849212	-5.3060155	5.4675045
H	-0.39393599	-5.75934001	4.12115459	H	3.6348490	2.4871913	-3.4467692
C	-2.28215423	-4.79544448	4.61999125	H	-5.8642220	-1.6835893	1.3541780
H	-2.34920417	-5.25910795	5.61647851	H	-3.8522246	-2.6054842	2.3403133
C	-3.28131249	-3.91055271	4.18281659	H	5.2085716	-2.4116419	2.0582486
H	-4.13593772	-3.67448291	4.83579802	H	6.0520768	-0.5953267	-0.5681745
C	-3.19990269	-3.32447656	2.90795560	H	7.0457423	-1.6998033	0.4300298
H	-3.98105442	-2.63039383	2.56488486	H	-0.9516464	2.0647203	-3.9079655
P	1.46904740	0.48427378	4.11591716	H	-0.9095411	2.8289303	-5.5220387
P	3.93357568	3.17043358	-0.36420615	H	-0.4779310	-5.8750255	4.0693541
P	1.05231508	-0.47956080	-4.25139480	H	7.4908378	-1.3978160	-1.2756154
P	4.15683544	-2.82907774	0.29980380	H	3.9459559	-3.6256643	2.2626548
Co	-0.46748453	1.45490908	-0.17180804	H	1.3943868	2.0370762	-4.9255547
Co	1.07525868	-0.17690378	-2.12206184	H	6.2140205	-4.5946838	2.8580933
Co	2.51954450	1.56121520	-0.26607980	H	-4.6735444	-1.0089922	-2.0633138
Co	2.61870552	-1.35105553	0.04336690	H	6.8365800	-4.2362163	1.2256895
Co	1.22337559	0.29954881	1.99059749	H	-0.1606609	-4.8144331	1.8385568
Co	-0.37336964	-1.41379860	0.14748024	H	-1.5744939	1.1788291	-5.3346011
Se	-1.25348013	-0.19005530	-1.71857099	H	-6.7963128	-1.8679249	-3.0387428
Se	0.96333775	2.16041114	-1.91177304	H	0.7822183	1.0895603	-6.3096275
Se	3.37597242	-0.03551926	-1.76817459	H	6.3377215	-3.6586602	-1.0442883
Se	3.50115033	0.31627409	1.46445913	H	5.4110570	-2.5447176	-2.0861274
Se	1.20346318	-2.04083041	1.78191557	H	5.5532546	-5.4637714	1.4480146
Se	-1.13010751	0.19491096	1.75237066	H	-9.0205492	-3.6016595	-2.0975464
Se	1.10257837	-2.41529972	-1.40758167	H	3.3453453	-0.0187348	-4.9189043
Se	1.04018492	2.54409580	1.26908306	H	-4.4820780	-4.4560720	0.5571743

Zn	-3.11654310	-0.05003898	0.08642128
P	-2.02013783	-2.79363500	0.38821125
P	-2.19431083	2.75111578	-0.26504102
N	-3.61296659	1.82295943	0.00686851
N	-3.50062391	-1.94889749	0.18579927
C	-4.87143396	2.30911971	0.40481043
C	-5.74748951	1.44057231	1.11146148
H	-5.40377629	0.42044883	1.35264992
C	-7.02525058	1.84664419	1.50815482
H	-7.66667178	1.13034881	2.04763654
C	-7.50185952	3.14996285	1.24230380
C	-6.63155403	4.01682370	0.55295113
H	-6.96366292	5.04298073	0.32371982
C	-5.35230365	3.61644089	0.13583092
H	-4.72417481	4.33077984	-0.41205619
C	-8.87841079	3.58702308	1.68941499
H	-9.67100443	2.91197662	1.30175496
H	-9.11236343	4.61247283	1.34076944
H	-8.97138649	3.58359903	2.79717564
C	-4.75304774	-2.50702567	-0.12699163
C	-5.13677819	-3.84185777	0.16309698
H	-4.43134438	-4.52085871	0.65951164
C	-6.41577185	-4.31541838	-0.16965260
H	-6.67040517	-5.36050679	0.07284976
C	-7.38042467	-3.49879248	-0.79140907
C	-7.00029934	-2.16849886	-1.07847061
H	-7.71788068	-1.48920423	-1.56752864
C	-5.72473150	-1.68888942	-0.76577870
H	-5.45919856	-0.64908962	-1.02112044
C	-8.75672748	-4.01428404	-1.14621714
H	-8.93286016	-3.99538596	-2.24360099
H	-9.55862533	-3.39898521	-0.68498145
H	-8.89947585	-5.05901447	-0.80564272
H	-1.2015318	-1.1568154	-4.4195919
H	1.6516084	-4.7842155	-0.0377345
H	2.8189743	-5.5997222	1.0539045
H	-6.5493792	-5.3455184	-0.4666739
H	-1.8097099	-2.9533964	-2.6123047
H	3.2765897	-2.3022983	-3.7795942
H	-1.9177817	-5.9472444	0.5288038
H	-8.1151213	-4.1640607	-3.5259949
H	2.3831187	-0.6681884	-6.2745353
H	4.6436050	-5.2982382	-0.7282994
H	-8.3249437	-5.2484951	-2.1165748
H	3.4565864	-4.4914828	-1.7887641
H	0.0114148	-2.4398317	-4.4010451
H	-0.7044167	-0.7046815	-6.9074668
H	4.0488025	-2.3821729	-5.3979012
H	2.3612970	-6.3599328	-0.5006304
H	2.3747122	-2.9713198	-5.1721029
H	0.5214544	-2.0091560	-6.8905707
H	-1.2002243	-2.3944184	-6.6288278
H	-1.8788893	-4.7624458	-4.3345914
H	-1.9401634	-7.7484776	-1.1839625
H	-1.9234491	-7.1737213	-3.6284813
N	-3.3232282	2.0406761	-0.0031092
N	-3.2900195	-2.0458894	-0.0666151
P	1.6186265	0.1684408	4.1138605
P	4.0742092	3.1173412	-0.4647153
P	-1.8512951	2.8890555	0.0304507
P	-1.8395735	-2.8699726	0.2488518
P	4.1984287	-2.9921391	-0.0483550
P	1.0284573	-0.2593802	-4.2791560
Cr	-3.1075102	-0.0112248	0.1275813
Co	1.4050212	0.1039929	1.9777814
Co	-0.2464381	1.4549676	-0.0360922
Co	2.7015053	1.4811265	-0.2487290
Co	-0.2224164	-1.4561969	0.0798949
Co	2.7181590	-1.4425072	-0.0979274
Co	1.1293671	-0.0987562	-2.1372965

Se	1.3292066	2.3904232	1.4304254
Se	-0.9834532	0.0582407	1.7514323
Se	3.6844821	0.1040109	1.3963877
Se	1.1085536	2.2208556	-1.8013987
Se	1.3568212	-2.2198809	1.6467452
Se	-1.2300905	-0.0645351	-1.6157982
Se	3.4484094	-0.0581531	-1.8488407
Se	1.1513323	-2.3773318	-1.5868073
O	-4.6349358	-0.0152780	1.6349382

1-Mn			
0 6			
C	2.4227982	-3.6454122	-1.8743693
C	3.5155169	-3.3011892	-2.6972019
H	4.2359428	-2.5487133	-2.3437936
C	3.6853800	-3.9150226	-3.9501638
H	4.5474290	-3.6402238	-4.5777062
C	2.7661027	-4.8786919	-4.3964873
H	2.9048236	-5.3659436	-5.3741682
C	1.6615171	-5.2110417	-3.5924065
H	0.9275870	-5.9540160	-3.9416865
C	1.4829323	-4.5896375	-2.3458152
H	0.5990499	-4.8358897	-1.7383853
C	2.2433023	-4.1662003	1.0167351
C	2.2388848	-5.5419675	0.7085383
H	2.2197727	-5.8756817	-0.3388023
C	2.2837701	-6.5041158	1.7331419
H	2.2810587	-7.5742103	1.4727816
C	2.3469049	-6.1058144	3.0771430
H	2.3897478	-6.8602165	3.8780071
C	2.3651033	-4.7356259	3.3927747
H	2.4275280	-4.4117517	4.4432118
C	2.3068624	-3.7749314	2.3729558
H	2.3190465	-2.7025983	2.6258295
C	-2.0712198	-2.1158012	4.7591493
H	-2.5471017	-1.9262846	5.7455640
H	-2.8822970	-2.4042229	4.0585267

1-Co(NTs)			
0 6			
C	2.1360042	-3.2519726	1.7324237
C	1.2690004	-4.3351256	2.0036161
H	0.2755722	-4.1517847	2.4409076
C	1.6502627	-5.6484733	1.6869282
H	0.9712638	-6.4844655	1.9170053
C	2.8851928	-5.8933806	1.0607408
H	3.1815689	-6.9232730	0.8077127
C	3.7273647	-4.8164953	0.7409410
H	4.6842259	-4.9934226	0.2264409
C	3.3580415	-3.5006517	1.0714551
H	4.0145840	-2.6604635	0.7987451
C	1.4298031	-1.4102908	3.9623880
C	1.0394001	-2.4973500	4.7709499
H	0.8982607	-3.4942661	4.3327124
C	0.8520215	-2.3299816	6.1539733
H	0.5537557	-3.1938333	6.7684052
C	1.0535167	-1.0753799	6.7511949
H	0.9135958	-0.9478819	7.8358995
C	1.4511654	0.0121950	5.9543654
H	1.6332926	0.9968488	6.4123961
C	1.6374635	-0.1526391	4.5731027
H	1.9687901	0.6975502	3.9591153
C	4.2025065	-0.5681826	2.5963158
C	4.5578193	-1.6122292	3.4919436
H	3.8918458	-2.4733124	3.6299252

C	-1.0358599	-3.2377882	4.8802755
H	-0.5200644	-3.4248460	3.9168223
H	-1.5285413	-4.1852268	5.1820197
H	-0.2664936	-3.0113494	5.6457025
C	-2.7116616	0.7128614	4.8251561
H	-2.4446180	1.7046851	4.4045854
H	-3.6655232	0.4278986	4.3321130
C	-2.8716790	0.7861989	6.3468476
H	-3.1459670	-0.1906266	6.7955980
H	-3.6792486	1.4997110	6.6132831
H	-1.9488050	1.1383027	6.8502627
C	0.0589285	-0.1794872	5.1878922
H	-0.2113939	-0.4800065	6.2243747
H	0.8227881	-0.9018320	4.8325002
C	0.6208714	1.2435108	5.1547953
H	0.8975653	1.5464952	4.1252654
H	1.5348149	1.3140736	5.7788994
H	-0.1020916	1.9908701	5.5391239
C	-3.3728942	-4.7202817	-1.2792783
H	-2.3404648	-4.9239615	-0.9259877
H	-4.0111692	-5.5557633	-0.9189292
C	-3.4178997	-4.6439968	-2.8084178
H	-4.4508596	-4.5156270	-3.1900425
H	-3.0176892	-5.5787734	-3.2527011
H	-2.7999226	-3.8047816	-3.1870942
C	-5.5682290	-2.8334846	-1.1318028
H	-5.3501856	-2.4777019	-2.1600823
H	-6.0977388	-3.8068528	-1.2302276
C	-6.4343341	-1.8095254	-0.3958749
H	-6.7072764	-2.1448432	0.6252663
H	-7.3775377	-1.6241216	-0.9501233
H	-5.9001139	-0.8433099	-0.2972413
C	-4.3407648	-3.8804700	1.3225556
H	-3.3794834	-4.2709373	1.7198356
H	-4.5826331	-2.9958115	1.9486809
C	-5.4480582	-4.9356139	1.4087768
H	-6.4315542	-4.5437044	1.0788394
C	5.7647734	-1.5772929	4.2063893
H	5.9972857	-2.4106058	4.8899988
C	6.6862111	-0.5206894	4.0687523
C	6.3346778	0.5202451	3.1804348
H	7.0142718	1.3775652	3.0463927
C	5.1270067	0.5071009	2.4760120
H	4.8779629	1.3615898	1.8285476
C	7.9876063	-0.4895861	4.8367314
H	8.0967075	-1.3782707	5.4895332
H	8.0614765	0.4114145	5.4830647
H	8.8657124	-0.4642025	4.1561174
C	1.5849951	3.0274264	-2.6170828
C	2.7185769	2.4281568	-3.1932364
H	3.4140107	1.8418438	-2.5789059
C	2.9899942	2.5869911	-4.5639457
H	3.8905646	2.1081132	-4.9764704
C	2.1275061	3.3463153	-5.3693762
H	2.3405453	3.4776152	-6.4419769
C	0.9883085	3.9464735	-4.7986423
H	0.3089548	4.5472900	-5.4237095
C	0.7139416	3.7845466	-3.4323521
H	-0.1770312	4.2614981	-2.9953299
C	0.9928349	4.5529537	-0.2722730
C	1.7738233	5.5753470	-0.8583362
H	2.4849536	5.3319726	-1.6611192
C	1.6545180	6.9028327	-0.4179218
H	2.2725500	7.6865365	-0.8826282
C	0.7552270	7.2294739	0.6110970
H	0.6598568	8.2721611	0.9522023
C	-0.0210595	6.2187879	1.2017851
H	-0.7298523	6.4656642	2.0075097
C	0.0988929	4.8899324	0.7631337
H	-0.5118121	4.1003053	1.2228315
C	3.6969606	3.1371776	0.3707293
C	4.9598892	3.1845253	-0.2739309
H	5.1420253	2.5570895	-1.1610777
C	5.9870356	3.9940777	0.2351111

H	-5.5703421	-5.2775901	2.4576919
H	-5.2265471	-5.8374410	0.8019620
C	-5.8223506	2.4512818	-0.4287481
H	-6.0423667	1.4137559	-0.1011311
H	-6.5470617	3.1138604	0.0915165
C	-5.9844841	2.5825068	-1.9448037
H	-5.8192728	3.6216312	-2.2943739
H	-7.0120494	2.2934555	-2.2485190
H	-5.2777000	1.9191283	-2.4820323
C	-4.5674677	3.1507548	2.0734006
H	-4.9358155	2.1722018	2.4489065
H	-3.5947236	3.3152050	2.5818005
C	-5.5519142	4.2786381	2.3989178
H	-6.5459930	4.1295829	1.9298332
H	-5.7203123	4.3347091	3.4947148
H	-5.1763392	5.2714894	2.0780388
C	-3.8062634	4.5418390	-0.3967729
H	-3.6048542	4.4036007	-1.4792126
H	-4.7561264	5.1148918	-0.3140499
C	-2.6483064	5.2998863	0.2568445
H	-2.8232622	5.4838267	1.3364184
H	-2.5041375	6.2852040	-0.2319018
H	-1.7000784	4.7341171	0.1553540
C	-2.5833868	1.0803067	-5.0610428
H	-2.4330989	1.0198546	-6.1609007
H	-3.3615165	0.3329877	-4.7992511
C	-3.0273627	2.4850642	-4.6497941
H	-3.1470426	2.5578472	-3.5505170
H	-4.0005218	2.7399305	-5.1177792
H	-2.2965154	3.2602692	-4.9574378
C	0.2756298	1.6814121	-4.8410154
H	0.0916525	2.6086621	-4.2583405
H	1.2411496	1.2864181	-4.4607250
C	0.3486908	1.9682013	-6.3441710
H	0.5641088	1.0564616	-6.9377226
H	1.1617390	2.6929407	-6.5579403
H	-0.5896910	2.4104617	-6.7363041
H	6.9587752	4.0050627	-0.2853081
C	5.8075075	4.7879395	1.3875567
C	4.5529278	4.7213929	2.0346072
H	4.3853067	5.3089821	2.9523578
C	3.5208862	3.9113207	1.5464492
H	2.5622735	3.8527243	2.0812216
C	6.9052960	5.6900364	1.9030249
H	7.9059837	5.3468928	1.5727435
H	6.9083628	5.7410982	3.0110222
H	6.7796539	6.7316258	1.5331196
P	-2.9933799	1.7260242	3.4186661
C	-2.3928833	0.9985759	5.0370260
H	-1.3333155	0.7191366	4.8596076
H	-2.3884487	1.8246720	5.7800383
C	-3.1753812	-0.1953157	5.5911031
H	-2.6860629	-0.5721179	6.5123367
H	-4.2194056	0.0698487	5.8539258
H	-3.2000462	-1.0343009	4.8675899
C	-2.3787610	3.4915324	3.5540545
H	-1.2715319	3.4037759	3.5569871
H	-2.6389063	3.9642926	2.5840351
C	-2.8664465	4.3443284	4.7298946
H	-2.3997897	5.3504467	4.6903442
H	-3.9648505	4.4951528	4.7163066
H	-2.6005322	3.9071801	5.7138924
C	-4.8304027	1.9001532	3.7164795
H	-5.2410850	0.8704159	3.6716398
H	-4.9680286	2.2599420	4.7597806
C	-5.5597903	2.8043654	2.7209010
H	-6.6535665	2.7885847	2.9060487
H	-5.2259984	3.8595181	2.7899602
H	-5.3864503	2.4632374	1.6812474
P	-4.7184245	1.6066182	-2.3178046
C	-4.1999859	2.8045219	-3.6588643
H	-3.5604166	2.2147873	-4.3486650
H	-5.1174465	3.0777661	-4.2242260
C	-3.4610228	4.0569999	-3.1844802

C	-0.6932695	-1.0487612	-5.3069982
H	-1.4636469	-1.7866056	-4.9983327
H	-0.9158785	-0.7724236	-6.3609853
C	0.7078868	-1.6511085	-5.1855782
H	1.4932726	-0.9543424	-5.5422045
H	0.7872605	-2.5765829	-5.7909526
H	0.9460800	-1.9217458	-4.1374926
C	2.0454455	4.2490715	-0.8407595
C	1.8630212	5.6068539	-0.5083707
H	1.7171828	5.9068119	0.5391302
C	1.8910504	6.5963042	-1.5074015
H	1.7485211	7.6523051	-1.2291144
C	2.1138481	6.2445412	-2.8475262
H	2.1429740	7.0212431	-3.6274107
C	2.3102983	4.8936405	-3.1851467
H	2.5014763	4.6082391	-4.2312981
C	2.2698597	3.9043337	-2.1923518
H	2.4227331	2.8471094	-2.4605450
C	2.1015361	3.6539753	2.0443267
C	1.0751123	4.5077020	2.5077252
H	0.1970870	4.7079191	1.8762726
C	1.1553014	5.0934750	3.7816634
H	0.3518900	5.7641162	4.1244672
C	2.2497335	4.8174860	4.6198689
H	2.3108277	5.2763026	5.6189915
C	3.2591822	3.9463308	4.1785637
H	4.1160159	3.7163671	4.8308089
C	3.1857440	3.3669012	2.9002156
H	3.9758619	2.6846515	2.5537676
P	-1.4435676	-0.4700844	4.1160423
P	-3.8995953	-3.1759340	-0.3572128
P	-1.0129054	0.4629964	-4.2516635
P	-4.1271910	2.8277046	0.2795415
Co	0.5059684	-1.4475364	-0.1597824
Co	-1.0439545	0.1685572	-2.1182608
Co	-2.4898311	-1.5609921	-0.2614267
Co	-2.5904841	1.3439855	0.0327347
H	-3.1493323	4.6743067	-4.0518236
H	-4.0922654	4.6943926	-2.5325773
H	-2.5503667	3.7917139	-2.6114068
C	-5.9026327	2.6116136	-1.2789482
H	-6.2967187	1.8991623	-0.5241127
H	-5.2595104	3.3162319	-0.7108494
C	-7.0369790	3.3493049	-1.9970345
H	-7.6662099	3.8945565	-1.2631147
H	-6.6595852	4.0999573	-2.7206487
H	-7.7072227	2.6589677	-2.5486449
C	-5.8546832	0.5012128	-3.3138676
H	-6.4564546	1.1540719	-3.9828495
H	-5.1839482	-0.0963171	-3.9662152
C	-6.7593590	-0.4173694	-2.4911224
H	-7.3298481	-1.0999589	-3.1540983
H	-6.1650532	-1.0389954	-1.7930415
H	-7.4959404	0.1531920	-1.8896660
P	-4.0162416	-3.5643972	0.6737010
C	-4.3726699	-3.9757200	2.4640102
H	-4.8486497	-4.9800642	2.4895676
H	-3.3767460	-4.0778221	2.9438501
C	-5.2260216	-2.9492161	3.2119863
H	-5.3068876	-3.2161367	4.2855983
H	-4.7806410	-1.9363293	3.1445192
H	-6.2562453	-2.8889319	2.8058785
C	-5.7182528	-3.4980685	-0.0955962
H	-6.1661011	-2.5532310	0.2779255
H	-5.5386143	-3.3304129	-1.1782786
C	-6.6538197	-4.6894093	0.1334229
H	-7.6255525	-4.5188460	-0.3750446
H	-6.2387230	-5.6351035	-0.2705780
H	-6.8748577	-4.8524553	1.2078962
C	-3.3491231	-5.2154223	0.0986591
H	-2.3678201	-5.3256641	0.6061933
H	-4.0163630	-6.0048305	0.5081250
C	-3.1868830	-5.3714028	-1.4149413
H	-2.7205454	-6.3484441	-1.6569719

Co	-1.1993094	-0.2948503	1.9867722
Co	0.4114738	1.4045664	0.1424710
Se	1.2989222	0.1794665	-1.7321111
Se	-0.9264279	-2.1627742	-1.8977977
Se	-3.3475896	0.0236448	-1.7739665
Se	-3.4791656	-0.3134332	1.4613437
Se	-1.1751656	2.0385930	1.7677154
Se	1.1674421	-0.1882758	1.7750854
Se	-1.0682059	2.4028421	-1.4153417
Se	-1.0093513	-2.5360301	1.2778257
Mn	3.0399347	0.0541520	0.0911024
P	2.0240348	2.8369209	0.3753619
P	2.2076675	-2.7886913	-0.2398115
N	3.6188847	-1.8741227	0.0436618
N	3.5011057	2.0136043	0.1587549
C	4.8816798	-2.3764455	0.4042418
C	5.7898664	-1.5069229	1.0706814
H	5.4614647	-0.4807245	1.3080357
C	7.0759557	-1.9203639	1.4298849
H	7.7418076	-1.2041764	1.9393273
C	7.5321776	-3.2316243	1.1643295
C	6.6313528	-4.0996557	0.5170792
H	6.9462619	-5.1322173	0.2919087
C	5.3416679	-3.6927189	0.1397341
H	4.6880554	-4.4100728	-0.3736692
C	8.9205681	-3.6740913	1.5671623
H	9.7054213	-3.0306115	1.1148002
H	9.1219546	-4.7173506	1.2525885
H	9.0650049	-3.6247073	2.6681983
C	4.7499190	2.5946989	-0.1227366
C	5.1088941	3.9369664	0.1671255
H	4.3813065	4.6105140	0.6388012
C	6.3904762	4.4256463	-0.1327639
H	6.6251769	5.4756076	0.1092374
C	7.3817023	3.6178118	-0.7233545
C	7.0264212	2.2806557	-1.0131094
H	7.7659602	1.6091166	-1.4799517
H	-4.1594450	-5.3262821	-1.9460046
H	-2.5386319	-4.5736194	-1.8306026
P	-0.1364097	-2.0065023	-3.6600065
C	-1.3924089	-2.4347046	-4.9767036
H	-0.8509955	-2.9976129	-5.7677061
H	-2.0982930	-3.1463024	-4.4991728
C	-2.1481988	-1.2477559	-5.5773306
H	-2.8969418	-1.5959667	-6.3185704
H	-2.6848506	-0.6797574	-4.7905506
H	-1.4681744	-0.5415345	-6.0950235
C	0.7304219	-3.6492219	-3.4758719
H	-0.0300568	-4.3470988	-3.0645979
H	0.9612087	-3.9970530	-4.5068287
C	1.9924662	-3.6387315	-2.6099388
H	2.4481856	-4.6498682	-2.5913091
H	2.7585449	-2.9244935	-2.9745435
H	1.7579554	-3.3696309	-1.5606535
C	1.1097613	-0.9363821	-4.5339653
H	0.6296474	0.0576173	-4.6509434
H	1.9500585	-0.7872106	-3.8218451
C	1.6593825	-1.4531036	-5.8671868
H	2.4155200	-0.7390250	-6.2509793
H	2.1749286	-2.4280182	-5.7559716
H	0.8766146	-1.5621401	-6.6462370
N	3.0312521	-0.5267377	1.8117612
N	2.6873453	2.2537555	-0.0998005
N	4.4230818	-0.4709297	-0.9524024
P	1.6647294	-1.4939884	2.1114535
P	1.2257348	2.7874154	-0.8080307
Co	3.2271030	0.3923991	0.0606354
Co	-0.1022540	-0.8825332	0.9626143
Co	-0.4097584	1.3617706	-0.4431227
Co	-2.3518001	0.7312714	1.6100383
Co	-3.1524606	0.6456264	-1.1925857
Co	-2.7958113	-1.8333782	0.3007133
Co	-0.9305449	-1.1338387	-1.8486970
Se	1.1117079	-0.3458729	-0.9444328

C	5.7499310	1.7855063	-0.7312378
H	5.5022550	0.7409324	-0.9853560
C	8.7607322	4.1485626	-1.0431628
H	8.9737741	4.1105987	-2.1334687
H	9.5565338	3.5556108	-0.5433676
H	8.8759405	5.2019528	-0.7191150
Se	-0.0822201	1.2660056	1.8671109
Se	-2.4551445	2.4970023	0.0465643
Se	-4.3628459	-0.1132043	0.7021805
Se	-3.2136970	-1.5706637	-1.9987435
Se	-0.7645777	-2.8397415	-0.2541278
Se	-1.3345452	1.0357739	-2.6185873
Se	-1.8761302	-1.4349394	2.4175815
S	5.1163893	-0.4084955	-2.3975047
O	5.6515293	0.9573373	-2.7265208
O	4.2447030	-1.0281051	-3.4576753
C	6.5692807	-1.4830928	-2.2516116
C	7.4447127	-1.3327610	-1.1609171
C	6.8378622	-2.4192928	-3.2596541
C	8.5925628	-2.1315398	-1.0888106
H	7.2130002	-0.6069479	-0.3672777
C	7.9957319	-3.2108687	-3.1736335
H	6.1332562	-2.5184268	-4.0980652
C	8.8919133	-3.0825196	-2.0928244
H	9.2739334	-2.0180405	-0.2298885
H	8.2066745	-3.9475265	-3.9659897
C	10.1385807	-3.9320180	-1.9982606
H	10.2151424	-4.6425158	-2.8443850
H	11.0555453	-3.3051829	-2.0001198
H	10.1573705	-4.5216059	-1.0573779

1-Cr(NTs)

0 7			
C	2.4114938	-3.5137187	0.4115578
C	1.7804163	-4.7385931	0.7260585
H	1.0149499	-4.7732197	1.5172166
C	2.1329561	-5.9137063	0.0458796
H	1.6441788	-6.8646232	0.3098846
C	3.1072109	-5.8784863	-0.9688538
H	3.3865272	-6.8025499	-1.4987501
C	3.7133871	-4.6584586	-1.3071478
H	4.4665220	-4.6154306	-2.1089068
C	3.3642883	-3.4779658	-0.6254794

H	3.8242398	-2.5190172	-0.9096858
C	2.1393129	-2.4904290	3.0869838
C	3.0477635	-3.5082399	3.4557353
H	3.6299439	-4.0329864	2.6857265
C	3.2170396	-3.8602472	4.8044328
H	3.9292879	-4.6560744	5.0721630
C	2.4874488	-3.1990866	5.8062572
H	2.6219145	-3.4761593	6.8635362
C	1.5845383	-2.1842727	5.4499605
H	1.0068789	-1.6603823	6.2273544
C	1.4088153	-1.8380813	4.1008531
H	0.6938947	-1.0512948	3.8187904
C	4.3653583	-0.8773696	1.9114366
C	5.4073450	-1.8203859	1.7723697
H	5.3635681	-2.5557565	0.9572845
C	6.4919042	-1.8244466	2.6628772
H	7.2893644	-2.5746499	2.5334940
C	6.5864133	-0.8909287	3.7153435
C	5.5415117	0.0498601	3.8478065
H	5.5809710	0.7941285	4.6597581
C	4.4520987	0.0562758	2.9694344
H	3.6410498	0.7877892	3.0885282
C	7.7640625	-0.8816558	4.6626020
H	8.4188758	-1.7623097	4.5110981
H	7.4345034	-0.8816800	5.7226519
H	8.3885600	0.0269216	4.5224102
C	1.3668185	3.4580197	-2.2920383
C	2.4097282	2.9785274	-3.1082827
H	3.1347739	2.2521541	-2.7156658
C	2.5246731	3.4184089	-4.4402376
H	3.3558084	3.0422733	-5.0564788
C	1.6002308	4.3317776	-4.9702612
H	1.6967947	4.6796767	-6.0107238
C	0.5489212	4.8034286	-4.1624400
H	-0.1823777	5.5197892	-4.5684681
C	0.4291080	4.3655328	-2.8352955
H	-0.3947881	4.7434147	-2.2106864

C	1.0464398	4.5053223	0.3574059
C	1.7188891	5.6539069	-0.1178058
H	2.3131033	5.6021132	-1.0411399
C	1.6413038	6.8651668	0.5869556
H	2.1730165	7.7504016	0.2050622
C	0.8933538	6.9477357	1.7739651
H	0.8319391	7.9000176	2.3236804
C	0.2241070	5.8101781	2.2534363
H	-0.3670051	5.8655444	3.1807691
C	0.2997716	4.5979997	1.5483407
H	-0.2303742	3.7079401	1.9150076
C	3.6957610	3.1458010	0.4766007
C	4.6985169	3.7650854	-0.3025884
H	4.7798061	3.5255825	-1.3716612
C	5.6085153	4.6529378	0.2861012
H	6.3857390	5.1153335	-0.3441010
C	5.5568158	4.9615975	1.6626436
C	4.5514478	4.3411100	2.4336453
H	4.4781259	4.5646323	3.5105332
C	3.6403580	3.4465977	1.8559733
H	2.8516109	2.9806253	2.4651228
C	6.5657203	5.8946053	2.2919614
H	7.4977387	5.3530626	2.5662034
H	6.1732761	6.3584021	3.2190421
H	6.8595773	6.7084312	1.5984357
P	-2.6211594	1.0691222	3.8732311
C	-1.9799245	0.0551942	5.3151105
H	-0.9225814	-0.1661852	5.0628299
H	-1.9662916	0.7263719	6.2005762
C	-2.7362581	-1.2338769	5.6461631
H	-2.2415371	-1.7646884	6.4857310
H	-3.7831411	-1.0367664	5.9535026
H	-2.7509945	-1.9248869	4.7801489
C	-1.8893123	2.7492674	4.2709743
H	-0.7928477	2.6083499	4.1610128
H	-2.1928887	3.3979335	3.4228630
C	-2.2312024	3.4043630	5.6132003

H	-1.7174933	4.3843204	5.7018528
H	-3.3175455	3.5967433	5.7255700
H	-1.9077234	2.7952411	6.4818929
C	-4.4199232	1.2738176	4.3466592
H	-4.8927078	0.2885569	4.1543021
H	-4.4610460	1.4460077	5.4448235
C	-5.1665276	2.3724120	3.5883555
H	-6.2424702	2.3747476	3.8597242
H	-4.7650995	3.3822498	3.8093433
H	-5.0915904	2.2132838	2.4950000
P	-4.9136099	1.9670014	-1.5611204
C	-4.5183042	3.3964022	-2.7042967
H	-3.9554876	2.9477529	-3.5494729
H	-5.4828936	3.7648720	-3.1165933
C	-3.7192622	4.5431697	-2.0826278
H	-3.4781047	5.3082224	-2.8491415
H	-4.2782735	5.0513834	-1.2708014
H	-2.7654139	4.1780092	-1.6521681
C	-5.9823606	2.7603875	-0.2490369
H	-6.3058096	1.9212814	0.4018588
H	-5.2792490	3.3577341	0.3686038
C	-7.1758347	3.6051404	-0.7056909
H	-7.7242684	4.0040467	0.1731138
H	-6.8657390	4.4772320	-1.3164590
H	-7.9040424	3.0196417	-1.3033476
C	-6.1584904	1.0611541	-2.6291732
H	-6.8170297	1.8213536	-3.1030171
H	-5.5622717	0.5990642	-3.4438007
C	-6.9861189	-0.0014727	-1.9043327
H	-7.6223036	-0.5603760	-2.6213337
H	-6.3313294	-0.7314942	-1.3892213
H	-7.6575059	0.4424353	-1.1412750
P	-4.0087916	-3.6516217	0.3498890
C	-4.2166856	-4.3668532	2.0670175
H	-4.7115108	-5.3568310	1.9612733
H	-3.1846271	-4.5568006	2.4292423
C	-4.9766784	-3.4804150	3.0556483

H	-4.9706096	-3.9309460	4.0694547
H	-4.5135416	-2.4758867	3.1250847
H	-6.0365608	-3.3401210	2.7603530
C	-5.7723254	-3.4487980	-0.2391297
H	-6.1644957	-2.5767879	0.3253672
H	-5.6867199	-3.1038191	-1.2910186
C	-6.7103661	-4.6548435	-0.1269982
H	-7.7193581	-4.3965127	-0.5110046
H	-6.3520905	-5.5235547	-0.7161836
H	-6.8394690	-4.9922545	0.9215728
C	-3.4351340	-5.1871339	-0.5553260
H	-2.4080053	-5.3780012	-0.1797331
H	-4.0693949	-6.0343096	-0.2144548
C	-3.4338952	-5.0883727	-2.0822427
H	-3.0031920	-6.0067083	-2.5319929
H	-4.4562611	-4.9645274	-2.4940479
H	-2.8259886	-4.2258190	-2.4223570
P	-0.6456287	-1.2950674	-4.0437377
C	-2.0398370	-1.2718691	-5.2919077
H	-1.6210517	-1.6453216	-6.2516172
H	-2.7605748	-2.0387175	-4.9371548
C	-2.7439058	0.0705717	-5.4927892
H	-3.5728239	-0.0301496	-6.2238853
H	-3.1692034	0.4404404	-4.5383947
H	-2.0544388	0.8510412	-5.8734442
C	0.0147660	-3.0149448	-4.3627265
H	-0.7515925	-3.7050030	-3.9508434
H	0.0277974	-3.1672589	-5.4644184
C	1.3847767	-3.3064713	-3.7508498
H	1.6771419	-4.3605385	-3.9332812
H	2.1794570	-2.6587838	-4.1724235
H	1.3770274	-3.1520974	-2.6541947
C	0.6549737	-0.1778891	-4.7806296
H	0.2742564	0.8554540	-4.6404776
H	1.5297296	-0.2552333	-4.0999923
C	1.0615400	-0.4282337	-6.2361003
H	1.8455033	0.2964782	-6.5381714

H	1.4810374	-1.4435633	-6.3896416
H	0.2145083	-0.3029496	-6.9414207
N	3.2373859	-0.8492964	1.0313443
N	2.7408997	2.2440846	-0.0972811
N	3.8950417	-0.0325416	-2.0476631
P	1.9085482	-1.9666588	1.3133051
P	1.1526241	2.8754743	-0.5371467
Cr	3.2873641	0.4386092	-0.3750712
Co	0.0073164	-1.1899147	0.7310669
Co	-0.4384743	1.4723894	-0.2367543
Co	-2.1657635	0.3869235	1.8835652
Co	-3.2632980	0.8198928	-0.8004206
Co	-2.7995782	-1.8869732	0.1579235
Co	-1.1282519	-0.7999034	-2.0105196
Se	0.9884252	-0.1609422	-1.1099568
Se	0.1442837	0.8196476	1.9448499
Se	-2.3966085	2.4167845	0.6917500
Se	-4.2703726	-0.2710004	1.0435962
Se	-3.4157140	-1.1956485	-1.9875358
Se	-0.8506004	-2.8014131	-0.7808426
Se	-1.5804602	1.4888078	-2.3022899
Se	-1.6554136	-1.9017492	2.2173051
S	5.4127483	0.4675004	-1.8199647
O	5.3737945	0.8344574	-0.2967672
O	5.9178629	1.5198156	-2.7389666
C	6.5663771	-0.9106444	-1.9783297
C	7.4656012	-1.2040776	-0.9440313
C	6.5955217	-1.6259161	-3.1899864
C	8.4034761	-2.2341085	-1.1300722
H	7.4217244	-0.6319944	-0.0064716
C	7.5322343	-2.6538632	-3.3520569
H	5.8877863	-1.3773521	-3.9947116
C	8.4547274	-2.9756531	-2.3280386
H	9.1144254	-2.4651481	-0.3206438
H	7.5549227	-3.2177808	-4.2986975
C	9.4626615	-4.0839820	-2.5248674
H	10.1033010	-3.8937915	-3.4115385

H	10.1261171	-4.1948435	-1.6454447
H	8.9615234	-5.0601557	-2.6958722

[**1**-Fe]$^+$		**1**-FeI			
1 6		0 6			
C	2.4853453613,-3.4542852979,-2.0297073722	C	2.57812979	-4.61856153	4.64318820
C	3.5439517507,-2.9921374672,-2.8391201551	C	1.98986745	-5.37767023	3.61920569
H	4.2164052456,-2.2102982533,-2.4567782568	C	2.93449477	-3.28222772	4.39430741
C	3.7453743421,-3.534036573,-4.1201856536	C	-4.54624423	-5.91775885	0.56624551
H	4.5813128029,-3.1723501219,-4.7382671811	C	-4.54369081	-3.10506136	3.32306988
C	2.8919599423,-4.5384471328,-4.6054418407	C	1.76404711	-4.80940882	2.35371355
H	3.0580703475,-4.970213182,-5.6042393415	C	-0.06419914	-1.56050849	5.34217207
C	1.8209516259,-4.987462572,-3.8125261616	C	-1.47139349	-0.96495798	5.34003652
H	1.1431056847,-5.7678507976,-4.1910879907	C	2.69776206	-2.70900475	3.13601054
C	1.6095748084,-4.4411314382,-2.5366715147	C	-3.59341808	-4.73683982	0.35719468
H	0.7588459132,-4.7890804603,-1.9312368176	C	-5.31147704	-3.01012970	2.00561583
C	2.3449395259,-4.1495472206,0.8245943459	C	2.11411322	-3.46773947	2.09669544
C	2.5595856095,-5.4856844423,0.4258784299	C	-3.35647318	1.13059787	4.90681520
H	2.6466831882,-5.7415652524,-0.6396613158	C	8.68469492	-3.54833778	1.60612263
C	2.6850919459,-6.5029782768,1.3879103056	C	-0.56324842	2.02824686	6.48582026
H	2.8527135379,-7.540611167,1.0608721834	C	6.24476505	-4.02932048	1.03200332
C	2.6124354608,-6.1975712329,2.7556515474	C	0.85223939	-4.95488244	-0.83178981
H	2.718782938,-6.9947597845,3.5070947191	C	7.27731030	-3.10349605	1.28134297
C	2.411817116,-4.8662059559,3.1608534161	C	-5.73925493	-3.06264906	-0.77636039
H	2.3661085018,-4.6164249537,4.2318074164	C	4.94510949	-3.62210085	0.69647412
C	2.2708796138,-3.8511559214,2.2038060774	C	0.84525577	-5.94805981	-1.82396162
H	2.1116739172,-2.8103555086,2.5277826393	C	-0.50702805	1.77743427	4.97524700
C	-2.1215628097,-2.3199486922,4.6511281883	C	-3.79027261	2.52528499	4.45373357
H	-2.6135972167,-2.1759610048,5.6367859304	C	6.94235121	-1.73429510	1.19731946
H	-2.9205109266,-2.5927915784,3.9306746335	C	-5.39923955	-3.43745629	-2.21740367
C	-1.0703879895,-3.4297519175,4.7459175376	C	1.86051192	-3.96403484	-0.81344588
H	-0.5384385138,-3.5783500912,3.7845731397	C	4.60983421	-2.24626125	0.60169993
H	-1.55518535,-4.3922240835,5.0081154899	C	5.64678729	-1.31480702	0.87872882
H	-0.3163259992,-3.2208878098,5.5308133978	C	1.82243288	-5.94370632	-2.83504895
C	-2.8076802175,0.5005237422,4.8241467596	C	2.82348668	-3.95323197	-1.84420659
H	-2.5447455876,1.5133951863,4.4540556069	C	2.80126374	-4.93711886	-2.84852413
H	-3.7504808059,0.2270847389,4.3040710197	C	5.87067626	2.58485207	2.51545562

C	-2.9944208375,0.5029367734,6.3448453449
H	-3.2733912518,-0.4934032433,6.7436568108
H	-3.8110870544,1.1996170997,6.6249588341
H	-2.0845053266,0.8377905984,6.8815745828
C	-0.0251614967,-0.3662122378,5.1872966056
H	-0.3041270984,-0.7201606727,6.203996733
H	0.7568532563,-1.0589110606,4.8128360525
C	0.5073166968,1.0675958118,5.2329852856
H	0.798504394,1.4303857056,4.2269523017
H	1.4072353342,1.1220209951,5.8779387952
H	-0.2366125311,1.7793875946,5.6429546311
C	-3.3172618707,-4.6881471234,-1.5045361448
H	-2.2801329112,-4.8913615828,-1.1652030674
H	-3.9375119853,-5.5524564619,-1.1841036073
C	-3.3752330087,-4.5348748669,-3.027429198
H	-4.413670169,-4.4185642309,-3.3963888337
H	-2.9530111288,-5.4353385919,-3.5181935254
H	-2.7846131476,-3.6619513338,-3.3721311648
C	-5.5479290657,-2.8445698545,-1.2552234035
H	-5.3383507221,-2.4399958811,-2.2670099459
H	-6.0615066988,-3.8203643086,-1.3991369969
C	-6.4310825465,-1.8742265679,-0.4689112712
H	-6.6922747045,-2.2612435684,0.536502818
H	-7.3806850183,-1.6888814578,-1.0108202054
H	-5.9239342254,-0.8982038127,-0.3306662779
C	-4.2967500135,-3.9966314168,1.1456951243
H	-3.3282257665,-4.3895203221,1.5225582988
H	-4.5555605076,-3.1479596728,1.8134851252
C	-5.3844476121,-5.0752946908,1.180352735
H	-6.3755605812,-4.687157791,0.8711574078
H	-5.4970913287,-5.4664147391,2.2123461262
H	-5.1458610229,-5.9438528879,0.5337146734
C	-5.8727986731,2.3891843777,-0.3639114783
H	-6.0794657904,1.3395429456,-0.067613617
H	-6.6055454219,3.0237287795,0.1785999874
C	-6.0401007659,2.5700358929,-1.8741682008
H	-5.8941668393,3.6229866751,-2.187648955

C	8.26602116	3.43799481	2.36843365
C	4.65858980	2.19707067	1.93185448
C	-6.80461775	2.03664719	0.57200978
C	6.97006782	2.99546594	1.72844955
C	-2.77108517	-2.81419132	-4.78740496
C	-5.72759218	3.12217120	0.65852762
C	1.53562656	3.86854476	2.52476593
C	1.78613800	4.82038809	3.52663871
C	4.48673142	2.21429372	0.52380737
C	6.80356775	2.99190850	0.32788891
C	-2.58916700	-1.31584209	-5.04114799
C	5.59050961	2.61388477	-0.26750432
C	0.30150515	-1.62720409	-4.63937691
C	2.10024009	4.00815298	1.24205021
C	2.60955948	5.92619394	3.25882501
C	0.52447341	-1.88405693	-6.13333238
C	-5.26334847	2.94072254	-2.18028853
C	-3.59167181	4.70253735	-0.51733439
C	2.93340767	5.12027797	0.98313895
C	3.18471987	6.07094699	1.98500017
C	1.89882293	3.76344586	-1.58950638
C	-0.88685473	0.99232247	-5.21920359
C	-4.48435193	5.88372149	-0.91055176
C	-4.42942392	3.07375921	-3.45562915
C	2.78900377	3.46946741	-2.63930716
C	1.02597005	4.86763783	-1.71214383
C	0.43669694	1.72886152	-5.00853926
C	2.82597823	4.28487715	-3.78568455
C	1.06744449	5.68059368	-2.85444188
C	1.97175137	5.39339262	-3.89418912
H	2.76661081	-5.06932426	5.62992458
H	1.71437565	-6.42883110	3.79801042
H	3.40847485	-2.67954567	5.18440659
H	-3.99538005	-6.87721938	0.47671576
H	-5.01590354	-5.90792282	1.57075593
H	-3.94027161	-4.03270998	3.39404051
H	-0.03162502	-2.48524297	5.95323749

H	-7.0645595451,2.2765229487,-2.1816215431	H	-5.24628519	-3.09654370	4.18225518
H	-5.3279576822,1.9374679989,-2.4403259665	H	-1.78676553	-0.68119319	6.36787983
C	-4.6254381729,3.0341304276,2.1646896541	H	-2.20765390	-1.71063476	4.97417361
H	-4.9702821462,2.0380277156,2.515497852	H	-5.36157356	-5.94135614	-0.18543705
H	-3.6555908524,3.2107899258,2.6745642492	H	-2.77635012	-4.73772409	1.10976808
C	-5.6361420815,4.1293692744,2.5213041904	H	-6.04118431	-3.84398342	1.91570128
H	-6.6303245574,3.9636620783,2.0594778634	H	-3.85210491	-2.24712557	3.43825154
H	-5.794422771,4.15459223,3.6190916813	H	0.68551393	-0.85937109	5.76202400
H	-5.2893945007,5.1385629471,2.2211753971	H	1.33563013	-5.43466014	1.55884322
C	-3.8761154638,4.5076673349,-0.2663829223	H	0.26385234	-1.83037447	4.31939136
H	-3.6676265426,4.4036527783,-1.351231288	H	-3.30857139	1.07404858	6.01602622
H	-4.8346334925,5.0640598644,-0.1752977109	H	2.98665394	-1.66452908	2.94687705
C	-2.7370515364,5.2648751494,0.4205725327	H	9.11590860	-2.96578094	2.44684503
H	-2.9270334029,5.4178275665,1.5020783814	H	-0.35703766	1.11044651	7.07286325
H	-2.608332141,6.2653602678,-0.0397142386	H	-3.08040082	-4.79618487	-0.62594868
H	-1.7759102608,4.7223471624,0.3135427733	H	-4.09412873	0.36953941	4.57673846
C	-2.6491148874,1.2874199649,-4.9974785323	H	-5.89744855	-2.06747741	1.96965201
H	-2.5087739287,1.2717026679,-6.0997262877	H	0.04947104	-4.93884265	-0.07946501
H	-3.4301311098,0.5338627717,-4.7641509854	H	6.46026015	-5.10880755	1.09466995
C	-3.0785418323,2.6780809064,-4.5275441231	H	-1.54693703	2.42241331	6.81263806
H	-3.20134293,2.7104671847,-3.4266857954	H	-6.49473293	-3.76052238	-0.35426261
H	-4.0485649822,2.958251293,-4.9860245885	H	8.72079995	-4.62083808	1.88295204
H	-2.3427422472,3.4590474144,-4.8061640569	H	0.06101841	-6.72113686	-1.81594817
C	0.2205799329,1.8574599157,-4.7937983104	H	0.20045053	2.77805597	6.77990618
H	0.0479359772,2.7624010993,-4.1736656026	H	-4.97363215	-4.45855134	-2.29646436
H	1.1894440412,1.4414257762,-4.4455466396	H	4.18564218	-4.38961608	0.50059059
C	0.2737225123,2.2027381289,-6.2859116466	H	-4.80265943	2.76419457	4.84008831
H	0.4722255349,1.314445309,-6.9186982902	H	9.36637185	-3.40888496	0.73840076
H	1.0916094953,2.9266738405,-6.4801720078	H	0.49871525	1.42687237	4.66275513
H	-0.6642352456,2.671185371,-6.6457562839	H	-3.10178997	3.31633888	4.81426799
C	-0.7766136423,-0.8515898525,-5.3508350318	H	7.71065561	-0.97043467	1.39907509
H	-1.5432952754,-1.5984674491,-5.0552192272	H	-6.18463315	-2.04604492	-0.73464229
H	-1.0216960519,-0.5368771446,-6.3884164927	H	-3.82238660	2.58969530	3.34756237
C	0.6265011572,-1.4577062024,-5.2846461627	H	-6.30795251	-3.40678920	-2.85343445
H	1.4034833469,-0.749930385,-5.6370335173	H	-0.68556213	2.71397448	4.40637719
H	0.6870226742,-2.3586617348,-5.9272850298	H	5.42178245	-0.23697552	0.86469806
H	0.8920307592,-1.7698013123,-4.2547347067	H	-4.66533716	-2.72808298	-2.64519043

C	2.0328076777,4.301326481,-0.6205787742	H	1.81253961	-6.71904328	-3.61696829
C	2.028103338,5.6419646777,-0.182002955	H	5.97062948	2.55812071	3.61306386
H	1.974825401,5.8765833068,0.890670054	H	8.52625391	2.80919092	3.24442497
C	2.1143490214,6.6931817034,-1.1115082413	H	-6.35958942	1.02400180	0.65240438
H	2.1109464724,7.7344026804,-0.7542651609	H	3.82083296	1.86025453	2.55966650
C	2.219581173,6.418855025,-2.4837975409	H	-2.77806894	-3.04227516	-3.70306384
H	2.2949623665,7.2436402827,-3.2087262894	H	-7.53384305	2.14795921	1.40088543
C	2.2380050498,5.0843767223,-2.926532319	H	9.11141234	3.39462157	1.65344495
H	2.3352536695,4.8609439345,-3.9999694635	H	3.59135743	-3.16512354	-1.86611907
C	2.1374266932,4.0334338879,-2.0039474671	H	0.89225433	3.00253617	2.73385030
H	2.1512788145,2.9901624892,-2.3563629784	H	-5.24477681	3.11206703	1.65758358
C	2.0474799736,3.5386318403,2.2210218083	H	-3.72862888	-3.17099010	-5.21897237
C	1.0413436389,4.4024407192,2.710168136	H	1.33185246	4.69778827	4.52223167
H	0.1832762777,4.6689901015,2.0752081354	H	3.56253457	-4.91212667	-3.64345757
C	1.1267092907,4.9262440046,4.0100386521	H	-1.95786831	-3.41291575	-5.24419611
H	0.3443496664,5.6092800804,4.3750377679	H	8.19902155	4.48623880	2.73429698
C	2.204719826,4.5789887535,4.8433012047	H	-7.37518407	2.09046554	-0.37694492
H	2.2713472774,4.9928147953,5.8610865217	H	0.14795656	-2.57472100	-4.08102557
C	3.1930168447,3.6991140997,4.3727795474	H	-3.48134573	-0.74745577	-4.70500943
H	4.0371119534,3.4176454915,5.0208055416	H	-6.18200664	4.12800018	0.52703377
C	3.1153871278,3.1786770503,3.0695599793	H	7.64585331	3.28979454	-0.31784749
H	3.891841464,2.4922114774,2.7019571596	H	2.80455676	6.67492043	4.04243420
P	-1.5142983917,-0.6385640688,4.0968377599	H	1.20140442	-1.16590409	-4.18118352
P	-3.8802468191,-3.2136075082,-0.501314983	H	-5.80397204	1.97169510	-2.18223412
P	-1.0715252315,0.6260356308,-4.2465944936	H	-2.46868062	-1.11488638	-6.12774962
P	-4.1925014643,2.7786225964,0.3616605999	H	5.49266569	2.60398422	-1.36219170
Co	0.5001518956,-1.3964875399,-0.2024715538	H	-3.20544907	4.81447440	0.51828989
Co	-1.068914465,0.2436780541,-2.1068845384	H	-0.34812233	-2.36631306	-6.61957362
Co	-2.4824723558,-1.5676544508,-0.3286635096	H	1.39281628	-2.56005355	-6.27400436
Co	-2.6227611055,1.3057990831,0.0672714177	H	-6.03390564	3.74093285	-2.12217230
Co	-1.2357369963,-0.3734631934,1.960502615	H	-5.39022375	5.96590869	-0.27541430
Co	0.3660010765,1.3798937144,0.1935911754	H	-2.68879283	4.65154386	-1.16133680
Se	1.2886933117,0.2646532901,-1.7594596605	H	-3.68934531	2.25194425	-3.52921233
Se	-0.9099685812,-2.0894558822,-1.973212835	H	3.45240841	2.59445742	-2.56083093
Se	-3.3614871939,0.0499320907,-1.7817208377	H	3.39365790	5.24405528	-0.00786534
Se	-3.5016117945,-0.4061771149,1.4241495904	H	0.74767364	-0.95170628	-6.69020116
Se	-1.2333387865,1.959876702,1.8316365496	H	3.83764772	6.93028454	1.76706349

Se	1.1443529345,-0.2310339593,1.8185785662
Se	-1.112577319,2.4426726088,-1.3264262283
Se	-1.0006621256,-2.5804223691,1.1790447767
Fe	2.8153171914,0.0908747916,0.1024092766
P	1.9520730147,2.8357274202,0.5118310371
P	2.2170605554,-2.722433441,-0.3530018362
N	3.5606297231,-1.707652032,-0.0139386739
N	3.3977013709,1.9464543477,0.2544524501
C	4.848574825,-2.1167228211,0.3837328132
C	5.6151866459,-1.2409510996,1.1986857028
H	5.1677129623,-0.2859551151,1.5201561025
C	6.912577227,-1.5704128732,1.5990679911
H	7.4742975108,-0.8599530143,2.2267457492
C	7.5110999551,-2.7962968261,1.2260987094
C	6.7451300714,-3.6692860935,0.4268916631
H	7.1779698358,-4.6334275212,0.1149604405
C	5.4461617464,-3.3457894215,0.0076129753
H	4.8971093352,-4.053906497,-0.6271264874
C	8.9052586367,-3.1532676445,1.6838951484
H	9.6292137967,-2.3430458084,1.4572785739
H	9.2701886058,-4.0797486235,1.199559093
H	8.9417233534,-3.3150637327,2.7827505167
C	4.6669036323,2.4690363323,-0.0612601213
C	5.1246268743,3.7487853297,0.3414468754
H	4.4726752011,4.4070465755,0.9309595117
C	6.4137064627,4.1875780549,0.0046249363
H	6.7358657058,5.1883029447,0.334729054
C	7.3064371898,3.3850712672,-0.7346435757
C	6.8468415579,2.1088781481,-1.1350940617
H	7.5103013446,1.4505529628,-1.718786532
C	5.5610875201,1.6640637317,-0.8170925086
H	5.223085726,0.6719464106,-1.1589875964
C	8.690849054,3.8643768377,-1.1011891298
H	8.7972578683,3.9944634118,-2.1995709919
H	9.4698291849,3.137333051,-0.7899693078
H	8.9261122378,4.8367200766,-0.6265446757

H	-1.74627054	1.65659374	-4.98884978
H	0.56135347	2.04909806	-3.95535758
H	0.31830356	5.09916843	-0.90021517
H	-0.99982277	0.67548482	-6.27915839
H	1.31288102	1.10396646	-5.27435278
H	-3.92645102	6.83660260	-0.79838989
H	-5.08246303	3.02825828	-4.35177677
H	-4.81873008	5.82658230	-1.96624493
H	-3.86961338	4.02989582	-3.49714459
H	0.47592390	2.64293640	-5.63495701
H	3.53218895	4.04610621	-4.59599134
H	0.39129642	6.54631490	-2.93430726
H	2.00650430	6.03482022	-4.78866986
N	3.33942588	-1.74658185	0.23118495
N	3.27495132	1.77048290	-0.07567333
P	-4.30198831	-3.00786329	0.42558440
P	-1.70438883	0.53810817	4.25054998
P	1.87290402	-2.60582164	0.46091872
P	-4.31733356	2.97725282	-0.56702118
P	1.83505629	2.70445565	-0.05883736
P	-1.13279386	-0.53101859	-4.16295880
Fe	3.29177794	-0.05408441	-0.81401363
Co	-2.82985789	-1.46009594	0.16425585
Co	-1.52090864	0.25025029	2.12035071
Co	0.11805747	-1.33241603	0.30253241
Co	-2.86715486	1.43150358	-0.20318400
Co	0.06790626	1.45054590	0.03388846
Co	-1.32081750	-0.22130853	-2.03547634
Se	-1.40516367	-2.10172394	1.91403970
Se	-3.80653231	0.16188150	1.55130176
Se	0.81286488	0.24641458	1.89496483
Se	-1.27536833	-2.44429240	-1.29171524
Se	-3.62571820	-0.22077342	-1.67893896
Se	-1.52867399	2.50168769	1.40544273
Se	0.98585507	-0.09264632	-1.50228944
Se	-1.30491858	2.12622480	-1.80233902

I(Iso=126.9)	4.73329348	-0.27795354	-2.98185800

VITA

Ben grew up in San Diego, CA and in 2018 he completed his undergraduate degree in Chemistry at Pitzer College in Claremont, CA. During college, Ben was a member of the Pomona-Pitzer Men's Soccer Team where he played goalkeeper all four years and was the Team Captain as a senior. As an undergraduate, Ben did research with Professor Jeffery Gustafson at San Diego State University and Professor Adam Johnson at Harvey Mudd College. Ben began graduate studies at the University of Washington in July 2018 where he worked with Professor Alexandra Velian. In May 2023, Ben received a Doctor of Philosophy degree in Chemistry. During his time in graduate school, he received multiple awards including the NSF Graduate Research Fellowship and the Clean Energy Institute Graduate Fellowship. In his free time, Ben can be found exploring Seattle's food scene, cooking, and cheering on his favorite sports teams.